EXPERIMENTAL INVESTIGATION OF THE AERODYNAMICS OF A CLASS 43 HIGH SPEED TRAIN

UNIVERSITY OF BIRMINGHAM

Martin Gallagher

A thesis submitted to the University of Birmingham for the degree of

DOCTOR OF PHILOSOPHY

School of Civil Engineering

College of Engineering and Physical Sciences

University of Birmingham

B15 2TT

23rd September 2016

ABSTRACT

This study aims to investigate the aerodynamic phenomena of passenger trains by undertaking a series of experimental investigations into the aerodynamics of a Class 43 high speed train (HST). A contextual research background is presented with regards to two significant aerodynamic pheoneona - slipstreams and crosswinds. Model scale experiments were undertaken on a 1/25th scale HST model at the transient aerodynamic investigations (TRAIN) rig moving model rig facility in order to measure slipstreams at a range of trackside positions and with different ballast heights. Crosswind effects were investigated through two model-scale tests and an extensive campaign of innovative train-based surface pressure measurements onboard an operational HST. A wind tunnel test investigated the flow field and pressure distribution around an HST power car and calculation of aerodynamic loads. A symmetrical pair of pressure taps at the train nose enabled yaw angle to be calculated at full scale. A scale-model test using a crosswind generator was undertaken and the magnitudes of aerodynamic loads compared very favourably with the wind tunnel data. The novel full scale it has been possible it isolate open-air data and gusts, and estimate the overturning forces due to crosswinds by a considered approach to surface pressure measurements.

ACKNOWLEDGEMENTS

I begin and thanking both of my academic supervisors, Professor Chris Baker and Dr Andrew Quinn. It has been both a pleasure and a privilege to work with both of you and your combined knowledge on the fascinating study of train aerodynamics and continued input throughout this study has been invaluable.

Thanks are given to the EPSRC for funding of the project "The measurement of train aerodynamic phenomena under operational conditions". This project was most certainly a team effort, and I would like to thank all of the academics and staff involved, as well as the industry stakeholders in this project - Network Rail, Railway Safety and Standards Board and Mott Macdonald. Thanks to Professor Mark Sterling and Dr Hassan Hemida for the valuable contributions made throughout the project, and in particular for the advice and feedback given during annual reviews. I would like to thank former TRAIN rig manager Dr Sarah Jordan for her ongoing optimism and valuable help with the experimental campaigns - such as teaching me how to use and cope with the TRAIN rig, drilling holes and sticking things on a rather important New Measurement Train, and with setting up the full scale slipstream measurement system, organising the trip and sharing in the dismay of their cancellation. I must also thank the new TRAIN rig manager Dr David Soper for his help undertaking almost the entirety of the TRAIN rig tests, his uncanny ability to fix any problem at the TRAIN rig in a more sophisticated manner than just "hitting it with a hammer", and also his advice on treating model scale data with caution - "if it seems to be real, it's an illusion".

With regards to the full scale train based measurements on the NMT, I would like to thank Dr John Easton and Rhys Davies (and numerous other members of the electrical engineering team) for designing the data acquisition hardware and software that made analysing the NMT data much more simple and straightforward, and also for designing a system robust enough to last almost 3 years. Additionally, Ed Steward and Paul Weston deserve thanks for their help in installation of the system and calibration of the equipment. Dr Andrew Quinn deserves a second mention for being the mastermind behind the NMT tests.

Specific thanks to Terry Johnson from RSSB for his continued input and interest throughout the project and suggestions for experimental work. Mr Steve Burrows from Network Rail who facilitated visits to the NMT, and also the train technicians from RVEL, Simon, Peter and Steve who took time away from their busy schedules to supervise and assist during any inspections and maintenance work on the NMT.

I would like to also thank my other academic colleagues - Dominic Flynn, Tim Gilbert, Matthew Haines, Francesco Dorigatti, Adam Jackson and Justin Morden. The many conversations and suggestions made during this project, as well as helping with experiments and research were invaluable. In particular I would like to thank Justin who undertook a project in parallel with this one, and was a great help with setting up the full scale experiments and also for his help with the model scale tests at the TRAIN rig. I would also like to thank the two students who helped me undertake tests at the TRAIN rig - Charlène and Aleks.

I would like to thank Derwent Patterns Ltd were responsible for constructing the TRAIN rig model and various ballast shoulders for the slipstream experiments, and Mike Vanderstam in the civil engineering laboratories for helping with the wind tunnel work.

Finally, I would like to thank my friends and family for their support, advice and love. My brothers and sisters - Joe, Kirstie, Maria and Steven, and of course most of all my parents - you've all been supportive and have (at the very least pretended to) taken an interest in this work, and for that I am grateful.

CONTENTS

LIST OF FIGURES

Chapter 1

Chapter 2

Chapter 3

Chapter 4

Chapter 5

Chapter 7

Chapter 8

Chapter 10

Chapter 11

LIST OF TABLES

LIST OF SYMBOLS

A_{ref}	Reference side area of vehicle (60 m^2)
A_S	Area of discreet rectangular surface
b	Track gauge (1435 mm)
C_η	Coefficient of generic aerodynamic force or moment (η = X, Y, Z, Mx, Mx,lee)
C_η^*	Coefficient of generic aerodynamic force or moment per unit length
$C_{\eta,floor}^*$	Partial coefficient of generic aerodynamic force or moment per unit length considering underbody pressures
$C_{\eta,loop}^*$	Partial coefficient of generic aerodynamic force or moment per unit length considering loop pressures
C_P	Coefficient of pressure
$C_{\theta,\varphi}$	Coefficient of yaw
E_{BIAS}	Bias error
E_{RAND}	Random error

E_{TOTAL}	total error
F_η	Aerodynamic force or moment
F_S	Force on discreet rectangular surface
f	Frequency
f_{cut}	Cut-off frequency of filter
f_{samp}	Sampling frequency
H	Form parameter
$I_{u,v,w}$	Turbulence intensity
i, j	Pressure tap in loop id
$K_{\theta,1}$	Cubic yaw coefficient (from wind tunnel tests)
$K_{\varphi,1}$	Cubic yaw coefficient (from CWG tests)
K_{NLC}	Non-linear calibration factor
K_{ACC}	Actual cubic calibration factor
k	Pressure tap identifier
L	Length of train
L_{ref}	Reference height (3.9 m for the HST but sometimes taken as 3 m)
L_{ux}	Streamwise length scale

M_η	Generic aerodynamic moment
$M_{X,lee}$	Lee-rail overturning moment
N	Number of samples
N_{samp}	Sample number
n	Reduced number of samples
P	Pressure
P_{AMB}	Ambient pressure
P_{dyn}	Dynamic pressure
P_{stat}	Static pressure
P_{total}	Total pressure
Q	Dynamic pressure
R	Gas constant
Re	Reynolds number
St	Strouhal number
T	Temperature in Kelvin
t	Time
t_{samp}	Time of sample

U	Streamwise velocity
$U_{2\sigma}$	TSI velocity
U_{cor}	Corrected streamwise aerodynamic vehicle speed
U_{res}	Uncorrected streamwise aerodynamic vehicle speed
U_{uncor}	Resultant horizontal velocity
u, v, w	Velocity components in -x, y and z directions
u', v', w'	Turbulent fluctuations of u, v, w
V	Lateral horizontal velocity
V_{train}	Train speed
V_{wind}	Wind speed
W	Vertical velocity
x, y, z	Cartesian axes
Y	Distance from COT to train side wall
Y_{tap}	Distance of tap from COT
y'	Distance from train side wall
Z_{tap}	Height of tap above TOR
z'	Height above ground level or platform level

List of Greek symbols

β	Angle of onset wind
δ^*	Displacement thickness
θ	Yaw angle (in reference to wind tunnel data)
ρ	Density of air
φ	Yaw angle (in reference to TRAIN rig crosswind data)

List of abbreviations

ABL	Atmospheric boundary layer
BRB	British Railways Board
CEN	European Committee for Standardisation
CFD	Computational fluid dynamics
CRWC	Characteristic reference wind curve
CWC	Characteristic wind curve
CWG	Crosswind generator
ELR	Engineer's line reference
EPSRC	Engineering and Physical Sciences Research Council
HST	Class 43 high speed train
ICE2	Intercity Express 2 high-speed train
LG	Light gate
LS	Light source
RMSE	Root-mean squared error

RWDI	Rowan Williams Davies and Irwin Inc
STBR	Single track ballast and rail
TFI	Turbulent Flow Instrumentation
TRAIN rig	Transient aerodynamics investigations rig
TSI	Technical Specification for Interoperability
UoB	University of Birmingham
WT	Wind tunnel (RWDI test)

CHAPTER 1

INTRODUCTION

1.1 Outline of this study

This thesis presents an experimental study at both full scale and model scale of the aerodynamics of a single train type - the Class 43 High Speed Train (HST). This PhD study forms an integral part of a larger research project undertaken by the University of Birmingham (UoB) known as "***The Measurement of Train Aerodynamic Phenomena under Operational Conditions***", which was funded by the Engineering and Physical Sciences Research Council (EPSRC). Appendix L describes the background, aim and objectives of the EPSRC funded project. Section 1.2 presents the research background of this PhD project and section 1.3 explains the motivation behind this study. Section 1.4 sets out the aim and objectives of this study, and section 1.5 outlines the structure of this thesis.

1.2 Research background

1.2.1 High speed rail in the UK

The term "high speed" is a relative term and not new - the "Mallard" steam train (figure 1.1a) reached 126 mph in 1938 - the same speed most trains in the UK run at today (Nock, 1983). In order to optimise the operation of passenger trains across the UK's rail network, it is necessary to increase the overall speeds at which trains travel. European experience suggests that high-speed rail should receive 80-90% of traffic for journeys less than 500 km, and 50% of traffic up to about 800 km (Hall and Chen, 2011). Wolmar (1999), discussed the historical development of the UK rail network, and much of what remains today is an antiquated Victorian system without much dedicated high speed straight track. However, with planned developments of high speed lines in the UK, such as the High Speed 2 (HS2) development that will initially link London to Birmingham (Department for Transport, 2010), and the existing HS1 lines for the Channel Tunnel Rail Link, the study of the aerodynamic phenomena of high speed trains is of increasing relevance to the UK situation.

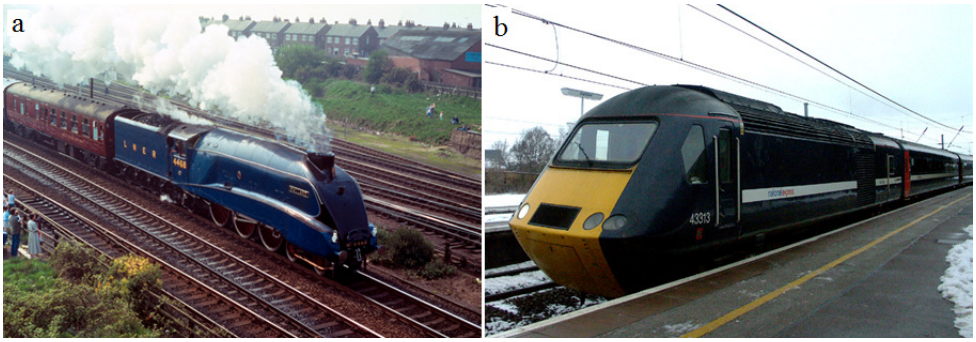

Figure 1.1 - (a) British LNER 'Mallard' (GBIV, 2013), and (b) the Class 43 HST (Langsdale, 2009).

1.2.2 The Class 43 HST

This study is focussed on the Class 43 High Speed Train, shown in figure 1.1b. The reason for the selection of this train was that Network Rail (NR) own a HST power car that was installed with measurement equipment as part of this project (see chapter 9). It should be noted that, by the European definition in the High-Speed Rolling Stock Technical Specification for Interoperability (HS RS TSI), that "high speed" is classified as a train that runs at speeds of at least 250 kph (European Commission, 2008). The Class 43 HST has a maximum line speed of 200 kph and so (slightly confusingly) is not regarded as "high speed" by conventional definitions. For the purposes of this study, however, the abbreviation HST refers solely to the Class 43 train.

The HST first came into service in 1976 and 194 of the trains remain in service in 2016 (Nock; 1983; Marsden, 2016). When introduced it was the fastest diesel hauled locomotive and regularly runs at speeds of 200 kph (125 mph, hence the train was "marketed" as the Intercity-125) (Nock, 1983). There are plans to phase out and replace the existing HST fleet (Hitachi Rail Europe, 2016), though it could potentially run for another 20 years (Railway Gazette, 2011).

In normal operating conditions, the HST operates with two Class 43 power cars at either ends, with a rake of usually 7-8 Mk. III coaches (i.e., a 2+7 or 2+8 formation). The overall power car length is 17.4 m, each Mk. III coach is 22.6 m long and the intercarriage gaps are approximately 0.86 m (BRB, 1979). Each power car is fitted with an [MTU 16V4000 R31R] diesel engine (Marsden, 2016), and the locations of the engine, exhaust and cooling fan are shown on the general arrangement of the HST power car in figure 1.2. The nose profile of the HST is somewhat unconventional in that it has an apex, and along the train sides the HST

underbody is unshielded compared to more contemporary high speed trains (such as the ETR-500 or ICE2).

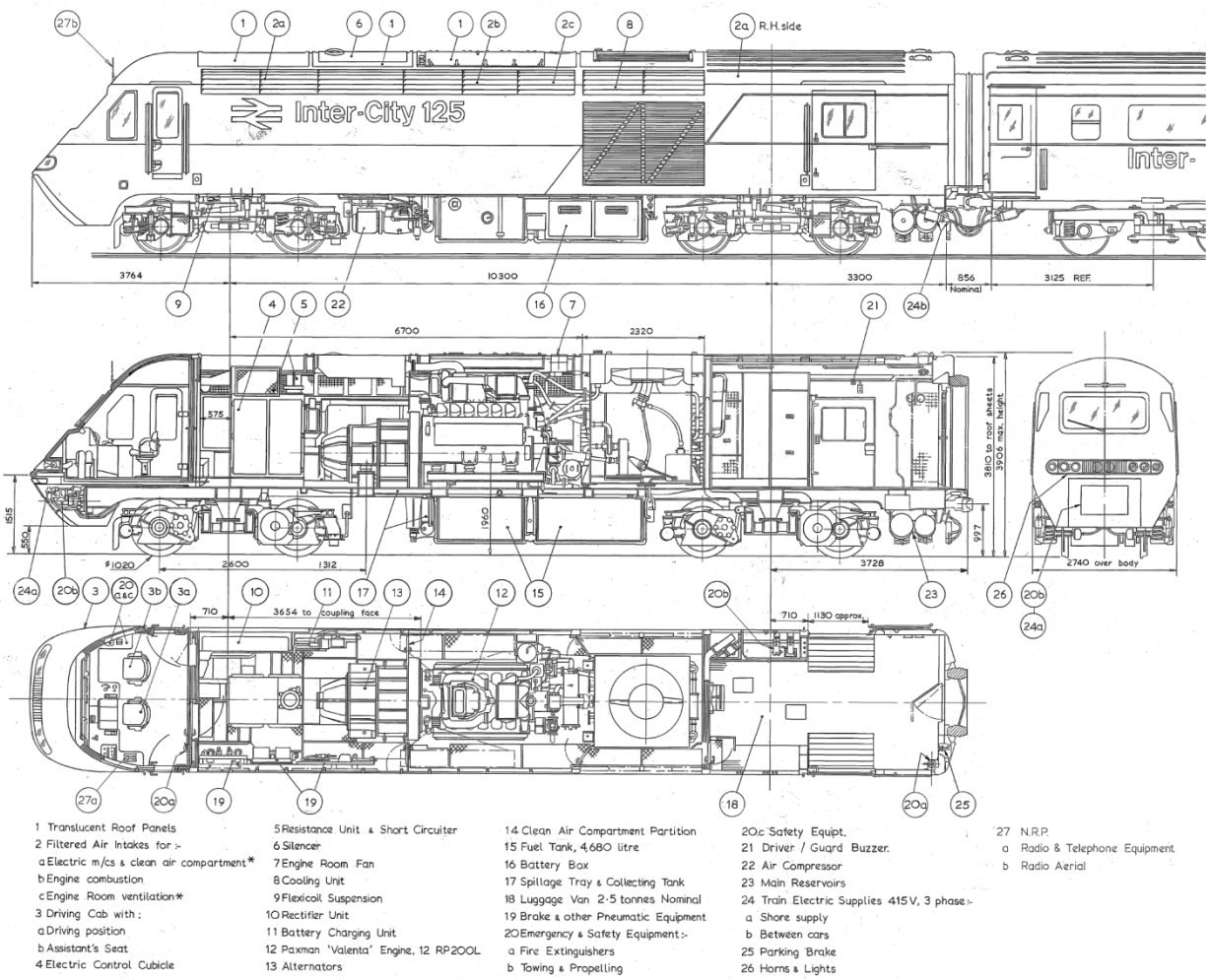

Figure 1.2 - General arrangement of the HST power car (BRB, 1979).

1.2.3 Aerodynamic phenomena - slipstreams

A moving train will disturb the air around it and hence increase the local air velocity, which is known as a slipstream. Slipstreams are potentially be hazardous to passengers and trackside workers and displace light wheeled equipment (Sterling et al., 2008a; Free, 2007; Baker, 2010). A moving train also affects the local static air pressure, which can cause fatigue loading on trackside structures (Zhou et al., 2014). Broadly speaking, the magnitudes of slipstream velocity increases in proportion with train speed, and pressures scale with the square of train speed. Given the expected increases in operational train speeds, the study of slipstreams is of continued interest to engineers.

Slipstream investigations usually consist of measuring the air velocity and pressure at a fixed trackside potion for a number of train passages. Full scale tests are usually expensive and complex to set up. The HS RS TSI (known henceforth as the TSI) sets requirements for full scale slipstream measurements such as the minimum number of train passages, permissible ambient wind conditions and infrastructure requirements, as well as legal limits of maximum permissible slipstream velocities (European Commission, 2008, 2010). Model scale tests are often cheaper and more time-efficient, however there is the question of whether or not model scale experiments represent the reality of full scale. The RAPIDE project (RAPIDE Consortium, 2001), reported in Sterling et al., (2008a), compared the slipstream of an ICE2 train at model scale with full scale data, and found that there were similarities in the slipstream velocities, however there were also notable differences related to differences in flow development due to scaling issues.

Studies at both full scale (Baker et al., 2013 a, b) and model scale (Johnson and Holding, 2003, Bell et al, 2014) have also found that the slipstream can be affected by changes in

infrastructure, such as ballast height and platforms. In this respect, model scale investigations are potentially very useful to quickly investigate differences in infrastructure and then make a case for more complex and costly full scale investigations. Infrastructure in the UK is often very different to that in Europe - UK platforms are usually higher and ballast height is usually lower in the UK, which raises the question of the applicability of European legislation to the UK case.

1.2.4 Aerodynamic phenomena - crosswinds

Natural winds can result in lateral forces and hence an overturning moment on a train that can result in derailment due to overturning with potentially very severe consequences. Current guidelines in the TSI require the calculation of non-dimensional force and moment coefficients, which are usually obtained from wind tunnel tests. These coefficients are then used in a numerical simulation that accounts for the dynamics of the train, and the maximum permissible wind speeds are subsequently calculated across a range of operational train speeds. Wind tunnel studies require validation, and have been found to be sensitive to slight changes in the model geometry, particular in the underbody and ground configuration (Rocchi et al., 2016; Baker et al., 2009). There is also some disagreement as to the extent of the effects of simulating the relative vehicle-ground motion on the force and moment coefficients (Dorigatti, 2013; Sakuma and Hibino, 2013). Natural winds are turbulent and vary due to topography, meteorological conditions and also height above ground, and are difficult to simulate in a wind tunnel and to standardise; low turbulence intensity and uniform flow wind tunnel tests are prescribed which do not represent the complexity of natural winds. This raises

the question of whether or not this surface pressures and forces obtained from this type of test reflect reality.

1.3 Motivation

Between 1972 and 2005 there were 29 incidents in the UK that may have been a result of slipstreams (Free, 2007). None of these incidents resulted in a fatality, but many of these involved unattended light wheeled equipment such as trolleys and pushchairs. It was estimated that the total value of loss (VOL) due to slipstream related incidents in the UK in 2005 was about £41,000, though had a single fatality occurred between 1972-2005, the VOL would have increased a little over four times this amount (Free, 2007). Two high profile incidents occurred in 2015 and both involved a push chair being pulled into a moving freight train and resulting in a fatality (Bowman, 2015; Tages Anzeiger, 2015). Train induced air flows can also have an adverse effect on passengers and line side workers, such as causing discomfort, distress or destabilisation (Jordan et al., 2008; Baker, 2015). There are therefore legal safety limits in the TSI for maximum permissible slipstream velocities which a train must meet before it is certified for use. Scale model tests are often used in the initial stages of aerodynamic design, though there disagreement about how well these tests can predict the magnitudes of slipstreams at full scale.

While crosswind incidents are thankfully quite rare, and tend to occur most on narrower gauge track or high bridges (Baker et al, 2009, Andersson et al., 2004), there have serious incidents involving derailment due to crosswinds passenger trains resulting in fatalities (CNN, 2007; Japan Times, 2008). Additionally, freight train containers are susceptible to displacement due to crosswinds and serious incidents have occurred in the UK (RAIB, 2009) and Australia (ATSB, 2008). The measurement of crosswind effects at full scale is difficult

and experimental data is quite limited in this respect. The full scale train based measurements of pressures on an HST power car undertaken as part of this study present an innovative and novel experimental case to study the effects of crosswinds in the real world, and then to compare these findings with model scale data.

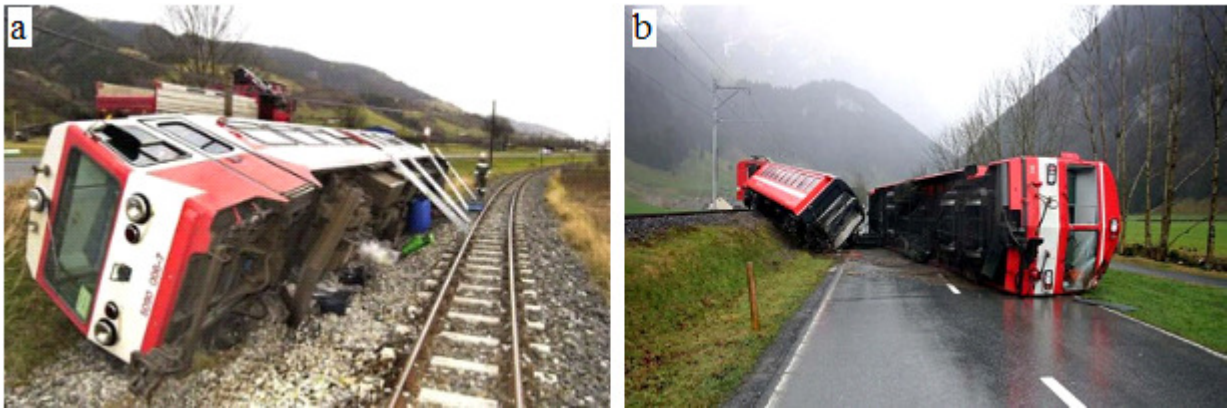

Figure 1.3 - Crosswind incidents (a) Austria in 2002 (Rolén et al., 2004) and (b) incident in Switzerland, 2007, during Kyrill storm (Grazzini and Romani, 2011).

As passenger numbers and train speeds are both expected to increase (Raghunathan et al., 2002), the risk associated with aerodynamic phenomena such as slipstreams and crosswinds will also increase. Further study of train slipstreams and crosswinds is therefore not only necessary from an engineering and academic perspective, but also from an ethical standpoint. This detailed study of both slipstreams and crosswinds on a single train type will also create a comprehensive data set that can be used for computational fluid dynamics (CFD) benchmarking.

1.4 Research aim and objectives

The overall aim of this study was to investigate the differences between full scale and model scale experimental results for both slipstream and crosswind effects on the HST.

This aim was realised by undertaking a variety of physical experiments at both full scale and model scale in order to measure aerodynamic phenomena in the real world and compare these results to model scale results.

The specific research objectives of this PhD study were as follows:

1. To undertake a thorough literature review on the aerodynamic phenomena of passenger trains, with a particular focus on slipstreams and crosswinds, in order to conduct experimental studies that address gaps in the current state of knowledge. Concerning slipstreams, is it possible to use model-scale experiments to accurately replicate the flow field at full-scale, and hence predict the magnitudes of velocities and pressures? And concerning crosswind effects on the train, is the application of quasi-steady theory in the estimation of magnitudes of aerodynamic forces and moments in the real world?
2. To develop a methodology for measurement of slipstream velocities and static pressure transients at model scale that is compliant with existing codes of practise and develops a further understanding of the Transient Aerodynamics Investigations rig (TRAIN rig).
3. To perform a number of slipstream measurements at model-scale in order to investigate how the slipstream velocity and static pressure transients caused by an HST are affected with respect to different fixed trackside measurement positions (both

lateral and vertical), and also with ballast height, and to use these results to aid in the design of full-scale measurements.

4. To analyse wind tunnel results on the surface pressures on an HST power car to investigate the general flow field and how it results in overturning forces/moments, and also to aid in the design of pressure tap locations at full scale.
5. To develop a methodology to measure the surface pressures on a model scale train using a moving model and crosswind generator in order to compare this data with wind tunnel data across a range of yaw angles, and therefore consider effects of vehicle ground motion and Re number on the surface pressures.
6. To develop an experimental and analytical methodology for novel train based measurements at full scale to investigate the effects of crosswinds on the surface pressures and hence overturning forces on an HST power car.
7. To deliver a detailed set of experimental data at both full scale and model scale for use in CFD validation and for comparison with other experimental studies, and hence allow scrutiny of current design and testing methodologies and codes of practice.

1.5 Structure of thesis

The content of the remainder of this thesis is set out in the following chapters:

Chapter 2 presents a literature review that considers the results of various full scale and model scale investigations in order to consider the effects of slipstreams and crosswinds on high speed passenger trains.

Chapter 3 introduces the TRAIN rig facility and describes the experimental set up and testing procedure of the scale model slipstream tests at the TRAIN rig.

Chapter 4 describes the procedure by which scale model slipstream results were analysed following current conventions and discusses the errors and uncertainty associated with the measurements.

Chapter 5 presents the findings from the scale model slipstream tests, and describes the slipstream of an HST from a fundamental perspective by considering a range of trackside measurement positions with a typical UK ballast height.

Chapter 6 describes the experimental methodology for the model scale experiments to investigate the effects of crosswinds on an HST power car, and includes information about a static model wind tunnel test, and a moving model test utilising a crosswind generator at the TRAIN rig which was developed by (Dorigatti, 2013).

Chapter 7 describes the analytical procedure for the scale model crosswinds experiments, and how pressure data was converted into non-dimensional pressure coefficients. The standard methodology used at both model-scale and full-scale to calculate non-dimensional force and moment coefficients is defined.

Chapter 8 presents the experimental results in the form of non-dimensional coefficients for both of the model scale crosswind tests. The wind tunnel data is used to give an overall illustration of the surface pressure distribution over the HST power car by consideration of the nose, the main length of the power car and the underbody separately. The TRAIN rig crosswind results are presented and then compared with the static wind tunnel results at key pressure tap positions at the train nose and in a loop of taps around the rear of the power car.

Chapter 9 describes the experimental set up of full scale train based measurements of the pressures on a HST power car that records pressures continuously as it travels across the entire UK rail network.

Chapter 10 describes the data processing methodology for the large quantity of data obtained from the full scale train based measurements introduced in chapter 9, and focuses on how data was categorised, the isolation of open air data, and then conversion of the surface pressures at the nose into yaw angle and aerodynamic vehicle speed, and hence conversion of the pressures around the loop into non-dimensional pressure coefficients and force/moment coefficients. Two methodologies used to calculate mean pressure coefficients with respect to yaw angle are introduced, and the identification of instantaneous gusts is also described.

Chapter 11 presents the results from the full scale train based measurements and compares two different approaches to analysing the data - scatter plots and regression models of pressure coefficient against yaw and a yaw angle bin methodology (developed at model scale) where pressure data was sorted according to yaw angle. The variation in aerodynamic forces with respect to yaw angle is considered by considering both mean pressure coefficients and instantaneous values from "gusts". The full scale results are then compared with the model scale results from the wind tunnel.

Chapter 12 draws conclusions about the different components of experimental work undertaken as part of this PhD study in order to address the research objectives set out in section 1.4. Suggestions for further work are made based on the findings of this study.

In addition, a series of detailed reference information has been provided as appendices which are set out as follows:

Appendix A presents a description of the TRAIN rig facility.

Appendix B presents the findings from three preliminary slipstream investigations to investigate the effect of ensemble size, train sped and underbody geometry.

Appendix C presents the detailed results from the experiments undertaken in order to assess the effect of ballast shoulder height on slipstream development of an HST, a Class 66 freight train and an ICE2 (a streamlined passenger train).

Appendix D presents full-scale data from measurements of the slipstream on an HST from a previous study (Baker and Quinn, 2012).

Appendix E describes calibrations performed on pressure measurement sensors.

Appendix F presents a detailed error and uncertainty analysis for all of the experiments undertaken in this study.

Appendix G considers the underbody pressures from the wind tunnel test in detail.

Appendix H provides additional methodological information and results from the TRAIN rig crosswind tests.

Appendix I describes an additional wind tunnel test undertaken in order to consider the air flow impinging on the HST nose without a crosswind.

Appendix J describes the preliminary data processing and analytical procedure when considering the large data set obtained from the full scale crosswind tests.

Appendix K presents detailed results from the full scale crosswinds tests based on a regression analysis of surface pressures with respect to crosswind magnitude.

Appendix L describes the EPSRC project aims and objectives, and how these were achieved in this study.

Appendix M presents this author's publications.

CHAPTER 2

LITERATURE REVIEW

2.1 Introduction

Chapter 2 presents a literature review on train aerodynamic phenomena that are of relevance to this study. The aim of this chapter is to provide a contextual background related to two key areas of interest in train aerodynamics - slipstreams and crosswinds. Section 2.2 sets out preliminary definitions of fluids in motion of relevance to train aerodynamics. Section 2.3 describes the effects of the moving train on the air flow i.e., the slipstream, and also on static air pressure. Section 2.4 considers the investigation of the effects of natural winds on the train, with specific focus on overturning forces due to crosswinds and how these effects are measured and evaluated at model-scale.

2.2 Preliminary definitions of fluid motion

This section describes conventional terms that are used to describe fluids in motion, and while the focus is on slipstreams, definitions presented in this section should also be considered to be general definitions of fluids in motion. More specific definitions are introduced as they are considered throughout this study. Definitions specific to crosswinds are introduced in section 2.4. Definitions in this section assume a stationary frame of reference and a moving train, and are based on conventions specified in BS EN 14067-4:2005 (CEN, 2005).

2.2.1 Definition of Cartesian axes and velocity vector components

Figure 2.1.1 shows the Cartesian axis definitions and corresponding velocity vectors and figure 2.1.2 shows each of the axes relative to the train (and also defines the convention for crosswinds adopted in this study). The x-axis origin is defined from the train nose (defined further in section 4.3 but for now taken as the tip of the train nose) and is negative in the direction of travel, the y-axis origin is usually defined from the track centreline (COT), or occasionally from the train wall side (nearest to any measurement equipment) denoted as y'. The z axis origin is defined from the top of the rail (TOR), or above ground level (i.e., cess or platform), denoted as z'. Air flow is considered as vector components u, v and w along these axis definitions respectively, and positive air flows follow the positive Cartesian axis definition (with the exception of streamwise flow which is in the opposite direction to the x axis and is positive in the direction of train travel). It should be noted that a slightly different convention is adopted when crosswinds are considered in section 2.4.

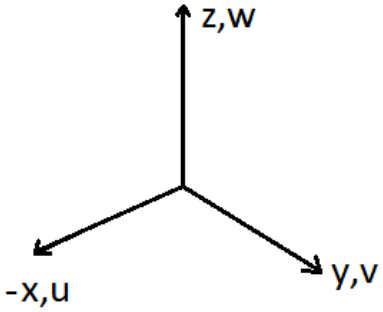

Figure 2.1.1 - Definitions of Cartesian axes and vector flow components for slipstream measurements. Origin is at train nose, COT and TOR.

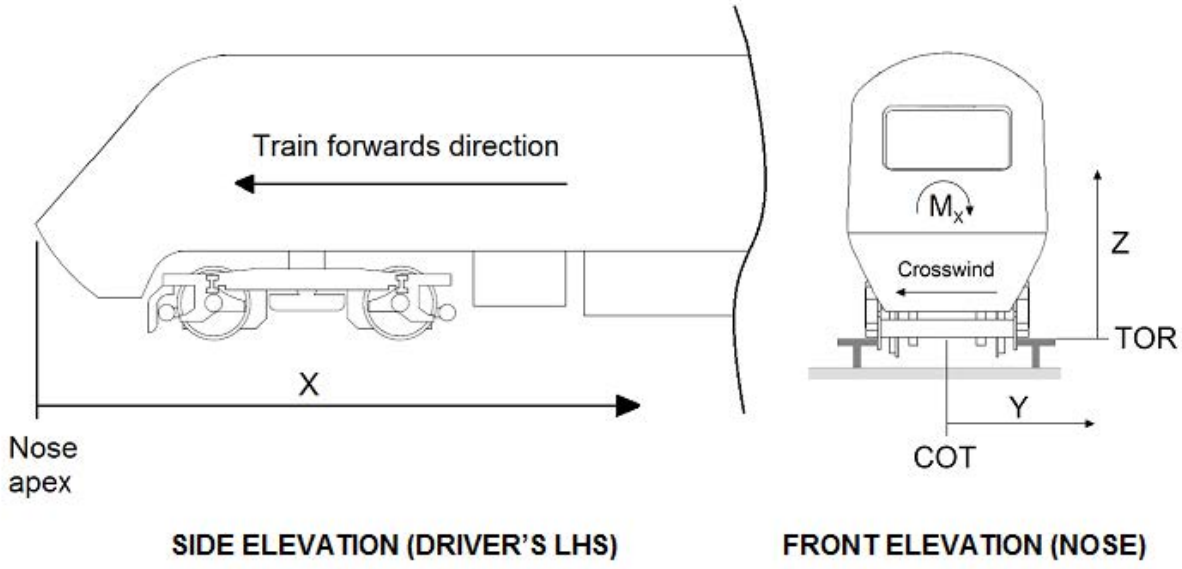

Figure 2.1.2 - Illustration of positive Cartesian axes (and moment) relative to origin on train.

2.2.2 Normalised velocity and pressure

It is common in aerodynamic investigations for results to be presented in a dimensionless form, since this allows easier comparison between different tests and Re numbers. Resultant horizontal velocity, U_{res}, is often of most interest and is defined as:

$$u_{res} = \sqrt{u^2 + v^2} \tag{2.1}$$

Velocities are typically normalised by dividing by (scalar) train speed, V_{train}, resulting in:

$$U = \frac{u}{V_{train}} \tag{2.2a}$$

$$V = \frac{v}{V_{train}} \tag{2.2b}$$

$$W = \frac{w}{V_{train}} \tag{2.2c}$$

$$U_{res} = \frac{u_{res}}{V_{train}} \tag{2.2d}$$

When pressure is discussed in the context of train slipstreams, it is the local static air pressure that is considered, and given that pressure is typically measured with a differential pressure transducer, static pressure, ΔP_{stat}, is defined as:

$$\Delta P_{stat} = P_{stat} - P_{\infty} \tag{2.3}$$

Where P_{stat} is the static gauge pressure at the measurement position and P_{∞} is the reference free stream pressure measured away from the air flow - this calculation is usually performed "physically" by the two pneumatic connections on the differential transducer (which measures the difference in pressure between the two pneumatic connections). Pressures are

conventionally presented as pressure coefficients, C_P, where ΔP_{stat} is divided by the dynamic pressure:

$$C_P = \frac{\Delta P_{stat}}{\frac{1}{2}\rho V_{train}^2} \tag{2.4}$$

Where ρ is the density of air, calculated as:

$$\rho = \frac{P_{AMB}}{RT} \tag{2.5}$$

Where P_{AMB} is the ambient total barometric pressure, R is the gas constant of air, usually taken as 287 J/kg.K, (CEN, 2010), and T is the temperature in Kelvin. Effects of humidity have generally been neglected in this study, however, section F.3.1.2 discusses the effects of humidity on air density during error analysis.

2.2.3 Turbulence intensity and ensemble averaging

Train slipstreams (and natural winds) are three dimensional and turbulent flows (Sterling et al., 2008a; Baker, 2014a), For a three dimensional velocity time series, the vector flow components can be decomposed into the (time averaged) mean (overbar) and fluctuating (') components:

$$u = \bar{u} + u' \tag{2.6a}$$

$$v = \bar{v} + v' \tag{2.6b}$$

$$w = \bar{w} + w' \tag{2.6c}$$

Turbulence intensity is then defined along any axis as the standard deviation of the relevant fluctuating velocity component divided by the mean of that velocity component:

$$I_u = \frac{\sigma_{u'}}{\bar{u}} \tag{2.7a}$$

$$I_v = \frac{\sigma_{v'}}{\bar{v}} \tag{2.7b}$$

$$I_w = \frac{\sigma_{w'}}{\bar{w}} \tag{2.7c}$$

As a general qualitative description, turbulence intensities of 0.2 and above are regarded as a high/very high turbulence level, 0.05 to 0.2 are a moderate turbulence level, less than 0.05 is a low turbulence level and less than 0.01 are very low turbulence levels (Pope, 2000). Turbulence is often described as random, and calculation of a reliable mean depends on a large quantity of data, i.e., an ensemble. Slipstream velocities and pressure transients are often presented in the form of ensemble averages calculated from the average of 'N' number of train passages (runs):

$$\bar{U} = \frac{1}{N}\sum U_N \tag{2.8a}$$

$$\bar{V} = \frac{1}{N}\sum V_N \tag{2.8b}$$

$$\bar{W} = \frac{1}{N}\sum W_N \tag{2.8c}$$

$$\overline{U_{res}} = \frac{1}{N}\sum U_{res,N} \tag{2.8d}$$

$$\overline{C_P} = \frac{1}{N}\sum C_{P,N} \tag{2.8e}$$

Where the subscript N is used to denote the value is obtained from a single run. When a transient slipstream velocity is considered, the definition of turbulence intensity is calculated at a given position in time (or distance assuming constant train speed between runs) - i.e., at a fixed location along the train - the reason for this is that train slipstreams have different and distinct flow regions. Turbulence intensity is defined as the standard deviation of the ensemble divided by one minus the ensemble average velocity to account for the fixed frame of reference (Sterling et al., 2008a), defined later in equation 4.15. Typically, turbulence intensity is only considered the streamwise direction and within the train boundary layer (section 2.3.2.2).

2.2.4 Integral length and time scales

There are nine integral length scales, each defined for any velocity component about any Cartesian axis as $L_{\xi,\eta}$ where ξ = u, v or w and η = x, y or z, and length scale can be calculated according to EDSU 74030 (1974) as:

$$L_{\xi,\eta} = \int_0^\infty \rho_\xi(\eta' - \eta)\, d(\eta' - \eta) \tag{2.9}$$

Where $\rho_\xi(\eta' - \eta)$ is the cross correlation coefficient relative to the generic velocity component ξ, given as (EDSU, 1974):

$$\rho_\xi(x' - x) = \frac{\overline{\xi(x,y,z,t) \cdot \xi(x',y,z,t)}}{\sigma_\xi(x,y,z,t) \cdot \sigma_\xi(x',y,z,t)} \tag{2.10a}$$

$$\rho_\xi(y' - y) = \frac{\overline{\xi(x,y,z,t) \cdot \xi(x,y',z,t)}}{\sigma_\xi(x,y,z,t) \cdot \sigma_\xi(x,y',z,t)} \tag{2.10b}$$

$$\rho_{\xi}(z^{'} - z) = \frac{\overline{\xi(x,y,z,t) \cdot \xi(x,y,z',t)}}{\sigma_{\xi}(x,y,z,t) \cdot \sigma_{\xi}(x,y,z',t)} \tag{2.10c}$$

Where an overbar is used to denote the mean over a time interval sufficiently large to assume a stationary flow.

There are three integral time scales, defined relative to a fixed measurement position as (EDSU, 1974):

$$T_{\xi} = \int_{0}^{\infty} \rho_{\xi}(\tau)\, \delta\tau \tag{2.11}$$

Where $\rho_{\xi}(\tau)$ represents the autocorrelation coefficient expressed as a function of lag, τ, given as:

$$\rho_{\xi}(\tau) = \frac{\overline{\xi(t) \cdot \xi(t+\tau)}}{\sigma_{\xi}^{2}} \tag{2.12}$$

Again, an overbar denotes a mean value over a sufficiently long time period to support the assumption of a stationary flow (EDSU, 1974).

2.2.5 Boundary layer equations

When considering a two dimensional boundary layer, the streamwise u-component velocities (at fixed z positions) at increasing distances from the wall can be plotted to give an estimation of the boundary layer development (Baker et al., 2001). Through integration of this

conventional boundary layer representation along the y-axis, displacement thickness (δ^*) and momentum thickness (θ^*) can be calculated as (Schlichting, 2010):

$$\delta^* = \int_0^\infty \left(1 - \frac{u(y)}{u_0}\right) dy \tag{2.13}$$

$$\theta^* = \int_0^\infty \left(\frac{u(y)}{u_0}\right)\left(1 - \frac{u(y)}{u_0}\right) dy \tag{2.14}$$

Where $u(y)$ is the velocity at a given y distance from the wall, and u_0 is the free stream velocity. Displacement thickness (illustrated on figure 2.2) measures the distance a reference plane would be moved from the body (i.e., train surface) to maintain the same mass flow rate but without the presence of a boundary layer, (Durbin and Medic, 2007; Kundu and Cohen, 2010). Momentum thickness is related to displacement thickness, but is the distance that would have to be moved for the total momentum (rather than mass/velocity flux) to be equal to that between the body surface and reference plane. Both are defined for two dimensional incompressible flow. Form (or shape) parameter (***H***) is given as (Schlichting, 2010):

$$H = \frac{\delta^*}{\theta^*} \tag{2.15}$$

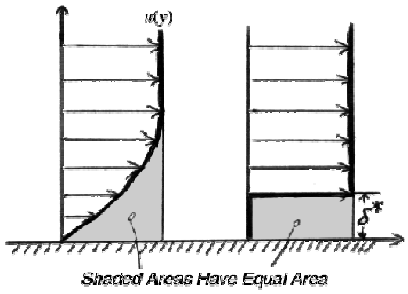

Figure 2.2 - Illustration of displacement thickness (Banks, 1999).

2.2.6 Strouhal number

The Strouhal number is a dimensionless quantity related to the frequency of vortex shedding, and therefore is useful when considering the trailing vortices shed from the tail of the train (discussed in section 2.3.2.3), and defined as:

$$St = \frac{f L_{ref}}{U} \tag{2.16}$$

Where f is the frequency of vortex shedding and L is the characteristic length (also termed hydraulic diameter), conventionally taken as the train height.

2.3 Slipstreams and pressure transients

2.3.1 Issues associated with train slipstreams

Section 1.3 introduced the potential hazards and risks associated with train slipstreams, such as the effect on wheeled equipment and passenger stability/comfort (Pope, 2007; Free, 2007; Jordan et al., 2008, Baker, 2015). Given that these latter terms are somewhat subjective, and the variability of physical characteristics within the population (height, weight etc), it is unsurprising that the numerous studies to investigate what is an "unsafe" wind velocity have shown variation, with unsafe wind velocities ranging from about 10 - 25 m/s (Baker, 2015).

The response of an individual to a sudden gust was investigated by Jordan et al., (2008), by subjecting 31 people to a "gust", i.e., an increase in mean wind velocity from 0-20 m/s in 0.2 to 0.3 s. The authors found that the wind speed required to cause loss of balance was a

function of the person's orientation, height and weight. A subsequent study by Jordan et al., (2009), concerned with slipstream velocities on passengers, found that the percentage of people displaced increased as either train speed was increased or distance from the platform edge decreased, and also acknowledged that the "gusts" considered in Jordan et al., (2008) were not necessarily representative of slipstream gusts. The current requirement in the UK is that a yellow safety line should be positioned 1.5 m from the platform edge at stations where trains may pass at speeds greater than 100 mph (but less than 125 mph, in which case passengers are not permitted on the platform) (Railway Safety and Standards Board, 2015). This distance of 1.5 m was adopted following a series of tests by the British Railways Board (BRB) in the early 1970s, based on a limited safe wind speed of 17 m/s (BRB, 1971). Soper et al., (2014), found that freight train slipstreams regularly break safety limits behind the UK yellow safety line, indicating that train geometry as well as speed also plays a significant role.

2.3.2 Physical consideration of train induced air flows and pressures

The slipstream of a typical passenger train can be considered in terms of different flow regions, which were defined for a zero crosswind case by Baker et al., (2001) as comprising five regions along the length of the train passage, which was later simplified by Baker (2010), as three distinct regions:

- Nose region (including upstream region);
- Boundary layer region - i.e., along the main length of the train (which can be considered in terms of the flow along the side, roof and underbody separately);
- Wake region - i.e., after the train has passed (including the near and far wake).

A typical train slipstream is shown in figure 2.3 and the various flow regions are labelled - a consideration of these regions is presented in the proceeding subsections.

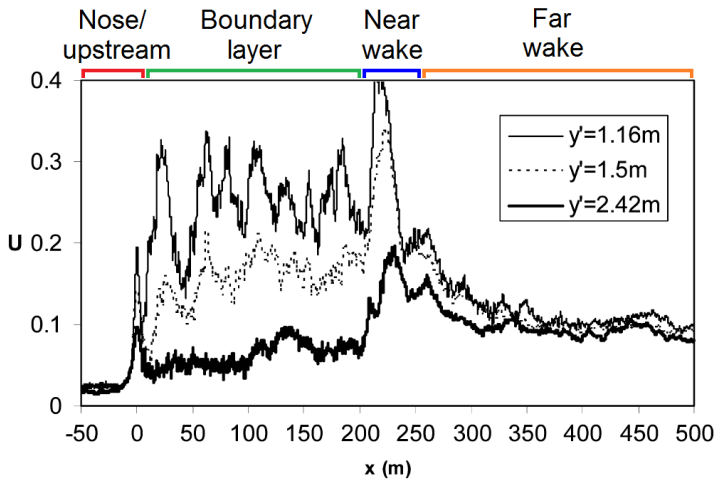

Figure 2.3 - Typical train slipstream for 8 car 206 m long ICE2 showing flow regions (Sterling et al., 2008a).

2.3.2.1 Nose region

As the train nose passes a fixed measurement position, there is a local velocity peak with a duration of about 0.1-0.2 s, but its magnitude is generally less than in other flow regions (Sterling et al., 2008a). Figure 2.3 shows the ensemble averages for normalised air velocity for an 8 car ICE2 train at increasing distances from the train side. There is a short and relatively low velocity peak at the nose, and the magnitude of this peak decreases as distance from the train increases, which is also shown in the expanded view of the nose velocity peaks of an ICE service car in figure 2.4 (Baker, 2010). It was also noted by Baker, (2010), that the

standard deviation of this ensemble (from figure 2.4) was small in all cases (of the order 0.02-0.03) suggesting little variation between runs.

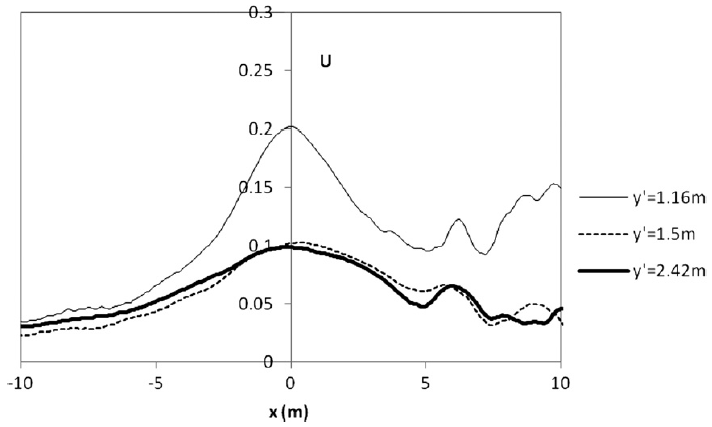

Figure 2.4 - Resultant horizontal velocity peak at nose for ICE service car (z' = 0.5 m) at increasing distances from train side (Baker, 2010).

Figure 2.5.1 shows the ensemble averaged slipstream velocity components (u and v), and resultant horizontal velocity (U) of an S103 Velar train tested as part of the AeroTRAIN project, and figure 2.5.2 shows expanded ensemble the velocities at the train nose (Baker et al., 2014a). The streamwise u-component velocity has a positive peak followed by a negative peak, and is of similar form to the static pressure pulse (which is generally a consistent sinusoidal pulse, as shown in figure 2.6) as would be excepted for an inviscid flow (Baker, 2010; Baker et al., 2014a). The lateral v-component is positive, indicating that the train nose pushes air away from it, and figure 2.5.2 shows that this component largely determines the nose peak magnitude (Baker et al., 2014a). The ensemble nose peak therefore reflects the "bluntness" of the train nose, and streamlined trains typically have normalised nose velocity

peaks of 0.05 to 0.07, which roughly double in magnitude for blunter trains (Baker et al., 2014a). Given the relatively low magnitude and duration of the nose peak, it is unlikely to cause passenger instability (Sterling et al., 2008a), however, scale model tests on a "very blunt" train - a Class 66 freight train - found the normalised nose peak to be about 1.2 and lasted for a duration of 0.5 s (Soper, 2014), which could affect passenger safety.

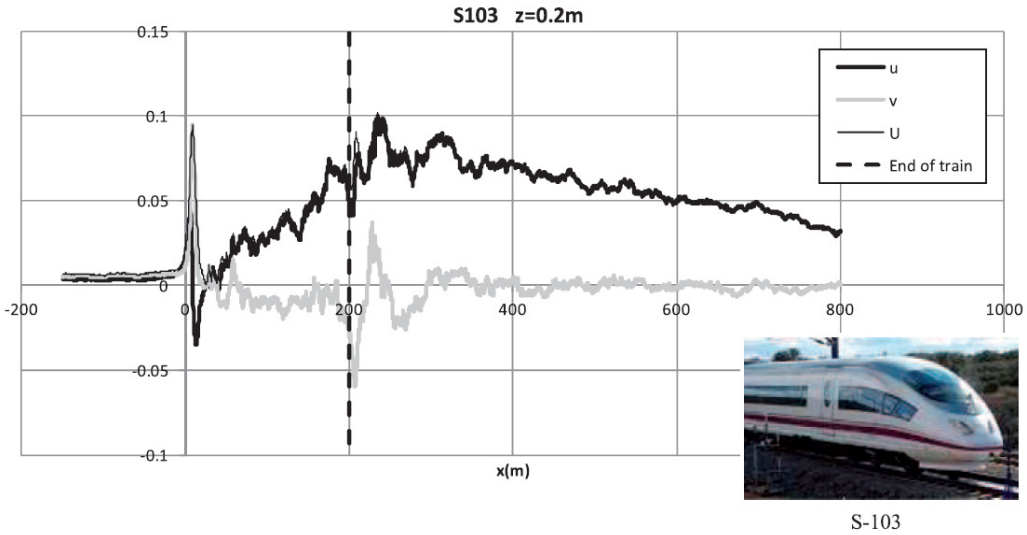

Figure 2.5.1 - Normalised ensemble average slipstream velocity horizontal components (u and v) and resultant (U) for S-103 train (Baker et al., 2014a).

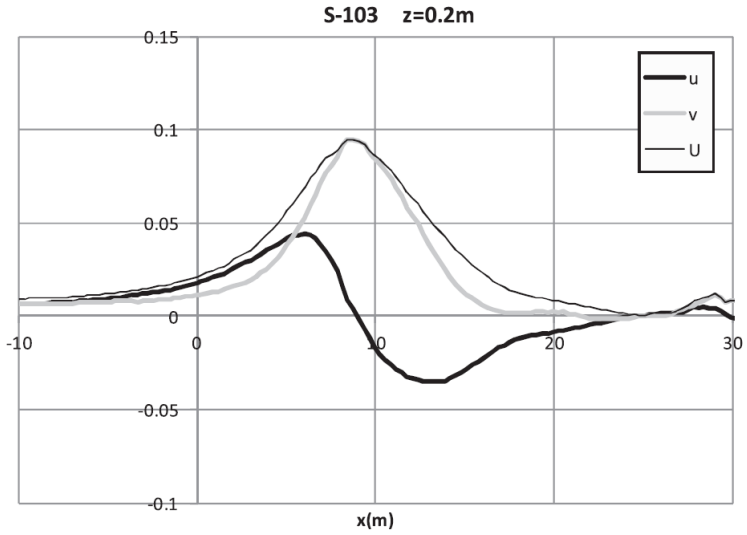

Figure 2.5.2 - Expanded view of ensemble average slipstream velocity horizontal components (u and v) and resultant (U) for S-103 train nose peak (Baker et al., 2014a).

Figure 2.6 shows the static pressure time history for the passage of two ETR 500 trains travelling in opposite directions, measured on one of the trains and for a single passage. There is a sinusoidal pulse - a sharp increase in pressure followed immediately by a sharp decrease, and this general pattern is consistent regardless of train type (Zhou et al., 2014; CEN 2005). As with velocity, the more blunt a train nose profile, the larger the pressure pulse (Baker, 2010; Gilbert, 2014; Soper, 2014). It can also be seen that the form of the graph is virtually identical between two runs, which illustrates that, unlike for velocity measurements, obtaining an ensemble from a large number of runs may not be necessary for static pressure measurements (Baker, 2010). A similar (but reverse) sinusoid is observed at the tail passage, but it is generally of lower magnitude that the nose peak for conventional passenger trains (i.e., with a trailing loco) (Zhou et al., 2014; CEN, 2005). Static pressures can cause fatigue

loading on structures and passing trains due to their cyclic nature (Fujii, 1995; Baker et al, 2014c, d), and may also lead to passenger discomfort or distress (Johnson, 2011).

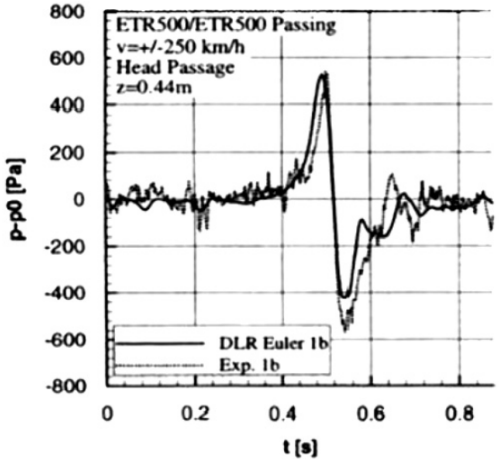

Figure 2.6 - Pressure pulse caused by passage of two ETR500 trains passing each other relative to one of the trains - predictive equation in bold and experimental data in thin-black (Mancini and Malfatti, 2001).

2.3.2.2 Boundary layer region

After the nose peak there is a development of a boundary layer along the train sides and roof (Baker, 2010), which appears to reach equilibrium after the first carriage and grows steadily along the length of the train (Baker et al., 2001; . The development of the boundary layer is dependent on the Re number and the train geometry i.e., the nose shape, the cross sectional profile (though this is generally consistent for most passenger trains), and roughness of the surface which includes underbody roughness/shielding, intercarriage gap size (Baker et al., 2001; Sterling et al., 2008a, Quinn et al., 2009, Baker at el., 2013a; Soper, 2014).

It was shown by Brockie and Baker, (1990), that the boundary layer of a full-scale HST has a complex, non-equilibrium and probably three-dimensional nature. Conventional methods of analysis - namely by considering the boundary layer as 2D - proved to be useful to illustrate the boundary layer properties, which has been echoed by Sterling et al. (2008a). Brockie and Baker, (1990), also found that for a 1/76th scale model HST, the boundary layer over the roof was more complex than the train sides - possibly arising due to a divergent flow around the front half of the leading power car which 'washed up' from the nose and over the roof, thickening the boundary layer, and this finding was also reported in a different study by Baker et al., (2001). It was however noted that the second half of the HST power car showed a more diminished and conventional profile (Brockie and Baker, 1990). The authors also found that, unlike at model scale where there was a noticeable growth in boundary layer thickness and displacement thickness, a full-scale HST showed little growth along the train. It was noted by Baker, (2010), when reporting on the work of Sterling et al, (2008a), that model-scale form parameters (equation 2.15) of the roof and side boundary layers showed little difference and both were below the value of 1.4 for an equilibrium boundary layer. It has also been observed that slipstream velocity usually decreases with measurement height, showing that underbody roughness (from bogies etc) had a major effect on the boundary layer flow (Baker et al., 2014a).

Full scale measurements conducted on a 206 m ICE service train, described by Sterling et al., (2008a) shown in figures 2.7 and 2.8, showed that there were large values of displacement thickness near the nose of the vehicle, which were not replicated at model-scale (figure 2.4). It was suggested by Baker, (2010), that this may be due to the existence of an unrealistic laminar boundary layer near the vehicle nose in scale model tests, which would not exist at the higher Re number of full-scale.

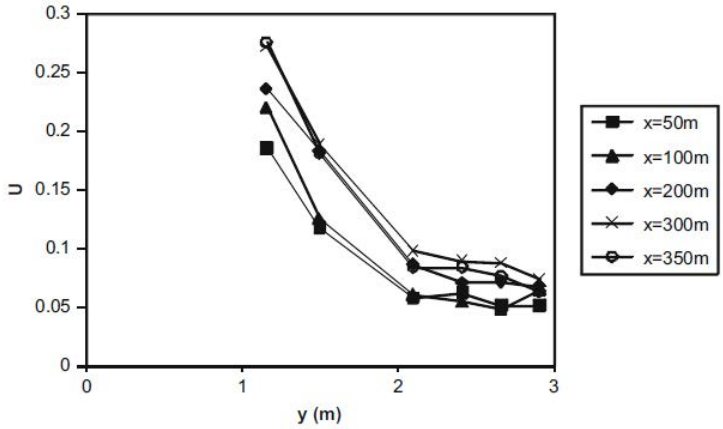

Figure 2.7 - Velocity profiles within boundary layer for ICE service car (Sterling et al., 2008a).

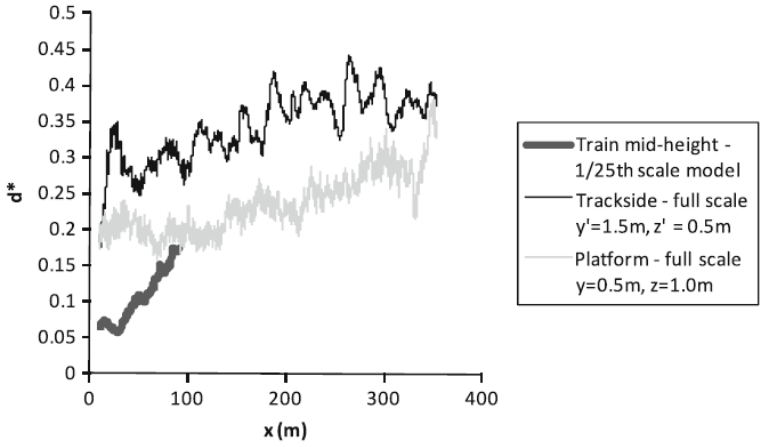

Figure 2.8 - Development of boundary layer displacement thickness for full-scale and scale model ICE (Baker, 2010, taken from Sterling et al., 2008a).

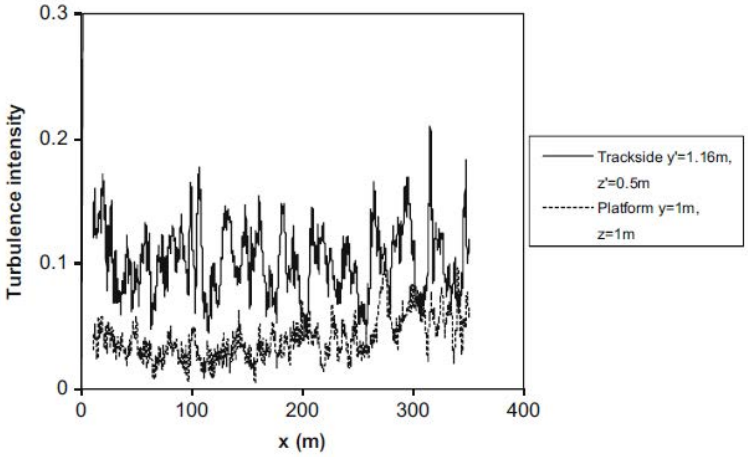

Figure 2.9 - Turbulence intensities for ICE service car (Sterling et al., 2008a)

Figure 2.9 illustrates the turbulence intensity for both trackside and platform measurements of the ICE service train from Sterling et al., (2008a). As can be seen, the turbulence intensity is essentially constant, perhaps very slightly increasing, along the train length, and unsurprisingly, that the trackside I_u is higher than measurements made with a platform. The values of I_u, of the order 0.05 to 0.1, are typical of flat plate boundary layers (Baker, 2010). The growth of the boundary layer is affected by scale - i.e. the Reynolds number (De Graaff and Eaton, 2000; Baker et al., 2001), and also the train length (Baker et al., 2001, Sterling et al., 2008a). The HST model used in this study is a 2+2 configuration, compared with a 2+7 or 2+8 configuration typical at full-scale. At full-scale there is a more rapid growth in the boundary layer near the nose of the train compared to model-scale, and this will affect the nature of the slipstream in this region at model-scale (Baker, 2010). Figure 2.10 compares the slipstreams for full-scale and moving model rig (MMR) tests, and shows that the main features such as nose and wake peaks are consistent, but there is a more rapid boundary layer growth at model-scale. At full-scale, for an ICE2 train, the integral time scale in the boundary

layer region was less than 0.1 s, and Baker, (2010), concluded that flow unsteadiness in the boundary layer region was unlikely to affect the safety of trackside workers based on the findings of the human response time to gusts of 0.2-0.3 s from Jordan et al., (2008), though Baker, (2010) and Sterling et al., (2008a) acknowledged that this was only true for a high speed passenger train and that air flows within a freight train boundary layer (considered in Sterling et al., 2008a, and Soper, 2014) do pose a risk.

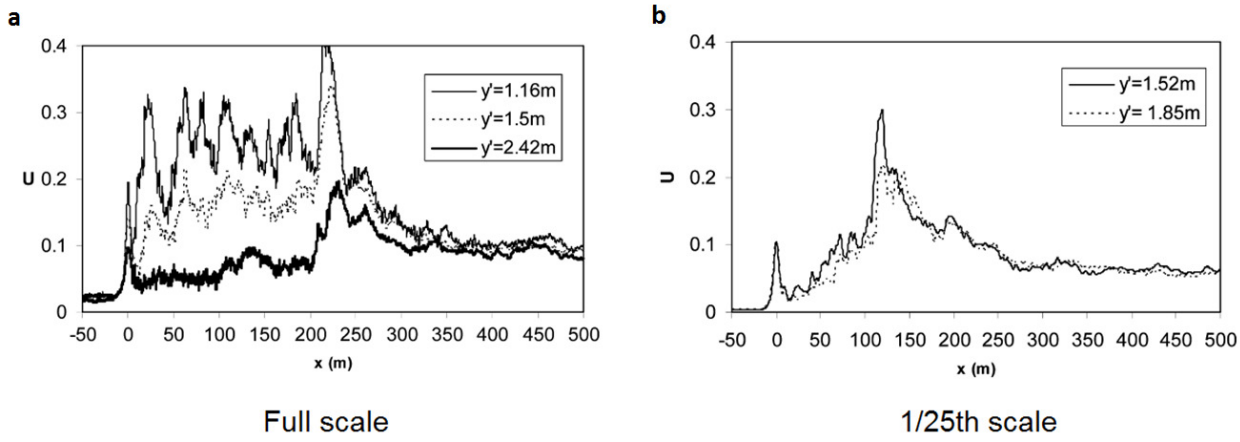

Figure 2.10 comparison of slipstreams from (a) full-scale and (b) model-scale for ICE train, z' = 0.5 m (Sterling et al., 2008a).

The intercarriage gaps fall within the boundary layer region, but it was reported by Brockie and Baker, (1990), that the intercarriage gaps were shown to have ***no apparent effect*** on the growth of the boundary layer. Larger geometric discontinuities, however, have been found to affect the slipstream. Baker et al., (2014a), found a large velocity peak at the position where two train sets were joined, but the authors acknowledged that the ensemble size was small (8 runs). Soper, (2014), found that gaps between rectangular freight containers created large and

distinct local velocity and pressure peaks. It was noted by Quinn et al., (2009), when considering the underbody flows, that the presence of intercarriage gaps affected pressure field beneath the train and the track bed, and a local velocity peak was found where two train sets were joined. Figure 2.11 shows ensemble pressure and velocity measurements under a train from Quinn et al., (2009). It can be seen that there is a large sharp sinusoidal pressure pulse at the nose of the train, regular negative peaks corresponding to intercarriage gap locations, and a smaller pressure pulse at the tail passage. The slightly larger Cp pulse at 10 s, and equivalent peak in mean velocity in figure 2.11, corresponds to the larger gap where the two 10 car train sets were joined together. The dependency of pressures on train geometry was also noticed by Ido et al., (2008), who studied different underbody geometries using a moving belt wind tunnel, and Hemida et al., (2010), who conducted an LES on a 1/50th scale train on a modelled rotating rail rig. For most modern passenger trains, the effect of small geometrical discontinuities do not have a significant effect on boundary layer growth (Muld et al., 2014, Bell et al., 2015), however, the unshielded bogie region is likely to have a significant effect and increase magnitude of the train induced slipstream and pressure (Baker et al., 2014a).

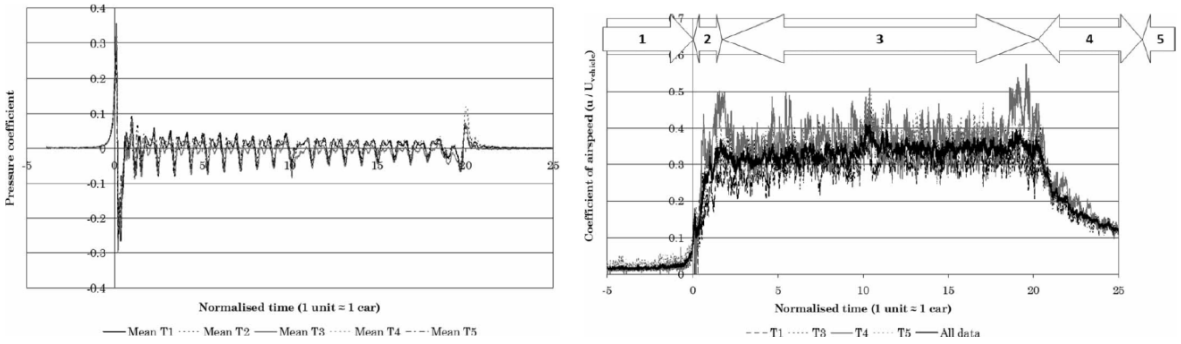

(a) (b)

Figure 2.11 - (a) normalised pressure and (b) normalised velocity beneath Class 373 train (Quinn et al., 2009).

2.3.2.3 Wake region

The wake is the region after the train has passed, and for most normal passenger trains at operational speeds, is highly turbulent, with the largest turbulence scales (Baker, 2010, Bell et al., 2015). It can be sub-categorised as the near and far wake (Baker et al., 2001).

The near wake of a train is the region immediately after the tail end of the train has passed, and the boundary layer has separated, and generally for passenger trains there is a sharp velocity peak shortly after the train passage (Baker et al., 2014a). It is distinguished from the far wake by the large unsteady flow structures giving rise to the maximum slipstream velocities which are potentially the most hazardous (Sterling et al., 2008a, Bell et al., 2014, Bell et al., 2015), however this is only true for typical passenger trains - trains with blunter noses may show larger velocity peaks in the nose and boundary layer regions (Baker et al., 2013; Soper et al., 2014; Flynn et al, 2014).

Baker, (2010), concluded that the large scale unsteady turbulent flow structures in the near wake region are not only hazardous to passengers and trackside workers, and may also be a significant cause of train drag, also acknowledged by Tian et al., (2015). Sterling et al., (2008a), conjectured that large flow structures - counter-rotating trailing helical vortices, form at the tail of the train as the turbulent boundary layer sheds, and rotation is created by downwash from the roof and tail of the train and the flow along the train sides (Bell et al., 2015). Baker et al., (2014a), found that trains with more streamlined tail profiles showed sharper increase in slipstream velocity in the near wake peaks than for trains with blunter tails. The trailing vortices spread out, moving downwards and outwards over time (Bell et al., 2015, Weise et al., 2006, Soper et al., 2016, Bell et al., 2016a, b, c), and some researchers posit that they exhibit span wise oscillations (Schulte-Werning et al., 2001; Muld et al., 2012;

Yao et al., 2013). Sterling et al., (2008a) found these flow structures to have time scales of ~0.15 s immediately after the train passage, which increased to about 0.3-0.4 s at 20-30 m downstream of the train tail. Sterling et al., (2008a), also concluded that accurate measurement of the wake flow structures depends on the phase of the vortices, and hence they may also be missed by the "cancelling out" effect of ensemble averaging (Sterling et al., 2008a). Baker, (2001) undertook wavelet analysis on the model-scale ICE2 measurements reported in Sterling et al., (2008a), and found peaks in the power spectra in the wake at Strouhal numbers of 0.03 and 0.5 (based on a hydraulic diameter as the nominal train height of 3 m) - the former identified as the regular "pumping" action of the wake and the latter with higher frequency fluctuations within the shear layers. These values disagreed somewhat with full-scale Strouhal numbers calculated by Sterling et al., (2008a) (based on the same hydraulic diameter), and computational work carried out by Schulte-Werning et al., (2003), (on an unspecified hydraulic diameter though is probably close to 3 m) who both found Strouhal numbers of around 0.15, which were close to values of 0.2 found by Bell et al., (2016b). Sterling et al., (2008a), suggested that the much lower Strouhal numbers from Baker, (2001), may in part be due to differences in scale associated with boundary layer growth and hence shear layer thickness.

It has been discussed by many authors (Baker, 2010; Flynn et al., 2016; Sterling et al., 2008a; Xu and Ding, 2006), that in general, a crosswind can significantly increase the magnitude and complexity of slipstream effects - particularly in the near wake. The study of crosswind effects at full-scale is challenging because of the stochastic nature of the wind and phase dependency on the trailing vortices, and therefore a very large number of runs are needed form a meaningful ensemble (Baker et al., 2014a). Figure 2.12 presents the results of moving model rig tests with and without crosswind and shows larger slipstream velocities with

crosswind. It was noted by Jordan, et al., (2009), and in the AeroTRAIN project (Baker et al., 2014a), that a crosswind can lead to a reduction in slipstream velocity close to the train (in the y-direction) and an increase in slipstream velocity further from the train, as the vortex is advected with the wind. Because of the complexity and lack of full-scale data, the effects of crosswinds on slipstreams has not been investigated in this study. but remains a key area of interest for wind engineers.

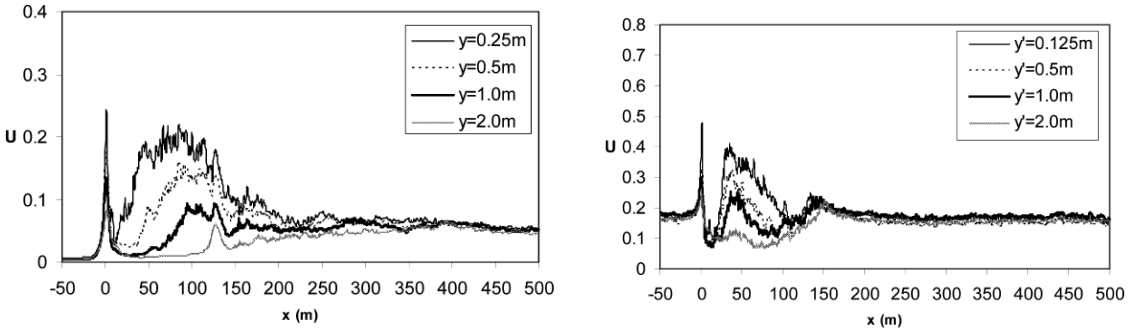

No crosswind With crosswind

Figure 2.12 - Comparison of slipstream measurements with and without a crosswind for a 4 car ICE at the TRAIN rig, z' = 2.25 m (Sterling et al., 2008a).

The far wake region follows the near wake and is characterised by a gradual decay in slipstream velocity and its standard deviation (Baker et al., 2001; Sterling et al., 2008a; Soper, 2014), eventually reaching the initial air velocity, though it has been noted that the time for velocities to return to the initial values are quite long, equivalent to several train lengths (Soper, 2014). Baker et al., (2014a), defined the far wake as occurring at distances greater than 100 m after the train passage, and found the velocity decay in the far wake to fit an exponential profile, with exponents close to -0.5 regardless of train type. Far wake flows generally do not have magnitudes that are of concern to safety.

2.3.3 Review of current codes of practise and legislation regarding train slipstreams

Legal European limits for aerodynamic phenomena are set out in the TSI. In addition, a series of European Standards (CEN codes) exist that prescribe methodologies for assessment of aerodynamic phenomena.

The TSI prescribes a methodology for calculating the maximum gust velocity of a train slipstream - a minimum of 20 runs at full-scale must be taken with ambient wind conditions less than 2 m/s. Slipstream velocities are measured at fixed vertical positions relative to TOR or platform ground level (given in table 2.1) and horizontal positions always 3 m from COT (European Commission, 2008, 2014). Data is then filtered using a moving average filter with a period of 1 s, and the maximum resultant horizontal air velocity, U_{max}, of each run is found. The TSI gust velocity ($U_{2\sigma}$) is defined as the mean of these maxima plus two standard deviations:

$$U_{2\sigma} = \overline{U_{max}} + 2\sigma_{U_{max}} \tag{2.17}$$

There are two points to note from the changes to the TSI; the permitted height of the ballast has increased and all measurements now take place in open air and without a platform as a consequence of the AeroTRAIN work (considered in Baker et al., 2014a, b). While this change is logical for the majority of European scenarios, i.e., larger ballast heights and lower platforms than in the UK (Soper et al., 2016; Johnson and Holding, 2003), this change must be treated with caution for the UK case. Figure 2.13 shows a comparison between the slipstream measured with a low (German) and high (UK) platform (0.3 m and 1 m high) from scale model tests undertaken as part of the RAPIDE project (Johnson and Holding, 2003;

RAPIDE Consortium, 2001), and shows that the higher platform has a much lower slipstream velocity. It should be noted that the vertical position relative to the train was different, and therefore differences in the slipstream may not solely be attributable to modification and attenuation of the flow due to the larger platform (Baker et al., 2014a). Similar findings were found at full-scale by Baker et al., (2014a). Given that the addition of a platform decreases slipstream velocity, it is this author's view that equivalent open air measurements with no platform are not necessarily pragmatic for the UK, and could lead to over-conservative design.

It was also hypothesised that the ballast height could affect the slipstream velocity, and if this was true then the permissible range of ballast heights (as in table 2.1) could encourage bias when test sites are selected during train design/certification. Additionally, given that in reality the main concern is the effect of slipstreams on people and wheeled equipment, measurement positions at a fixed position from TOR could be well away from the centre of gravity of a typical person (or piece of equipment) standing 3 m from the COT if the ballast height is large. Or conversely, if the ballast height is very low (as is the case in most of the UK), large slipstream velocities may recorded at the TSI position of 0.2m above TOR, but this finding would not in itself have much practical significance, except perhaps the effect on tools and equipment. Further consideration of the effects of ballast height is presented in (Bell et al., 2014; Soper et al., 2016), the latter is based on experiments undertaken as part of this study which are presented in chapters 3 to 5.

Table 2.1 - TSI limit values of slipstream velocities for a train running at 200 kph (European Commission, 2008, 2014).

Legislation	Scenario	z	$U_{2\sigma}$ (m/s)
TSI 2008	Open track with ballast height of 0.75 m (±0.25 m)	0.2 m above TOR	20
	With platform ≤ 240 mm above TOR	1.2 m above platform	15.5
TSI 2014	Open track with ballast height of 1 m (±0. 5 m)	0.2 m above TOR	20
	Open track with ballast height of 1 m (±0. 5 m)	1.4 m above TOR	15.5

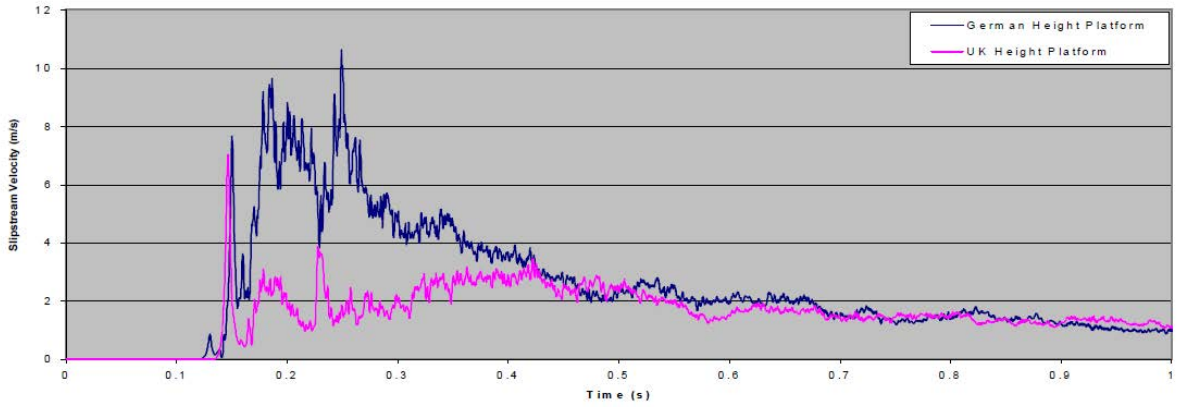

Figure 2.13 - Slipstream velocities of ICE2 from TRAIN rig tests for two platforms (pink shows UK height of 1 m, blue shows German height of 0.3 m above TOR), measured 1 m from platform edge and 1.4 m above platform (Johnson & Holding, 2003).

2.3.4 Closing remarks on slipstream research

The slipstream of a train is a complex three-dimensional phenomena, and in the real world slipstreams are affected by train type and speed, ambient wind conditions and infrastructure scenarios. The main issues with slipstreams are the effects of winds on people and equipment, and static pressures can cause (fatigue) loading on structures (Zhou et al., 2014). Current standards and legislation based on homologation requirements, while simple and somewhat logical, may not necessarily be pragmatic for the UK, and given that both the number of passengers and train speeds are expected to increase, further study of the flow field around high-speed trains can only be beneficial. Full scale tests measure reality, but given the complexity of the railway system, they are often expensive and complicated to set up. Model scale tests are usually quicker and cheaper and have been shown to, in some cases, be able to replicate the main flow features around a train. The expectation is that, provided that Re number effects and differences in model and full-scale train geometries are successfully mitigated, the flow development in the boundary layer and wake should be comparable between full-scale and model-scale. This is not the case, however, and there are clearly issues associated with differences in scale, primarily with boundary layer development (which is more rapid at model-scale), and as yet, there is no consensus as to the extent to which model-scale data represents reality. The same comment could also be applied to CFD, and the collection of model-scale slipstream data is integral to the advancement of CFD through validation of computational models.

2.4 Effects of crosswinds on trains

2.4.1 Natural winds

The atmospheric boundary layer (ABL) develops due to natural winds and friction from the surface of the earth (Garrat, 1994). Natural winds can be highly variable and turbulent, and affected by meteorological conditions, topography, terrain and infrastructure (Garrat, 1994; Baker 2015). The ABL can be considered to take a conventional logarithmic profile of mean wind velocity (figure 2.15) where velocity is zero at the earth's surface (no-slip condition) and increases as height (z) increases (Surry and Johnson, 1986; Garrat, 2004). Therefore when the effects of winds on trains (which are close to the ground) are considered, the variations in velocity with height are of significance.

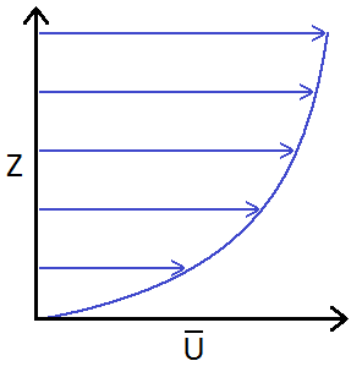

Figure 2.14 - Illustration of generic logarithmic ABL profile ($\bar{U}$ denotes the mean horizontal flow).

For consideration of natural winds, the conventional frame of reference is to align the x-axis (and hence u component) with the direction of the mean horizontal wind velocity. The Cartesian axes and vector components correspond as in figure 2.1.1.

The logarithmic vertical wind profile can be approximated as (Blackadar and Tennekes, 1968):

$$\overline{U}(z) = \frac{u_*}{K_{VK}} ln\left(\frac{z}{z_0}\right) \tag{2.18}$$

Where u_* is the surface friction velocity, K_{VK} is the Von Kármán constant (~0.41) and z_0 is the surface roughness length - values are given in ESDU, (2002) for different topographies. It is suggested that this logarithmic approximation is valid for z < 30 m (EDSU, 2002) or z < 200m (Dyrbye and Hansen, 1999), which in most cases are height ranges applicable to trains.

The wind velocity at a given instant can be considered in terms of the mean and the turbulent fluctuations (as in equations 2.6a to 2.6c). In order to apply this decomposition to this study, it is necessary to make the following assumptions (Dorigatti, 2013):

- the flow is stationary given a large enough time interval;
- the mean wind velocity (in any vector component) depends only height;
- small changes in height do not affect the wind direction.

Instantaneous wind velocity (V) was therefore defined by Dorigatti, (2013), based on George (2013) as:

$$V(x, y, z, t) = \overline{U}(z)\mathbf{i} + [\mathrm{u}'(\mathrm{x,y,z,t})\mathbf{i} + \mathrm{v}'(\mathrm{x,y,z,t})\mathbf{j} + \mathrm{w}'(\mathrm{x,y,z,t})\mathbf{k}] \tag{2.19}$$

Where $\overline{U}$ is the mean wind at a given time, which is only a function of height (z), **i**, **j** and **k** are unit vectors associated with the x, y and z axes respectively and u', v' and w' are the turbulent flow fluctuations which are affected also by position in three-dimensional space, and given a sufficiently long time interval have zero mean (Reynolds, 1895). Turbulence intensity is at its maximum close to the ground, and is sensitive to height within the range of heights

considered in this study on the effect of ABL on trains. Turbulence intensity of the ABL is therefore also defined as a function of height:

$$I_{u,v,w}(z) = \frac{\sigma_{u,v,w}(z)}{\overline{U}(z)} \tag{2.20}$$

The turbulence intensity within the height ranges considered in this study is expected to be about 10-30%, based on full-scale measurements reported in Baker et al., (2004) and Surry and Johnson, (1986), though of course varies significantly with geographical location, topography/infrastructure and meteorological conditions.

2.4.2 Air flow relative to a stationary and moving train

When the effect of winds on trains are considered, a different convention is adopted in this study and wind velocities are resolved relative to the x-axis of the train. This section aims to set out the conventions for considering winds on a stationary and moving train.

The air flow on a stationary train (as is typical of wind tunnel tests) can be considered in quite straightforward terms, as shown on figure 2.15, where the yaw angle can be defined as either an instantaneous or mean value depending on how the onset wind is considered. The wind profile can be assumed to take either a logarithmic profile or a uniform flow profile depending on the wind tunnel boundary layer simulation (or lack thereof), however for the purposes of this study it has been assumed there is no variation in u_{wind} over the train height.

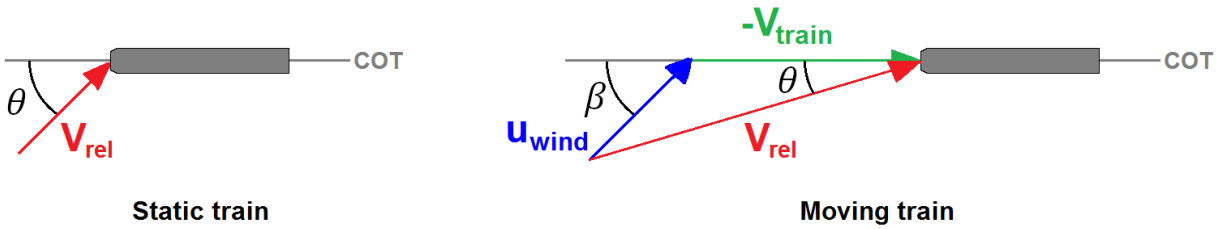

Figure 2.15 - Air flow relative to stationary and moving train.

A moving train experiences an airflow reverse to the direction of travel when taking the train as the reference frame. Resultant wind velocity is defined as:

$$V_{rel} = \sqrt{(\overline{U_{wind}}(z)\sin\beta)^2 + (V_{train} + \overline{U_{wind}}(z)\cos\beta)^2} \tag{2.21}$$

Yaw angle therefore depends on V_{train}, U_{wind} and β - the angle between the onset wind and the x-axis of the train (i.e., the COT), and these terms are related by trigonometry as:

$$\theta(z) = \arctan\left(\frac{\overline{U_{wind}}(z)\sin\beta}{V_{train} + \overline{U_{wind}}(z)\cos\beta}\right) \tag{2.22}$$

When the motion of the train is simulated, such as in moving model tests with a crosswind (for example Sakuma, 2013; Dorigatti, 2013; Soper, 2014), the yaw angle is defined as in figure 2.15 and in this study is always defined as positive when cross flow impinges on the driver's LHS.

Dorigatti, (2013), acknowledged that the vertical velocity profiles of the air flow relative to the moving train (taking the moving train as the frame of reference and hence the "stationary" air as a uniform flow) is different to the logarithmic boundary layer profile of the ABL, resulting in a skewed velocity profile illustrated in figure 2.16. However, by comparison of

static and moving model tests, Dorigatti, (2013), found negligible effect of the skewed wind profile as both tests showed pressure distributions within experimental error. It was acknowledged by Baker, (2010) that, when considering moving model simulations through a crosswind, by logic the significance of the skewed velocity profile must depend on train speed, with the resultant air flow more like the logarithmic profile at low speeds, and more like a uniform flow at high speeds. Premoli et al., (2016), undertook CFD simulations of a stationary train compared to a moving train when subject to a crosswind, and found a small (~5%) reduction in the side force and rolling moment coefficients (defined later in equations 2.25a and 2.25d) with the static model case. When considering wind tunnel tests at low yaw angles, Cheli et al., (2010), noted that the boundary layer effects would not be representative of the realistic air flow of a moving train. Morden et al., (2015), also noted that in wind tunnel tests, upstream effects, such as separations from the splitter plate and any ground simulation, could affect the flow field - particularly at lower yaw angles.

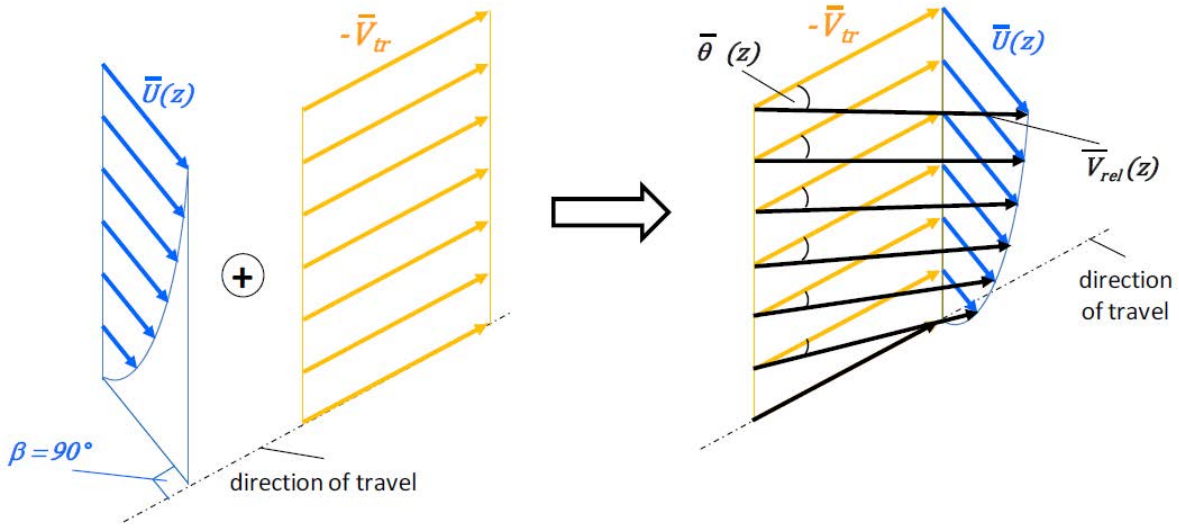

Figure 2.16 - Illustration of skewed wind velocity profile relative to a moving train (from Dorigatti, 2013).

2.4.3 Wind loading on a train

Natural winds in the ABL can result in overturning forces which can result in derailment. The forces acting on a vehicle are expressed relative to the x, y and z axes as drag, side and lift forces, and moments about each axis correspond to roll (x), pitch (y) and yaw (z) - only rolling moments about the x axis and the lee-ward rail (lee-rail moments) are of interest in this study. Force and moment are defined as:

$$F_\eta = \frac{1}{2} C_\eta \rho A_{ref} V_{rel}^2 \tag{2.23a}$$

$$M_\eta = \frac{1}{2} C_\eta \rho A_{ref} L_{ref} V_{rel}^2 \tag{2.23b}$$

Where C_η is a non-dimensional coefficient related to any force or moment (i.e., η = X, Y, Z), A_{ref} is a full-scale reference area, usually taken as the side area of one car and L_{ref} is the reference lever arm length, usually taken as the train height. Baker et al., (2008), and Xu and Ding, (2006), stated that derailment due to lee-rail overturning is a more likely scenario than flange climbing when considering the effects of crosswinds. Lee-rail moment is related to roll moment and lift force by:

$$M_{X,lee} = M_X + (F_Y \frac{b}{2}) \tag{2.24}$$

Where b is the track gauge and UK standard gauge = 1435 mm.

Non-dimensional force and moment coefficients are typically found through experiments, and the coefficients of interest to this study (drag, side and lift forces, roll moment and lee-rail moment coefficients), are defined respectively as (Baker, 1991a):

$$C_X = \frac{F_X}{\frac{1}{2}\rho V_{rel}^2 A_{ref}} \quad (2.25a)$$

$$C_Y = \frac{F_Y}{\frac{1}{2}\rho V_{rel}^2 A_{ref}} \quad (2.25b)$$

$$C_Z = \frac{F_Z}{\frac{1}{2}\rho V_{rel}^2 A_{ref}} \quad (2.25c)$$

$$C_{M_X} = \frac{M_X}{\frac{1}{2}\rho V_{rel}^2 A_{ref} L_{ref}} \quad (2.25d)$$

$$C_{M_{X,lee}} = \frac{M_{X,lee}}{\frac{1}{2}\rho V_{rel}^2 A_{ref} L_{ref}} \quad (2.25e)$$

Forces and moments coefficients are usually obtained from low turbulence (I_u < 2.5%) wind tunnel tests, though CEN, (2010) describes a predictive equation based on train type and geometry. Currently, moving model tests are not regarded as "CEN compliant" (CEN, 2010), though in theory could represent a more realistic test case (Sakuma and Hibino, 2013). In the wind tunnel, forces are generally measured in two ways. Global forces (i.e., on the train as a whole) can be measured with strain gauges or dynamometers, however there are issues associated with mechanical vibrations, discussed at length by Dorigatti, (2013). A different approach is to measure surface pressures on the train and then integrate the pressures from each tapping to estimate the relevant forces and moments - this method was developed in Sanquer et al., (2004), and Quinn et al., (2007), and its application in this study has been described in detail in section 7.2.2. Typically, pressure coefficients are measured on a model surface, defined as:

$$C_{P_k} = \frac{P_k - P_0}{\frac{1}{2}\rho V_{rel}^2} \tag{2.26}$$

Where the subscript k defines an individual pressure tap, P_k is the total static pressure at any pressure tap and P_0 is the reference static pressure. Pressure coefficients are then integrated across the entire train surface to give force and moment coefficients (rather than forces). The use of loops of pressure taps around a train can not only provide useful information about the flow field (Baker and Sterling, 2009; Dorigatti, 2013; Rocchi et al., 2016) but also allows accurate calculation of force and moment coefficients given an adequate number of pressure taps that are essentially equal to global values measured by a force balance (Sanquer et al., 2004).

2.4.4 Unsteady crosswind effects on trains

Forces due to crosswinds can be thought of as steady - arising from the mean velocity component (Baker, 1991a), or unsteady - arising due to turbulent fluctuations (Baker, 1991b, c; Dorigatti, 2013, Sterling et al., 2008b), though unsteady effects are convoluted by the turbulent flows induced by the train and the dynamics of the vehicle.

The quasi-static assumption is usually made when considering the effect of the ABL on trains, which assumes that time domain fluctuations in the onset wind velocity correspond to fluctuations in pressures (hence forces) on the train - essentially that fluctuations are caused by turbulence buffeting (Baker, 1991b). Strictly speaking this assumption is incorrect, mainly due to frequency domain effects of vortex shedding from a moving vehicle which can affect the power spectra of the force fluctuations (Baker, 1991b,c; Sterling et al., 2008b). The near

wake region and windward wall-roof junctions are usually the dominant regions for vortex shedding (Baker, 1991b; Orellano and Schober 2006; Baker and Sterling, 2009). Robinson and Baker, (1986), found that free-stream turbulence affected mean force and moment coefficients, and concluded that the effects were due to an interaction of the free stream turbulence and the train wake. If this is true, then there is an implication for wind tunnel tests on shorter train models (i.e., fewer coaches), as the wake phenomena would not be representative due to differences in boundary layer development (see section 2.3.2.2) and possibly also tail geometry affecting the wake (Bell et al., 2016c).

A "correction factor" (known as the aerodynamic admittance) can be used to relate fluctuations in the onset wind to fluctuations in the forces on a train (Baker, 1991b; Baker, 2003; Sterling et al., 2008b), though frequency domain effects are not considered in this level of detail in this PhD study.

Cooper, (1984), and Baker, (1991b) noted that the quasi-static assumption appears valid for full-scale gusts of relatively long duration (Baker, 1991, quoted about 4-5s for trains) - lower timescales may be damped to some extent by the vehicle suspension (Baker et al., 2011b). Baker, (1991c) concluded that gusts of period 1-3 s were of sufficient time to cause train instability. Andersson et al., (2004), and Li et al., (2013) also noted the importance of gust build up time on the train dynamics. Short build up times (i.e., a sudden gust such as on a train exiting a tunnel) of less than 1 s can have significant and undesirable effects on the dynamics of the train, whereas gusts of length greater than 1 s can potentially be treated as a constant wind (Lippert, 1999; Andersson et al., 2004).

Baker et al., (2004), noted that there was a significant effect of the suspension on the side force coefficient at full-scale, with higher side force coefficients (hence rolling moment

coefficients) when the suspension was unlocked and the train was at zero degrees cant. The highest side force and rolling moment coefficients were found with locked suspension and at 6° cant deficiency, due in part to the increased side area. Lift coefficients from complementary wind tunnel measurements were lower than at full-scale, and it was concluded to be due to geometric discrepancies in the ground roughness between the different scales (Baker et al., 2004), highlighting the need for care when simulating local roughness of the ground in wind tunnel tests.

2.4.5 Effect of infrastructure and train geometry

As discussed in section 2.4.1, the height of the train above ground results in a higher velocity of the ABL. Bridges and viaducts potentially experience the highest magnitude winds not only due to boundary layer effects (equation 2.18) but also due to the "funnelling" effect within valleys (Barry and Chorley, 1968). Conversely, cuttings (i.e., where the train is shielded) have been shown to greatly decrease the magnitudes of aerodynamic forces (Zhang et al., 2015). Increasing the height of the embankment can also increase the wind velocity due to boundary layer effects and also the effect of wind speed up (by mass continuity) as wind flows up the embankment. Diedrichs et al., (2007), investigated the effect of wind speed up on a 6 m high embankment through CFD calculations. Speed up factors between roughly 1.2-1.3 were found and the authors suggested that it may be logical to reduce permissible wind speeds on embankments (discussed in section 2.5.5). Baker, (1985), found increases in velocity of about 70% for an 8 m high embankment compared with a flat ground case - this larger value is likely due to a combination of speed up and boundary layer effects. A wind tunnel study of a 1:10th scale ETR 500 train with a flat ground scenario compared to a 6 m embankment was

undertaken by Cheli et al., (2010), who also compared the use of different reference wind speed measurements by considering the upstream undisturbed wind flow and the flow over the embankment separately. The authors found that at lower yaw angles (up to 30°), the flat ground data using the upstream undisturbed reference wind velocity showed no significant differences to the embankment data when considering the wind velocity over the embankment as the normalising reference. The authors concluded that flat ground wind tunnel tests could be acceptable to evaluate overturning forces and moments in the lower yaw angle ranges typical of full-scale high-speed passenger trains. When the pressure field was considered, Diedrichs et al., (2007) noted that speed up increased the magnitude of negative pressures over the roof and windward wall-roof junction, and the larger suction pressure at the latter region reduced the side force coefficient. Diedrichs et al, (2007), also concluded that a 10% increase in height corresponded to an equal percentage decrease in permissible wind speed, and hence that higher embankments impair the crosswind stability of railway lines. Both Diedrichs et al., (2007) and Cheli et al., (2010) acknowledged that lift force is particularly sensitive to the underbody flows, which suggests that the underbody and track geometry and the relative vehicle-ground motion could play a significant role. Rocchi et al., (2016) carried out wind tunnel tests on a 1:10 scale model based on the German InterReigo train with different underbody geometries of increasing complexity and blockage (open, moderate and full/complex) with a single track ballast and rail (STBR) scenario (as prescribed in CEN, 2010), and both the power car and trailing coach were fitted with pressure taps. No significant variation in $\overline{C_{M_{X,lee}}}$ for the power car was observed between the open and complex underbody geometries at lower yaw angles (up to about 20°), but at yaw angles of 25° and above the moderate and complex underbody geometries showed higher values of $\overline{C_{M_{X,lee}}}$ that increased by a greater percentage than the increase in side area. The pressure data showed that

increasing the underbody complexity and blockage resulted in higher magnitudes of suction pressures over the roof (at half the power car length) which would have increased the magnitude of $\overline{C_Z}$.

2.4.6 Comparison between model-scale and full-scale tests

An investigation to compare aerodynamic forces between full-scale field tests and a wind tunnel test on an equivalent scale model of an 80 m long generic commuter train was undertaken by Suzuki and Hibino, (2016). The full-scale model was positioned on a viaduct in a coastal region where peak gusts of 30 m/s or greater were measured several times a year, and the tests were carried out for over three years. The wind tunnel flow simulation aimed to replicate the ABL through use of turbulence generating elements, though the turbulence intensities were slightly lower than at full-scale (Cooper, 1984). Additionally, a uniform flow was also simulated in the wind tunnel, and a comparison of side and lift force coefficients between the two wind tunnel simulations are shown on figure 2.17.1 - the important finding to note in relation to this study is that at yaw angles up to 30° the uniform flow and boundary layer flow tests compare very closely for side and lift force. The addition/omission of underbody equipment was also investigated, which can significantly affect the flow field around a train (Robinson and Baker, 1990; Copley, 1987; Rocchi et al., 2016). The addition of underbody equipment was found to increase the side force coefficient (at both full and model scale) by about 30%, which was significantly larger than the change in the side area of the car. A smaller increase was also observed on lift force coefficients with the addition of underbody equipment at higher yaw angles. Good agreement was found in side and lift forces between

the wind tunnel (with an ABL simulation) and full-scale, shown on figure 2.17.2, though the full-scale data showed a higher degree of scatter at lower yaw angles.

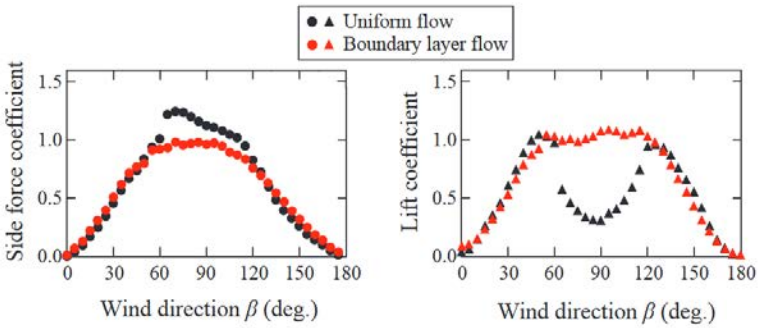

Figure 2.17.1 - Comparison of side and lift force coefficients from uniform flow and ABL wind tunnel simulations (Suzuki and Hibino, 2016).

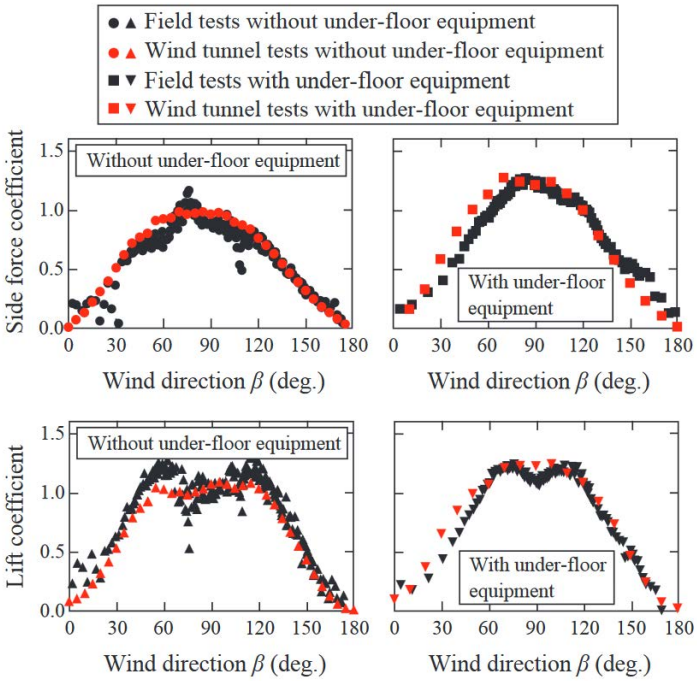

Figure 2.17.2 - Comparison of (a) side and (b) lift for ABL wind tunnel simulation and full-scale data (Suzuki and Hibino, 2016).

When comparing full-scale and wind tunnel data for pressure distributions on a mobile home, Surry and Johnson, (1986) found significant disagreement - the wind tunnel data showed negative suction peaks (on the windward roof) of lower magnitude than at full-scale. It was acknowledged that the wind tunnel flow was not representative of the ABL and turbulence intensity was lower at model-scale, and the authors also eluded to the complexity of replicating full-scale flow phenomena in the wind tunnel, a sentiment echoed by Cooper, (1984).

2.4.7 Application of codes of practise and legislation

The TSI (European Commission, 2014) sets out legislation on the evaluation of risk due to crosswinds for Class 1 high-speed vehicles ($\geq$ 250 kph), trains falling below this speed are considered an open point in the TSI (Paradot et al., 2015). Low speed trains also tend to be smaller (hence less mass and a lower restoring moment - see equation 2.27) and also less aerodynamically profiled which can affect the flow field (Giappino, 2016). Assessment of crosswind effects for trains < 250 kph (such as the HST) is based on CEN part 6 (CEN, 2010; European Commission, 2014), which outlines procedures for obtaining force and moment coefficients and subsequent calculation of characteristic wind curves (CWCs). This study is focussed on the first step (obtaining force and moment coefficients), therefore only a brief description of the subsequent assessment is presented.

There are three different methodologies to evaluate train safety performance in relation to crosswinds that are prescribed in CEN part 6. Listed in increasing level of accuracy (and hence complexity), they are defined in CEN, (2010), as:

- Simple two dimensional model;
- Advanced quasi-static method;
- Time dependent multi-body simulation (MBS).

These methods are described briefly in the sections that follow. There are additional methods available but in general all conform to the same strategy. The lee rail moment coefficients are obtained from wind tunnel tests, predictive formulae (which are conservative) or CFD simulations (though these require validation). The dynamic response of the train (due to both crosswinds and vehicle travel), and basic geometrical properties are accounted for in some form of numerical model, and finally, wheel unloading is considered in a limit-state style calculation in order to obtain CWCs, shown in figure 2.18. The CWC shows the "limit" wind speeds across a range of operational train speeds and is compared with characteristic reference crosswind curves (CRWCs) in the TSI - if the CWC is lower than the CRWC then the train is regarded as safe.

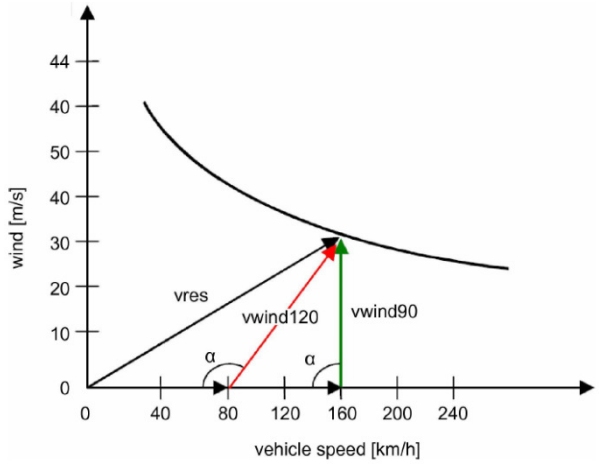

Figure 2.18 - Generic CWC showing geometric calculation approach (from TSI, 2008).

2.4.7.1 Simple two dimensional model

The vehicle can be treated using two dimensional analysis as a three mass model, though this method is the least accurate accepted method and therefore is conservative (CEN, 2010). The stability of the vehicle is dependent on the moment equilibrium of all moments on the train:

$$\sum M = f_{\Delta Q}\frac{1}{f_m}M_m + M_{CoG} + M_{la} + M_{X,lee} \tag{2.27}$$

Where $f_{\Delta Q}$ is a wheel unloading factor (of 0.9), and f_M is a factor related to uncertainty in the modelling methodology and is always greater than 1 - values are given in CEN part 6, and is taken as 1.2 for passenger vehicles (CEN, 2010), M_m is the restoring moment due to the vehicle mass, M_{CoG} is related to the lateral movement of the centre of gravity and M_{la} is due to the uncompensated lateral acceleration (due to cant deficiency). The lee-rail moment, $M_{X,lee}$, is calculated from equation 2.25e across the range of yaw angles over which $C_{M_{X,lee}}$ was measured (and should be shown at 10° steps from 10° to 90° according to CEN, 2010). The CWC is then calculated across this yaw based on the criterion that $\sum M = 0$.

2.4.7.2 Advanced quasi-static method

This method is similar to the simple two dimensional method, however it requires a more complex model that aims to model more accurately the suspension, body stiffness, forces between adjacent cars, the lateral displacement of the wheel on the track etc. CEN, (2010), suggests a five body model is appropriate for most trains. The criterion for the calculation of the CWC is that of 90% wheel unloading.

2.4.7.3 Time dependent MBS using Chinese hat wind scenario

A MBS program and a gust profile are used to model the forces on an unloaded vehicle (or additionally an eccentrically loaded vehicle if less favourable). A "Chinese hat" gust profile is typically used, which assumes that there is no temporal variation of velocity, rather that the velocity varies along the length of the track - an example is shown in figure 2.19. The mean horizontal wind component is assumed to be perpendicular to the train and temporal variations in the gust direction are assumed to be zero, and the train speed is assumed constant. When considering the unloaded car of the train as a frame of reference, the gust time series can be illustrated as in figure 2.19 (b).

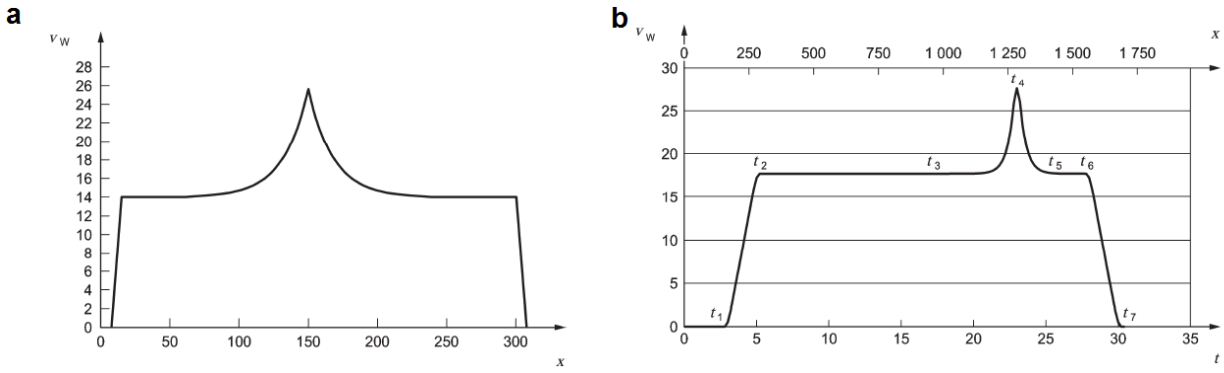

Figure 2.19 - Generic Chinese hat gust profile (a) spatial profile along track and (b) deterministic temporal wind profile taking train as frame of reference.

A three dimensional model is used that is more complex than that used in the advanced quasi-static method. MBS is therefore believed to be the most accurate and hence least conservative approach of calculating the forces and moments on the most sensitive car, though Baker,

(2013) has questioned the accuracy of this methodology given the large uncertainty associated with the natural wind.

Paradot et al., (2015), calculated the CWC of a wide range of European vehicles as part of data collected from the AeroTRAIN project using an MBS at zero cant. The lee-rail moment coefficients of the vehicles are shown in figure 2.20.1 and the corresponding CWCs are shown in figure 2.20.2. The M6Bx, which had the highest $C_{M_{X,lee}}$ has the lowest CWC, and conversely the InterRegio which had the lowest values of $C_{M_{X,lee}}$ has the highest CWC. This indicates that the aerodynamic profile of the train is dominant in determination of overturning risk - Andersson et al., (2004), suggested that crosswind effects contribute about 60% towards 100% wheel unloading, the remaining 40% are related to dynamics accounted for in the MBS. It should be noted that figure 2.20.2 was calculated with zero lateral acceleration (i.e., zero cant deficiency), and Andersson et al., (2004), estimated that lateral acceleration could account for 14% of 100% wheel unloading.

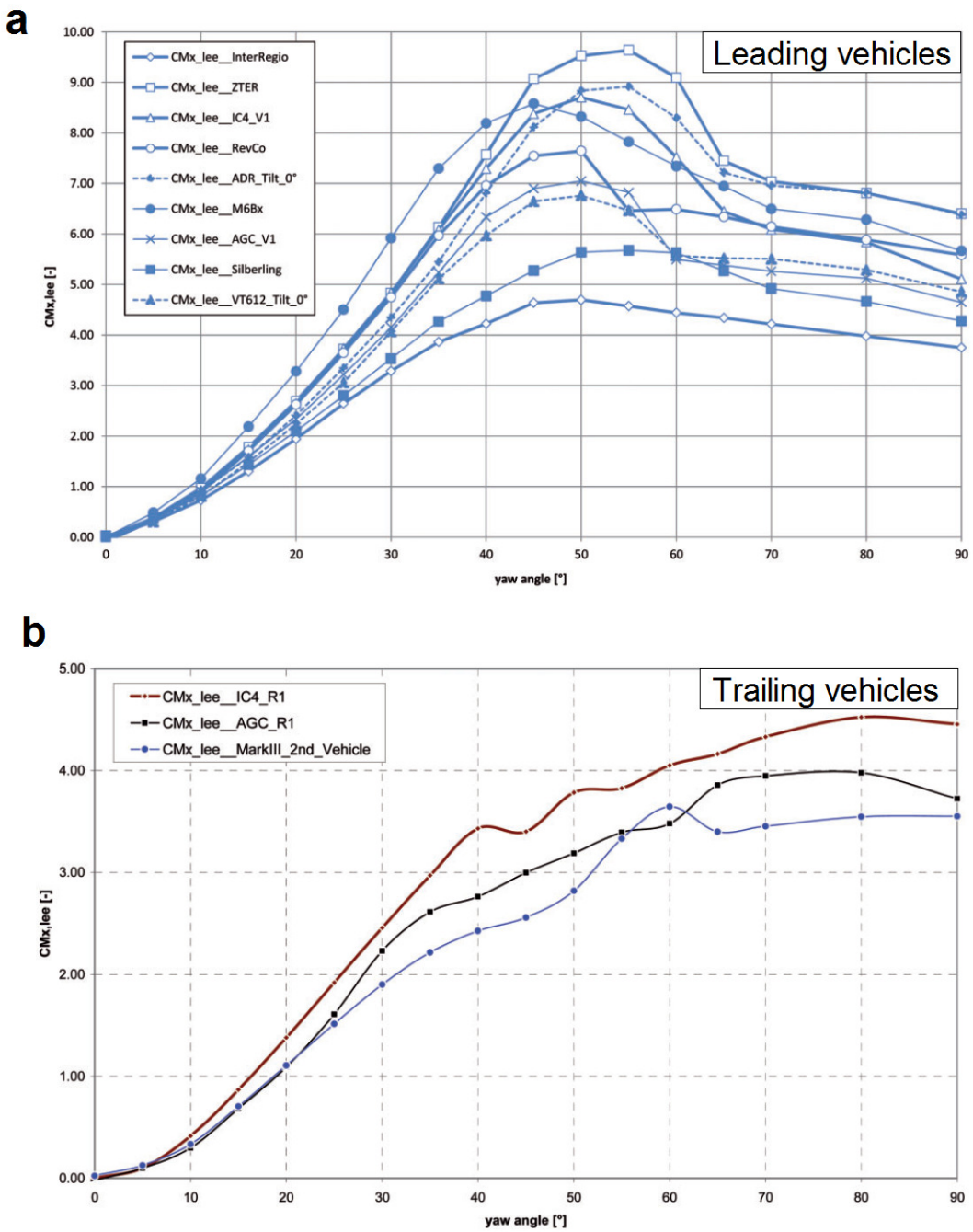

Figure 2.20.1 - Lee rail moment coefficients for a range of train types showing (a) leading vehicle and (b) trailing vehicles (Paradot et al., 2015).

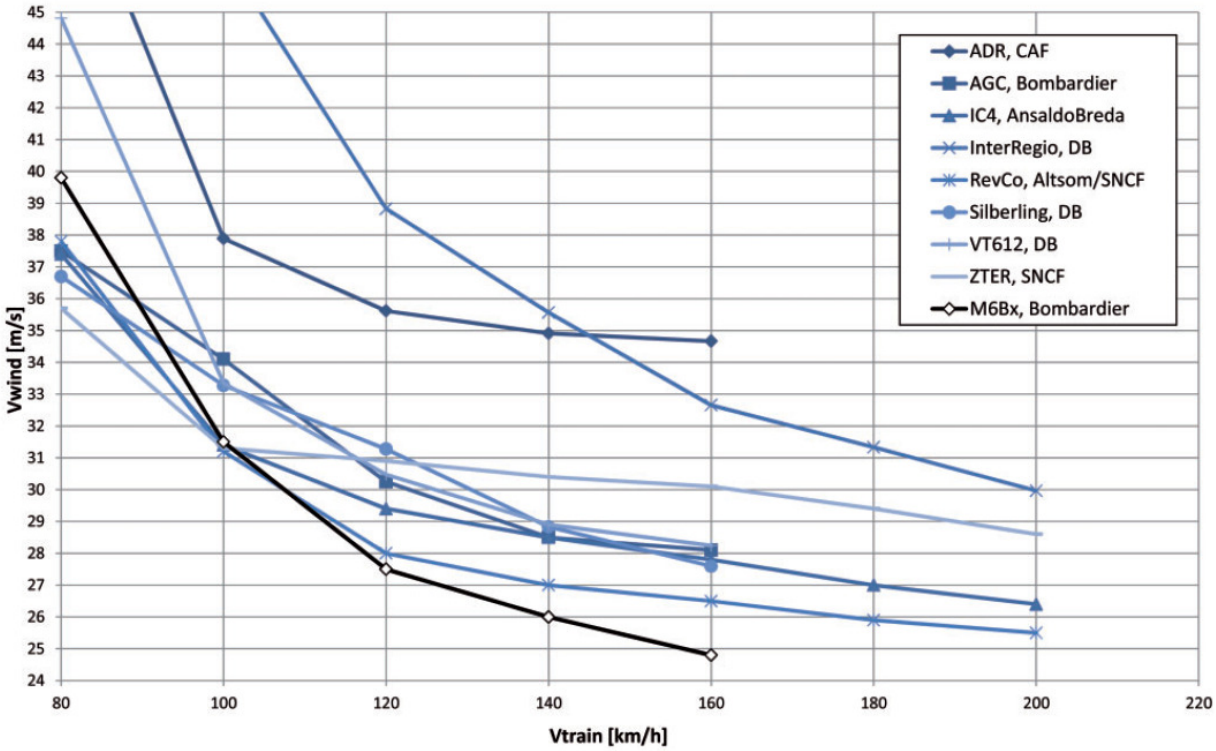

Figure 2.20.2 - CWC obtained from MBS for range of European trains (Paradot et al., 2015).

2.4.8 Crosswinds closing remarks

The measurement of aerodynamic forces arising due to crosswinds is still a major concern regarding railway safety. High winds have resulted in overturning accidents, but it must be acknowledged that additional factors such as track irregularities and the dynamic response of the train can also have a significant role. The wind relative to a moving vehicle can be resolved into vector components relative to the axis of train travel, however the vertical velocity profile of the ABL will differ from the "uniform block" velocity profile caused by the movement of the train (relative to the train). Wind tunnel measurements, while commonplace, cannot replicate the skewed velocity profile of a moving train, and simulation of the ABL is difficult to replicate. For this reason, CEN prescribes low turbulence uniform flow wind tunnel tests, which appears to be for the sake of simplicity of standardisation. Moving model experiments are less common due to the smaller number of facilities capable of undertaking these tests, and further work is required before these can be considered in codes of practice. The effect of increasing embankment height was found to increase the magnitude of side force coefficient and hence lee-rail moment - the most critical parameter for overturning, as a result of both the vertical logarithmic velocity profile of the ABL and also wind speed up over the embankment. Viaducts (at elevated heights above the ground) may also experience significantly higher winds than in a flat-ground or cutting case. At full-scale, gust build up time has been shown to be a factor and low build up times (such as a train exiting shielded environment) can be particularly unfavourable. Comparisons between wind tunnel and full-scale data on static trains have shown fairly good agreement despite the widely recognised difficulties in replicating the ABL in the wind tunnel. However, there is clearly a knowledge gap given the uncertainty in the measurement and simulation of the natural wind compared with the uniform and smooth flow found in a wind tunnel. Additionally, little work has been

undertaken on the measurement of pressures and forces between model-scale and full-scale around a moving train rather than more conventional static tests.

CHAPTER 3

MODEL-SCALE SLIPSTREAM TESTS - EXPERIMENTAL METHODOLOGY

3.1 Introduction

Chapter 3 describes the physical experimental setup of the measurement of slipstreams and pressure transients at model scale.

Scale model tests were undertaken at the TRAIN rig which is described briefly in section 3.2, and in further detail in appendix A. The HST model is described in section 3.3. The trackside instrumentation is described in section 3.4. The aims and objectives of the tests are set out in section 3.5 and section 3.6 describes the experimental set up.

Full scale measurements of the slipstream of a HST at operational speed were undertaken on the West Coast Mainline (WCML) at Uffington - appendix D describes the tests and presents the full scale results.

3.2 TRAIN rig facility

The TRAIN rig is a purpose built moving model test facility owned and operated by the University of Birmingham. The facility is capable of propelling 1:25th scale models at up to 80 m/s down a straight 150 m long test track. The track bed is a concrete slab, approximately 0.8 m wide and 1 m above the ground. The tracks are made from stainless steel I-beams with a centre to centre spacing equivalent to UK standard gauge. The length of the TRAIN rig is divided approximately into three 50 m sections:

- The firing section where the model is accelerated to the testing speed using a catapult effect from large elastic bungee ropes and a mechanical system of winches (described in section A.2).
- The testing section where slipstream velocities and pressure transients can be measured in an open air test section, and also includes a circular tunnel and crosswind generator (CWG) shown in figure 3.1 (see also section A.3). The crosswind generator is described in more detail in section 6.3.
- The braking section which is described briefly in section A.4, where the train model is decelerated using a system of ropes/pulleys and the friction within a mechanical piston.

The TRAIN rig has been used extensively in experimental work such as the TRANSAERO project (Johnson and Dalley, 2002) and RAPIDE project (Sterling et al., 2008a), and can be used to investigate the effects of infrastructure such as platforms (Johnson and Holding, 2003), tunnels/confinement (Baker et al., 2014c, d; Gilbert, 2013) and ballast height (Soper et al., 2016). Additionally, it can provide validation for CFD experiments (Soper et al., 2014,

Flynn et al., 2014), and be used to measure the effects of crosswinds on trains (Soper, 2014, Dorigatti, 2013).

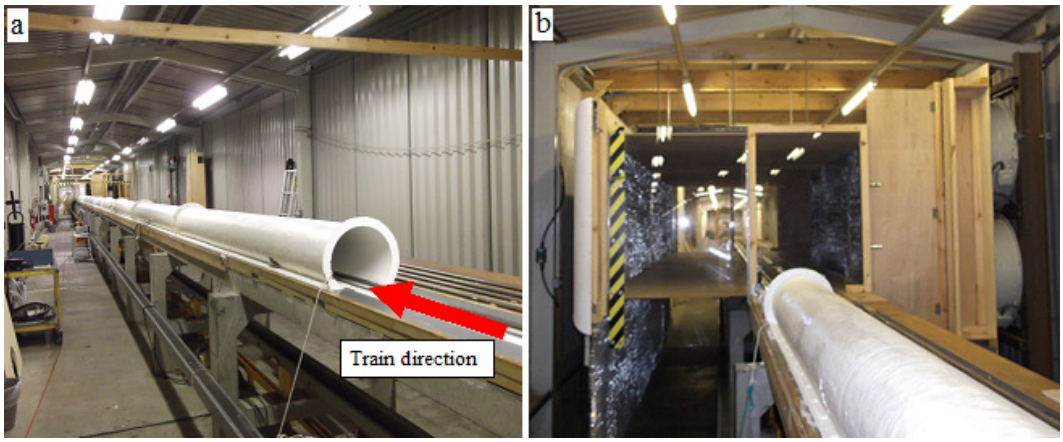

Figure 3.1 - Internal view of TRAIN rig facility (a) circular tunnel and (b) crosswind generator.

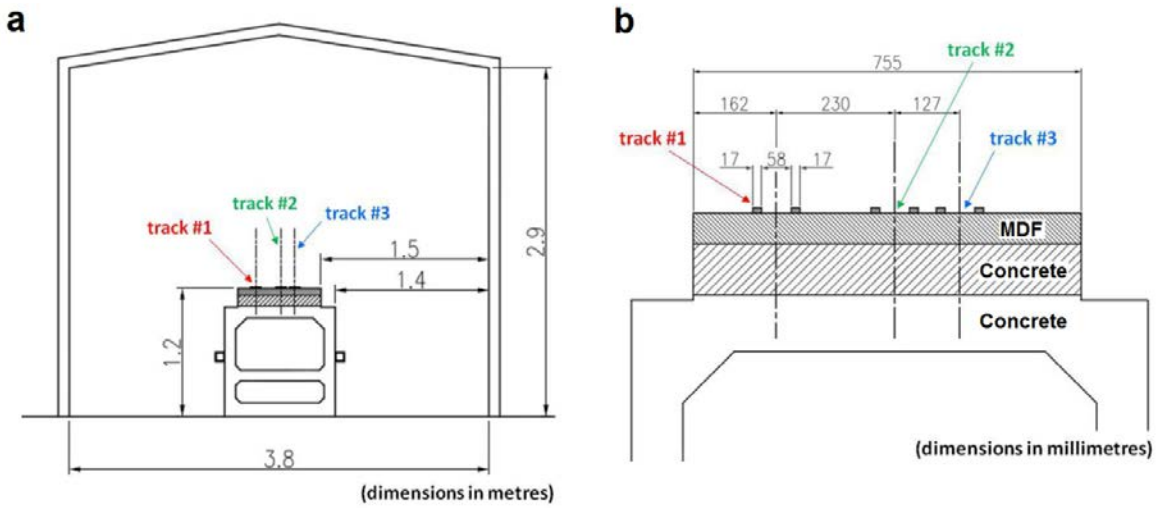

Figure 3.2 - Dimensions of TRAIN rig facility cross section - train travels on track #1 and direction of travel is into plane of view (Dorigatti, 2013).

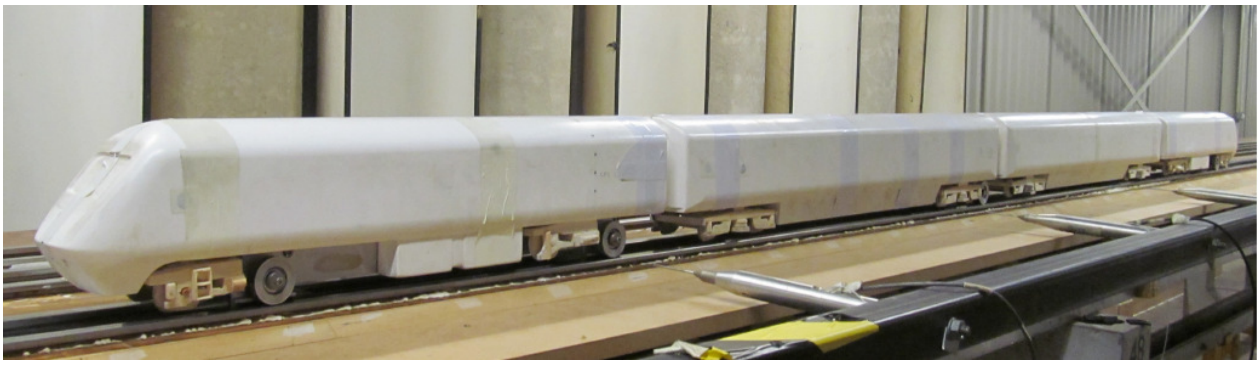

Figure 3.3 - HST model at the TRAIN rig with leading and trailing power cars and rake of two Mk III coaches.

3.3 HST model development

A 1:25th scale HST (in a 2+2 consist) was tested at the TRAIN rig. The model consists of a rectangular hollow section spine onto which the firing chassis and trailing wheels (figures 3.6.1 and 3.6.2) are attached with bolts. The outer shell of the model is constructed using glass reinforced polymer (GRP), which is connected to the spine using circular hollow section bars at both ends of each car mounted in wooden fittings (shown later in figure 6.8.4). The two shell sections are additionally secured with tape, which adds to the strength of the model and prevents unrealistic air flow into and out of the model itself. The bogies are modelled using balsa wood (figures 3.4.1 and 3.5.1) and are screwed directly onto the model shell. The external dimensions and the size of large details of the bogies are representative of those at full scale but smaller details are not modelled accurately; figures 3.4.1 to 3.5.2 compare the undercarriage area of the HST and Mk. III coach models to full scale.

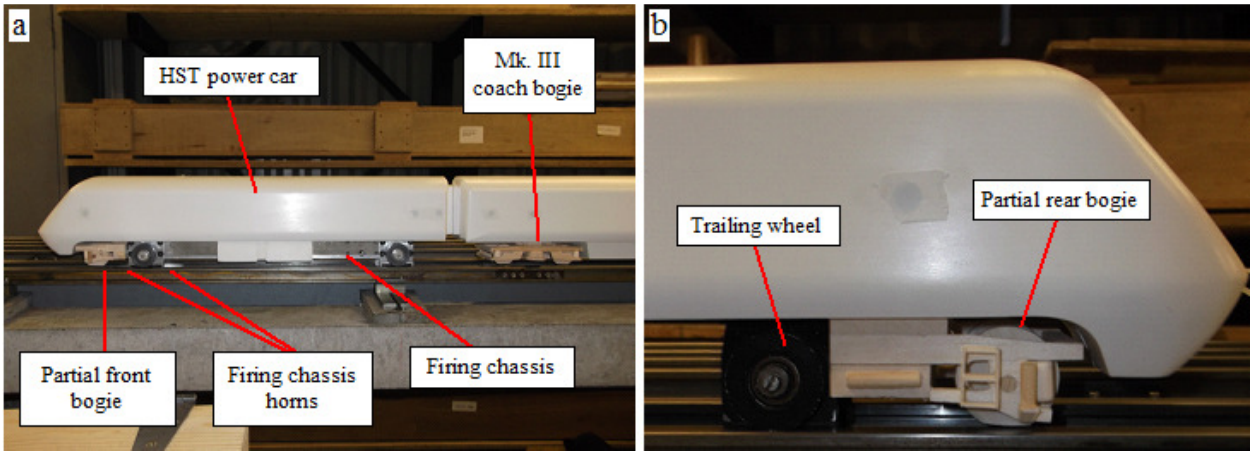

Figure 3.4.1 - HST power car (a) leading power car and (b) trailing power car partial bogie and trailing wheel.

Figure 3.4.2 - Full scale HST power car (a) entire power car (Wilson, 2015), and (b) bogie (Read, 2013).

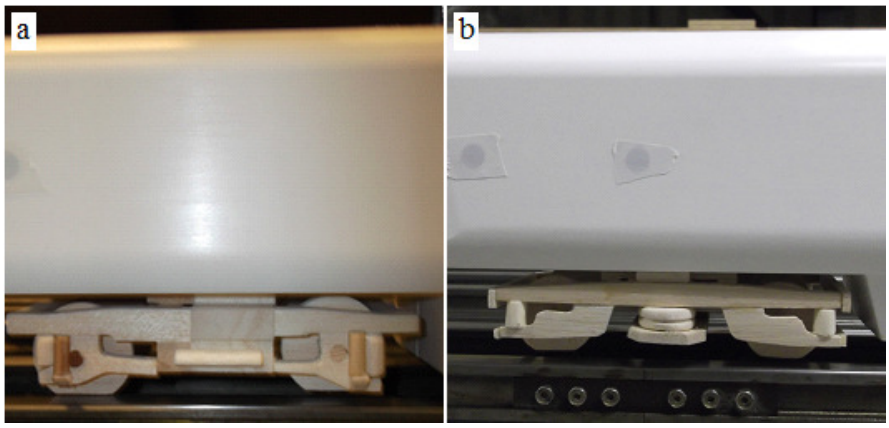

Figure 3.5.1 - Balsa wood bogies (a) full power car bogie (located on trailing power car) and (b) Mk. III coach bogie.

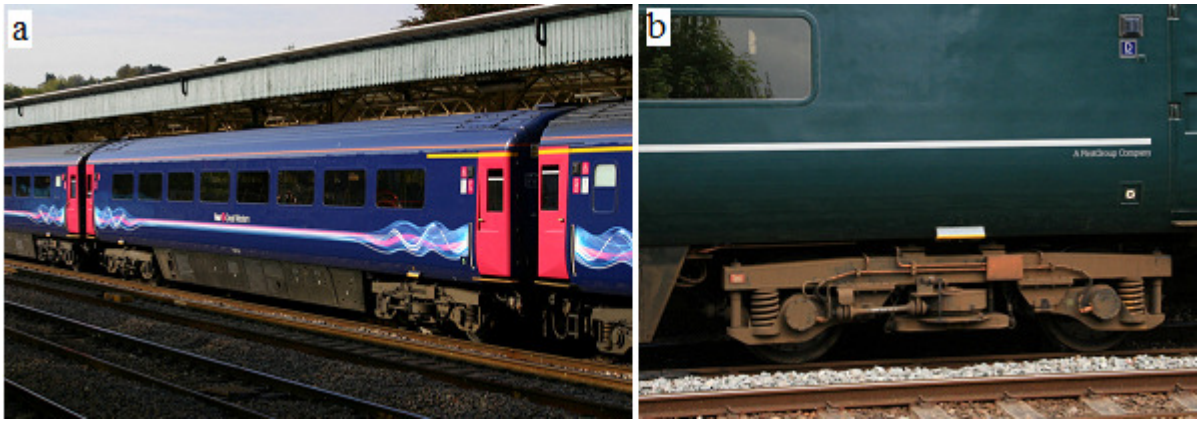

Figure 3.5.2 - Full scale Mk III coach (a) entire coach (Read, 2009), and (b) bogie (Read, 2016).

The train model travels on a stainless steel wheel set bolted directly onto the model spine, consisting of a firing chassis (figure 3.6.1) and two sets of trailing wheels (figure 3.6.2). The wheels are connected to axles mounted in a U-shaped piece of aluminium which has flanges below each wheel. These flanges fit within the web of the I-beam train tracks and prevent any lateral and vertical movement of the train. Also shown are the black deformable polymer packs, which are fixed to the web of the trailing wheel which reduce lateral movement and vibration of the train on the tracks, while adding minimal resistance to the forward motion of the train. The firing chassis has two spikes/horns, which hook onto the firing and braking ropes (see appendix A). The trailing wheel diameter is 0.98 m at full scale, which is slightly less than at full scale (1.0 m). Trailing wheels were positioned at the same positions as the wheels at full scale (and the balsa wood bogies were cut) in order to achieve a more accurate full-scale representation.

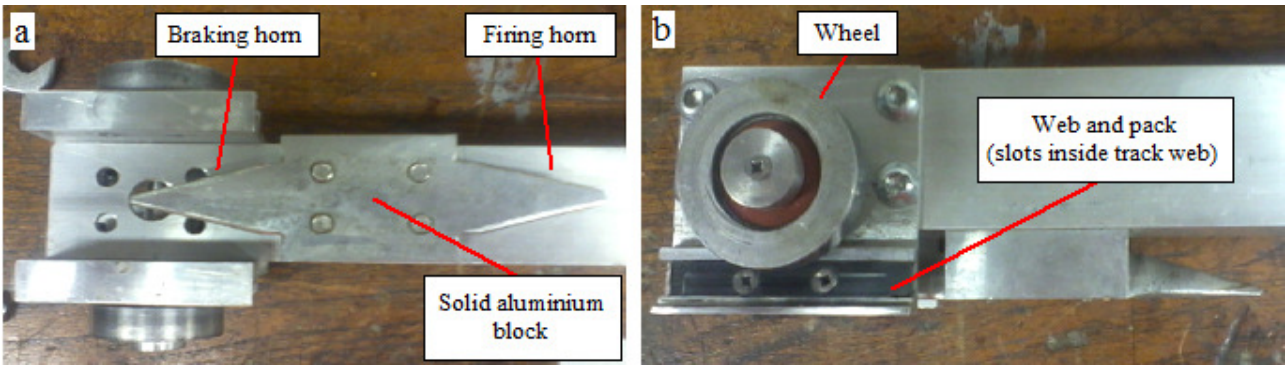

Figure 3.6.1 - Main features of firing chassis front (a) underside and (b) side view (Soper, 2014).

Figure 3.6.2 - Trailing wheel within track web.

3.4 Trackside instrumentation

3.4.1 Cobra probes

Air velocity and static pressure were measured using Cobra probes (figure 3.7) manufactured by Turbulent Flow Instrumentation (TFI). The probe is 150 mm long and the head contains four 0.5 mm diameter pressure taps (figure 3.8). A reference pressure port at the tail of the probe was connected via pneumatic tubing to a location away from the air flow. The non-dimensionalised ratios of pressures from each tap are compared to pre-supplied calibration data, and the calculation of instantaneous air velocity in three components (to ±0.5 m/s and within 2 - 40 m/) and static pressure (within ±5 Pa) to be calculated (TFI, 2012). The probes have been used extensively at the TRAIN rig for slipstream measurements (Dorigatti, 2013; Gilbert 2013; Soper, 2014) and in other studies across academia and industry (TFI, n.d.). The advantages of such probes are that they are smaller and more suitable for model-scale tests than conventional anemometers (less flow interference and a greater precision in y-axis and z-

axis positioning from COT and TOR), they are more robust than conventional hot-wires and are supplied with software that has all the necessary calibration files already installed.

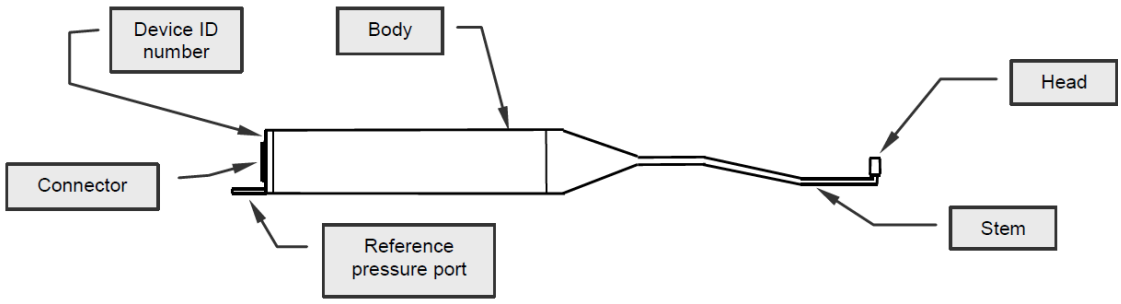

Figure 3.7 - Diagram of main features of a Cobra probe (TFI, 2012a).

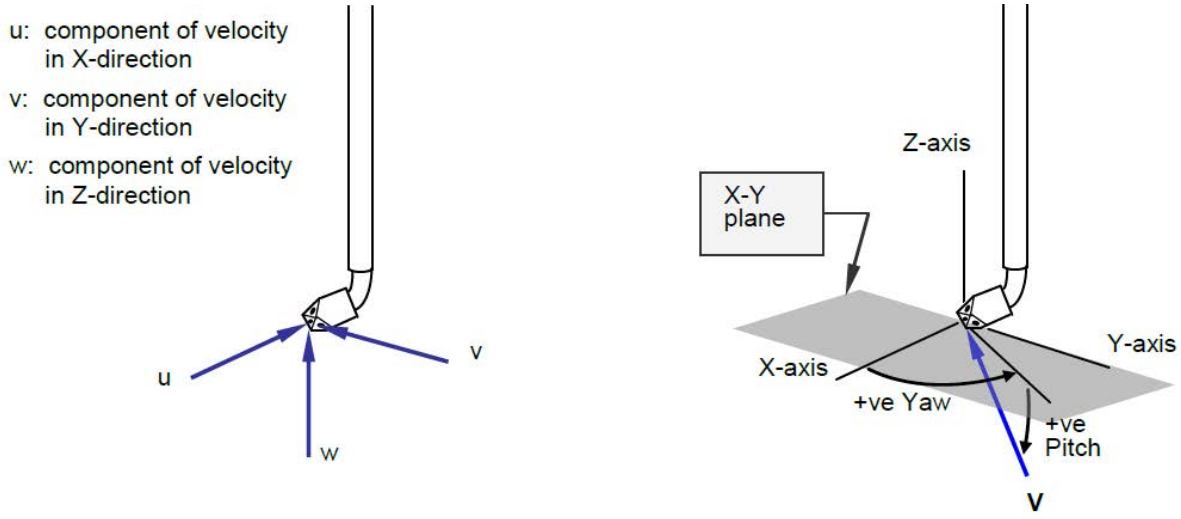

Figure 3.8 - Diagram showing axis configuration for a Cobra probe (TFI, 2012a). X-axis is aligned with primary (U) flow component.

The probe head has a ±45° cone of acceptance about its primary axis, and so any flow that is outside of this cone will not be recorded, resulting in zero values in the instantaneous data time series. This was most noticeable in the nose region of the slipstream (see sections 4.5 and 5.3.1).

The probes are also sensitive to mechanical vibration that is caused by the initial firing of the train model and the movement of the model on the track. This noise manifested as a non-zero velocity but was less than the minimum velocity capability of the probes of 2 m/s. To physically reduce the effects of mechanical vibration, the probes were mounted on a robust horizontal stand that was not in direct contact with the track structure (figure 3.12).

3.4.2 Train speed measurements

Train speed was measured using two photo-electric position finders, referred to as light gates (LG). These sensors work by using a light source and a detector to create a ray of light across the tracks. When two LG pairs are spaced some distance apart, 1 m in the case of this investigation, the speed of the train is calculated by a bespoke interface box, which displays the speed immediately allowing the speed of each run to be checked. A second pair of LGs were set up roughly 6 m further along the track in the direction of train travel to allow the deceleration of the train through the test section to be estimated. A linear deceleration was assumed over this relatively short distance of the test section, and was generally less than 0.5 m/s when the HST was fired at 40 m/s. The vertical height was consistent for each light gate to ensure that the LG beam was broken at the same position relative to the train nose.

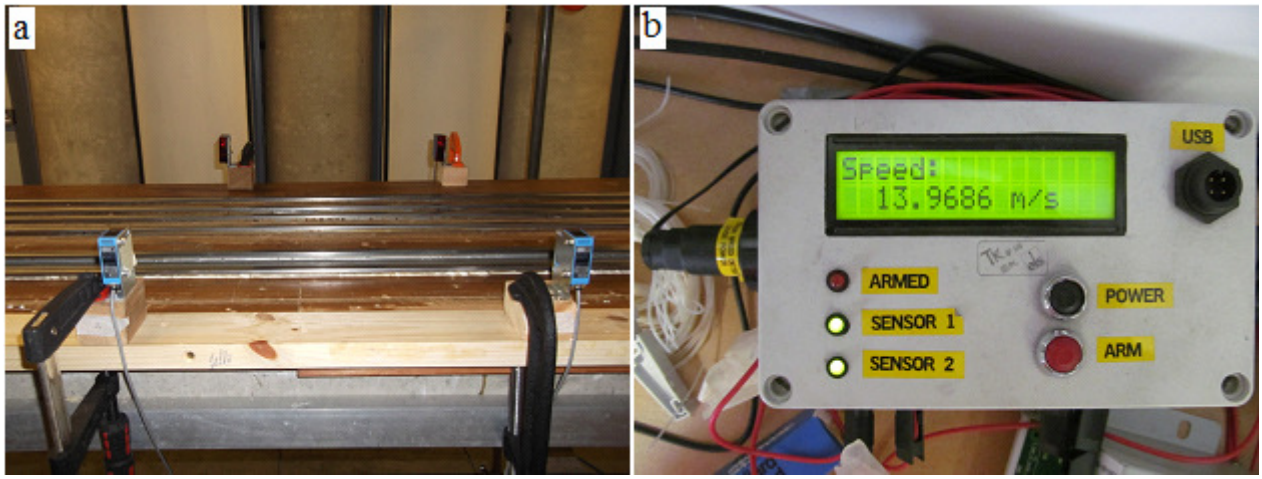

Figure 3.9 - (a) - Set of light gates spaced at 1 m, and (b) - light gate speed display box.

3.4.3 Ambient conditions

The ambient temperature and humidity were recorded using a Oregon Scientific BAR208HGA weather station, to an accuracy of ±0.1°c and ±1% respectively. The ambient pressure was recorded by a GBP3300 Digital Barometer to ±100 Pa shown in figure 3.10. Ambient conditions were manually recorded just before the train was fired for each run in an Excel spreadsheet, and the temperature and pressure were always inputted into the TFI control software for the Cobra probes.

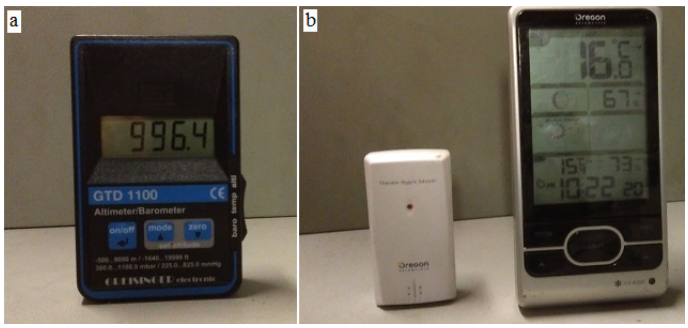

Figure 3.10 - Ambient condition monitors (a) barometer and (b) weather station (temperature and humidity).

3.5 Aims and objectives of slipstream experiments

3.5.1 Preliminary investigations

The aim of these measurements was to investigate the slipstream of the HST in order to determine appropriate testing parameters for later investigations, such as ground configuration, ensemble average size, train speed and measurement positions. Three separate investigations were carried out:

- Four sets of 20 runs at train speeds of 20, 30, 40 and 50 m/s to investigate Re number effects on the slipstream and pressure transient of the HST, and also to determine the optimum speed for testing the HST.
- A large ensemble (100 runs) at a single measurement position (3 m from COT, 0.2 m from TOR) with a ballast height of 0.3 m to consider the effect of ensemble size.
- One set of 20 runs at 3 m from COT, 0.2 m above TOR with a 0.3 m ballast height with the HST model fired in reverse to investigate the effects of the firing chassis on the slipstream (in the nose region and start of the boundary layer region). Note that this test was undertaken after the majority of the slipstreams tests were completed.

The findings from the preliminary investigations are presented in appendix B.

3.5.2 Detailed flow characterisation of the HST

The aim of this test was to measure the slipstream of the HST at various fixed trackside positions and with a ballast height of 0.3 m (which is typical of most of the track in the UK, and matched the ballast height at the Uffington test site). The measurement positions are

specified in table 3.2, which also includes the measurement positions for the ballast height tests (described in section 3.5.3) since these were part of the same testing campaign.

3.5.3 Effect of ballast height on flow development

The aim of this test was to investigate the effect of different ballast heights on the flow development and magnitudes of slipstream velocities and static pressure transients of an HST, and also a Class 66 freight train and ICE2 - all models are at 1:25th scale. It was hypothesised that by increasing the ballast height, the trailing vortices would have a larger spatial volume to spread out into and hence the wake peaks in slipstream velocity, when measured at the trackside TSI position, would decrease as ballast shoulder height was increased. A range of measurement positions (defined in table 3.2 and figure 3.13) were selected in order to conduct a detailed investigation. The findings from this investigation have been published in Soper et al., (2016), and the results for the freight train and ICE2 are presented in appendix C - this PhD study focuses solely on the HST.

Table 3.1 - Summary of properties for the HST, ICE2 and Class 66 trains used for the ballast shoulder investigations (lengths given at model scale)

Train type	Length (mm)	Width (mm)	Train height from TOR (mm)	Investigative train speed (m/s)	Reynolds number ($\times 10^5$)	Configuration
HST	3275	110	156	40	4.2	2+2
Freight	7950	106	156	33.5	3.5	loco and 8 containers
ICE2	4215	123	156	40	4.2	2+2

3.6 Experimental set up

The open air test section was instrumented with four Cobra probes that were mounted on a rigid stand that allowed four probes to be mounted horizontally at the same height above TOR. The stand was only in contact with the ground, i.e., there was no load path between the concrete track bed and the stand in order to mitigate the effects of mechanical vibration. The probes were spaced at intervals corresponding to 20 m at full scale, which allowed each probe to be considered independent (European Commission, 2008). The actual distances between the Cobra probes and the light gates are shown in figure 3.11. The horizontal distances of the probes were staggered so that probe D would be the furthest distance from COT and probe A would be the closest to COT in order to reduce the effects of flow interference.

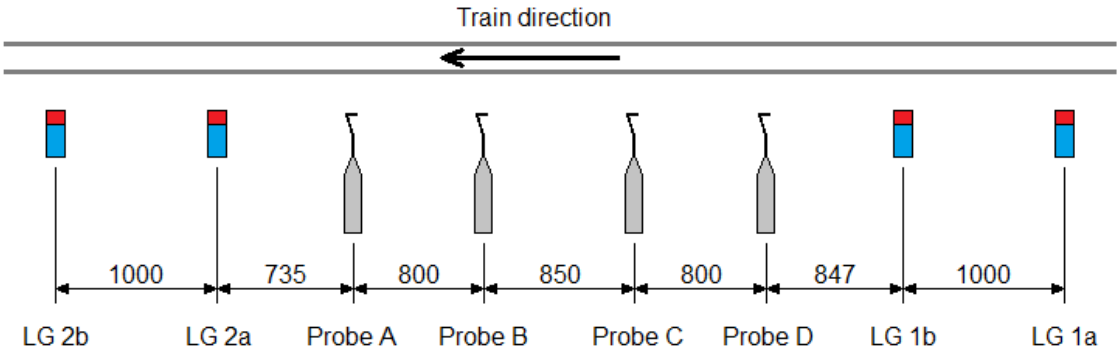

Figure 3.11 - Overview of testing section to show Cobra probe and light gate positions.

3.6.1 Ground configurations and measurement positions

The HST model on the TRAIN rig tracks and ground is shown in figure 3.12, and a rear elevation of the HST on the tracks with the probe measurement positions is shown in figure 3.13. A range of ballast heights were tested with the HST; which included full scale heights of 0 m, 0.3 m, 0.75 m, 1 m and 1.5 m. The Cobra probe positions shown in figure 3.13 were not tested for every ground configuration - table 3.2 lists the Cobra probe measurement positions for each ballast shoulder height. It should be noted that the tracks at the TRAIN rig are not representative of full scale rails, which effectively increases the vertical distance between the cess level and the TOR by 0.3 m (i.e., TOR to cess is 1.05 m). The required ballast height for wind tunnel tests in CEN is 825 mm (see figure 6.3) and the total height with rails is 1 m from TOR to cess level. The results from the 0.75 m ballast height in this experiment should therefore be comparable to those made with a CEN compliant ballast given the closeness of the total height of the TOR to cess.

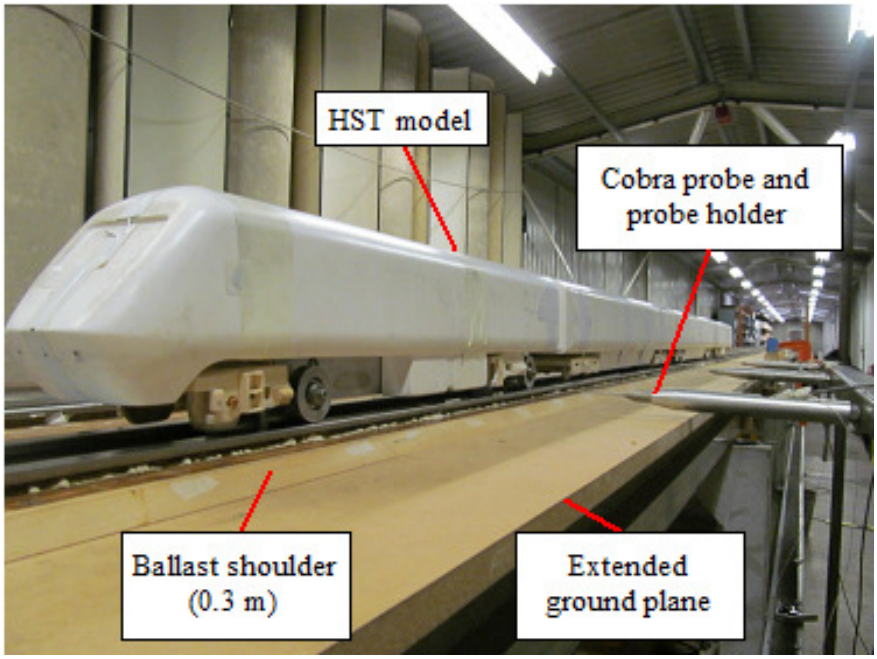

Figure 3.12 - HST in the open air test section at TRAIN rig showing ballast shoulder ground configuration and Cobra probes.

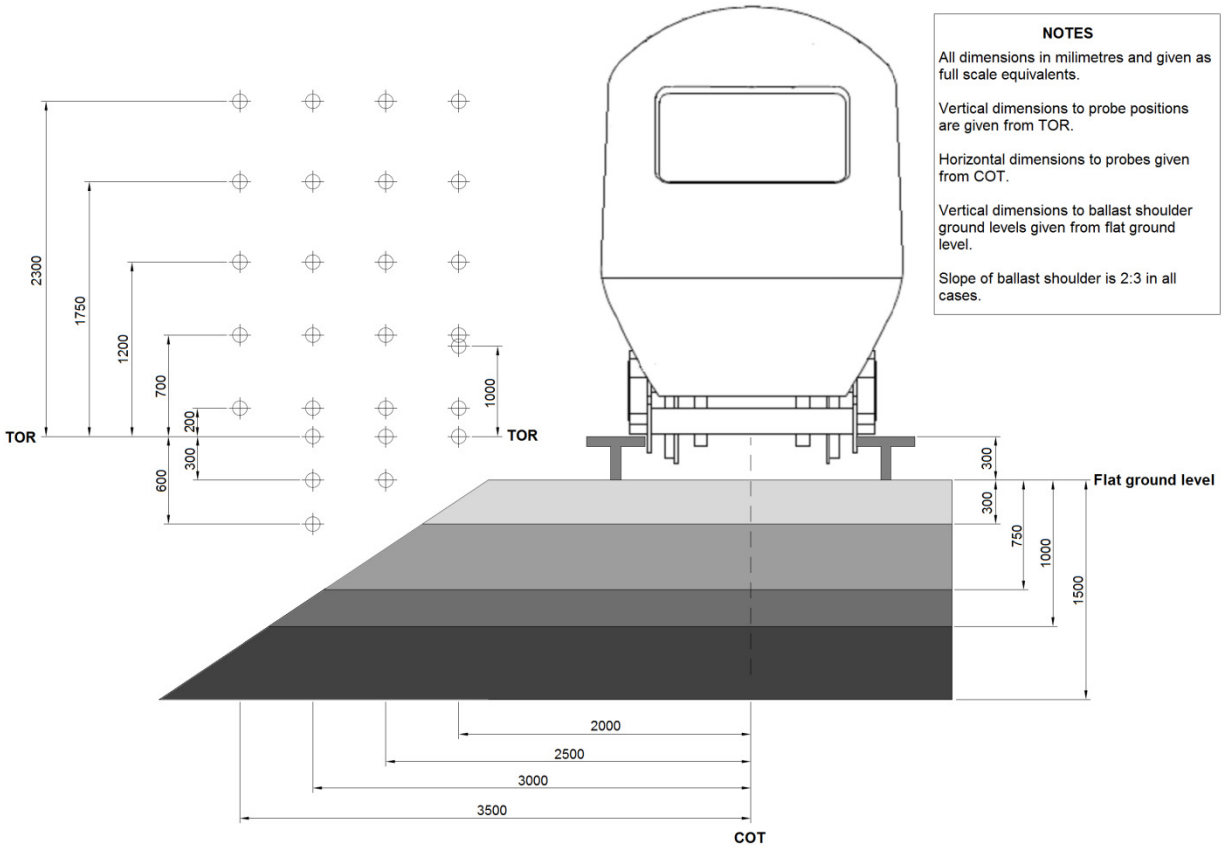

Figure 3.13 - Rear elevation of HST on TRAIN rig tracks to show Cobra probe measurement positions and different ground configurations (all dimensions are at full scale).

Table 3.2 - Full scale equivalent Cobra probe measurement positions for slipstream measurements of the HST for different ballast heights.

Key: x = HST only, **X** = HST and freight, **X*** = HST, freight and ICE2.

Measurement position		Ballast height (m)				
From COT (m)	From TOR (m)	0.0	0.3	0.7	1.0	1.5
2.0	0.0	**X**	**X**	**X**	-	**X**
	0.2	**X**	**X**	**X**	-	**X**
	0.7	**X**	**X**	**X**	-	-
	1.0	-	**X**	-	-	-
	1.2	**X**	**X**	**X**	-	**X**
	1.75	-	x	-	-	-
	2.3	-	x	-	-	-
2.5	-0.3	-	**X**	**X**	-	**X**
	0.0	-	**X**	-	-	**X**
	0.2	-	**X**	-	-	**X**
	0.7	-	**X**	-	-	-
	1.2	-	**X**	-	-	-
	1.75	-	x	-	-	-
	2.3	-	x	-	-	-
3.0	-0.6	-	-	**X**	**X**	**X**
	-0.3	-	**X**	**X***	**X**	**X***
	0.0	**X**	**X**	**X**	-	**X**
	0.2	**X***	**X**	**X***	**X**	**X***
	0.7	**X**	**X**	**X**	-	-
	1.2	**X***	**X**	**X***	**X**	**X***
	1.75	-	x	-	-	-
	2.3	-	x	-	-	-
3.5	0.2	-	x	-	-	x
	0.7	-	x	-	-	-
	1.2	-	x	-	-	-
	1.75	-	x	-	-	-
	2.3	-	x	-	-	-

CHAPTER 4

MODEL-SCALE SLIPSTREAM TESTS - ANALYTICAL METHODOLOGY

4.1 Introduction

Chapter 4 outlines the procedure by which raw data was acquired and converted into a useful format. Acquisition and conversion of the data is described in section 4.2. Preliminary data alignment and conversion to normalised variables is described in section 4.3, and secondary processing such as realignment by resampling the data is described in section 4.4 along with the application of a low-pass filter. The subsequent stages of analysis, such as the ensemble averaging procedure, calculation of standard deviations and boundary layer properties (turbulence intensity and displacement thickness) are described in section 4.5. Section 4.6 considers the experimental errors and uncertainties associated with the measurements (see appendix F for more detail). Section 4.7 describes application of the TSI gust analysis (introduced in section 2.3.3) to the model scale experiments.

4.2 Data acquisition and conversion

Scale model slipstream and static pressure data was recorded by Cobra probes (described in section 3.4.1). Data sampling parameters were specified before each run and manually entered into the graphical user interface (GUI) software supplied with the probes, shown in figure 4.1. Data was sampled at 5000 Hz, and then processed by the TFI data acquisition software to prevent data aliasing - data was oversampled by a factor of 2, passed through a digital low-pass anti-aliasing filter, then data was down-sampled by a factor of 2 (TFI, 2012a) hence the output data files were at 5000 Hz. For the HST model running at 40 m/s, this corresponds to one sample every 8 mm at model scale (0.2 m at full scale). The probes were set to sample for 20 seconds which ensured that there would be at least 10 seconds of data after the tail passage of the train to meet TSI requirements (European Commission, 2008). A total of four Cobra probes were used for each run and they were connected to the four available channels on the A/D unit (figure 3.8) supplied by TFI, which allowed the four probes to sample data simultaneously. The data files from each run were saved on the PC in the format 'TRAIN_GROUND_RUN.extension' where train was either HST, F66 or ICE2, "ground" defined the ballast shoulder, run was the run number and the file extension was in the format '.thA' where "th" meant time history and A represented the probe i.e., probe A was in channel 1, probe B was in channel 2 etc. A total of four data files were obtained for each run; each file was approximately 1.6 MB and contained four columns for u, v, w and static pressure (in m/s and Pa respectively). The raw data files were converted to a readable format using a Matlab script "readTHfile" written by TFI, which produced vector variable outputs for each velocity component and static pressure, as well as single value outputs for temperature and ambient pressure. This allowed analysis to be automated to assure the quality of the processed data.

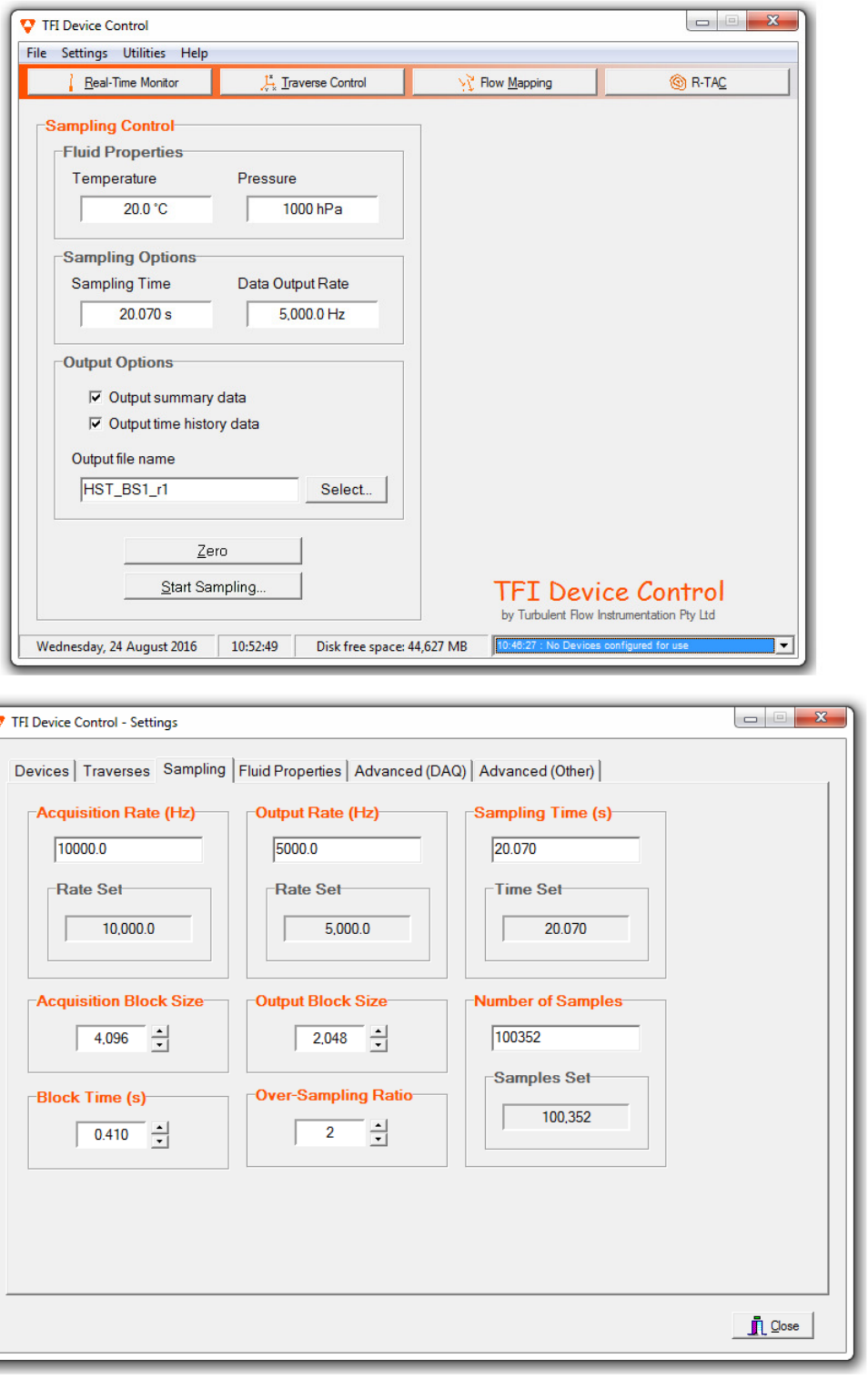

Figure 4.1 - Graphical user interface of the TFI software.

4.3 Data alignment and non-dimensionalised variables

The data was sampled at a constant frequency (F_{samp}) and for a constant duration. The time (in seconds) at a given point in the data relative to the origin is defined as:

$$T_{samp} = \frac{N_{samp} - 1}{F_{samp}} \tag{4.1}$$

Where N_{samp} is the sample number relative to the origin.

During processing, the origin (T = 0 s) was defined as the nose passage of the train, defined as the time at which the minimum static pressure created by the nose pulse was recorded - this method also resulted in good alignment with the nose peak due to the inviscid nature of the nose flow (Baker, 2010, Baker et al., 2013a).

The convention for slipstream velocities and pressures is to normalise the data with respect to train speed and dynamic pressure (as in equations 2.2 and 2.4). At the TRAIN rig, train speed was calculated by two pairs of light gates which recorded the speed of the HST nose as it broke the beams. A linear deceleration was assumed throughout the test section, and $V_{train|r}$ (train speed per run) was calculated and assumed constant for each individual probe (i.e., deceleration while the train passed the probe was disregarded). The normalised values for the three velocity components are therefore:

$$U(t)_r = \frac{u(t)_r}{V_{train|r}} \tag{4.2a}$$

$$V(t)_r = \frac{v(t)_r}{V_{train|r}} \tag{4.2b}$$

$$W(t)_r = \frac{w(t)_r}{V_{train|r}} \tag{4.2c}$$

Where upper case U, V and W are the normalised velocity components of the dimensional velocity components u, v and w, (t) indicates that these are instantaneous values with respect to time, the subscript r defines each individual run.

Much of the analysis that follows concerns the resultant of the horizontal velocity:

$$U_{res}(t)_r = \sqrt{U(t)_r{}^2 + V(t)_r{}^2} \tag{4.3}$$

Static pressure $(P(t)_r - P_{AMB|r})$ was normalised to pressure coefficients $C_p(t)_r$ using the following equation:

$$C_p(t)_r = \frac{P(t)_r - P_{AMB|r}}{\frac{1}{2}\rho_r V_{train|r}^2} \tag{4.4}$$

Where $P(t)_r$ is the total instantaneous static pressure and $P_{AMB|r}$ is the ambient pressure recorded with the barometer per run. The Cobra probe software automatically calculates the static pressure $(P(t)_r - P_{AMB|r})$. The density of air for each run is defined as:

$$\rho_r = \frac{P_{AMB|r}}{RT_r} \tag{4.5}$$

Where T_r is the ambient temperature in Kelvin for each run.

The x axis was expressed as model scale distance by:

$$x = V_{train|r} T_{samp} \tag{4.6}$$

As all the TRAIN rig models were 1:25th scale, distance can be represented as full scale distance by multiplying by 25,

$$x_{FS} = x \times 25 \tag{4.7}$$

Though it was preferred to normalise the x axis with respect to train length:

$$x_{norm} = \frac{x}{L_{train}} \tag{4.8}$$

Where L_{train} is the length of the train in metres at model scale.

It should be noted that regardless of the x-axis definition, all data was aligned at the positive peak of the nose pressure pulse in all proceeding analysis (in most cases corresponding to the maximum value from equation 4.4).

4.4 Secondary data processing: resampling and filtering

The run to run variability in train speeds was permitted to be within ± 3% of the nominal investigative train speed, V_{train} (given in table 3.1 for each train tested) as required by CEN, (2005). For the HST, V_{train}= 40 m/s, hence all runs between 38.8 m/s < $V_{train|r}$ < 41.2 m/s were acceptable. Data was resampled to the nominal investigative train speed to reduce x-axis misalignment which would affect the ensemble quality at the tail. The consequence of resampling the data is a change in the sampling frequency related to the differences between $V_{train|r}$ and V_{train},

$$F_{resamp|r} = F_{samp} \frac{V_{train|r}}{V_{train}} \tag{4.9}$$

Where $F_{resamp|r}$ is the modified sampling frequency of each resampled run. It was therefore necessary to apply the low-pass filter to the raw data signal before it was resampled. However, in order to apply the low-pass filter, the data needed to be a continuous time series. The Cobra probes would record instantaneous zero values (of u, v, w and P) when the air flow fell outside of the ±45° cone of acceptance, resulting in gaps in the data . This was most notable in the nose region (for all runs) and arising due to a recirculating airflow from the nose (and hence a negative streamwise U component) illustrated in the ensemble average shown in figure 4.3. The zero values were removed and the data was temporarily linearly interpolated to allow the application of a filter. A first-order low-pass Butterworth filter with a cut-off frequency of 650 Hz was applied to the data using the "butter" and "filt" functions on Matlab, (Mathworks, 2010), in order to remove any high frequency portion of the signal that was above the maximum frequency response of the Cobra probe. The data was then adjusted for phase shift due to the filtering by realigning the x-axis origin at the nose pressure pulse maximum. Each filtered and temporarily interpolated run was then resampled using the "resample" function on Matlab, (Mathworks, 2010), with respect to train speed. Once the data had been resampled, the temporarily interpolated data was removed from each run.

4.5 Slipstream velocity data analysis

The TSI and CEN both state that an ensemble average should be formed by taking an average of U_{res} from at least 20 acceptable runs (European Commission, 2008; CEN, 2005). This process requires that a moving train should pass a stationary probe at a fixed axial coordinate

position (y, z) a number of times, hence a time domain signal is recorded "N" times. The ensemble average is defined as:

$$\bar{c}(x) = \frac{1}{N}\sum_{r=1}^{N} c_r(x) \tag{4.10}$$

Where N is the number of independent measurements, i.e., the ensemble size.

The ±45° cone of acceptance of the Cobra probe results in instantaneous values of zero whenever the flow falls outside of this cone - figure 4.2 shows the raw data from a single run with the zero values included. A "moving window" ensemble was therefore adopted and N was defined at each x-axis interval (i.e., each sample once data had been resampled). When taking an ensemble average, the zero value data was disregarded which therefore decreased the ensemble size, N, at specific positions - most notable in the nose region. The lower case n refers to the moving ensemble size at a given position, i.e., $n(x) \leq N(x)$. Figure 4.3 shows the percentage of good data (i.e., percentage of real values out of the ensemble size) as a function of sampling time with respect to the ensemble average, and shows that the majority of zero values were recorded at the nose of the train (i.e., 50% good data indicates equivalent moving ensemble size). Other types of sensors such as ultrasonic anemometers and hot wires do not have the same issues of data drop out, though they are not as convenient to use as Cobra probes at the TRAIN rig. It should also be noted that data drop out in the nose region is not of primary concern since that the largest slipstream magnitudes (that are of interest in this study) are in the train wake, and given that the nose flow is inviscid (Baker, 2010) a smaller ensemble size should be acceptable in the nose region anyway.

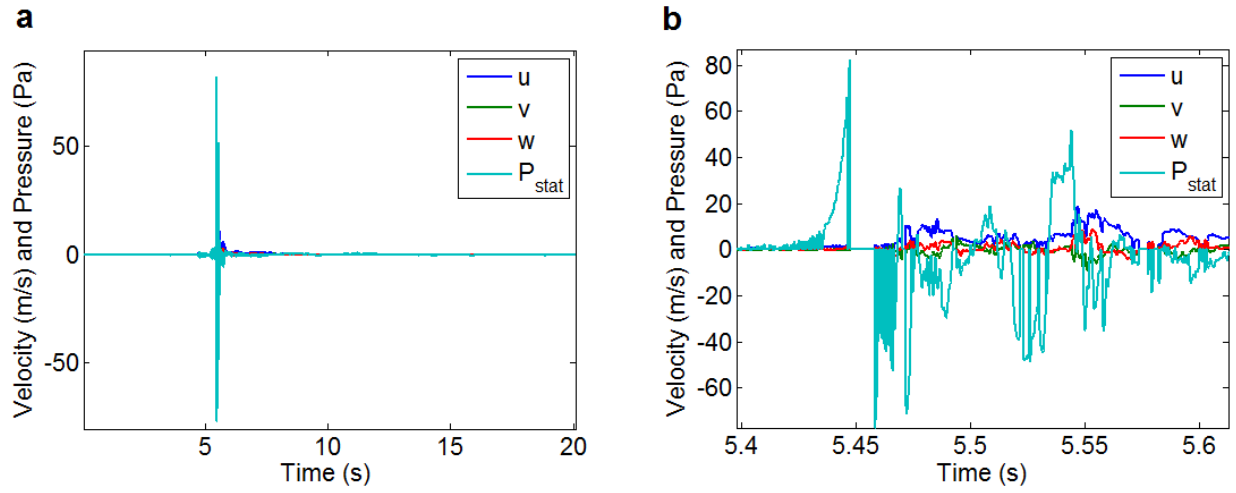

Figure 4.2 - Velocity and pressure for an individual raw run of the HST at 3 m from COT and 0.2 m above TOR showing zero values in the data - (a) entire sampling duration and (b) train passage).

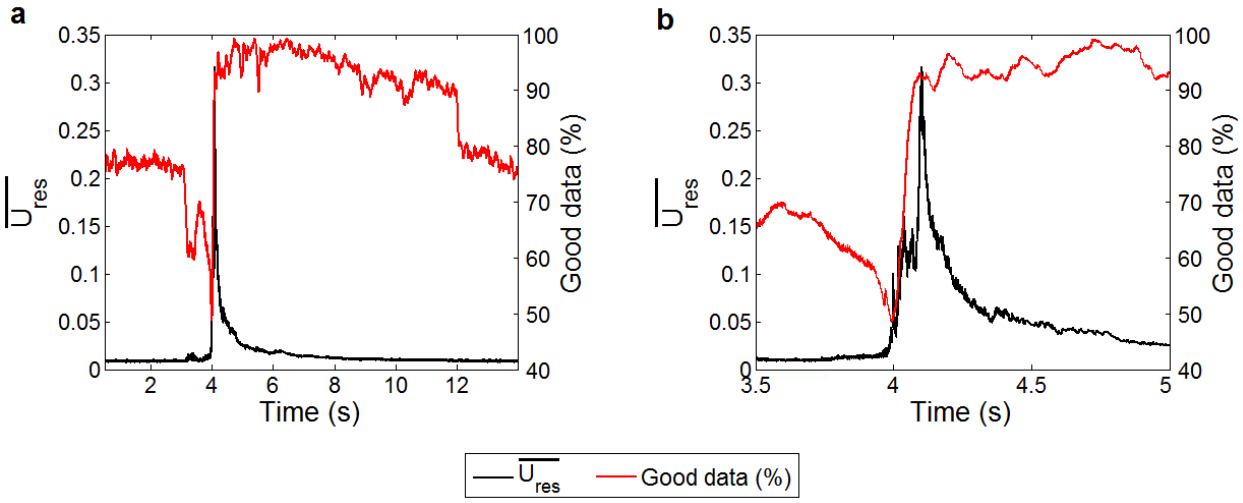

Figure 4.3 - Percentage of good data relative to ensemble average slipstream velocity (in red) and ensemble average velocity (in black) for (a) entire sampling duration and (b) during the train passage, at 3 m from COT and 0.2 m above TOR for ballast height of 0.3 m taken from 100 runs. X-axis is in time (the ensemble was arbitrarily aligned at 4 s).

The variance $var(x)$ and standard deviation $\sigma(x)$ are defined as follows:

$$\overline{c^2}(x) = \frac{1}{n}\sum_{r=1}^{n} c_r^2(x) \tag{4.11a}$$

$$var(x) = \overline{c^2}(x) - \bar{c}(x)^2 \tag{4.11b}$$

$$\sigma(x) = \sqrt{var(x)} \tag{4.12}$$

Note that an ensemble average, variance and standard deviation can be calculated this way from any individual vector or resultant velocity component or from static pressure or pressure coefficients. An overbar is used to define an ensemble averaged time series, hence $\overline{U}$, $\overline{V}$, $\overline{W}$, $\overline{U_{res}}$ and $\overline{C_p}$ define the ensemble averages of the individual velocity components, resultant horizontal velocity and pressure coefficient respectively.

4.5.1 Turbulence intensity

The movement of the train, no-slip condition and viscosity of air create shear, which results in turbulence within the boundary layer (Baker, 2010). For flows that are non-stationary such as a slipstream, where there are different flow regions (Baker, 2010), it is only appropriate to consider the turbulence intensity within the boundary layer region.

As the train is moving in relation to the velocity probe, a moving frame of reference approach needs to be taken (Sterling et al., 2008a). For slipstreams, and within the boundary layer region, turbulence intensity, $I_u(x)$, at a given distance, x, is expressed as the ratio of the

standard deviation of the streamwise ensemble velocity, $\sigma_u(x)$, to one minus the normalised streamwise ensemble mean, $1 - (\overline{U}(x))$:

$$I_u(x) = \frac{\sigma_u(x)}{(1 - (\overline{U}(x)))} \tag{4.13}$$

4.5.2 Displacement thickness

Displacement thickness considers the two-dimensional boundary layer, which for the three-dimensional and highly turbulent boundary layer of a train is only slightly appropriate - however it is felt to give a useful indication of boundary layer thickness (Sterling et al., 2008a; Baker, 2010). Given that the train is moving passed a fixed measurement point, the definition of displacement thickness in equation 2.13 is adapted, resulting in:

$$\delta^* = \int_{y'=0}^{\infty} U \, dy \tag{4.15}$$

Essentially, δ^* is calculated through integration of the horizontal boundary layer profile between the train side wall and the boundary layer edge.

4.6 Error analysis

Errors were calculated as the sum of bias limit (due to equipment inaccuracies) and random uncertainty within the ensemble (defined in equations F.1 to F.3). The procedure and the results of the error analysis are described in detail in appendix F. Figure 4.4 shows the bias limit, random uncertainty and total error for all measurement positions tested for the 0.3 m

ballast height, where measurement positions are presented in ascending distance from COT, then within each block (i.e., all positions at fixed distance from COT) for ascending height above TOR (and are defined in table F.3.1.2).

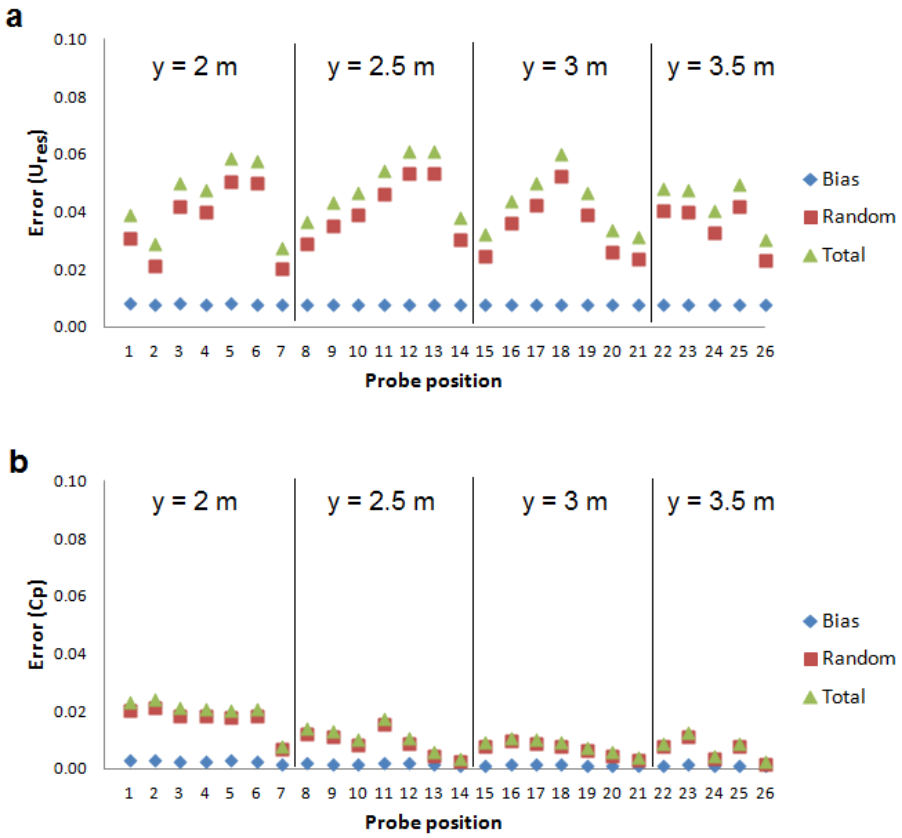

Figure 4.4 - Absolute errors - bias error, random uncertainty and total error for 0.3 m high ballast for all measurement positions (defined in table F.3.1.2) for (a) resultant horizontal velocity and (b) pressure coefficient.

Figure 4.4 shows that the errors are more sensitive to vertical measurement position than for distance from COT, and that random uncertainty is the largest contribution to total error for measurements of both U_{res} and C_P. The values of errors are similar to those found by Soper,

(2014), who used the same methodology to calculate errors based on Dorigatti, (2013), and found absolute total errors of approximately 0.06 - though the errors for the HST are slightly lower, due mostly to the higher train speed therefore lower fractional contribution of train speed uncertainty divided by train speed (since the same equipment was used) - see equation F.1. Overall values of error, taken as the mean plus two standard deviations of all of the total errors, are 0.06 and 0.02 for $\overline{U_{res}}$ and $\overline{C_P}$ respectively (roughly equivalent to a velocity of 2.4 m/s and a pressure of 19 Pa at 40 m/s).

4.7 TSI analysis

The TSI analysis was described in section 2.3.3and this section describes the application of the TSI procedure to model scale tests. The resultant horizontal velocity component is then obtained using equation 4.3. The TSI (which applies to full-scale tests) requires that each run is then filtered using a low-pass 1 second moving average filter at full-scale, and so the filter period is converted to model-scale by:

$$T_{model\ scale} = \frac{z_{train|model\ scale}}{z_{train|full\ scale}} \times \frac{V_{train|full\ scale}}{V_{train|model\ scale}} \times T_{full\ scale} \tag{4.16}$$

Where $T_{model\ scale}$ and $T_{full\ scale}$ are the moving average periods (in seconds) at model and full scale, $z_{train|model\ scale}$ and $z_{train|full\ scale}$ represent the train heights at model and full scale (the fractional expression is 1/25 in all cases), and $V_{train|model\ scale}$ and $V_{train|full\ scale}$ are the nominal train speeds.

The maximum resultant horizontal velocity, $U_{res|r}(\max)$, of each filtered run is then found resulting in an ensemble of N peak velocity values. The mean of these maxima, $\overline{U_{res}}(\max)$, is found by:

$$\overline{U_{res}}(max) = \frac{1}{N}\sum_{r=1}^{N} U_{res|r}(max) \tag{4.17}$$

The TSI value, $U_{2\sigma}$, is then calculated as the peak gust within this ensemble assuming a normal distribution (which is sensible based on previous studies on guests such as Baker et al., 2014b), with a 95% confidence interval, i.e., the mean plus two standard deviations of the ensemble of $U_{res|r}(\max)$:

$$U_{2\sigma} = \overline{U_{res}}(max) + 2\sigma_{TSI} \tag{4.18}$$

The TSI value can be represented as a dimensional value at full scale by multiplying by the full scale train speed which is 55.6 m/s for the HST:

$$U_{2\sigma|full\ scale} = U_{2\sigma} V_{train|full\ scale} \tag{4.19}$$

CHAPTER 5

MODEL-SCALE SLIPSTREAM TESTS - RESULTS AND DISCUSSION

5.1 Introduction

Chapter 5 presents the experimental results from the TRAIN rig tests to investigate the slipstream and pressure transients of an HST. The results of the tests that consider the effect of ballast height on flow development have been published in Soper et al., (2016), and full results are presented in appendix C, and so ballast height effects are not considered at length in this chapter. Preliminary slipstream experiments are presented in appendix B, and consider the effect of ensemble size, train speed and the underbody (by firing the HST in reverse). From these initial investigations a train speed of 40 m/s and ensemble size of 20 runs were selected. The effects of firing the train in reverse are discussed in section 5.6. Section 5.2 presents the HST ensemble averages for slipstream velocities and pressures for the 0.3 m ballast height scenario (where the majority of measurements were made). Section 5.3 considers the main flow regions defined in Baker, (2010); the nose, boundary layer and wake regions with a 0.3 m ballast height. Section 5.4 briefly considers the effects of ballast height on the slipstream of an HST, Class 66 freight train and the ICE2. Section 5.5 presents the TSI

analysis of gusts for the HST at the prescribed measurement positions (see table 2.1), and discussion and closing remarks are made in section 5.6.

5.2 Ensemble averages of velocity and pressure with 0.3 m ballast height

All figures presented in this section are formed from 20 run ensemble averages. Consideration of the ensemble size is presented in section B.2.

The ensemble average velocity vector components are shown at positions of 3 m from COT and 0.2 m and 1.2 m above TOR for the 0.3 m ballast height in figure 5.1. Generally, the magnitude of $\overline{U_{res}}$ is dominated by the streamwise velocity, $\overline{U}$, the exception is at the nose region (considered in section 5.3.1). The vertical component ($\overline{W}$) shows low magnitudes along the train sides, and the negative component immediately after the train passage indicates some element of downwash from the roof in the near wake from a tailing vortex.

The effect of underbody equipment - namely the firing chassis shown previously in figure 3.6.1 - was considered in an additional experiment reported in appendix B where the HST model was fired in the reverse direction (i.e., firing chassis was at the rear of the train). Figure 5.1.2 compares the ensemble averages $\overline{U_{res}}$ and $\overline{C_P}$ for the forwards and reverse directions at 3 m from COT and 0.2 m above TOR. There is quite clearly an effect from the firing chassis; a relatively large velocity peak was observed after the nose peak, and the average velocity was greater along the length of the train when the HST was fired in the forwards direction. In the reverse direction, the wake velocity peak was greater. The firing chassis also has an apparent

effect on the nose pressure coefficient - when the HST was fired in the forwards direction there is an asymmetry about the x axis (i.e., the negative peak is larger than the positive peak), and also both the positive and negative peaks are larger when the HST is in the forwards direction. The effect of the firing chassis on the pressure peak has been noted in previous studies (Gilbert, 2013), but this is the first time such an effect was seen on $\overline{U_{res}}$. It should be stressed that only a single measurement position was tested with the HST model in the reverse direction due to time constrains, therefore it is difficult to draw firm conclusions from figure 5.1.2. However, given that in this study the wake flows are of most interest, the HST was fired in the forwards direction to prevent interference in the near wake flows from the firing chassis.

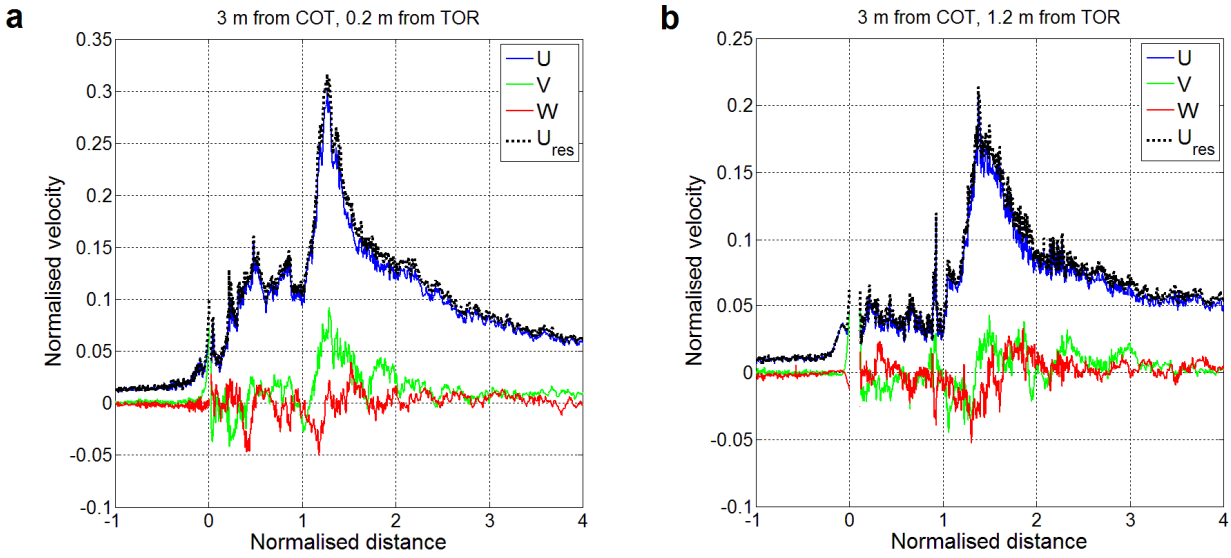

Figure 5.1.1 - Comparison of ensemble averaged velocity vector components, and resultant horizontal velocity at 3 m from COT and (a) 0.2 m above TOR, (b) 1.2 m above TOR, both with 0.3 m ballast height.

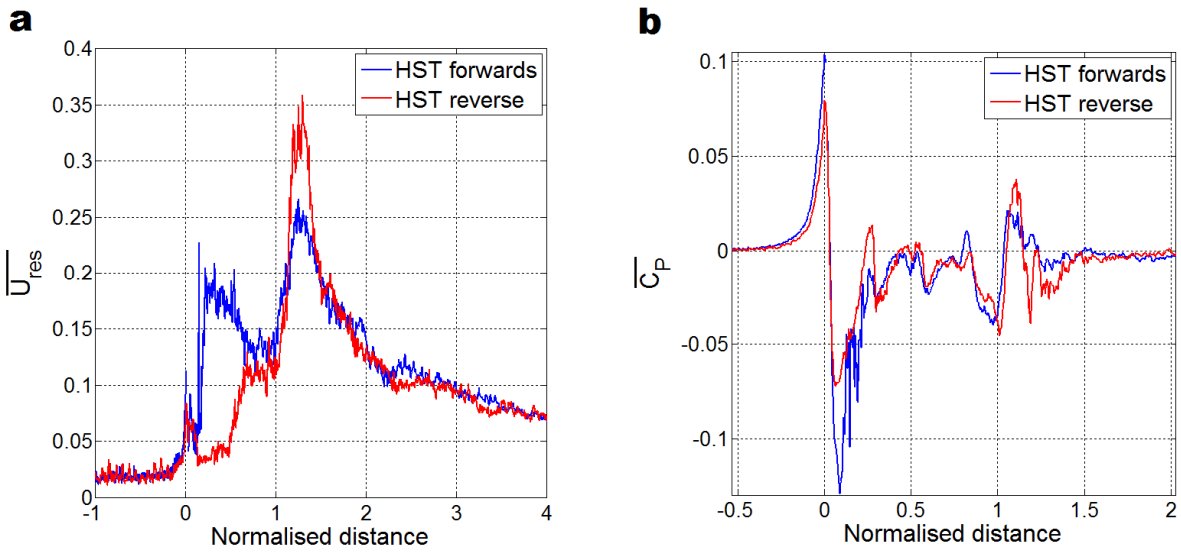

Figure 5.1.2 - Comparison of HST in the forwards (blue) and reverse (red) directions for (a) ensemble average velocity and (b) ensemble pressure coefficient at 3 m from COT and 0.2 m above TOR.

The ensemble averages of $\overline{U_{res}}$ and $\overline{C_P}$ are shown in figure 5.2 at heights of 0.2 m and 1.2 m above TOR and at increasing distances from the COT. The effect of changing the vertical height of the probe is shown in figure 5.3. Figure 5.2 shows that as the distance from the COT is increased, there is a decrease in slipstream velocity in all of the flow regions (as seen in previous studies such as Sterling et al., 2008a). The large velocity peak immediately after the nose passage at 2 m from COT decreases significantly as the distance from COT is increased and at 3 m this nose peak is approximately 80% lower than 2 m from COT which is much larger than the reduction in the near wake velocity peak (which decreases by about 20% from 2 m to 3 m from COT). The large velocity peak immediately after the nose peak can also be seen on figure 5.2 (b) at 2 m from COT. There is a decrease in velocity in the boundary layer region as distance from COT is increased, which is more noticeable at 0.2 m above TOR. The boundary layer region is considered in more detail in section 5.3.2. At 1.2 m above TOR there

is very little difference in slipstream velocity between measurement positions of 3 m and 3.5 m from COT. Static pressure also decreases as distance from COT is increased.

The ensemble average velocity and pressure are shown in figure 5.3 across a range of heights above TOR for distances of 2 m and 3 m from the COT. Figures 5.3 (a) shows that $\overline{U_{Res}}$ is larger at low heights (up to 0.7 m above TOR) which is believed to be due to the roughness of the unshielded bogie region and is consistent with full scale studies (such as the AeroTRAIN work reported in Baker et al., 2014a). There is a slight decrease in the pressure coefficients as height increases, most notable when considering the head pressure pulse at 2 m from COT (as in figure 5.3a), though at 3 m from COT $\overline{C_P}$ shows little variation with height which suggests that train geometry only has a significant effect on static pressure close to the train sides. The overall form of the $\overline{C_P}$ time series is similar across all heights, and is consistent with previous studies (Mancini and Malfatti, 2001; Zhou et al., 2014). Figure 5.3 (a) and (b) shows three small negative peaks between the head and tail pressure pulses which correspond to the intercarriage gap locations. The large velocity peak immediately after the nose peak is most apparent at 2 m from COT, and this peak is present at heights of up to 1.75 m above TOR. The x-axis position of this peak corresponds with the large negative peak in pressure coefficient. In the most extreme case, i.e., close to the ground and the train sides, this velocity peak is most pronounced and as distance from the train increases to 3, to 3.5 m, this velocity peak is not detected (as shown in figure 5.2). Given that this peak is localised to measurement positions closer to the ground and train sides, and that it was not found in the reverse direction, it is believed that this peak is caused by a combination of the HST nose geometry and the underbody equipment at the nose of the train giving rise to trapped air beneath the train (which effectively changes the train nose geometry to a more bluff profile). Section B.4 describes tests where the model was fired in reverse (i.e., a different underbody geometry at

the nose) which found significant differences in velocity in pressure at 3 m from COT and 0.2 m above TOR. Figure 5.3 shows that at 2 m from the COT and 0.2 m above TOR, the nose pressure pulse is an asymmetric sinusoid (about the x-axis) where the negative peak is about 60-70% greater than the positive peak, and it is believed that this is also as a result of the underbody geometry.

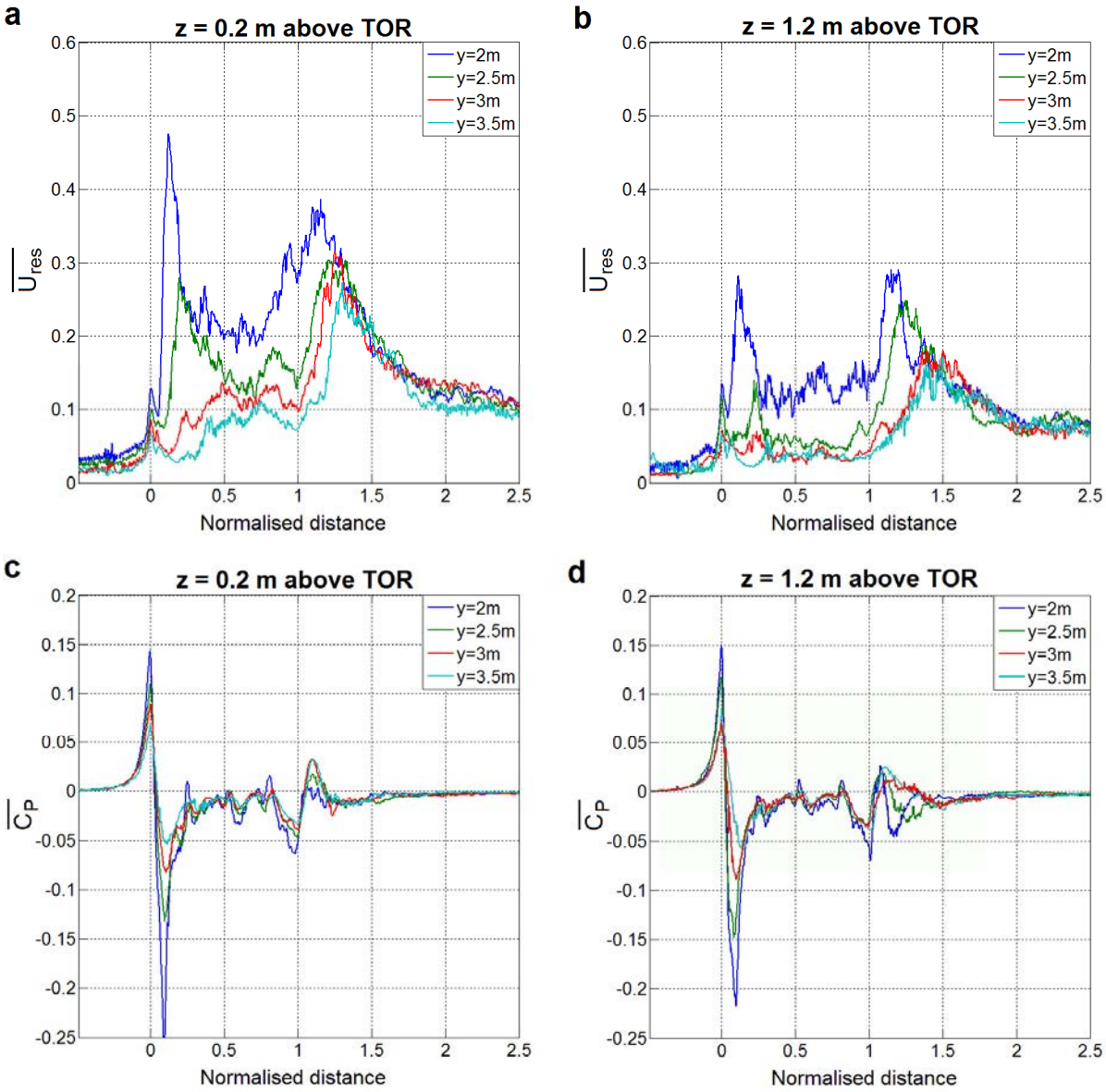

Figure 5.2 - Ensemble averages for HST with 0.3 m high ballast at increasing distances from COT (shown by coloured lines) - (a) and (b) show $\overline{U_{Res}}$ at 0.2 m and 1.2 m above TOR, and (c) and (d) show corresponding $\overline{C_P}$.

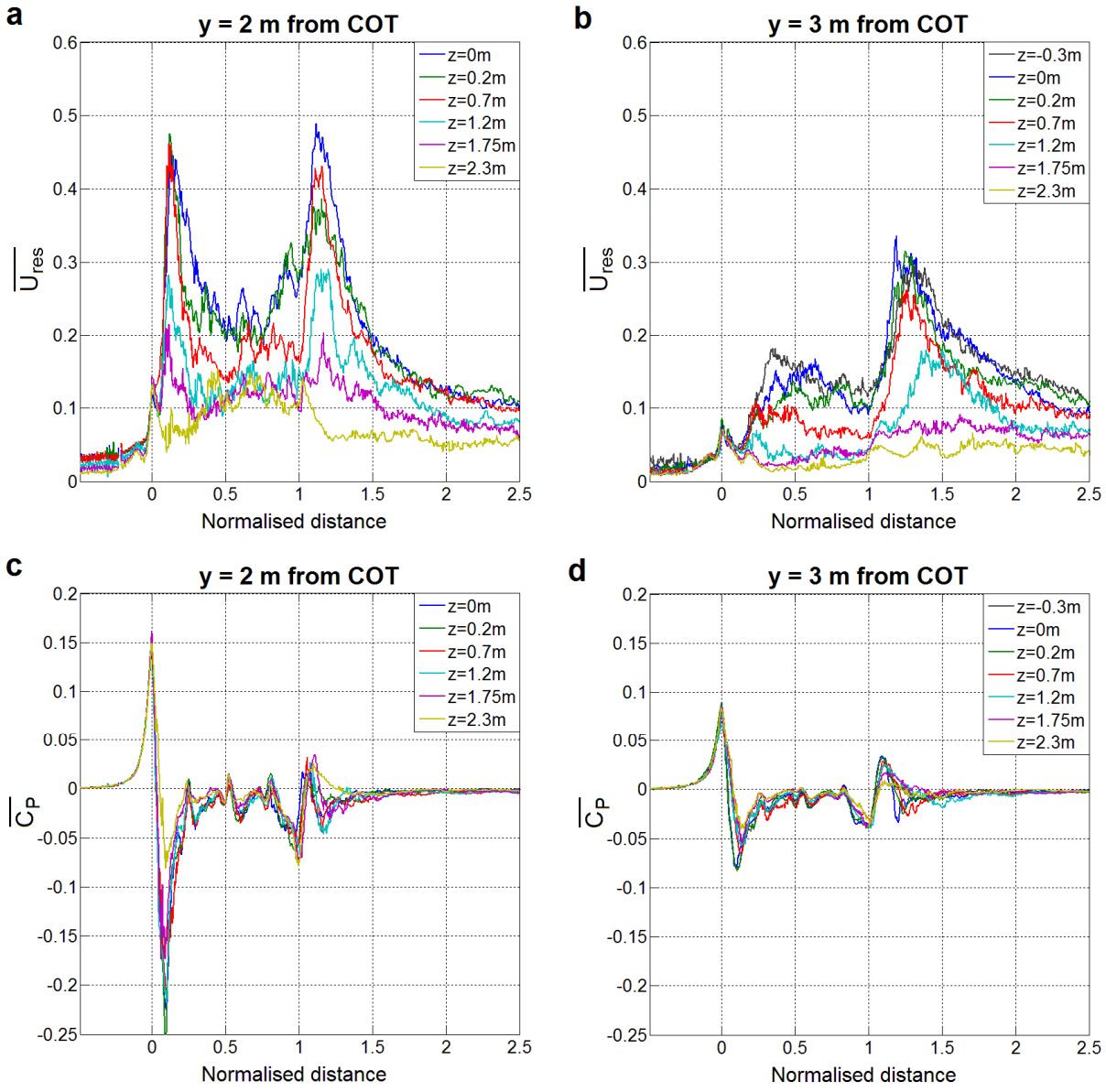

Figure 5.3 - Ensemble averages for HST with 0.3 m high ballast at increasing heights from TOR (shown by coloured lines) - (a) and (b) show $\overline{U_{Res}}$ at 2 m and 3 m from COT, and (c) and (d) show corresponding $\overline{C_P}$.

5.3 Slipstream velocities in different flow regions

5.3.1 Nose region

The nose region can be considered inviscid, and is usually well defined for most trains with a clear and reproducible peak in velocity and a sinusoidal pressure pulse (Sterling et al., 2008a; Baker, 2010; Baker et al., 2014a). For the HST model, the underbody equipment that is required to carry the model along the tracks is not representative of the full scale geometry - see figure 3.6.1). The HST slipstream shows a "secondary" velocity peak, and this was most pronounced at positions closer to the train and the ground, though this secondary peak was not apparent in the reverse direction. This section attempts to consider the "real" nose peak.

Figure 5.4 shows the horizontal velocity components, resultant horizontal velocity and pressure coefficient at the train nose at 0.2 m above TOR and at increasing distances from COT. The dashed part of the graphs show linearly interpolated data which is solely for illustrative purposes to show the Cobra probe "drop out". The streamwise components must therefore be interpreted with caution at x-axis distances greater than 0 m as it is expected that a reverse flow occurs in line with the pressure pulse (Baker et al., 2014a), which has not been detected due to limitations of the equipment. The magnitude of the resultant nose velocity peak increases as lateral distance to the nose decreases (consistent with the findings of Baker et al., 2014a), and the same can be said for each vector component and also static pressure. The "roughness" of the graphs can be attributed to both limitations in the working velocity range and accuracy of the probes and the limited spatial distribution of data points. The velocities at the nose are within the range 1 - 4 m/s, and the working range of the probe is 2 - 40 m/s. One point of interest is that the U component remains positive (i.e., no data drop out)

while the pressure coefficient is negative. The lateral V component matches the pressure coefficient very closely indicating an inviscid flow. It is also interesting to note that the magnitudes of the U and V components are very similar, unlike the findings of Baker et al., (2014a), but given the limitations of the probes it is not certain whether this is a true representation of the nose velocities of a full scale HST.

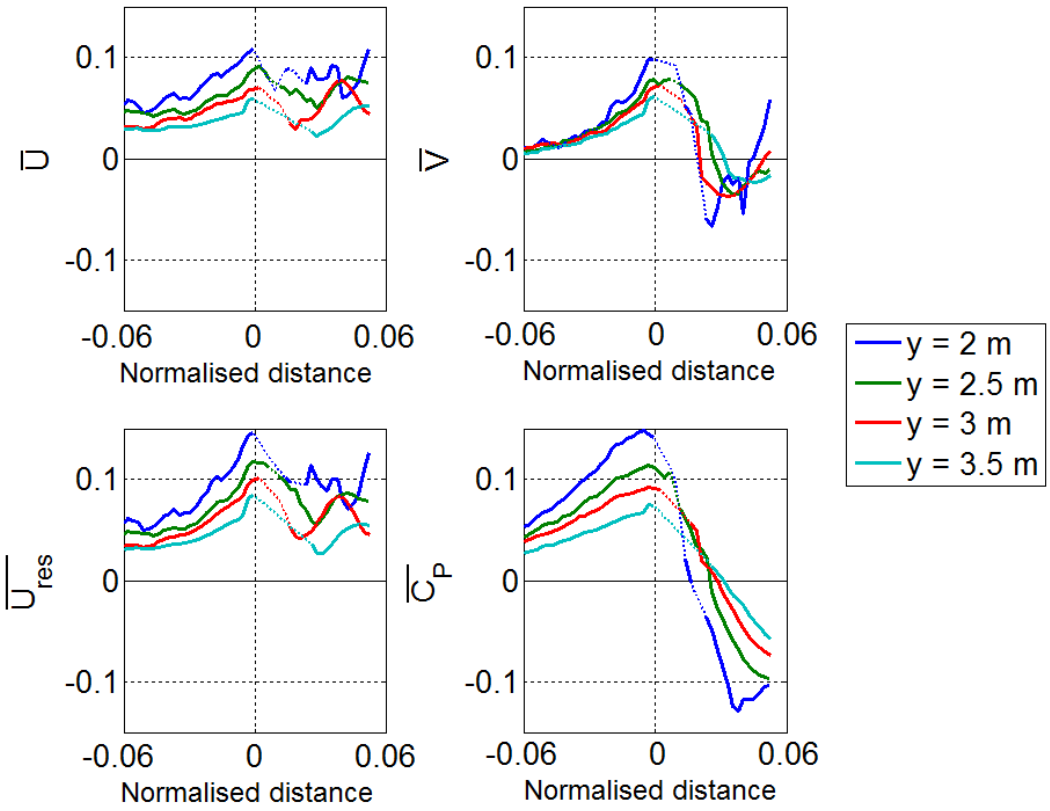

Figure 5.4 - Nose peaks of $\overline{U}$, $\overline{V}$, $\overline{U_{res}}$ and $\overline{C_P}$ at 0.2 m from TOR and increasing distances from COT. Dotted lines show interpolated data due to Cobra probe drop out. A normalised distance of 0.06 is equivalent to 5 m at full-scale.

5.3.2 Boundary layer region

As shown previously in figures 5.2 and 5.3, there is a large and possibly unrealistic secondary nose peak in the start of the boundary layer region. This peak may arise due to a combination of the HST nose profile channelling air downwards and then this accelerated flow encounters the firing chassis resulting in a shed vortex. The definition of the boundary layer region may be obscured by the additional flow immediately after the nose passage. For the purposes of this study, the boundary layer is defined as normalised distances of between 0.2 and 1 of the 4 car train length, though it should be noted that interference from this nose peak can be seen at normalised lengths of up to 0.5. The velocity profiles with respect to distance from COT are shown for a range of heights in figure 5.5 at normalised distances of 0.75 and 0.9 along the train.

Figure 5.5 shows that there appear to be two distinct boundary layer thicknesses - the boundary layer has a higher velocity and hence thickness closer to the ground, ($z < 0.2$ m) and a lower thickness at heights above 1.2 m. At 0.7 m above TOR there is a "transition" velocity profile that fits neither category. The larger velocities closer to the ground arise due to the underbody roughness which produces a higher slipstream velocity (Baker et al., 2014a), compared with the smooth train sides at heights above 1.2 m. By considering the streamwise turbulence intensity, shown in figure 5.6, at 2 m from COT the turbulence intensity close to the ground is approximately double the turbulence intensity closer to the roof. The variation in velocity profiles with respect to height shown in figure 5.5 match the variation in turbulence intensity magnitude. At 0.7 m above TOR, it is believed that the highly turbulent flow closer to the ground interacts with the less turbulent flow along the upper half of the train walls.

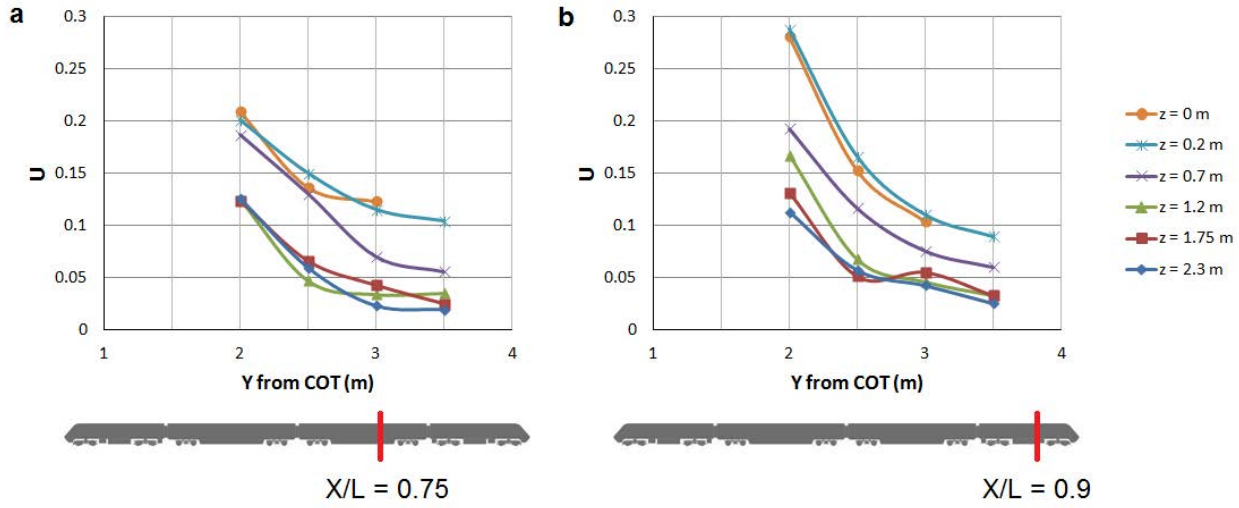

Figure 5.5 - Normalised velocity profiles at normalised distances of X/L = 0.75 (a) and 0.9 (b) for different heights above TOR.

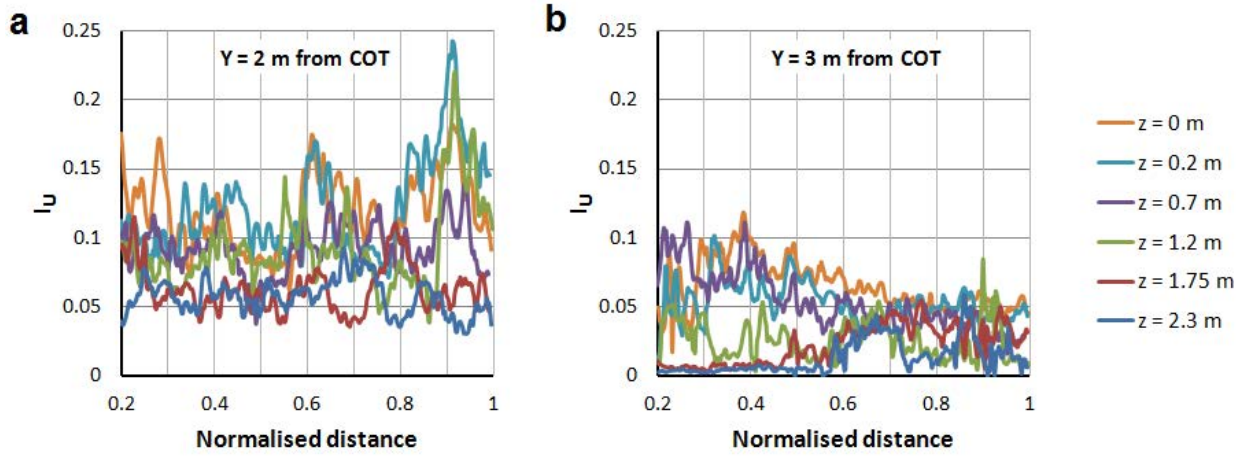

Figure 5.6 - Streamwise turbulence intensity at (a) 2 m from COT and (b) 3 m from COT for increasing heights above TOR for 0.3 m ballast height.

Displacement thickness was calculated according to equation 4.15, by fitting an exponential curve through the existing data and to assume a no-slip condition at the train surface, then an integration of this instantaneous exponential function between the train surface and the 99% boundary layer limit (i.e., when the exponential function of U equalled 0.01). Given that the number of data points in the integral was only four, and that figures 5.5 and 5.6 have illustrated the complex turbulent and 3D nature of the boundary layer, it is accepted that the values of δ^* are not entirely accurate or realistic, but should give a reasonable illustration of boundary layer thickness (Sterling et al., 2008a).

5.3.3 Wake region

The ensemble averages (in figures 5.2 and 5.3 for example) show that the largest velocities occur in the near wake region. It should be noted that when individual runs are considered, larger peaks may occur in the boundary layer region (i.e., the secondary nose peak) - this is discussed further in section 5.5. Figure 5.2 showed that the magnitude of the wake peak (and the entire slipstream overall) increases as distance from COT decreases, which is in line with many investigations of slipstreams in open air (Sterling et al., 2008a and Baker et al., 2014a for instance). It is hypothesised (and supported by considerable evidence from physical and computational studies - see section 2.3.2.3) that the wake flow of a conventional streamlined high-speed train consists of counter rotating trailing vortices that are shed from the train tail, and it is believed that their rotation occurs in part due to downwash from the roof and over the sloped tail (Bell, 2016b,c; Muld, 2012), which depends on the flow remaining attached to the tail profile. This may not be the case on the HST due to the relatively steep slope of the tail compared to most conventional passenger trains, and as such the HST may be considered in

aerodynamics terms fall somewhere between a conventional streamlined passenger train and a bluff/blunt train.

The far wake flow is shown by a gradual decay in slipstream velocity, and this was found to fit an exponential profile with a negative exponent. In this study, the far wake was defined between normalised distances of 1.5 < X/L < 5. To investigate the effects of measurement position (from COT and TOR) and also ballast height, an exponential curve was fitted to $\overline{U_{res}}$ in the far wake using the "fit" function in Matlab (Mathworks, 2010). Figure 5.7 shows an example of this curve fitting for the 0.3 m high ballast profile at heights of 0.2 m and 1.2 m above TOR for increasing distances from COT. The exponential best-fit curves are compared in figures 5.8 and 5.9 at fixed positions to consider the effects of ballast height.

Figure 5.7 shows that the form of the velocity decay is consistent regardless of measurement position, and the offsets between 0.2 m and 1.2 m above TOR are due to the higher near wake peaks at 0.2 m above TOR. When the wake decay (between normalised x-axis distances of 1.5 to 3) is compared between different ballast heights in figures 5.8 and 5.9 there is a clear (albeit quite small) difference - the larger ballast heights show a more rapid decay in velocity at positions closer to the ground (in figure 5.8) but at 1.2 m above TOR the form of the exponential fits is very close for both 0 m and 1.5 m high ballast. This is unsurprising since larger ballast heights have a greater volume for the wake flows to dissipate their energy within.

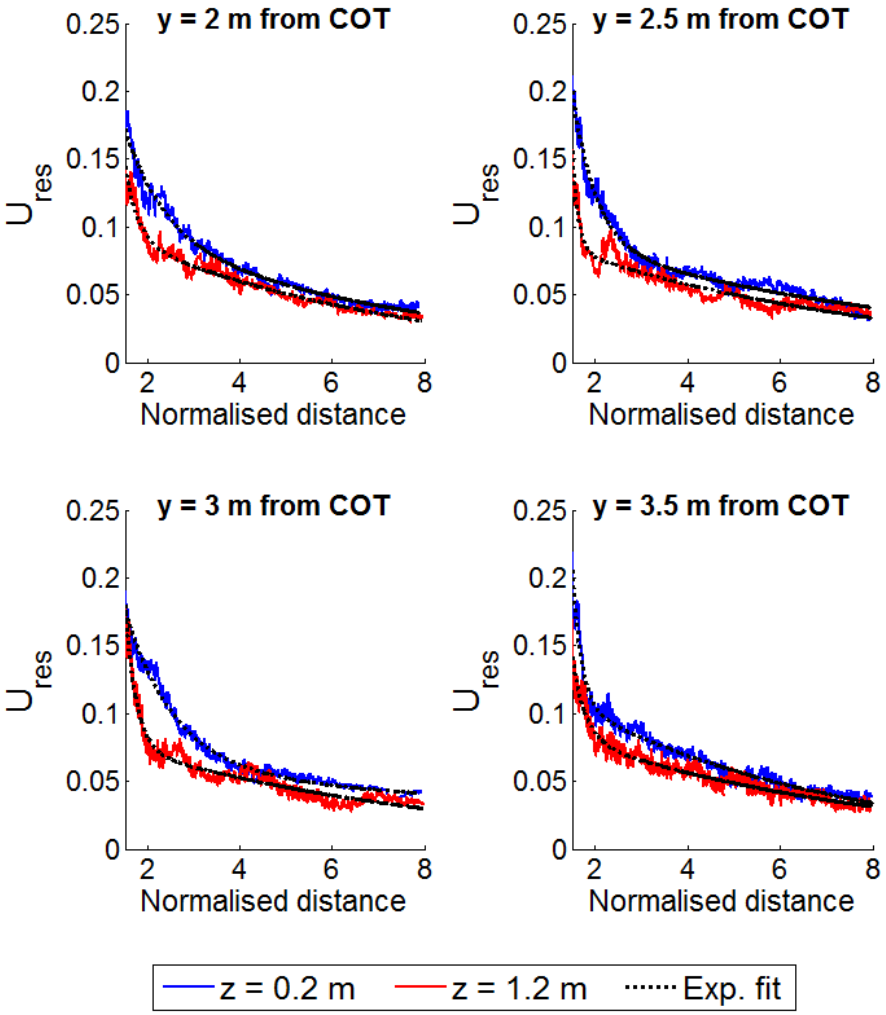

Figure 5.7 - Examples of far wake velocity and exponential curve fitting at z = 0.2 m and 1.2 m above TOR for y = 2 m to 3.5 m for 0.3 m ballast height.

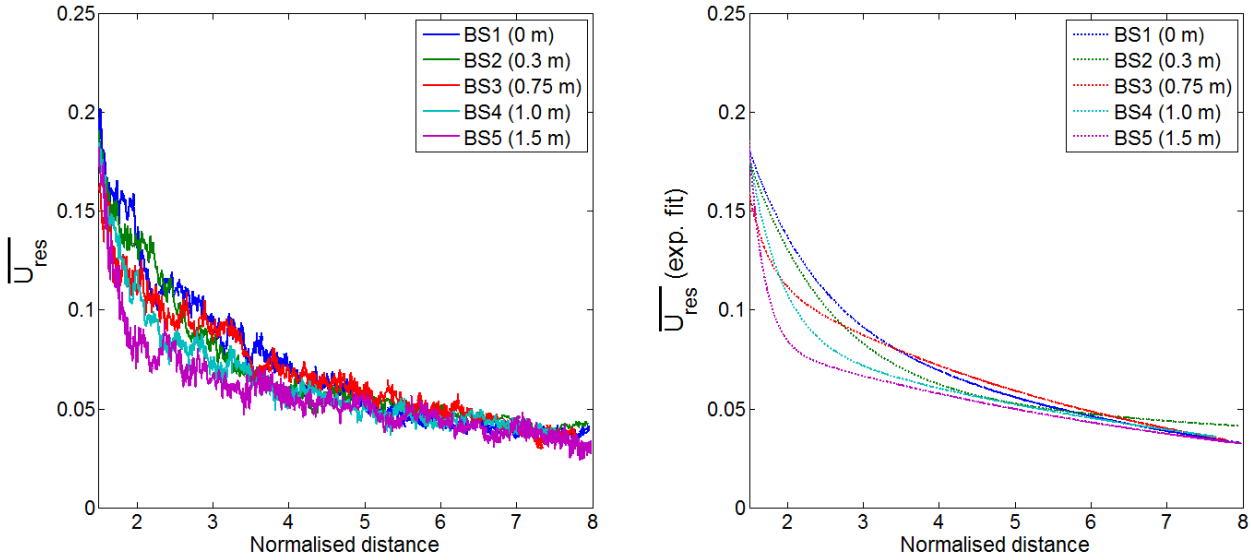

Figure 5.8 - Far wake velocities for different ballast heights at y = 3 m from COT and z = 0.2 m above TOR - solid lines are raw ensemble averages and dotted lines are exponential best fits.

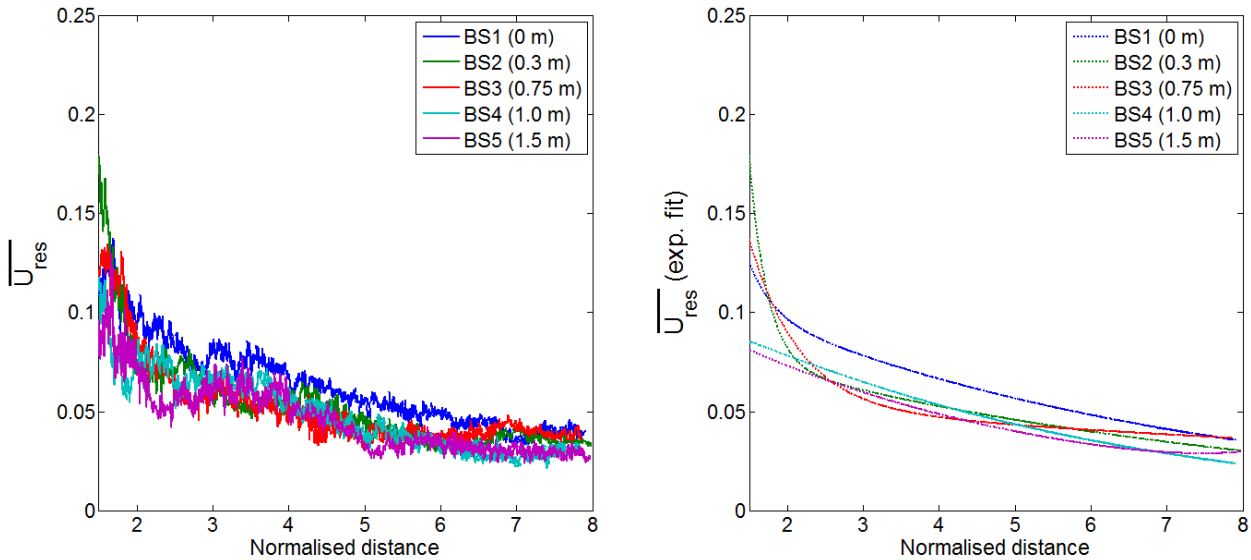

Figure 5.9 - Far wake velocities for different ballast heights at y = 3 m from COT and z = 1.2 m above TOR - solid lines are raw ensemble averages and dotted lines are exponential best fits.

5.4 Effects of ballast height on flow development

Appendix C presents the entire set of results from the ballast height investigations for all trains tests as ensemble averages of velocity and pressure. In summary, the HST showed some ballast height effects in the boundary layer region but no significant effects (i.e., outside of experimental uncertainty) were noted in the wake. The differences in the HST boundary layer region may also be due to differences in an unrealistic flow (the secondary velocity peak) caused by the firing chassis, and so while there are ballast height effects, these should be treated with caution when applying these findings to the real world. The ICE2 showed significant differences in slipstream velocity - the near wake peaks decreased by 50% as ballast height increased from 0 m to 0.75 m at the TSI trackside measurement position, though this result should also be treated with caution (see section 5.4.2). The freight train slipstream showed no effect with regards to changes in ballast height. The static pressure showed no notable differences with respect to ballast height regardless of train type. Soper et al., (2016), considers these findings further.

5.4.1 HST slipstream results

Figure 5.10 compares the slipstream of the HST for different ballast heights at fixed trackside positions. The main differences between ground simulation and slipstream velocity occur in the boundary layer region and at positions close to the ground, i.e., at the trackside measurement position in the TSI, shown in figure 5.10 (a). The larger peak in the near wake on figure 5.10 (a) appears to be an anomalous result (suggesting that a larger ensemble size would have been beneficial). In figure 5.10 (b), at the higher measurement position of 1.2 m

above TOR and 3 m from COT (close to the new TSI measurement position of 1.4 m above TOR), ballast height appears to have no significant effect on the ensemble average velocity in the boundary layer region. There is perhaps some effect in the near wake in figure 4.10 (b) - such as the larger magnitude of the wake peak with flat ground than with a 0.75 m to 1.5 m ballast height - though this is not conclusive. Generally, however, the nose and wake peaks appear unaffected by ballast height close to the ground, however the secondary velocity peak due to the firing chassis, apparent in figure 5.10 (a), is very much attenuated as ballast height increases.

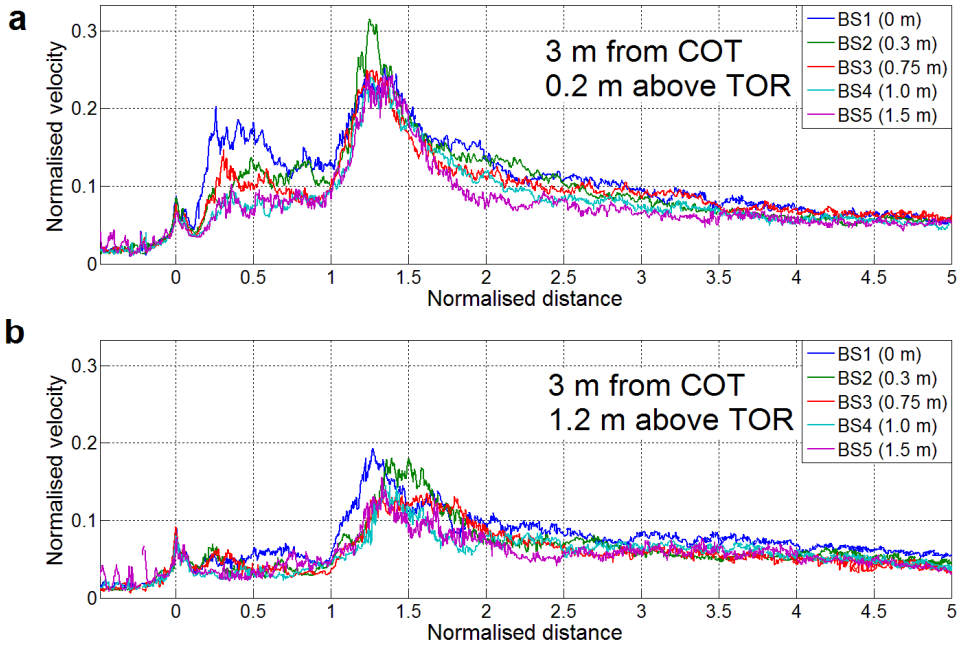

Figure 5.10 - Comparison of the resultant slipstream velocity for the HST with different ballast heights at (a) z = 0.2 m and (b) x = 1.2 m above TOR, both at y = 3 m from COT.

5.4.2 ICE2 and Class 66 freight train results

The results for the ICE2 and freight train are shown at the trackside TSI measurement position with different ballast heights. There are clear differences in the slipstream of the ICE2, particularly in the near wake, due to ballast height. Figure 5.11 shows that the largest wake peak was with a flat ground case. It must be noted that the near wake peak is in fact higher with a 1.5 m high ballast than a 0.75 m high ballast - this difference may arise simply due to the limited ensemble size and the phase dependent nature of wake vortex shedding. It could possibly be hypothesised, that the effects of ballast height are more significant at low ballast heights, and perhaps that the ranges of ballast height specified in the TSI could be in an "insensitive" region, however clearly further measurements (further measurement positions and different train geometries) are needed to consider this hypothesis adequately. There are differences in the ICE2 boundary layer velocities, though these are very low given the shielded underbody of the model - the unshielded HST has a boundary layer velocity roughly twice the magnitude of the ICE2. There are no apparent differences in the freight train slipstreams across the range of ballast heights considered.

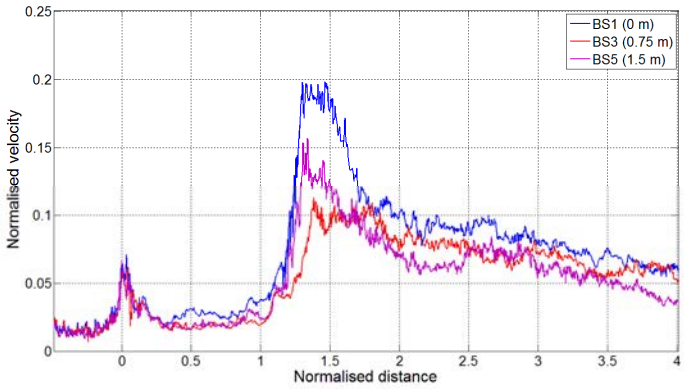

Figure 5.11 - Comparison of the resultant slipstream velocity for the ICE2 with different ballast heights at z = 0.2 m from TOR, y = 3 m from COT.

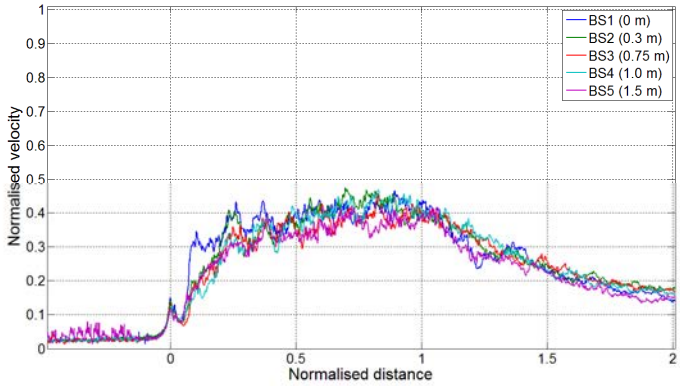

Figure 5.12 - Comparison of the resultant slipstream velocity for the Class 66 freight train with different ballast heights at z = 0.2 m from TOR, y = 3 m from COT.

5.5 TSI gust analysis of the HST

The TSI analytical procedure (described in sections 2.3.3 and 4.7) considers the maximum velocity of each filtered run. The procedure requires a 1 s gust filter, however it was noted in Jordan et al., (2008), that the response time of a person to a gust that could lead to instability was about 0.3 s. The TSI analysis was therefore performed twice, considering both a 1 s and a 0.3 s period of the moving average filter. The effect of filtering on a single run is shown on figure 5.13 - note that the x-axis has been adjusted to account for phase shift from the filtering. The 0.3 s filter preserves the "form" of the slipstream, but reduces the magnitude of the sharp wake peak. The 1 s filter, when applied to model scale data with shorter train lengths, has obscured the form of the slipstream and flow regions can no longer be clearly identified.

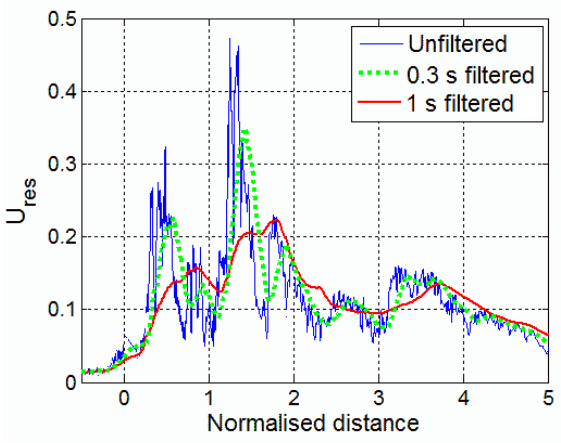

Figure 5.13 - Effect of moving averaging filters on a single run at trackside TSI position (3 m from COT, 0.2 m from TOR) with 0.3 m ballast height.

Figure 5.14 shows the position of the maximum gust in relation to the normalised x-axis position of the train for the 100 run ensemble (considered in section B.2) at the trackside TSI position. When unfiltered data is considered, the majority of the maxima fall in the near wake, however there are a significant number of maxima in the boundary layer region, most likely due to the secondary nose peak. When the data was 0.3 s and 1 s filtered, the majority of the maxima fell within the near wake, and the mean, standard deviation and value of $U_{2\sigma}$ decreased. This general shift is of course caused primarily by the increase in the phase shift created by increasing the filter period, but it is of interest to note that the TSI procedure (i.e., using a larger filter period) could be used to mitigate the effects of artificial velocity peaks caused by unrealistic train geometry.

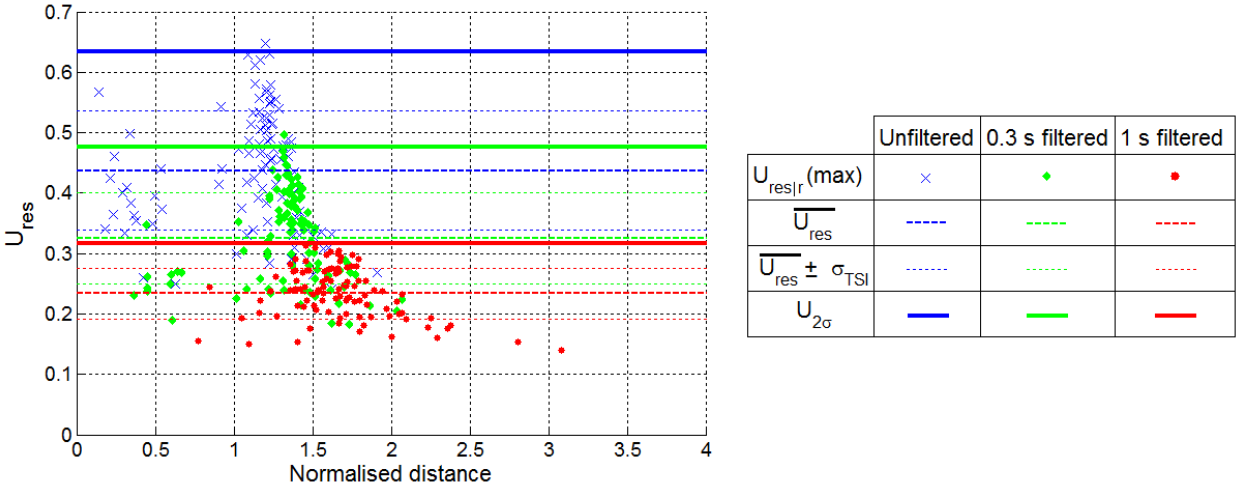

Figure 5.14 - Positions of maximum velocity for 100 run ensemble at TSI trackside position with 0.3 m ballast height showing unfiltered (blue), 0.3 s filtered (green) and 1 s filtered (red) data, also showing mean, standard deviation and $U_{2\sigma}$ for each filtering case.

The normalised and dimensional full scale TSI values (equation 4.19) are given for each ballast height in tables 5.1 and 5.2 for the trackside and open air platform measurement positions. Note that the actual platform position is meant to be at 1.4 m above TOR (European Commission, 2014), and while this position was not tested it is felt that 1.2 m above TOR should show similar slipstream magnitudes as 1.4 m above TOR.

When the trackside values are considered, the HST does not break the limit value of 20 m/s when a 1 s filter was applied. There may be slight differences as a result of ballast height - the lower ballast heights of 0 m and 0.3 m show slightly higher (roughly 10%) mean velocities than ballast heights of 1 m and 1.5 m. The values of $U_{2\sigma}$ for the 1.5 m ballast height are similar to flat ground, which is due to the larger standard deviation - it is felt a larger ensemble size may allow further scrutiny of this unexpected result. When a 0.3 s filter was

applied, all of the values of $U_{2\sigma}$ break the TSI limit for all ballast heights, though not by a great amount. As discussed in section 2.3.1, the effects of gusts on people is open to conjecture, though the prescribed 1 s moving average period may be too long and filter out potentially hazardous gusts of lower time scales, given the research of Jordan et al., (2008). Were this reconsidered in the TSI, then there could be implications for trains that are currently regarded as "safe". The measurements at 1.2 m above TOR (close to the TSI platform position) in table 5.2 allow the same point to be made - a 0.3 s filter results in values of $U_{2\sigma}$ that break current limits but a 1 s filter shows values of $U_{2\sigma}$ below the TSI limit of 15 m/s. When considering the 1 s filtered data, the largest value of $U_{2\sigma}$ was with the flat ground case, suggesting that ballast height can affect flow some distance from the ground. However, given that UK platforms are taller and reduce slipstream velocity quite considerably, as shown in figure 2.13 from Johnson and Holding, (2003), it is doubtful that ballast height would, in reality, have much effect with the presence of a platform. Therefore the fact that the 0.3 s filtered values of $U_{2\sigma}$ are slightly higher than the limit value of 15 m/s does not in itself raise safety concerns when slipstreams on a platform are considered.

Table 5.1 - Trackside TSI values at y = 3 m from COT, z = 0.2 m above TOR.

	Ballast height (m)	1 s moving average filter			0.3 s moving average filter		
		$\overline{U_{max}}$	$\sigma_{U_{max}}$	$U_{2\sigma}$	$\overline{U_{max}}$	$\sigma_{U_{max}}$	$U_{2\sigma}$
Non-dimensional	0	0.22	0.039	0.29	0.30	0.063	0.42
	0.3	0.21	0.039	0.29	0.32	0.071	0.46
	0.75	0.20	0.038	0.27	0.29	0.068	0.42
	1.0	0.19	0.045	0.28	0.26	0.072	0.41
	1.5	0.19	0.048	0.29	0.28	0.074	0.43
Dimensional full scale	0	12.0	2.2	16.3	16.7	3.5	23.7
	0.3	12.0	2.2	16.3	17.8	4.0	25.7
	0.75	11.0	2.1	15.3	16.1	3.8	23.7
	1.0	10.5	2.5	15.6	14.6	4.0	22.6
	1.5	10.7	2.7	16.1	15.9	4.1	24.1

Table 5.2 - Platform TSI values at y = 3 m from COT, z = 1.2 m above TOR.

	Ballast height (m)	1 s moving average filter			0.3 s moving average filter		
		$\overline{U_{max}}$	$\sigma_{U_{max}}$	$U_{2\sigma}$	$\overline{U_{max}}$	$\sigma_{U_{max}}$	$U_{2\sigma}$
Non-dimensional	0	0.16	0.038	0.24	0.24	0.068	0.37
	0.3	0.15	0.036	0.22	0.21	0.061	0.34
	0.75	0.13	0.035	0.20	0.18	0.056	0.30
	1.0	0.13	0.031	0.19	0.18	0.048	0.27
	1.5	0.12	0.039	0.20	0.18	0.061	0.30
Dimensional full scale	0	9.2	2.1	13.5	13.2	3.8	20.8
	0.3	8.2	2.0	12.3	11.9	3.4	18.7
	0.75	7.4	1.9	11.3	10.3	3.1	16.5
	1.0	7.1	1.7	10.6	9.8	2.7	15.2
	1.5	6.7	2.2	11.1	10.0	3.4	16.9

5.6 Further discussion and closing remarks

The slipstream is typically represented as the resultant horizontal velocity, which is dominated by the streamwise U velocity component. The slipstream of an HST shows the main flow regions - nose, boundary layer and wake. The nose passage results in a small peak in the U and V components and a sinusoidal pressure pulse, and as distance from COT is increased the magnitudes of these velocity and pressure peaks decrease. Immediately after this nose peak it was found that there was a large and sharp streamwise velocity peak at measurement positions that were both close to the ground and train sides, and this peak was, in some cases, larger than the near wake peak (at 2 m from COT and 0.2 m above TOR for instance). Firing the HST model in reverse (i.e., the firing chassis was trailing) is considered in appendix B, and it was found that this secondary nose peak was not present in the reverse direction. The magnitude of the negative peak of the nose pressure pulse was also lower in the reverse direction. While only a single measurement position was tested (3 m from COT and 0.2 m above TOR), this test suggests that this peak arises as a result of the HST nose profile which channels air downwards towards the ground and the higher underbody blockage from the firing chassis. When full scale data was considered (appendix D), some of the individual runs showed large velocity peaks closer to the nose. This suggests that there is an intermittent flow at the HST nose that is not characteristic of more conventional/modern high speed trains. When the boundary layer region was considered, it was found that the HST has a complex and three dimensional boundary layer, which was thicker and more turbulent closer to the ground, most likely due to the unshielded underbody (boundary layer velocities were much higher than for the ICE2 which has a more shielded underbody). The autocorrelations (presented in Soper et al., 2016) showed that within the boundary layer region most of the energy was at

time scales of less than 0.4 -0.5 s, i.e., low scale turbulent fluctuations. The largest slipstream velocities were generally in the near wake region, and the magnitude of the wake peaks decreased as both distance from COT and distance from TOR increased. When the effects of ballast height were considered, the HST showed lower velocities in the boundary layer region at 3 m from COT and 0.2 m above TOR as the ballast height was increased, suggesting that ballast height has an effect on flow development closer to the ground. There were no definite differences observed in the near wake peaks with different ballast heights for the HST or Class 66 freight train, however, the ICE2 showed a clear reduction in wake peak as ballast height increased. The ICE2 results support the hypothesis that increasing ballast height reduces the slipstream velocity at the TSI measurement position (3 m from COT and 0.2 m from TOR) as there is a larger volume for the trailing vortices to spread out into with larger ballast heights, which supports the findings of Bell et al., (2014) who also found a reduction in the wake peak with a similar shaped train to the ICE2. The slipstream of the ICE2 (at the TSI trackside measurement position) showed little sensitivity at ballast heights of 1 m and 1.5 m (i.e., the upper portion of the TSI range) but was sensitive between ballast heights between 0.5 m to 1 m, which suggests that further work is required to consider the TSI limits of ballast height. The fact that the Class 66 freight train and HST do not support this hypothesis could suggest that the near wake flows of these trains are different. There is no clear wake peak in the freight train slipstream (discussed further in Soper, 2014) suggesting that the wake flow of a freight train is a recirculation, and that downwash of the roof flow over the tail is needed to create rotation of the shear layers to result in trailing vortices (Muld, 2012, Bell, 2016b, c). The HST nose/tail profile is different to most conventional high speed trains - there is a slightly steeper downwards slope from the roof to the tail "tip" which is at a height of 1.6 m above TOR. The trailing vortices of an HST may therefore have a smaller diameter/scale and

shed closer to the roof, which could explain the lack of sensitivity of wake peaks to ballast height. The effect of tail profile on the wake was investigated by Bell et al., (2016c) who reached a similar conclusion - steeper tails showed lower slipstream magnitudes due to the lack of helical trailing vortices. The far wake flows of the HST show slight sensitivity to ballast height - though far wake flows are not considered hazardous. A TSI gust analysis found that, at the open air measurement positions of 3 m from COT and 0.2 m and 1.2 m above TOR, the largest velocities occurred mostly in the near wake. Both a 1 s moving average filter, as prescribed in the TSI, and a 0.3 s moving average filter based on Jordan et al., (2008), were applied to the data and it was found that the HST did not break safety limit values with a 1 s filter but did break safety limits when a 0.3 s filter was applied, however it is not necessarily pragmatic to infer that the HST is "unsafe". Open air measurements to assess slipstream velocities on a platform may not be appropriate in the UK, as the platforms are larger than in mainland Europe and have been shown to reduce slipstream velocities (Johnson and Holding, 2003). For trackside measurements, the TSI measurement position is very close to ground level and away from the centre of gravity of a typical person, given that typically the ballast height in the UK is lower than in mainland Europe. As height above TOR is increased, the slipstream of an HST decreases, and the TSI velocities at 1.2 m above TOR, 3 m from COT, were slightly below the TSI limit of 15.5 m/s with a 0.3 s filter except for with the flat ground case, though it is unlikely that ballast height would affect platform slipstreams in reality.

CHAPTER 6

MODEL-SCALE CROSSWIND TESTS - EXPERIMENTAL METHODOLOGY

6.1 Introduction

Chapter 6 describes the experimental procedure for two scale model tests which aimed to measure the surface pressures on a HST power car when subject to crosswinds over a range of yaw angles. A commercial wind tunnel test is described in section 6.2. The second test involved a moving model through a crosswind. Section 6.3 describes the crosswind generator at the TRAIN rig facility and section Section 6.4 describes the experimental set up these tests.

6.2 Commercial wind tunnel test

A wind tunnel test was undertaken by Rowan Williams Davies and Irwin Inc. (RWDI) in order to investigate the surface pressures on a HST power car across a range of yaw angles. This wind tunnel was also used in Baker and Sterling, (2009). It should be noted here that this was a commercial test, and therefore some details of the experimental set up and procedure, and also some elements of the data analysis, were not provided by RWDI.

The aim of this test was to investigate the flow field and hence overturning forces on an HST by measuring the surface pressures on an HST power car across a range of yaw angles. Understanding the flow field was important in determination of regions of the train that showed a good relationship between yaw angle and surface pressure, in order to aid in the design of the pressure tap system at full-scale on the NMT. Pressures were measured on the leading vehicle which typically experiences the largest forces (Dorigatti et al., 2012; Sakuma and Hibino, 2013), in order to compare with data from the full-scale tests (chapters 9 to 11).

6.2.1 Experimental set up

6.2.1.1 Pressure tap set up

A 1/25th scale HST power car was fitted with 313 surface pressure taps. Figure 6.1.1 shows the locations of the pressure taps on the power car, and is reproduced at a higher magnification in appendix G. The pressure taps were located mostly over nose of the train, and in loops around the circumference of the power car, shown in figures 6.1.2 and 6.1.2 - underbody pressures are considered separately in appendix G and hence underbody taps are

not shown on figure 6.1.3. The normalised distances of the loops of taps shown in figure 6.1.3 from the front of the train are given in table 6.1 and figure 6.1.2. Each pressure tap was connected to a piece of 2 mm diameter tubing that was glued inside the drilled pressure tap hole and flush with the outer surface of the train. The lengths of pneumatic tubing were not specified by RWDI.

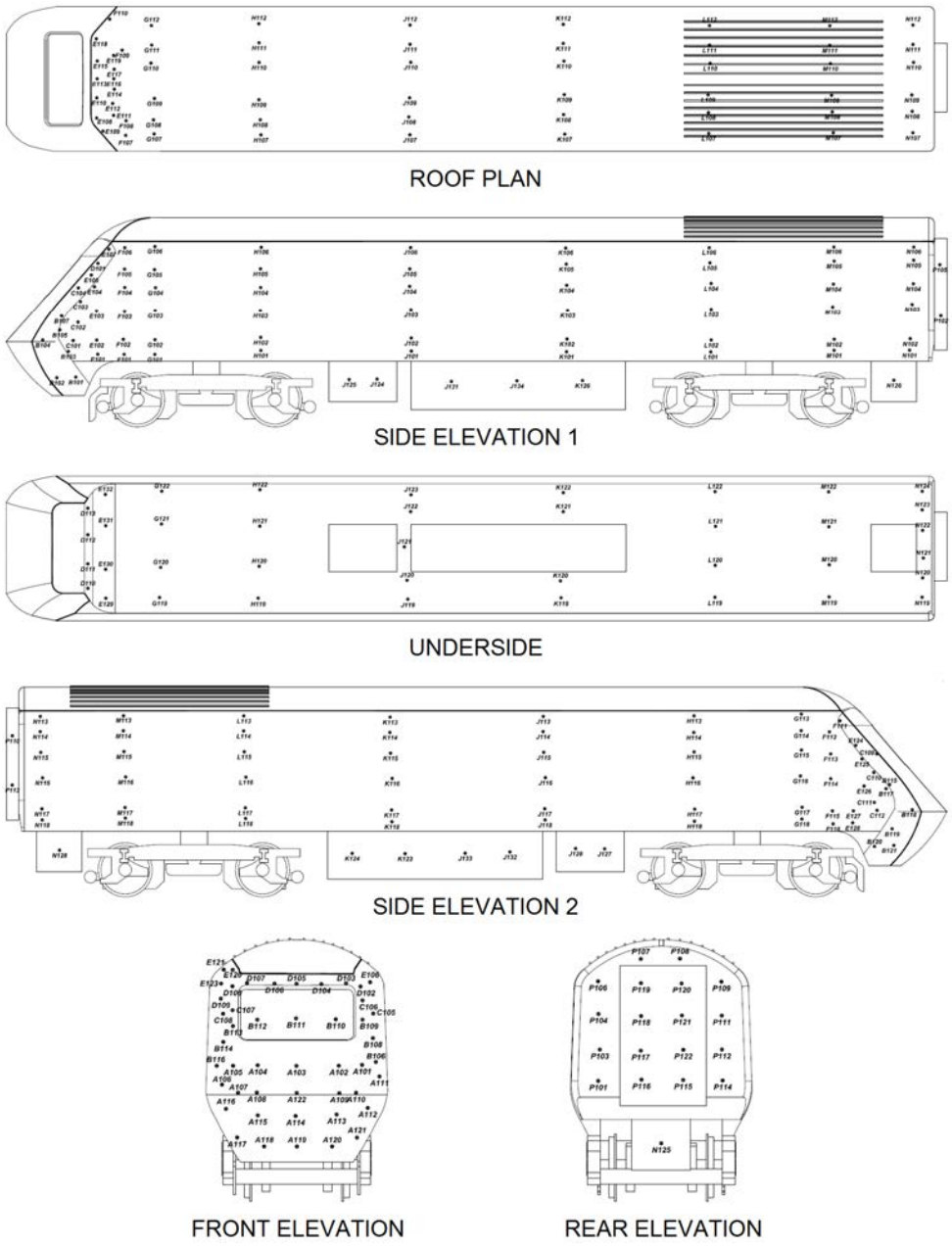

Figure 6.1.1 - Locations of pressure taps on 1/25th scale wind tunnel HST model from RWDI.

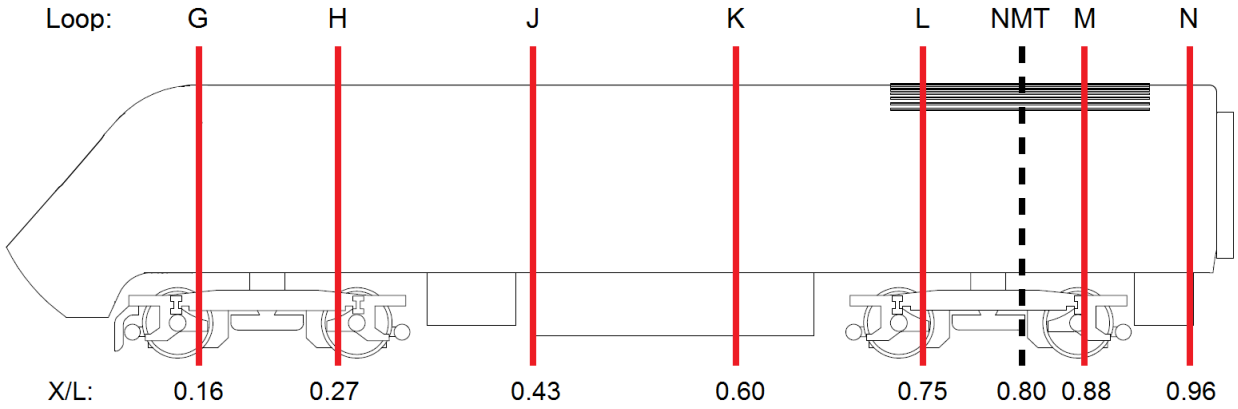

Figure 6.1.2 - Locations of pressure tap loops around HST power car (red bars show wind tunnel loops and dashed line shows location of loops on NMT and TRAIN rig model).

Table 6.1 - Distances of pressure tap loops on wind tunnel model from train nose.

Loop letter	Normalised distance from train nose (X/L)	Total number of pressure taps in loop	Tap references
G	0.16	22	G101 - G122
H	0.27	22	H101 - H122
J	0.43	23	J101 - J123
K	0.60	22	K101 - K122
L	0.75	22	L101 - L122
M	0.88	22	M101 - M122
N	0.96	24	N101 - N124

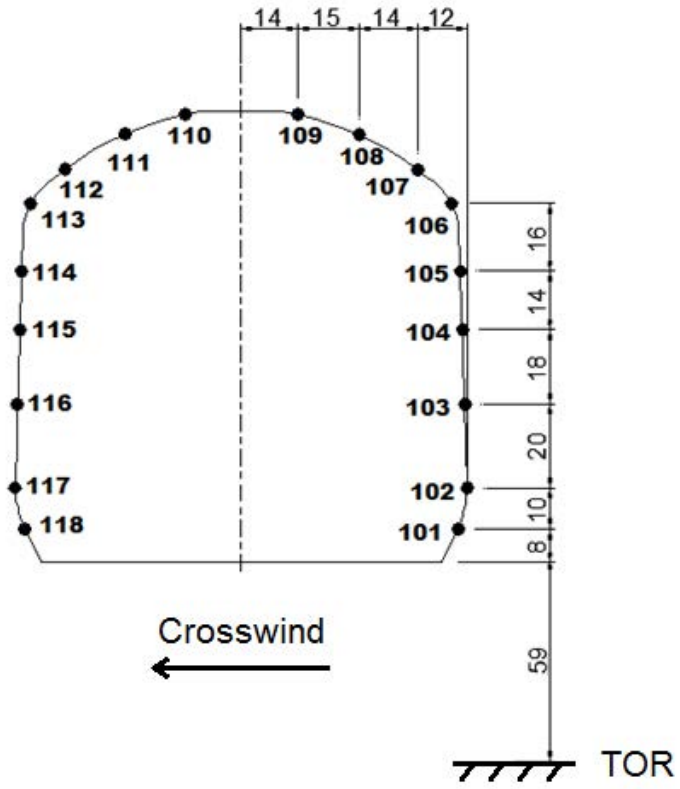

Figure 6.1.3 - Section of the HST wind tunnel model to show a loop of tapping points around train walls and roof. Dimensions in millimetres and at model-scale.

6.2.1.2 HST model and ground set up

The HST model was constructed from a 3D printed plastic shell and the external dimensions were within 2 mm (at model-scale) of the equivalent full-scale dimensions as required in CEN. The bogies were also 3D printed and were fixed to the model by screws running through the bogie and into the floor of the train, shown in figures 6.2.2. A Mk. III was also constructed in the same way as the power car and was attached to the single track ballast and rail (STBR) ground configuration immediately after the power car, shown in figure 6.2.2 (b). The coach was not fitted with any pressure taps, but was necessary to prevent unrepresentative flow separation effects at the rear of the power car. The power car and coach were not mechanically connected (i.e., a small gap was left), as required in CEN part 6 to minimise vibration (CEN, 2010).

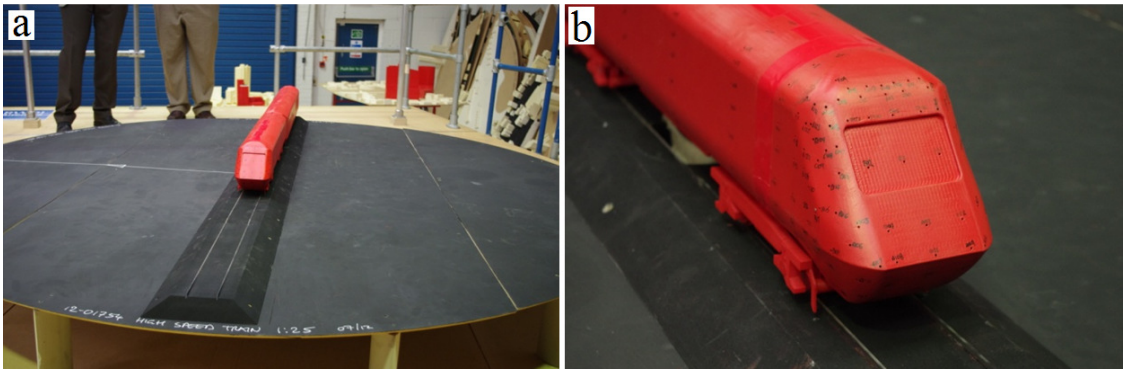

Figure 6.2.1 - HST model mounted on STBR ground piece on a splitter plate and turntable.

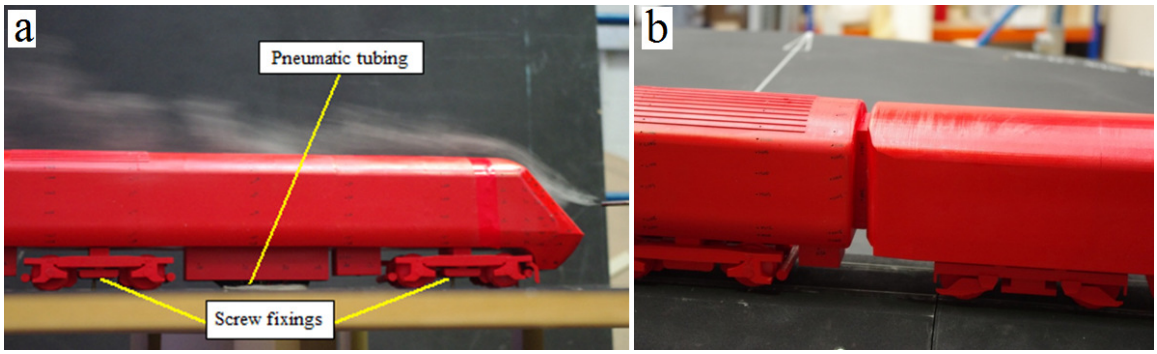

Figure 6.2.2 - Location of screw fixings and pneumatic tubing beneath the HST model and junction between (a) HST power car and (b) Mk. III coach.

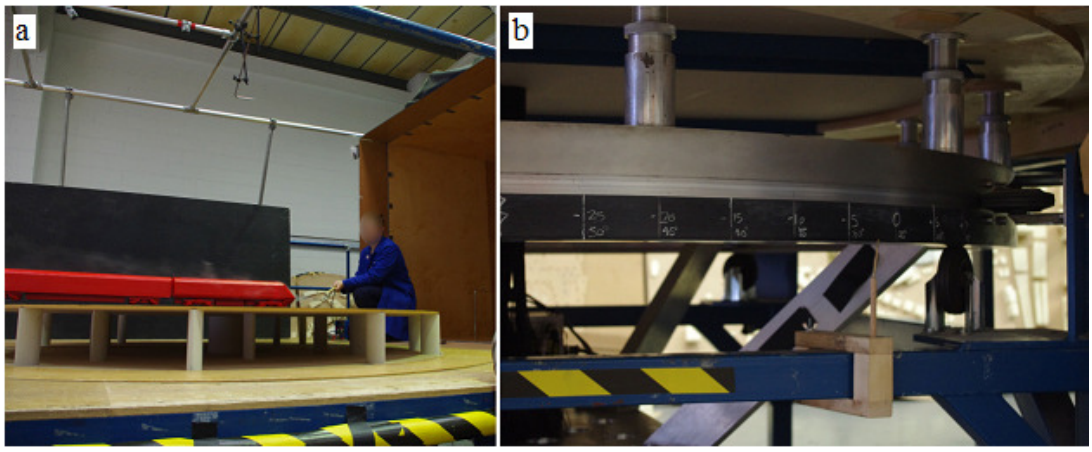

Figure 6.2.3 - (a) HST model on splitter plate outside of the wind tunnel and (b) underside of turntable.

The train was fixed to a STBR ground configuration, and is shown in figure 6.3.1. The ballast height was 0.825 m from the cess to top of ballast, and 1.0 m from the cess to TOR at full-scale, and the ballast widths were 3 m and 5.55 m at the top and base of ballast respectively, therefore the cross section of the STBR complies with requirements of CEN, shown in figure

6.3 (CEN, 2010). The only aspects of the STBR simulation dimensions that did not comply with CEN were at the leading edge of the ground simulation. The upstream sloped edge (shown in figure 6.4) had a 45° slope from cess level to the top of the ballast, 0.5 m upstream of the train nose, which was a larger than the angle of 30° specified in CEN, and also the leading edge of the STBR was not radiused as is recommended in CEN. This slope was found to cause flow separation which affected the air flow to pressure taps at the nose of the train in a separate wind tunnel test conducted as part of this study a zero yaw angle, described in appendix I, and this was also found in CFD simulations on the same wind tunnel set up by Morden et al., (2014).

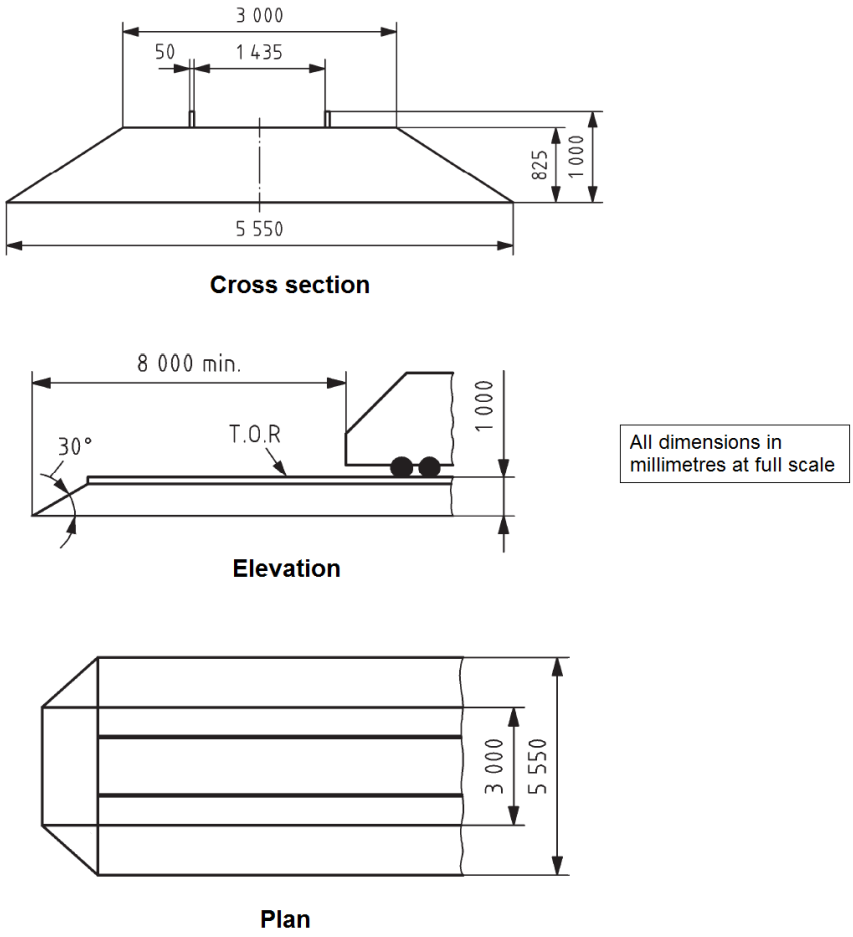

Figure 6.3 - Ground configuration requirements for wind tunnel tests (CEN, 2010).

Figure 6.4 - 45° slope at leading edge of STBR configuration.

6.2.1.3 Wind tunnel set up

The HST model and ground configuration were fixed to the a splitter plate and turntable shown in figure 6.2.3. The sloped front edge of the ground configuration, which was thought to affect the flow to the nose taps, was positioned approximately 10-20 mm from the leading edge of the turntable. The turntable and model were situated just outside of the wind tunnel oriface as shown in figure 6.5. The upper surface of the turntable (cess level) was 200 mm above the wind tunnel floor at model-scale, in order to negate the wall boundary layer effects of the wind tunnel.

The wind tunnel velocity was measured using a pitot static probe positioned 1.5 m upstream of the centre of the HST model and ground set up (i.e., 1.5 m from the centre of the circular splitter) and at a height of 120 mm from the TOR at model-scale (equivalent to a reference height of 3 m at full-scale). The pressure time series data from this reference probe was not provided by RWDI, which limits analysis in chapter 8 to consider only steady effects.

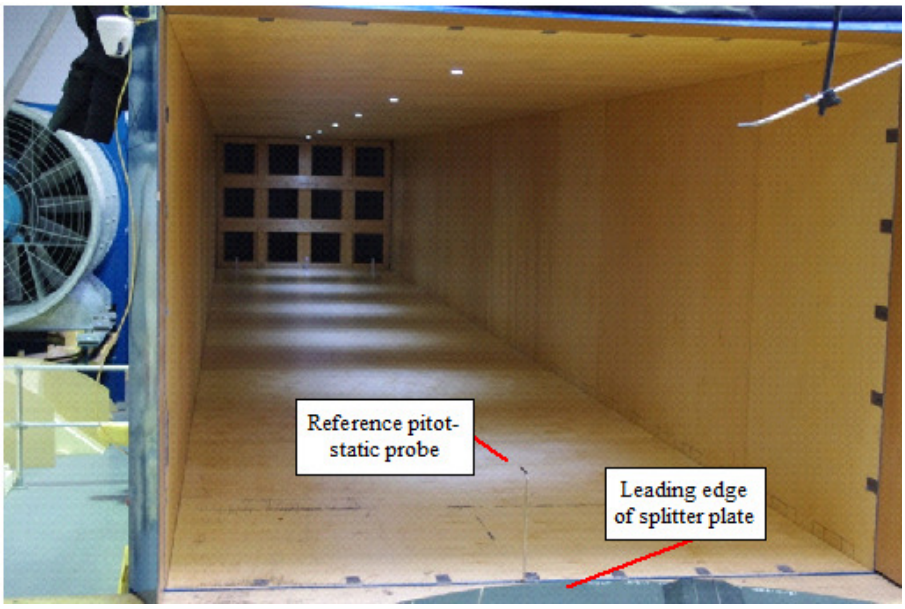

Figure 6.5 - Positions of pitot-static probes and turntable in the RWDI wind tunnel.

6.2.2 Experimental procedure

The pressure tap (and reference probe) data was sampled by a data logger at 512 Hz for 120 s. This procedure was repeated at yaw angles from 0° to 50° in 5° increments, and hence time series data for each pressure tap was obtained. The analytical methodology of this data is presented in section 7.2. Analysis of the pressure tap data at the front of the train indicated that the wind tunnel flow was stable for the duration of the sampling time, i.e., the fans had reached their maximum power as the mean flow component did not show any significant changes for the sampling duration.

Two tests were conducted by RWDI using the same wind tunnel and experimental set up shown in figure 6.4. The main difference between these tests was that one test had a clear wind tunnel (figure 6.5) with no additional turbulence generation (i.e., besides that caused by

the fans) so is known henceforth as the "smooth flow test", and the second test used roughness elements to generate a higher turbulence intensity, so is known as the "higher turbulence test", and was intended to consider Re number sensitivity by "simulating" the effects of a higher Re number by increasing the turbulence intensity (though this resulted in a slight reduction in the mean wind tunnel free stream velocity). Note also that the "smooth flow" test actually had a turbulence intensity greater than 2.5% as specified in CEN (2010).

The Re number for both tests (table 6.2) fell below the CEN limit of 2.5 x 10^5, which would require velocity of about 25 m/s. Table 6.2 also shows the main parameters of the crosswind tests at the TRAIN rig, (mean velocities are resultant of train speed and crosswind speed - see also table 6.4).

Table 6.2 - Key parameters from scale model crosswind tests on a 1/25th scale HST.

Test description	Mean velocity (m/s)	Re number ($\times 10^5$)	Turbulence intensity (I_u)	Yaw angles tested
RWDI Smooth flow	13.2	1.4	5.5%	0° - 50° (5° increments)
RWDI higher turbulence	11.5	1.2	10%	0° - 50° (5° increments)
TRAIN rig crosswind generator	24 - 46	2.5 - 4.8	17%	15° - 30° (5° increments)

6.3 Description of the TRAIN rig crosswind generator

Tests were conducted at the TRAIN rig using a crosswind generator (CWG) which was built and investigated by Dorigatti, (2013) as part of a PhD project. The CWG is shown in figure 6.6 and the dimensions of the CWG are shown in figures 6.7.1 and 6.7.2. The airflow within the CWG is generated by a total of 16 axial flow fans [Ziehl-Abegg, FC071-4DF.7M.V6] (Ziehl-Abegg, 2010), arranged in two rows of eight as shown in figure 6.7.1. The fans are connected to a steel frame, and operate in suction to generate flow perpendicular to the tracks. The CWG itself is an enclosed structure along 6.35 m of track, and the crosswind fetch is 1.685 m and flat ground configuration is simulated. Air can enter the CWG through a hexagonal "honeycomb" flow straightener over the inlet surface and also through small opening portals to allow the transit of the model train which have a slight effect on the lateral velocity component and static pressure close to the CWG "edges" (see figures 6.8.1 to 6.8.3). The CWG is contained entirely within the TRAIN rig building envelope, so the air flow is an open circuit, i.e., it recirculates within the building after being expelled by the fans.

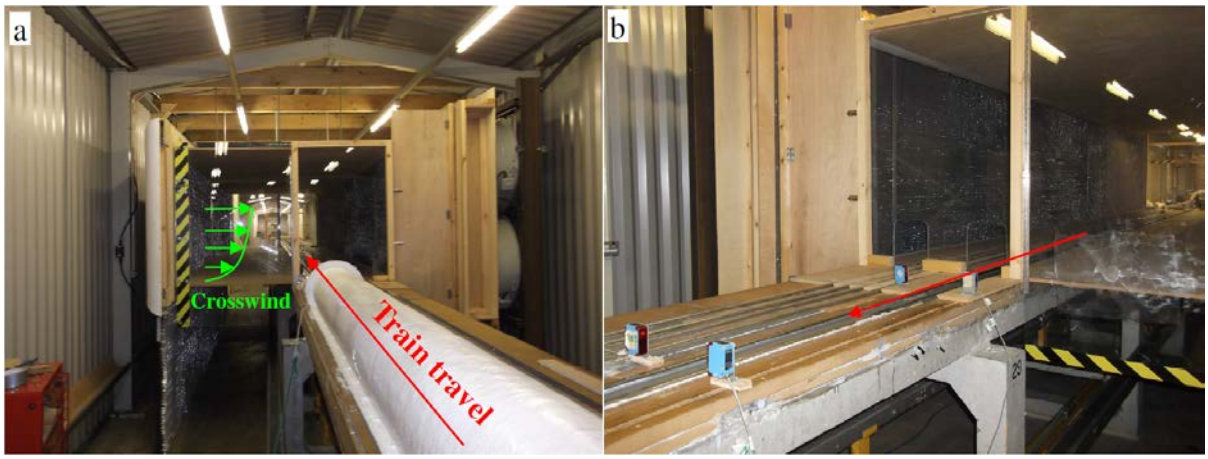

Figure 6.6 - The CWG at the TRAIN rig (a) entrance flow direction and (b) light gates at exit.

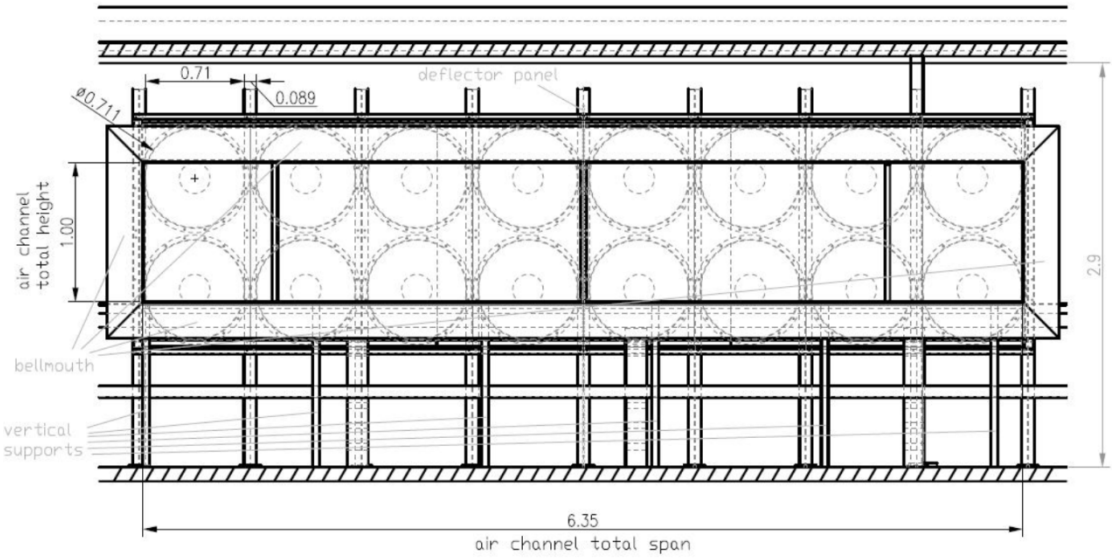

Figure 6.7.1 - Fan arrangement and external dimensions of the CWG (from Dorigatti, 2013).

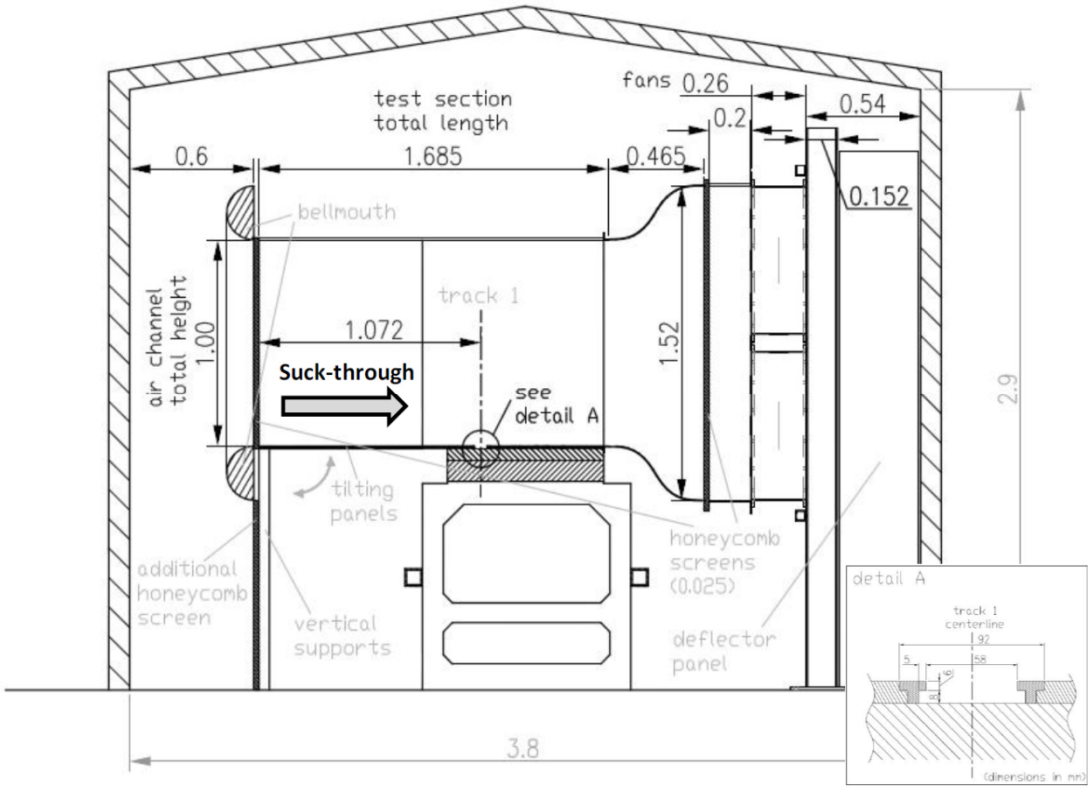

Figure 6.7.2 - Cross sectional view of the CWG (from Dorigatti, 2013).

6.3.1 Crosswind velocity characteristics

The air velocity within the crosswind generator varies significantly across the length of the track, due mainly to the proximity of the fans to the track, and the gradient of the axial velocity of the fan blades (hence air velocity) along the radius of each fan. Note that when the flow of the fans is considered in this section, the streamwise (u) component is in the main direction of the flow (i.e., perpendicular to the direction of train travel), the v component is defined as parallel and contrary to the direction of train travel, and the w component is vertically upwards.

Figure 6.8.1 shows the time averaged velocity profiles taken by Dorigatti, (2013), at a reference height of 3 m at full-scale and at the centre of track, across the span of the crosswind generator in 0.1 m steps (at model-scale). Velocity and static pressure were measured using Cobra probes mounted on retort stands. The vertical lines on figure 6.8.1 indicate the inter-fan gaps. The average span-wise flow characteristics are presented in table 6.3. Figure 6.8.1 (a) shows that there is limited span-wise uniformity of the streamwise flow across the CWG, and there is also limited span-wise uniformity in the integral length scale and turbulence intensity shown in figure 2.4.3. Figure 6.7.1 (b) shows that the lateral and vertical velocity components begin to diverge from ~0 m/s at approximately span-wise positions 52 and 12, due to the entrance and exit portals of the CWG respectively. The static pressure shown in figure 6.8.2 is also affected in these regions, and as a result, experimental data from the crosswind tests has been discarded when the train is close to the entrance/exit. A retest of the CWG flow characterisation by Soper, (2014), found good agreement (within 4%) of mean velocity and a similar uniform span-wise distribution of static pressure to that shown

in figure 6.8.2. The velocities and pressures shown in figures 6.8.1 and 6.8.2 from Dorigatti, (2013), were used in analysis of the data collected in this study.

Given this spanwise non-uniformity in velocity, there are no positions inside the CWG when all of the cars will experience the same yaw angle. It is therefore only possible to test a single location at a time. The analytical methodology (described later in section 7.3) therefore considers single loops (i.e., x-axis positions) of pressure taps independently and assumes the velocity within the CWG to take it's mean value at the different locations along the CWG span (as in figure 6.8.1).

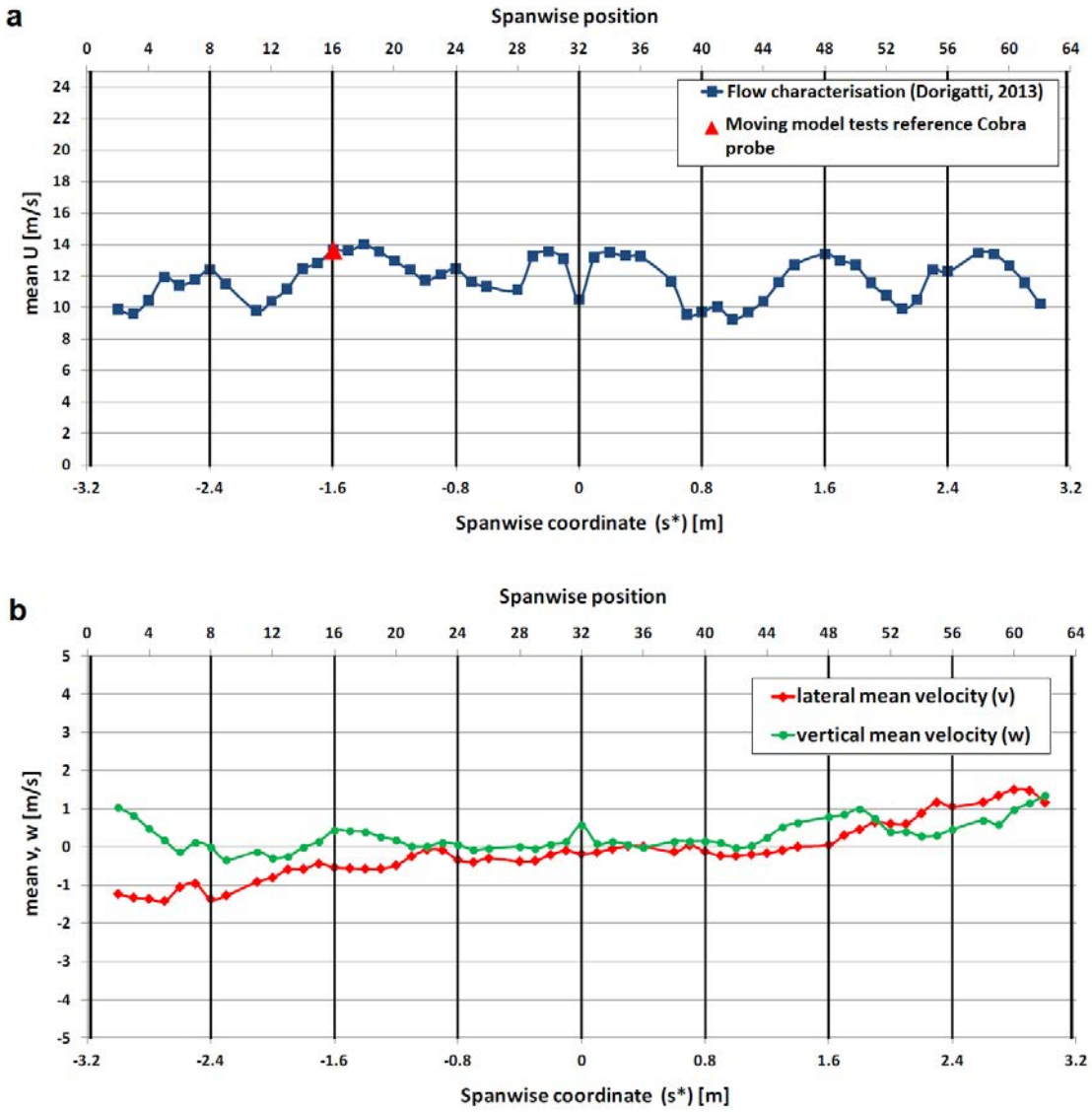

Figure 6.8.1 - Time averaged mean velocity across CWG (a) streamwise, (b) lateral and vertical components (Dorigatti, 2013).

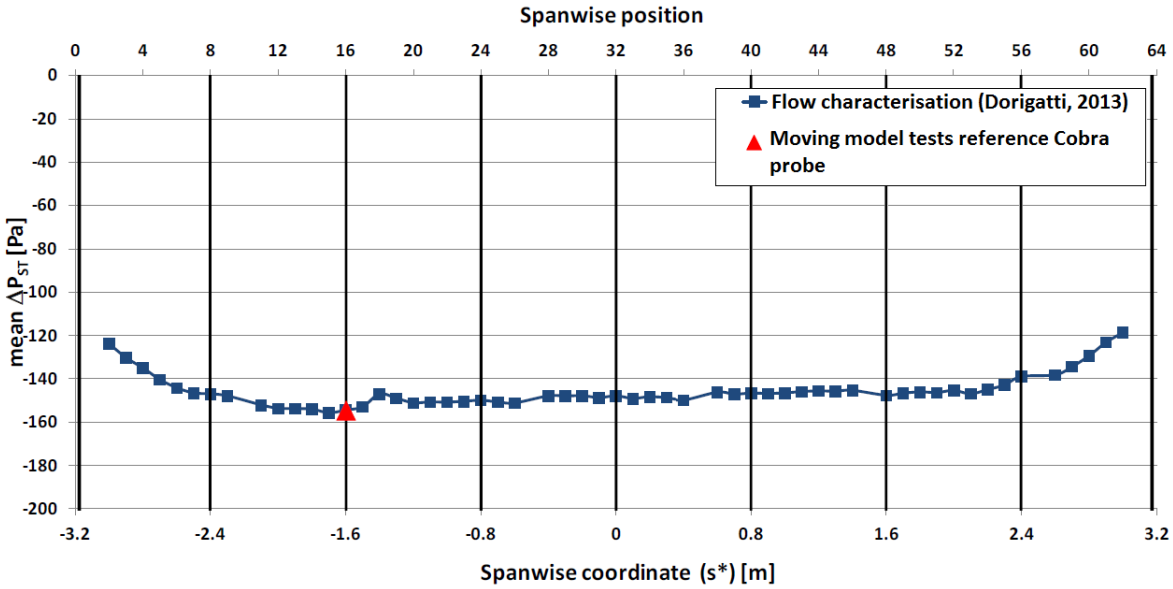

Figure 6.8.2 - Time averaged differential static pressure across the CWG (Dorigatti, 2013).

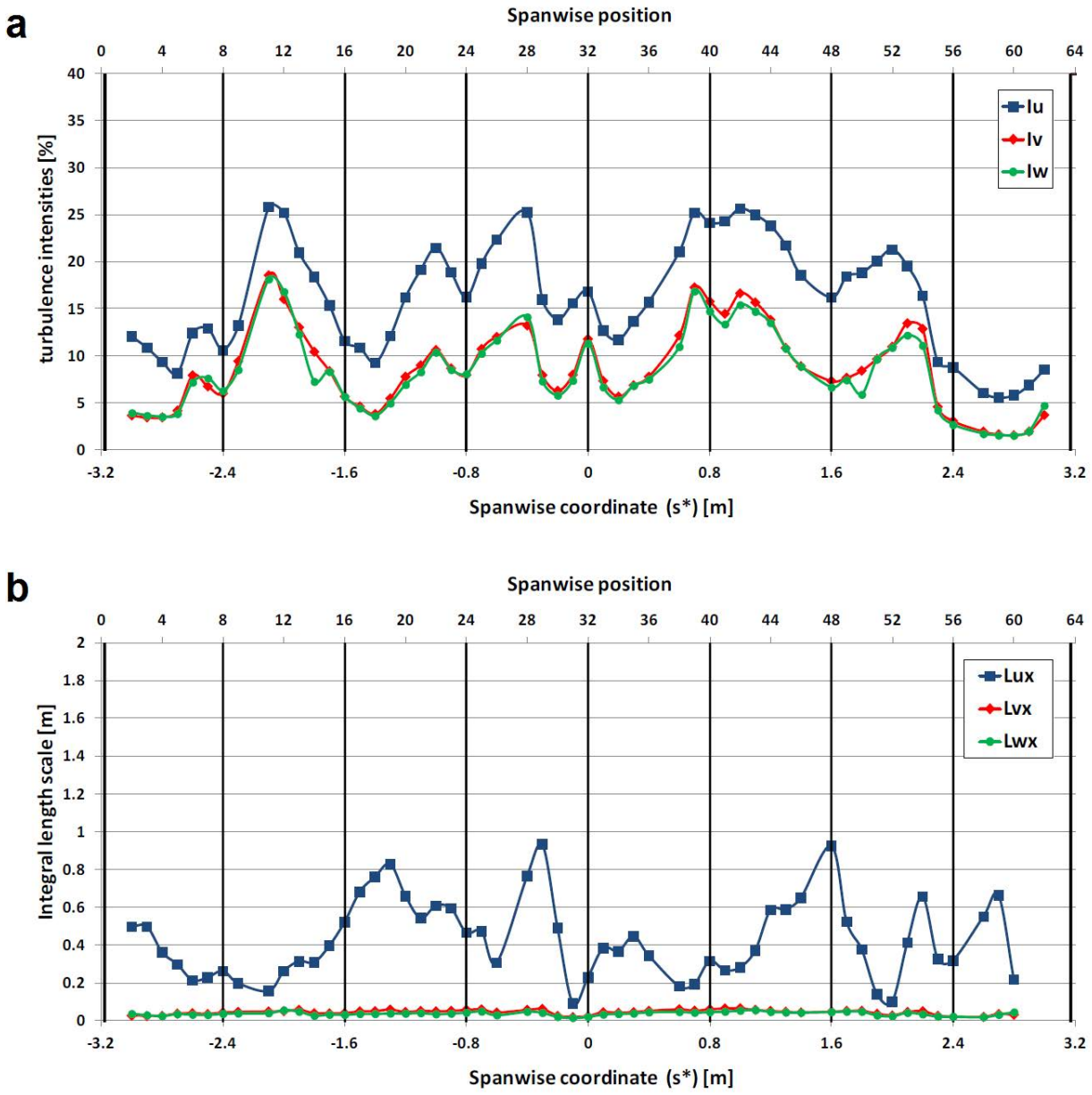

Figure 6.8.3 - (a) Turbulence intensities and (b) streamwise integral length scales across the CWG (Dorigatti, 2013).

The turbulence intensity and streamwise length scales also exhibit clear span-wise variation as shown in figure 6.8.3. The vertical velocity profile shows a typical logarithmic boundary layer profile that is about 0.2 m to 0.4 m thick (at model-scale) where thickness slightly with varies with span-wise position.

Table 6.3 - Span-wise average flow properties from flow characterisation (Dorigatti, 2013).

$\overline{U}$ (m/s)	$\overline{v}$ (m/s)	$\overline{w}$ (m/s)	ΔP_{stat} (Pa)	I_u (%)	I_v (%)	I_w (%)	L_{ux} (m)	L_{vx} (m)	L_{wx} (m)
12	0.0	0.2	-150	17	9	9	0.42	0.05	0.04

6.4 Experimental set up

Surface pressures on 1:25th scale HST model were measured as it was was fired through the CWG. The aim of these tests was to investigate the surface pressures at the same pressure tap positions as at full-scale over a range of yaw angles, and also to compare with the wind tunnel data , though it should be noted that the wind tunnel pressure taps were slightly different x-axis positions (along the train) to those used in the moving model tests (see figure 6.1.2), which matched full scale, i.e., X/L = 0.8. Following the methodology of Dorigatti, (2013), and Soper, (2014), a double averaged crosswind velocity (i.e., spatial average across the CWG span of the temporal mean velocities) of 12 m/s was taken in order to calculate train speeds necessary to acheive yaw angles of 15° to 30°, in 5° increments (table 6.4). Previous work has only considered a single yaw angle, therefore it is felt that this work should aid in the development of moving model crosswind studies. Each yaw angle consisted of 15 runs at

each investigative train speed, though equipment issues resulted in two additional 10 run ensembles needing to be conducted (see section H.2).

Table 6.4 - Investigative train speeds, corresponding yaw angles and required tensions for firing. Re number based on train height of 3.9 m and CWG velocity of 12 m/s.

Yaw angle (degrees)	Train speed (m/s)	Re number (10^5)	Tension (kN)
15	44.8	4.5	7.2
20	33.0	3.4	6.1
25	25.7	2.8	5.5
30	20.8	2.3	5.1

Tests were undertaken by firing the model train through the CWG after initiating the model data logger and allowing the CWG fans to reach full power.

The overall experimental set up was arranged so that transient data, from the HST passing a stationary Class 66 freight train model, and through a circular cross sectioned tunnel, could also be acquired by the pressure measurement system onboard the HST model in the same runs. The experimental set up for the transient tests is described in section H.3, but the results are not presented in this study.

6.4.1 Onboard data acquisition system

6.4.1.1 Onboard data logger

A bespoke onboard data logger, used in the crosswind tests conducted by (Dorigatti, 2013), and Soper, (2014), and previously in the AeroTRAIN project (European Commission, 2015),

was installed inside the 4 car HST model in the passenger coach behind the leading power car. The data logger was mounted on the model spine (figures 6.9.1 to 6.9.2) along with the pressure transducers (figure 6.10). The logger was capable of sampling 16 channels of data at 4000 Hz. The data was saved onto an integrated 4 GB SD card, and transferred to a PC after ever run using a USB interface and specialist software, which was also used to set the data logger to sample after some start up time delay.

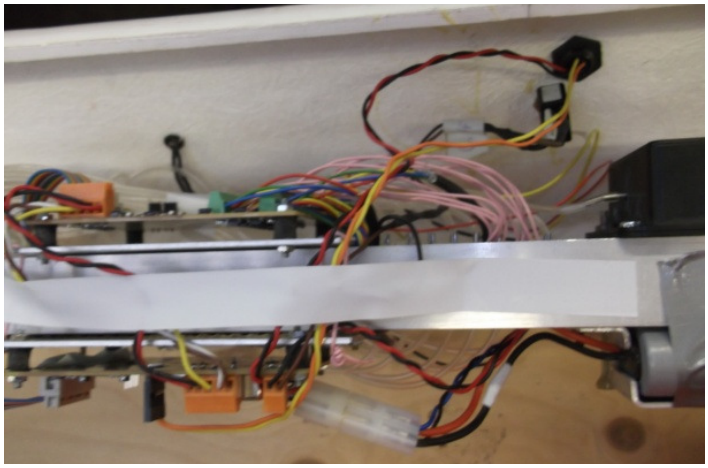

Figure 6.9.1 - Plan view of the datalogger fixed to the train model spine.

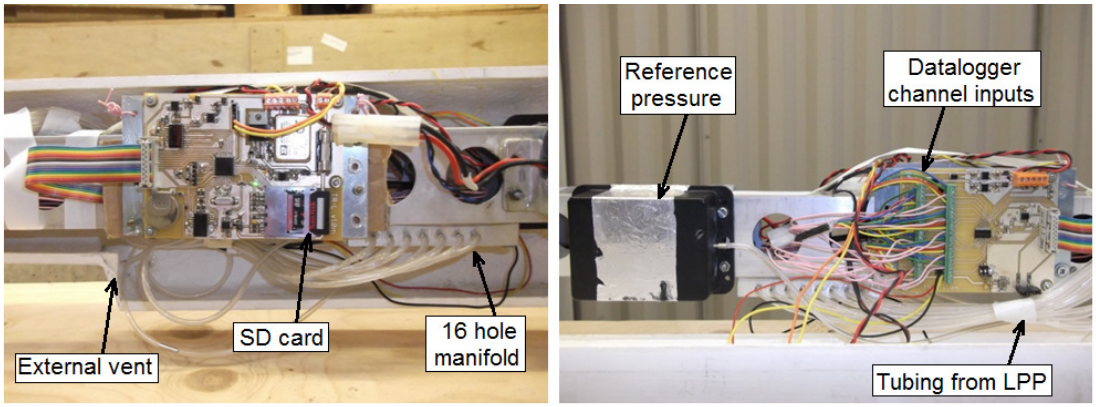

Figure 6.9.2 - Main features of the onboard data logger.

It was observed during the tests that certain channels of the datalogger did not function correctly (five channels altogether - see section H.2), most likely due to a short circuit between the signal and power cables as a result of the large mechanical forces on the train and minimal space within the train itself. A second test was therefore required, comprising two sets of 10 runs at 20° and 25° yaw angle.

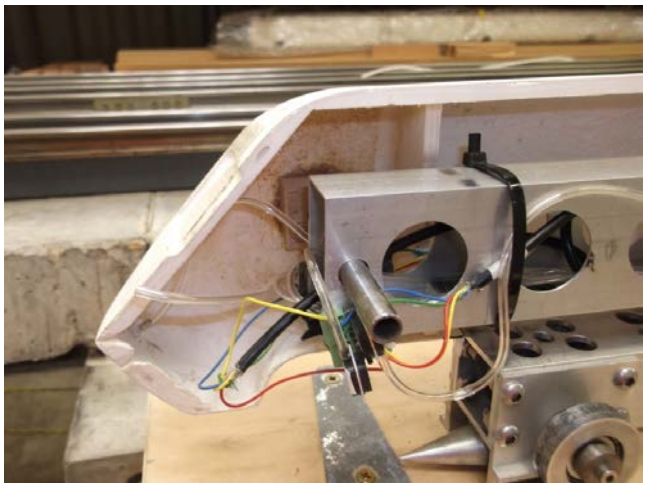

Figure 6.10 - Pressure tapping point and transducer at train nose.

6.4.1.2 Differential pressure transducers

Channels 1 to 15 of the data logger were connected to Sensortechnics HCLA0050DB differential pressure transducers (Sensortechnics, n.d.), with shielded multicore signal cables run through the spine of the model. This type of transducer was chosen as they are capable of an almost linear voltage to pressure response at pressures between ±2500 Pa, compared with the lower range transducers (±1250 Pa) used by Dorigatti (2013), and Soper (2014). Preliminary runs found that the pressures within the tunnel were expected to exceed 2000-3000 Pa, and in order to acquire usable train based measurements of tunnel transients for

further work during the same experimental runs, the larger operating range was preferred. A subsequent calibration of the onboard pressure measurement system (appendix E) found the best fit curves to fit a cubic equation (equation 7.14). The locations of pressure taps in the CWG tests are shown on figure 6.11, and a pressure tap at the nose is shown in figure 6.10.

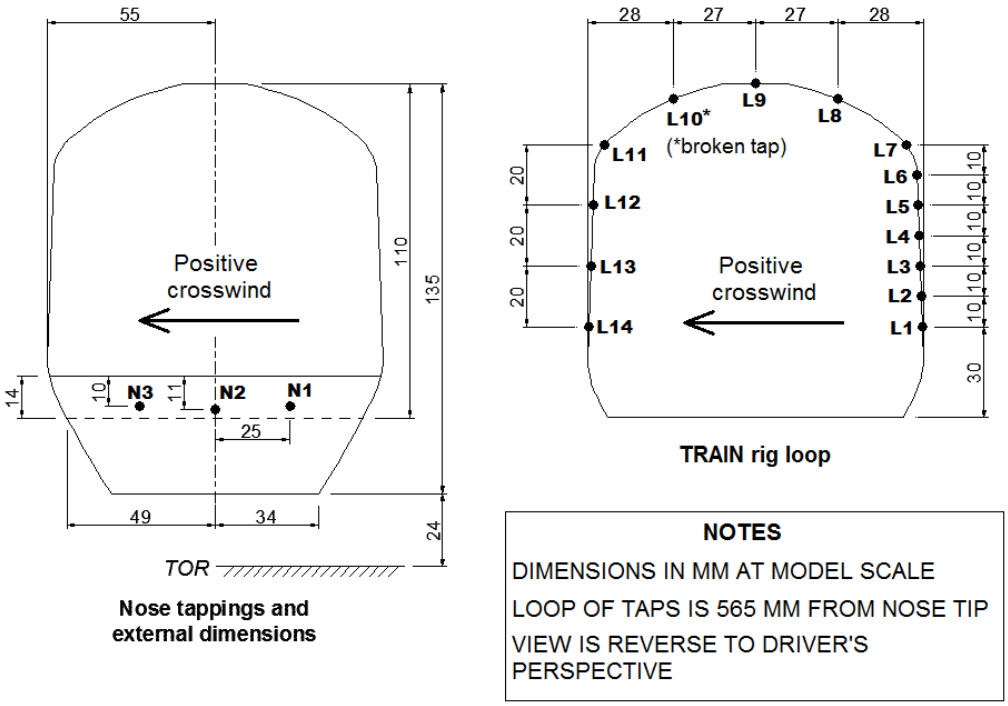

Figure 6.11 - Locations of pressure taps on TRAIN rig HST power car model at train nose and loop. Nose tap positions N1 - N3 were also tested on wind tunnel model and at full-scale on the NMT.

6.4.1.3 Light sensor

Channel 16 on the onboard data logger was used for a light detecting phototransistor (VISHAY-TEPT5600 sensor) (Vishay, 2011) housed on the leeward side of the train, exactly 1 m from where the train nose would break a light gate beam, in order to align the onboard data with the external systems. The light sensor would record a ~4.6 V signal at the ambient light conditions inside the building, and would drop sharply to between ~0-2 V when passing a light source (shown in figure 7.4).

6.4.1.4 Power supply

The system was powered using a 8 V battery pack, though the voltage to the transducers was limited to a ~5 V DC supply resulting in a very consistent background voltage (i.e., the voltage at ~0 Pa pressure difference across the differential transducer). The battery was charged between each run as the data was transferred to a PC by the same electrical connection, housed on the leeward side, next to the on/off switch (figure 6.12).

6.4.1.5 Pneumatic system

The high pressure port (HPP) of each differential pressure transducer was connected to a tapping point by a 150 mm length of 3.2 mm outer diameter (o.d.), 1.6 mm inner diameter (i.d.) silicone tubing, which was shorter than those used by Dorigatti, (2013), who used tube lengths up to 600 mm, and did not have tube resonance issues. The low pressure port (LPP) of each transducer was connected to a 16-hole manifold by a 450 mm length of tubing, which was, in turn, connected to an inflexible reference pressure reservoir via a 200 mm length of

tubing. The connection between the manifold and reference pressure reservoir had an external vent (located as shown in figure 6.12) to allow the reservoir to return to the ambient pressure before each individual run. The vent also allowed a true reading of the background voltage to be taken at the beginning of each day.

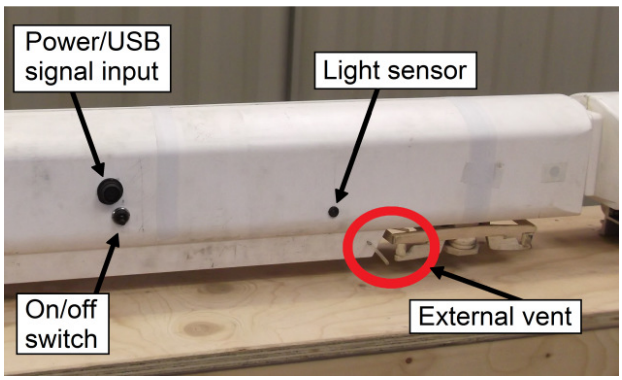

Figure 6.12 - External power and signal socket, logger power switch, light sensor and external reference pressure vent on leeward side of first carriage.

6.4.2 External set up

The experimental system comprised two Cobra probe data logging systems, a data logger dedicated to transient tunnel pressures and the onboard data logger. In order to synchronise the four systems, the analogue signal from each of the four photo-electric sensors used to measure train speed was recorded by each of the three external data loggers. Each logger was also set to sample at 4000 Hz to simplify subsequent data analysis. The crosswind test area is considered in more detail in figure 6.14.

6.4.2.1 Ambient conditions

The ambient temperature and humidity were recorded using the barometer and weather station described in section 3.4.3 (figure 3.10). Ambient conditions were noted at the start of each run in an Excel spreadsheet, and the temperature and pressure were always inputted into the TFI control software for the Cobra probes.

6.4.2.2 CWG set up

A single Cobra probe was set up in the crosswind generator at a height of 0.12 m above TOR, 0.2 m upstream of the track centreline and 4.2 m from the crosswind generator entrance (marked on figure 6.8.1 in red). This probe acted as a reference to ensure that the crosswind flow characteristics were consistent between runs, and analysis of the data from this probe found no significant differences in the mean crosswind velocity of each run.

Four sets of light gates were set up on either side of the CWG in two pairs spaced 1 m apart, to record the train speed for each run. It should be noted that the speeds obtained using these light gates were not directly used in the data analysis - the purpose of the light gates was to give an instant indication of whether the run was at an acceptable train speed. An LED light source was mounted on the first light gate sensor (figure 6.13.1 and 6.14), which would add a marker to the onboard data file at the instance where the train nose broke the second light gate (as the train mounted light sensor was 1 m from the position the train nose broke the second light gate beam). This allowed a consistent alignment marker at a fixed position between different data acquisition systems. Three additional light sources - 650 nm, 3 V, 1.5 mW lasers (figure 6.13.2) - were positioned inside the crosswind generator and spaced

approximately 2 m apart. Figure 6.14 shows the exact distances between the point where the beam struck the onboard light sensor). The advantage of this set up was a more accurately obtained position of the train within the crosswind generator than to simply assume a linear velocity decrease as in previous studies (Dorigatti, 2013 and Soper, 2014).

Figure 6.13.1 - Two pairs of light gates spaced 1 m apart, with LED light source on first (RHS) light gate.

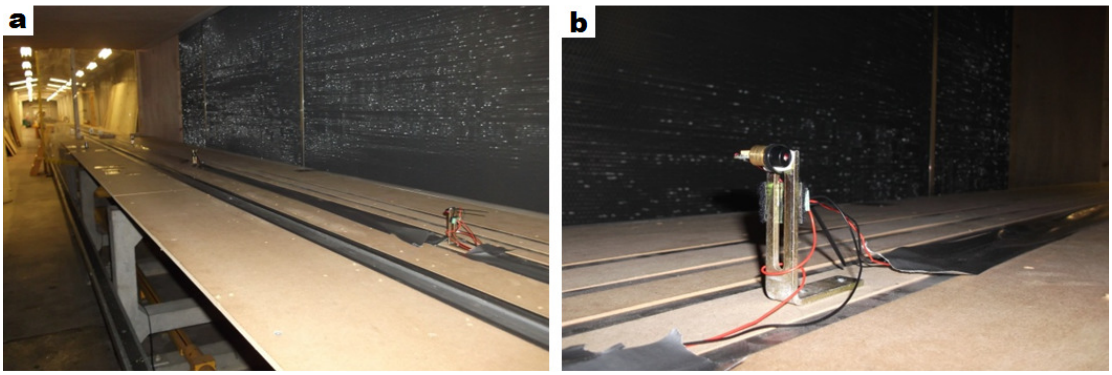

Figure 6.13.2 - (a) Three laser light sources inside CWG, (b) mounting of a laser.

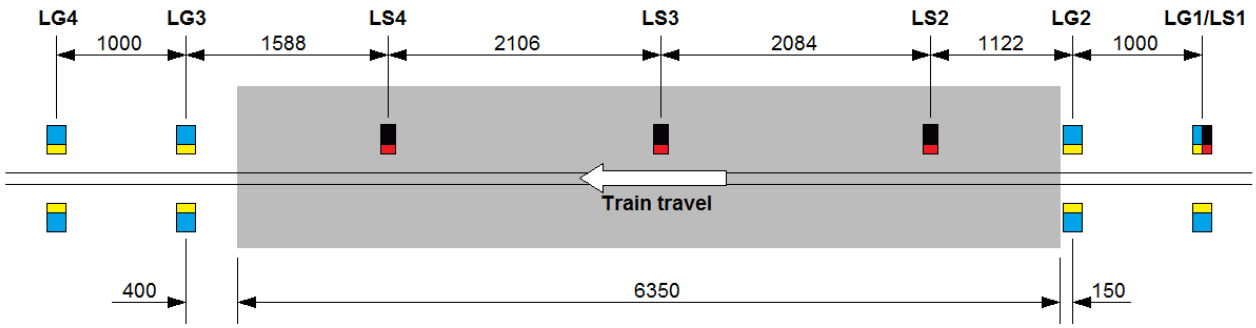

Figure 6.14 - Light gates 1 - 4 (LG) and light sources (LS) 1-4 relative to the crosswind generator (in grey). Dimensions in millimetres.

CHAPTER 7

MODEL-SCALE CROSSWIND TESTS - ANALYTICAL METHODOLOGY

7.1 Introduction

Chapter 7 describes the analytical procedure for the two scale model tests to measure the pressures on a 1:25th scale HST in a crosswind. Section 7.2 describes the analytical methodology for the RWDI wind tunnel data, which is fairly brief as the data was received by the UoB already converted to aerodynamic coefficients. The general methodology for calculating force and moment coefficients is presented in section 7.2.2, which is of relevance to the TRAIN rig CWG tests and the full-scale measurements. Section 7.3 describes the analytical methodology for the tests at the TRAIN rig using the CWG.

7.1.1 Definitions

In all of the crosswind investigations surface pressures were measured from pressure taps. Much of the analytical procedure is consistent between all pressure taps regardless of position. Where an equation can be applied to any pressure tap, the subscript "k" has been used to define the tap. Where analysis is focussed on a specific loop of pressure taps (when aerodynamic forces and moments are considered), the subscripts i and j have been used to denote the pressure tap number and loop number respectively.

Yaw angle is defined as θ when wind tunnel measurements are considered, and defined as φ when the TRAIN rig CWG tests are considered - the reason for this is that parameters from both tests were used to estimate yaw at full-scale, therefore it is necessary to distinguish between the two yaw angles at this stage.

7.2 Wind tunnel analytical methodology

Each pressure time series was sampled at 512 Hz and for 120 s. Data received by the UoB from RWDI was in the form of pressure coefficient time histories for each tap, and mean force and moment coefficients for the entire power car. Data from the reference probe was not provided.

The time averaged mean and standard deviations of pressure coefficient have been used in this study, and were calculated from the pressure tap time series in the conventional way. Assumptions had to be made about the experimental procedure and measurement equipment

in order to calculate the bias limit, and hence estimate the total error for each measurement. Error analysis is considered in section 7.2.3 and in more detail in Appendix F.

7.2.1 Analysis of pressure coefficient data

It has been assumed that instantaneous pressure coefficients were calculated for each pressure tap using:

$$C_{P_k}(t) = \frac{P_{k,Total}(t) - P_{Stat}(t)}{\bar{Q}} \tag{7.1}$$

Where $P_{k,Total}(t)$ was the instantaneous total pressure of a given pressure tap, k, assumed to be measured by the HPP of a pressure transducer, and $P_{Stat}(t)$ was the instantaneous static pressure from the pitot static probe and this was the pressure applied to the LPP of each transducer. $\bar{Q}$ was time averaged dynamic pressure and assumed to be recorded by a single differential pressure transducer across the total and static ports of the pitot-static probe for each yaw angle tested.

7.2.2 Calculation of force and moment coefficients

Force and moment coefficients were defined in equations 2.25a to 2.25e (though drag force is not considered in this study). A methodology to calculate these coefficients based on the measurement of the surface pressure distribution over a vehicle has been used successfully in previous studies at both model-scale (Sanquer et al., 2004, Dorigatti, 2013; Soper, 2014) and full-scale (Quinn et al., 2007). This method involves converting the model geometry into a

simplified model composed of discreet rectangular surfaces (discretisation), where each surface is "centred" on a pressure tap. The edges of each surface are extended to the midpoint between two adjacent pressure taps (or the container edges for end taps). The assumption was made that the pressure recorded by the pressure tap (subscript "k") was constant and uniformly distributed across the corresponding rectangular surface (subscript "S"). The pressure (or pressure coefficient) recorded by the pressure tap was multiplied by the discrete rectangle area of each surface (A_S) to obtain a dimensional force (F_S) or force coefficient (C_{F_S}) acting normal to, and at the centre of, each surface:

$$F_S = P_k A_S \tag{7.2}$$

$$C_{F_S} = \frac{C_{P_k} A_S}{A_{ref}} \tag{7.3}$$

Where A_{ref} is the reference side area of the vehicle, taken as 60 m^2 for the HST power car.

The dimensional side force (F_{Y_S}) and lift force (F_{Z_S}) on each surface are found through trigonometry by considering the angle between the horizontal (y-axis) and the line normal to each surface, θ_S:

$$F_{Y_S} = F_S \cos\theta_S \tag{7.4a}$$

$$F_{Z_S} = F_S \sin\theta_S \tag{7.4b}$$

Similarly the non-dimensional side and lift force coefficients on each surface, C_{Y_S} and C_{Z_S} respectively, are defined as:

$$C_{F_{Y,S}} = C_{F_S} \cos\theta_S \tag{7.5a}$$

$$C_{F_Z,S} = C_{F_S} \sin\theta_S \tag{7.5b}$$

Figure 7.1 shows the definition of θ_S for all orientations of surfaces considered (assuming a positive pressure), and is defined such that $\theta_S \leq 90°$. If a negative pressure is considered, the axis definitions as shown on figure 7.1 for force vectors F_{Y_S} and F_{Z_S} are reversed.

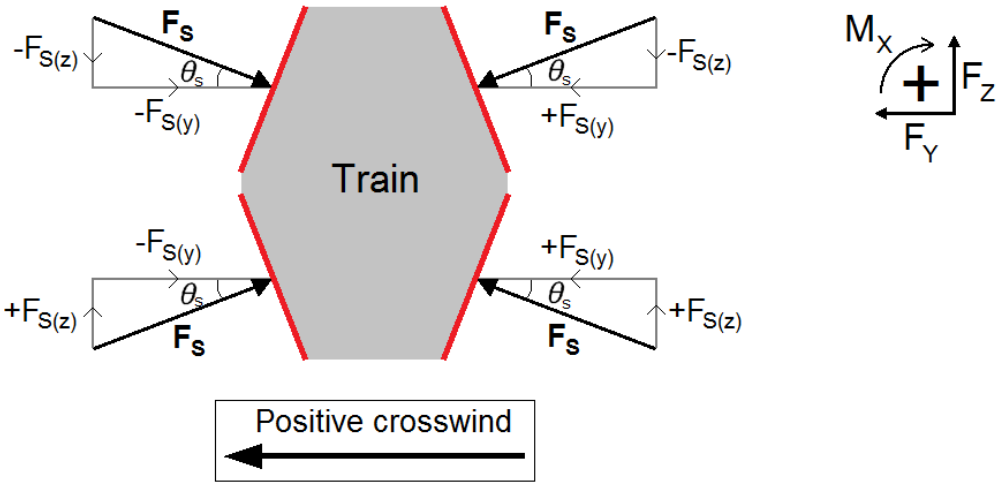

Figure 7.1 - Definition of θ_S and vector forces resolved in the y and z axes (side and lift) for all surface (subscript "S") orientations considered.

Total side force and lift force are calculated as the sum of the side and lift forces on each surface:

$$F_Y = \sum_{N_S} F_{Y_S} \tag{7.6a}$$

$$F_Z = \sum_{N_S} F_{Z_S} \tag{7.6b}$$

Where N_S is the number of surfaces. Dimensional overturning moment and lee-rail moment are calculated as:

$$M_X = \sum_{N_S}(F_{Y_s}L_{Z,S}) + \sum_{N_S}(F_{Z_s}L_{Y,S}) \tag{7.7a}$$

$$M_{X,lee} = \sum_{N_S}(F_{Y_s}L_{Z,S}) + \sum_{N_S}(F_{Z_s}L^*_{Y,S}) \tag{7.7b}$$

Where $L_{Z,S}$ is the vertical component of the distance from TOR to the midpoint of each surface, $L_{Y,S}$ is the horizontal component of the distance from COT to the midpoint of each surface (defined as positive from COT to windward side) and $L^*_{Y,S}$ is the same as $L_{Y,S}$ but from the leeward rail.

Non-dimensional force coefficients are defined:

$$C_Y = \sum_{N_S} C_{F_Y,S} \tag{7.8a}$$

$$C_Z = \sum_{N_S} C_{F_Z,S} \tag{7.8b}$$

Non dimensional moment coefficients are defined as:

$$M_X = \frac{(\sum_{N_s} C_{F_Y,S}L_{Z,S}) + \sum_{N_s}(C_{F_Z,S}L_{Y,S})}{L_{ref}} \tag{7.9a}$$

$$M_{X,lee} = \frac{(\sum_{N_s} C_{F_Y,S}L_{Z,S}) + \sum_{N_s}(C_{F_Z,S}L^*_{Y,S})}{L_{ref}} \tag{7.9b}$$

Where $L_{Z,S}$ is the vertical height of the midpoint of each surface from TOR, $L_{Y,S}$ and $L^*_{Y,S}$ are the horizontal distances of each surface midpoint from the COT and leeward rail respectively and L_{ref} was taken as the train height at full-scale (3.9 m).

In this study only a single loop of pressure taps around the walls and roof were measured during the CWG tests and at full-scale. Force/moment coefficients are defined for a single loop, i.e., coefficient per unit length of the train, as C^*_η. For the wind tunnel measurements, C^*_η can be expressed as the sum of the partial force and moment coefficients per unit length considering the walls and roof (loop) and the underbody (floor) separately:

$$C^*_\eta = C^*_{\eta,loop} + C^*_{\eta,floor} \tag{7.10}$$

Note that the underbody contribution to C^*_Y is taken as zero given that all pressure taps are on a horizontal surface. Additionally, an overbar is used on $\overline{C^*_\eta}$ to denote that it was obtained from time averaged $\overline{C_{P_k}}$.

Finally, the calculation of total force and moment coefficients on the power car was found through integration of the values of C^*_N across the length of the power car, and the widths of each 1 m strip were adjusted so that the edges of each strip were at the centre of each loop of taps (illustrated in figure 7.2.2). Figure 7.2.1 shows the simplified HST model discretisation for any of the loops of pressure taps on the RWDI wind tunnel model (the underbody is shown in appendix G). Each of the coloured lines on figure 7.2.1 represents a surface, S, (labelled on the outside of the train outline) and the corresponding pressure tap (labelled on the inside of the train outline). The areas of each surface and corresponding pressure tap, along with the angle of each surface, θ_S, are given in table 7.1.

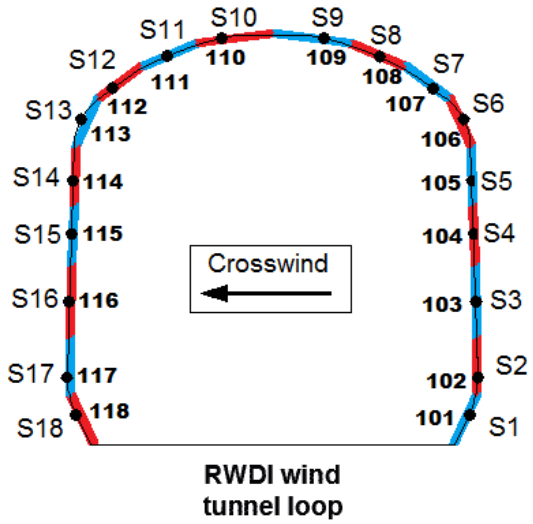

Figure 7.2.1 - Model discretisation showing surfaces 1 to 14 (red and blue) and corresponding pressure taps for RWDI wind tunnel rig model.

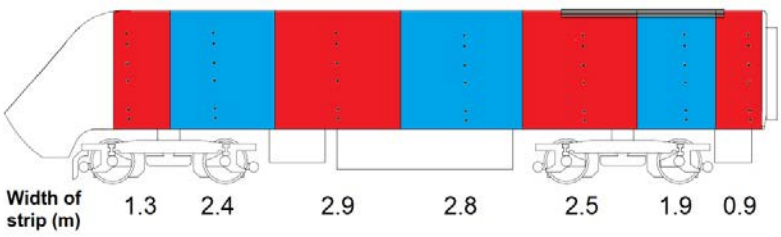

Figure 7.2.2 - Widths (at full-scale) and locations of extended strips used to calculate overall forces and moments on the HST power car from the wind tunnel pressure taps.

Table 7.1 - Areas and angles of discrete model geometry surfaces and corresponding pressure taps for wind tunnel model.

Surface number	Pressure tap	A_S (m^2)	θ_S (°)
1	101	0.38	19
2	102	0.46	2
3	103	0.59	2
4	104	0.50	2
5	105	0.47	2
6	106	0.43	30
7	107	0.44	57
8	108	0.51	68
9	109	0.65	77
10	110	0.65	77
11	111	0.51	68
12	112	0.44	57
13	113	0.43	30
14	114	0.47	2
15	115	0.50	2
16	116	0.59	2
17	117	0.46	2
18	118	0.30	19

7.2.3 Error and uncertainty analysis

The calculation of errors for the wind tunnel data was based on a series of assumptions regarding the experimental set up and equipment accuracy. Appendix F describes the calculation procedure and assumptions made in detail. Errors were defined as the sum of the bias limit and random uncertainty (equations F.1 to F.3), and are expressed as absolute values of the mean pressure coefficients. Errors were calculated for all pressure taps and at all yaw angles. The wind tunnel errors presented in this study are only rough estimates - however they are believed to be within the correct order of magnitude and allow comparison between

different regions of the train and yaw angles (Dorigatti, 2013). Figure 7.3 shows the bias, random and total uncertainties for both of the RWDI wind tunnel tests. The bias limit was found to be the largest contribution to total error - the random uncertainty was low because of the large sample size. The first ~120 pressure taps are at the nose of the train and exhibit higher errors than the taps along the length of the main power car body. Errors at the train nose were on average about 0.01 - 0.04 C_P higher than those along the length of the power car, and that errors were not sensitive to yaw angle at yaw angles up to about 30°. The different regions around the loops (windward wall, roof and leeward side wall) showed little difference in the values of error at lower yaw angles. However, at 45°, larger errors were found at the windward wall-roof junction which is a separation point, and the larger errors are in line with previous studies (Dorigatti, 2013; Soper, 2014).

The second RWDI wind tunnel test was at a slightly lower velocity and higher turbulence intensity, and unsurprisingly the errors were slightly higher (figure 7.3). The larger bias limit was mostly as a result of the lower wind tunnel test speed (hence dynamic pressure) as in equation F.1, and the larger random uncertainty was due to the higher standard deviation due to the higher streamwise turbulence intensity. For the purposes of this study, nominal and consistent errors have been assumed for all pressure taps either at the nose or in loops around the length of the power car, and these are given in table 7.2.

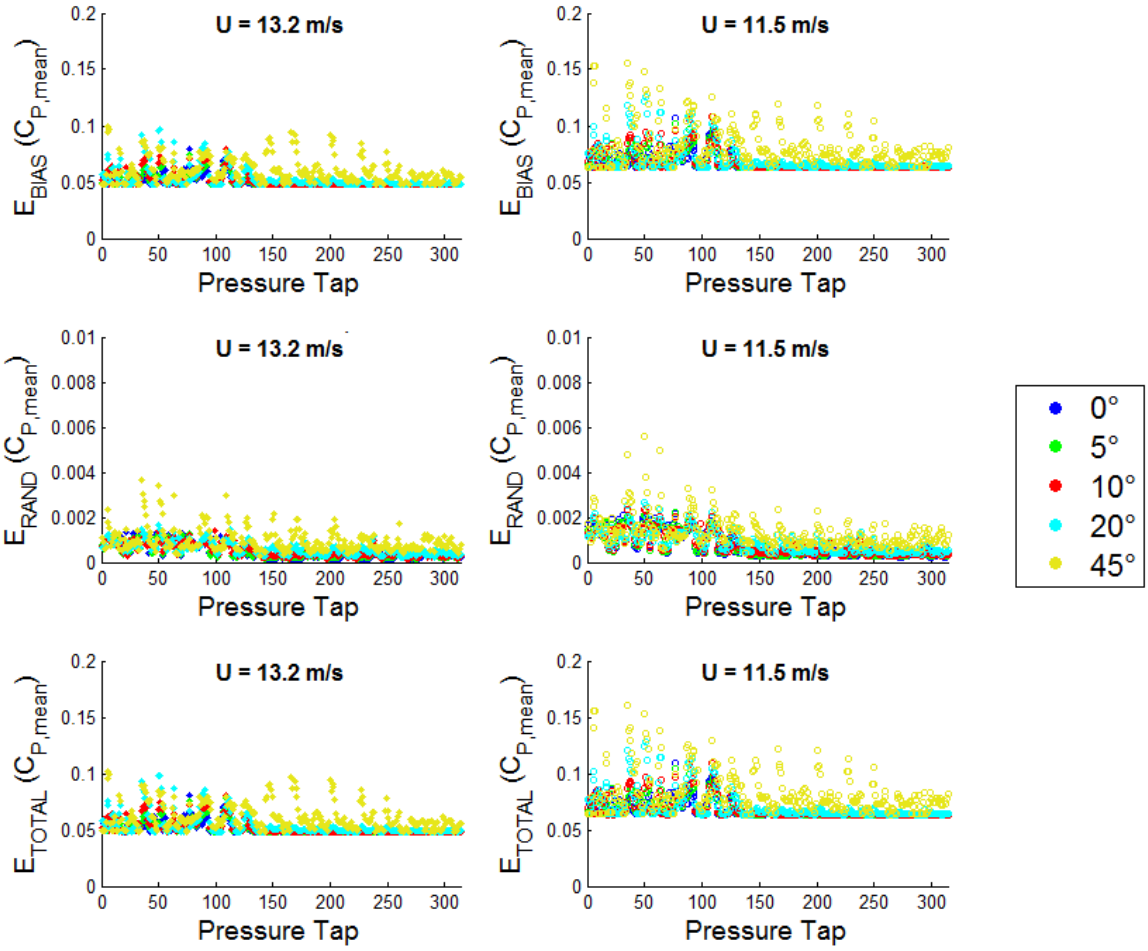

Figure 7.3 - Bias, random and total errors for both RWDI wind tunnel tests.

Table 7.2 - Nominal total errors for both RWDI wind tunnel tests.

Location of pressure taps	E_{Total} $(\overline{C_P})$	
	U = 13.2 m/s	U = 11.5 m/s
Nose	0.06	0.07
Loop	0.05	0.06

7.3 TRAIN rig crosswind tests analytical methodology

Tests were conducted at the TRAIN rig using the crosswind generator and the onboard data logger at yaw angles of 15° to 30°. The overall procedure for these tests is described in this section. Additional specific details about this test are provided in appendix H.

The overall strategy for processing the data post-acquisition was as follows:

- Each data file from the onboard data logger was checked to ensure that all the light sources have been detected (all light sources were successfully detected on every run);
- Isolate data from when the train is in the crosswind generator using the LED light source (mentioned in section 6.3.2.2) as a reference position;
- Using the light sources and onboard light sensor, a column of distance inside the crosswind generator was created, assuming linear decelerations between light sources. The nose taps and loop taps were considered separately during analysis because of their different positions on the train. Train speed, streamwise aerodynamic velocity and crosswind velocity (hence yaw angle) were then obtained as a function of time.
- Voltage data from each transducer was converted to pressure data, which was then low-pass filtered then normalised to pressure coefficients.

The processing of the data was automated entirely using Matlab to ensure that all analysis was correct and of the same quality. The format of the collected data is described in section H.4.

7.3.1 Data isolation

The first stage of data processing was to align all the data files from the different data loggers. For each independent system, the second light gate being triggered (which corresponded to the onboard light sensor registering the LED) was used as a reference marker. The onboard light sensor was able to successfully record the LED light source and three lasers on every run, though the raw voltage change was often inconsistent between light sources. To detect these points the gradient of the voltage time series of the light sensor was considered rather than the peak raw voltage, as the voltage would always decrease sharply when passing a light source. Figure 7.4 shows an entire raw run - the initial peak in voltage between 11 s and 11.5 s is the moment the model was fired (the acceleration of the model is seen on channels 1 - 3), there is then a large pressure transient as the train passes through the tunnel and the light sources at the CWG can be seen as the vertical black lines.

Given that the exact positions of the light sources were known relative to the CWG (see figure 6.14), the distances relative to the CWG entrance were added to the data when a light source was detected. A constant train speed was assumed between the light sources and a distance time series was created by interpolation for the nose and loop taps separately.

The onboard pressure data was then trimmed using the distance time series to distances between 0 m and 6.35 m (i.e., the span of the CWG) for both the nose taps and loop of taps, and then the data near the entrance and exit portals was discarded. For both the nose and loop of taps the first 1.2 m of data was removed. Soper, (2014), removed all data after 5.7 m following the methodology of Dorigatti, (2013), however, it was noted that when considering the nose taps (see figure 7.5.1) that there was a large increase in pressure coefficient at 5 m through the CWG - all data after this point was therefore discarded.

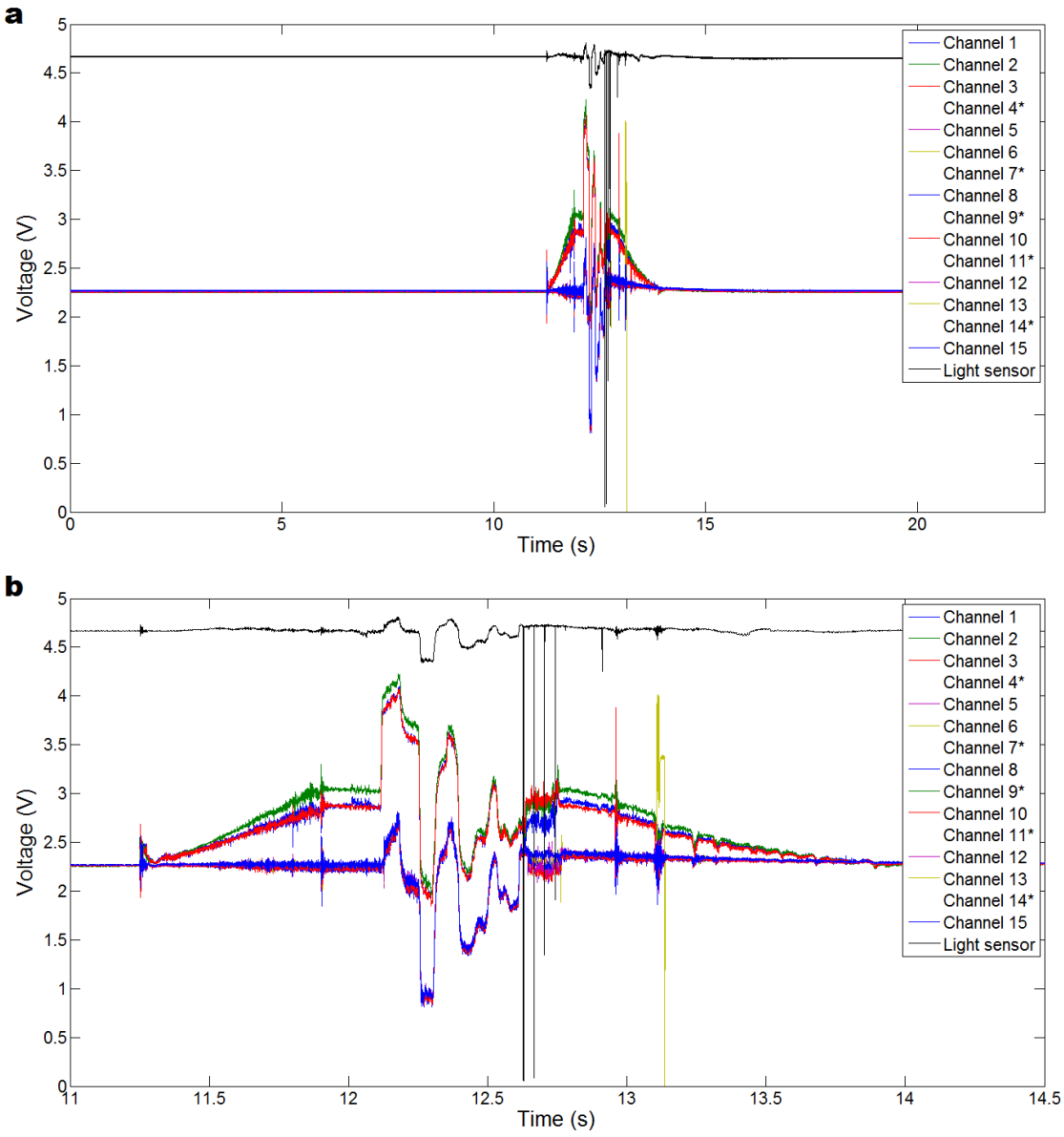

Figure 7.4 - Raw voltage time series from onboard data logger (a) for 20 s of sample time, (b) zoomed in showing the entire train run.

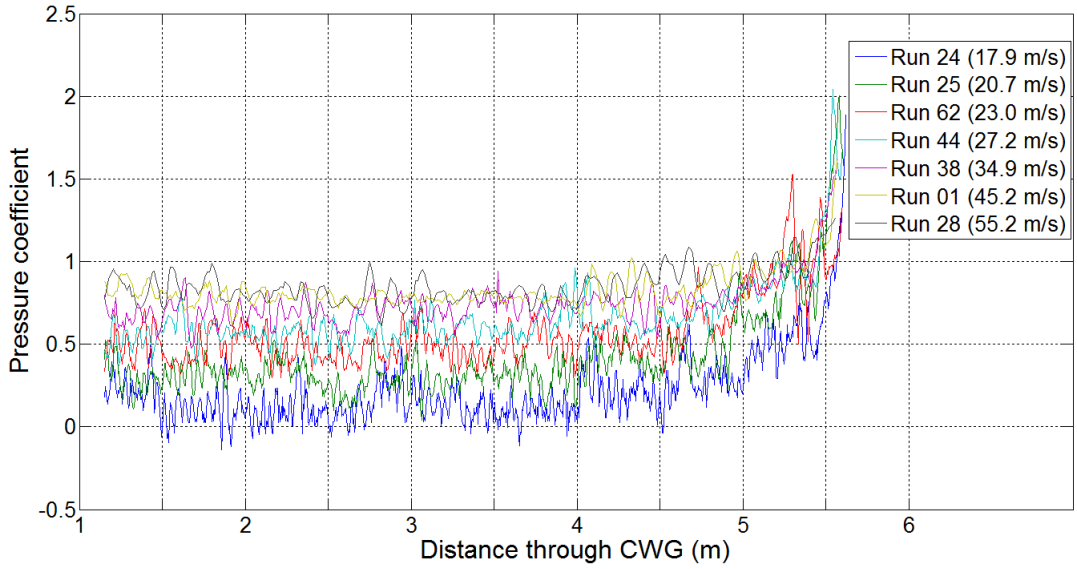

Figure 7.5.1 - Pressure coefficient time history of 7 unfiltered runs at different speeds for the central nose tap (tap N2).

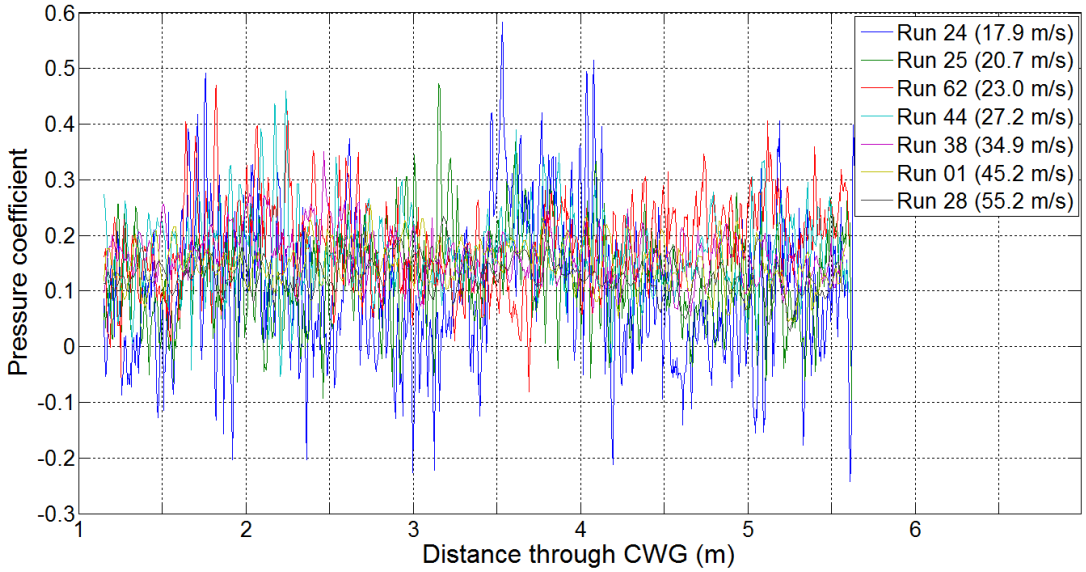

Figure 7.5.2 - Pressure coefficient time history of 7 unfiltered runs at different speeds for the windward wall tap (tap L1).

7.3.2 Low-pass filtering

Previous studies have found that mechanical interference caused by the fan blades results in resonant noise in the pressure tap time series (Dorigatti, 2013; Soper, 2014). The power spectrum was obtained by performing a Fourier transform on the fluctuating component of the raw voltage time series (decomposed by subtracting the mean voltage) using the Fast Fourier Transform function "fft" on Matlab (Mathworks, 2010). The power spectra of the raw data at different pressure taps and train speeds were investigated and no train speed effects were observed in the power spectra (section H.5 considers this in detail), suggesting that the frequency of mechanical vibrations due to the model (assumed to scale to train speed) had no apparent effect on the recorded data. This highlights the efficacy of using the onboard data logger rather than a force balance which can be sensitive to mechanical vibration (Dorigatti, 2013).

Figure 7.6 shows the power spectra from raw and filtered data from a single run for key pressure taps. A peak in the raw data power spectrum was found at frequencies between about 130 Hz to 200 Hz, and was present for each of the different pressure taps and independent of train speed. This range is in agreement with Dorigatti, (2013) who found a resonant peak at about 135 Hz, and concluded this to be due to interference caused by the fan blades. Data was filtered by using a low-pass second-order Butterworth filter with a cut off frequency of 100 Hz. The frequency spectra of the filtered data, illustrated in red on figure 7.6, shows that the resonant peak observed at 100-200 Hz has successfully been removed and the majority of the original signal unaltered. The effect of this filtering on individual runs measured by the windward tap at 20°, and the spatial (span-wise) ensemble average pressure coefficient is shown in figure 7.7. All proceeding analysis considers the data after it has been filtered.

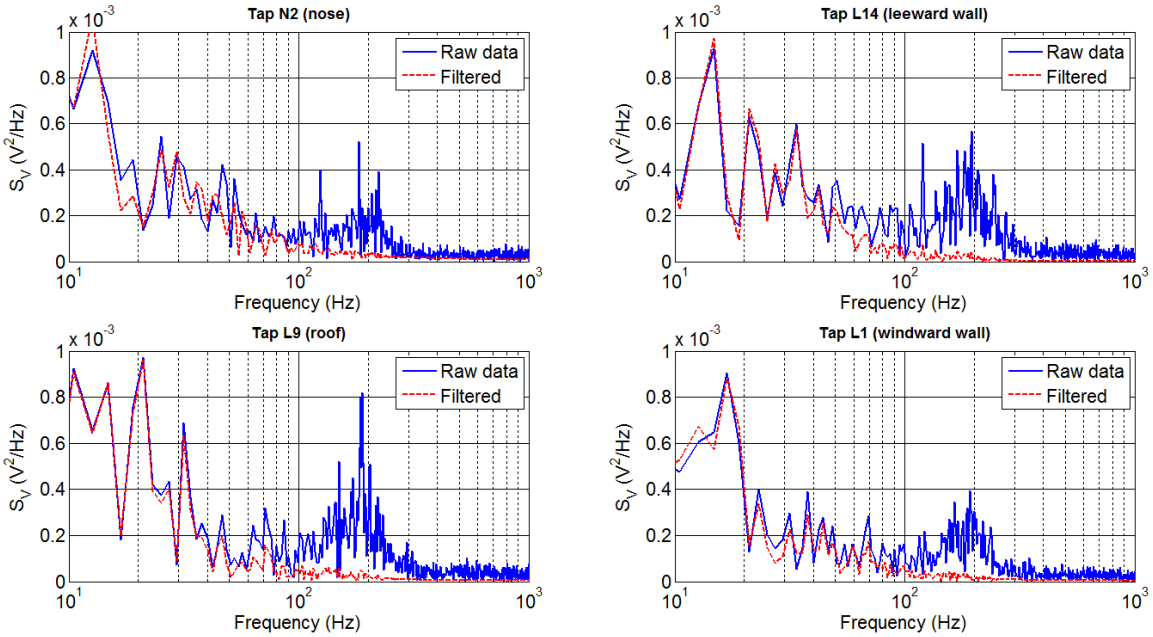

Figure 7.6 - Power spectra of single run voltage time series for raw and filtered data at key tapping positions.

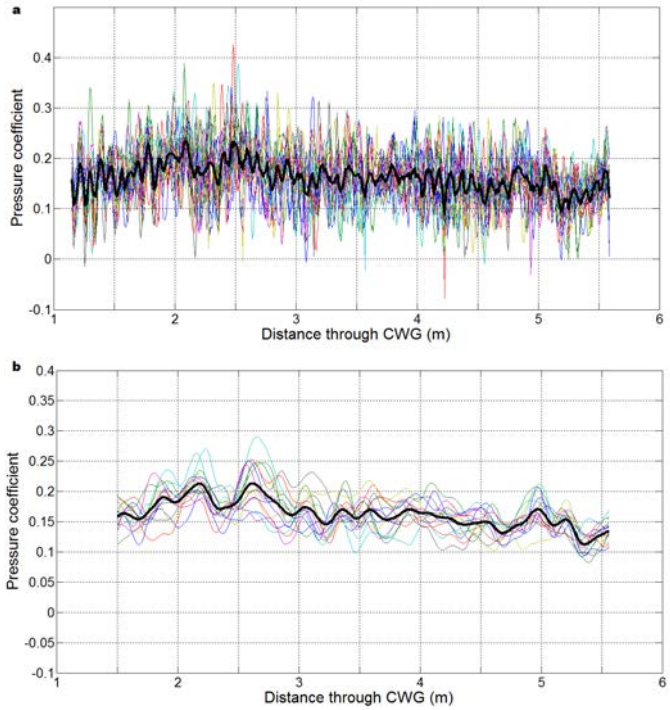

Figure 7.7 - Individual runs (15) and ensemble in dark black for (a) unfiltered and (b) filtered data for tap 15 (windward side in loop at 15° yaw angle).

7.3.3 Data conversion

Data acquired by the data logger was recorded as the voltage of the output signal of each pressure transducer and sampled at 4000 Hz. The pressure transducers output a digital voltage signal, $\Delta V_k(t)$, defined as:

$$\Delta V_k(t) = V_k(t) - V_{0,k} \tag{7.11}$$

Where $V_k(t)$ is the voltage at a given instant in time, t. The background voltage $V_{0,k}$, i.e., voltage at 0 Pa differential pressure was calculated by:

$$\Delta V_{0,k} = V_{0,k,Run} - V_{0,k,AMB} \tag{7.12}$$

$$V_{0,k} = V_{0,k,Run} - \Delta V_{0,k,} \tag{7.13}$$

Where $V_{0,k,Run}$ is the mean voltage for 5 s of data before each individual run (while the train is stationary), and $V_{0,k,AMB}$ is the voltage obtained from an open vent test at the start of each day, i.e., the voltage of each transducer when both the HPP and LPP are open to the atmosphere. It should be noted that the difference, $\Delta V_{0,k}$, was very low - of the order of less than 0.5% of $V_{0,k,Run}$, and can be therefore be approximated as zero.

The voltage signal, $\Delta V_k(t)$, was converted to instantaneous pressure, $\Delta P_k(t)$, following an empirical equation based on the calibration described in appendix E:

$$\Delta P_k(t) = K1_{ACC,k}\Delta V_k^3(t) + K2_{ACC,k}\Delta V_k^2(t) + K3_{ACC,k}\Delta V_k(t) \tag{7.14}$$

Where coefficients $K1_{ACC,k}$, $K2_{ACC,k}$ and $K3_{ACC,k}$ are obtained from a cubic best fit of calibration data for each transducer and given in table E.4.2. It should be noted here that the calibration of the onboard system (in appendix E) did not result in a clear cubic calibration, though the cubic calibration model resulted in the lowest errors for most of the pressure transducers than compared to linear calibration models, though the errors for a linear calibration were generally also very close to the cubic model (i.e., <0.5% difference in absolute percentage error) - see "Calibration 3" on figure E.7.

The measured voltage is an output from the transducer based on the difference in pressure between the HPP, $P_k(t)$, and the LPP (reference pressure reservoir), P_{Ref}, expressed as:

$$\Delta P_k(t) = P_k(t) - P_{Ref} \tag{7.15}$$

It has been assumed that $P_{Ref} = P_{ATM}$ for the duration of each run, where P_{ATM} is the ambient atmospheric pressure in the room (recorded with a digital barometer during each run).

7.3.4 Calculation of pressure coefficients

The mean CWG velocity and static pressures, shown in figures 6.8.1 and 6.8.2, are a function of distance through the CWG. However, in this analysis the data was considered in the time domain to reflect the actual analytical process.

The vehicle speed is related to both the distance of the train through the CWG (which was marked on the data by the light sensor channel), and the time at which the train passes the light sensors, where the time is defined as:

$$t = \frac{n_{sample} - 1}{f} \tag{7.16}$$

Where n_{sample} is the sample number and f is the sampling frequency. The time origin was initially taken as the instant the light sensor passed the first light source.

A uniform deceleration (with a linear gradient $m_{V,tr,(LN-1)}$) between light sources is assumed,

$$m_{V,tr,(LN-1)} = \frac{V_{tr,(LN)} - V_{tr,(LN-1)}}{V_{tr,(LN-1)}} \tag{7.17}$$

Where $V_{tr,(LN)}$ is the train speed at the midpoint between two light sources (numbered 1 to 4, denoted by subscript *LN*). Train speed can be estimated using:

$$V_{tr}(t) = V_{tr,(LN-1)} - (m_{V,tr,(LN-1)} \times t_{(LN-1):LN}) \tag{7.18}$$

Where $V_{tr}(t)$ is the train speed at any given moment in time inside the crosswind generator. Note that a linear extrapolation of the velocity gradient, $m_{V,tr,(LN-1)}$, is assumed for all positions after the fourth (and final) light source.

$V_{tr}(t)$, is slightly different for the nose and loop tapping points. The nose taps and loop of taps are spaced 0.65 m apart, and the light source is 1 m from the nose taps. As a result, the nose taps and loop taps have slightly different distance and time series as the nose taps move through the CWG faster than the loop taps. The distance origin was defined at the entrance portal and wall (i.e., the start of the CWG), and the time origin was then redefined as the instant that the pressure taps passed the distance origin (i.e., once the taps had passed through the entrance portal).

The mean flow velocity, in both the streamwise and transverse directions, $\bar{u}(t)$ and $\bar{v}(t)$ respectively, is a function of distance through the CWG, x, and can also be thought of as a function of normalised distance, $d_{Sn,Norm}$ between the any two adjacent of the 64 measurement positions (i.e., the distance between two measurement positions 0.1 m apart, divided by 0.1 m). The change in velocity between two adjacent measurement positions, denoted with subscripts Sn and $Sn+1$, is assumed to vary linearly with distance, such that:

$$\bar{u}(t) = \bar{u}_{Sn} + d_{Sn,Norm}\,(\bar{u}_{Sn+1} - \bar{u}_{Sn}) \tag{7.19a}$$

$$\bar{v}(t) = \bar{v}_{Sn} + d_{Sn,Norm}\,(\bar{v}_{Sn+1} - \bar{v}_{Sn}) \tag{7.19b}$$

Where $\bar{u}_{Sn}$ and $\bar{v}_{Sn}$ are the mean velocities obtained from the flow characterisation outlined in section 6.3.1 for each measurement position (Dorigatti, 2013). The time averaged mean static pressure at a given time in the CWG, $\overline{P_{Stat}}(t)$, can be expressed in the same form:

$$\overline{P_{Stat}}(t) = \overline{P_{Stat}}_{Sn} + d_{Sn,Norm}\left(\overline{P_{Stat}}_{Sn+1} - \overline{P_{Stat}}_{Sn}\right) \tag{7.19c}$$

The term $\bar{v}(t)$ is defined as positive in the direction of train travel, and so the aerodynamic vehicle speed in the direction of train travel, $\bar{U}_{tr,Aero}(x)$, is given by:

$$U_{tr,Aero}(t) = V_{tr}(t) - \bar{v}(t) \tag{7.20}$$

The resultant wind velocity, $\overline{U}_{Res}(t)$, and instantaneous yaw angle, $\varphi(t)$, are given by:

$$\overline{U}_{Res}(t) = \sqrt{(U_{tr,Aero}(t))^2 + \bar{v}(t)^2} \tag{7.21}$$

$$\varphi(t) = \arctan(\frac{\bar{v}(t)}{U_{tr,Aero}(t)}) \tag{7.22}$$

Note that an over bar has been used on $\overline{U}_{Res}(t)$ as it comprises two time averaged values, though its value is an instantaneous function of distance through the CWG (i.e., time). The density of air, ρ, was then calculated according to equation 4.5, and the instantaneous pressure coefficient per transducer is defined as:

$$C_{P_k}(t) = \frac{\Delta P_k(t) - \overline{P_{Stat}}(t)}{\frac{1}{2}\rho(\overline{U}_{Res}(t))^2} \tag{7.23}$$

Note that the subscript φ is used to define the term $C_{P_k}(t)$ when considering a specific yaw angle, φ.

7.3.5 Average pressure coefficients (yaw angle bins)

Following the trim of data and conversion to pressure coefficients, the data was saved as two data files (one for the nose taps and one for the loop) for each run containing the filtered pressure coefficient time series within the working length of the CWG, and a column of instantaneous yaw angle. The data was then binned according to the instantaneous yaw angle

into nominally sized bins of ±1.5° between 15° to 30° in 5° steps. The mean pressure coefficient for each channel (i.e., tapping point) for each yaw angle was calculated by:

$$\overline{C_{P_{k,\varphi}}} = \frac{\sum_{i=1}^{N_{bin,\varphi}} C_{P_{k,\varphi}}(t)}{N_{bin,\varphi}} \tag{7.24}$$

Where $N_{bin,\varphi}$ is the bin size at a given yaw angle.

Mean yaw angle, $\bar{\varphi}$, for each bin was found in the same way from instantaneous yaw, $\varphi(t)$. For all cases, $\bar{\varphi}$ was within 0.1° of the target yaw angle, and the $\varphi(t)$ followed a normal statistical distribution within each bin, shown in figure 7.8. Standard deviations for each pressure tap and yaw angle bin, $\sigma_{k,\varphi}$, were therefore calculated assuming a normal statistical distribution of pressure coefficients within each bin and in the conventional way ($\sigma_{k,\varphi}$ is considered in the error analysis in appendix F). These quantities are given for each pressure tap and yaw angle in table 8.2. Figure 7.8 shows a negative skew when the yaw angle range of ±2.5° is considered at (i.e., more of the data falls within the lower angle bin range). This skew resulted in a decrease in the mean spanwise yaw angle of about 1° when the bin sizes were ±1.5° (see figure H.14), however subsequent analysis has not accounted for this reduction as a 1° change in yaw angle would not have a significant effect (i.e., no greater then experimental uncertainty) on the surface pressure distributions (shown in section 8.3). It should also be noted that the coefficients presented in table 8.1 were obtained from the actual mean yaw angles of each bin (rather than nominal investigative yaw angles).

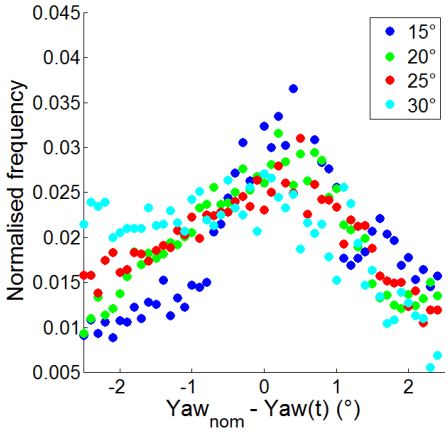

Figure 7.8 - Statistical distribution of instantaneous yaw angles, yaw(t), (in 0.1° bins) for all data collected within ±2.5° of the nominal investigative yaw angles, Yaw_{nom}.

7.3.6 Calculation of force coefficients

Side force coefficients per unit length were calculated for the loop of pressure taps. As discussed in appendix H, certain channels on the data logger did not function correctly and therefore a second test was undertaken to test the broken tap positions. Force coefficients are therefore only considered at yaw angles of 20° and 25°, i.e., where all pressure taps have usable data. The geometrical discretisation of the TRAIN rig model is shown in figure 7.9, and the specific areas of each finite geometry element are given in table 7.3. Note that tap L10 did not function throughout the tests, however, the pressures from tap L10 should be quite accurately represented by the adjacent taps, given the uniformity of pressures over the leeward roof side at the rear of the power car (see figure 8.6 for instance). Given the position of this tap the effect on side force coefficient (which is of most interest in this study) will be negligible since tap L10 is on the lee-ward roof side, so only provides a contribution to lift force. The methodology follows that in section 7.2.2. Forces and moments were only

considered in terms of the partial coefficients per unit length, C_{η}^{*}, as no underbody taps were tested (see equation 7.10).

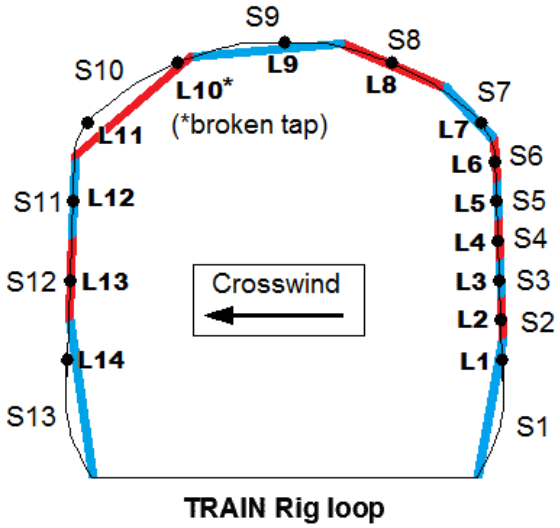

Figure 7.9 - Model discretisation showing surfaces 1 to 13 (red and blue) and corresponding pressure taps for TRAIN rig model (tap L10 has been omitted from analysis).

Table 7.3 - Areas and angles of discrete model geometry surfaces and corresponding pressure taps.

Surface number	Pressure tap	A_S (m^2)	θ_S (°)
1	L1	0.90	6
2	L2	0.31	2
3	L3	0.31	2
4	L4	0.31	2
5	L5	0.31	2
6	L6	0.32	3
7	L7	0.55	41
8	L8	0.81	68
9	L9	1.24	95
10	L11	1.08	59
11	L12	0.60	2
12	L13	0.62	2
13	L14	1.03	5

7.3.7 Error analysis

Analysis of error is presented in detail in Appendix F, and follows the methodology used in previous studies with the CWG (Dorigatti, 2013; Soper, 2014). As in equations F.1 to F.3, error was defined as the sum of the bias limit and the random uncertainty. Bias limit was calculated through propagation of error (Taylor, 1997), and considered the span wise mean pressure of each individual run. The maximum bias limit of the bias errors from all individual runs at a given nominal investigative yaw angle was taken, conservatively, as the bias limit for a given tap and yaw angle. Random uncertainty considered the standard deviation of the span-wise mean pressures for each ensemble for each tap a given yaw angle, assuming a normal distribution of the span wise mean pressures and with a 95% confidence level. Span-wise mean ensemble averages of pressures and forces are given in appendix H. The random

uncertainty was also calculated from the standard deviations of each bin (see table 8.2) and was significantly lower than random uncertainty based on the span-wise mean pressures. For consistency with previous studies (Dorigatti, 2013; Soper, 2014) the larger values of random uncertainty were used to conservatively calculate total error as the sum of bias and random uncertainty. Table 7.4 presents the absolute errors used in later analysis.

The mean of the maximum total errors, $\overline{E_{TOTAL(\max)}}$, is higher at 25° yaw angle than at 20°. The main reason for this is that a lower investigative train speed was required at 25°, hence a higher fractional component of error due to the fixed uncertainty of train speed measurements. The errors were found to be highest on the leeward side wall and the nose, and the highest bias and random errors were, as was also the case in the RWDI wind tunnel study, identified at the windward side wall and roof junction. When considering a loop of taps towards the rear a the Class 390 power car model, Dorigatti, (2013), found the total error to be consistent around this loop, with absolute total errors of just less than 0.05 of the mean C_P. The values presented in table 7.4 for the HST are within the same magnitude as the errors found by Dorigatti, (2013), and the individual contributions of bias and random uncertainty to total error are similar - bias is usually similar to, but slightly higher than, the random uncertainty for most taps. The values of $\overline{E_{TOTAL(\max)}}$ have been shown as error bars in subsequent figures in chapter 8.

Table 7.4 - Bias limit, random uncertainty and total uncertainty for each pressure tap from CWG tests at 20° and 25° yaw.

	Tap	E_{BIAS}(max)		E_{RND}		E_{TOTAL}(max)		$\overline{E_{TOTAL}}$(max)	
		20°	25°	20°	25°	20°	25°	20°	25°
Nose	N1	0.024	0.045	0.019	0.027	0.043	0.072	0.047	0.058
	N2	0.036	0.035	0.015	0.018	0.051	0.053		
	N3	0.039	0.038	0.007	0.012	0.046	0.050		
Leeward side wall	L14	0.043	0.041	0.016	0.019	0.059	0.060	0.053	0.062
	L13	0.048	0.044	0.017	0.018	0.065	0.061		
	L12	0.028	0.050	0.009	0.014	0.037	0.064		
Roof	L11	0.015	0.017	0.013	0.012	0.028	0.029	0.037	0.048
	L9	0.022	0.024	0.020	0.017	0.041	0.041		
	L8	0.018	0.032	0.010	0.034	0.029	0.066		
	L7	0.025	0.028	0.026	0.029	0.051	0.057		
Windward side wall	L6	0.011	0.020	0.007	0.015	0.018	0.036	0.024	0.034
	L5	0.015	0.020	0.008	0.012	0.024	0.033		
	L4	0.017	0.028	0.009	0.009	0.026	0.037		
	L3	0.011	0.028	0.011	0.008	0.021	0.037		
	L2	0.024	0.025	0.011	0.008	0.035	0.034		
	L1	0.015	0.018	0.004	0.010	0.020	0.028		

CHAPTER 8

MODEL-SCALE CROSSWIND TESTS - RESULTS AND DISCUSSION

8.1 Introduction

Chapter 8 presents the results from the RWDI wind tunnel tests and the moving model TRAIN rig tests through the CWG. The wind tunnel data is more comprehensive - the entire power car was fitted with pressure taps and a larger range of yaw angles were tested than the CWG tests at the TRAIN rig. The wind tunnel data presented in section 8.2 has therefore been used to give a more overall picture of the distribution of pressure at various yaw angles on the HST power car. The CWG data presented in section 8.3 has been analysed in order to compare with the wind tunnel data for validation and also to develop and validate methodologies for analysing data on the NMT. The results presented in this chapter are discussed later in comparison with the full-scale crosswind measurements in chapter 11.

8.2 Wind tunnel results

The majority of the experimental results presented in this section are for the "smooth flow" test at a higher wind tunnel speed of 13.2 m/s, since the results from the "higher turbulence" test are very similar. The higher turbulence test was undertaken in order to consider Re number effects, since the Re number of the smooth flow test was lower than the minimum required in current codes of practice (CEN, 2005) - see section 6.2.2 for experimental details. Given that the two wind tunnel tests showed very similar results (i.e., mean pressure coefficients within experimental uncertainty), it can be concluded that the Re number of the smooth flow test was adequately high to negate any Re number sensitivity. It should also be noted that the Re number of the smooth flow test was 1.4×10^5. Rocchi et al., (2009), also found no significant Re number effects in the range of 1.4×10^5 - 3.0×10^5 during wind tunnel tests on a generic passenger train.

In the results that follow, the positions of these pressure taps are defined according to the normalised positions. Longitudinal distances are defined as X/L, where X is the distance of the pressure tap from the train nose, (X = 0 is the tip of the train nose) and L is the power car length from the nose tip to the mid-point of the inter-carriage gap. Lateral distances are defined as Y_{Tap}/Y_{Train} where Y_{Train} is half of the width of the train (Y = 0 is at the COT) and defined as positive towards the windward side of the train. Vertical distances are defined as Z_{Tap}/Z_{Train} where Z_{Tap} is the vertical distance of the tap above TOR and Z_{Train} is the train height from TOR.

When pressures are considered around a loop of pressure taps, the pressure tap locations are defined by the anticlockwise circumferential distance around the train, where the origin is at

the bottom corner of the leeward side wall. Section 8.2.1 considers the pressures at the train nose and section 8.2.2 considers the pressures acting along the main length of the power car.

8.2.1 Pressures around train nose

The flow field around the train nose was considered in order to locate suitable pressure tapping points at full scale which could be used to calculate yaw angle from surface pressures. The surface pressure distribution across the front face of the HST for yaw angles of 0° to 50° is shown on figure 8.1. A triangular mesh was constructed using the "delauney" function on Matlab (Mathworks, 2010). The triangulation approach was used because of the irregular spacing of the pressure taps. The pressure tap positions are shown as black circles on each graph, and no extrapolation was performed on the data, hence there are gaps between the coloured mesh and train outline. The colour scaling is consistent with later figures (8.5 and G.3) for ease of comparison.

Figure 8.1 shows that at low yaw angles (0° to 5°) the surface pressure distribution appears fairly symmetrical about the vertical plane. At 0° yaw angle there is a slight asymmetry in the pressure distribution about the vertical axis, with a slightly higher positive pressure on the leeward side (i.e., the LHS on figure 8.1) indicating a slight yaw angle offset. At lower yaw angles, the nose stagnation point - a high positive pressure coefficient close to unity, can be seen on figure 8.1 at normalised heights of Z_{Tap}/Z_{Train} = 0.3 - 0.5 (the nose tip is at Z_{Tap}/Z_{Train} = 0.4). As the yaw angle increases up to 50°, this stagnation point shifts towards the windward side of the train and both the magnitude and spatial coverage of the negative pressure on the leeward face of the nose increases, indicating that at yaw, the flow is

accelerated across the curved nose "edge" between the nose and windward wall, and there is a region of separation at the edge of the nose and leeward wall.

Figure 8.2 shows the horizontal $\overline{C_P}$ profile for lines of pressure taps at yaw angles of 0°, 5°, 10°, 20° and 30° for normalised heights of $\overline{Z_{Tap}}/Z_{Train}$ = 0.2 to 0.8. An overbar is used to denote that the height is the average of all the horizontal taps as there are some small differences in Z_{Tap} between taps within each horizontal line. At $\overline{Z_{Tap}}/Z_{Train}$ = 0.2, $\overline{C_P}$ is parabolic, with a maxima roughly at the train centreline at 0° yaw angle (slightly offset to the leeward side), and the position of this maxima shifts towards the windward side as the yaw angle increases, i.e., a shift in the centre of pressure. At $\overline{Z_{Tap}}/Z_{Train}$ = 0.4 to 0.7, the location of this maxima is less pronounced at lower yaw angles (0° - 10°), i.e., there is a fairly uniform and positive pressure between Y_{Tap}/Y_{Train} = -0.2 to 0.2 which coincides with the flat part of the HST nose, and a larger negative pressure is seen around the curved "edges" of the train nose. It can also be seen that the largest positive pressure coefficients of about 0.8, close to 1.0 which indicate the true stagnation point, are seen at the tapping positions closest to the nose apex at a normalised height of 0.4. At $\overline{Z_{Tap}}/Z_{Train}$ = 0.8 there are slight peaks in $\overline{C_P}$ at Y_{Tap}/Y_{Train}= ± 0.35 at yaw angles of 20° to 30°, which are from pressure taps immediately adjacent to the cab window recess and at slightly lower normalised heights than the rest of the pressure taps - these peaks are believed to show local pressure discontinuities due to cab window recess, which is similar to findings from previous research (Lawrence and Harrison, 1977).

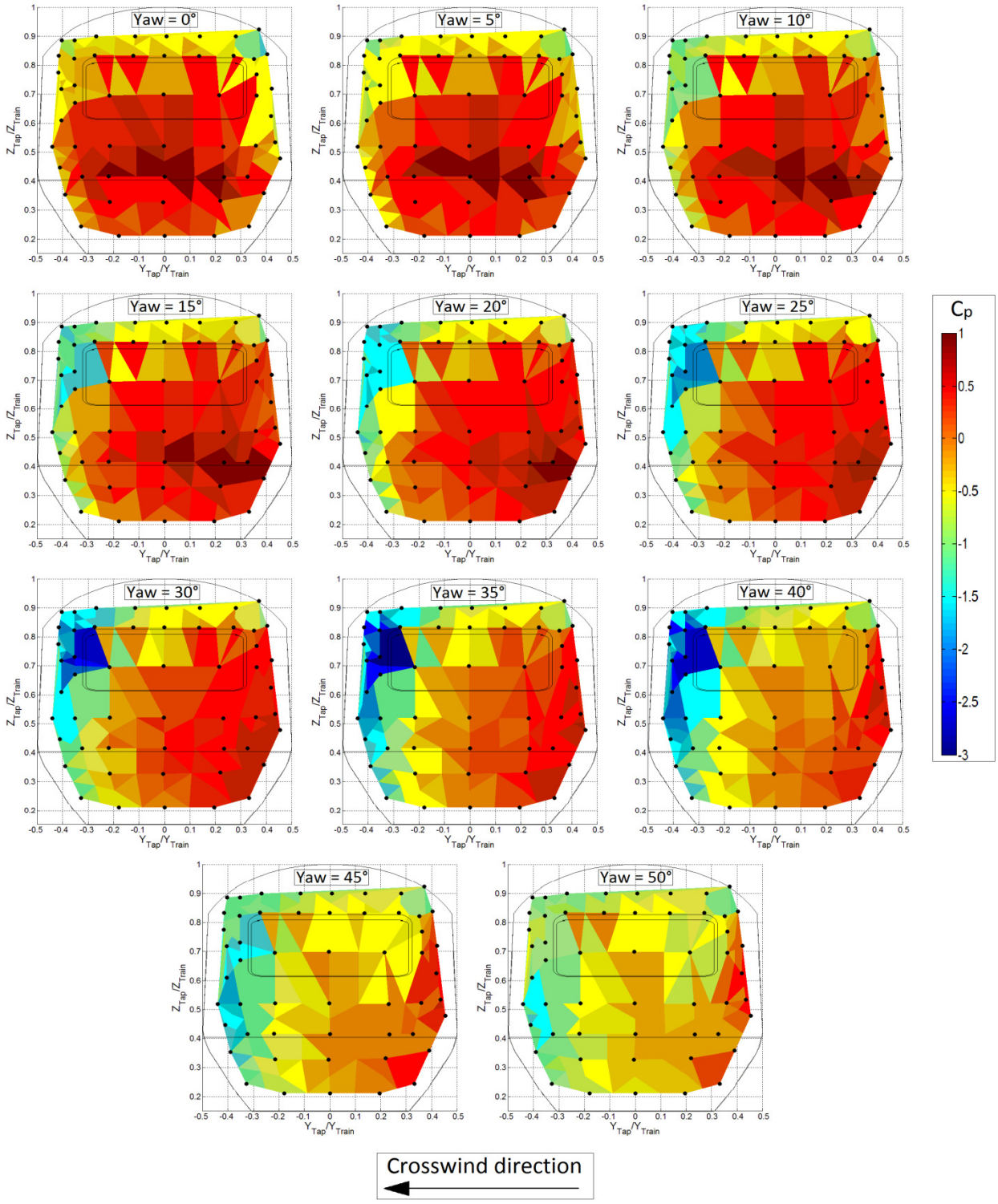

Figure 8.1 - Pressure distribution over HST nose for yaw angles of 0° to 50°.

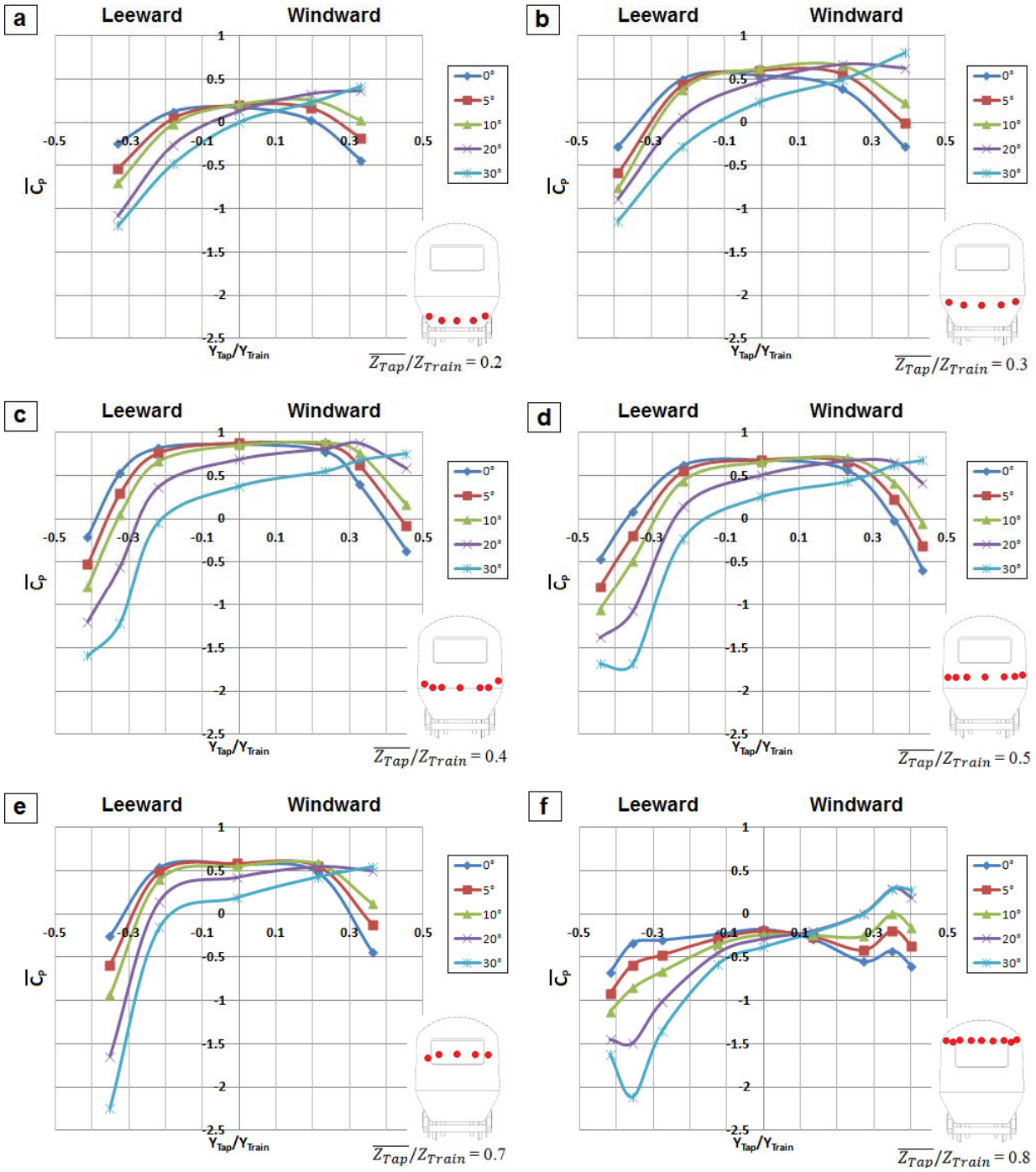

Figure 8.2 - Horizontal pressure profiles at the HST nose at heights of $\overline{Z_{Tap}}/Z_{Train}$ = 0.2 to 0.8 for yaw angles between 0° - 30°.

8.2.2 Calculation of yaw angle from pressure data

The purpose of considering the surface pressure distribution at the nose of the HST was to enable the calculation of yaw angle at full-scale, by developing a quantitative empirical equation to relate pressure differentials across the nose to yaw angle. The principal behind this approach has been applied extensively in the aerospace industry, and is commonly known as a flush airdata sensing (FADS) system, which relates vehicle based pressure measurements to air quantities, such as air velocity and yaw angle (Whitmore et al., 1995; Sami et al., 2009).

When the differences in $\overline{C_P}$ between symmetrical pairs of pressure taps at the nose are considered $\left(\overline{C_{P_{windward}}} - \overline{C_{P_{leeward}}}\right)$, the relationship between the difference in $\overline{C_P}$ and yaw angle can be considered almost linear for θ = 0° to 20°:

$$\left(\overline{C_{P_{windward}}} - \overline{C_{P_{leeward}}}\right) = m_\theta \theta + \theta_{offset} \tag{8.1}$$

Where m_θ is a linear gradient and θ_{offset} is the wind tunnel yaw offset (taken as -3°). The term $\left(\overline{C_{P_{windward}}} - \overline{C_{P_{leeward}}}\right)$ is in reality a function of two unknowns - yaw angle (θ) and relative wind velocity (V_{rel}). Equation 8.1 is valid for the wind tunnel (and moving model) tests given that these quantities were known. In reality, at full-scale, these quantities are in fact functions of each other and both unknown (see equations 2.21 and 2.22 and figure 2.15). At full-scale, it is therefore necessary to consider the pressure differential at the train nose independently of yaw angle (see equation 8.2).

Figure 8.3 illustrates equation 8.1 for various tapping pairs at the train nose. The results for tapping positions W1 - L1 and W3 - L3 on figure 8.3 (the letters "W" and "L" which preclude the tap number define the windward and leeward side taps) are very similar, suggesting that

there was little sensitivity to height in the region below the nose tip. The outer pairs of pressure taps closest to the train edges (pairs 2, 4, 5 and 6) showed a larger differential of $\overline{C_P}$ than the tap pairs closer to the train centreline (pairs 1 and 3). There is also little difference between the two wind tunnel tests.

Tap pair 3 on figure 8.3, located at Z_{Tap}/Z_{Train}= 0.3, was chosen as the location of the pressure taps at full scale, because of the good relationship with yaw angle and differential $\overline{C_P}$, and good agreement between the two different wind tunnel tests (U = 11.5 and 13.2 m/s). If error and accuracy are considered, it would have been more favourable to locate pressure taps in the outer positions (such as L2 and W2) since the magnitudes of the recorded values were higher and therefore the percentage errors would be lower. However, during installation of full-scale pressure tap system, it was not practical to locate the taps on these outer surfaces (due to the physical construction of the lower part of the HST nose shell which would have impeded installation of the tapping points and pneumatic tubing). The more central tap positions were therefore a slight compromise, but nonetheless can enable estimation of yaw angle from pressure coefficients.

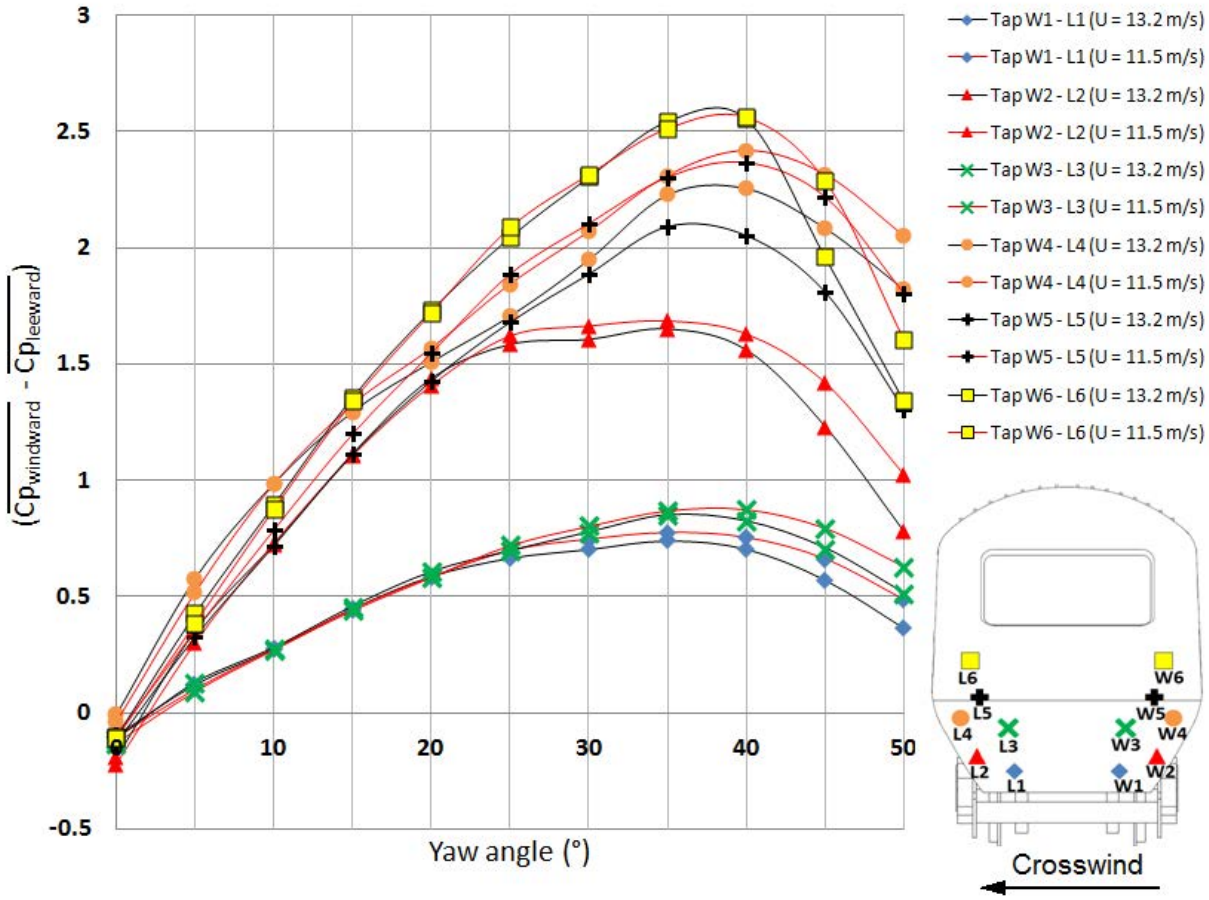

Figure 8.3 - Variation in $\left(\overline{C_{P_{windward}}} - \overline{C_{P_{leeward}}}\right)$ with yaw angle at the train nose between symmetrical pairs of pressure taps, at mean streamwise wind tunnel velocities of 13.2 m/s and 11.5 m/s.

At full-scale it was not possible to convert the dimensional pressures into pressure coefficients without first knowing the yaw angle (in order to calculate resultant aerodynamic speed and hence dynamic pressure - see section 10.2.3.4). In order to develop a function to calculate yaw from dimensional pressures, the wind data tunnel needed to consider a pressure differential that was independent of dynamic pressure (i.e., wind tunnel velocity), which was achieved by dividing $\left(\overline{C_{P_{windward}}} - \overline{C_{P_{leeward}}}\right)$ at tap positions W3 and L3 (as on figure 8.3) by the

pressure coefficient recorded by the central pressure tap (tap N2 on figure 6.11). This gave a non-dimensional coefficient of yaw, C_θ:

$$C_\theta = \frac{C_{P_{windward}}(\theta) - C_{P_{leeward}}(\theta)}{C_{P_{centre}}(\theta)} \tag{8.2}$$

Where $C_{P_{windward}}$, $C_{P_{centre}}$ and $C_{P_{leeward}}$ refer to pressure coefficients (or dimensional pressures) from the nose taps positions shown on figures 6.1 and 9.5, and are a function of yaw (θ). On subsequent figures in this section, these terms are abbreviated to $C_{P,w}$, $C_{P,c}$ and $C_{P,l}$. These definitions are fixed for the geometrical tap positions .

Figure 8.4.1 shows non-corrected C_θ plotted against yaw angle for both of the RWDI tests. The is an offset in the yaw angle of about -3° at zero nominal yaw angle, which may be due to either the wind tunnel flow, or possibly the addition of the STBR ground configuration which has been shown to affect the flow to the train nose - see appendix I. The data was then corrected to account for θ_{offset} of about -3° for the wind tunnel tests by subtracting θ_{offset} from all of the yaw angles (i.e., a y-axis shift), resulting in the zero-corrected data shown in figure 8.4.2. The data from the TRAIN rig CWG test (presented later in section 8.3.1) has also been shown on figure 8.4.2, and an assumed y-intercept of zero was included by definition in the TRAIN rig data. An immediate point to note is that the TRAIN rig data shows a much higher gradient than the wind tunnel data (discussed further in section 8.3.1). It also should be stressed that this "correction" of the wind tunnel data may not strictly speaking be correct, particularly if the offset was caused by the STBR (since the physical geometry immediately upstream of the train would change as yaw angle changed, which could affect the apparent yaw angle at the train nose). An alternative correction would be to treat the zero yaw case as "independent", i.e., $C_\theta = 0$ at zero yaw, but to leave higher yaw angles uncorrected - this

would cause the wind tunnel and moving model results to compare more favourably than shown in in figure 8.4.2. Nonetheless, it will be seen in chapter 11 that the estimation of yaw angle at full-scale is challenging and that use of either the wind tunnel or moving model data does not result in a true estimation of yaw angle, regardless of how any yaw angle offset correction is applied.

Cubic best-fit polynomials were fitted to the data in figure 8.4.1 using the a least squares regression model (Microsoft Corporation, 2007) which resulted in an empirical equation to calculate yaw angle (θ) from coefficient of yaw as:

$$\theta = K_{\theta,1}C_{\theta}^{3} + K_{\theta,2}C_{\theta}^{2} + K_{\theta,3}C_{\theta} \tag{8.3}$$

Where the terms $K_{\theta,1}$, $K_{\theta,2}$ and $K_{\theta,3}$ are cubic yaw coefficients obtained from the cubic best fit models from the wind tunnel test and are given in table 8.1 for both of the wind tunnel tests and the TRAIN rig data. Note also that the subscript θ defines coefficients and yaw angle or coefficient calculated from the wind tunnel data (based on the "smooth flow" test results at 13.2 m/s) and the subscript φ defines that the coefficients were calculated from the TRAIN rig CWG data. Coefficient of yaw (equation 8.1) is henceforth defined in a general sense as $C_{\theta,\varphi}$. It must be stressed that equation 8.2 is only considered valid for yaw angles between $-25° \leq \theta \leq 25°$.

Table 8.1 - Yaw coefficients from wind tunnel ($K_{\theta,1,2,3}$) and TRAIN rig data ($K_{\varphi,1,2,3}$).

Test	Yaw coefficients		
	$K_{\theta,\varphi,1}$ (deg^{-2})	$K_{\theta,\varphi,2}$ (deg^{-1})	$K_{\theta,\varphi,3}$ (deg)
RWDI (U = 13.2 m/s)	-0.0719	-2.0493	15.724
RWDI (U = 11.5 m/s)	-0.1339	-2.3532	17.133
TRAIN rig CWG	5.2811	-15.012	33.766

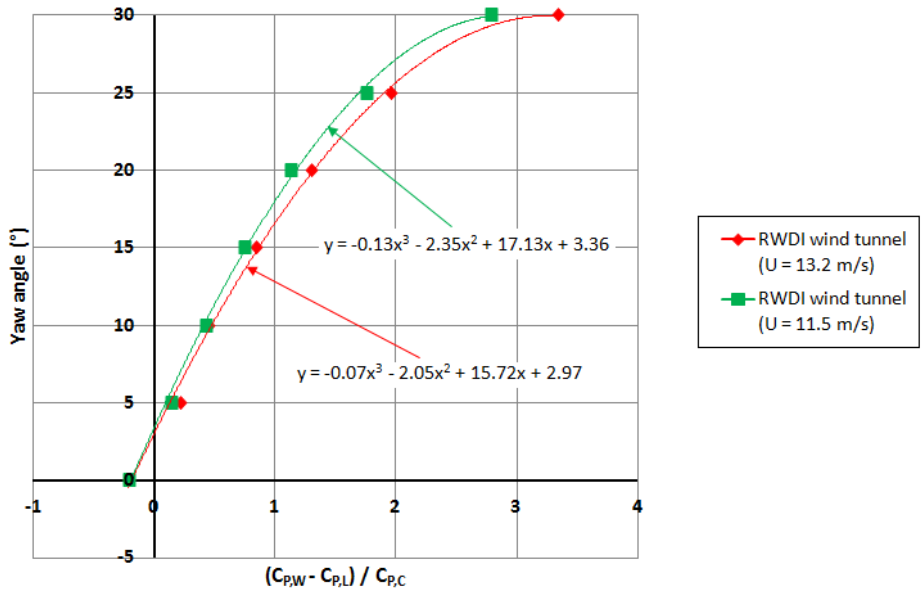

Figure 8.4.1 - Relationship between C_θ and yaw angle for all wind tunnel tests (wind tunnel is not zero-corrected).

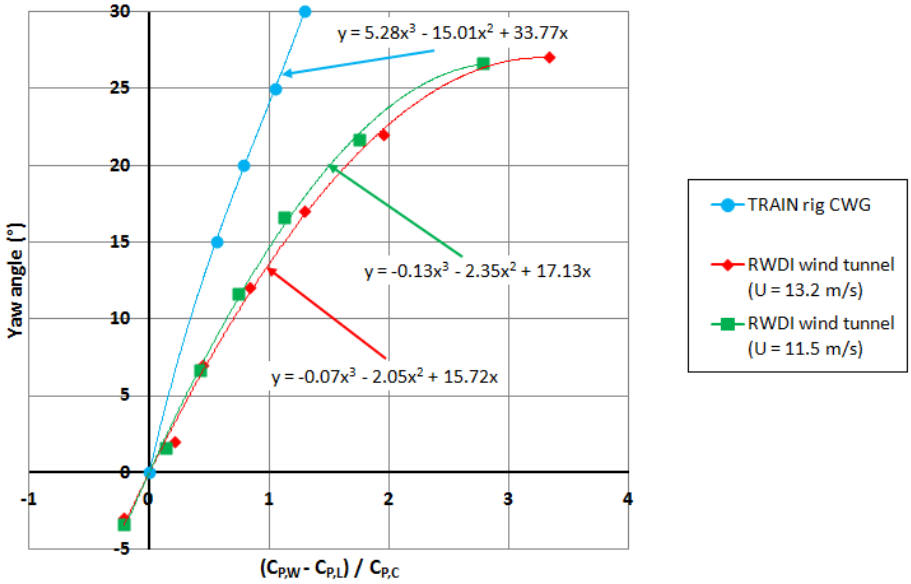

Figure 8.4.2 - Relationship between $C_{\theta,\varphi}$ and yaw angle for all scale model tests (wind tunnel data is zero-corrected).

8.2.3 Pressure distribution along length of power car

Pressure coefficients were measured in loops at various distances along the leading power car (figures 6.1.2 and 6.1.3). The main purpose of this section is to show how the pressure develops over the train walls and side of the HST power car as the normalised distance X/L is increased across a range of yaw angles , and hence consider how pressures and forces act along the length of the power car in the crosswind case. As it was impracticable to locate pressure taps on the underbody of the HST at the TRAIN rig (due to the firing chassis) or at full scale, the underbody region has not been considered in detail in this section - Appendix G describes the underbody pressures in more detail.

The variation in surface pressure with yaw angle acting on the overall main body of the power car is shown on the shaded surface plots in figure 8.5 (with the same colour shading as in figure 8.1). The train wall-roof junctions are shown with horizontal dashed lines, and the vertical axis is the normalised circumferential distance around the train. The shaded surface covers an area that is essentially the train walls and roof stretched out and projected onto a single rectangular plane. The regular spacing of pressure tap points and overall rectangular surface permitted a more typical mesh to be constructed using the "gridfit" function on Matlab developed by D'Errico, (2005). At zero yaw $\overline{C_P}$ over the main length of the train walls and roof is about zero and there is a region of negative pressure at the train nose-roof junction indicating a flow separation. As the yaw angle increases this region of negative pressure shifts towards the leeward side (seen on the nose pressures in figure 8.1). At 20° to 30° positive pressure develops on the windward side wall which is of slightly higher magnitude closer to the train nose and a suction pressure develops over the train roof and leeward side. At 40° there are two distinct separation regions as vortices are shed from the train nose and delta wing vortices shed from the windward wall-roof junction.

Figure 8.6 to shows the variation in $\overline{C_P}$ between yaw angles of 0° to 50° for loops of tapping points at increasing distances from the train nose (i.e., X/L). The train wall-roof junctions are shown as vertical dashed, and the windward side wall is at 7.5 m to 5.25 m, the roof is at 5.25 m to 2.25m and the leeside wall is from 2.25 m to 0 m. The magnitudes of pressures are largest closer to the nose, and there is a larger and more evenly distributed negative $\overline{C_P}$ over the roof at X/L = 0.27 (figure 8.6b), arising due to divergent streamwise flow from the train nose-roof and also from separation of the leeward face. As distance from the nose increases, a well defined suction peak at the windward wall-roof junction and the position of peak is consistent with a large number of other studies on passenger trains, for example, Lawrence

and Harrison, (1977); Dorigatti, (2013); Morden et al., (2015); Rocchi et al., 2016). Of interest to full-scale is the pressures at the rear of the car at X/L = 0.75 and 0.88. Figures 8.6 (e) and (f) show very similar magnitudes of $\overline{C_P}$ suggesting that the latter half of the power car length is not greatly affected by body end effects at the nose and the pressures therefore give a more accurate representation of the overall pressure distribution on the train (Lawrence and Harrison, 1977), which supports the chosen position of the loop of taps at X/L = 0.8 at full scale. At the very end of the power car (X/L = 0.96) the pressure distribution is of slightly lower magnitude - this is believed to be due to the proximity of the intercarriage gap.

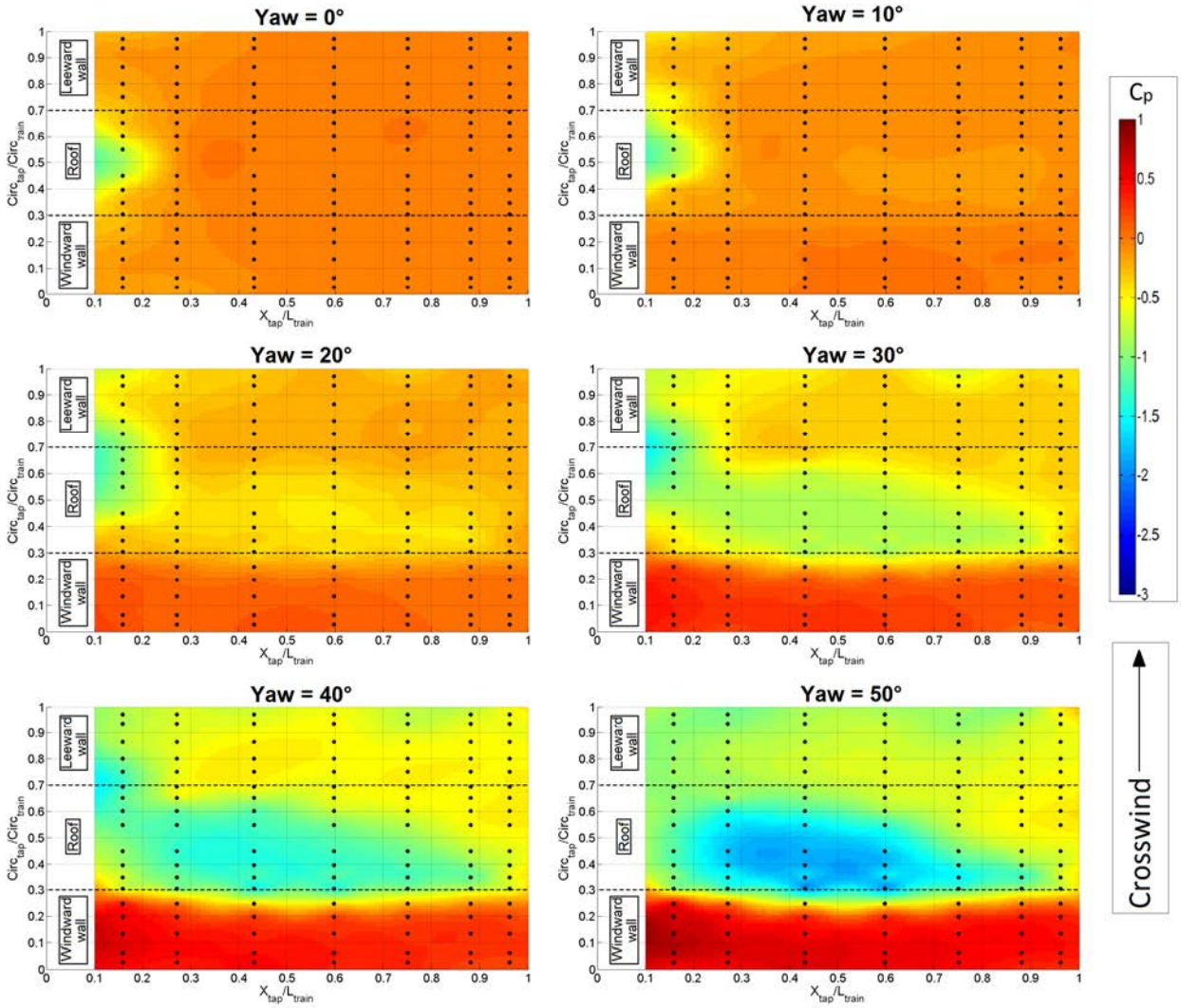

Figure 8.5 - Shaded plot of $\overline{C_P}$ over main length of power car body at θ = 0° to 50°. Y-axis is the train circumference and wall-roof junctions are marked with horizontal dashed lines.

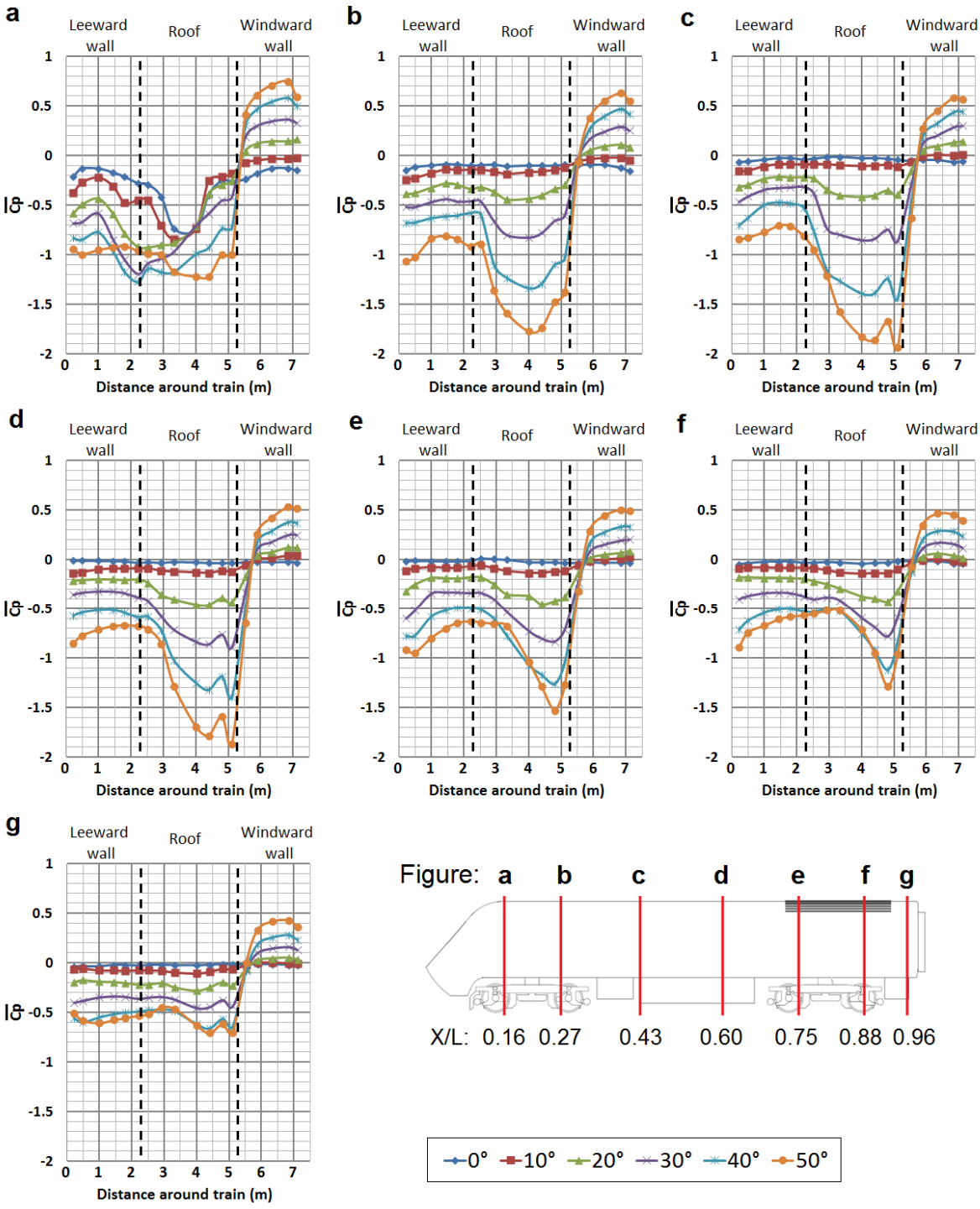

Figure 8.6 - Pressure distribution around loops at 0° to 50° at increasing X/L.

8.2.4 Underbody region

Previous analysis has focussed on pressure distributions around the train walls and roof. The underbody region is not of great importance in this study, but has been considered in more detail in appendix G. The overall pressure distribution across the underbody shows pressure coefficients close to zero, and there are slightly positive pressures on the windward side and negative pressure on the leeward side, though the geometrical features (bogies, blocks etc) significantly affected the local pressures. The rectangular blocks at the track/train centreline were found to create blockage, and at yaw, a region of stagnation (indicated by a positive pressure) developed on the windward side of the block and a corresponding negative pressure on the leeward side of the block. Of most interest in this study are the pressures around the rearward bogie, and the contribution of underbody pressures at this location to forces and moments at the loop at location full-scale at X/L = 0.8 (which was roughly at the bogie centreline - figure 6.1.2). Figure 8.7 shows the pressure distributions either side of the rear bogie. A net positive pressure was seen in the loop immediately upstream (at X/L = 0.75) and a net negative pressure was seen at the loop immediately after the bogie. It was assumed that integration of the pressures from the loops at X/L = 0.75 and 0.88 (taking the width of each strip as 0.5 m) would give an indication of the lift force and hence moments due to pressures beneath the train at this location. This process is described in more detail in section G.3. Figure 8.8 shows the partial lift force and moment coefficients integrated across both loops from both the underbody region ("floor") and from the roof and side walls ("loop"), for both wind tunnel tests across the yaw angle range tested. The results from both RWDI wind tunnel tests are almost identical, and are within the experimental uncertainties presented in table 7.2. The magnitudes of $C^*_{\eta,loop}$ are much higher than $C^*_{\eta,floor}$ in all cases - the underbody force

coefficients are essentially zero. This is due not only to the relatively lower magnitudes of pressures in the underbody region than across the loop, but also that the positive pressures just ahead of the bogie and the negative pressures just after the bogie effectively cancel each other during summation. For the purposes of the TRAIN rig CWG tests and full-scale experiments, the underbody pressures, and hence lift force and moment coefficients, can be considered to be zero at X/L = 0.8.

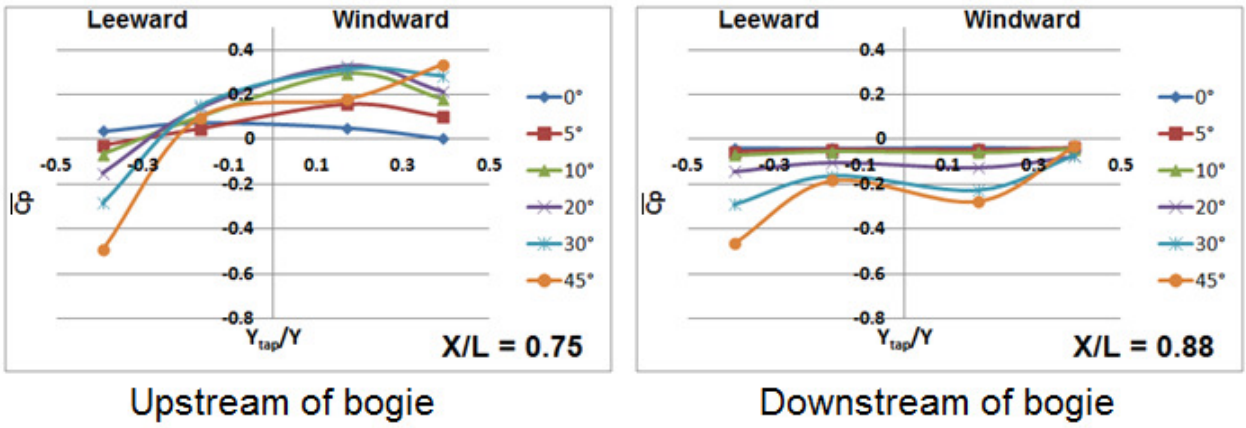

Figure 8.7 - Pressure coefficients along strips of taps (in y-direction) either side of rearward bogie at (X/L = 0.75 and 0.88).

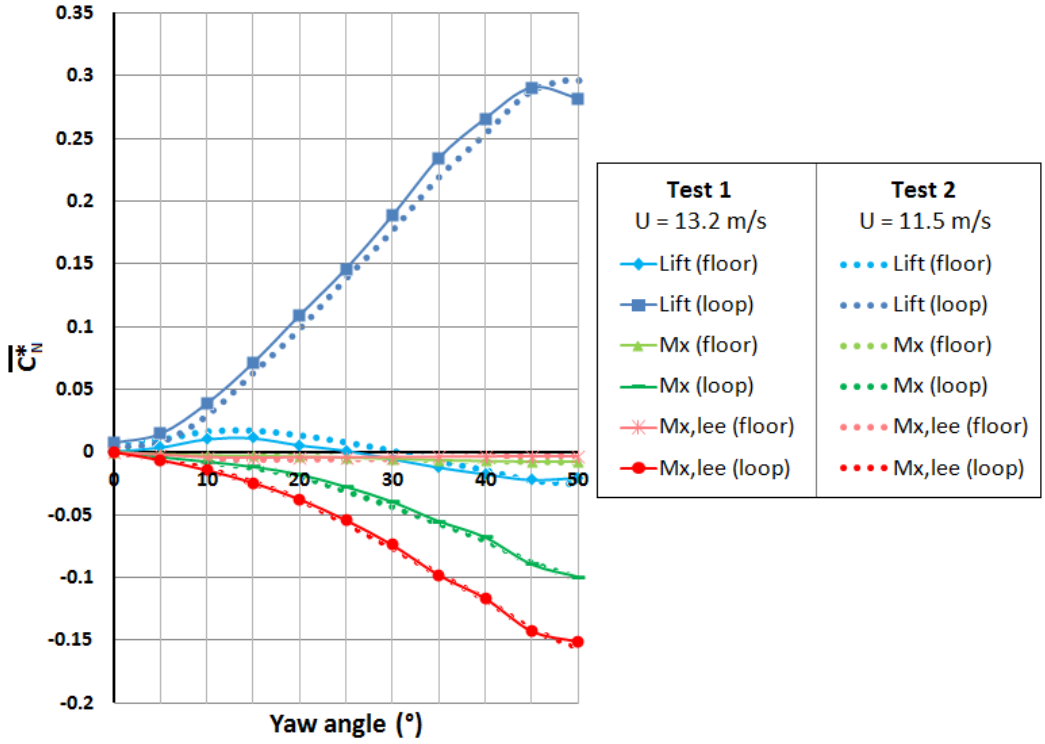

Figure 8.8 - Comparison of $C^*_{\eta,loop}$ and $C^*_{\eta,floor}$ at X/L = 0.8 for both wind tunnel tests.

8.2.5 Force and moment coefficients per unit length

Force and moment coefficients per unit length were calculated as the sum of partial coefficients $C^*_{\eta,loop}$ and $C^*_{\eta,floor}$ (equation 7.10). Section G.3 shows a comparison of the force and moment coefficients from the loop and roof separately, and generally speaking, the values of $C^*_{\eta,floor}$ were about one order of magnitude lower than $C^*_{\eta,loop}$. This section considers the total values of $\overline{C^*_\eta}$ along the train length (the overbar denotes that they were obtained from $\overline{C_P}$). Figure 8.9 shows the variation of $\overline{C^*_\eta}$ along the length of the train, and the forces reflect the pressure distributions considered in section 8.2.3.

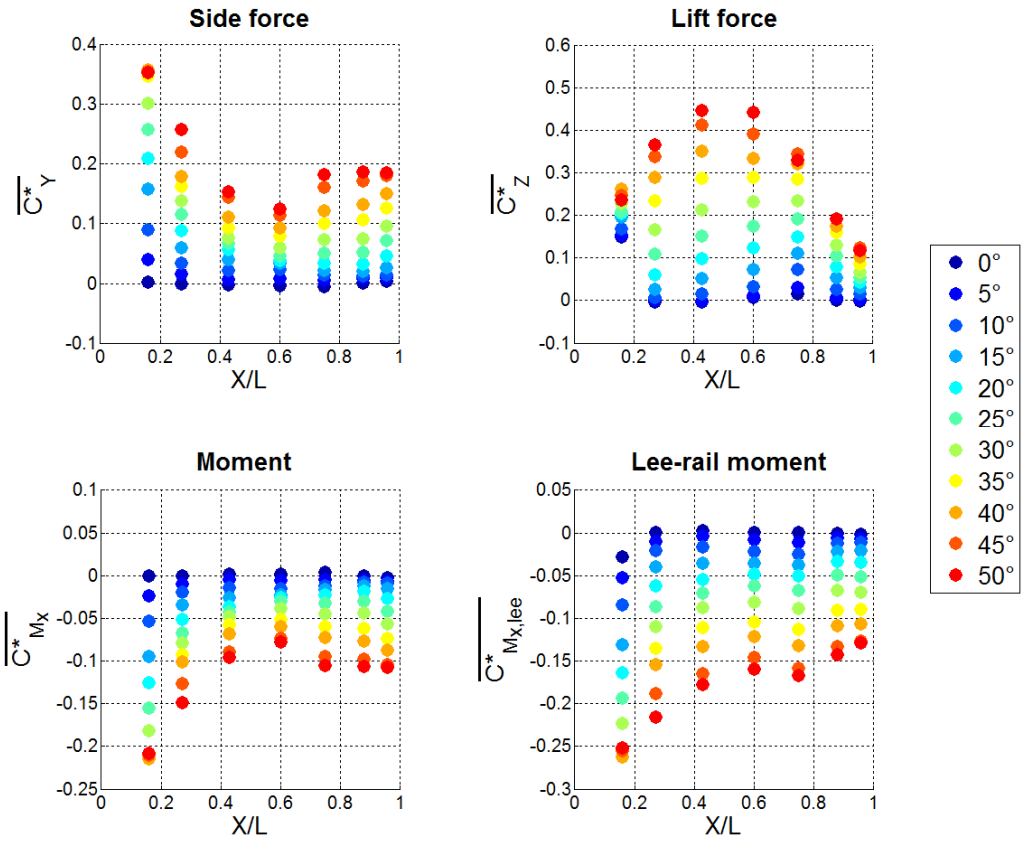

Figure 8.9 - Values of $\overline{C_\eta^*}$ along length of power car from "smooth flow" wind tunnel test.

Side forces are a measure of the difference in pressure between the windward side wall and the leeward side wall. Figures 8.5 and 8.6 showed that the windward wall experiences a positive pressure and the leeward side wall experiences a negative pressure - these two effects combine to result in a side force. The largest magnitude values of $\overline{C_Y^*}$ are seen closer to the train nose, and generally $\overline{C_Y^*}$ decreases from the nose up to about X/L = 0.6. Near the rear of the power car, at X/L > 0.7, $\overline{C_Y^*}$ slightly increases and remains fairly consistent and stable, indicating that body-end effects at the train nose at yaw are of less significance. A similar conclusion can be drawn for moment $\overline{C_{M_X}^*}$ and $\overline{C_{M_{X,lee}}^*}$ show little variation in length towards

the rear of the train. As was seen in the pressure distributions (figure 8.6), at the very rear of the power (X/L ~0.9) car there is a decrease in pressures corresponding to a lower $\overline{C_Z^*}$, though $\overline{C_{M_{X,lee}}^*}$ is not greatly affected. The consistent variation of $\overline{C_{M_{X,lee}}^*}$ with length towards the rear of the power car suggests that the loop location at full scale is representative of the typical pressure distribution (hence overturning forces) on the overall train.

8.2.6 Overall force and moment coefficients

The overall force and moment coefficients were calculated by RWDI by integration of all 314 pressure taps on the train. Figure 8.12.1 shows the overall values of $\overline{C_\eta}$ provided by RWDI. As yaw angle increases, the side force and lift forces increase due to the pressure distributions shown earlier. Figure 8.12.2 shows these coefficients calculated from the loops of pressure taps only (along the main length of the power car, including the underbody), i.e., disregarding the nose, and following the methodology described in section 7.2.2, and compares the two wind tunnel tests performed by RWDI. There is very good agreement between all values of $\overline{C_\eta}$ calculated from the loop taps. Figure 8.12.3 compares the data in figure 8.10.1 (overall $\overline{C_\eta}$) with the data shown in figure 8.10.2 ($\overline{C_\eta}$ from loop taps only). The values of $\overline{C_Y}$ in figure 8.10.3 are very close across the range of yaw angles, suggesting that side forces arise mostly due to loading on the main body of the train (when considering steady effects). There is a significant divergence of $\overline{C_Z}$ as yaw angle is increased, which is due to the separations over the train-roof which result in very large suction pressures that were not accounted for when only the loops were considered. The values of $\overline{C_{M_{X,lee}}}$ are therefore lower when the nose pressure taps are disregarded.

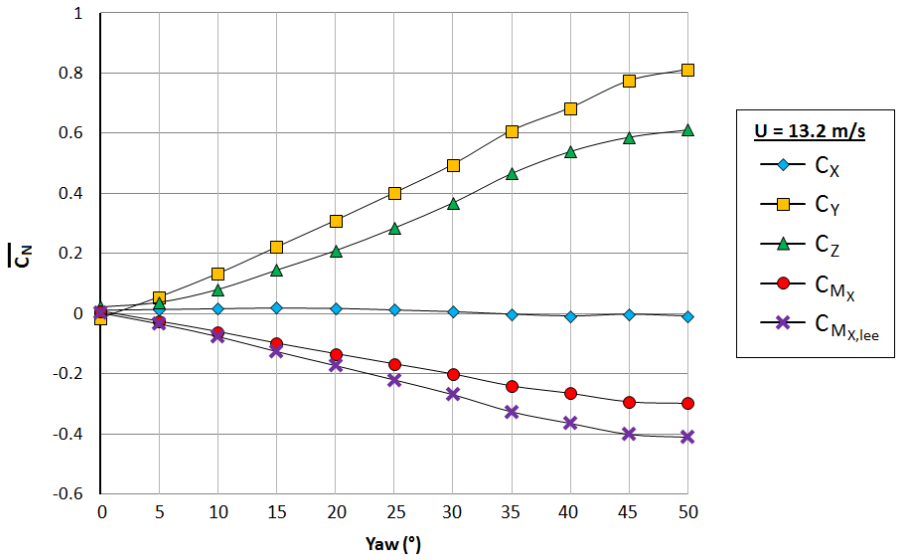

Figure 8.10.1 - Force and moment coefficients calculated by RWDI from all pressure taps.

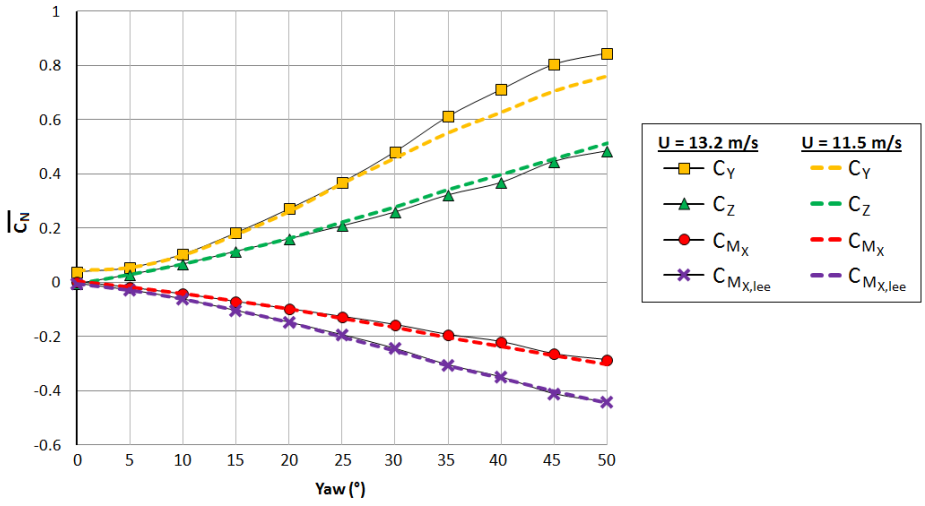

Figure 8.10.2 - Comparison of force and moment coefficients from both RWDI tests calculated from loops of pressure taps only.

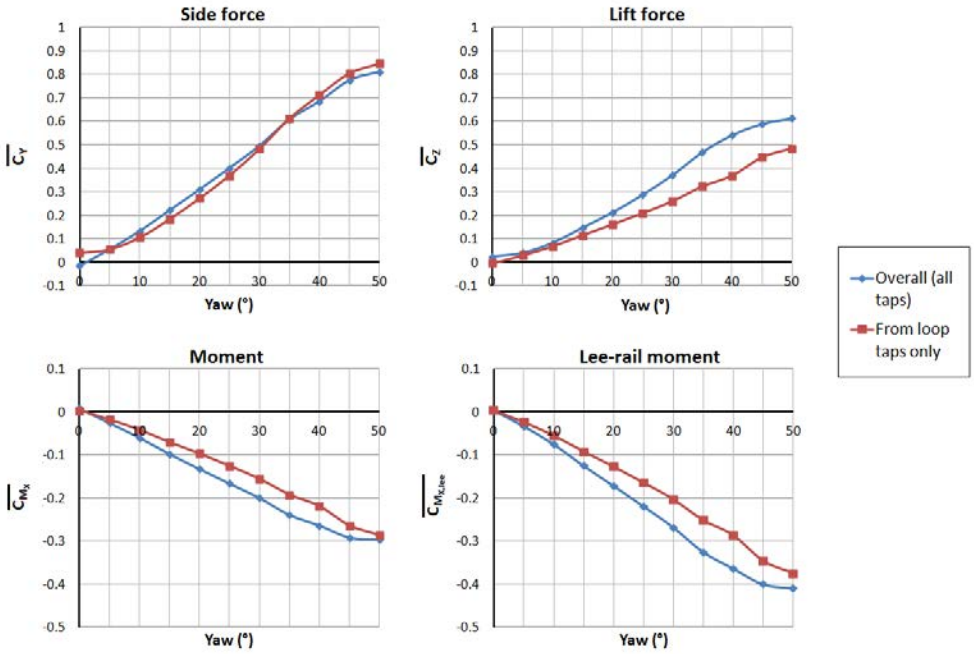

Figure 8.10.3 - Comparison between overall force and moment coefficients calculated from entire train and from loop taps only (data from U = 13.2 m/s test only).

8.3 TRAIN rig crosswind test results

This section considers the mean pressure coefficients obtained from the yaw angle bins methodology described in section 7.3.5. Ensemble averages of pressure across the span were also considered and though are not presented in this chapter (but are given in section H.6.2). This section focuses on comparing the results of these moving model tests with the static wind tunnel tests described previously in section 8.2. The mean pressures for each tap position and yaw angle, along with the standard deviations and random errors (based on equation F.2 and the bin standard deviation) are given in table 8.2 at the end of this chapter.

8.3.1 Pressures at train nose

Figure 8.11 compares the pressures for each of the three pressure taps on the nose between the CWG and RWDI tests. There is a slight difference between the data from the two wind tunnel tests - the higher turbulence wind tunnel test (shown as green squares) consistently shows a slightly higher pressure coefficient than the smooth flow test (shown as red diagonal squares). While this difference is within experimental error, the consistent nature of this offset suggests that may have been Re number effects (such as differences in the floor boundary layer at low turbulence resulting in a lower velocity at the height of the nose taps, or differences in the flow separation from the STBR). The results from the TRAIN rig CWG tests, shown on figure 8.11 as blue circles, show the same trend as the wind tunnel data - i.e., a higher positive pressure on the windward pressure tap than on the leeward side pressure tap. The magnitudes the pressure coefficient for all three taps decreases as the yaw angle is increased in the range of 20° to 30°, and the comparative magnitudes of the three pressure taps are similar for the TRAIN rig and wind tunnel data. The TRAIN rig results are, however, consistently substantially larger than the RWDI wind tunnel results, and this difference is larger than the combined experimental error of the CWG and wind tunnel tests (shown as error bars). At 25° - 30° yaw angle, the wind tunnel data shows a negative pressure coefficient, whereas the leeward nose pressure tap is positive in the TRAIN rig data. It is believed that this may be caused due to a combination of the different ground simulations and also differences in the undercarriage region between both trains. The CWG tests took place with a flat ground configuration where ground level was at the same height as the TOR. The firing chassis on the TRAIN rig model results in a much higher underbody blockage and was found to affect the slipstream and pressure transients of the HST (discussed in chapter 5) and also affected the pressure transients of the ICE2, discussed in appendix C and by Gilbert, (2013). It is believed

that the high underbody blockage of the TRAIN rig model, combined with the HST nose shape (which presumably forces air downwards), created higher pressures at the nose, which were possibly exacerbated due to constrictive the flat ground scenario. The main implication of this finding is that there are significant differences in the calculation of yaw angle at full scale depending on whether the cubic yaw coefficients (equation 8.3) are taken from the wind tunnel or TRAIN rig data.

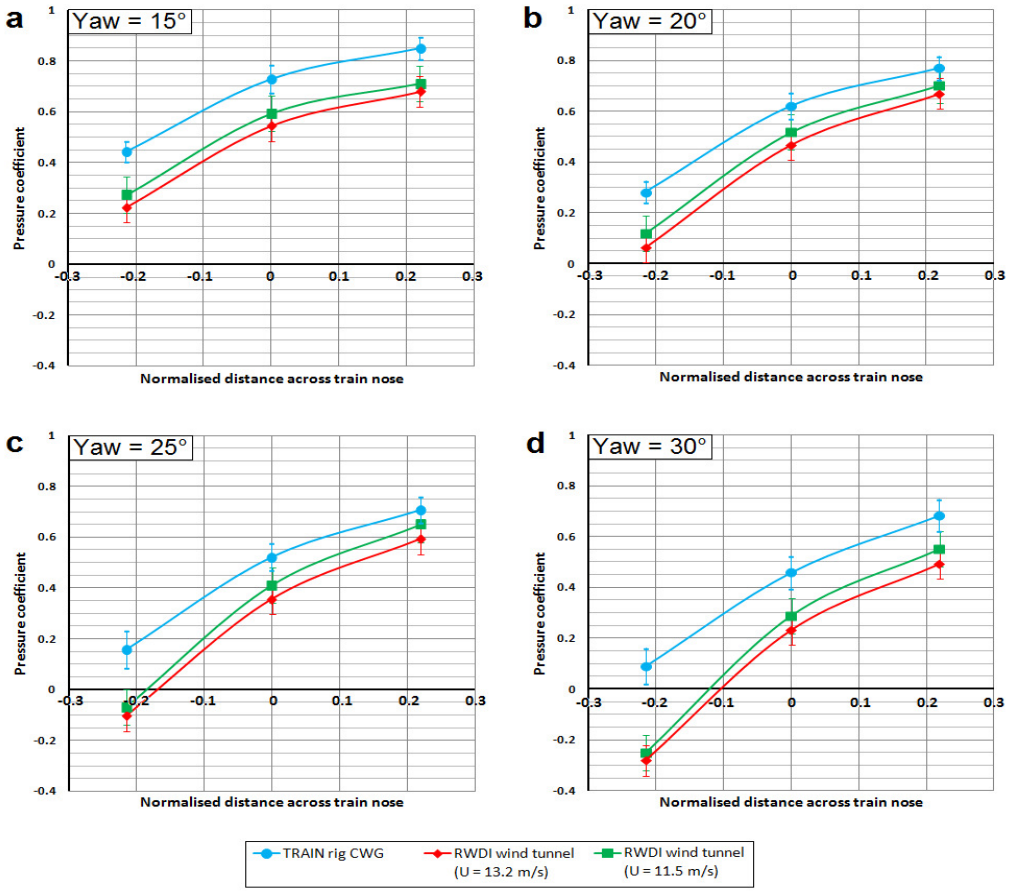

Figure 8.11 - Comparison of pressure distribution across train nose between wind tunnel and CWG tests data.

8.3.2 Pressures around loop at rear of power car

The main aim of the CWG tests was to investigate the pressures around the loop in order to consider the effects of vehicle movement on the magnitudes of pressures and forces. Figures 8.12.1 to 8.12.4 compare the pressure coefficients from the various wind tunnel tests with the CWG data. Error bars represent the total uncertainties defined in tables 7.2 and 7.4. The wind tunnel data was interpolated to form equivalent data at the CWG tests loop position (X/L = 0.8). At yaw angles of 15° and 30°, the CWG data is presented as individual data points due to the lower number of pressure taps. Generally speaking there is good agreement between the static and moving model tests - the positive pressure on the windward side wall, the negative peak at the windward wall-roof junction and negative pressure on the leeward side wall are all replicated and of similar magnitudes. At 20° and 25° the wind tunnel and CWG data are within experimental uncertainty, despite the differences in experimental set up and Re number. At 20° and 25° yaw (figures 8.12.2 and 8.12.3) there is a divergence of $\overline{C_P}$ across the leeward wall as distance towards the ground increases between the wind tunnel and CWG tests. Dorigatti, (2013) conducted static and moving model tests using the CWG with the same experimental set up and did not notice any significant differences in the pressure field around the rear of the train, which suggests that this difference may be due to the ground set up. The static pressure may be "higher" (less negative) with the flat ground case of the CWG tests due to the reduced volume for the air to flow into, compared to the STBR in the wind tunnel. The HST geometry may also have some role in the leeward wall $\overline{C_P}$ divergence. Dorigatti, (2013) used a Class 390 model which has a more shielded underbody region - as discussed in section 5.3.2 the slipstream of the HST is more turbulent closer to the ground, and there may therefore be interaction effects between the delta wing vortices shed from the

windward wall-roof junction and the leeward side boundary layer that also affect the flow field and hence pressure distribution. It should also be noted that there are differences in the two set ups regarding the underbody geometry (such as the high wind tunnel blockage created by the pneumatic tubing - figure 6.2.2a) that may affect flow field with crosswind. Despite the differences in set up, the comparison between the two tests can be regarded as very favourable. A final point of interest is that, on the leeward wall and at 20° and 25° yaw angles there is a discontinuity (more negative $\overline{C_P}$ than adjacent taps) at about 1.7 m around the loop in the moving model tests that is not present in the wind tunnel data. It is believed that this may be due to equipment errors (such as an issue with the data logger or the pressure transducer itself for this particular channel that was not identified during the tests). However, this "discontinuity could be said to fall within experimental error when considering the errors of this tapping location and the adjacent pressure taps.

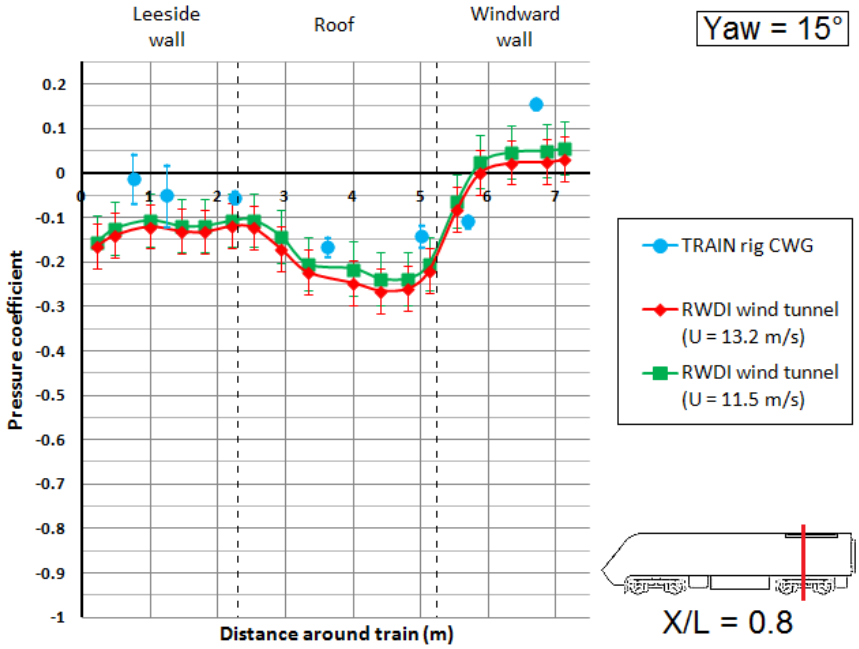

Figure 8.12.1 - Comparison of $\overline{C_P}$ between wind tunnel and CWG data around loop at 15° yaw.

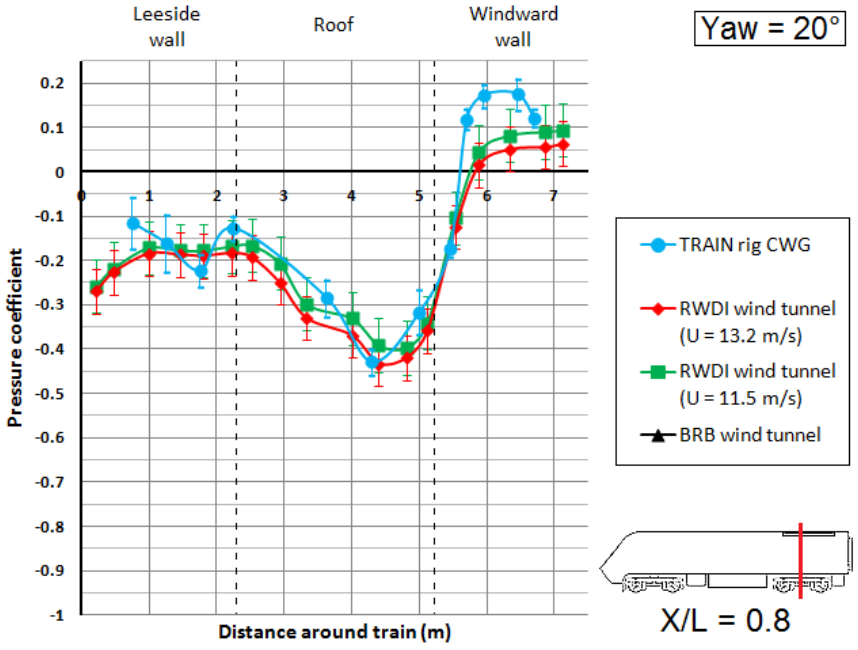

Figure 8.12.2 - Comparison of $\overline{C_P}$ between wind tunnel and CWG data around loop at 20° yaw.

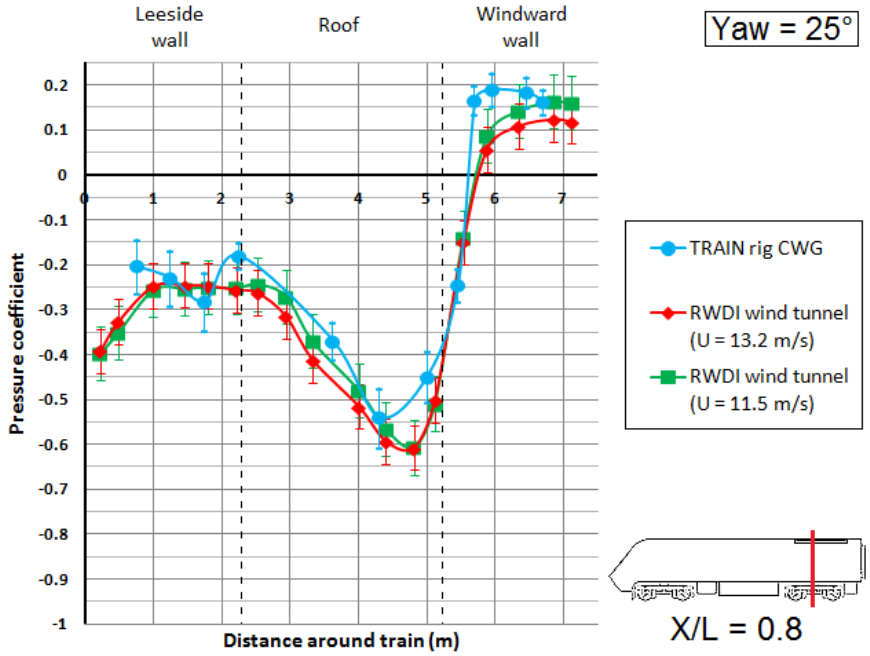

Figure 8.12.3 - Comparison of $\overline{C_P}$ between wind tunnel and CWG data around loop at 25° yaw.

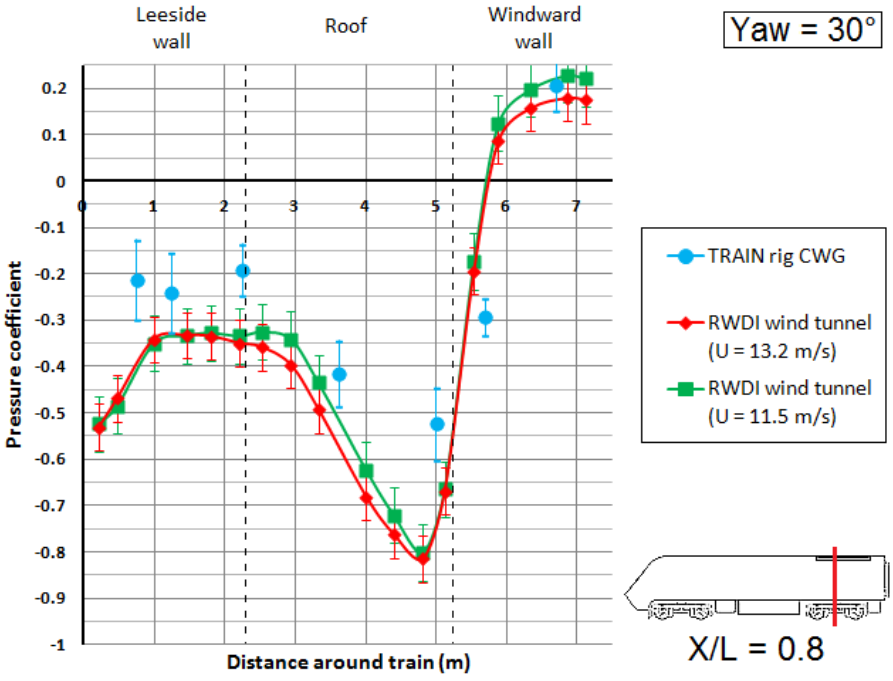

Figure 8.12.4 - Comparison of $\overline{C_P}$ between wind tunnel and CWG data around loop at 30° yaw.

8.3.4 Comparison of force and moment coefficients

The values of $\overline{C_\eta^*}$ from both tests at X/L = 0.8 are compared in figure 8.13. CWG data is only shown at yaw angles of 20° and 25°, but compares very favourably at these yaw angles (and well within the experimental uncertainties considered in appendix F). Given that the overall pressure distributions around the loop showed a good comparison between the wind tunnel and CWG data, the good comparison between force and moment coefficients is unsurprising. The wind tunnel values included underbody pressures but the CWG did have any underbody pressure taps, however the comparison between $\overline{C_Z^*}$ and hence $\overline{C_{M_{X,lee}}^*}$ is very close, which supports the conclusion that the positive and negative underbody pressures either side of the rearward bogie effectively cancel out during summation.

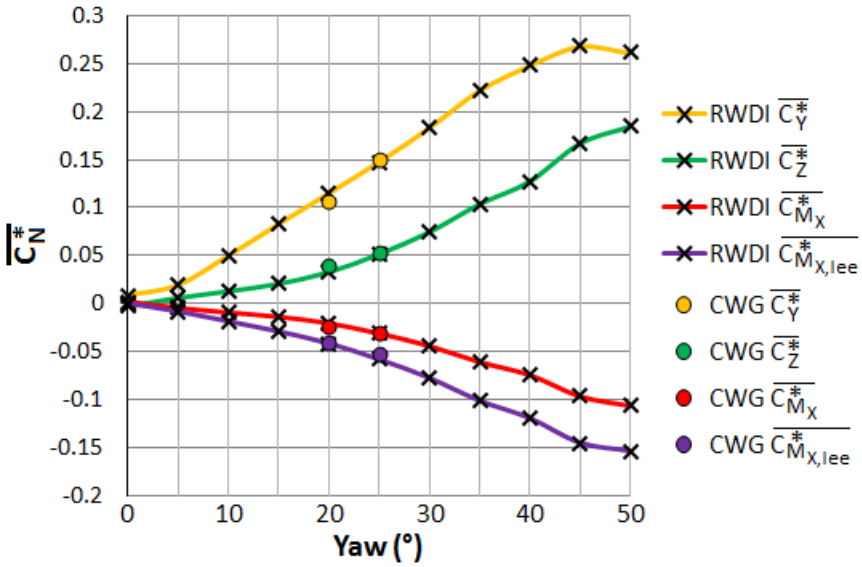

Figure 8.13 - Comparison of mean force and moment coefficients per unit length at X/L = 0.8 for wind tunnel and CWG data.

Table 8.2 - Mean pressure coefficients, standard deviations and random uncertainties for each pressure tap and yaw angle bin.

	Yaw (°)	Pressure tap																
		Nose			Leeward side wall					Roof		Windward side wall						
		N1	N2	N3	L14	L13	L12	L11	L9	L8	L7	L6	L5	L4	L3	L2	L1
$\overline{C_{P_{k,\varphi}}}$	15°	0.44	0.73	0.85	-0.01	-0.05		-0.05	-0.16		-0.14		-0.11				0.16
	20°	0.28	0.62	0.77	-0.12	-0.16	-0.22	-0.13	-0.28	-0.43	-0.32	-0.17	0.12	0.17	0.17	0.18	0.12
	25°	0.16	0.52	0.71	-0.20	-0.23	-0.28	-0.18	-0.37	-0.54	-0.45	-0.24	0.17	0.19	0.18	0.18	0.16
	30°	0.09	0.46	0.68	-0.21	-0.24		-0.19	-0.42		-0.52		-0.29				0.21
$\sigma_{k,\varphi}$	15°	0.139	0.103	0.074	0.068	0.073		0.048	0.083		0.108		0.025			0.032	0.036
	20°	0.165	0.137	0.115	0.110	0.102	0.075	0.074	0.107	0.150	0.161	0.054	0.061	0.060	0.043	0.033	0.033
	25°	0.183	0.180	0.160	0.105	0.091	0.053	0.072	0.111	0.115	0.170	0.072	0.051	0.063	0.060	0.037	0.035
	30°	0.200	0.212	0.177	0.094	0.080		0.088	0.118		0.156		0.062			0.054	0.056
$E_{RND,bin}$	15°	0.002	0.001	0.001	0.001	0.001		0.001	0.003		0.003		0.000			0.001	0.001
	20°	0.002	0.001	0.001	0.001	0.001	0.001	0.001	0.002	0.002	0.002	0.001	0.001	0.001	0.001	0.001	0.001
	25°	0.002	0.002	0.002	0.001	0.001	0.001	0.001	0.002	0.001	0.003	0.001	0.001	0.001	0.001	0.001	0.001
	30°	0.003	0.003	0.003	0.001	0.001		0.001	0.010		0.013		0.001			0.004	0.005

CHAPTER 9

FULL-SCALE CROSSWIND TESTS - EXPERIMENTAL SET UP

9.1 Introduction

Chapter 9 describes the experimental set up of the full scale train based measurements of pressures on an HST power car due to crosswinds. Section 9.2 introduces the New Measurement Train (NMT) on which the system was installed. Section 9.3 describes the different components of the onboard pressure measurement system.

9.2 The NMT

The NMT is owned and operated by Network Rail, and runs across the majority of the UK's rail network at operational speeds, covering most of the network in a roughly two week cycle. The main purpose of the NMT is rail inspection, and it typically runs in a 2+7 or 2+8 configuration with two Class 43 power cars and a rake of customised Mk. III coaches. Four Class 43 power cars are available for use on the NMT to ensure operational uptime when maintenance of a power car is necessary. The actual selection of the train formation varies on a daily to weekly basis depending on operational requirements and power car availability. Of the four power cars, car 43062 (named "John Armitt") was selected to be installed with an onboard pressure tap measurement system. This power car was chosen as it is the most geometrically similar to a Class 43 power car used for passenger trains as it has no buffers. The only major geometric difference to a passenger Class 43 car is that 43062 has a camera at the front of the nose and a spotlight at the driver cab roof, shown in figure 9.1.

The arrangement of a Class 43 power car was shown in figure 1.2. The diesel engine is positioned between the driver's cab and the luggage area. Air intakes for engine cooling are located on the train walls either side of the engine, and the engine exhaust and cooling fan array are located above the engine on the roof. It is worth noting here that the engine and air intakes, cooling array and exhaust system are upstream of the loop of pressure taps, and have been shown to affect the pressure tap data (discussed in appendix J).

The GRP front panel of the power car (figures 9.4 and 9.8) can be raised to allow access to the draw bar, and the panel itself is removable. The nose panel and adjacent curved walls are constructed from GRP, approximately 5 mm thick. The walls and roof of the power car in the luggage area are constructed from a steel shell of about the same thickness.

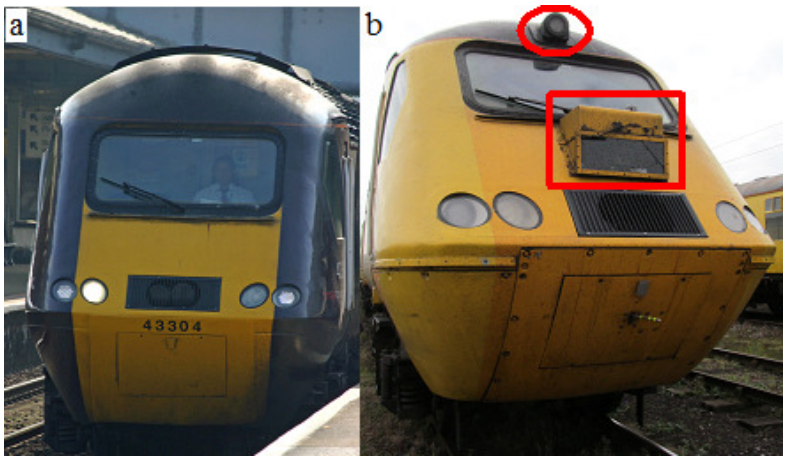

Figure 9.1 - Comparison of the front (a) a commercial Class 43 power car to (b) car 43062 on the NMT - spotlight is circled and a rectangular box is drawn around the nose camera.

9.3 Onboard data acquisition system

An onboard pressure measurement system was installed on car 43062 at Heaton train depot in Newcastle between 28/09/13 and 03/10/13. The entire system was bespoke and designed and built by the UoB. The system allows the measurement of surface pressures at the train nose and in a loop around the luggage area of the power car to be recorded whenever the power car is receiving an electrical supply, and therefore records whenever the power car is in operation. The system is designed to run continuously during the operation of the train, and to collect and synchronise data from different sources. The components of the system are described in the subsections that follow.

9.3.1 Reference pressures and environmental data

Three reference pressure sources were located in the luggage area of the power car. The reference pressure reservoir for all pressure taps was a partially sealed (PS) inflexible ceramic reservoir ($P_{ref|PS}$), which had a small opening which allowed the pressure to normalise to the ambient pressure over a time period of 30 s to 1 minute, but provided a stable reference for the comparatively low time scale pressure fluctuations that were of interest (such as crosswinds/gusts). Two additional reference sources were used to enable cross checking of this reference pressure. An open ended (OE) static pressure probe ($P_{ref|OE}$), shown in figures 9.2.1 and 9.2.2, was used to measure the total pressure within the luggage area (which is not air-tight), and an additional ceramic container ($P_{ref|CS}$) that identical to the main reference pressure reservoir but was completely sealed (CS). Additionally, and absolute barometric pressure was recorded by a sensor inside the onboard PC ($P_{ref|AMB}$).

The temperature inside the luggage area was recorded using a thermocouple located close to the open air reference probe (figure 9.2.2). A gyroscopic sensor [CRS07], (Silicon Sensing, 2013) was also mounted within the onboard PC that recorded the rate of overturning, though this data has not been used in this study.

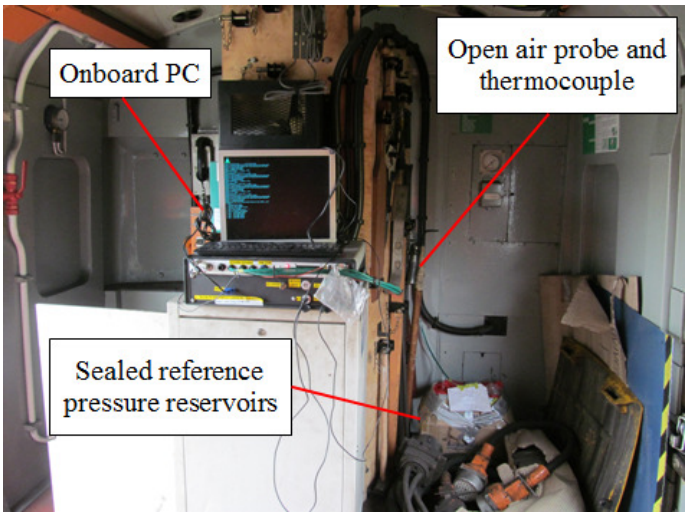

Figure 9.2.1 - Locations of reference pressures, thermocouple and onboard PC.

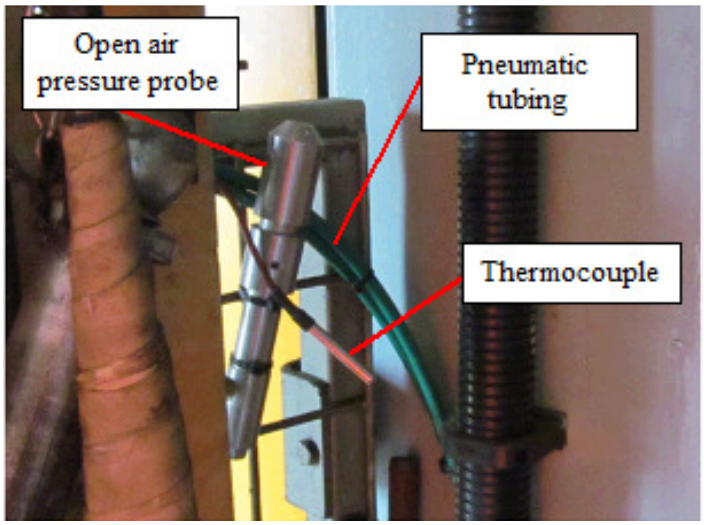

Figure 9.2.2 - Open air reference probe and thermocouple tip on the NMT.

9.3.2 Pressure measurement system

9.3.2.1 Modular pressure transducer box

Pressure transducers were fitted into modular pressure transducer boxes. Each box contained eight HCLA0050DB pressure transducers (Sensortechnics, n.d.), connected to printed circuit

board. For seven of these pressure transducers, the HPP was connected to an external stainless steel mounting point ("hose nipple") on the front of each box, and the LPP to a stainless steel manifold that connected to the reference pressure source. The eighth transducer had two external mounting points - one connection to the HPP and the second to the LPP - intended to be used as a separate measure of dynamic pressure from the pitot static probe at the train nose. The external mounting point acted as an adaptor between the pneumatic tubing (described in section 6.3.1.5) inside the pressure transducer box and the 9 mm o.d., 7 mm i.d. PVC tubing in the external pneumatic system between the modular box and the tapping point. The lower diameter tubing was run through the hose nipple and the cavity filled with an epoxy resin. The connections at the hose nipple and the reference pressure manifold were observed to be airtight during calibrations at pressures up to ±2500 Pa for a duration of 60 s.

The power to each modular box was provided by the onboard PC (nominally 5 V). The voltage signal output from each pressure transducer was transmitted via fibre optic cable from each modular box to the onboard PC. Cable was run through plastic conduit, which also contained the reference pressure tubing, and this conduit was securely fixed along existing cable and conduit lines on the train.

A total of four modular boxes were used; three were mounted on the inside of the luggage area on the train walls and roof, and one at the train front on the inner surface of nose panel. Each box was located as close to the pressure taps as was practicable in order to minimise the lengths of pneumatic tubing and hence reduce the effects of tube resonance. Resonance effects are addressed briefly appendix J. An end plate, which was fitted to the train using epoxy resin, contained six threaded studs to mount the box onto which allowed the box to easily be switched without re-fitting the end plate.

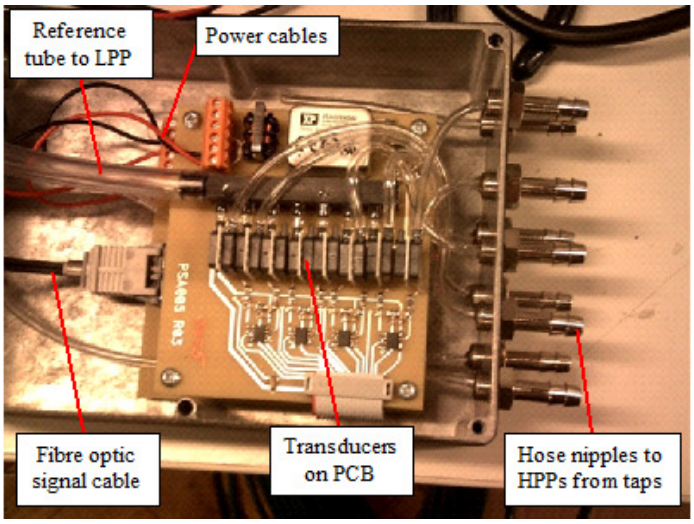

Figure 9.3 - Internal view of modular pressure transducer box.

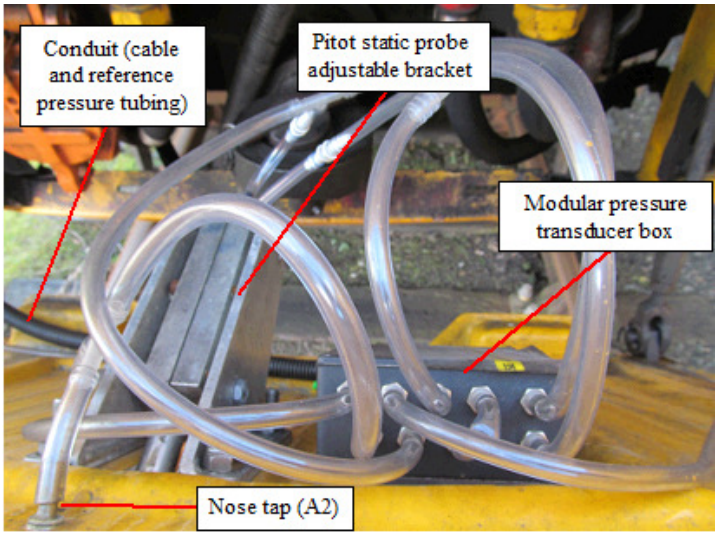

Figure 9.4 - Modular pressure transducer box and pitot probe bracket mounted on rear surface of nose drawbar access panel.

9.3.2.2 Pressure tapping points

The power car was fitted with three pressure taps at the nose of the train and 17 taps in a loop around the luggage area. The position of these pressure taps was decided based on data from the wind tunnel test described in section 8.2.1.2. Three nose taps were found to give a good

relationship with yaw angle in the wind tunnel (shown in figures 8.3 and 8.4.2), and so these tapping positions were chosen at full scale to calculate yaw angle (equation 8.3). The loop taps were expected to show the surface pressures (and hence overturning forces) on a strip towards the rear of the power car and hence give a representative indication of overturning forces and moments. A major factor in the position of the pressure taps in the loop was the practicality of working around existing equipment inside the train. One wall was accessible only through an equipment cupboard which was the limiting factor for choice in the distance of the loop along the train length (in the x direction). The taps also needed to be fitted around shelving for equipment in this cupboard, and the junction between the cupboard wall and roof was inaccessible. The opposite wall contained fire extinguishers and electrical wiring, and so the vertical spacing of taps was restricted. The locations of the pressure taps are shown in figure 9.5.

Each pressure tap point was constructed by drilling a 3 mm diameter hole through the train skin. A roughly 30 mm length of 8 mm o.d. and 3 mm i.d. stainless steel tube was glued to an aluminium base plate using an epoxy resin, and washers were glued onto the inner surface of the base plate to ensure that it was robust against forces and moments from any accidental damage. The aluminium base plate was then glued to the inner surface of the train skin with epoxy resin, so that the stainless steel tubing was inside the drilled hole but not protruding outside of the outer surface of the train, and the seal around the tap was airtight. The stainless steel tubing was tightly fitted inside the pneumatic tubing that connected to the modular box and drainage line. (figure 9.9b shows the tap construction).

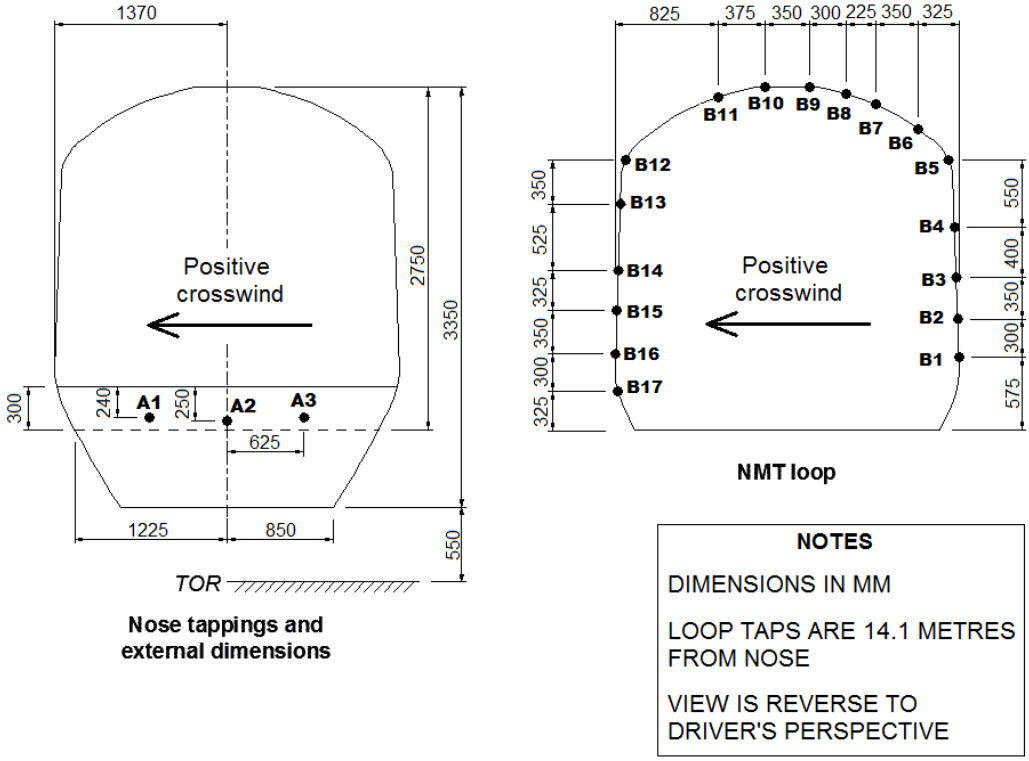

Figure 9.5 - Positions of pressure taps at full scale at train nose and loop of pressure taps located 14.1 m from the nose tip, i.e., X/L = 0.8).

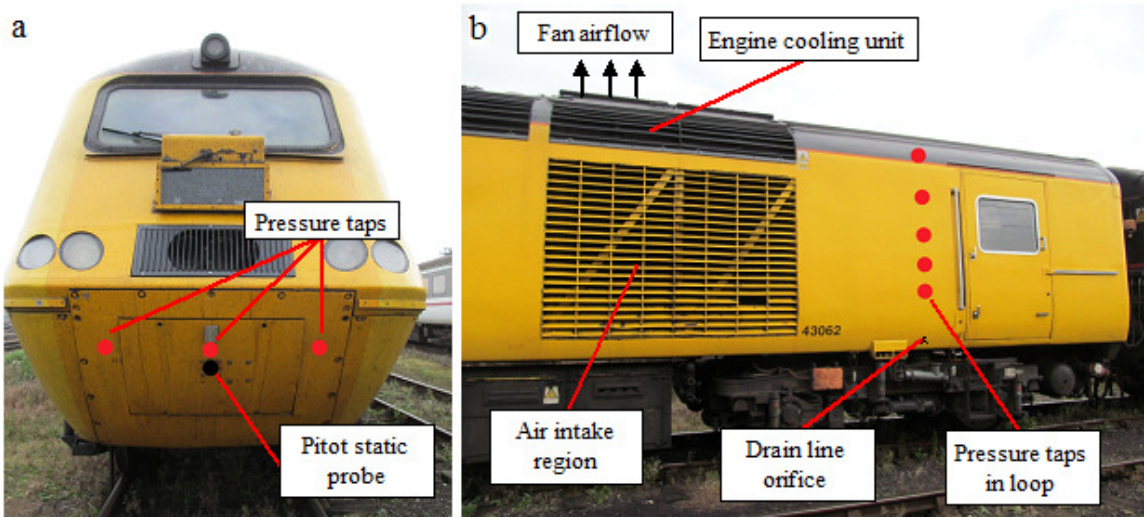

Figure 9.6 - External features - pressure taps and pitot static probe positions on the NMT.

9.3.2.3 Pitot-static probe

A custom built pitot static probe was fitted at the nose of the train in order to measure streamwise aerodynamic vehicle speed (i.e., the sum of the train speed and the resultant x-axis flow component arising due to natural winds). Once streamwise aerodynamic vehicle speed was known, and also the yaw angle, it was possible to calculate ambient wind speed and ultimately V_{rel} (see section 2.4.2 for background and section 10.2.3.4 for application). The probe was housed on an end plate that allowed the angle to be adjusted, and the design is shown in figure 9.7. The probe was then fitted onto the removable nose panel using four bolts through the adjustable bracket and GRP nose panel, and the probe was aligned horizontally using a spirit level. The probe tip was 260 mm below the nose apex. and 100 mm directly below tap A2 and at the train centreline. The aerodynamic vehicle speed, when calculated from the dynamic pressure from the pitot-static probe, was lower than the actual vehicle speed. A wind tunnel test was therefore carried out as part of this study to investigate the air flow at the nose of the train, and is described in Appendix I. Section 10.2.3.3 discusses how the aerodynamic vehicle speed was calculated, and this calculation was validated against the actual train speed from a built-in GPS tracker (see figure 10.2). The nose mounted pressure probe utilised three pressure transducers, one each for the total and static pressure connected to the HPP and the LPPs were connected to the reference pressure source inside the train, and one transducer had the HPP connected to the total pressure and the LPP to the static pressure to give an additional measurement of dynamic pressure for redundancy of the system in cause of faults.

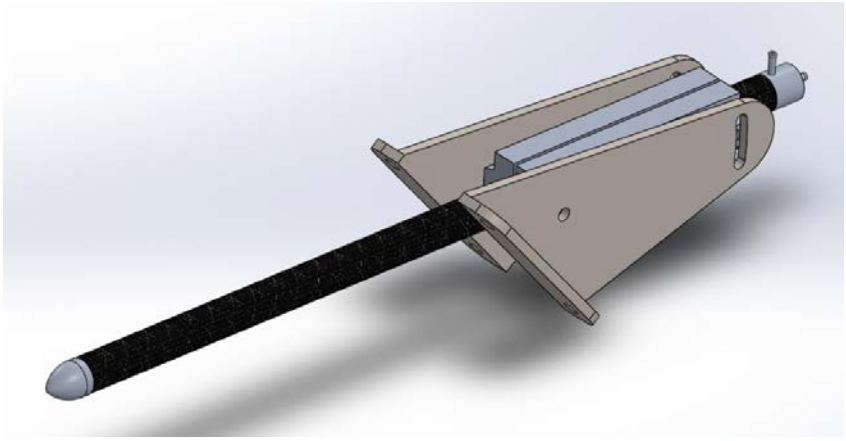

Figure 9.7 - 3D design of pitot probe and adjustable mounting bracket.

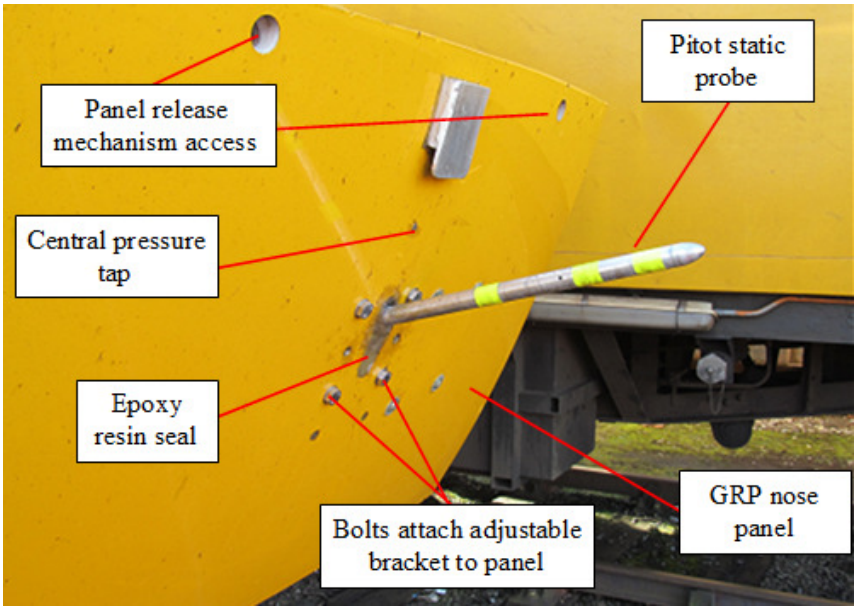

Figure 9.8 - Pitot static probe mounted on GRP panel - probe shaft is marked with fluorescent tape for safety reasons.

9.3.2.4 Pneumatic and drainage systems

Each pressure tap was connected to the pressure transducer by a sealed pneumatic circuit that had to allow drainage of water. The connection from the pressure tap to the HPP of the transducer can be considered in three stages; the tap to the drainage junction, the drainage junction to the modular box and the external connection on the box to the HPP of the transducer. The total lengths of tubing ranged from 0.4 m to 1.6 m, and tubing lengths are given in table J.3 for each pressure tap.

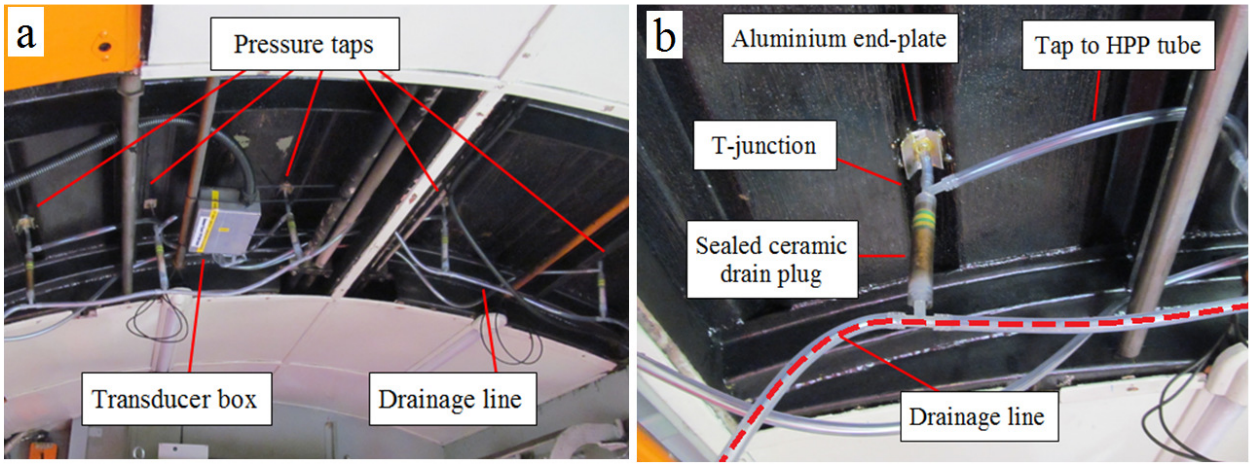

Figure 9.9 - (a) pressure taps on the roof and drainage line and (b) drainage system for an individual pressure tap on NMT roof.

The drainage junction was made using a T-piece connector. The junction had one leg that connected to the pressure tap via a short length of tubing (80 mm), and another to the pressure transducer box. The third leg was connected to a larger diameter PVC tube that housed a ceramic drain plug (figure 9.9b). This drainage tube was aligned vertically downwards so that the majority of water would flow down this tube under gravity. The connection between the T-piece and the drainage plug tube was made airtight by fitting the 9 mm o.d. tube over the T-

piece leg, which created an airtight seal as it was housed in the larger diameter tubing and PVC adhesive tape was wrapped around the drain plug to ensure it was sealed within the tube. The ceramic drain plug and allowed water to pass through slowly due to gravity and capillary action into the drainage line. The drainage line led to openings at the bottom of each of the walls for the loop of pressure taps. The nose pressure taps did not require a drain line after the drain plug as the area behind the nose of the train was open to the atmosphere, hence water would drain onto the tracks.

9.3.2.5 GPS and train speed data

Two GPS systems were installed; a GPS tracker installed inside the onboard PC that recorded whenever the pressure system was powered on, and the existing GPS system on the NMT. The existing GPS feed provided train speed as a vector (and was negative when car 43062 was trailing), and also gave engineer's line reference (ELR) so this feed was potentially more useful, however, this feed required the entire train to be powered on as well as the correct carriage configuration, so this data feed was sporadic (though all available data has been saved for future use). Both systems gave very similar results, so the intermittency of the existing onboard GPS feed was not a significant issue, and the GPS tracker installed inside the bespoke PC was used for automated data analysis (since both systems gave GPS position - latitude and longitude, as well as train speed, which were the primary interests in this study and that train direction could be determined in quite a straightforward way from the pressures at the train nose).

9.3.2.6 Onboard computer

A custom built PC that ran bespoke data acquisition software on a Linux operating system was secured on top of an existing electrical equipment cabinet (figure 9.10). The PC case was fitted with mounting and connection points for reference pressure tubing and the thermocouple on the front face. Power to the PC was provided from the existing power supply on the train. Once the PC was turned on, it would begin sampling data continuously after a brief start up time (~1-5 minutes). The PC was capable of sampling data at 128 Hz for the pressure and environmental data. The internal GPS tracker data was sampled at 1 Hz, and the existing onboard GPS feed was sampled at 50 Hz. The software on the PC was capable of synchronising the various data feeds with a consistent start point. The data acquisition process is discussed in section J.2.

Figure 9.10 - Onboard PC mounted on electrical equipment storage cabinet.

Data was temporarily saved on the hard disk drive of the PC and then complete data files (separated into 15 minute segments of synchronised data) were written to a 128 GB USB flash drive, which could be manually removed/replaced and posted to the University of Birmingham. Data was collected on a fortnightly cycle and analysed immediately in order to detect any faults (section J.5.5) that would require immediate maintenance of the data acquisition system.

9.3.3 System overview

An overview of the electrical and pneumatic systems are shown in figure 9.11. Pneumatic components (i.e., pressure taps labelled A1-A3 and B1-B17, the pitot static probe and the three external reference pressure sources) are shown as blue blocks, with blue lines corresponding to pneumatic tubing. Electrical sensors are shown as white blocks, and black lines show power/signal cables (drawn as a single line) - the exception is the existing "Network GPS" feed that is powered externally (so is only a signal cable). All pressure transducers use the partially sealed reference pressure as the reference pressure - a manifold was installed inside the case of the onboard PC to enable multiple pneumatic connections. Finally, two additional pressure transducers were situated inside the onboard PC (not shown on figure 9.11) to measure reference pressures (see equations 10.4a and 10.4b). Further details about the experimental set up are provided in appendix J.

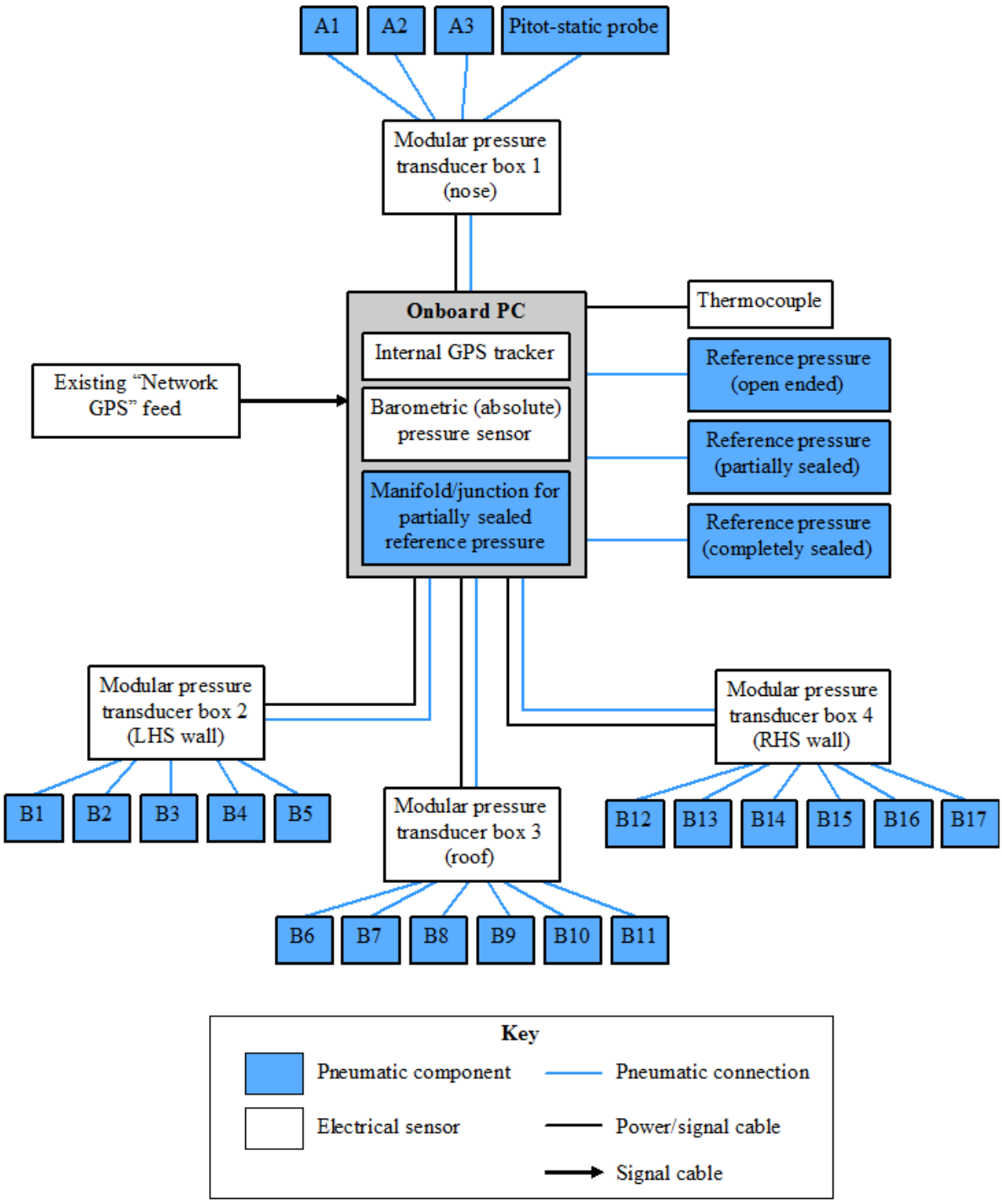

Figure 9.11 - Schematic overview of data acquisition system at full-scale on the NMT.

CHAPTER 10

FULL-SCALE CROSSWIND TESTS - ANALYTICAL METHODOLGY

10.1 Introduction

Chapter 10 describes the analytical methodology for the full scale train based measurements of pressures at full scale on the NMT power car. The data processing procedure is described in detail in appendix J, and this chapter considers the data once all of the different sources (pressures, GPS etc) had been collected together. The initial conversion of voltage signals to nominal pressures is described in section 10.2.1, and the categorisation criteria of data files are defined in section 10.2.2. Section 10.2.3 describes the process of conversion of nominal pressures to corrected pressure coefficients in several stages - obtaining the actual background voltages of each transducer, calculating the true aerodynamic speed and yaw angle and hence resultant aerodynamic speed required to normalise the corrected pressure data. Section 10.2.4 describes the low-pass filtering and section 10.2.5 describes how open air data was isolated. Section 10.2.6 describes the discretisation of the train used in the calculation of force and moment coefficients. Section 10.3 describes the two methodologies that were used to obtain mean pressure coefficients, and also defines "gusts" that have also been considered in the discussion of results. Error analysis is presented in section 10.4 and in detail in section F.6.

10.1.1 Overview of data collected

Data was collected by the onboard PC from the different pieces of equipment and synchronised by the onboard PC. Pressure data was sampled at 128 Hz and GPS data at 1 Hz, and data was saved in 15 minute segments. A total of 3050 hours raw data have been collected from the NMT between 03/10/13 and 22/06/15. Of this raw data, 113.3 hours of "open air" data have been identified and used in subsequent analysis to some extent. Section 10.2.2 describes how data was categorised and table 10.2 lists the quantity of data collected for each category.

10.2 Data processing

The data processing strategy can be thought of in various stages. The first stage was collection of all data into a single data file of pressures, train speed, GPS location etc, which is described in section J.4. Data files were then categorised based on the train speed, direction and quality of the data obtained. Background voltages of each transducer were obtained from data where the train was stationary, and used to recalculate the pressures for each pressure tap (see section 10.2.3.1). The dynamic pressure from the pitot-static probe was converted to "true" aerodynamic vehicle speed (section 10.2.3.3) and yaw angle was calculated from the pressure taps at the nose, which enabled result wind velocity to be calculated and used to normalise the pressure data to coefficients (section 10.2.3.4). Given the very large quantity of data collected from the NMT measurements it was necessary to automate as much of the processing as possible to ensure the data was all of consistent quality and to save time.

10.2.1 Pressure data - preliminary processing

10.2.1.1 Conversion to nominal pressures

The voltage signal of each transducer (ΔV_k) was converted into a nominal pressure, i.e., not yet accounting for voltage offsets in the background voltage ($V_{k,0}$) between each transducer since this was performed later (section 10.2.3.1).

The voltage output of each transducer was converted to pressure (in Pa) by:

$$\Delta V_k = V_k - V_{k,0} \tag{10.1}$$

$$P_k = K_{NLC} \Delta V_k \tag{10.2}$$

Where $V_{k,0}$ is the background voltage at 0 Pa differential pressure, and K_{NLC} is the nominal linear calibration coefficient (defined in appendix E), and equal to 2500 PaV^{-1}. For the purposes of preliminary analysis, $V_{k,0}$ was taken as 2.25 V since the data needed to be analysed to some extent first before actual background voltages were obtained.

10.2.1.2 Reference pressures

Three reference pressure sources were used and were described in section 9.3.1. The pressure from each pressure tap can thus be expressed as:

$$P_k = P_{k,total} - P_{ref,PS} \tag{10.3}$$

Where $P_{k,total}$ is the total pressure applied to the HPP of each transducer. The only exception

is the single pressure transducer dedicated to dynamic pressure of the pitot-static probe (see equation F.13.1). Two additional reference pressure channels were recorded, and defined as:

$$P_{ref1} = P_{ref,CS} - P_{ref,PS} \tag{10.4a}$$

$$P_{ref2} = P_{ref,OE} - P_{ref,PS} \tag{10.4b}$$

Therefore it was possible to also adopt either $P_{ref,CS}$ or $P_{ref,OE}$ as the normalising reference pressure for each pressure tap, by adding either equation 10.4a or 10.4b to equation 10.2 (i.e., equation 10.5).

10.2.2 Data categorisation

Each data file was categorised according to various criteria, and the overall procedure is shown in the flow chart in figure 10.1. The criteria for each category are described in more detail in table 10.1. The procedure was implemented in four stages (numbered 0 to 3) and was hierarchical, i.e., only data that passed stage 1 would be sub-categorised in stage 2, and so on. Stage 0 checked that there was an adequate quantity (at least 10 s) of data in the file. Stage 1 considered the actual quality of the pressure data - if the key components of the system functioned correctly the data was regarded as "good". Nose sensors were critical and all of the data channels had to be functioning for data to be considered "good" since dynamic pressure and yaw angle were needed to obtain pressure coefficients. Within the loop, all of the modular pressure transducer boxes had to be functioning, but individual broken pressure channels were permitted. Stage 2 considered the quantity of working pressure channels, i.e., whether or not was there enough spatial coverage around the loop to perform meaningful open air analysis. Stage 3 considered the operation of the train - i.e., speed and direction, and therefore whether

the data was appropriate for open air analysis (running). It should be noted that a file was defined as containing forwards running data if at least a 10 s block of the data in the file met this criteria, and hence at stage 3, an data file may have fit into more than one category. Table 10.2 surmises the quantity and obtained possible uses of data in each category. It must be stressed that the categorisation was based on the appropriateness of the data for open air analysis - bad and unacceptable data may still have been useful for analysis of pressure transients, but this was outside the scope of this study.

Table 10.1 - Data categorisation criteria.

Stage	Categories	Criteria
0	Has data	At least 10 s of data (file length of at least 1280 rows).
	No data	Failure to meet above criterion.
1	OK	All modular pressure transducer boxes must be OK. All data channels on the nose must be OK.
	Bad	Failure to meet criteria for "OK".
2	Good	All modular transducer boxes working, and majority of pressure channels functioning correctly - minimum of four good pressure taps on each of the walls and roof (i.e., at least 12 working taps).
	Acceptable	All modular transducer boxes working, and minimum of three good pressure taps on LHS wall and roof and two good pressure taps RHS wall.
	Unacceptable	Failure to meet above criteria for "Good" or "Acceptable".
3	Forwards running	Train speed (from GPS data) above 20 m/s. Car 43062 was leading, i.e., corrected train speed (see 10.2.3.3) from front pitot was within ±30% of mean train speed for duration train was above 20 m/s.
	Reverse running	Train speed (from GPS data) was above 20 m/s. Car 43062 was leading, i.e., corrected streamwise aerodynamic speed (equation 10.7) from front pitot was low (i.e., ±50 Pa)
	Slow running	Train speed (from GPS data) was below 20 m/s but above 0.5 m/s. Train direction irrelevant.
	Stationary running	Train speed (from GPS data) was below 0.5 m/s.
	Unacceptable running	Failure to meet above criteria for running (miscellaneous files with GPS data failure).

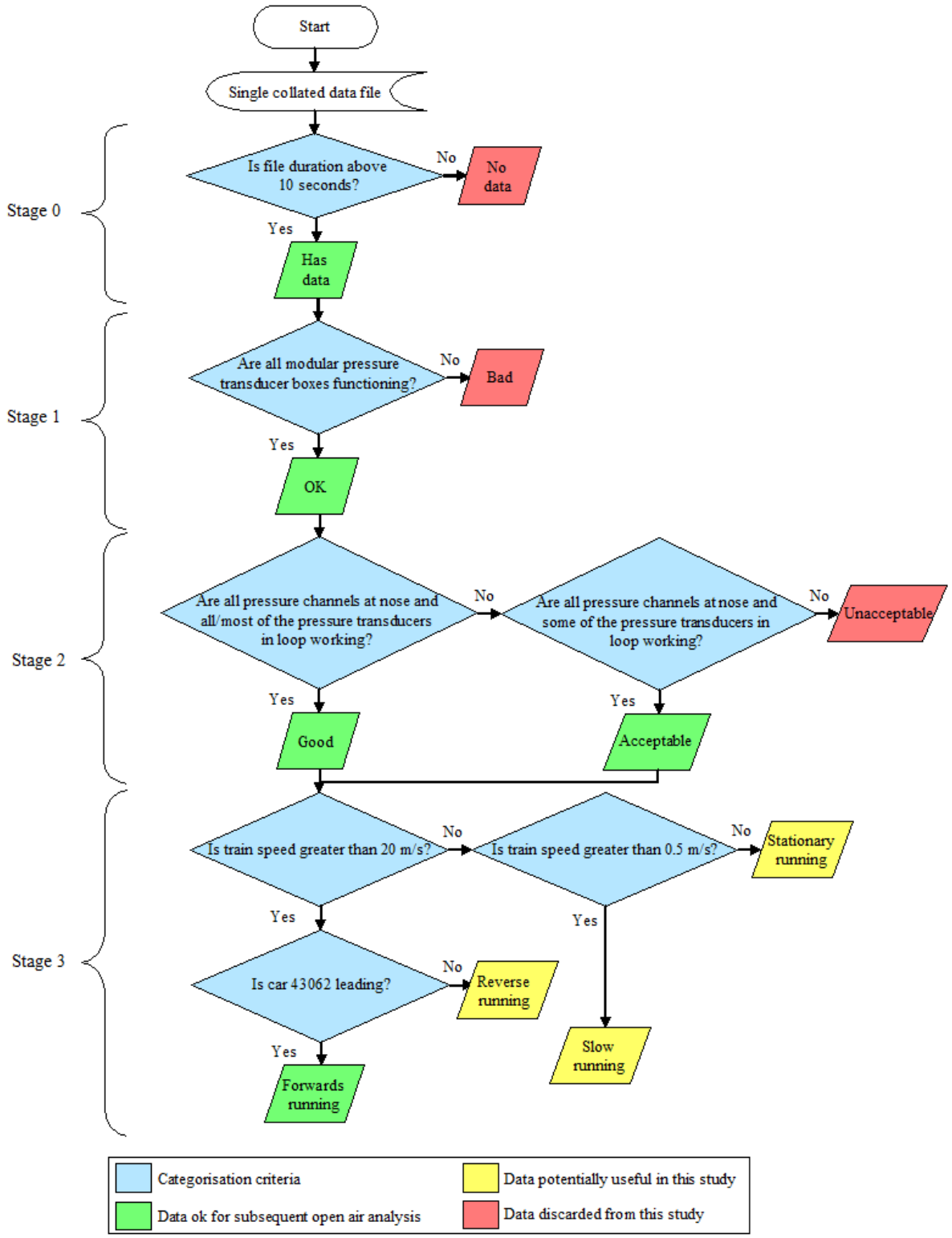

Figure 10.1 - Overview NMT data file categorisation procedure.

Table 10.2 - Possible uses of data in each category, and quantity obtained.

Stage	Categories	Possible use(s) of data	Quantity of data obtained		
			Files	Hours	Percentage (of all data)
0	Has data	Subsequent analysis.	12734	3051	100
	No data	Discarded.	13990	0	0
1	OK	Open air analysis. Transients analysis.	10360	2299	75
	Bad	Pressure tap specific analysis of transients.	3630	752	25
2	Good	Open air analysis of pressures and calculation overturning forces on loop of taps. Effects of passing trains and tunnels on pressures around train.	1770	373	12
	Acceptable	Open air analysis of pressures and less accurate calculation overturning forces on loop of taps. Effects of passing trains and tunnels around train.	6115	1378	45
	Unacceptable	Pressure tap specific analysis of transients.	2475	548	18
3	Forwards running	Consideration of variation in surface pressures and forces with yaw angle. Transients analysis.	2642	639	21
	Reverse running	No open air analysis undertaken. Transients analysis, e.g., comparing pressure transients from a single tunnel for forwards and reverse running.	211	51	2.7
	Slow running	No open air analysis undertaken, but high yaw angles could be considered. Transients analysis.	2070	647	21
	Stationary running	Obtaining background voltages for working pressure channels ($V_{k,0}$). Very high yaw angles could be considered. Transients of moving train passing a stationary train.	2324	39	1.3
	Unacceptable running	Analysis of pressure transients.	7	2	0.1

10.2.3 Pressure data - secondary processing

10.2.3.1 Background voltages and pressure recalculation

All good data that was defined as stationary running was used to obtain background voltages. As the experiments took place in the real world, the effects of natural winds on the train resulted in pressure fluctuations on the stationary train. A conservative approach was therefore taken to define parts of data where the ambient wind conditions were stable, assuming the corresponding fluctuations in pressure were random and low amplitude (i.e., of zero mean over a sufficient time interval). Once a data file had been categorised as "stationary running" a one minute segment of the data file was considered and the following conditions had to be met in order for that portion of the data to be considered as representative of zero differential pressure:

- Train speed less than 0.22 m/s (0.5 miles per hours);
- Maximum fluctuations in pressure from each pressure tap within ±15 Pa of the time averaged pressure for a 1 minute period. This had to be true for all working pressure channels.

If these conditions were met the 1 minute period was extended by one sample and the process repeated until the conditions were no longer met. If the conditions were not met then the 1 minute window was shifted sample one sample and the check procedure repeated. The temporal mean values for each tap were defined as $V_{0,k}(t_{epoch})$ where the term t_{epoch} defines the Unix epoch time stamp at which $V_{0,k}$ was calculated. The uncertainty associated with the background voltages is considered in section F.6.1.1 and figure F.5 shows $V_{0,k}(t_{epoch})$ across a 1 year period.

Once background voltages were obtained, the pressures from each data file (regardless of its categorisation as defined in table 10.1) were recalculated using the new values of $V_{0,k}$ by equations 10.1 and 10.2.

10.2.3.2 Reference pressure modification

When considering open air analysis, one issue was that variations in pressure due to elevation were apparent on the data (shown in figure 10.3.2 for example). This was due to the reference pressure source of the LPP of each transducer - a partially sealed reservoir which would normalise with the ambient pressure over a time period of about 30 s - 1 minute (Quinn et al., 2016). All pressure tap data was therefore normalised by $P_{ref,OE}$, i.e., the pressure inside the luggage area measured with the open ended probe. This resulted in a very stable mean pressure across the entire duration of each data file (see section J.5.2).

$$\Delta P_k = \left(P_{k,HPP} - P_{ref,PS}\right) + \left(P_{ref,PS} - P_{ref,OE}\right) \tag{10.5}$$

10.2.3.3 Calculation of streamwise aerodynamic vehicle speed

To convert pressures to pressure coefficients it was necessary to calculate U_{res} from the streamwise aerodynamic vehicle speed U and the yaw angle. Both of these quantities required data from wind tunnel tests, which introduces additional uncertainty into the measurements which is discussed in appendix F. The streamwise aerodynamic vehicle speed was calculated as:

$$U_{uncor}(t) = \sqrt{2\frac{1}{\rho}P_{dyn}(t)} \tag{10.6}$$

Where the subscript "*uncor*" defines that the velocity is uncorrected. Figure I.5.1 and table I.2 in appendix I shows the air velocity recorded at the pitot static probe position from a wind tunnel test on a 1:25th scale HST at zero yaw. It was found that the presence of the train resulted in an air velocity that was about half of the velocity recorded with no train in place. Corrected streamwise vehicle speed was therefore recalculated as:

$$U_{cor}(t) = C_{dyn} U_{uncor}(t) \tag{10.7}$$

Where C_{dyn} is the empirical conversion factor obtained from the wind tunnel test and equal to 2.1. A check was performed on this conversion factor by considering all good open air data where the instrumented power car was leading and the train speed was above 20 m/s, equivalent to about 60 hours of data. The values of $U_{uncor}(t)$ and $U_{cor}(t)$ were plotted against $V_{tr}(t)$ (train speed from the GPS tracker) and are shown in figure 10.2 (note that data has been filtered and resampled at 1 Hz). The gradient of $U_{cor}(t)$ against $V_{tr}(t)$ is very close to unity. If the assumption is made that over a sufficiently long time interval, the fluctuations in natural wind velocity on the NMT should take a mean value of zero, then this wind tunnel calibration factor can be considered to be remarkably accurate.

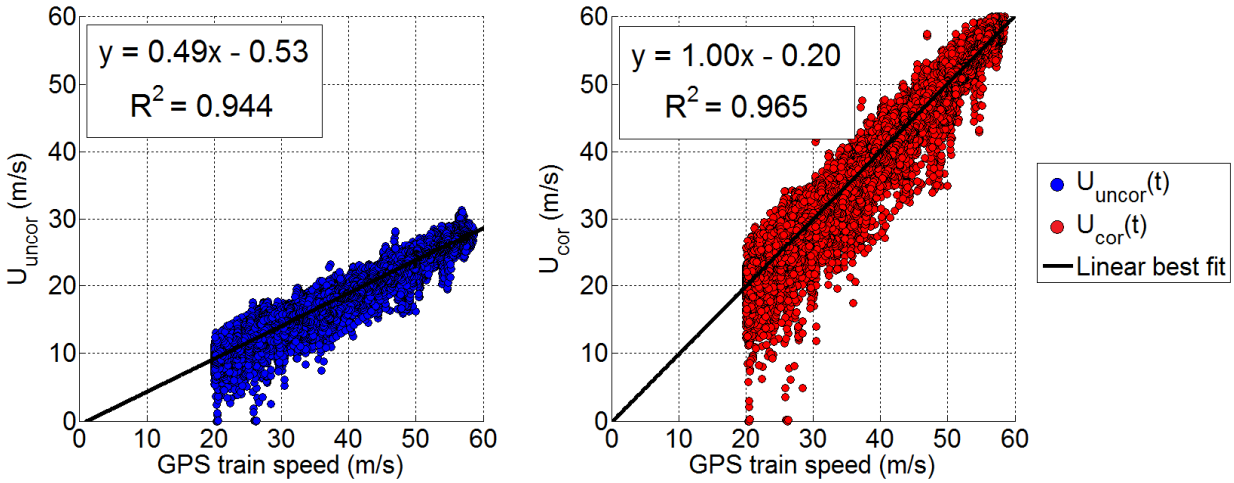

Figure 10.2 - Linear best fit of U_{uncor} and U_{cor} against train speed for forwards running at train speeds above 20 m/s.

10.2.3.4 Calculation of yaw angle and pressure coefficients

Yaw angle was calculated from the nose pressure taps following the procedure described in section 8.2.2, and two yaw angles were defined based on the values of $K_{\theta,1,2,3}$ from the higher Re number RWDI wind tunnel data, and $K_{\varphi,1,2,3}$ from the TRAIN rig CWG data. There are therefore two definitions of instantaneous yaw angle depending on which empirical coefficients are used, and $\theta(t)$ defines yaw calculated from the wind tunnel test coefficients and $\varphi(t)$ defines the yaw angle from the TRAIN rig tests. Instantaneous yaw angle was calculated as:

$$C_{\theta,\varphi}(t) = \frac{\Delta P_{A3}(t) - \Delta P_{A1}(t)}{\Delta P_{A2}(t)} \tag{10.8}$$

$$\theta(t) = K_{\theta,1}C_{\theta,\varphi}^3(t) + K_{\theta,2}C_{\theta,\varphi}^2(t) + K_{\theta,3}C_{\theta,\varphi}(t) \tag{10.9a}$$

$$\varphi(t) = K_{\varphi,1}C^3_{\theta,\varphi}(t) + K_{\varphi,2}C^2_{\theta,\varphi}(t) + K_{\varphi,3}C_{\theta,\varphi}(t) \quad (10.9b)$$

Where $\Delta P_{A1,2,3}$ are the pressures from nose taps A1, A2 and A3 which are defined by their physical position (shown in figure 9.5), and the constants $K_{\theta,1,2,3}$ and $K_{\varphi,1,2,3}$ are defined in table 8.1. The resultant wind velocity was calculated from yaw angle as:

$$U_{res,\theta,\varphi}(t) = \frac{U_{cor}(t)}{cos(\theta(t), \varphi(t))} \quad (10.10)$$

Where the notation "θ, φ" implies that a value was calculated for both of the yaw angles calculated from equations 10.9a and 10.9b. The crosswind velocity component perpendicular to the train was calculated as:

$$V_{\theta,\varphi}(t) = \frac{U_{res,\theta,\varphi}(t)}{sin(\theta(t), \varphi(t))} \quad (10.11)$$

Pressures were then normalised to pressure coefficients by:

$$C_{P_k}(t) = \frac{\Delta P_k}{\frac{1}{2}\rho(U_{res,\theta,\varphi}(t))^2} \quad (10.12)$$

Analysis of each file was therefore undertaken twice based on values of $\theta(t)$ and $\varphi(t)$.Two data files were then saved that containing the unfiltered data as pressure coefficients, yaw angle, the ambient wind velocity components, GPS position and train speed, for each yaw angle.

10.2.4 Data filtering

In order to mitigate the effects of high frequency and magnitude pressure fluctuations which arise either due to turbulence, electrical and mechanical noise and tube resonance, pressure data was filtered with a low pass moving average filter with a 1 s period, and the filtered data was saved as a new data file. The choice of the 1 s filter period was that previous studies have indicated that gusts of period 1-3 s can result in train instability (Baker, 1991a). Use of a moving average filter resulted in a phase shift in the data, which was accounted for during data isolation by temporarily appending zeros to the start of the data file during the data isolation procedure (section 10.2.5), then removal of these zeros once the open air data had been isolated. The 1 s filtered data file was then resampled to create an additional smaller sized file (used in analysis described in section 10.3.1). It should be pointed out that at this stage there were three versions of the data file:

- Raw data;
- 1 s filtered data;
- 1 s filtered data resampled at 1 Hz.

The most significant issue noted with the data was that the roof taps showed an increase in noise, shown in figure 10.3.1, which appeared quasi-periodic. It was believed that this was due to the engine cooling array - large fans that expel air from the roof which were located ahead of the loop of pressure taps, and presumably are controlled by a thermostatic control unit within the engine cooling system. The frequency spectra of this noise at the roof taps was analysed in section J.5.3. When the roof fans were presumed to be turned on more of the signal power was at frequencies between 1-10 Hz suggesting additional noise. The 1 s filter was successful in removing the noise, however the mean suction pressures over the roof were

significantly greater when the roof fans were switched on (of the order of 200-500 Pa) and no method of reliably identifying or correcting the data has been developed in this study. Pressure data over the roof (and hence mean lift forces and overturning moments) presented in chapter 11 are therefore to be interpreted with caution.

10.2.5 Isolation of open air data

In this study the focus was on obtaining data that only consisted of open air running. Open air data, for the purposes of this investigation, is defined as train speeds above 20 m/s (72 kph) and without any effects from infrastructure or passing trains. A "pressure transient" is defined as a change in pressure created by (in most cases) a passing train or tunnel. Pressure transients were identified and removed from the data files, which at this stage were a continuous time series, but after this process there would be discontinuities, hence why any data filtering was carried out prior to data isolation. Transients were identified in the raw data, and removed from the raw, filtered and 1 s resampled data files in parallel.

Different approaches were used to categorise different types of pressure transient, and the overall strategy was conservative - given the aim of this study and the very large quantities of data, it was felt better to remove a lot of false positives (i.e., segments of data incorrectly identified as pressure transients) than to aim for a higher level of accuracy in detecting transients. It should be noted that many of the "false positives" have in fact been manually identified as gusts and hence considered in later open air analysis. An iterative approach was adopted, and broadly speaking the level of accuracy decreased with each pass of the data

through an identification algorithm. Section J.5.2 describes the procedure by which transients were removed in detail and gives examples of the different type of pressure transient.

Figure 10.3.1 shows an example of the first 500 s of a 15 minute data file , showing one pressure tap from each side wall and the roof. The horizontal black bars indicate the positions where pressure transients were detected. There are two passing trains at t = 10 s and t = 460 s, and a tunnel at t = 400 s (shown more clearly in figure 10.3.2). The green graph indicates the roof pressure tap and shows quasi-periodic increases in the magnitude of the pressure fluctuations, which are believed to arise due to the engine cooling array (considered in detail in section J.5.3), in some cases these fluctuations were identified as pressure transients and removed from the data. There is a slight rise in the pressure from all taps at about t = 260 s, which corresponds to a change in elevation - given the train speed and change in pressure it is estimated to be a rise of about 10-20 m over a distance of roughly 2.5 km.

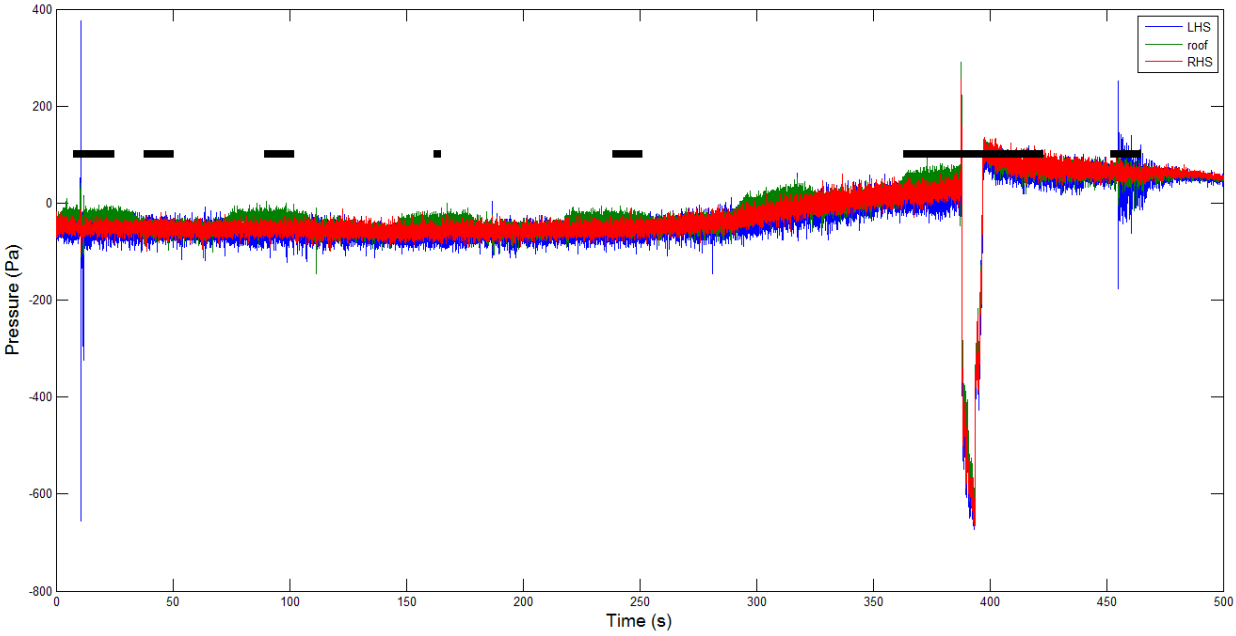

Figure 10.3.1 - NMT pressure tap time series around loop, with black bars indicating the detection of pressure transients.

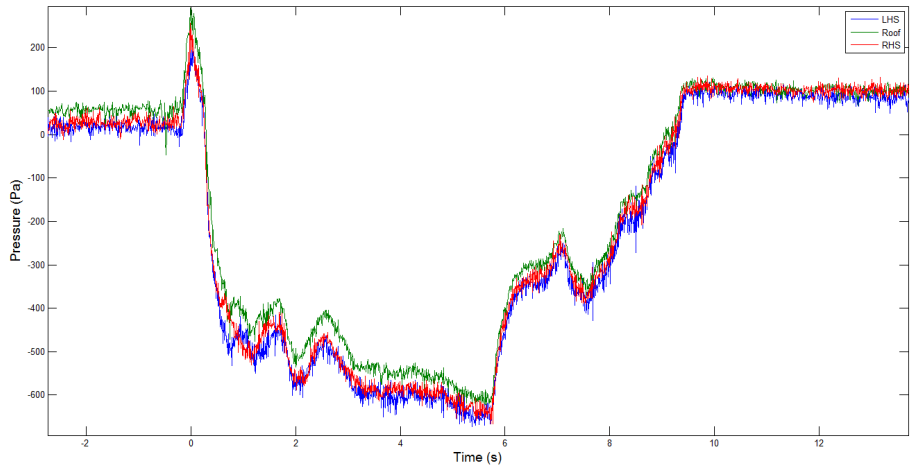

Figure 10.3.2 - Example of tunnel transient (from figure 3.3.10) at <400 s.

10.2.6 Calculation of force and moment coefficients

The methodology for calculating force and moment coefficients follows that described in section 7.2.2, based on previous studies (Sanquer et al., 2004; Quinn et al., 2007; Dorigatti 2013; Soper 2014). The discretised model of the loop of pressure taps is shown in figure 10.4, and table 10.3 lists the details of each rectangular surface. Data from taps B4 and B7 was omitted from the calculation of forces due to issues noted with these taps (discussed in appendix K).

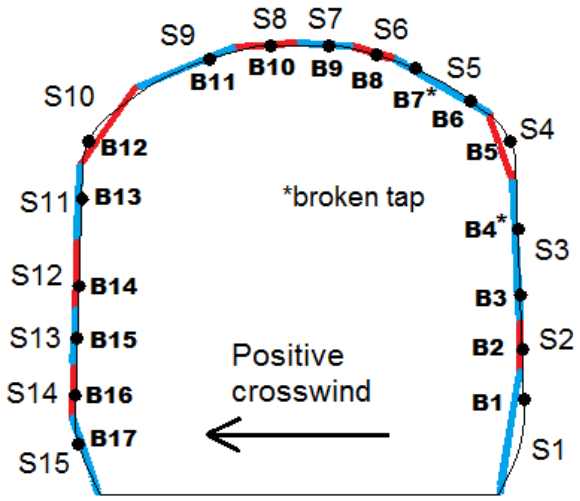

Figure 10.4 - Discretised model of NMT loop - pressure taps B4 and B7 have been omitted.

Table 10.3 - List of surfaces, corresponding pressure taps and surface properties for NMT loop.

Surface number	Pressure tap	A_S (m^2)	θ_S (°)
1	B1	0.81	9
2	B2	0.39	2
3	B3	1.05	2
4	B5	0.51	25
5	B6	0.83	60
6	B8	0.34	73
7	B9	0.39	88
8	B10	0.42	88
9	B11	0.78	74
10	B12	0.71	60
11	B13	0.54	2
12	B14	0.53	2
13	B15	0.40	2
14	B16	0.39	2
15	B17	0.58	19

10.3 Analysis of open air data

Open air data was analysed on the basis of the quasi-static assumption, i.e., that instantaneous fluctuations in the wind velocity result in corresponding fluctuations in the surface pressure distribution and hence forces on the vehicle. Each instantaneous data sample was considered independent and was sorted based on instantaneous yaw angle (calculated from both equations 10.9a and 10.9b - i.e., data was effectively analysed twice). This method was similar to the yaw angles bin methodology used successfully for the TRAIN rig CWG tests (described in section 7.3.5), and has been used in other studies (Quinn et al., 2007, Soper, 2014).

In total, just over 100 hours of good open air data were obtained once transients and bad data had been removed from data categorised as "forwards running". This data was analysed and presented following two main approaches:

- Regression analysis of scatter plots of pressure coefficient against yaw angle (section 10.4.3);
- Pressure coefficient data sorted into yaw angle bins for each tap (section 10.4.2).

10.3.1 Scatter plots and regression analysis

This analysis considered the 1 s filtered resampled data files - resampling was necessary to reduce the quantity of data given the limited of computing power of a desktop PC. Appendix K presents the scatter plots for each of the pressure taps in the loop against yaw angles obtained from the WT and CWG coefficients separately. Three regression models were

chosen - linear, quadratic and cubic, and applied to the scattered data - note that positive and negative yaw angles were considered to be separate and independent. Analysis of these regression models found a large degree of scatter, and that R^2 values increased as the polynomial order of the regression model increased (appendix K presents the detailed results of the regression analysis). Values of pressure coefficient were then obtained from the linear regression models (as these gave the most realistic data) for each pressure tap.

10.3.2 Yaw angle bin methodology

This approach considered the non-resampled 1 s filtered data, and follows the methodology used for the TRAIN rig CWG tests described in section 7.3.5. Pressure coefficients were sorted into bins according to the instantaneous yaw angle at 5° ±2° intervals from -20° to 20°. The mean and standard deviation of each bin then were calculated assuming a normal distribution of data in each bin. The quantity of data in each bin and standard deviations are given in tables F.10.1.1 to F.10.2.2 during uncertainty analysis.

10.3.3 Analysis of gusts

It was of interest to consider segments of data identified as "gusts". Often these were incorrectly identified as pressure transients and removed from the open air data, and a number of these were manually identified as false positives and reintegrated into the open air data analysis described in sections 10.3.1 and 10.3.2. Gusts were identified based on a peak in yaw angle over a time period of 1 s or higher (based on Baker, 1991a), unlike a shorter and sharper

duration yaw angle peak as a result of a passing train. Based on this observation, a Matlab function was developed to identify "gusts" from the non-isolated continuous data files after the data had been 1 s filtered. Figure 10.5 shows the definition of a generic gust.

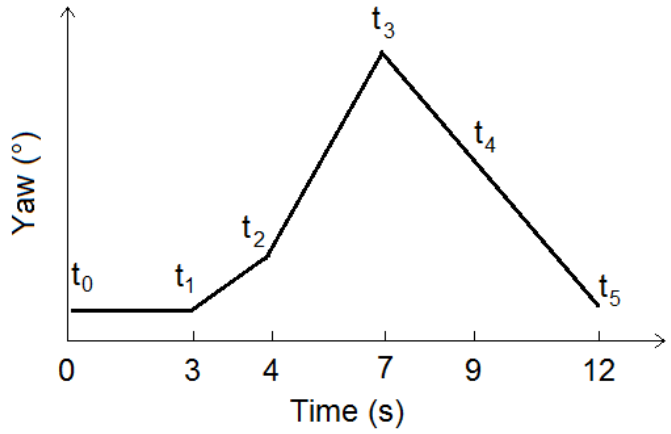

Figure 10.5 - Generic gust profile time history.

The criteria for the gust were that:

- between t_0 and t_1 the yaw angle must not exceed 2 in magnitude, and the minimum time between (t_1 - t_0) is 3 s;
- between (t_1 and t_2) is a "buffer" stage in the build up time, where yaw angle may take any value, and the maximum length of (t_2 - t_1) is 1 s;
- yaw angle at t_3 is defined as the gust peak yaw, and must not exceed 20°;
- the magnitude of the temporal mean yaw between (t_2 and t_4) must be greater than 5°, and the minimum length of (t_4 - t_2) is 1 s;
- gust end is at t_5 which is the time at which the magnitude of yaw angle is less than 2°;
- train speed must be 15 m/s or greater , no two adjacent pressure taps in the loop may have faults and all sensors at train nose must function.

Once gusts were identified, data was manually categorised as either "gusts" and "not gusts" (since a large number (~30%) of the data segments identified as gusts were in fact pressure transients caused by passing trains). The analysis was undertaken twice based on the values of $\theta(t)$ and $\varphi(t)$ (equation 10.9a and 10.9b). A total of 174 "gusts" were identified based on $\theta(t)$ and 498 gusts were obtained from $\varphi(t)$. Values of $C_{\eta}^{*}(t)$ were then obtained from the pressure tap time history for each gust, and considered with respect to yaw angle in section 11.4.

10.4 Error and uncertainty analysis

Errors were quantified for the loop of pressure taps in terms of the bias, random and total errors (equations F.1 to F.3), and the methodology followed that used for the model scale tests and is described in detail in section F.6. The values obtained may not necessarily account for all sources of uncertainty, such as the effects of the engine cooling fans, the uncertainty in calculation of yaw angle or the train speed correction (equation 10.7). The values of errors are shown in figure 10.6. Note that the errors for taps B4 and B7 are very low, and following regression analysis these pressure taps have been considered to be "faulty" and hence omitted from all analysis. The errors over the roof (taps B6 to B11) are, unsurprisingly, higher than for the side walls when both bias and random error is considered, and this is believed to be as a result of the engine fans. Random uncertainty was obtained based on the root mean square errors (RMSE) of the linear regression models (see appendix K), since this was higher than random error calculated based on the standard deviations of each yaw angle bin. Random errors are lower than bias errors due to the very large quantity of data.

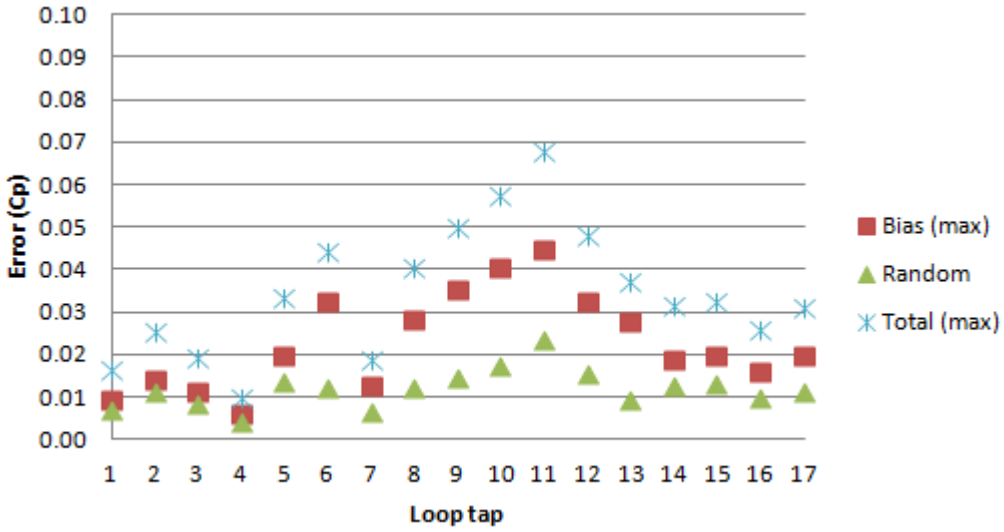

Figure 10.6 - Experimental errors (bias, random and total) for each of the loop pressure taps.

CHAPTER 11

FULL-SCALE CROSSWIND TESTS - RESULTS AND DISCUSSION

11.1 Introduction

Chapter 11 presents the main results from the full scale crosswind tests. Section 11.2 briefly considers the differences in yaw angles (θ and φ). Section 11.3 considers the different results from the two methodologies of obtaining mean pressure coefficients; results from the scatter plots methodology are presented in section 11.3.1 and the yaw angle bin results are presented in section 11.3.2. Section 11.4 considers examples of the time domain variation in pressures and forces with respect to φ for different examples of gusts (defined in section 10.3.3), and also considers the 1 s peak values of for each of the gusts. Comparison of force and moment coefficients based on all methodologies of obtaining pressures is presented 11.5, and closing remarks are made in section 11.6.

11.2 Distribution of yaw angles

Section 10.2.3.4 discussed that yaw angle (hence all subsequent analysis) was calculated twice depending on the yaw coefficients (see table 8.1) from the WT and CWG tests. Throughout this chapter, comparisons are drawn between the two yaw angles, so the definition that θ refers to yaw calculated from the wind tunnel cubic yaw coefficients and φ is yaw angle obtained from the TRAIN rig CWG test cubic yaw coefficients is worth restating.

Figure 11.1 shows the quantity of full scale data in 1° yaw angle bins calculated from both the WT and CWG yaw coefficients. There appears to be a slight bias towards positive yaw, though the majority of the data is within the low yaw angle range (less than ± 5°). The values of θ are much less spread than φ which of course results from the different definitions of yaw (as in figure 8.4.2).

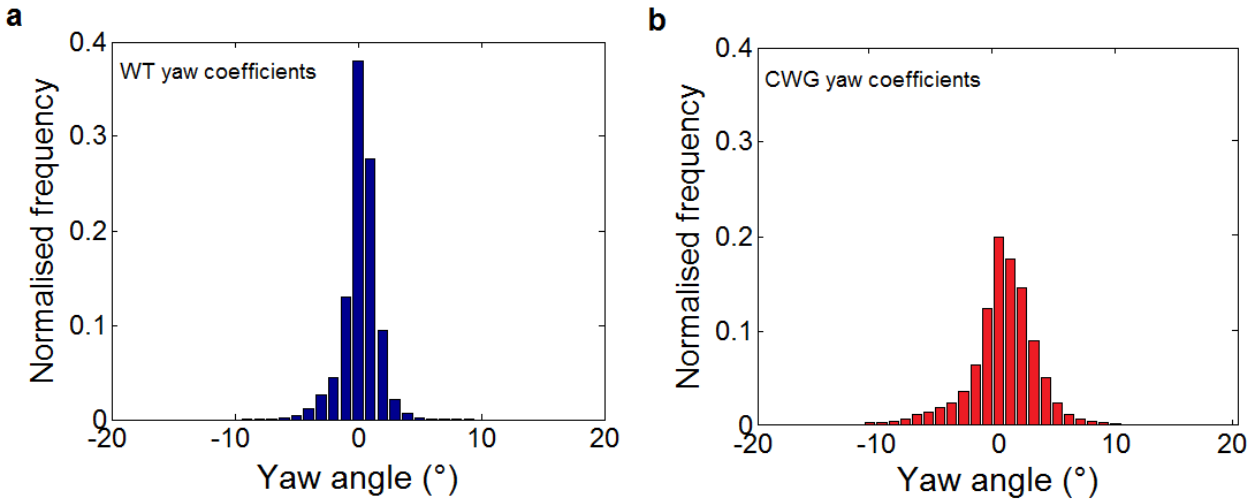

Figure 11.1 - Distribution of yaw angles for scatter plot pressure data.

11.3 Pressure distribution around the loop

11.3.1 Scatter plots and regression analysis

Pressure data was considered separately for each pressure tap and the relationship between pressure coefficient and yaw angle was investigated. Scatter plots of pressure coefficient against yaw angle for each pressure tap are presented in appendix K. For each scatter plot, a linear, quadratic and cubic best fit regression model was fitted using the "polyfit" function on Matlab (Mathworks, 2010) and positive and negative yaw angles were considered independently. The coefficients of each regression model are given in tables K.2.1 and K.2.2, and the validity of these models is discussed further in appendix K. It was found that quadratic and cubic models had the best fit with the data (i.e., highest R^2 values and lowest RMSE) but these models often predicted behaviour that was unrealistic, such as pressure coefficients greater than unity or sharp decreases in negative pressure coefficient on the windward side wall as yaw angle increased (see tap B17 on figure 11.2 for instance). A linear regression model was found to be the least accurate (statistically speaking), but resulted in the most "realistic" results for each pressure tap, i.e., whether or not the pressure coefficient of each would increase or decrease with respect to increasing yaw angle, though it is acknowledged that the variation of pressures for any of the loop pressure with respect to yaw angle was not found to be linear in the wind tunnel data (section K.4). Figure 11.2 shows the scatter plots and regression models for all of the pressure taps in the loop, and are based on θ (i.e., wind tunnel yaw coefficients). The scatter plots shown in figure 11.2 are shown more clearly and compared with equivalent scatter plots based on φ in appendix K. The range of φ (see appendix J) is approximately double that of θ, and as yet it is uncertain whether θ or φ is most realistic.

The pressure data exhibits a high degree of scatter as yaw angle increases, though general trends are apparent . The windward taps shows a positive gradient and the leeward taps show a negative gradient as yaw increases. The roof pressure taps, within the yaw angle range investigated, show a quadratic trend with a maxima at about zero yaw and then very low pressure coefficients at yaw angles of 10°. Previous research indicates that as a crosswind impinges on a train there is a separation at the windward wall-roof junction which results in a frequency domain vortex shedding phenomenon over the roof (Baker, 1991b). It is therefore unsurprising that at about ±10° yaw there are very low and scattered pressure coefficients over the roof, indicating an intermittent flow feature that may be cancelled out during the averaging process in the wind tunnel test data. It is quite striking that the magnitudes of the suction pressures are very high compared to the values from the wind tunnel data (which is shown later in figure 11.5 for comparison). There may also be influences from the engine cooling fan on the roof pressure taps.

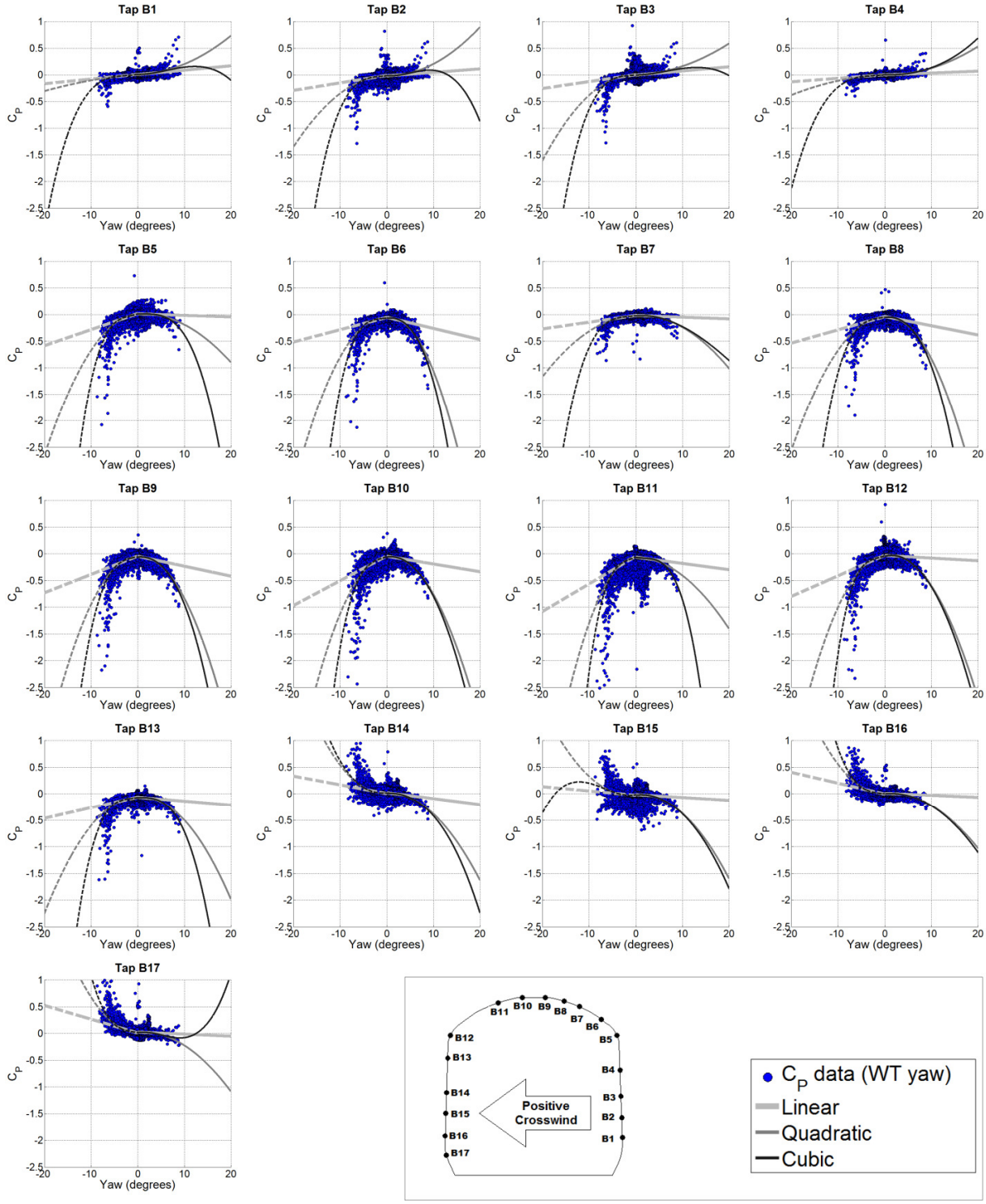

Figure 11.2 - Scatter plots of $C_{P_k}(t)$ against yaw (θ) and best fit models for each pressure tap.

There is an asymmetry in the pressure distributions at the roof for the positive and negative yaw angles. Taps B9 and B10 (either side of the roof centreline) show a larger quantity of large suction $C_{P_k}(t)$ values when negative yaw angles are considered, and the linear regression gradient is therefore higher for negative yaw angles. In fact, the magnitude of the linear gradient (given in tables K.2.1 and K.2.2 for positive and negative yaw respectively) is larger for the negative yaw angle range when most of the working pressure taps are considered regardless of their location (taps B4 and B7 have been discarded from subsequent analysis). The case where the linear best fit gradients are closest is seen on tap B6, which is unexpected since this pressure tap is at the wall-roof corner i.e. the separation point, therefore this tap was expected to show a negative gradient of larger magnitude at positive yaw angles (given that this is the location where a suction peak is expected). When considering the remainder of the taps, the asymmetry in gradient between positive and negative yaw angles is not necessarily unexpected, insofar as that taps on the windward side at positive yaw will of course be on the leeward side at negative yaw and therefore the physical flow characteristics and hence pressures are expected to be different. It is therefore simpler to compare the distribution of pressures around the loop as a whole at both positive and negative yaw angles to consider this point further.

Figures 11.3.1 compares the pressures around the loop that were calculated from the linear regression models at both positive and negative yaw angles, and the wind tunnel data has been shown for comparison. At negative yaw angles the NMT pressure tap positions have been inverted (so that the lowest tap on the windward wall is always on the RHS of the figure). Error bars are representative of the total error for each pressure tap (shown in figure 10.6 for full scale and table 7.3 for the wind tunnel data). Figure 11.3.2 is in the same format but based on φ rather than θ.

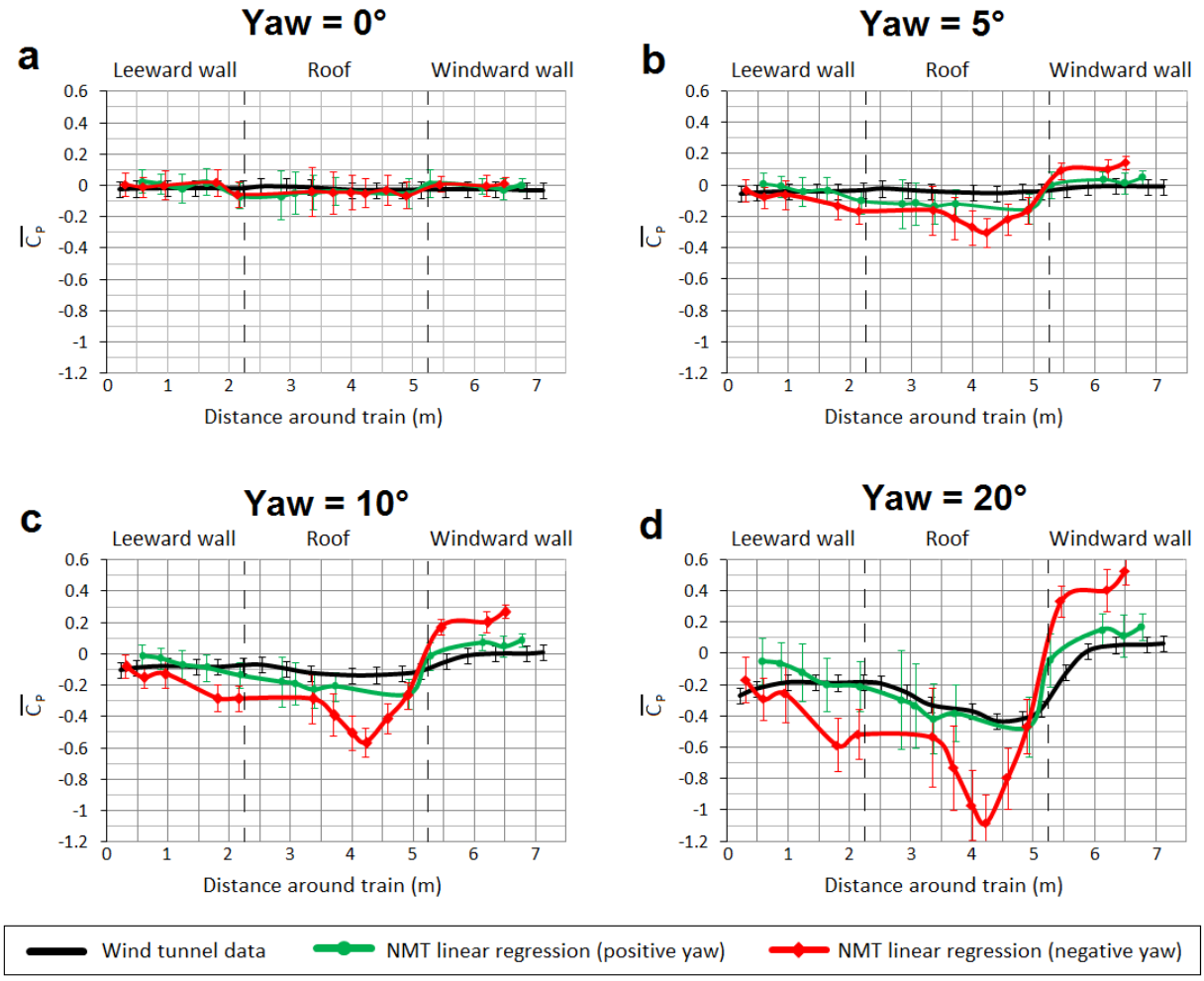

Figure 11.3.1 - Distribution of $\overline{C_P}$ around loop between wind tunnel and NMT data obtained by linear regression for positive and negative yaw angles, based on θ.

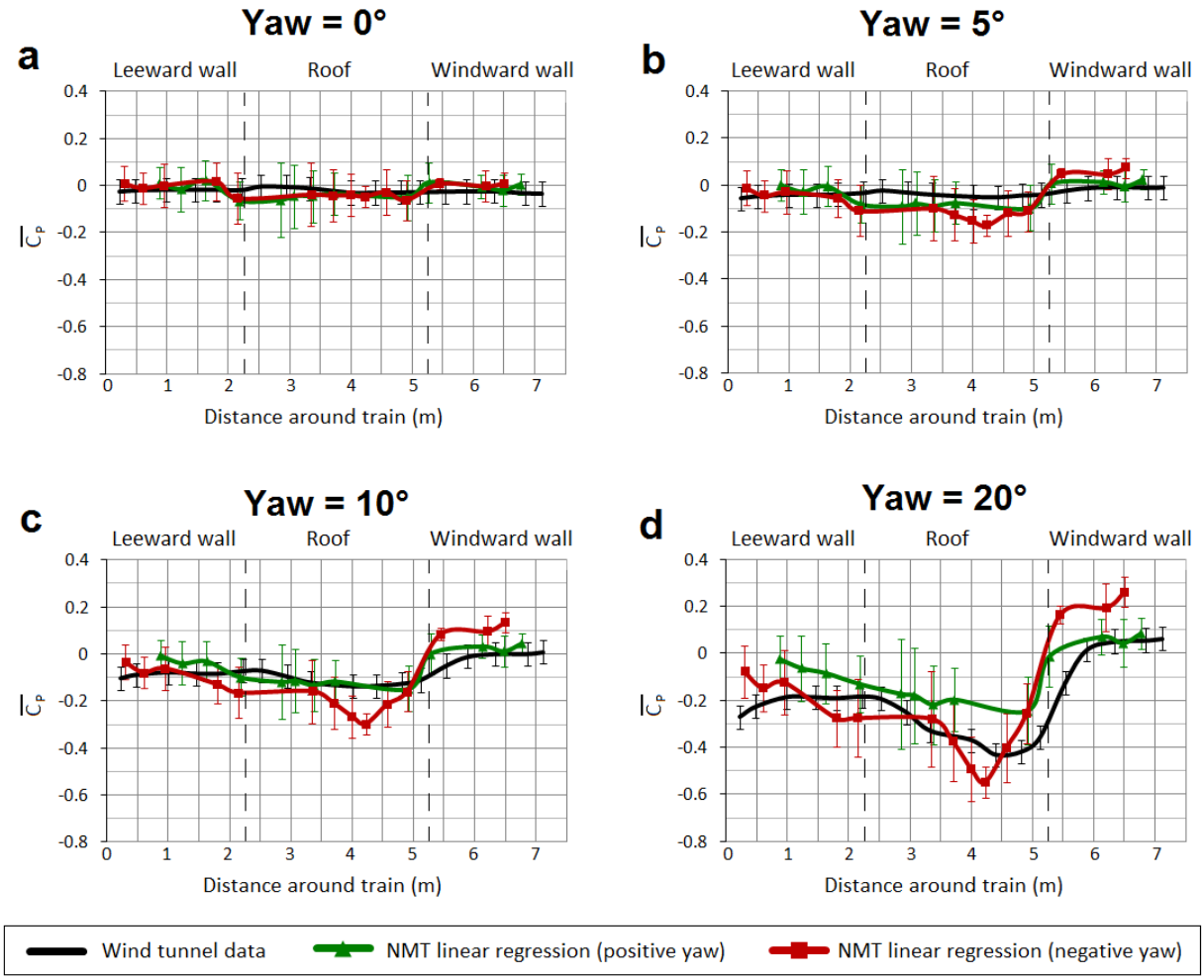

Figure 11.3.2 - Distribution of $\overline{C_P}$ around loop between wind tunnel and NMT data obtained by linear regression for positive and negative yaw angles, based on φ.

The differences between values of $\overline{C_P}$ calculated at positive and negative yaw angles are quite pronounced for both θ and φ, with negative yaw angles showing higher magnitudes of pressures around the loop. Relating this finding to the slight skew shown in figure 11.1, it could be suggested that there is an offset issue with one of the nose pressure taps despite the data having been "zeroed" following a stringent procedure (section 10.2.3.1). No clear "offset" issues were found, but it may be possible that the pressure transducers show different linear responses, however there is no calibration data for the NMT system to address this further. Generally, the pressures obtained from linear regression are close to the wind tunnel pressures and are mostly within experimental error. The full scale data based on φ appears to be slightly more favourable overall, though very good comparison is seen on figure 11.3.1 (d) with positive yaw (shown in green), though this may simply be fortuitous.

11.3.2 Yaw angle bins results

Figures 11.4.1 and 11.4.2 show the mean pressure coefficients obtained from the yaw angle bins methodology in the same format as figures 11.3.1 and 11.3.2, i.e., positive and negative yaw angles are shown and compared with the wind tunnel data. Figure 11.4.1 shows the data based on yaw angle calculated from the wind tunnel coefficients at yaw angles of magnitude 0° to 10°. There is very good agreement (within experimental error) between the positive and negative yaw angle data, unlike the regression analysis results in section 11.3.1, which could suggest that the discrepancy between positive and negative yaw angles obtained from the regression models is related to flaws in the use of a linear best fit model. It is, however, very conspicuous that the full-scale data is significantly different to the wind tunnel data at 10°. The full scale data shows much higher positive and negative pressure coefficients around the

loop, though the qualitative pressure distribution generally matches that found in the wind tunnel, albeit at a much higher yaw angle. Figure 11.5 shows the pressure distribution from the wind tunnel data for comparison - the full scale yaw bin data at 10° yaw shown in figure 11.4.1 (c) is of closest magnitude to the wind tunnel data at about 30° to 40°. If the data based on the CWG yaw calculation coefficients is considered in figure 11.4.2, the same conclusions can be reached - there is good agreement in pressure distribution between positive and negative yaw angles and the full scale data shows larger magnitudes of pressure coefficients than the wind tunnel data. The main difference between figures 11.4.1 and 11.4.2 is that the CWG yaw calculation results in higher yaw angles than the wind tunnel data (given the same pressures at the NMT nose). The fact that both figures 11.4.1 and 11.4.2 show higher magnitudes of pressures at a given yaw angle than the wind tunnel could suggest that in both cases the yaw angle was underestimated, though it should be noted that at 10° (figure 11.4.2c) the full scale and wind tunnel data compares very well and is with experimental uncertainty, unlike figure 11.4.1 (c) where very large suction pressures can be seen, again suggesting that θ is much lower than the true yaw angle.

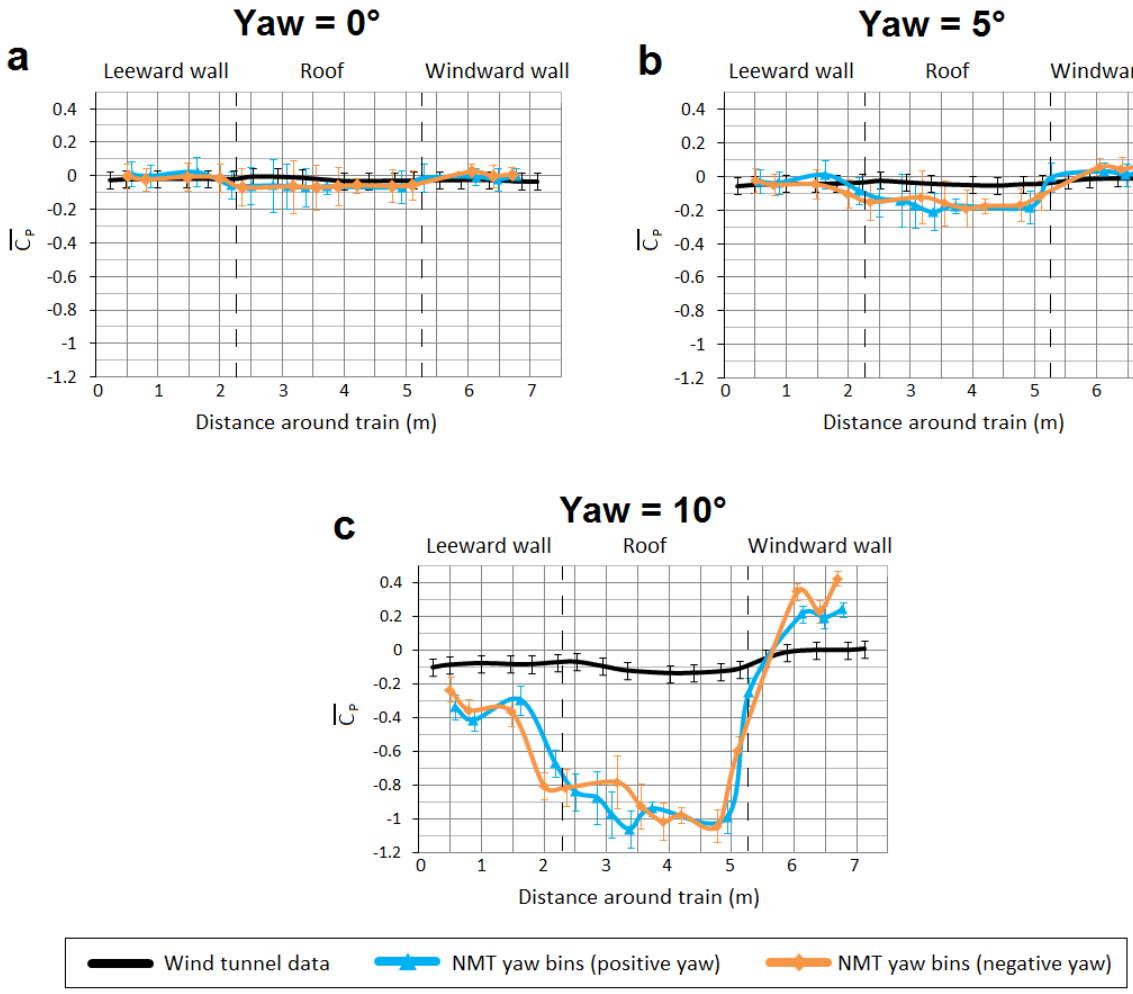

Figure 11.4.1 - Distribution of $\overline{C_P}$ around loop between wind tunnel and NMT data obtained from yaw angle bins for positive and negative yaw angles, based on θ.

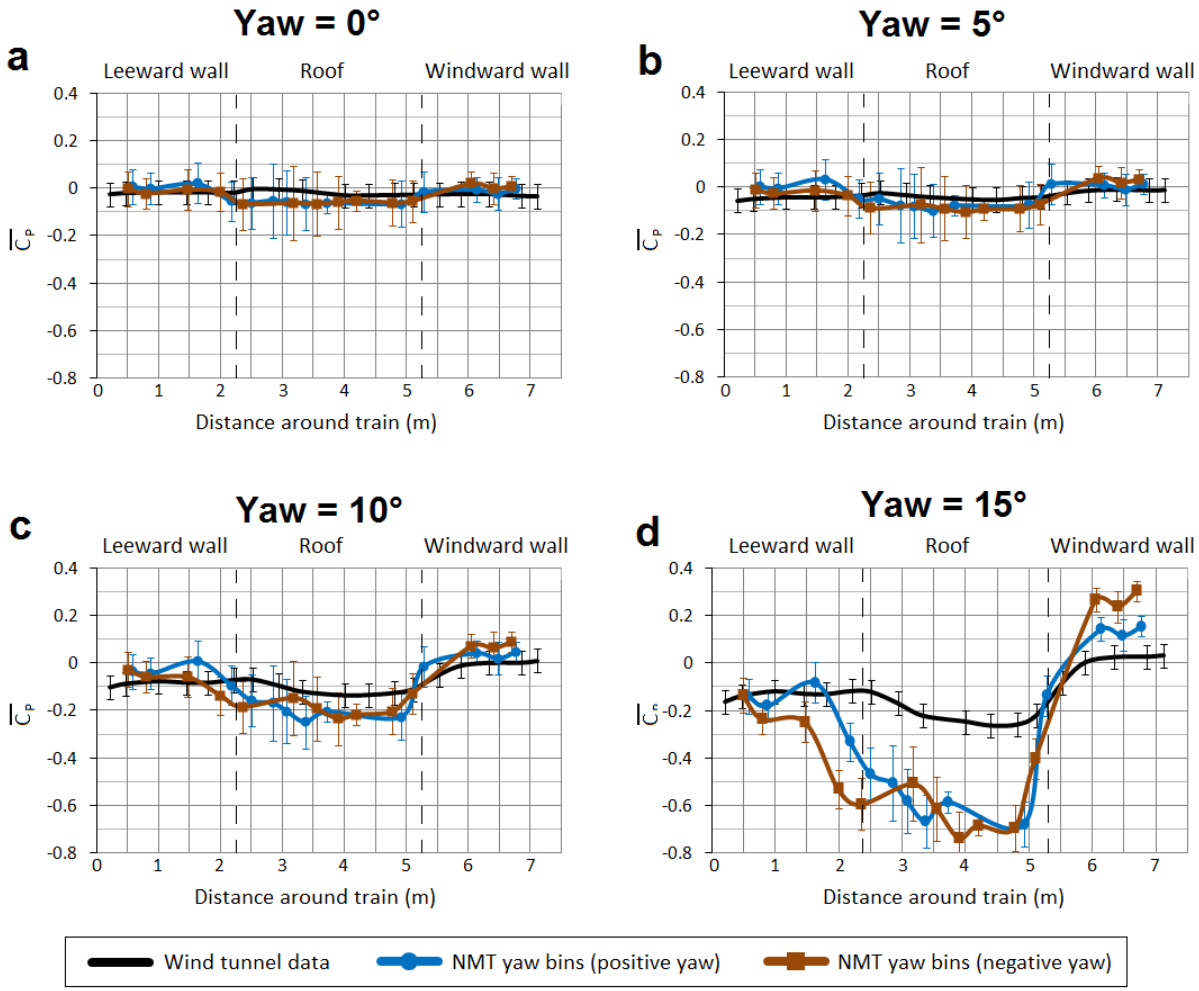

Figure 11.4.2 - Distribution of $\overline{C_P}$ around loop between wind tunnel and NMT data obtained from yaw angle bins for positive and negative yaw angles, based on φ.

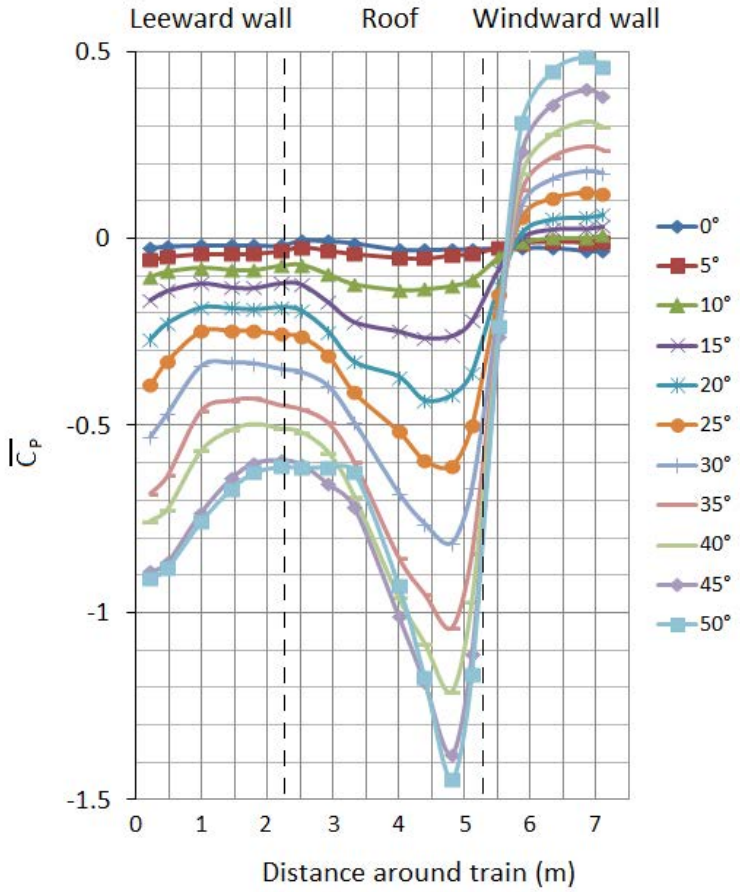

Figure 11.5 - Wind tunnel $\overline{C_P}$ around NMT loop position (from 13.2 m/s test) at yaw angles of 0° to 50°.

11.4 Gust results

The bin data presented in section 11.3 indicated that the yaw angle calculation based on the wind tunnel data significantly underestimated yaw angle at full scale, and hence the gusts analysis focuses on the data that had been processed using yaw angle based on the CWG coefficients.

Examples of six different gusts are shown in figure 11.6.1, which shows the yaw angle and the pressures from taps B1 and B16 (relative to whether or not the tap was on the windward or leeward side - all gusts in figure 11.6.1 were considered positive). The values of C_Y^*, C_Z^* and $C_{M_{X,lee}}^*$ are shown for the same six gusts in figures 11.6.2 to 11.6.4.

When the yaw time history of the gusts is considered, gust (a) shows a profile closest to the "generic gust" shown in figure 10.5 and has a duration of about 4 - 5 s. The windward side tap shows an increase in pressure that correlates very closely with yaw angle, and the leeward side tap shows a corresponding (albeit slightly "rougher") negative pressure, possibly indicating turbulence of a delta wing vortex. Gust (b) shows two yaw angle peaks of roughly the same magnitude and duration (~4 s), and the windward pressure correlates very well with yaw angle, though the leeward pressure does not show any notable effect. Gust (c) shows a crosswind of long duration and relatively high magnitude, and there are three distinct yaw angle peaks which correlate well with the windward pressure tap. The leeward pressure tap shows a reflection of the windward pressure, though the leeward suction pressure is of lower magnitude. It is interesting to note that the yaw angle is consistently at 10° between the pressure peaks, but the windward pressure coefficient is about 0.05 and the leeward pressure coefficient is close to zero. Gust (d) shows a smaller magnitude gust followed by a larger

magnitude gust and gust (e) shows a gust with a long build up time. Gust (f) shows a gust where the windward tap appears insensitive to yaw angle, however figures 11.6.2 and 11.6.4 show that the C_Y^* and $C_{M_{X,lee}}^*$ are well defined and correlate with yaw angle. For all gusts shown, C_Y^* correlates well with respect to yaw angle in the same way as windward wall pressure. For example, the value of C_Y^* increases sharply in line with the sharp increase in yaw angle in 11.6.2 (b), but shows a more gradual and almost exponential profile in 11.6.2 (e). The smaller peak in gust (d) at 2 s does not result in a large increase in C_Y^* and has no apparent effect on $C_{M_{X,lee}}^*$. It is again interesting to consider gust (c); in figure 11.6.2 (c) between the clear peaks in C_Y^* the vales of C_Y^* are zero/slightly negative despite the yaw angle of 10°. The peaks of C_Z^* shown in figure 11.6.3 closely match the peaks of yaw angle and C_Y^*. However, it is believed that the values of suction pressures over the roof are larger than would be expected due to the engine exhaust and cooling fans (see figure 1.2 and section J.5.3). The values of C_Z^* may in some cases be overestimates of the actual uplift force (assuming that the downwards force generated by the fans offsets the increase in lift). For example, in the wind tunnel test at 45° yaw angle (i.e., the maximum yaw angle tested) the value of $\overline{C_Z}$ calculated for the entire power car was about 0.6 (using the same reference area of 60 m^2 as was used to obtain C_Z^* for the full scale loop). Figure 11.6.3 shows values of C_Z^* greater than 1.0 at yaw angles of about 15°. In fact the values of C_Z^* appear to vary greatly with respect to yaw angle by considering the gusts shown in figure 11.6.3. The values of $C_{M_{X,lee}}^*$ shown in figure 11.6.4 must therefore be interpreted with care, given the large differences in C_Z^*. At present, it is promising to see that for all gusts the values of $C_{M_{X,lee}}^*$ clearly correlate with yaw angle when gusts are considered.

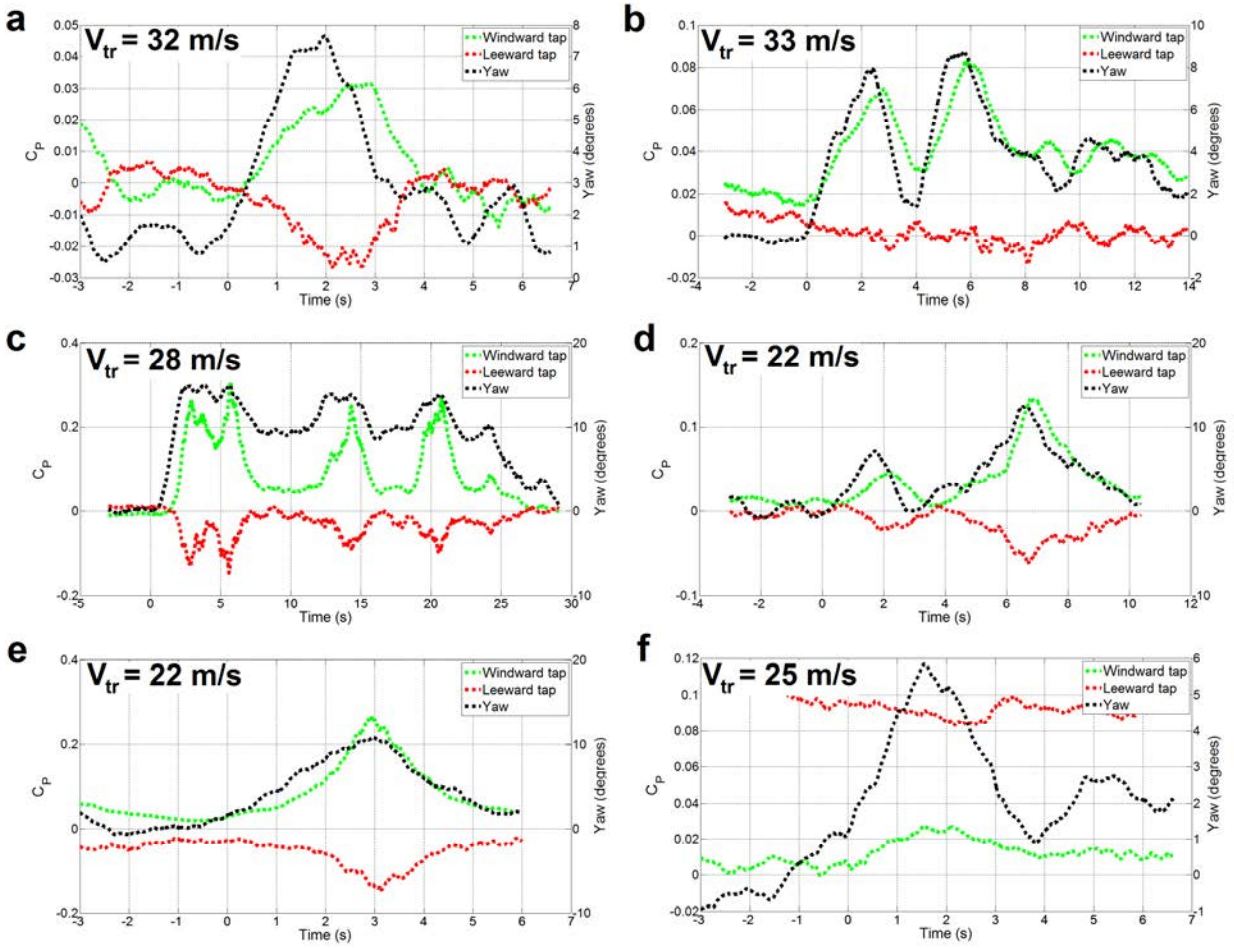

Figure 11.6.1 - Examples of gusts at full scale and corresponding pressures coefficients from opposite tapping points (B1 and B16) (black - yaw, green - windward tap, red - leeward tap).

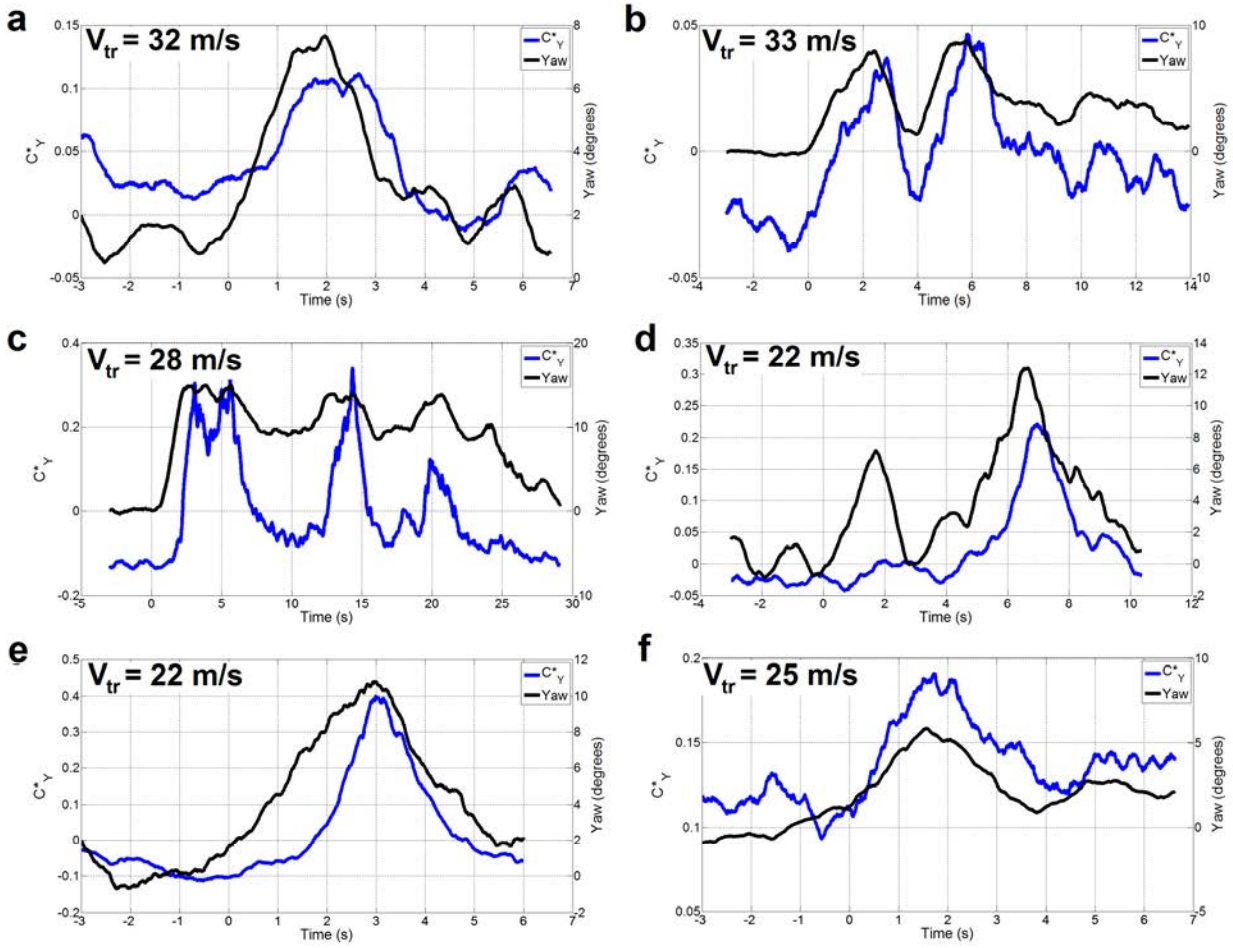

Figure 11.6.2 - Examples of gusts showing yaw (black) and corresponding values of C_Y^* (blue).

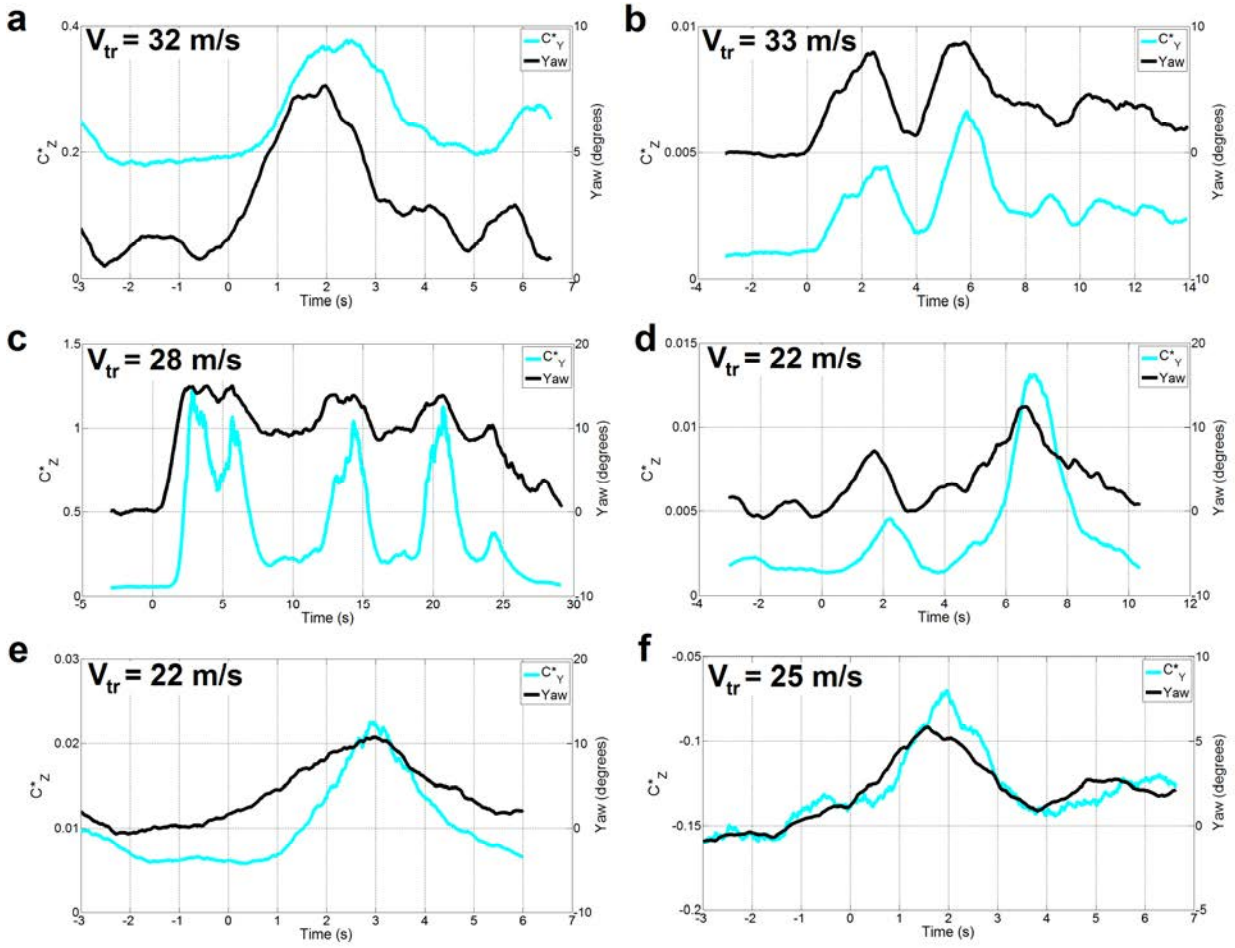

Figure 11.6.3 - Examples of gusts showing yaw (black) and corresponding values of C_Z^* (cyan).

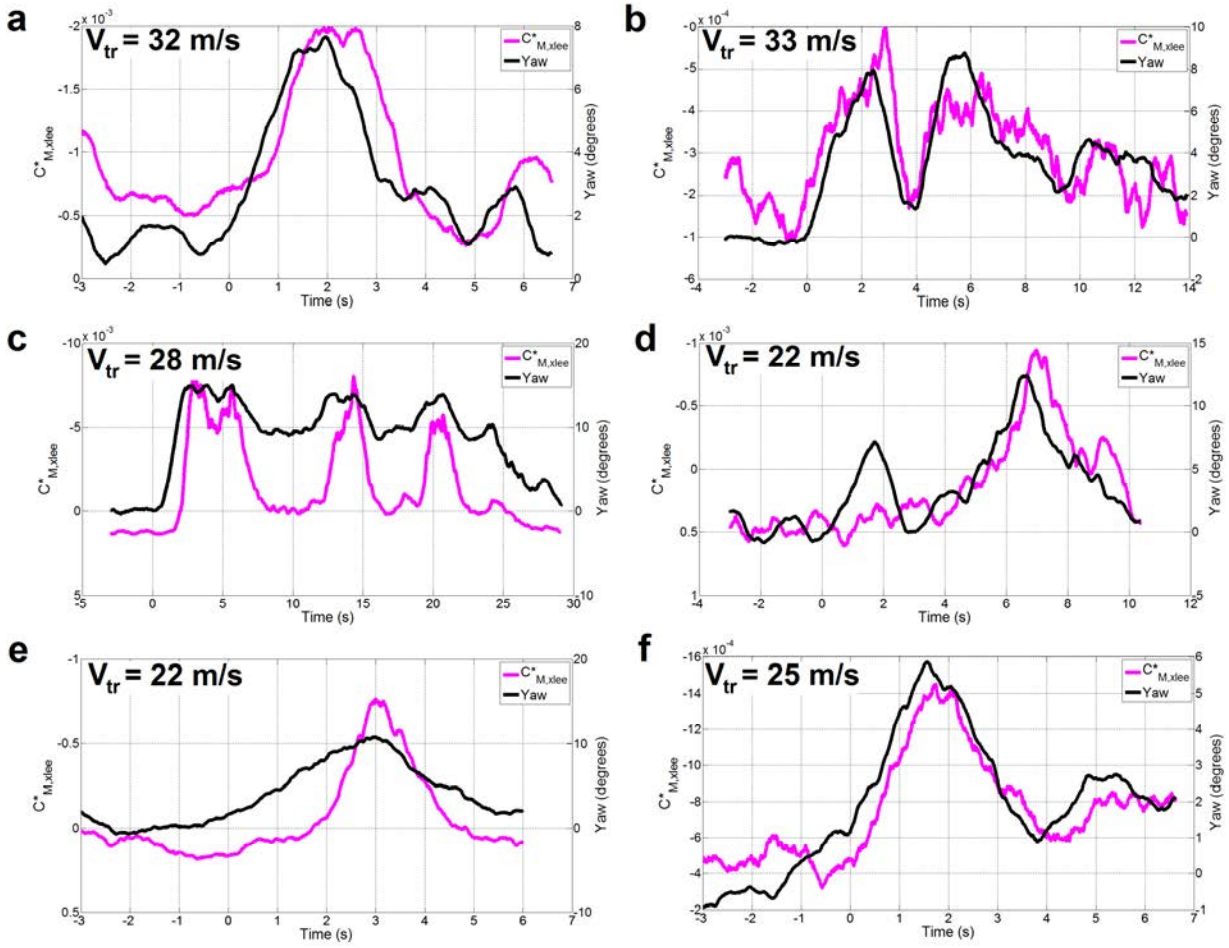

Figure 11.6.4 - Examples of gusts at full scale, yaw (black) and corresponding values of $C^*_{M_{X,lee}}$ (magenta). The y-axis direction is reversed on the LHS (i.e., $C^*_{M_{X,lee}}$ is negative).

The peak values of C_η^* for all gusts considered are shown in figure 11.7.1 and 11.7.2 against the yaw angle at which the peaks were measured (θ and φ respectively).

While it must be stressed that the ensembles of "gusts" cannot be considered exhaustive, the results do suggest that the qualitative variation of peak forces and moments with respect to yaw is sensible. As seen previously, the different values of yaw (θ and φ) result in significantly different trends in the linear best fit (see appendix K), i.e., a change in the gradient by a factor of about 2 since $\theta(t)$ is twice the value of $\varphi(t)$.

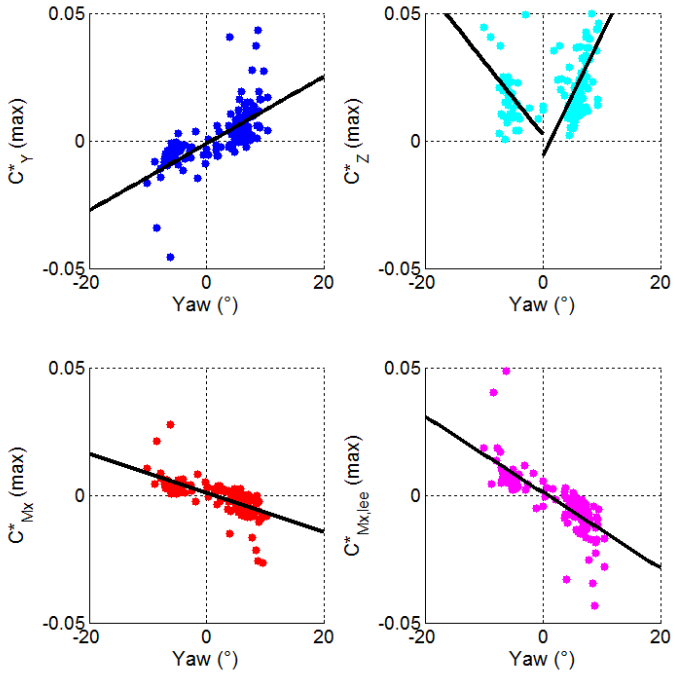

Figure 11.7.1 - Peak values of C_η^* against θ for gusts and linear best fit approximations.

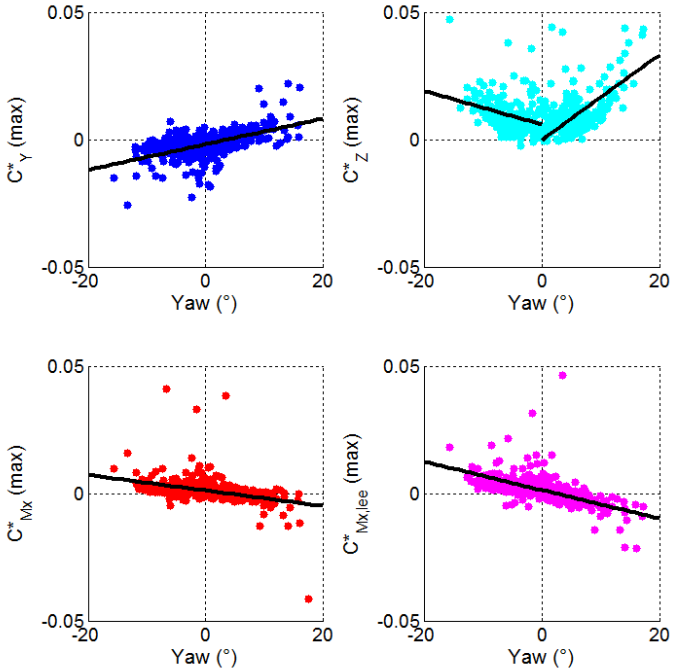

Figure 11.7.2 - Peak values of C_{η}^{*} against φ for gusts and linear best fit approximations.

11.5 Force and moment coefficients

Values of force and moment coefficient per unit length were obtained based on the mean pressure distributions shown in section 11.3. Figure 11.8.1 shows $\overline{C_\eta^*}$ obtained from the regression analysis (i.e., from the data in figures 11.3.1 and 11.3.2), and figure 11.8.2 shows $\overline{C_\eta^*}$ obtained from the yaw bins methodology. In both cases, $\overline{C_\eta^*}$ was calculated for positive and negative yaw independently and is shown for both θ and φ, and the wind tunnel data (based on pressures shown in figure 11.5) is shown for comparison.

Both figures 11.8.1 and 11.8.2 show the same trends as the pressure distributions shown in section 11.3. The linear regression pressure data (figure 11.8.1) shows magnitudes of $\overline{C_\eta^*}$ that are closest to the wind tunnel data, however the yaw bin data shows a close relationship with the wind tunnel data up to about 10°, after which there is a large increase in the magnitude of $\overline{C_\eta^*}$. This is most pronounced in the lift force on figure 11.8.2 when considering θ - the pressure distribution at 10° shown in figure 11.4.1 (c) showed a greatly larger negative pressure over the roof, and consequently there is an equally large lift force compared to the wind tunnel data. The "best" results on figure 11.8.2 appear to be taken from the pressure distributions based on φ for the yaw bins methodology at lower yaw angles. The same conclusion could be made for the force coefficients shown in figure 11.8.1 based on the regression models.

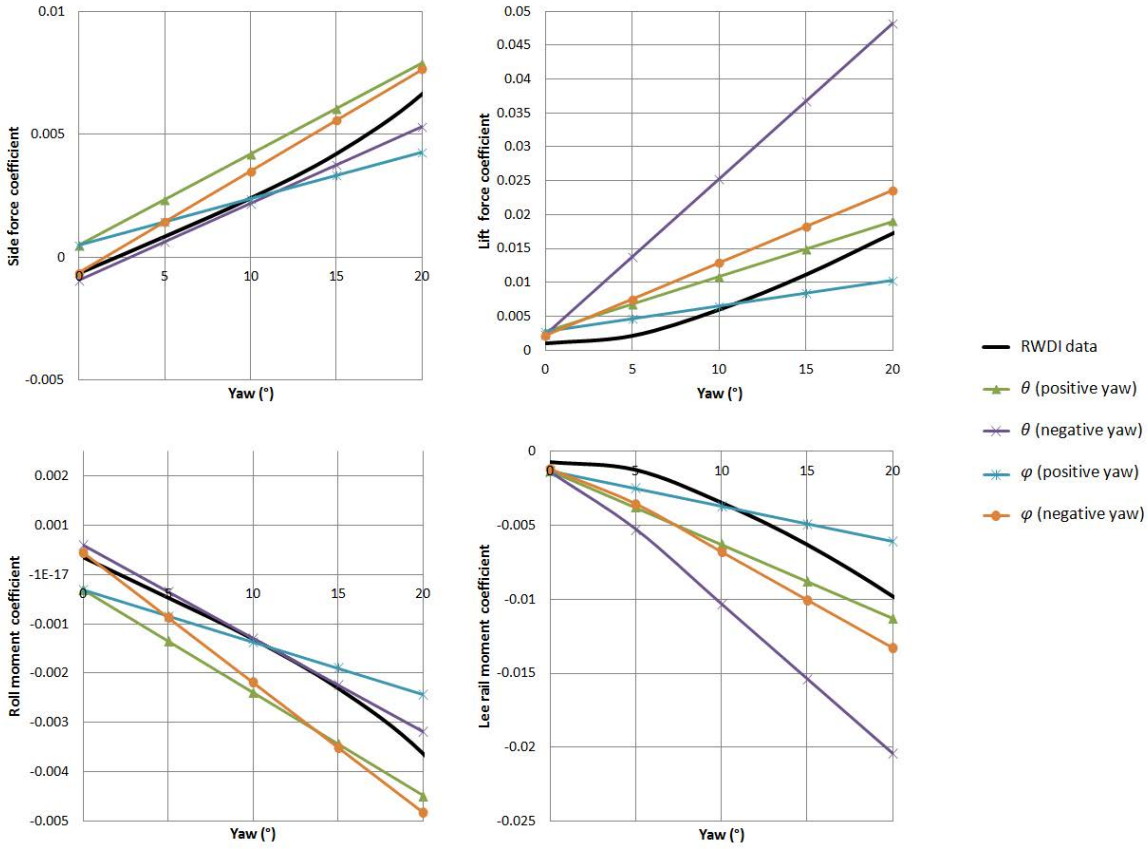

Figure 11.8.1 - Comparison of $\overline{C_{\eta}^{*}}$ based on "scatter plot linear regression" pressure data for both θ and φ from 0° to 20° yaw angle.

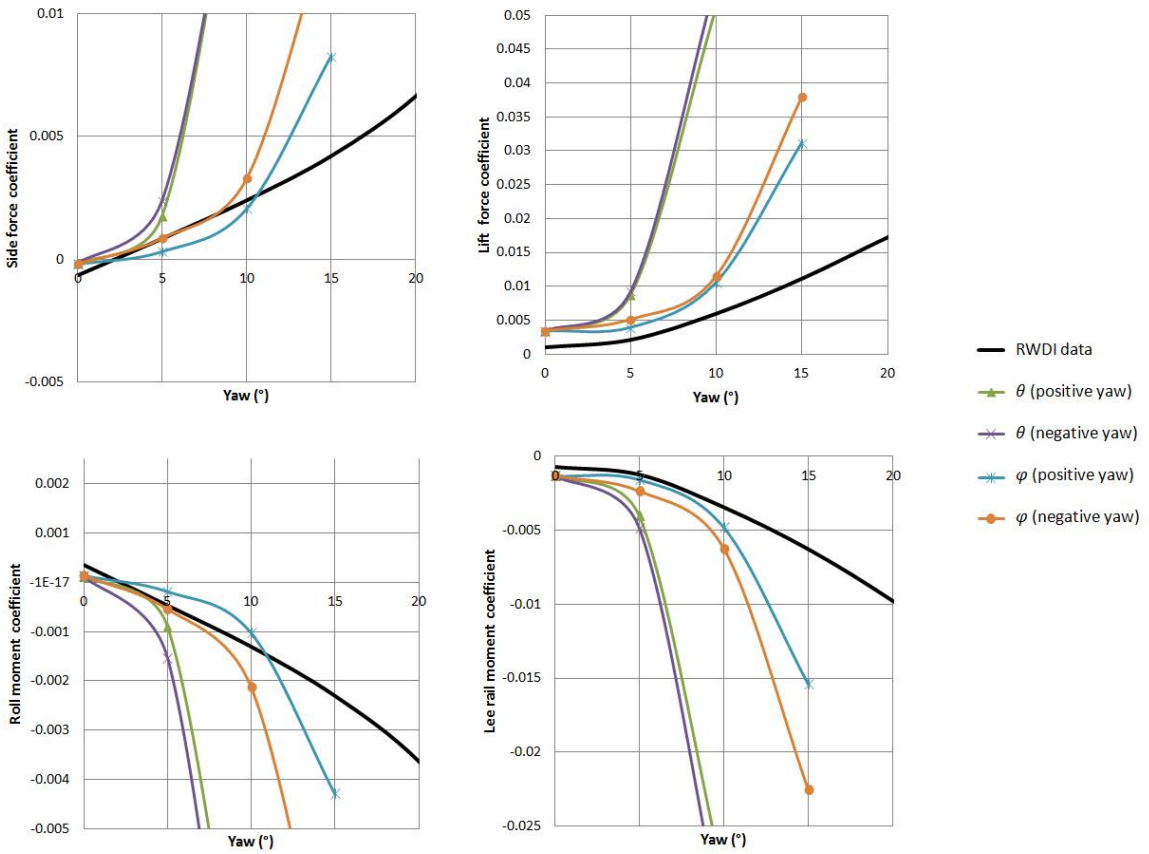

Figure 11.8.2 - Comparison of $\overline{C_{\eta}^{*}}$ based on "yaw bin" pressure data for both θ and φ from 0° to 20° yaw angle.

11.6 Closing remarks

Two methodologies were applied to the NMT data set in order to obtain mean pressure coefficients across a range of yaw angles in operational conditions. The yaw angle was calculated based on coefficients obtained from scale model tests based on the pressures at the nose of the train. The main point to make from the analysis in this chapter is that the different methodologies and calculations of yaw angle all resulted in very different results.

Considering both the pressure distributions and the resulting force coefficients in sections 11.3 and 11.6 respectively, it appears that generally speaking, φ is the more realistic approximation of the true yaw angle (on the assumption that the pressures and forces from the wind tunnel should be representative of pressure distributions at full scale). Considering the model-scale test results (figure 8.13), the magnitudes of pressures at the train nose were significantly different between the wind tunnel and moving model tests. The moving model results showed pressures at the nose taps that were significantly higher than those from the wind tunnel and the differences were outside of experimental error. The yaw angles calculated from the TRAIN rig data were approximately twice as great as from the wind tunnel yaw coefficients. It was posited that this may be in part due to differences in the underbody geometry (given the effects on the HST slipstream) and also the HST nose profile and differences in ground simulation. Another possibility is that there was in fact a boundary layer along the STBR/splitter plate in the wind tunnel. Given the low height of the nose taps, even a slight boundary layer could significantly reduce the air velocity at this location, which would decrease the magnitude of the pressure coefficients. The moving model tests would have had a uniform block velocity profile in the train direction and therefore there would not be boundary layer effects, and of course this situation represents the reality of the moving train at full scale.

A slightly concerning finding is that when the regression models were considered, the positive and negative yaw angles showed different pressure distributions. This could suggest that there is an offset issue with one of the nose pressure taps, effectively resulting in an asymmetry in the calculation of yaw angle. The yaw bin data, however, does not show any clear signs of a yaw asymmetry as the pressure distributions are within experimental uncertainty.

Analysis of gusts showed that the fluctuations in yaw angle of a time period greater than 1 s, which reflect fluctuations in the onset wind, correlated very well to fluctuations in aerodynamic forces.

In closing, the following recommendations are made to improve analysis of this large full scale data set:

- A detailed calibration of all equipment should be undertaken.
- It may be possible to develop a "correction" to yaw angle, though at present more benchmark data is required.
- Two wind tunnel tests on the HST model should be undertaken - a uniform flow and boundary layer flow test. This will help to ascertain whether there were boundary layer effects in the RWDI tests. This test could be performed at the TRAIN rig, following the methodology of Dorigatti, (2013) and undertaking a static model test in the CWG to compare to the results in chapter 8.
- Analysis of gusts has shown that the yaw angle, while not necessarily accurate, does correlate very well with surface pressures and forces. If a larger ensemble of gusts were created, and the yaw angles bin methodology undertaken on this larger ensemble, taking φ as the yaw, it is expected that this methodology would yield the most accurate results.
- An algorithm should be developed to identify segments of data where the engine cooling fans are switched on and hence remove this interference from the data.

CHAPTER 12

CONCLUSION

12.1 Introduction

The main aim of this project was to compare the aerodynamics of an HST at model scale and at full scale. This aim was achieved through undertaking a number of model-scale investigations in order to compare with full-scale data, particularly with respect to crosswind tests. Section 12.2 considers how each research objective set out at the start of this study has been fulfilled, and similarly section L.2.3.1 considers the specific objectives of the EPSRC project.

12.2 Conclusions related to each research objective

Objective 1: To undertake a thorough literature review on the aerodynamic phenomena of passenger trains, with a particular focus on slipstreams and crosswinds, in order to conduct an experimental studies that address gaps in the current state of knowledge.

A literature review presented in chapter 2 outlined the basic definitions by which aerodynamic phenomena are analysed and described, and collected together the findings from various experimental studies at both full scale and model scale on the measurement of train slipstreams and the effects of natural winds on a train.

- Current legislation (TSI) sets testing procedures at full-scale and maximum permissible slipstream velocities, however, the TSI may not be suited to the UK which has different infrastructure to most of mainland Europe. It was found from a previous study that ballast height may affect flow development around a train, but there is a range of ballast heights permitted by the TSI for test site criteria. The assessment of slipstreams can also be carried out by model scale tests or by CFD (which requires validation), and procedures are outlined in CEN.
- Full-scale and model-scale measurements of typical passenger slipstreams show three distinct flow regions. The nose region is characterised by a relatively low magnitude velocity peak (dominated by the lateral V component) and a sinusoidal pulse in static air pressure - both of these increase in magnitude with the "bluntness" of the train nose. The boundary layer along the main length of the train is three dimensional and turbulent, though generally does not have velocities of high enough magnitude to be a safety concern. Differences in roughness (such as underbody shielding) and scale (Re number) can affect the boundary layer development. The near wake region usually

shows the largest velocity peaks as a result of the large flow structures which can have both a velocity and time scale large enough to pose a risk (and is therefore of most concern to engineers). These flow structures decay in the far wake, and this decay fits an exponential profile - this knowledge could be useful for validation of CFD models.

- Comparisons between full scale and model scale measurements have in some cases shown good agreement, however, the data set is limited in that there are few studies that have measured the same train type at both scales.
- Natural winds within the ABL are turbulent and vary significantly with topography, meteorological conditions and infrastructure. Low turbulence wind tunnel tests do not represent reality in this respect, but are the prescribed method for obtaining force and moment coefficients needed to obtain CWCs, and previous studies have shown that slight changes in wind tunnel set up and modelling geometry can have a significant effect on these coefficients. Given that scale-model wind tunnel tests can give different results (namely values of the critical parameter $C_{M_{X,lee}}$ used to obtain the CWC), both to each other and to reality, there are potentially safety implications for how the results of low turbulence wind tunnel tests should be applied to the real world, as in reality natural winds can be considerably different.

Objective 2: To develop a methodology for measurement of slipstream velocities and static pressure transients at model scale that is compliant with existing codes of practise and develops a further understanding of the TRAIN rig.

The experimental and analytical test procedures were described in chapters 3 and 4, and a CEN compliant investigation of the slipstream of an HST was undertaken at the TRAIN rig facility.

- A 1:25th scale 4 car HST model designed specifically for use at the TRAIN rig was commissioned by the UoB specifically for this project. The model construction also allowed an integrated data logger system to be housed inside of the model in line with previous studies (Dorigatti, 2013; Soper 2014).
- Typically, 20 - 40 runs can be undertaken in a single day and the variation in train speed between runs that are set up with the same tensile force in the firing system is usually less than 3%, therefore the TRAIN rig can efficiently meet the requirements of CEN.
- Preliminary studies were undertaken (see appendix B) to investigate the effects of train speed, ensemble size and underbody geometry on the train slipstream. A train speed of 40 m/s and ensemble size of 20 runs were consequently selected and these met the requirements of CEN part 4, (2008).

Objective 3: To perform a number of slipstream measurements at model-scale in order to investigate how the slipstream velocity and static pressure transients of an HST are affected with respect to different fixed trackside measurement positions (both lateral and vertical), and also with ballast height, and to use these results to aid in the design of full-scale measurements.

A series of tests were undertaken with a 1:25th scale HST. The testing procedure and measurement positions of slipstream tests at the TRAIN rig are specified in chapter 3, and the analytical procedure is presented in chapter 4. The key results are presented in chapter 5, and more detailed results are presented in appendices B and C. A limited quantity of full-scale results are presented in appendix D.

- A detailed set of measurements were undertaken in open air to measure the slipstream of an HST with a ballast height of 0.3 m, at various positions from the centre of track and from the top of rail.
- The HST showed a slipstream that was similar to most conventional high speed trains, though the magnitudes of normalised velocity were higher than more contemporary trains (such as the ICE2) which have more streamlined nose/tail profiles and underbody shielding.
- A large velocity peak was observed after the nose peak at measurement positions closer to the ground and train sides, though this velocity peak was not found when the HST was fired in reverse. It is therefore concluded that this velocity peak is related to the unrealistic underbody geometry (i.e., the firing chassis) beneath the leading power car, therefore this velocity peak can be treated as artificial.

- Increasing the y-axis distance from the COT resulted in a significant decrease in the slipstream velocity at model scale at all z-axis measurement positions (above TOR), though given the issues with scale on the boundary layer development, results at distances greater than ~3 m from COT should be treated with caution. This shows that risk from slipstreams can be effectively mitigated by increasing the distances that people/light equipment are from the train sides (safety lines for example).
- Increasing the z-axis position above TOR allowed the effects from the underbody roughness to be considered - there was a thicker and more turbulent boundary layer closer to the unshielded underbody region (at heights of up to about 1.2 m above TOR) than the smaller and less turbulent boundary layer region over the smoother side walls.
- A TSI gust analysis found that when a 1 s moving average filter was applied to the data (as prescribed in the TSI) that the HST did not break safety limit values, however when a 0.3 s moving average filter was applied (in line with the findings of Jordan et al., 2008) the HST broke safety limit values at both the trackside and platform measurement positions (note that the TSI platform measurement position is 1.4 m above TOR, but data from 1.2 m above TOR was considered to be equivalent).
- The results from the detailed slipstream tests on the HST with a typical UK ballast height (0.3 m) enabled the fixed trackside measurement positions at full scale to be assessed and justified - however the full-scale tests did not take place, but are described briefly in appendix D.
- Increasing the ballast height resulted in a decrease in the HST slipstream velocity at measurement positions close to the ground ($z < 1.2$ m above TOR) within the boundary layer and far wake regions. A thicker boundary layer (i.e., larger

displacement thickness) was observed for a 0.3 m ballast height than a 1.5 m ballast height at 0.2 m above TOR. No clear differences were observed in the near wake velocities of the HST regardless of ballast height (and the near wake usually has the highest slipstream velocities so is of most concern during train design/certification). TSI gust analysis was undertaken at positions of 3 m from COT and 0.2 m and 1.2 m above TOR, and generally there was a slight decrease in $U_{2\sigma}$ as ballast height increased, however this slight decrease is within experimental uncertainty.

- The ICE2 slipstream showed clear differences in the near wake as a result of changing ballast height at 3 m from COT and 0.2 m above TOR, though only a limited number of measurement positions were tested with the ICE2.
- Ballast height had no effect on static pressure, and this is true for all of the measurement positions and for trains tested.

Objective 4: To analyse wind tunnel results on the surface pressures on an HST power car to investigate the general flow field and how it results in overturning forces/moments, and also to aid in the design of pressure tap locations at full scale.

RWDI were retained by the UoB to undertake a wind tunnel test on an HST power car and these results were presented in chapter 8.

- Only steady aerodynamic effects were considered due to the nature of the wind tunnel test (low turbulence and uniform flow, as required by CEN). At yaw, the lee-rail overturning moment arises as a result of a positive pressure on the windward side wall and a negative pressure on the leeward side wall which result in a side force, and a negative pressure across the roof which results in a lift force.

- Lee-rail moment per unit length (i.e., from a single loop of tappings) was highest close to the train nose and then decreased along the main length of the train - the lee-rail moment coefficients appeared to stabilise towards the rear of the power car, suggesting that this is an appropriate location for the loop of taps at full-scale.
- When the underbody pressures were integrated from loops either side of the rearward bogie, the integrated lift force and hence moment in the underbody region was effectively zero, indicating that the position of the loop of pressure taps on the NMT was satisfactory and that underbody pressures could be disregarded at this location.
- The differential of pressure coefficients at symmetrical pairs of pressure taps at the nose region showed an almost linear relationship with respect to increasing yaw angle, which enabled the identification of suitable pressure tap locations on the full scale tests on the NMT in order to calculate yaw angle within the yaw angle range of about $-20° \leq \theta \leq 20°$.

Objective 5: To develop a methodology to measure the surface pressures on a model scale train using a moving model and crosswind generator in order to compare this data with wind tunnel data across a range of yaw angles, and therefore consider effects of vehicle ground motion and Re number on the surface pressures.

Tests were conducted at the TRAIN rig and the HST power car was fitted with pressure taps at the nose and a around a loop towards the rear of the power car at the same positions as on the NMT. An integrated onboard data logger, developed by Dorigatti, (2013), was housed inside the HST model and recorded pressure data and light sensor

data. The light sensor and sources (which were at fixed positions inside the CWG) enabled train position to be marked on the pressure data time series. Chapter 6 describes the experimental set up.

- A range of yaw angles could be tested by changing the investigative train speed, assuming that the CWG flow was "constant" and approximately 12 m/s. The effect of changing the speed of the CWG fans was not investigated due to the need to undertake a flow characterisation for each fan speed, which was not feasible within the time constraints of this study.
- As a result of the span wise variation in crosswind velocities and linear train speed deceleration there was variation in the instantaneous yaw angle through the CWG. Data was therefore considered as independent samples and sorted into yaw angle bins, and this method gave reliable data, where the standard deviation of each bin was lower than the random uncertainty calculated following the method of Dorigatti, (2013). Despite the flow irregularity, this analytical procedure resulted in data that compared favourably with the wind tunnel data.
- There were differences in the underbody geometry between the static and moving tests - there was higher blockage beneath the TRAIN rig moving model than the RWDI wind tunnel model due to the larger wheel sets and firing chassis needed to propel the model along the tracks), and the TRAIN rig CWG had an unrealistic flat ground scenario (i.e., the ground was level with the TOR), whereas the RWDI wind tunnel test had a STBR configuration. There were also differences in the boundary layer of the flow - the wind tunnel was a uniform flow test whereas the CWG had a boundary layer.

- There was no noticeable difference in any of the force and moment coefficients per unit length despite the differences in experimental set up, since the pressure distributions around the loop of taps were very similar between the static and moving model tests.
- The pressure taps at the nose showed significantly larger pressures for the moving model tests and it is hypothesised that this may due to a combination of the HST nose profile and the higher underbody blockage at the nose. Alternatively, there may have been a floor boundary layer in the wind tunnel that resulted in a lower velocity close to the ground (and hence to the nose pressure taps). However, it was possible to accurately estimate yaw angle from the nose taps for the moving model test.

Objective 6: To develop an experimental and analytical methodology for novel train based measurements at full scale to investigate the effects of crosswinds on the surface pressures and hence overturning forces on an HST power car.

An HST power car used on the NMT was installed with an onboard pressure measurement system that recorded continuously during operation, resulting in a very large quantity of data. A hierarchical categorisation procedure and series of checks were used to isolate and format segments of useful data (see chapter 10 and appendix J).

- Open air data was isolated from each data file by aiming to identify and remove pressure transients - i.e., large fluctuations in pressure caused by passing trains and tunnels. The pressure transients have not been used in detail in this study, however the NMT system was validated against a previous test (see Quinn et al., 2016) and good

agreement was found. This database of pressure transients is potentially a very useful resource.

- A procedure was designed to identify and categorise pressure transients and gusts, which could form a useful database.
- Three pressure taps at the train nose were used to calculate yaw angle based on coefficients obtained from the wind tunnel and TRAIN rig CWG tests. The CWG tests showed a higher range of yaw angles, and it is believed that these coefficients resulted in a more realistic calculation of yaw angle based on the corresponding pressures around the loop and aerodynamic forces.
- Analysis of gusts showed that forces and moments correlated very well with respect to yaw angle in the time domain. A large ensemble of "gusts" may be a very useful and reliable data set.

Objective 7: To deliver a detailed set of experimental data at both full scale and model scale for use in CFD validation and for comparison with other experimental studies, and hence allow scrutiny of current design and testing methodologies and codes of practise.

This study has collected data from four detailed experiments - model scale slipstreams, wind tunnel and moving model experiments on surface pressures due to crosswinds and full scale train based measurements on the NMT. All of the experimental data has been made available as raw data and corresponding Matlab programs, allowing this author's analysis to be repeated. Processed data has been made available as part of this PhD thesis, in a journal paper (Soper et al., 2016) and several additional detailed papers will be

published as part of the academic outputs of the EPSRC project, and the work contained in this thesis will form a substantial portion of the published data.

12.3 Recommendations for future work

As a result of the findings of this study, the following recommendations for future work are suggested:

- The broad data set from these tests should be used as a reference database for CFD benchmarking - particularly as the wind tunnel data comprises two tests at different turbulence intensities and that the slipstream tests considered a large number of measurement positions with different ballast heights. The data is available in both "raw" and processed format along with the data processing algorithms developed on Matlab on the UoB file server.
- The underbody geometry at the TRAIN rig is significantly different to a real HST as a result of the metal firing chassis and wheel sets that are needed for mobility of the model on the track but are not to scale due to operational requirements of the TRAIN rig. The underbody was found to affect the slipstream in a brief preliminary test at the TSI trackside measurement position, and further tests across a range of measurement positions and train types to consider both forwards and reverse running would be useful in understanding how significant the differences in underbody are for different train types - the HST may be particularly sensitive due to its nose shape and unshielded underbody region. A detailed set of full scale slipstream measurements of the HST would be invaluable in distinguishing "real"

from "artificial" slipstream phenomena resulting from the train underbody, since the model scale and full scale data used to this effect in this study is limited to a single measurement position in each case, and detailed full scale data would also allow further scrutiny of the effects of model scale and allow validation of the tests described in chapters 3 to 5.

- Ideally, the CWG should be redesigned in order to increase the fetch and to allow simulation of ballast, embankments etc which has been shown to affect the magnitudes of force coefficients when tested in a wind tunnel. This would be invaluable with regards to developing CEN assessment of force and moment coefficients for moving model tests which are not yet covered in CEN since the findings of this study and Dorigatti, (2013), show that moving model crosswind tests are not only viable but also preferable to low turbulence wind tunnel tests.
- A static test in the CWG (following the methodology of Dorigatti, 2013) of the HST model would allow the differences between the moving model crosswind test and the RWDI wind tunnel test to be investigated further.
- The pressure transients from the circular tunnel at the TRAIN rig that were recorded during the crosswind tests, both relative to the train and to a fixed point on the tunnel, could aid in the development and validation of tunnel pressure transient simulation software.
- The gyroscopic sensor on the NMT has not been used in this study, however it may be possible to consider "gusts" (see section 11.4) with the rate of overturning from the gyroscopic sensor, and hence consider the effects of gust build up time discussed in Andersson et al., (2004), and the effects of infrastructure on the build up time from the GPS data. There could also be the possibility of correlating

onboard measurements with various trackside measurements. It could also be possible to observe the slipstream of the NMT and correlate this data to pressure data and reference wind speeds in order to investigate the effects of crosswinds on the slipstream.

- The pressure transient data from the NMT which was "discarded" in this study has many potential uses. It is the first time an experiment on this scale has been undertaken, and the availability of pressure transients from passing trains and tunnels across the entirety of the UK rail network is an invaluable resource. A database of tunnel pressure transients could be developed (using the GPS data) and allow revision of speed limits that may be in place due to aerodynamic reasons. Cases of passing trains within double track tunnels (i.e., potentially the worst case) could be examined. Assessment of loads due to passing trains could be greatly improved through the use of real data from the NMT, and the ability to isolate and also search through the data by GPS position could enable risk to be geographically considered. Finally, tunnel pressure transients could be used to remotely validate and calibrate the system - if the NMT were to travel through the same tunnel twice (and at similar speeds), a comparison between the two tunnel transients could allow the response of the pressure transducers to be compared within their working range, provided that the data was suitably normalised.

REFERENCES

ACIN, 2015. Betz Micromanometer User Guide. Available at http://www.acin.nl/documenten/betz_20140319141252_.pdf. Last accessed on 07/02/15

Andersson, E., Häggström, J., Sima, M., Stichel, S. 2004. Assessment of train overturning risk due to strong cross-winds. Proceedings of the Institution of Mechanical Engineers, Part F: Journal of Rail and Rapid Transit Volume 218 (3), 213–223.

ATSB. 2008. Rail Occurrence Investigation RO-2008-013. Technical report, ATSB Transport.

Baker, C.J. 1985. The determination of topograhical exposure factors for railway embankments. Journal of Wind Engineering and Industrial Aerodynamics, 21, 89-99.

Baker, C.J. 1991a. Ground vehicles in high cross winds part I: Steady aerodynamic forces. Journal of Fluids and Structures 5, 69-90.

Baker, C.J. 1991b. Ground vehicles in high cross winds Part II: Unsteady aerodynamic forces. Journal of Fluids and Structures, 5, 91-111.

Baker, C.J. 1991c. Ground vehicles in high cross winds part III: The interaction of aerodynamic forces and the vehicle system. Journal of Fluids and Structures 5, 221-241

Baker, C.J., Dalley, S.T., Johnson, T., Quinn, A., Wright, N.G., 2001. The slipstream and wake of a high-speed train. Proceedings of the Institution of Mechanical Engineers, Part F: Journal of Rail and Rapid Transport 215, 83-99.

Baker, C.J. 2001. Flow and dispersion in ground vehicle wakes. Journal of Fluids and Structures, 15(7), 1031-1060.

Baker, C.J., 2003. Some complex applications of the "wind loading chain". Journal of Wind Engineering and Industrial Aerodynamics, 91, 1791-1811.

Baker, C.J., Jones, J., Lopez-Calleja, F., Munday, J. 2004. Measurement of the cross wind forces on trains. Journal of Wind Engineering and Industrial Aerodynamics, 94, 547-563.

Baker, C.J., Bouferrouk, A., Perez, J., Iwnicki, D.S., 2008. The integration of cross wind forces into train dynamic calculations. World Congress on Rail Research, Seoul, S. Korea.

Baker, C.J., Sterling, M. 2009. Aerodynamic Forces on Multiple Unit Trains in Cross Winds. Journal of Fluids Engineering, 131.

Baker, C.J., Cheli, F., Orellano, A., Paradot, N., Proppe, C., Rocchi, D. 2009. Cross-wind effects on road and rail vehicles. Vehicle System Dynamics, 47:8, 983:1022.

Baker, C.J., 2010. The flow around high speed trains. Journal of Wind Engineering and Industrial Aerodynamics 98, 277-298.

Baker, C.J., Sterling, M., Quinn, A.D., Hemida, H., 2011. Standard Proposal - The measurement of train aerodynamic phenomena under operational conditions. University of Birmingham (submitted to EPSRC, ref: EP/I03842X/1), United Kingdom.

Baker, C. (2013). A framework for the consideration of the effects of crosswinds on trains. Journal of Wind Engineering and Industrial Aerodynamics Volume 123, 130–142.

Baker, C.J. 2014a. A review of train aerodynamics, Part 1 - Fundamentals. The Aeronautical Journal, 1201, 201-228.

Baker, C.J. 2014b. A review of train aerodynamics, Part 2 - Applications. The Aeronautical Journal, 1202, 345-382.

Baker, C.J., Quinn, A.D., Sima, M., Hoefener, L., Licciardello, R. 2014a. Full-scale measurement and analysis of train slipstreams and wakes. Part I: Ensemble averages. Proc. IMechE Part F: J. Rail and Rapid Transport, 228(5), 451-467.

Baker, C.J., Quinn, A.D., Sima, M., Hoefener, L., Licciardello, R. 2014b. Full-scale measurement and analysis of train slipstreams and wakes. Part II: Gust analysis. Proc. IMechE Part F: J. Rail and Rapid Transport, 228(5), 451-467.

Baker, C.J., Jordan, S., Gilbert, T., Quinn, A., Sterling, M., Johnson, T., Lane, J. 2014c. Transient aerodynamic pressures and forces on trackside and overhead structures due to

passing trains. Part 1: Model-scale experiments. Proceedings of the Institution of Mechanical Engineers, Part F: Journal of Rail and Rapid Transport, 228, 37-56.

Baker, C.J., Jordan, S., Gilbert, T., Quinn, A., Sterling, M., Johnson, T., Lane, J. 2014d. Transient aerodynamic pressures and forces on trackside and overhead structures due to passing trains. Part 2: Standards applications. Proceedings of the Institution of Mechanical Engineers, Part F: Journal of Rail and Rapid Transport, 228, 57-70.

Baker, C.J. 2015. Risk analysis of pedestrian and vehicle safety in windy environments. Journal of Wind Engineering and Industrial Aerodynamics, 147, 283-290.

Baker, C.J., Quinn, A.D., Hemida, H., Gallagher, M., Morden, J., Soper, D. 2016. The measurement of train aerodynamic parameters in operational conditions - trackside measurements. Aerovehicles 2 (conference), Göteborg, Sweden.

Banks, C. 1999. Boundary Layers: An Aerospace 503 Midterm. Available at: http://aerojockey.com/papers/bl/node2.html. Last accessed 14/03/13.

Barry, R.G., Chorley, R.J. 1968. Atmosphere, Weather & Climate (third edition, 1977 reprint). Methuen & Co, Ltd. London, UK.

Bell, J.R., Burton, D., Thompson, M.C., Herbst, A.H., Sheridan, J. 2014. Wind tunnel analysis of the slipstream and wake of a high-speed train. Journal of Wind Engineering and Industrial Aerodynamics, 134, 122-138.

Bell, J.R., Burton, D., Thompson, M.C., Herbst, A.H., Sheridan, J. 2015. Moving model analysis of the slipstream and wake of a high-speed train. Journal of Wind Engineering and Industrial Aerodynamics, 136, 127-137.

Bell, J.R., Burton, D., Thompson, M.C., Herbst, A.H., Sheridan, J. 2016a. Flow topography and unsteady features of the wake of a generic high-speed train. Journal of Fluids and Structures, 61, 168-183.

Bell, J.R., Burton, D., Thompson, M.C., Herbst, A.H., Sheridan, J. 2016b. Dynamics of trailing vortices in the wake of a generic high-speed train. Journal of Fluids and Structures, 65, 238-256.

Bell, J.R., Burton, D., Thompson, M.C., Herbst, A.H., Sheridan, J. 2016c. The effect of tail roof-angle on the unsteady wake structure and slipstream of high-speed trains. Aerovehicles 2 (conference), Göteborg, Sweden.

Blackadar, A. K. and Tennekes, H. 1968. Asymptotic similarity in neutral barotropic planetary boundary layers. Journal of Atmospheric Sciences Volume 25, 1015–1020.

British Broadcasting Corporation. 2007. BBC News: Strong wind topples Chinese train. Available at http://news.bbc.co.uk/1/hi/world/asia-pacific/6403959.stm. Last accessed 17/08/2016.

Brockie, N.J.W., Baker, C.J., 1990. The aerodynamic drag of high speed trains. Journal of Wind Engineering and Industrial Aerodynamics 34, 273-290.

Bouferrouk, A., Baker, C., Sterling, M., O'Neil, H., Wood., S. 2008. Calculation of the crosswind displacement of pantographs. BBAA VI International Colloquium on Bluff Bodies Aerodynamics and Applications. Milano, Italy.

Bowman, J. 2015. 'It was a tragic accident': Toddler killed when pram sucked onto tracks by high-speed train. The Mirror. Available at: http://www.mirror.co.uk/news/uk-news/it-tragic-accident-toddler-killed-5604996. Last accessed 20/08/16.

CEN. 2005. EN 14067-4 Railway applications - Aerodynamics Part 4: Requirements and test procedures for aerodynamics on open track. Technical report, CEN.

CEN. 2010. EN 14067-6 Railway applications - Aerodynamics Part 6: Requirements and test procedures for cross wind assessment. Technical report, CEN.

CNN. 2007. Sandstorm derails train in China; 4 die. Available at: https://web.archive.org/web/20070302073413/http://www.cnn.com/2007/WORLD/asiapcf/02/28/china.train.ap/index.html. Last accessed 08/03/15.

Cooper, K.R., 1984. The wind-tunnel simulation of surface vehicles. Journal of Wind Engineering and Industrial Aerodynamics, 17, 167-198.

Copley, J.M. 1987. The 3-D flow around railway trains. Journal of Wind Engineering and Industrial Aerodynamics, 26, 21.

D'Errico, J. 2005. Surface fitting using "gridfit" - Matlab file exchange (".m" file). Available at: http://uk.mathworks.com/matlabcentral/fileexchange/8998-surface-fitting-using-gridfit. Last accessed 08/07/16.

De Graaff, D., Eaton, J.K., 2000. Reynolds-number scaling of the flat-plate turbulent boundary layer. Journal of Fluid Mechanics 422, 319-346.

Department for Transport (UK). 2010. High Speed 2 documents. Available at: http://www.dft.gov.uk/pgr/rail/pi/highspeedrail/. Last accessed 22/10/13.

Diedrichs, B., Sima, M., Orellano, A., Tengstrand, H. 2007. Crosswind stability of a high-speed train on a high embankment. Proceedings of the Institution of Mechanical Engineers, Part F: Journal of Rail and Rapid Transport, 221, 205-225.

Dorigatti, F., Quinn, A.D., Sterling, M., Baker, C.J. 2012. Evaluation of crosswind effects on rail vehicles through moving model experiments. The Seventh International Colloquium on Bluff Body Aerodynamics and Applications, Shanghai, China.

Dorigatti, F. 2013. Rail vehicles in crosswinds: analysis of steady and unsteady aerodynamic effects through static and moving model tests. Ph.D thesis, University of Birmingham.

Durbin, P., Medic, G. 2007. Fluid dynamics with a computational perspective. Volume 10. Cambridge university press, UK.

Dyrbye, C., Hansen, S.O. 1999. Wind Loads on Structures. John Wiley & Sons Ltd.

EPSRC, 2011. The measurement of train aerodynamic phenomena under operational conditions. Available at: http://gow.epsrc.ac.uk/NGBOViewGrant.aspx?GrantRef=EP/I03842X/1. Last accessed 05/08/16.

ESDU. 1974. Characteristics of atmospheric turbulence near the ground. Part 1: definitions and general information, Data item 74030. Engineering Sciences Data Unit International plc, London.

ESDU. 2002. Strong winds in the atmospheric boundary layer Part 1: hourly-mean wind speeds, Data item 82026. Engineering Sciences Data Unit International plc, London.

European Commission. 2008. Technical specification for interoperability relating to the 'rolling stock' sub-system of the trans-European high-speed rail system. Document number C(2008) 648, 2008/232/CE, The Commission of the European Communities, February 2008.

European Commission. 2014. Concerning a technical specification for interoperability relating to the 'rolling stock' sub-system of the trans-European high-speed rail system. No 1302/2014. Official Journal of the European Union (2014).

European Commission. 2015. Final Report Summary - AEROTRAIN (AERODynamics Total Regulatory Acceptance for the Interoperable Network), March, 2015.

Fintelman, D.M. 2015. Influence of cycling position and crosswinds on performance and aerodynamics. Ph.D thesis, University of Birmingham.

Flynn, D., Hemida, H., Soper, D., Baker, C.J. 2014. Detached-eddy simulation of the slipstream of an operational freight train. Journal of Wind Engineering and Industrial Aerodynamics, 132, 1-12.

Flynn, D., Hemida, H., Baker, C.J. 2016. On the effects of crosswinds on the slipstream of a freight train and associated effects. Journal of Wind Engineering and Industrial Aerodynamics, 156, 14-28.

Free, P. 2007. Effective management of risk from slipstream effects at trackside and platforms; Appendix A1. Railway Safety and Standards Board, T425 Report.

Fujii, K., Ogawa, T. 1995. Aerodynamics of high speed trains passing by each other. Computers and Fluids, 24 (8), 897-908.

Garratt, J.R. 1994. The atmospheric boundary layer. Cambridge university press, UK.

George, W. 2013. Lectures in Turbulence for the 21st Century. Available at: http://www.uio.no/studier/emner/matnat/math/MEK4300/v13/undervisningsmateriale/tb_16january2013.pdf. Last accessed 23/06/15.

Giappino, S., Rocchi, D., Schito, P., Tomasini, G. 2016. Cross wind and rollover risk on lightweight rail vehicles. Journal of Wind Engineering and Industrial Aerodynamics, 153, 106-112.

Gilbert, T. 2013. Aerodynamics effects of high speed trains in confined spaces. Ph.D thesis, University of Birmingham.

Gill Instruments. 2015. Wind Master 3-Axis Ultrasonic Anemometer (data sheet). Available at: http://gillinstruments.com/data/datasheets/windmaster.pdf?iss=3.201603. Last accessed 19/02/15/

Google. 2016. Aerial photograph of TRAIN rig. Available at: https://www.google.co.uk/maps/@52.9099029,1.4600512,264a,20y,359.37h,34.91t/data=!3m1!1e3. Last accessed 24/03/16.

Grazzini, M., Romani, M. 2011. The use of SIMPACK in cross-wind analysis of a railway vehicle according to EN14067-6 2010 standard (Ansaldo Breda). SIMPACK user meeting, Salzburg.

Great British Innovations Vote. 2013. Great British Innovations Vote. Available at: http://www.topbritishinnovations.org/~/media/Voting/Images/Mallard_detail.jpg. Last accessed 13/01/13.

Greisinger. 2013. GPB 3300 Digital Barometer Technical Information. Available at: https://www.greisinger.de/files/upload/en/produkte/kat/k16_069_EN_oP.pdf. Last accessed 07/03/16.

Hall, P., Chen, C.L., 2011. The impacts of high-speed trains on British economic geography, a study of the UK's Intercity 125/225 and its effects. Journal of Transport Geography, 19, 689-704.

Hemida, H., Gil, N., Baker, C.J., 2010. LES of the Slipstream of a Rotating Train. Journal of Fluids Engineering, 132 (5).

Hitachi Rail Europe, 2016. Replacing diesel-powered HST rolling stock in the UK. Available at: http://www.hitachirail-eu.com/super-express-iep_57.html. Last accessed 14/08/16.

Japan Times. 2008. Wind blamed for fatal 2005 JR East accident. Available at http://www.japantimes.co.jp/news/2008/04/03/national/wind-blamed-for-fatal-2005-jr-east-accident/#.V9hn1zWlfaQ. Last accessed 19/08/16.

Johnson, T. 2001. Measurements of the effect on pressures of a porous tunnel entrance using a moving model rig. AEA Technology Rail, UK.

Johnson, T., Dalley, S. 2002. 1/25 Scale Moving Model Tests for the TRANSAERO Project. TRANSAERO - A European Initiative on Transient Aerodynamics for Railway System Optimisation, Part 3.

Johnson, T., Holding, J., 2003 Better understanding of high speed train slipstream velocities. World Congress on Railway Research. Edinburgh, UK.

Johnson, T. 2011. Basis of the 1.44 kPa criterion for the train passing pressure pulse. Technical note. RSSB; INS & RST Delivery Unit.

Jordan, S.C., Johnson, T., Sterling, M., Baker, C.J., 2007. Evaluating and modelling the response of an individual to a sudden change in wind speed. Building and Environment, 43, 1521-1534.

Jordan, S.C., Sterling, M., Baker, C.J., 2009. Modelling the response of a person to the slipstream generated by a passenger train. Journal of Rail and Rapid Transport (IMechE), 223, 567-579.

Khier, W., Breuer, M., Durst, F., 2000. Flow structure around trains under side wind conditions: a numerical study. Computers and Fluids, 29, 179-195.

Kundu, P.K., Cohen, I.M. 2010. Fluid Mechanics. Academic Press, San Diego, CA, USA.

Kwon, H., Park, Y.W., Lee, D., Kim, M.S., 2001. Wind tunnel experiments on Korean high-speed trains using various ground simulation techniques. Journal of Wind Engineering and Industrial Aerodynamics 89, 1179-1195.

Langsdale, P., 2009 43313 British Rail Class 43 HST diesel power car. Available at: http://train-photos.com.s3.amazonaws.com/5976.jpg. Last accessed 22/12/12.

Lawrence, G., and Harrison, D.J. 1977. The external pressure distribution acting on HST power cars with and without crossflow. British Railways Board, Research and Development Division, Derby, UK.

Lawson, T. 2001. Building Aerodynamics. Imperial College Press, London, UK.

Li, Y., Hu, P., Cai, C.S., McNeil, E.B., McNeil, N,S., Zhang, M., Qiang, S. 2013. Wind tunnel study of a sudden change of train wind loads due to the wind shielding effects of bridge towers and passing trains. Journal of Engineering Mechanics, 139 (9), 1249-1259.

Lippert, S. 1999. On Side Wind Stability of Trains. Kungliga Tekniska Högskolan Railway Technology, Stockholm.

List, R. J. 1971. Smithsonian Meteorological Tables (6th revision). Smithsonian Institution Press, Washington D.C., USA.

Mancini, G., Malfatti, A., 2001. Full scale measurements on high speed train ETR 500 passing in open air and in tunnels of Italian high speed line. TRANSAERO A European Initiative on Transient Aerodynamics for Railway System Optimization (Notes on Numerical Fluid Mechanics and Multidisciplinary Design (NNFM)) by Burkhard Schulte-Werning, Remi Gregoire, Antonio Malfatti, and Gerd Matschke. 101–122.

Marsden, C.J. 2016. Rail Guide (Seventh Edition). Ian Allan Publishing, Surrey, UK.

Mathworks, 2010. Matlab version 7.10.0.499, 2010. [Computer software]. The MathWorks Inc., Natick, Massachusetts.

McKenna, C., 2006. Photograph of the New Measurement Train next to regular HST. Available at: http://upload.wikimedia.org/wikipedia/commons/c/c3/Hornby_HST_43087%2BNMT_43062-02.jpg. Last accessed 22/10/13.

Mercker, E., Knape., H.W. 1989. Ground simulation with moving belt and tangential blowing for full-scale automotive testing in a wind tunnel. SAE Paper 890367.

Microsoft Corporation. (2007). Microsoft Excel 2007 [Computer Software].

Microsoft Corporation. (2015). Uffington Ordinance Survey map. Available at www.bing.com/maps/. Last accessed 21/02/2015.

Morden, J., Hemida, H., Baker, C.J. 2015. Comparison of RANS and Detached Eddy Simulation Results to Wind-Tunnel Data for the Surface Pressures Upon a Class 43 High-Speed Train. Journal of Fluids Engineering, 137.

Muld, T., Efraimsson, G., Henningson, D.S. 2012. Flow structures around a high-speed train extracted using proper orthogonal decomposition and dynamic mode decomposition. Proceedings of the Institution of Mechanical Engineers, Part F: Journal of Rail and Rapid Transport, 57, 87-97.

Nock, O.S., 1983. Two miles a minute (second edition). Patrick Stephens Limited, Cambridge, UK.

Oregon Scientific. 2016. Oregon Scientific BAR208HGA Advanced Weather Station with Atomic Time. Available at: http://www.oregonscientificstore.com/p-44-oregon-scientific-bar208hga-advanced-weather-station-with-atomic-time.aspx. Last accessed 07/03/16.

Orellano, A., Schober, M. 2006. Aerodynamic Performance of a Typical High-Speed Train. Proceedings of the 4th WSEAS International Conference on Fluid Mechanics and Aerodynamics, Elounda, Greece.

Paradot, N., Grégoire, R., Stiepel, M., Blanco, A., Sima, M., Deeg, P., Schroeder-Bodenstein, K., Johnson, T., Zanetti, G. 2015. Crosswind sensitivity assessment of a representative Europe-wide range of conventional vehicles. Proceedings of the Institution of Mechanical Engineers, Part F: Journal of Rail and Rapid Transport, 229(6), 594-624.

Pope, S.B. 2000. Turbulent Flows. University Press, Cambridge, UK.

Pope, C.W. 2007. Effective management of risk from slipstream effects at trackside and platforms. Railway Safety and Standard Board, T425 Report.

Posudin, Y. 2014. Methods of Measuring Environmental Parameters John Wiley & Sons, Hoboken, New Jersey, USA.

Premoli, A., Rocchi, D., Schito, P., Tomasini, G. 2016. Comparison between steady and moving railway vehicles subjected to crosswind by CFD analysis. Journal of Wind Engineering and Industrial Aerodynamics, 156, 29-40.

Quinn, A.D., Sterling, M., Robertson, A.P., Baker, C.J. 2007. An investigation of the wind-induced rolling moment on a commercial vehicle in the atmospheric boundary layer. Proceedings of the Institution of Mechanical Engineers, Part D: Journal of Automobile Engineering, 221, 1367-1379.

Quinn, A.D., Hayward, M., Baker, C.J., Schmid, F., Priest, J.A., Powrie, W. 2009. A full-scale experimental and modelling study of ballast flight under high-speed trains. Proceedings of the Institution of Mechanical Engineers, Part F: Journal of Rail and Rapid Transport, 224, 61-74.

Quinn, A.D., Baker, C.J., Gallagher, M. 2014. The measurement of aerodynamic phenomena in operational conditions on rail vehicles. Proceedings of the Second International Conference on Railway Technology: Research, Development and Maintenance

Quinn, A.D., Baker, C.J., Hemida, H., Gallagher, M., Morden, J., Soper, D. 2016. The measurement of train aerodynamic parameters in operational conditions - on vehicle measurements. Aerovehicles 2 (conference), Göteborg, Sweden.

Raghunathan, R.S., Kim, H.D., Setoguchi, T., 2002. Aerodynamics of high-speed railway train. Progress in Aerospace Sciences, 38, 469-514.

RAIB. 2009. Detachment of containers from freight wagons near Cheddington and Hardendale 1 March 2008. Technical report, DfT Accident Investigation.

Railway Gazette. 2011. HSTs are good to 2035. Available at http://www.railwaygazette.com/news/single-view/view/hsts-are-good-to-2035.html. Last accessed 07/02/14.

RAPIDE Consortium. 2001.Synthesis report of RAPIDE project. Aerodynamics workshop, Koln.

RCUK, 2016. Gateway to Research - The measurement of train aerodynamic phenomena under operational conditions. Available at: http://gtr.rcuk.ac.uk/projects?ref=EP/I03842X/1. Last accessed 05/08/16.

Read, M. 2004. UK Railway Pics. Available at: https://ukrailwaypics.smugmug.com/UKRailwayPics/Diesel-Locos-PostPrivatisation/EMD-class-66/Class-665-Freightliner/i-5DkDQN3. Last accessed 06/09/16.

Read, M. 2009. UK Railway Pics. Available at: https://ukrailwaypics.smugmug.com/Coaches/Mk3-HST-Trailers/401xx-Series-Mk3-TSMB-GN2G/i-2G8NvBM/A. Last accessed 06/09/16.

Read, M. 2012. UK Railway Pics. Available at: https://ukrailwaypics.smugmug.com/Daybyday/2012/2012-02-29-Exeter/i-vkwsNWm. Last accessed 06/09/16.

Read, M. 2013. UK Railway Pics. Available at: https://ukrailwaypics.smugmug.com/Daybyday/2013/2013-06-25-South-Wales/i-NcWQ4qM. Last accessed 06/09/16.

Read, M. 2016. UK Railway Pics. Available at: https://ukrailwaypics.smugmug.com/Coaches/Mk3-Coaching-Stock-Loco-hauled/Mk3-BFO-AE1G/i-PKdWQCM/A. Last accessed 06/09/16.

Reynolds, O. 1895. On the dynamical theory of incompressible viscous fluids and the determination of the criterion. Philosophical Transactions of the Royal Society of London. Volume 186, 123–164.

Robinson, C.G., Baker, C.J., 1990. The effect of atmospheric turbulence on trains. Journal of Wind Engineering and Industrial Aerodynamics, 34, 251-272.

Rocchi, D., Schober, M., Cheli, F., Orellano, A., Tomasini, G. 2009. Comparison of wind tunnel tests results on the ATM train. Euromech Colloquium (509), Vehicle Aerodynamics, Berlin, Germany.

Rocchi, D., Tomasini, G., Somaschini, C., Giappino, S. 2016. Underbody blockage effect on the aerodynamic coefficients of train vehicles. Aerovehicles 2 (conference), Göteborg, Sweden.

Rolén, C., Rung, T., Wu, D. 2004. Computational modelling of cross-wind stability of high-speed trains. European Congress on Computational Methods in Applied Sciences and Engineering, Jyväskylä, Finland

Sakuma, Y., Hibino, Y. 2013. Pressure fluctuations on a 1/10th scale train model moving through a cross wind. Railway Technical Research Institute, Tokyo, Japan.

Sami, I, Postlethwaite, I, Gu, D. 2009. Subsonic Tests of a Flush Air Data Sensing System Applied to a Fixed-Wing Micro Air Vehicle. Journal of Intelligent Robot Systems, 54, 275-295.

Sanquer, S., Barré, C., Dufresne de Virel, M, Cléon, L.M. 2004. Effect of cross winds on high-speed trains: development of a new experimental methodology. Journal of Wind Engineering and Industrial Aerodynamics, 92, 535-545.

Schlichting, H. 2010. Boundary-Layer Theory (8th edition). Originally published by McGraw Hill, New York, USA.

Schulte-Werning, B., Heine, B., Matschke, C. 2001. Unsteady wake flow characteristics of modern high-speed trains. Journal of Applied Mathematics and Mechanics, 81, 789-790.

Sensortechnics, No date. HCLA Series - Miniature amplified pressure sensors (data sheet). Available at: http://www.sensortechnics.com/cms/upload/datasheets/DS_Standard-HCLA_E_11629.pdf. Last accessed 09/03/15.

Silicon Sensing. 2013. CRS07 gyro (data sheet). Available at: http://www.siliconsensing.com/media/1166/crs07-00-0100-131-rev-2.pdf. Last accessed 04/02/16.

Soper, D., Baker, C.J., Sterling, M. 2014. Experimental investigation of the slipstream development around a container freight train using a moving model facility. Journal of Wind Engineering and Industrial Aerodynamics, 135, 105-117.

Soper, D., 2014. The aerodynamics of a container freight train. Ph.D thesis, University of Birmingham.

Soper, D., Gallagher, M., Baker, C.J., Quinn, A. 2016. A model-scale study to assess the influence of ground geometries on aerodynamic flow development around a train. Proceedings of the Institution of Mechanical Engineers, Part F: Journal of Rail and Rapid Transport.

Sterling, M., Baker, C.J., Bouferrouk, A., O'Neil, H., Wood, S., Pearce, W., Crosbie, E., 2008a. An investigation of the aerodynamic admittances and aerodynamic weighing functions of trains. BBAA VI International Colloquium on: Bluff Bodies Aerodynamics & Applications, Milan, Italy.

Sterling, M., Baker, C.J., Jordan, S.C., Johnson, T., 2008b. A study of the slipstreams of high-speed passenger trains and freight trains. Proceedings of the Institution of Mechanical Engineers, Part F: Journal of Rail and Rapid Transport, 222, 177-193.

Sterling, M., Quinn, A.D., Hargreaves, D.M., Cheli, F., Sabbioni, E., Tomasini, G., Delaunay, D., Baker, C.J., Morvan, H., 2010. A comparison of different methods to evaluate the wind induced forces on a high sided lorry. Journal of Wind Engineering and Industrial Aerodynamics 98, 10-20.

Surry, D., Johnson, G.L., 1986. Comparisons between wind tunnel and full scale estimates of wind loads on a mobile home. Journal of Wind Engineering and Industrial Aerodynamics, 23, 165-180.

Suzuki, M., Katsuji, T., Maeda, T. 2003. Aerodynamic characteristics of train/vehicles under cross winds. Journal of Wind Engineering and Industrial Aerodynamics, 91, 209-218.

Suzuki, M., Hibino, Y. 2016. Field Tests and Wind Tunnel Tests on Aerodynamic Characteristics of Train/Vehicles under Crosswinds. Quarterly Report of Railway Technical Research Institute, 57(1), 55-60.

Tabata, S. 1973. A simple but accurate formula for the saturation vapor pressure over liquid water. Journal of Applied Meteorology, 12, 1410-1411.

Tages Anzeiger. 2015. Einjähriger stirbt nach Unfall mit Güterzug [translation: Toddler dies after accident with freight train]. Available at: http://www.tagesanzeiger.ch/zuerich/region/Einjaehriger-stirbt-nach-Unfall-mit-Gueterzug/story/24124510. Last accessed 20/08/16.

Taylor, J. R. (1997). An introduction to error analysis: the study of uncertainties in physical measurements. University science books, CA, USA.

Tian, H., Huang, S., Yang, M. 2015. Flow structure around high-speed train in open air. Journal of Central South University, 22, 747-752.

Turbulent Flow Instrumentation (TFI). 2012a. Getting started - Cobra Probe. Available at: http://www.turbulentflow.com.au/Downloads/Getting%20Started%20-%20Cobra%20Probe.pdf. Last accessed 08/09/14.

Turbulent Flow Instrumentation (TFI). 2012b. Cobra Probe (flyer). Available at: http://www.turbulentflow.com.au/Downloads/Flyer_CobraProbe.pdf. Last accessed 08/09/14.

TFI. n.d. Cobra probe reference list with abstracts. Available at http://www.turbulentflow.com.au/Downloads/RefAbstracts_CobraProbe.pdf. Last accessed 06/03/14.

Vishay, 2011. Ambient Light Sensor - TEPT5600. Available at: http://www.vishay.com/. Last accessed on 08/05/2015.

Weise, M., Schober, M., Orellano, A. 2006. Slipstream velocities induced by trains. Proceedings of the 4th WSEAS International Conference on Fluid Mechanics and Aerodynamics, Elounda, Greece.

Whitmore, S.A., David, R.J., Fife, J.M. 1995. In-Flight Demonstration of a Real-Time Flush Airdata Sensing (RT-FADS) System. NASA Technical Memorandum number 104314. Available at: https://www.nasa.gov/centers/dryden/pdf/88381main_H-2053.pdf. Last accessed 11/12/2016.

Wiederhold, P. R. 1997. Water Vapor Measurement: Methods and Intrumentation. Marcel Dekker, Inc. New York, USA.

Wilson, P. T. 2015. 43070 Cotswold Rail.jpg. Available at: http://locomotive.wikia.com/wiki/File:43070_Cotswold_Rail.jpg. Last accessed 12/08/16.

Wolmar, C., 2009. Blood, Iron & Gold: How the railways transformed the world. Atlantic Books, London, UK.

Wolmar, C., 2003. Broken Rails: How Privatisation Wrecked Britain's Railways (second edition). MPG Books Ltd, London, UK.

Xu, Y. L., Ding, Q.S., 2006. Interaction of railway vehicles with track in cross-winds. Journal of Fluids and Structures 22, 295-314.

Yao, S., Sun, Z., Guo, D., Chen, D., Yang, G. 2013. Numerical study on the wake characteristics of high-speed trains. Acta Mechanica Sinica, 29(6), 811-822.

Yoshida, Y., Muto, S., Imaizumi, T. 1977. Transient aerodynamic forces and moments on model vehicles passing through cross-wind. International Automotive Engineering Congress and Exposition, Cobo Hall, Detroit, USA.

Zhang, J., Gao, G., Liu, T., Li, Z. 2015. Crosswind stability of high-speed trains in special cuts. Journal of Central South University, 22, 2849-2856.

Zhou, D., Tian, H., Zhang, J., Yang, M. 2014. Pressure transients induced by a high-speed train passing through a station. Journal of Wind Engineering and Industrial Aerodynamics, 135, 1-9.

APPENDIX A

DESCRIPTION OF TRAIN RIG FACILITY

A.1 Introduction

Appendix A provides a description of the TRAIN rig facility (introduced in chapter 3), which consists of three roughly 50 m long sections - the firing section, the test section and the braking section. A description of each of these sections is described in sections A.2 to A.4.

Figure A.1 - Aerial photograph of TRAIN rig (Google, 2016).

A.2 Description of propulsion system

A diagram of the tension/firing system is shown in figures A.2.1 and the firing process shown in figure A.2.2. The model train is propelled down the tracks using a catapult effect provided by a system of ropes and pulleys beneath the track bed. The energy to propel the model is provided by a set of elastic bungee ropes that are fixed at the firing end of the TRAIN rig, and are connected to the detachable part of the firing carriage (shown in figure A.4). An inflexible rope, defined as the firing rope, is fixed beneath the track bed and runs through pulleys on the firing carriage. This rope has a small loop at the free end that temporarily attaches onto a spike on the firing chassis of the model train (figure 3.6.1). The firing carriage itself consists of two components (shown in figure A.4). The main body of the firing carriage is connected the main winch via a robust steel cable. The recoiling part of the firing carriage is connected to the elastic bungee ropes and also houses the firing rope. The two pieces are secured in place using a temporary locking mechanism - a bell shaped bar on the recoiling part fits into a pincer style locking mechanism on the main body which is secured before the train is fired.

A smaller inflexible rope (retracting rope) runs between the rails above the track bed, and connects to the rear of the model train using a rubber band and cable tie. An electric retracting winch then pulls the train backwards on the tracks.

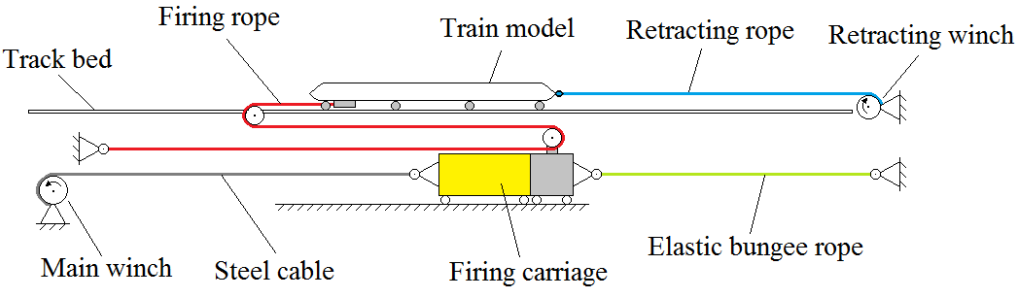

Figure A.2.1 - Components of TRAIN rig firing system

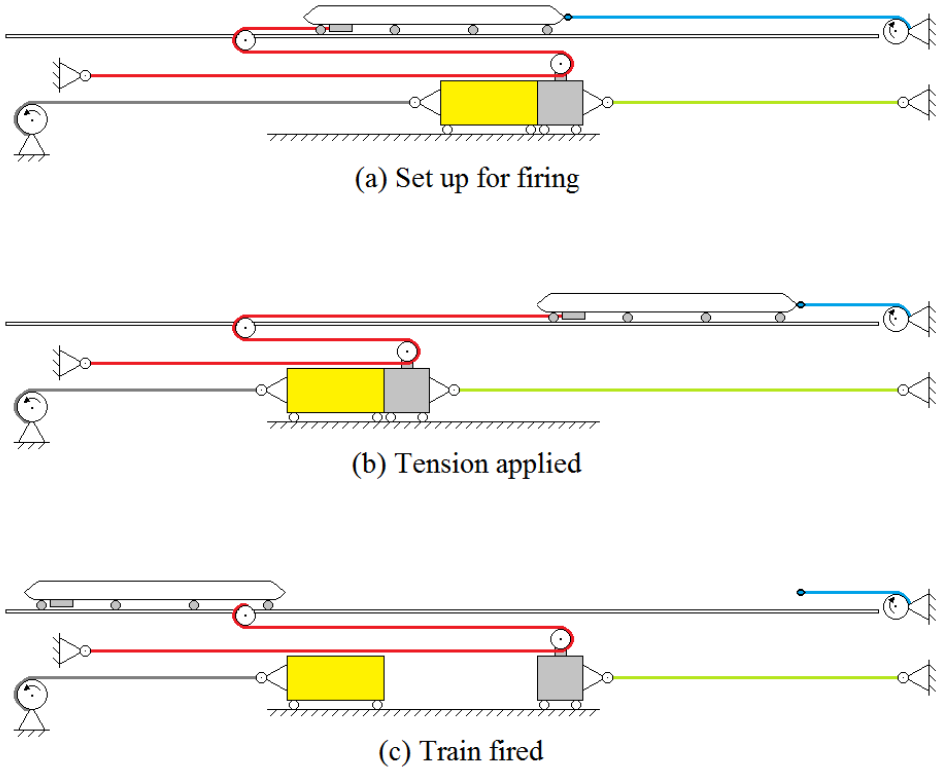

Figure A.2.2 - Firing procedure of TRAIN rig - direction of train travel is from RHS to LHS of page.

Figure A.3 - Rear of HST model showing loop that attaches to retracting rope (via a rubber band).

The system is controlled safely from a control panel in a separate room shown in figure A.5. The control panel allows the system to either be tensioned or de-tensioned by remotely operating the main winch. When tension is applied to the system, the main winch pulls the firing carriage towards itself (and hence stretches the elastic bungee ropes). As the system is put into tension, the firing rope extends (i.e., slackens) and the retracting rope simultaneously pulls the model train and firing rope backwards on the track, thus keeping the firing rope taut. A strain gauge between the steel cable and the firing carriage measures the tension in the system and this is displayed on the front face of the control panel to a precision of 0.01 kN, shown in figure A.5 (b) . The tension force is indicative of the speed of the train, and although some variation in train speeds is observed during testing, it is usual for most experimental runs to be within ± 3% of the investigative train speed as required by CEN once the necessary tension is known.

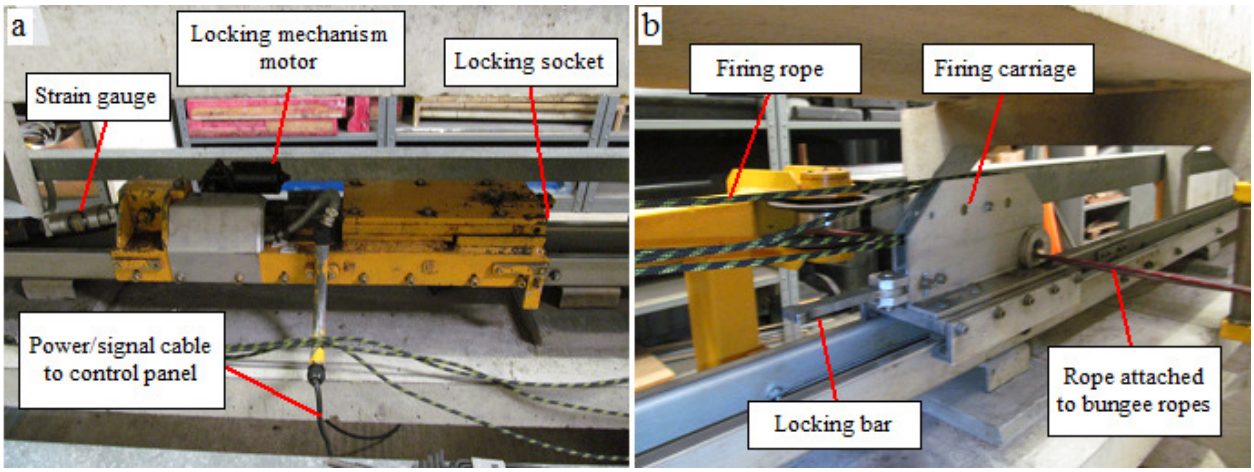

Figure A.4 - Components of the firing carriage - (a) main body of the carriage and (b) detachable part that recoils once fired

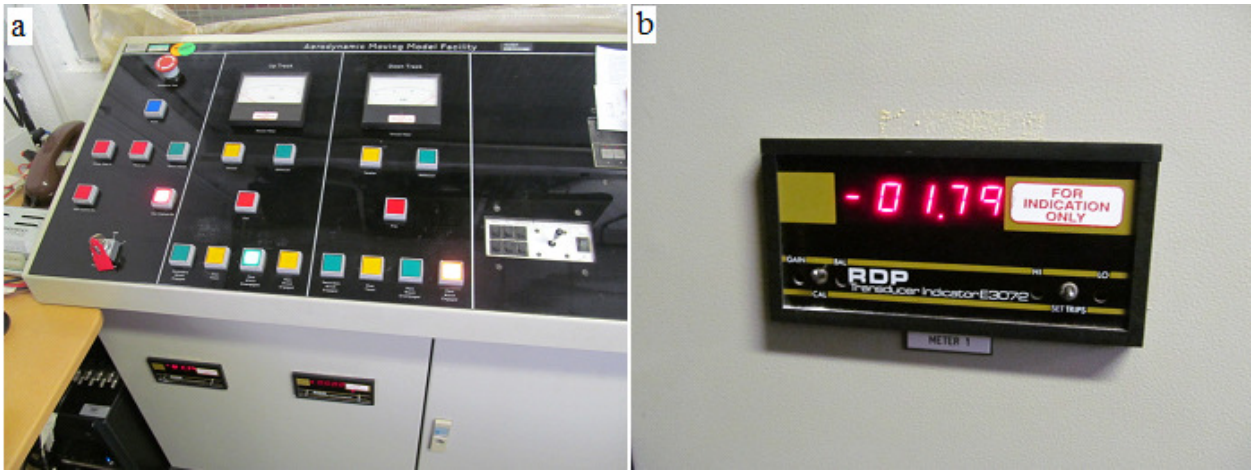

Figure A.5 - TRAIN rig control panel - (a) overview and (b) tension display in kN.

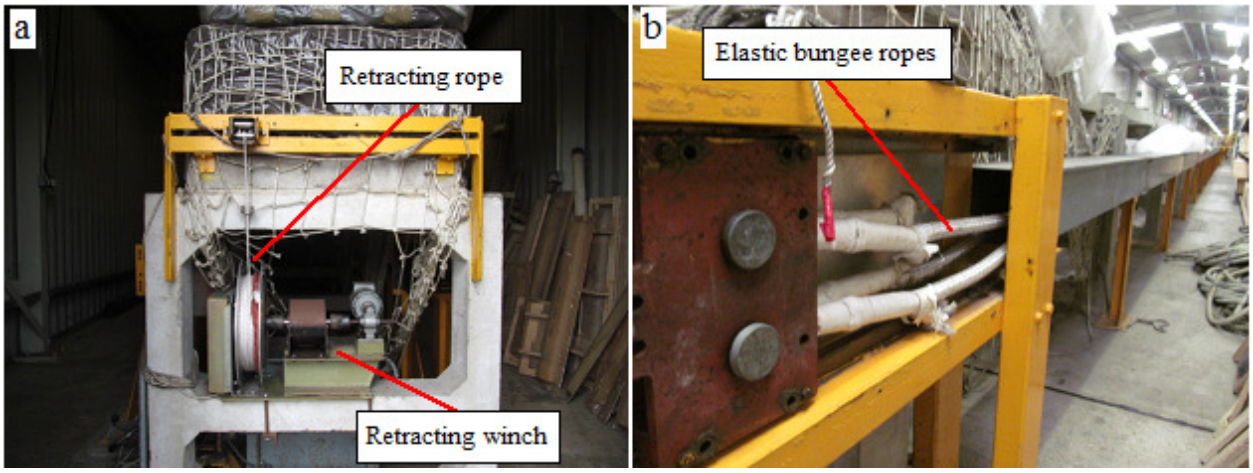

Figure A.6 - (a) - Retracting rope and winch and (b) - elastic bungee ropes.

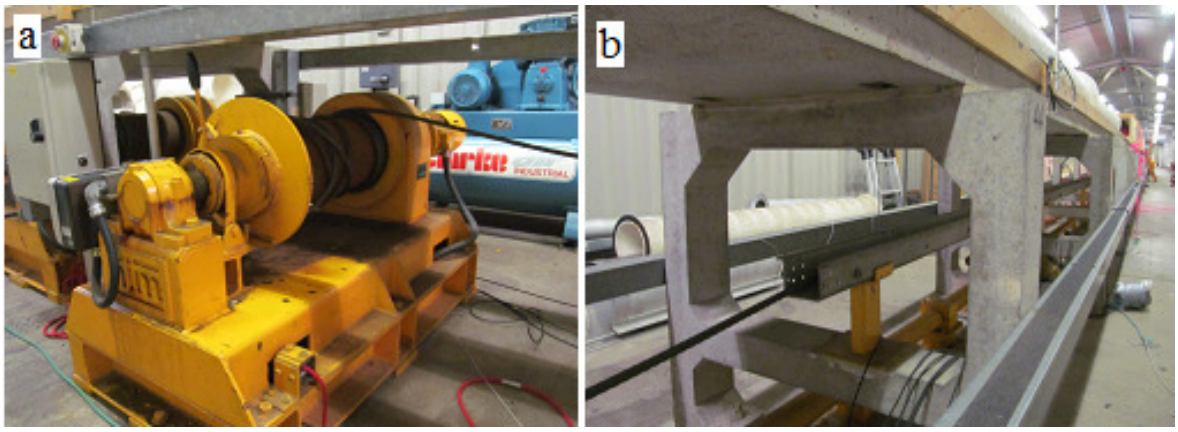

Figure A.7 - (a) Main winch and (b) robust steel cable in trough beneath track bed.

The model is fired using the control panel to operate a motor on the firing carriage that disengages the locking mechanism. The detachable part of the firing carriage, which is attached to the elastic bungee ropes and firing rope, recoils to its original position and the firing rope transfers the tensile load in the system to the train model. The rubber band connecting the train and the retracting rope breaks and the train model then travels along the

tracks freely under its own momentum and is free from any ropes. A decrease in train speed is observed, typically less than 1 m/s in the open air test section, which arises due to both mechanical and aerodynamic resistances.

A.3 Description of test section

The testing section consists of three main parts - an approximately 8 m long open air testing section, a cylindrical 22 m long tunnel and a 6.35 m long crosswind generator (CWG), which are shown in chapter 3.

The open air test section was used to measure the slipstream of the HST model. The ground plane is made from medium density fibreboard (MDF) which can be removed to allow different ground configurations (such as embankments/ballast shoulders) to be modelled.

The circular tunnel has a uniform cross section and was found to create pressures of up to 4 kPa on the train - this was found during the crosswind tests described in section 6.3. While the pressure transient data from the tunnel was collected, it has not been considered directly in this project. The data was, however, useful to ensure that the measuring equipment was not going to be damaged by the pressures within the tunnel due to the moving train during the CWG tests (i.e., the tunnel based pressure measurements were expected to give magnitudes of pressures similar to the pressures on the train, therefore the appropriate pressure transducers could be chosen).

The crosswind generator is immediately after the tunnel and uses two banks of 9 fans to create a 12 m/s crosswind perpendicular to the train tracks. The crosswind generator is described in detail in chapter 6.

A.4 Description of braking system

The train model is decelerated using a rope and piston. A brake rope runs through pulleys and is fixed to a piston, and it has a small loop at its free end. The loop is positioned in a metal trough between the tracks to ensure that the front facing spike of the firing chassis will enter the loop as the model is travelling (figure A.6). The rope then carries a tensile load to a piston which is contained within an approximately 8 m long cylinder. The inner surface of the cylinder is made from a deformable polymer and friction between the inner surface and the cylinder is sufficient to reduce the velocity to 0 m/s over a long enough time period (1-2 s) that does not create braking forces that are large enough to cause damage to the model train itself. The piston has a second rope attached to its rearward side that is used to pull the piston back to its original starting position after each run using an electronic winch. An emergency brake system is located at the end of the braking section that consists of a rope with a loop at its free end (similar to the normal brake rope loop as in figure A.6 a) and the fixed end of the emergency brake rope is attached to an elastic bungee rope to prevent very rapid deceleration of the moving model, though this system is not as effective as the normal brake system. Out of roughly 1000 runs undertaken at the TRAIN rig, only two runs resulted in the primary brake system failing, highlighting the effectiveness of the system if set up correctly.

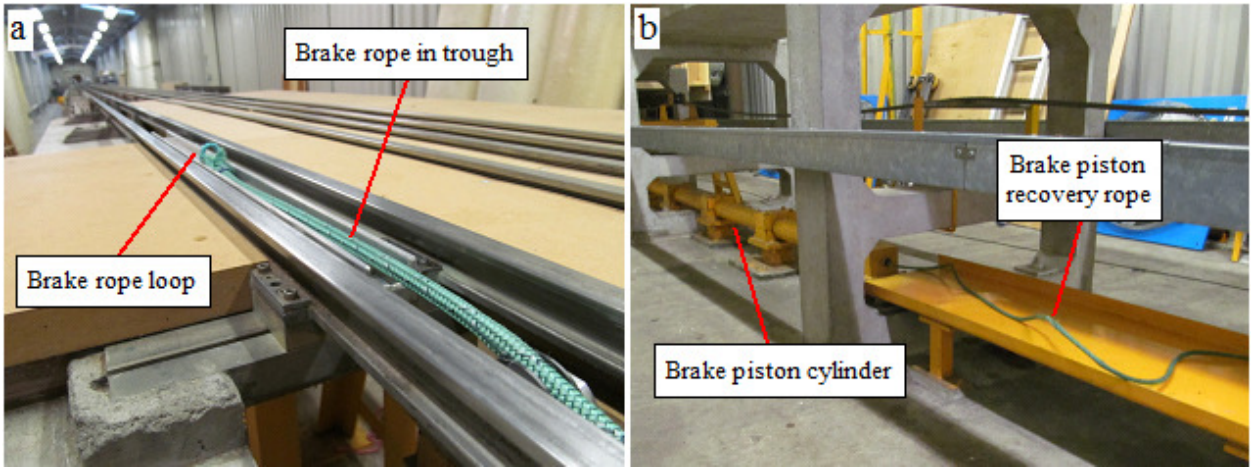

Figure A.6 - Brake system (a) - brake rope free end and (b) - brake piston and recovery rope.

A.3 Test procedure

At the start of the day the TRAIN rig needs to be set up ready to fire. The elastic bungee ropes are tightened using a mechanical winch to pull the ropes taut - they are then secured in place. The Cobra probes and supporting stand were set up to the correct measurement positions from COT and TOR and their positions checked with a ruler and set square. The PC that records the Cobra probe data was powered on and the probes were checked to ensure they were working correctly. The emergency brake was checked to ensure that the firing chassis horn would hook onto the brake rope loop. Power to the TRAIN rig firing system (needed to apply and control tension to the system) was controlled via the main control panel and required a key to power on the system.

Once the rig was set up for initial firing, the firing system and braking system were set up (usually simultaneously as each system requires one person in order to reduce set up time). The firing and braking ropes were checked for any wear/damage as each run was set up. Once

set up, the application of tension and subsequent firing was performed in the control room. Three CCTV cameras monitor the train model on the tracks, the firing rope beneath the tracks and the braking system to allow the key components to be monitored remotely and hence safely while tension is applied and the model is fired. Ambient temperature and pressure were recorded just before the train was fired and manually entered into both the TFI software itself and also into an Excel spreadsheet that served as a record of each run. Air humidity from the weather station, and the tension displayed on the TRAIN rig control panel, were also entered into the spreadsheet.

The Cobra probes were set to sample for a few seconds before the train was fired using the TFI software, and the was data stored locally on the PC for each run. The TFI software also showed a real time display of the data which acted as a method of checking that the data had been acquired correctly. The train speeds, as indicated from the light gate boxes (figure x.), were manually entered into the Excel spreadsheet - if the train speeds fell outside of the investigative train speed (40 m/s ±1.2 m/s for the HST) then the data from that run was discarded. This process was repeated until 20 acceptable measurements of velocity had been obtained at a given measurement position in order to form an ensemble average.

At the end of the day the Cobra probes and pressure transducers were stored securely in the workshop. The elastic bungee ropes were loosened (by slowly unwinding the winch that was used to tighten them) and then the electrical power to the TRAIN rig firing system was turned off - the key to control the power was securely stored.

APPENDIX B

ADDITIONAL MODEL-SCALE SLIPSTREAM EXPERIMENTS

B.1 Introduction

Appendix B presents the results from three additional slipstream studies on the HST:

- Ensemble size sensitivity study (section B.2);
- Re number effects (train speed) (section B.3);
- Effects of the underbody geometry (reverse firing) (section B.4).

The purpose of these studies was to develop the methodology for measuring slipstreams of the HST at the TRAIN rig. Each of the studies are described in sections that follow.

B.2 Ensemble size sensitivity analysis

B.2.1 Introduction

The TSI/CEN (European Commission, 2014, CEN, 2008) state that at least 20 independent runs should be undertaken when measuring slipstream velocity transients. To consider the effect of ensemble size on the calculated ensemble average, a set of 100 runs were undertaken as part of this study with a 0.3 m high ballast profile and at the TSI trackside measurement position of 0.2 m above TOR and 3 m from COT, and therefore all figures in this section are at this measurement position and ballast height.

B.2.2 Results and discussion

Figure B.1 shows the resultant horizontal velocity, U_{res}, of individual runs and the corresponding ensemble average and standard deviations (in bold and dashed black lines respectively) for ensemble sizes of 5 runs to 100 runs. Figure B.1 shows that at 50 runs the wake peak is sharper and that the ensemble mean is essentially identical to 100 runs. With 20 runs, the magnitude of the ensemble mean is similar to 50 and 100 runs, however the wake peak is slightly less defined. However, the main point of interest is the large slipstream velocity immediately after the nose peak - with smaller ensemble sizes (5-10) this peak is of similar magnitude to the wake. When the ensemble size is increased, the magnitude of the ensemble averaged nose peak decreases, suggesting that it is an intermittent flow feature that is effectively cancelled out by ensemble averaging (Sterling et al., 2008a).

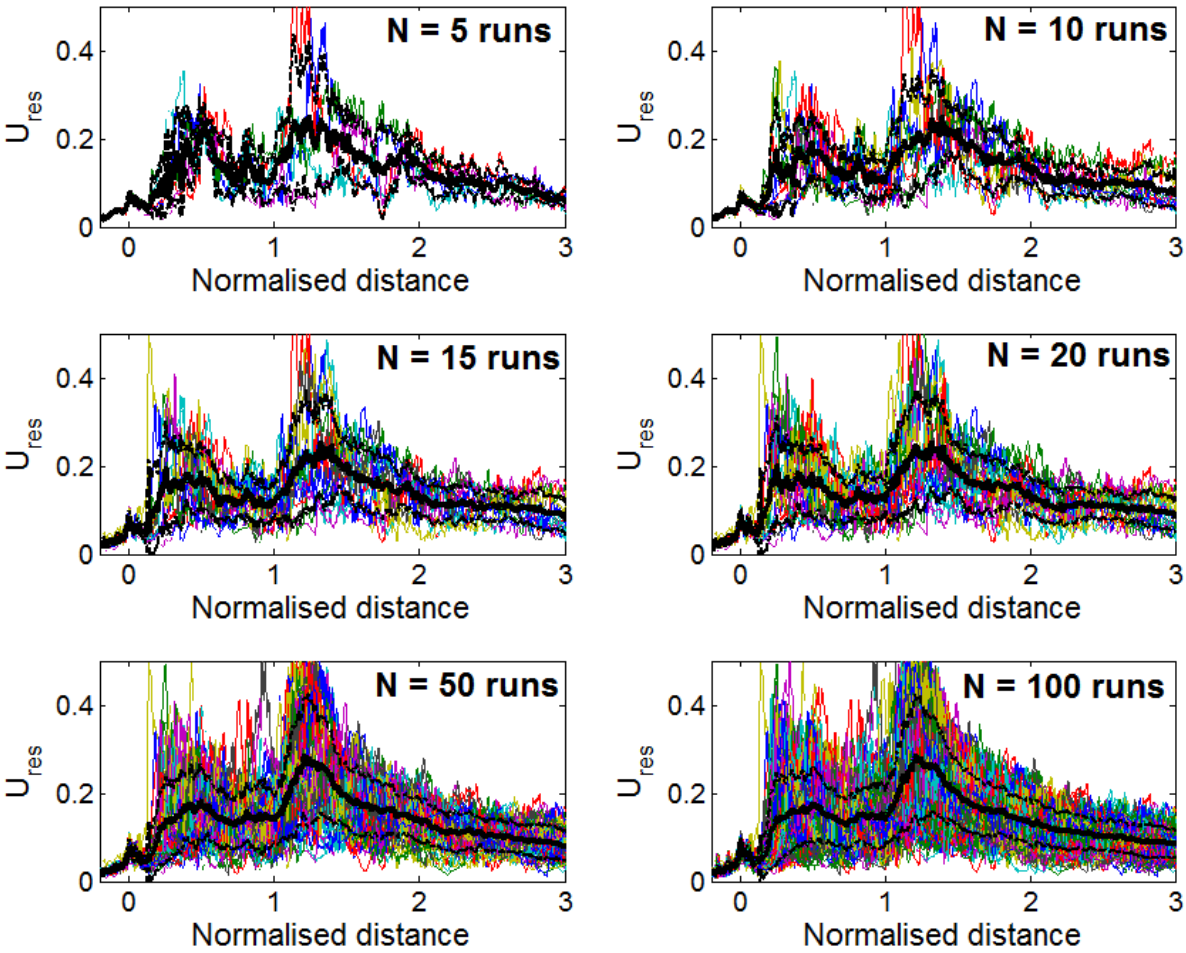

Figure B.1 - U_{res} of individual runs (coloured), ensemble average (black bold) and plus/minus one standard deviation (black dashed) for increasing ensemble sizes.

An illustration of increasing the ensemble size from 1 to 100 on the resultant (and normalised) horizontal velocity, its standard deviation and on static pressure is shown in figures B.2.1 to B.2.2. When considering $\overline{U_{res}}$ the nose appears to have little sensitivity to ensemble size, and the most significant effects are noticed at normalised distances of 0.25 (i.e., the secondary nose peak) and at 1.25 (i.e., the wake peak). If $\sigma_{U_{res}}$ is considered, the largest differences (when ensemble size is increased) are at normalised distances of about 0.1 to 0.6, again, the

region of the secondary velocity peak. When pressure is considered, there is considerably less colour "smear" indicating that pressures are not as sensitive to increasing the ensemble size, and that only a small number of runs are required - a finding consistent with previous studies (Baker, 2010, Soper, 2014).

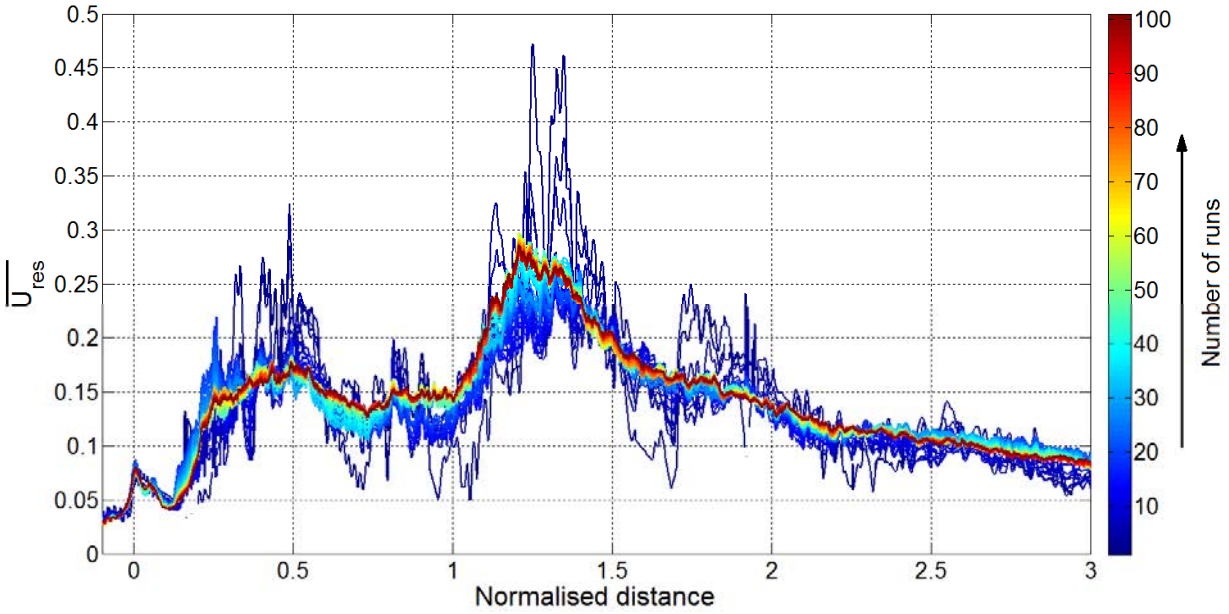

Figure B.2.1 - Effect of increasing ensemble size on resultant horizontal velocity ensemble.

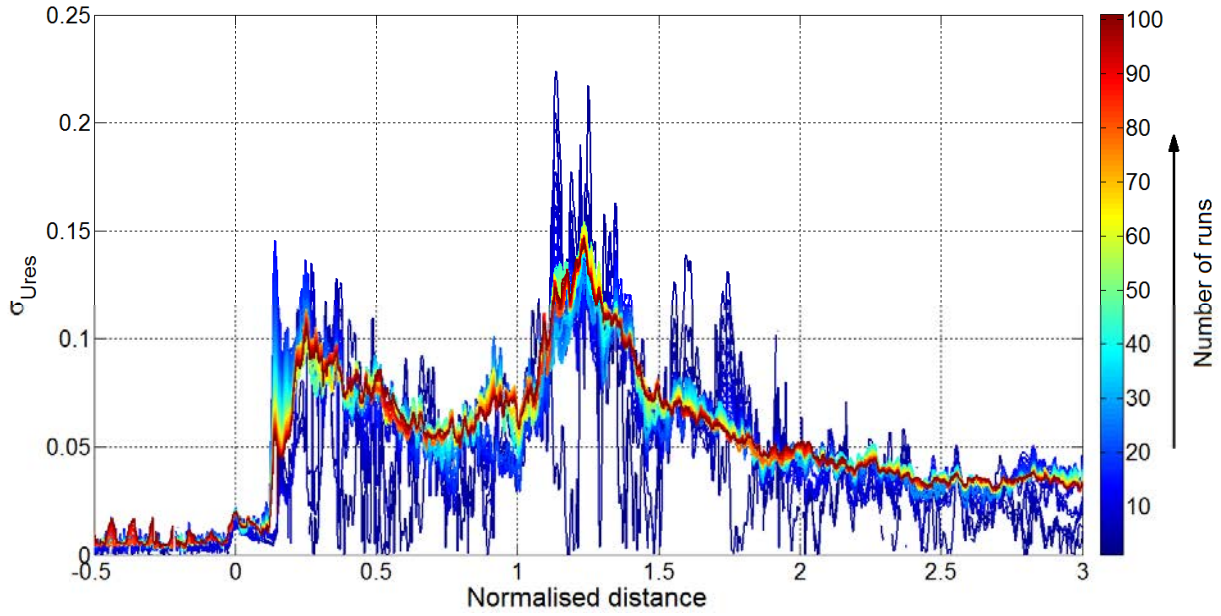

Figure B.2.2 - Effect of increasing ensemble size on resultant horizontal velocity standard deviation.

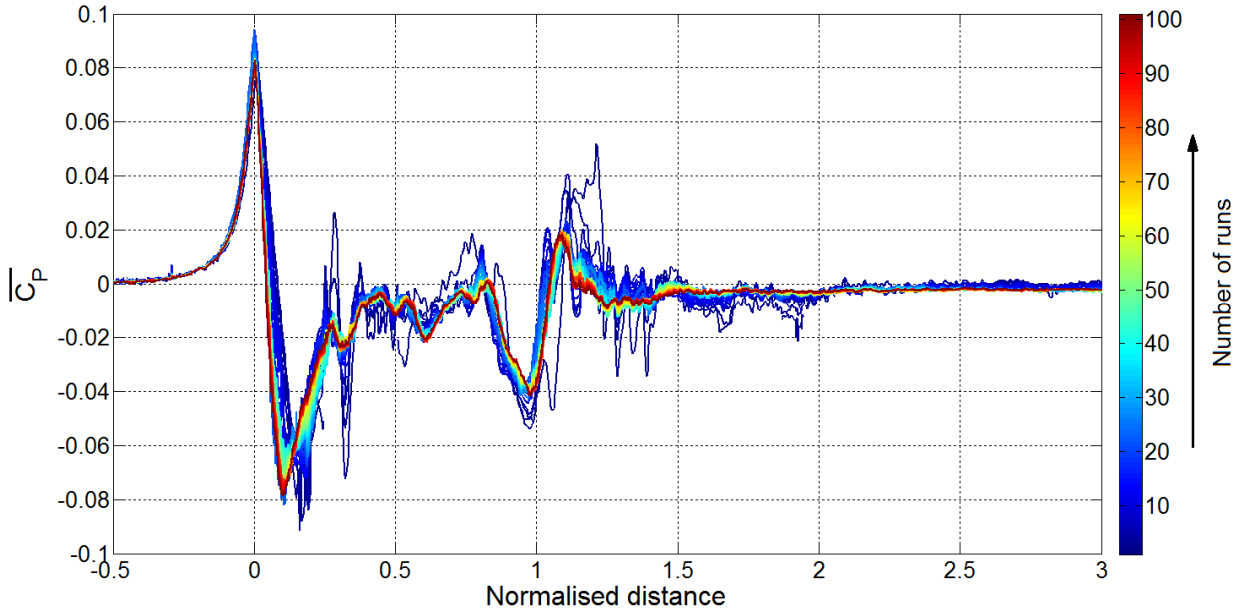

Figure B.3 - Effect of increasing ensemble size on resultant horizontal velocity ensemble.

For this particular study, the residual is defined as the difference between the 100 run ensemble average (or standard deviation) and the N run ensemble average or standard deviation (where N is greater than 1 and less than 100).

Figure B.4.1 shows the residuals of $\overline{U_{res}}$ and $\sigma_{U_{res}}$ calculated with respect to the 100 run ensemble, and similarly the residuals of $\overline{C_P}$ and σ_{C_P} are shown in figure B.4.2. As ensemble size increases, the residuals decrease. At 20 runs the residuals of velocity are less than 0.05 (i.e. a velocity of 0.The residuals show little difference between 20 and 30 runs which indicates that there is little benefit from increasing the ensemble size above 20 runs. The residuals of pressure coefficient are lower than for resultant velocity suggesting that a lower ensemble size is adequate for pressure measurements (though this is not of major importance in this study since Cobra probes record both velocity and pressure).

It should be noted that the ensemble size is also affected by the inability of the Cobra probe to record reverse flow. Figure 4.x shows the moving ensemble size (a phrase coined by Soper, 2014) of a 20 run ensemble at the TSI measurement position. The lower moving ensemble size is most notable at the train nose where a negative u-component flow occurs (as shown in figure 2.5.2).

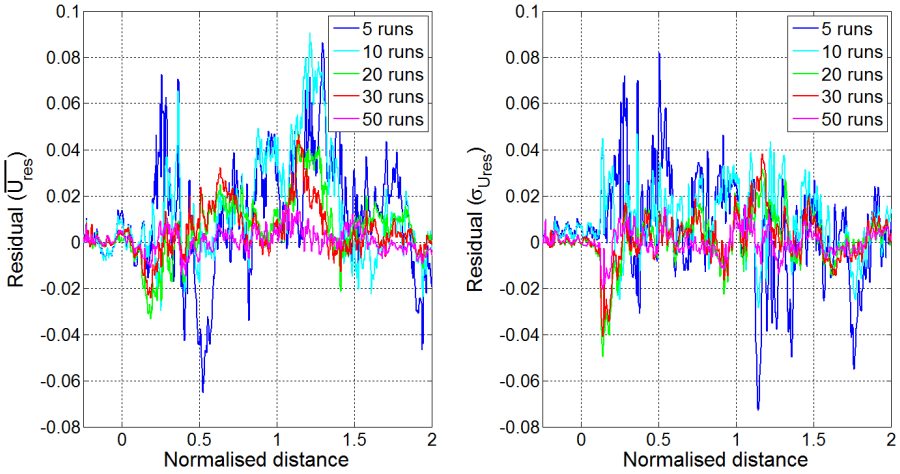

Figure B.4.1 Residual of $\overline{U_{res}}$ and $\sigma_{U_{res}}$ for ensemble sizes of 5 to 50 runs at 3 m from COT and 0.2 m above TOR for 0.3 m ballast height

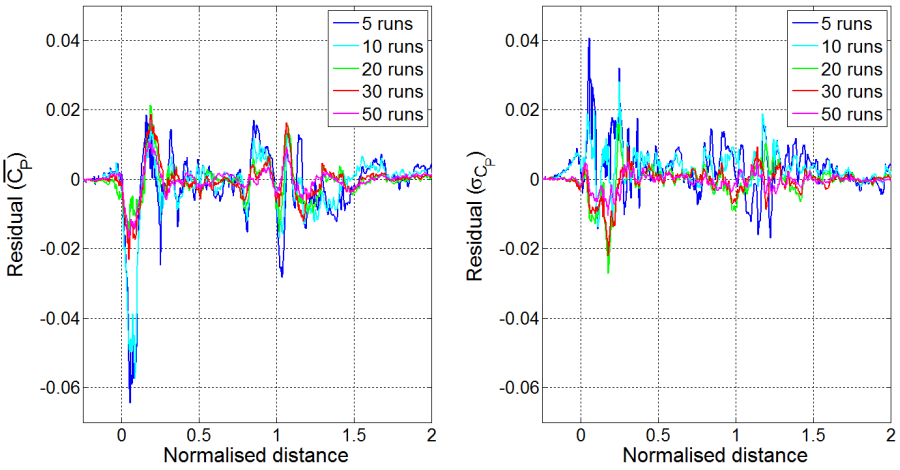

Figure B.4.2 Residual of $\overline{C_P}$ and σ_{C_P} for ensemble sizes of 5 to 50 runs at 3 m from COT and 0.2 m above TOR for 0.3 m ballast height

B.3 Effect of train speed

Preliminary experimental runs (not presented in this thesis) found the normalised resultant horizontal slipstream velocity (as in equation 4.3) to range from 0 to 0.08 at the nose peak, 0.1 in the boundary layer region and 0.2 to 0.3 in the wake region at a position of 3.5 m from COT and 2.3 m above TOR, i.e., the position that was tested from the train which should have the lowest slipstream velocity. In order to ensure that the slipstream velocities that were measured were above the minimum velocity that could accurately be measured by the Cobra probe of 2 m/s, 40 m/s was selected as the investigative train speed, which ensured that the significant flow features were mostly observed at air velocities above 2 m/s (equivalent to a normalised velocity of 0.05).

B.3.1 Introduction and description of test

The aim of this test was to investigate the effects of Re number on the ensemble averages of velocity and pressure by changing the train speed. Re number is defined as:

$$\mathrm{Re} = \frac{V_{train} L_{ref}}{\nu}$$

Where V_{train} is the train speed, L_{ref} is the reference length, taken as train height above TOR (given in table 3.1), and ν is the kinematic viscosity of air, taken as 1.5×10^{-5} m^2/s. Ensemble averages were measured at the TSI position (3 m from COT and 0.2 m above TOR) at train speeds of 20 m/s to 50 m/s with a ballast height of 0.3 m. The minimum Re number (as specified in CEN part 4) for model scale tests is Re = 2.5×10^5, equivalent to a 1:25th model train speed of 23.6 m/s. Note that sometimes the reference length is taken as 3 m, in which

case the minimum train speed increases to 31.3 m/s. In order to assess the Re number effects around this Re number range, train speeds of 20 m/s to 50 m/s were tested, equivalent to a Re number range of 2.1×10^5 to 5.2×10^5.

B.3.2 Results and discussion

The ensemble averaged velocity and pressure are shown in figure B.5. It should be noted that this data has not been filtered, though it was resampled as described in section 4.4. There are some slight differences in the ensemble averaged velocity for the different train speeds, however there is no clear effect of train speed. The nose peaks all have a similar value close to 0.1. The secondary velocity peak before the boundary layer is larger and more similar for the 20 m/s and 50 m/s ensembles (i.e., the opposite ends of the speed range tested). The wake peaks show a very similar form in terms of x-axis position and the "sharpness" of the peak, but higher values just above 0.3 were found for 30 m/s and 50 m/s than values of about 0.25 for 20 m/s and 40 m/s. There are also slight differences in the boundary layer, though again there is no clear relationship with respect to train speed, and the far wake is identical regardless of train speed. The static pressure results compare very favourably between the different train speeds. Figure B.6 shows the standard deviation of the velocity ensembles - the standard deviation of the secondary nose peak is large for the 20 m/s ensemble indicating that there may be some Re number dependency at the nose of the train, and that in all cases the variation in this secondary nose peak is high suggesting a phase-dependent vortex shedding phenomena. Given that the differences in ensemble average velocity are relatively low when compared to the standard deviation of the ensembles (shown in figure B.6), it is suggested that these differences arise due to random uncertainty and therefore that train speed has no

significant effect on the ensemble velocity or pressure at speeds of 30 m/s or higher, and hence that Re number effects are not of significance within this range of train speeds, and that 40 m/s was an appropriate speed at which to conduct the tests.

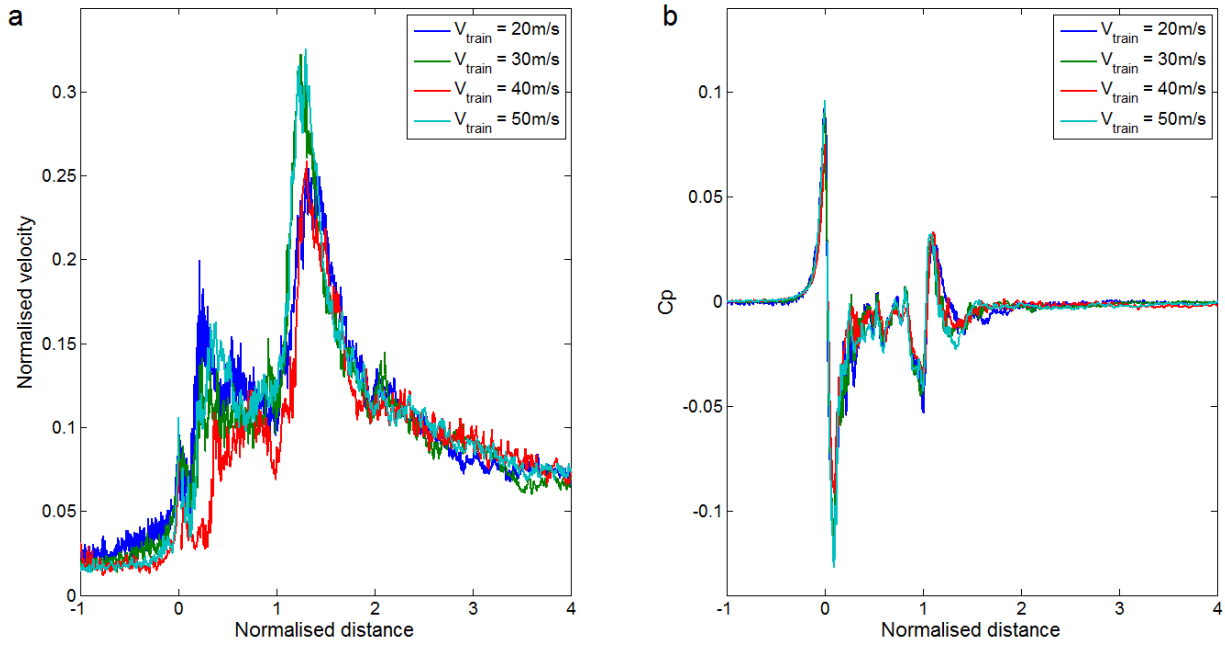

Figure B.5 - Comparison of ensemble averages - (a) normalised resultant horizontal velocity and (b) static pressure for different train speeds at 3 m from COT, 0.2 m from TOR.

The TSI gust analysis (described in section 4.7) was applied to each ensemble at each of the train speeds, and the TSI values are given in non-dimensional and full scale velocities in table B.1. The values of $U_{2\sigma}$ as full scale equivalents show little variation (less than 1 m/s) when 20 m/s is compared with any other investigative train speed. It should also be noted that these values consider velocity maxima only, though the differences in the boundary layer region seen on figure B.5 do not appear to result in significant differences in the TSI velocities. The values of $U_{2\sigma}$ at train speeds between 30 m/s to 50 m/s show very little difference, which suggests that 40 m/s is an appropriate speed to test at as the Re number is above the minimum

Re number required in CEN (taking L_{ref} as either train height or 3 m) and that there is little benefit in testing at any higher a train speed. There are disadvantages at higher train speeds such as increased setting up time and an increased rate of failure of key TRAIN rig components (such as the firing and braking ropes) due to the higher loads, which are time consuming to fix (equivalent to the time taken to carry out 10-20 runs).

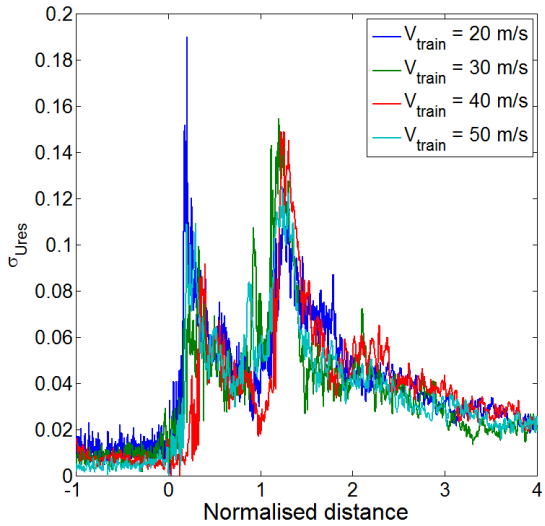

Figure B.6 - Comparison of standard deviation of slipstream velocity for different train speeds at 3 m from COT, 0.2 m from TOR.

Table B.1 - TSI gust analysis for different train speeds at trackside position (3 m from COT and 0.2 m above TOR)

Train speed (m/s)	Non-dimensional			Full scale equivalent (m/s)		
	$\overline{U_{max}}$	$\sigma_{U_{max}}$	$U_{2\sigma}$	$\overline{U_{max}}$	$\sigma_{U_{max}}$	$U_{2\sigma}$
20	0.21	0.036	0.28	11.5	2.0	15.6
30	0.21	0.041	0.30	11.9	2.3	16.5
40	0.21	0.039	0.29	12.0	2.2	16.3
50	0.22	0.037	0.29	12.3	2.1	16.5

B.4 Effect of underbody geometry

B.4.1 Introduction and description of test

The slipstream of the HST was noted to have a large velocity peak (when slipstreams were measured closer to the train and ground) which was not apparent in the slipstream of more conventional high speed passenger trains such as the ICE2. It was hypothesised that it may be due to a combination of the HST nose profile, which channels air downwards, the lack of underbody shielding of the HST (compared with the ICE2) and underbody blockage from the firing chassis (shown in figures 3.6.1 and 6.10). The firing chassis is situated about 1-3 m from the nose tip (at full scale) and creates a high blockage beneath the train which likely leads to trapped air beneath the train which effectively increasing the bluntness of the HST nose. A brief investigation was therefore undertaken after the majority of the slipstream tests (described in chapters 3 to 5) had been completed to assess the effect of firing the HST model in reverse. The aim of this test was to assess the influence of the firing chassis on the HST slipstream at measurement positions closer to the ground and train. Due to time constraints only a single measurement position was tested, and 20 runs were undertaken at the trackside TSI position of 3 m from COT and 0.2 m above TOR. The key geometric difference between the forwards and reverse running was that in reverse the firing chassis was trailing, and the firing chassis creates a higher blockage beneath and within the two metal wheels that the trailing wheels due to the position of the "horns" that are required to fire the model and catch onto the brake rope loop. Runs were undertaken with a flat ground scenario (expected to give the "worst case" i.e., the most flow constriction therefore highest velocities) and at 40 m/s. The data was not filtered but was resampled to reduce alignment errors while maintaining the original signal as best as possible.

B.4.2 Results and discussion

Figure B.7 compares the ensemble averages of the train running in the forwards direction to the reverse direction for the vector components and the resultant horizontal velocity. The resultant horizontal velocity plus or minus one standard deviation for both cases is shown in figure B.8.

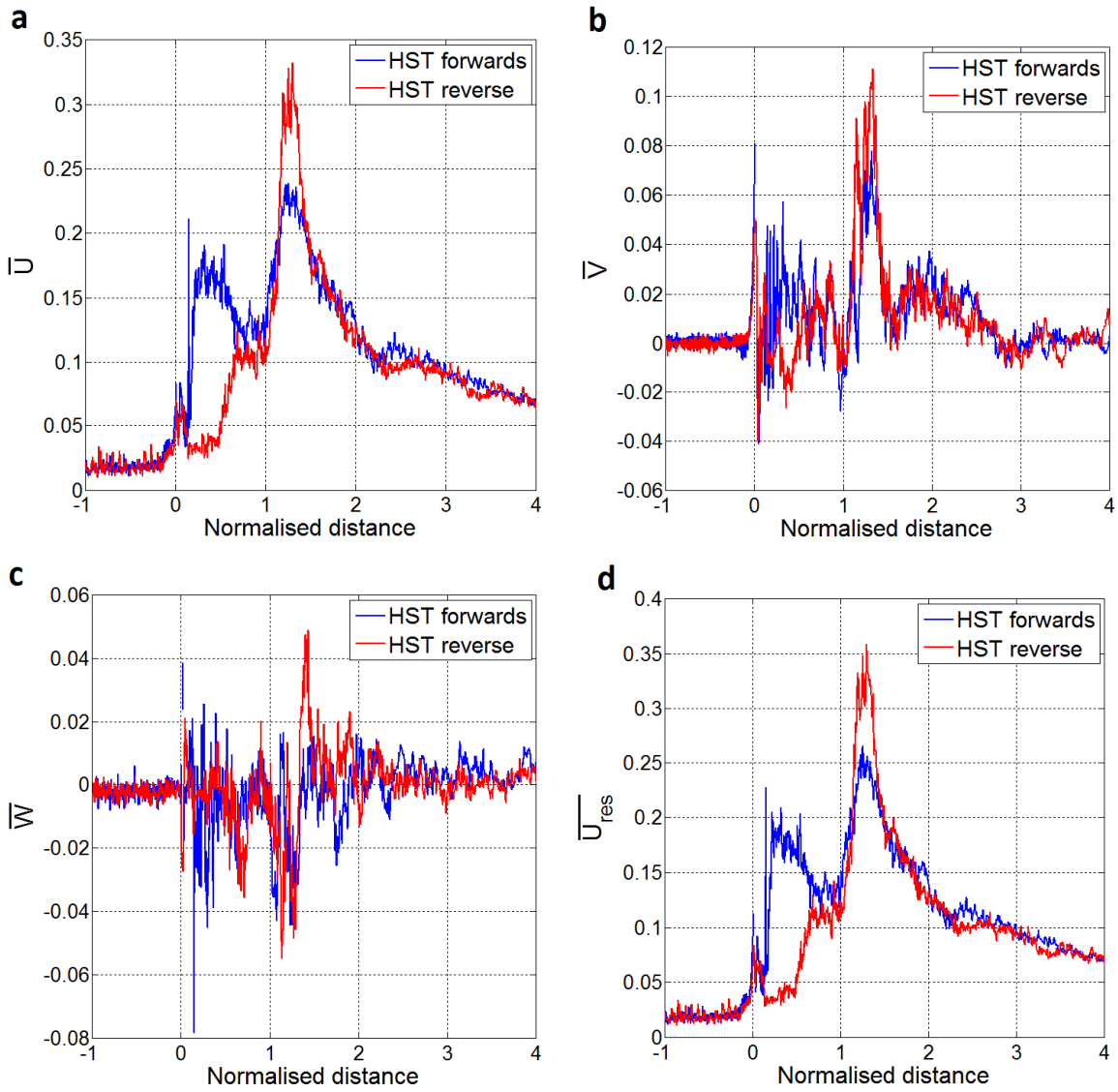

Figure B.7 - Comparison between HST running forwards and in reverse showing ensemble average vector components (a) to (c) and resultant horizontal velocity (d).

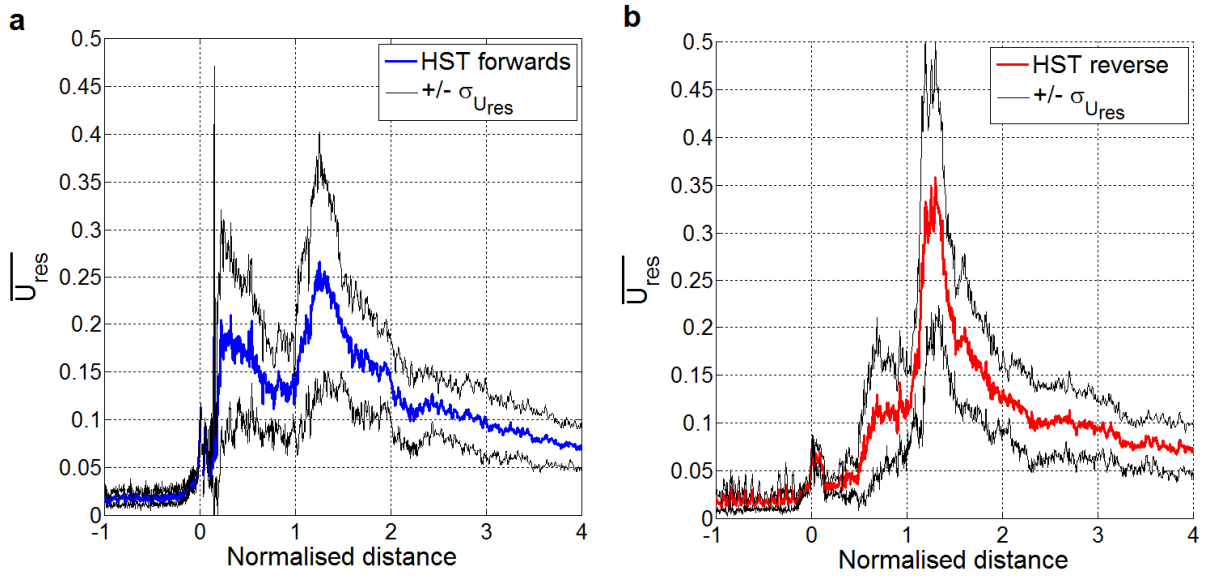

Figure B.8 - Comparison of ensemble average result horizontal velocity ± one standard deviation for (a) forwards and (b) reverse running

There are clear differences between the two data sets. At the "true" nose peak (at x = 0) the forwards running ensemble is slightly higher, and it can be seen that this is due to a higher magnitude of both u and v component velocities. The secondary nose peak in the "HST forwards" direction is of similar magnitude to the near wake, and is primarily a streamwise flow, though this peak is not apparent on the data where the train is in reverse. The standard deviation is also very low immediately after the nose passage when the HST is in reverse, compared to a very high standard deviation when in the forwards direction. When the wake peaks are considered, the reverse direction, where the firing chassis is at the rearward end of the HST model, shows both a larger wake peak and larger standard deviation.

The boundary layer regions, while of short length, also show differences - there is a fast growth of the boundary layer in the reverse direction, but in the forwards direction there is a

actually a reduction in slipstream velocity along the train length, which supports the idea that there are two separate flows in the forwards direction - the actual boundary layer and the nose-shed vortex, and these two flows most likely interact to give rise to an unrealistic boundary layer. The boundary layer does show similar values just before the wake, which could suggest that the firing chassis does not greatly affect the latter part of the boundary layer (though given the limited data quantity this is not certain), and hence the near wake flows, when running in the forward direction, have been considered acceptable in subsequent analysis. The near wake flows in the reverse direction are of higher magnitude, likely arising to a localised vortex shed from the firing chassis in combination with the trailing vortices from the tail. The far wake behaviour is identical regardless of direction.

The ensemble of pressure coefficient is shown in figure B.9, and there are also clear differences in the nose pressure pulse. The positive and negative peaks are lower and better defined in the reverse direction. In the forwards direction, the negative peak, and pressures immediately after this negative peak, clearly reflect the geometrical roughness of the firing chassis. The pressures along the main length of the train are very similar between the forwards and reverse directions, however the tail pressure pulse is of slightly higher magnitude when run in reverse. smaller initial nose peak aligned with the maximum pressure of the nose pulse and then a much larger nose peak aligned with the negative pressure peak of the nose pulse. The firing chassis may be partially causing the greatly larger secondary nose velocity peak.

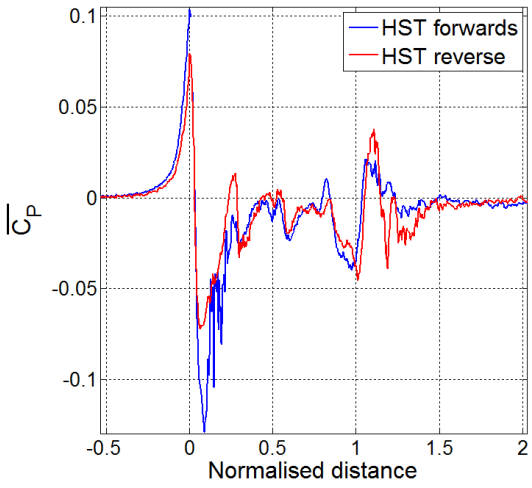

Figure B.9 - Comparison of ensemble averaged pressure coefficient for forwards and reverse running.

This test was only very brief and only considered a single ensemble and measurement position for a single train type, and of course cannot be taken as "proof". However, this finding does suggest that further study of the specific underbody modifications of the TRAIN rig is needed for different measurement positions and train types. There is also the question of whether the geometry at the nose during reverse running accurately represents the full scale geometry - given the geometric simplifications to the bogies and the lack of simulation of other full scale underbody equipment, the underbody immediately after the nose (the reverse direction) has less underbody blockage than at full scale. In the forwards direction, not only is the blockage higher, but the actual geometry is quite different to reality due to the horns and block of the firing chassis. It is also believed that given the HST nose profile, the HST may be particularly sensitive to underbody geometry at the train nose. Nonetheless, it is clear that further study of the underbody geometry would be of use for future model scale experiments.

If the additional trains tested during the ballast height effects are considered very briefly then possible effects of the firing chassis can be seen. It is interesting to note that the ICE2 pressure pulse was unusual (see pressure trace in figure B.10 for example), and consisted of a "double dip" negative pressure pulse at the nose. Gilbert, (2013), made the conclusion that the firing chassis was causing this pressure pulse and therefore Gilbert, (2013), removed the second pulse from the data. The firing chassis did not have any apparent effect on the ICE2 slipstream (i.e., no clear secondary nose velocity peak at 2 m from COT). Figure B.11 shows that the Class 66 freight train data shows a very large velocity peak (of 0.7) at 2 m from COT immediately after the nose passage, which Soper, (2014) concluded to be unsurprising given the very blunt nose profile of the freight train. However, the large peak of 0.7 is aligned with the large negative pressure peak at the same position, which suggests that this peak may be caused, in part, by the firing chassis.

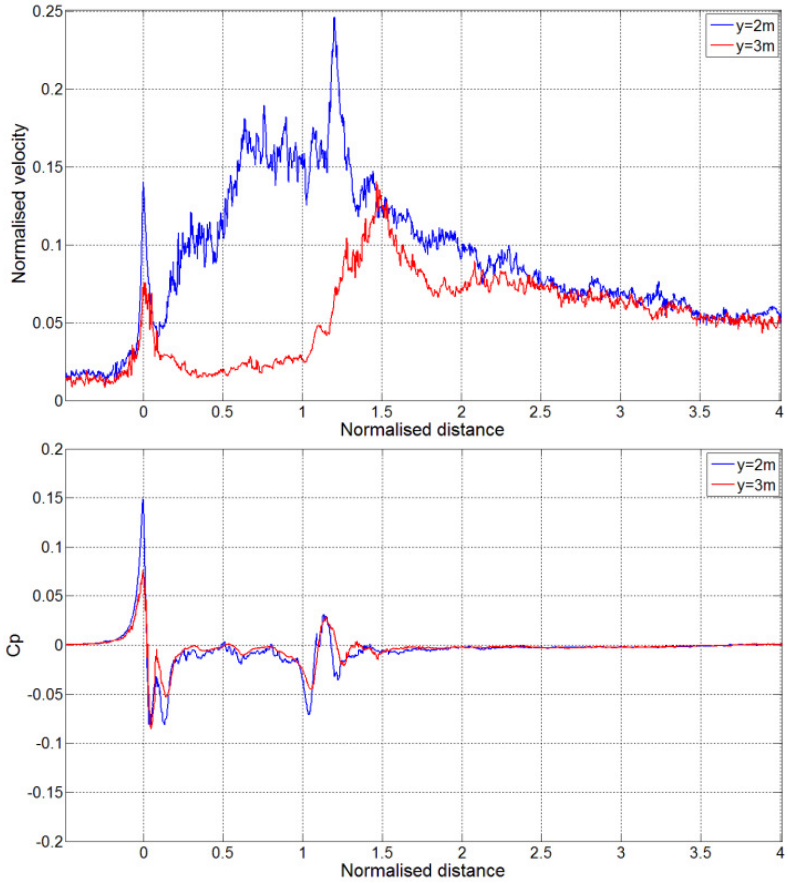

Figure B.10 - Ensemble averages of slipstream (LHS) and pressure (RHS) for ICE2 with 0 m ballast height at z = 1.2 m above TOR and y = 2.0 m and 3.0 m from COT.

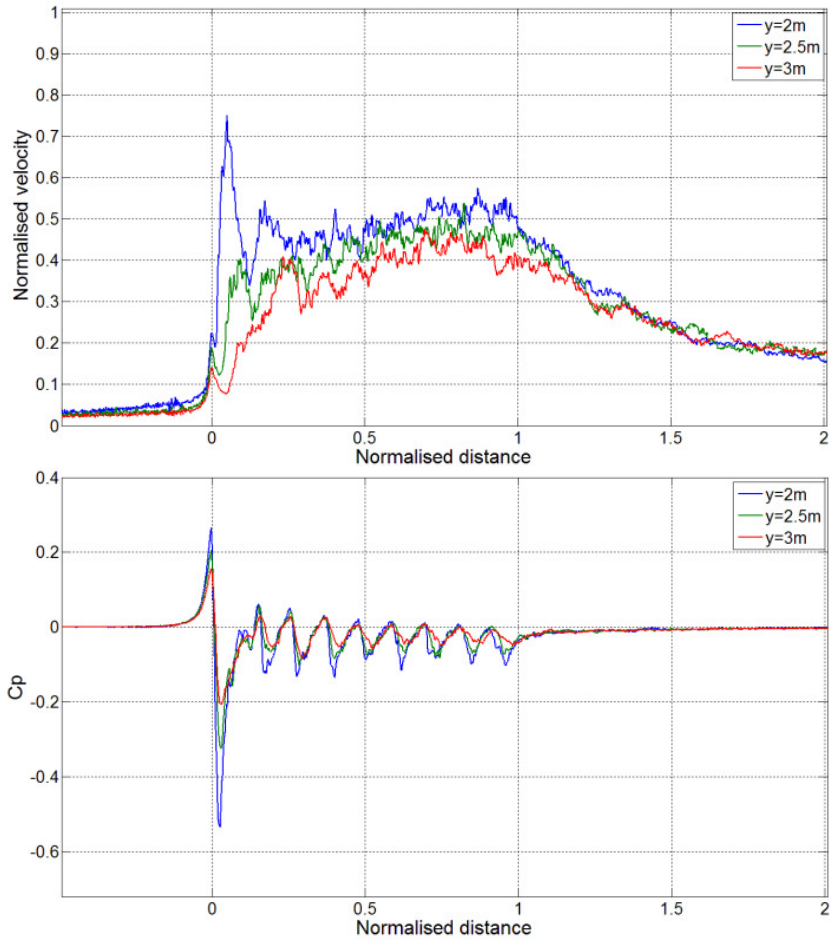

Figure B.11 - Ensemble averages of slipstream (LHS) and pressure (RHS) for freight train with 0.3 m ballast height at z = 0.2 m above TOR and y = 2.0 m, 2.5 m and 3.0 m from COT.

B.5 Closing remarks

Three separate experiments were undertaken in order to develop a more robust methodology for moving model tests to measure slipstreams and pressures at the TRAIN rig. The effect of changing ensemble size was found to reduce the standard deviation of the ensemble. The minimum number of 20 train passes, as specified in the TSI and CEN seems reasonable considering the results obtained with the HST - there was little measurable effect in the results

for a 20 run and 30 run ensemble. Static pressure can also be seen to have a more stable ensemble after a lower number of runs than for velocity. When considering the effect of train speed, it is clear that if the measured slipstream velocity and static pressure are suitably normalised (as in section 4.3) then results can be compared between different train speeds. A significant difference in the slipstream was noted at the TSI trackside measurement position between the HST being fired in the forwards direction and in the reverse direction due to geometrical differences in the underbody - most significantly the position of the firing chassis was found to increase slipstream velocities immediately after the firing chassis passed the measurement position, and a similar effect was noted for static pressure. It is unclear whether either the forwards or reverse direction accurately represents the full scale geometry, and only a single train type and measurement position was tested, however this finding certainly suggests the need for further work on the matter.

APPENDIX C

TRAIN RIG ENSEMBLE AVERAGES FOR HST, CLASS 66 AND ICE2

C.1 Introduction

Appendix C presents the full set of experimental results for all measurement positions tested (as specified in table 3.2) for the tests described in chapter 3. The aim of these tests was to investigate the slipstream of an HST with different ballast heights (described in section x.) However, in order to develop a more holistic investigation into the effect of ballast height on the slipstream of a train, two additional trains were tested - a Class 66 freight train with an unfavourable (i.e., largest slipstream magnitude) loading configuration, (Soper, 2014), shown in figure C.1.1, and the Intercity Express 2 (ICE2) passenger train shown in figure C.1.2. Like the HST, both the Class 66 and ICE2 are 1:25th scale models and both have been successfully tested previously at the TRAIN rig (Soper, 2014; Gilbert, 2013). The investigative parameters for the three trains are presented in table 3.1. The results presented in this appendix are in the form of ensemble averages, calculated following the process outlined in chapter 4, and in all cases consisted of 20 acceptable runs at each measurement position.

Figure C.1.1 - Class 66 freight train (a) full scale (Read, 2004) and (b) TRAIN rig model.

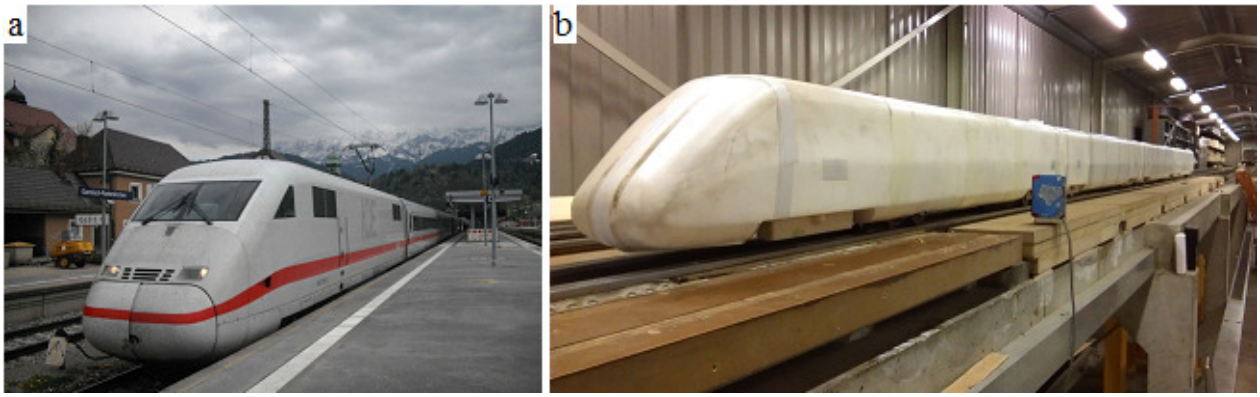

Figure C.1.2 - ICE2 passenger train - (a) full scale (Wikimedia Commons, 2011), (b) TRAIN rig model.

C.2 Results

C.2.1 Format of results

Results are presented in three different formats and each train is considered separately. Section C.2.2 presents the results for the HST, section C.2.3 is for the freight train and C.2.4 for the ICE2. Within each of these sections, the first subsection (C.2.N.1) presents the results at single heights above TOR and shows different distances from the COT on the same axis - i.e., horizontal rakes. The second subsection (C.2.N.2) shows the same data at fixed y-distances (from COT) and with different heights on the same graph, i.e., vertical rakes. In both sections C.2.N.1 and C.2.N.2 the results are presented in order of ascending ballast height. Finally, subsection C.2.N.3 considers different ballast heights at single measurement positions.

All results are presented as ensemble averages of normalised velocity ($\overline{U_{res}}$) on the LHS and pressure coefficient ($\overline{C_P}$) on the RHS and the train type, ground configuration and distances from COT and TOR are given in each figure caption. Table C.1 defines the ground configurations. Tables C.2.1 to C.4 lists the figure numbers and corresponding ground configurations and measurement positions for the data collected for each train, and are intended to serve as a list of contents for this appendix.

Table C.1 - Definitions of ground configurations

Ballast height (m)	Definition
0	1
0.3	2
0.75	3
1	4
1.5	5

Table C.2.1 - List of figures for HST (part 1 of 2).

Figure number	Ground configuration	Distance from COT (m)	Distance from TOR (m)
C.2.1	1	2, 3	0
C.2.2	1	2, 3	0.2
C.2.3	1	2, 3	0.7
C.2.4	1	2, 3	1.2
C.2.5	2	2.5, 3	-0.3
C.2.6	2	2, 2.5, 3	0
C.2.7	2	2, 2.5, 3, 3.5	0.2
C.2.8	2	2, 2.5, 3, 3.5	0.7
C.2.9	2	2, 2.5, 3, 3.5	1.2
C.2.10	2	2, 2.5, 3, 3.5	1.75
C.2.11	2	2, 2.5, 3, 3.5	2.3
C.2.12	3	2.5, 3	-0.3
C.2.13	3	2, 3	0
C.2.14	3	2, 3	0.2
C.2.15	3	2, 3	0.7
C.2.16	3	2, 3	1.2
C.2.17	5	2.5, 3	-0.3
C.2.18	5	2, 2.5, 3	0
C.2.19	5	2, 2.5, 3, 3.5	0.2
C.2.20	5	2, 3	1.2
C.2.21	1	2	0, 0.2, 0.7, 1.2
C.2.22	1	3	0, 0.2, 0.7, 1.2
C.2.23	2	2	0, 0.2, 0.7, 1.2, 1.75, 2.3
C.2.24	2	2.5	-0.3, 0, 0.2, 0.7, 1.2, 1.75, 2.3
C.2.25	2	3	-0.3, 0, 0.2, 0.7, 1.2, 1.75, 2.3
C.2.26	2	3.5	0.2, 0.7, 1.2, 1.75, 2.3

Table C.2.2 - List of figures for HST (part 2 of 2).

Figure number	Ground configuration	Distance from COT (m)	Distance from TOR (m)
C.2.27	3	2	0, 0.2, 0.7, 1.2
C.2.28	3	3	-0.6, -0.3, 0, 0.7, 1.2
C.2.29	4	3	-0.6, -0.3, 0.2, 1.2
C.2.30	5	2	0, 0.2, 1.2
C.2.31	5	2.5	-0.3, 0, 0.2
C.2.32	5	3	-0.6, -0.3, 0, 0.2, 1.2
C.2.33	3, 4, 5	2.5	-0.6
C.2.34	2, 3, 5	2.5	-0.3
C.2.35	2, 3, 4, 5	3	-0.3
C.2.36	1, 2, 3, 5	2	0
C.2.37	2, 5	2.5	0
C.2.38	1, 2, 3, 5	3	0
C.2.39	1, 2, 3, 5	2	0.2
C.2.40	2, 5	2.5	0.2
C.2.41	1, 2, 3, 4, 5	3	0.2
C.2.42	2, 5	3.5	0.2
C.2.43	1, 2, 3	2	0.7
C.2.44	1, 2, 3	3	0.7
C.2.45	1, 2, 3, 5	2	1.2
C.2.46	1, 2, 3, 4, 5	3	1.2

Table C.3 - List of figures for Class 66 freight train.

Figure number	Ground configuration	Distance from COT (m)	Distance from TOR (m)
C.3.1	2	2.5, 3	-0.3
C.3.2	2	2, 2.5, 3	0
C.3.3	2	2, 2.5, 3	0.2
C.3.4	2	2, 2.5, 3	0.7
C.3.5	2	2, 2.5, 3	1.2
C.3.6	1	2	0, 0.2, 0.7, 1.2
C.3.7	1	3	0, 0.2, 0.7, 1.2
C.3.8	2	2	0, 0.2, 0.7, 1.2
C.3.9	2	2.5	-0.3, 0, 0.2, 0.7, 1.2
C.3.10	2	3	-0.3, 0, 0.2, 0.7, 1.2
C.3.11	3	2	0, 0.2, 0.7, 1.2
C.3.12	3	3	-0.6, -0.3, 0, 0.2, 0.7, 1.2
C.3.13	4	3	-0.6, -0.3, 0.2, 1.2
C.3.14	5	2	0. 0.2, 1.2
C.3.15	5	2.5	-0.3, 0, 0.2, 1.2
C.3.16	5	3	-0.6, -0.3, 0, 0.2, 1.2
C.3.17	3, 4, 5	3	-0.6
C.3.18	2, 5	2.5	-0.3
C.3.19	2, 3, 4, 5	3	-0.3
C.3.20	1, 2, 3, 5	2	0
C.3.21	2, 5	2.5	0
C.3.22	1, 2, 3, 5	3	0
C.3.23	1, 2, 3, 5	2	0.2
C.3.24	2, 5	2.5	0.2
C.3.25	1, 2, 3, 4, 5	3	0.2
C.3.26	1, 2, 3	2	0.7
C.3.27	1, 2, 3	3	0.7
C.3.28	1, 2, 3, 5	2	1.2
C.2.29	2, 5	2.5	1.2
C.3.30	1, 2, 3, 4, 5	3	1.2

Table C4 - List of figures for ICE2.

Figure number	Ground configuration (BSX)	Distance from COT (m)	Distance from TOR (m)
C.4.1	1	2, 3	1.2
C.4.2	1	3	0.2, 1.2
C.4.3	3	3	-0.3, 0.2, 1.2
C.4.4	5	3	0.2, 1.2
C.4.5	3, 5	3	-0.3
C.4.6	1, 3, 5	3	0.2
C.4.7	1, 3, 5	3	1.2

C.2.2 HST results

C.2.2.1 HST results by height above TOR (z)

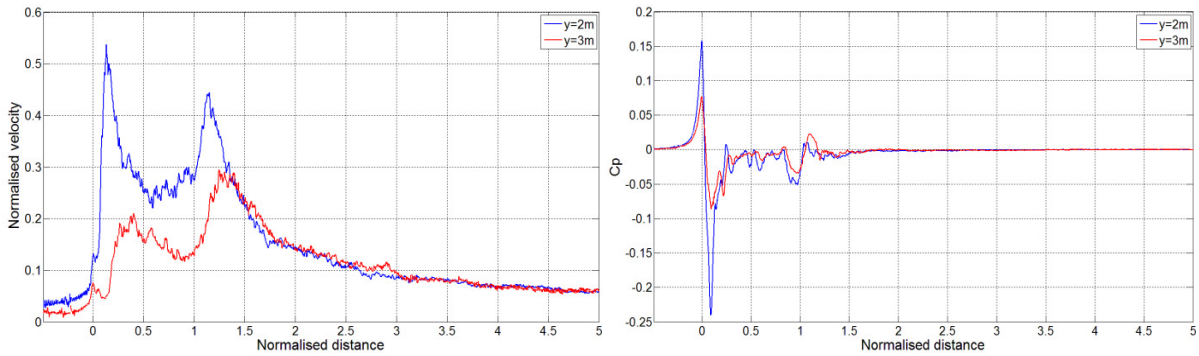

Figure C.2.1 - Slipstream and pressure for HST with BS1 at z = 0.0 m above TOR, y = 2.0 m and 3.0 m from COT.

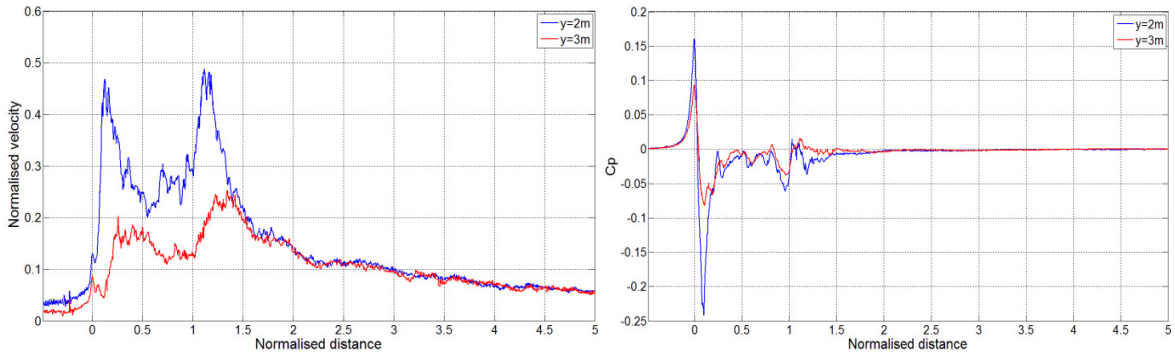

Figure C.2.2 - Slipstream and pressure for HST with BS1 at z = 0.2 m above TOR, y = 2.0 m and 3.0 m from COT.

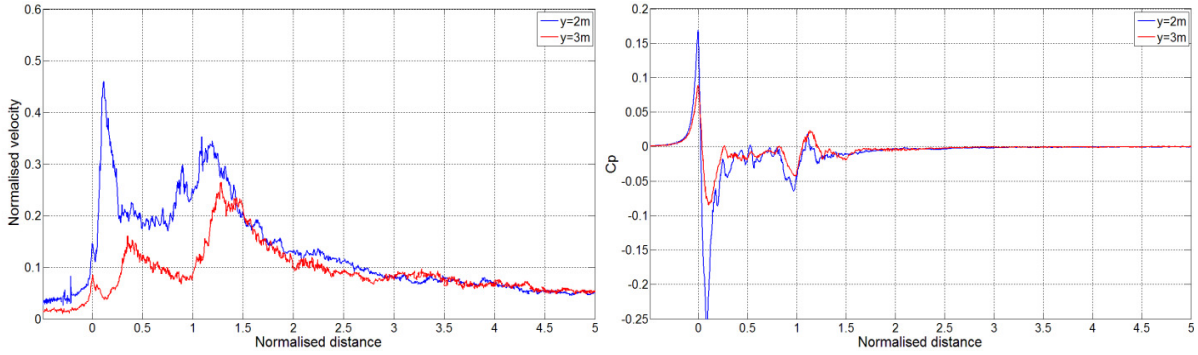

Figure C.2.3 - Slipstream and pressure for HST with BS1 at z = 0.7 m above TOR, y = 2.0 m and 3.0 m from COT.

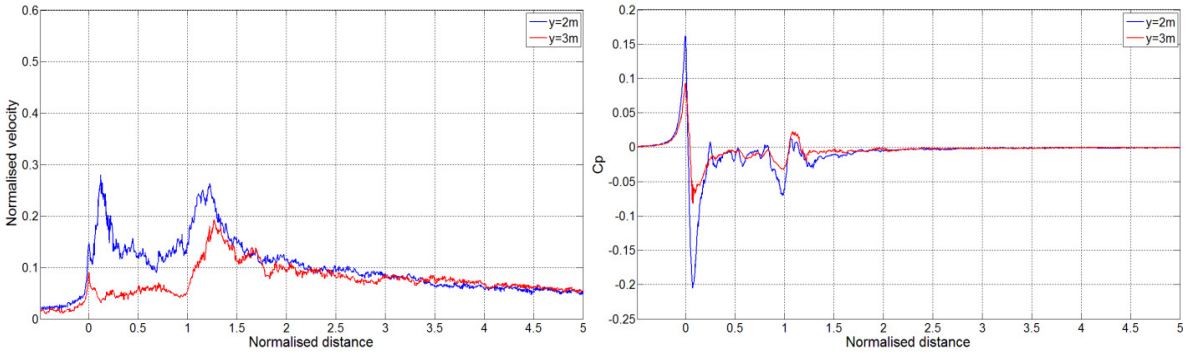

Figure C.2.4 - Slipstream and pressure for HST with BS1 at z = 1.2 m above TOR, y = 2.0 m and 3.0 m from COT.

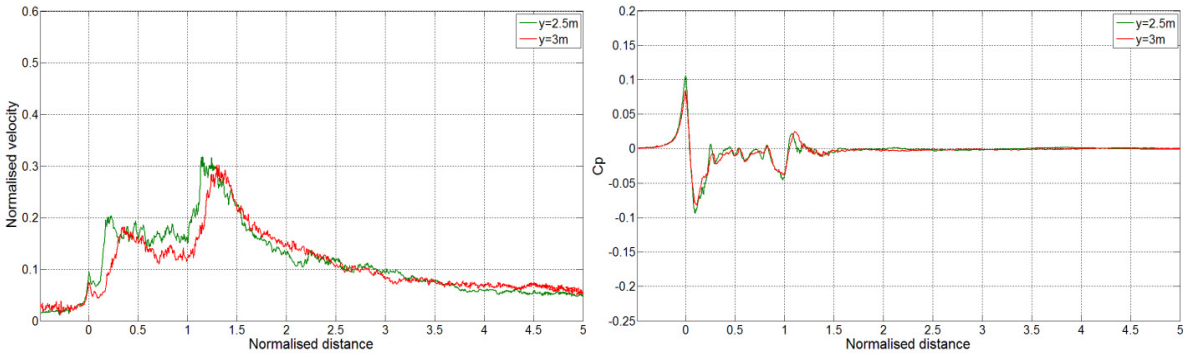

Figure C.2.5 - Slipstream and pressure for HST with BS2 at z = 0.3 m below TOR, y = 2.5 m and 3.0 m from COT.

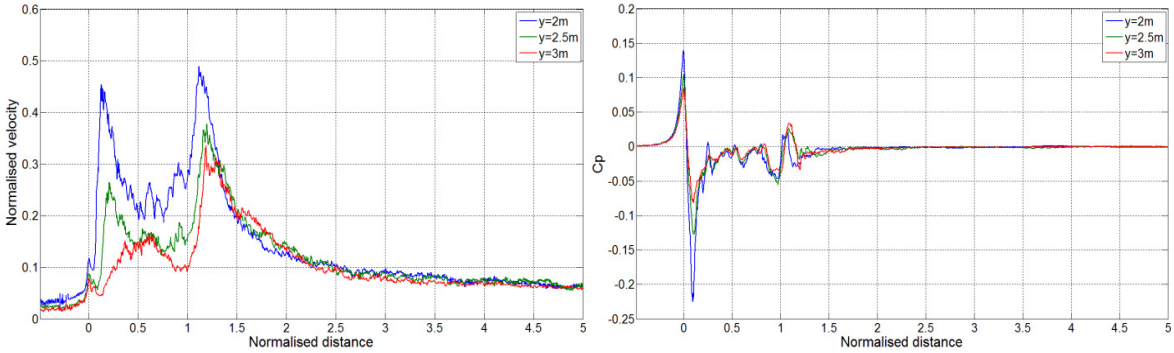

Figure C.2.6 - Slipstream and pressure for HST with BS2 at z = 0.0 m above TOR, y = 2.0 m, 2.5 m and 3.0 m from COT.

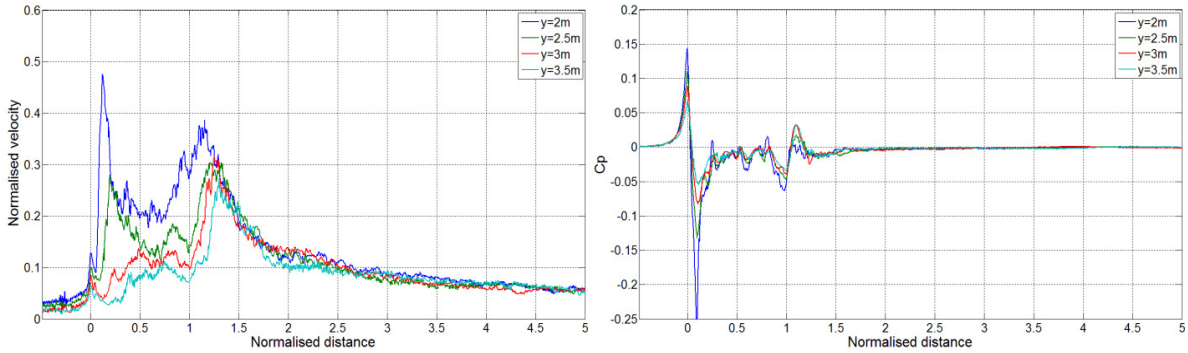

Figure C.2.7 - Slipstream and pressure for HST with BS2 at z = 0.2 m above TOR, y = 2.0 m, 2.5 m, 3.0 m and 3.5 m from COT.

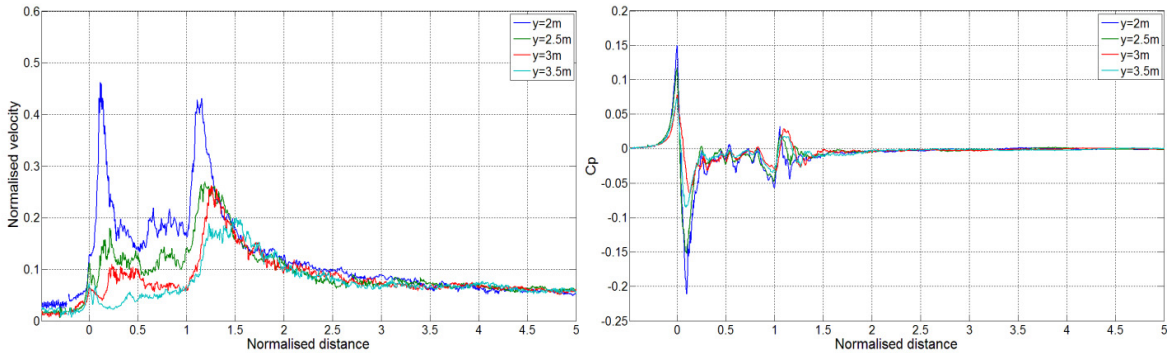

Figure C.2.8 - Slipstream and pressure for HST with BS2 at z = 0.7 m above TOR, y = 2.0 m, 2.5 m, 3.0 m and 3.5 m from COT.

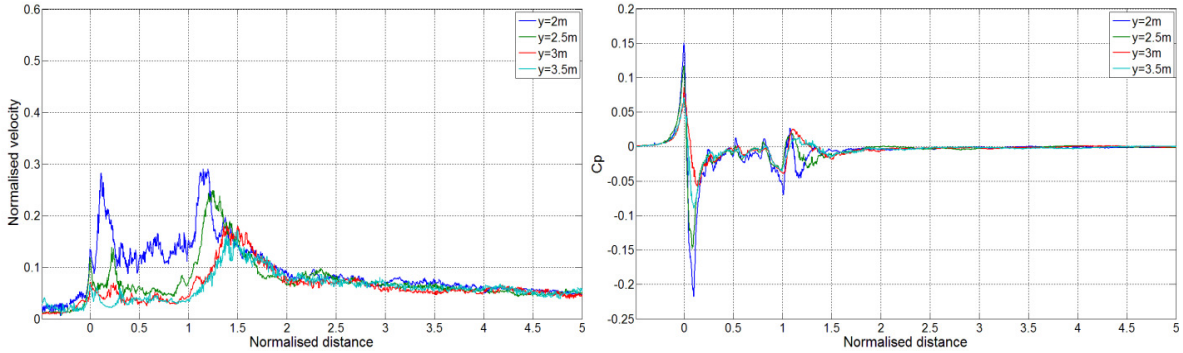

Figure C.2.9 - Slipstream and pressure for HST with BS2 at z = 1.2 m above TOR, y = 2.0 m, 2.5 m, 3.0 m and 3.5 m from COT.

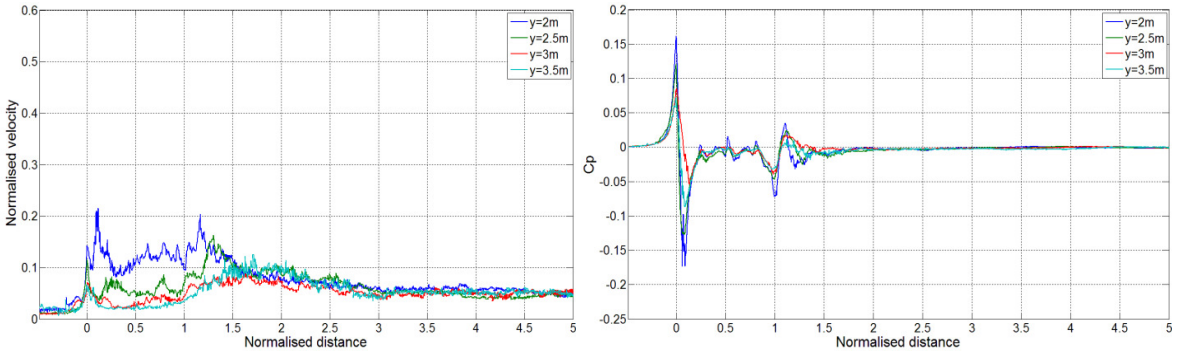

Figure C.2.10 - Slipstream and pressure for HST with BS2 at z = 1.75 m above TOR, y = 2.0 m, 2.5 m, 3.0 m and 3.5 m from COT.

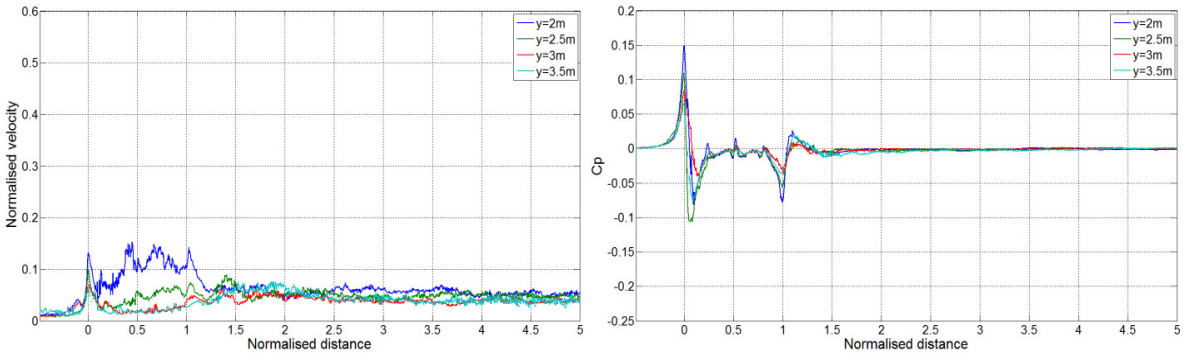

Figure C.2.11 - Slipstream and pressure for HST with BS2 at z = 2.3 m above TOR, y = 2.0 m, 2.5 m, 3.0 m and 3.5 m from COT.

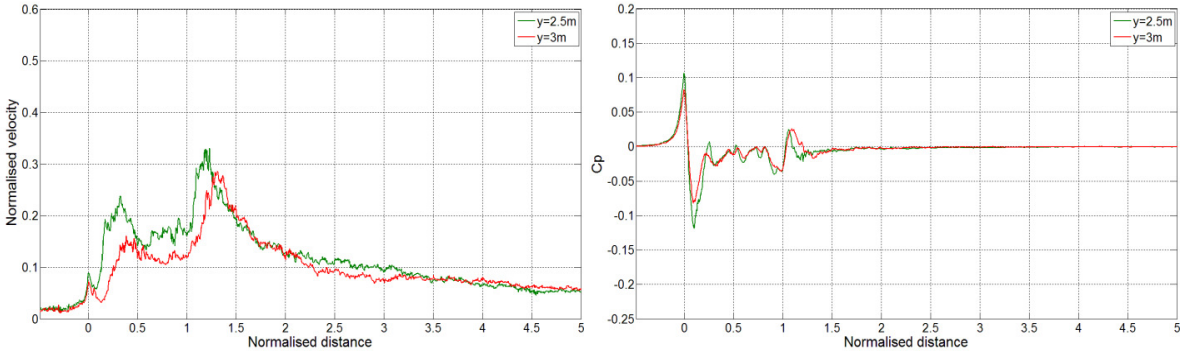

Figure C.2.12 - Slipstream and pressure for HST with BS3 at z = 0.3 m below TOR, y = 2.5 m and 3.0 m from COT.

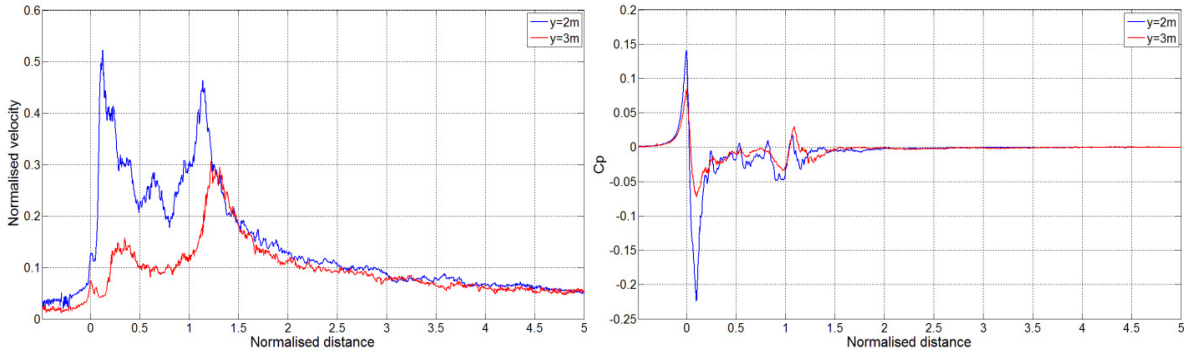

Figure C.2.13 - Slipstream and pressure for HST with BS3 at z = 0.0 m above TOR, y = 2.0 m and 3.0 m from COT.

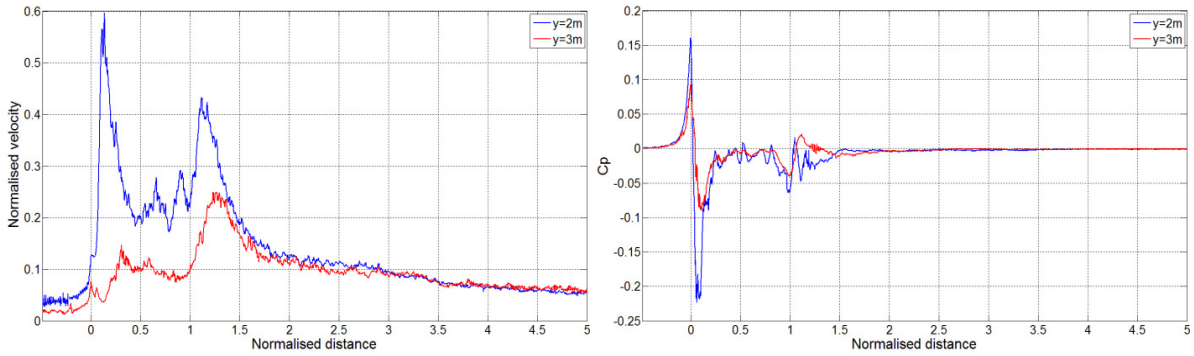

Figure C.2.14 - Slipstream and pressure for HST with BS3 at z = 0.2 m above TOR, y = 2.0 m and 3.0 m from COT.

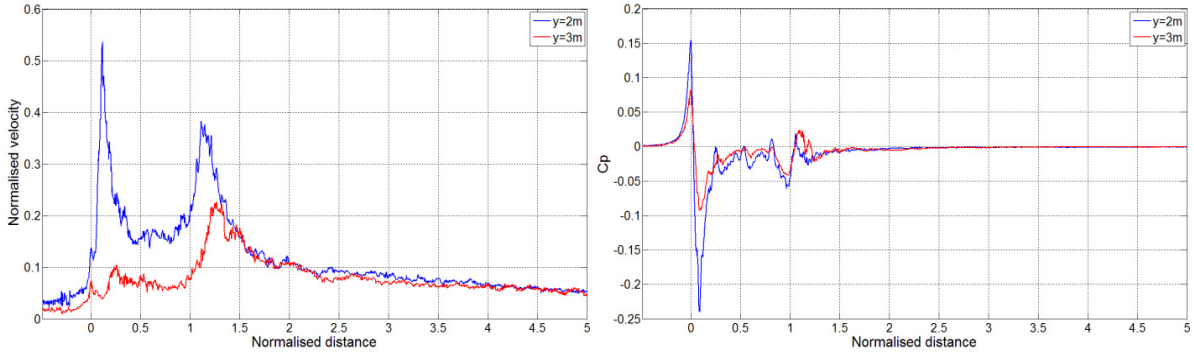

Figure C.2.15 - Slipstream and pressure for HST with BS3 at z = 0.7 m above TOR, y = 2.0 m and 3.0 m from COT.

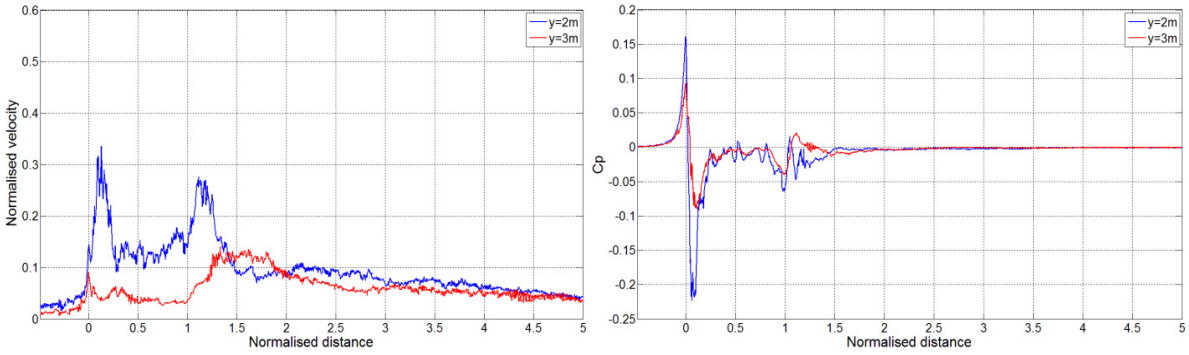

Figure C.2.16 - Slipstream and pressure for HST with BS3 at z = 1.2 m above TOR, y = 2.0 m and 3.0 m from COT.

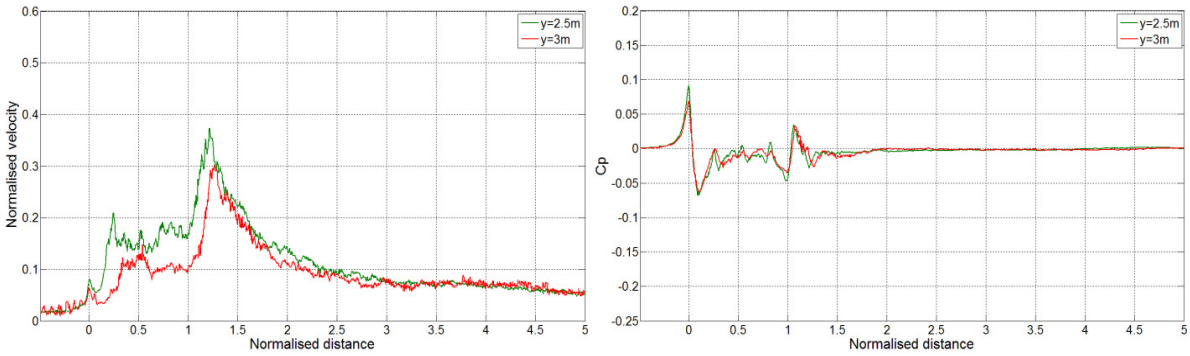

Figure C.2.17 - Slipstream and pressure for HST with BS5 at z = 0.3 m below TOR, y = 2.5 m and 3.0 m from COT.

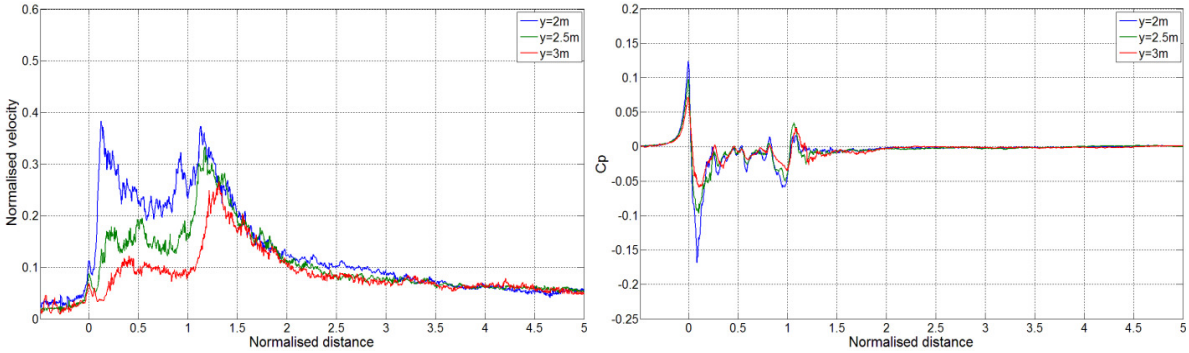

Figure C.2.18 - Slipstream and pressure for HST with BS5 at z = 0.0 above TOR, y = 2.0 m, 2.5 m and 3.0 m from COT.

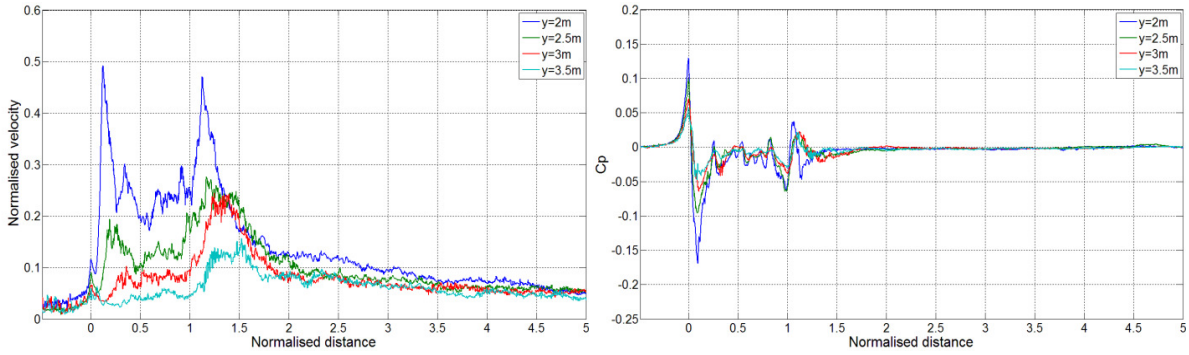

Figure C.2.19 - Slipstream and pressure for HST with BS5 at z = 0.2 above TOR, y = 2.0 m, 2.5 m, 3.0 m and 3.5 m from COT.

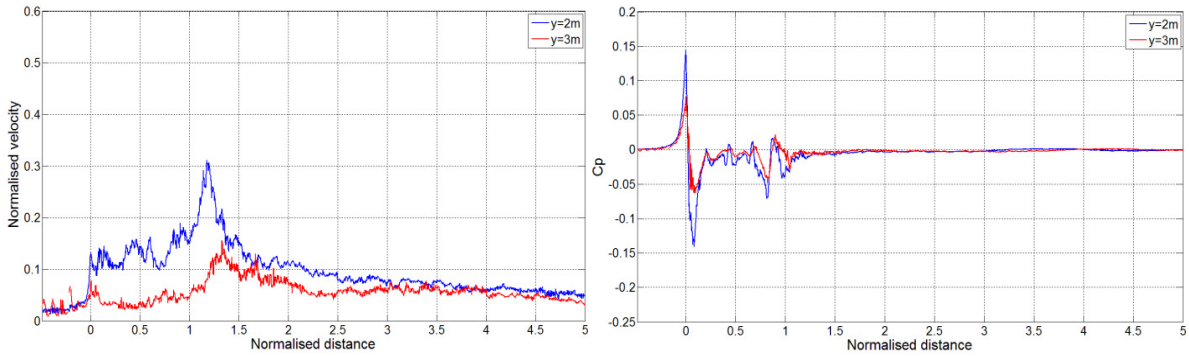

Figure C.2.20 - Slipstream and pressure for HST with BS5 at z = 1.2 m above TOR, y = 2.0 m and 3.0 m from COT.

C.2.2.2 HST results by distance from COT (y)

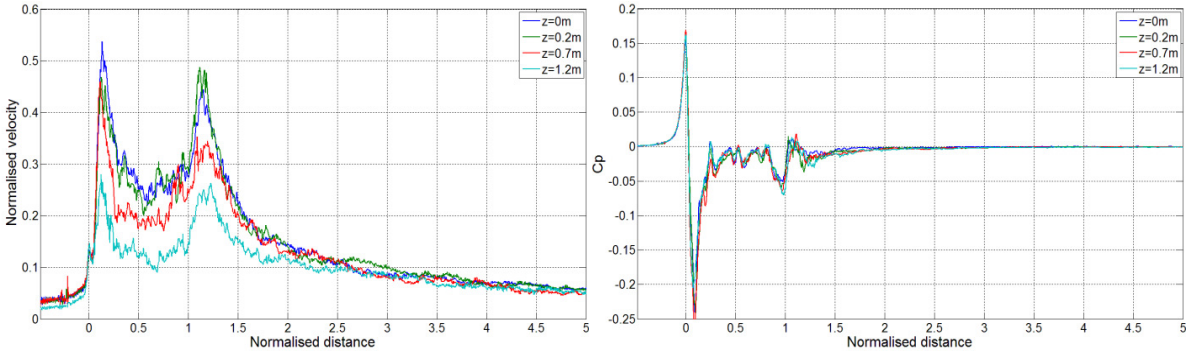

Figure C.2.21 - Slipstream and pressure for HST with BS1 at y = 2.0 m from COT, z = 0.0 m, 0.2 m, 0.7 m and 1.2 m from TOR.

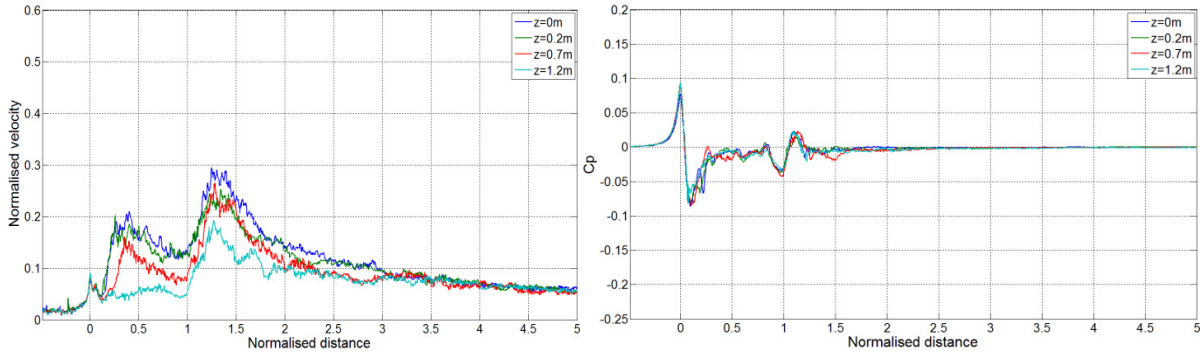

Figure C.2.22 - Slipstream and pressure for HST with BS1 at y = 3.0 m from COT, z = 0.0 m, 0.2 m, 0.7 m, and 1.2 m from TOR.

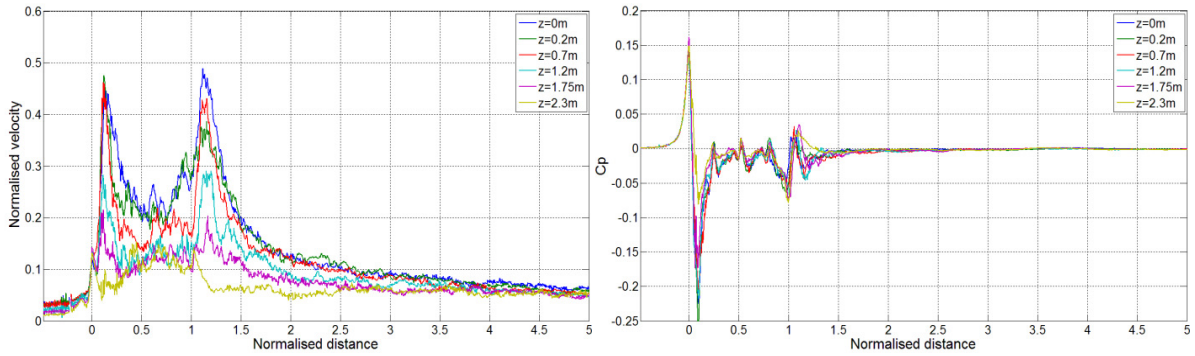

Figure C.2.23 - Slipstream and pressure for HST with BS2 at y = 2.0 m from COT, z = 0.0 m, 0.2 m, 0.7 m, 1.2 m, 1.75 m and 2.3 m above TOR.

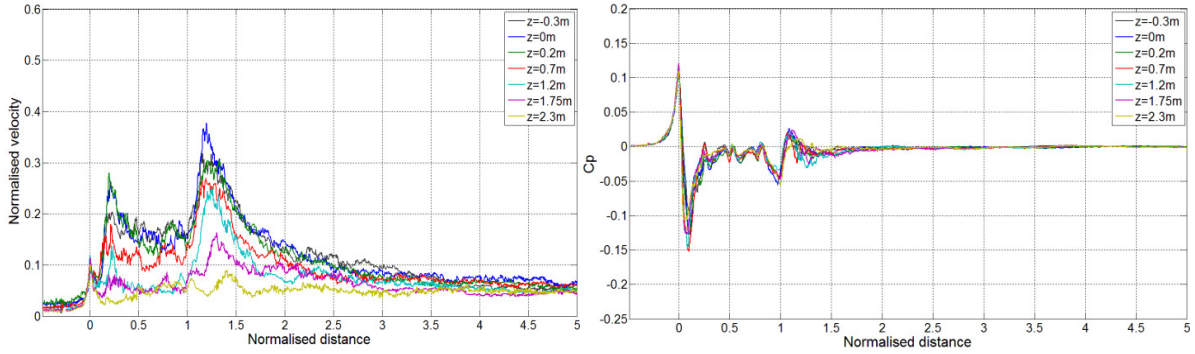

Figure C.2.24 - Slipstream and pressure for HST with BS2 at y = 2.5 m from COT, z = 0.3 m below and 0.0 m, 0.2 m, 0.7 m, 1.2 m, 1.75 m and 2.3 m above TOR.

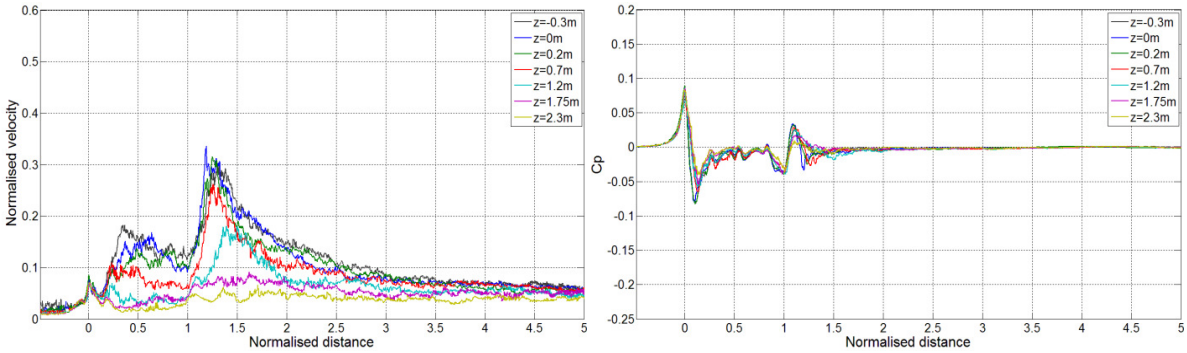

Figure C.2.25 - Slipstream and pressure for HST with BS2 at y = 3.0 m from COT, z = 0.3 m below and 0.0 m, 0.2 m, 0.7 m, 1.2 m and 2.3 m above TOR.

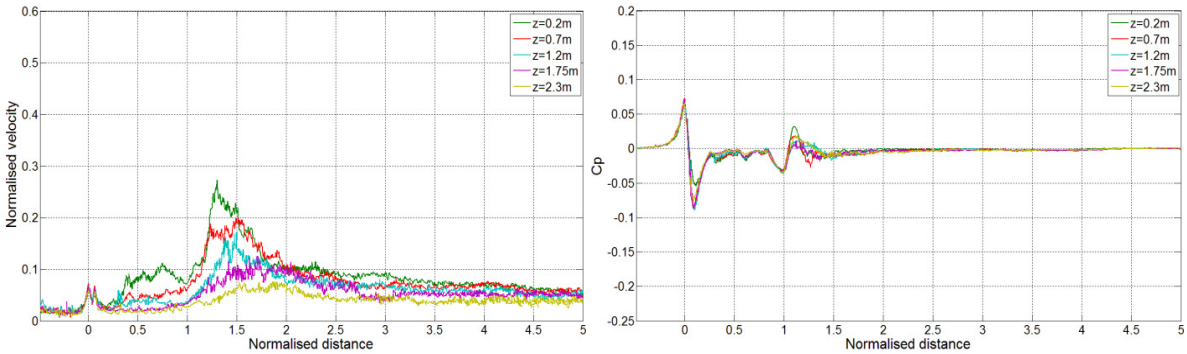

Figure C.2.26 - Slipstream and pressure for HST with BS2 at y = 3.5 m from COT, z = 0.2 m, 0.7 m, 1.2 m and 2.3 m above TOR.

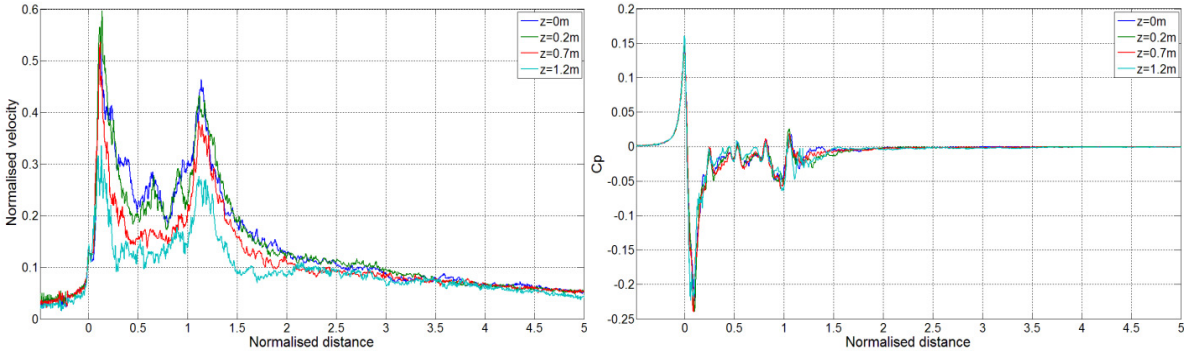

Figure C.2.27 - Slipstream and pressure for HST with BS3 at y = 2.0 m from COT, z = 0.0 m, 0.2 m, 1.2 m and 2.3 m above TOR.

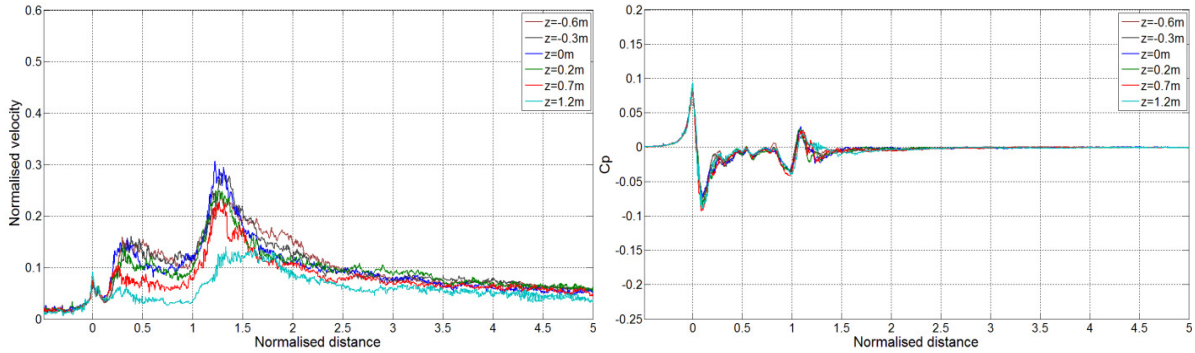

Figure C.2.28 - Slipstream and pressure for HST with BS3 at y = 3.0 m from COT, z = 0.6 m and 0.3 m below and 0.0 m, 0.2 m, 1.2 m and 2.3 m above TOR.

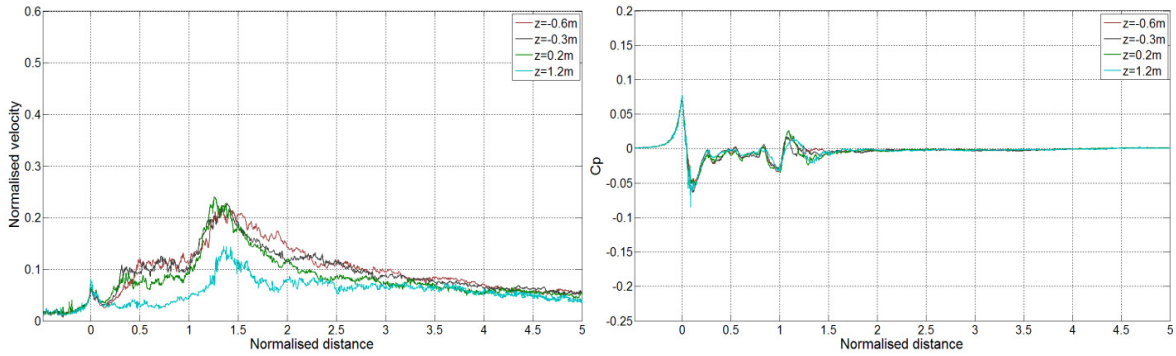

Figure C.2.29 - Slipstream and pressure for HST with BS4 at y = 3.0 m from COT, z = 0.6 m and 0.3 m below and 0.2 m and 1.2 m above TOR.

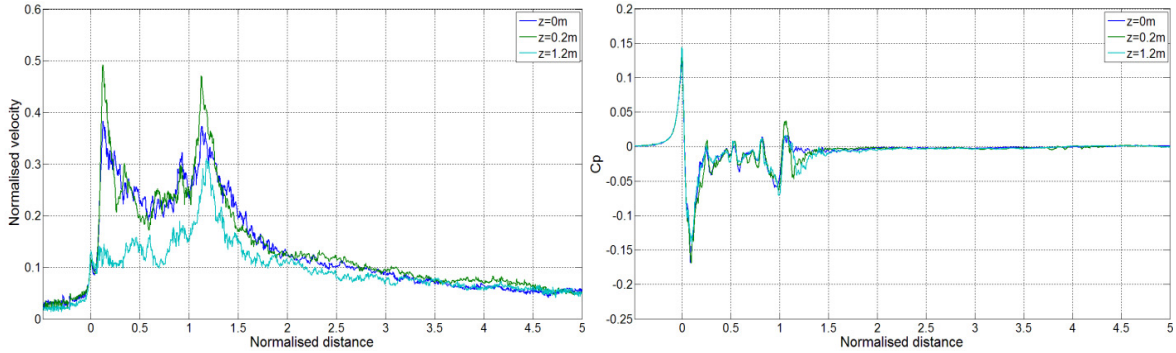

Figure C.2.30 - Slipstream and pressure for HST with BS5 at y = 2.0 m from COT, z = 0.0 m, 0.2 m and 1.2 m above TOR.

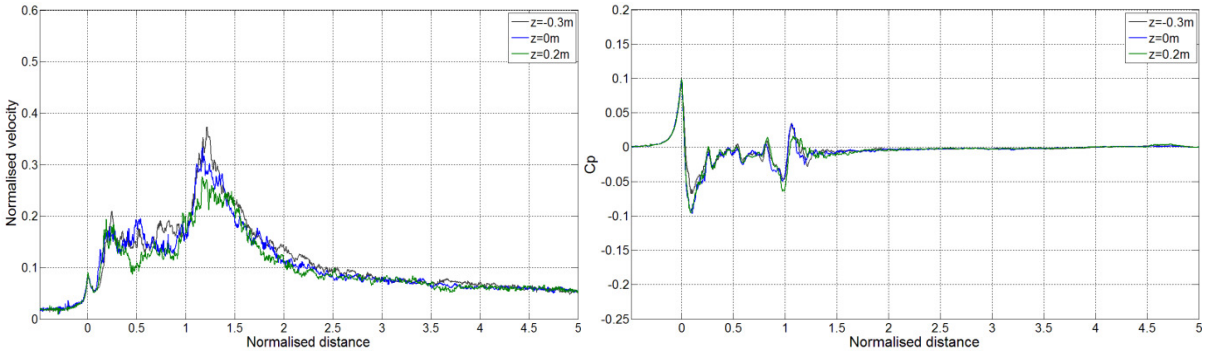

Figure C.2.31 - Slipstream and pressure for HST with BS5 at y = 2.5 m from COT, z = 0.3 m below and 0.0 m and 0.2 m above TOR.

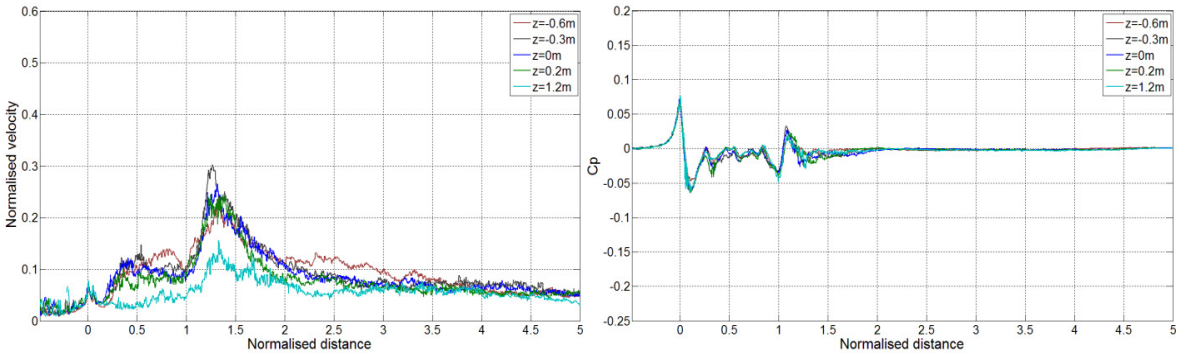

Figure C.2.32 - Slipstream and pressure for HST with BS5 at y = 3.0 m from COT, z = 0.6 and 0.3 m below and 0.0 m, 0.2 m and 1.2 m above TOR.

C.2.2.3 HST results by ballast height

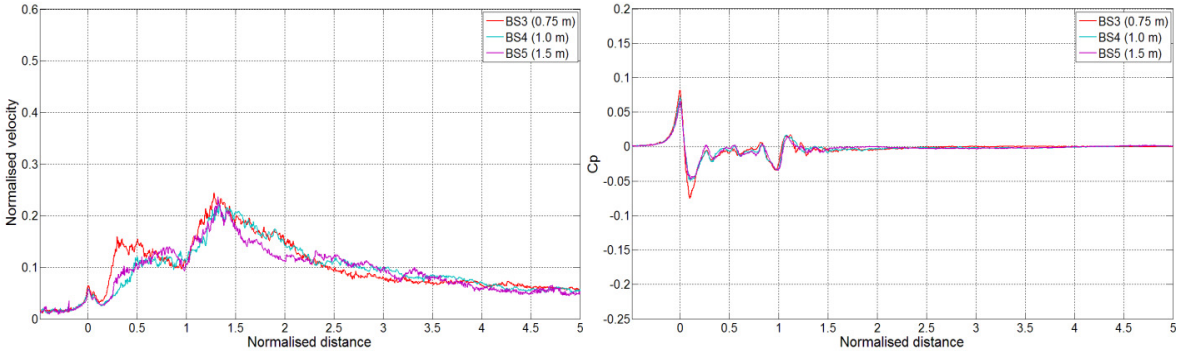

Figure C.2.33 - Slipstream and pressure for HST with BS3, BS4 and BS5 at y = 2.5 m from COT, z = 0.6 m below TOR.

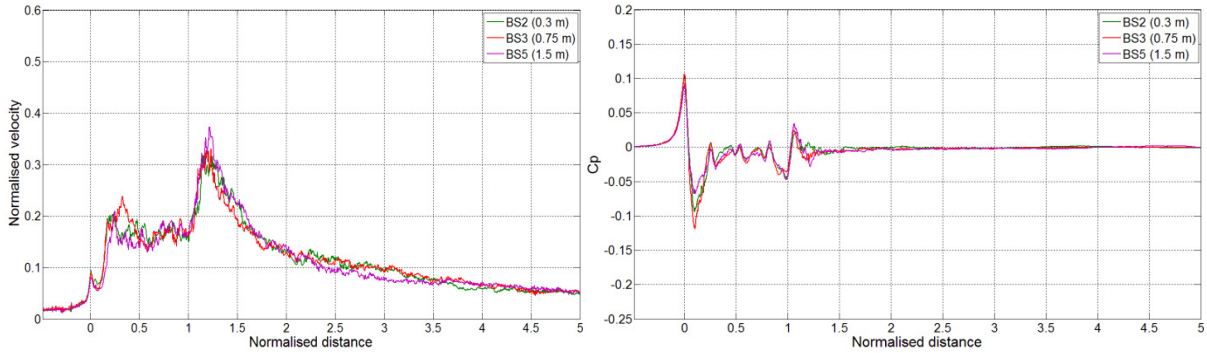

Figure C.2.34 - Slipstream and pressure for HST with BS2, BS3 and BS5 at y = 2.5 m from COT, z = 0.3 m below TOR.

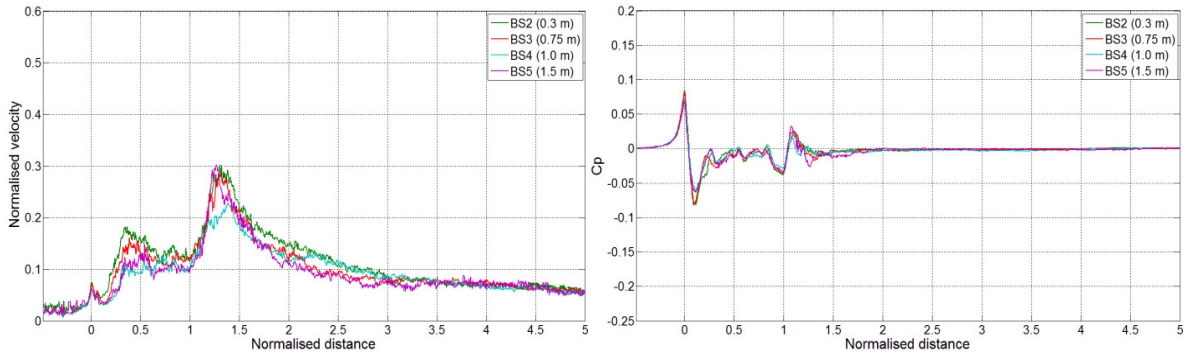

Figure C.2.35 - Slipstream and pressure for HST with BS2, BS3, BS4 and BS5 at y = 3.0 m from COT, z = 0.3 m below TOR.

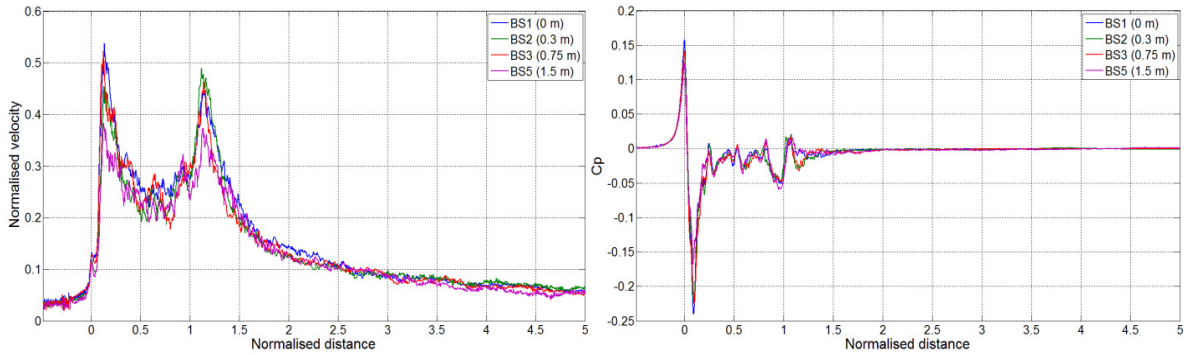

Figure C.2.36 - Slipstream and pressure for HST with BS1, BS2, BS3 and BS5 at y = 2.0 m from COT, z = 0.0 m above TOR.

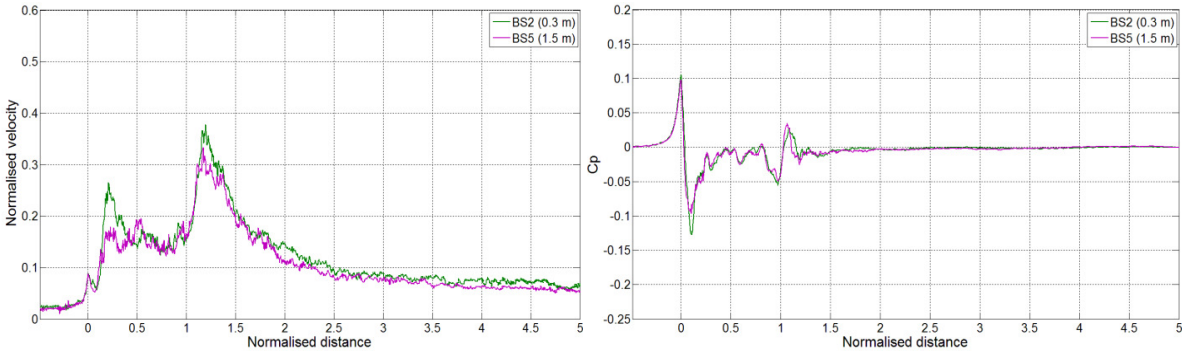

Figure C.2.37 - Slipstream and pressure for HST with BS2 and BS5 at y = 2.5 m from COT, z = 0.0 m above TOR.

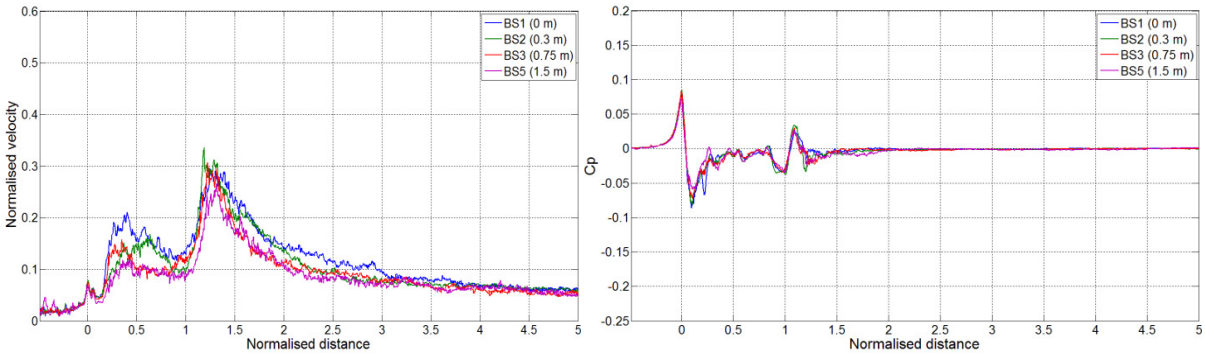

Figure C.2.38 - Slipstream and pressure for HST with BS1, BS2, BS3 and BS5 at y = 3.0 m from COT, z = 0.0 m above TOR.

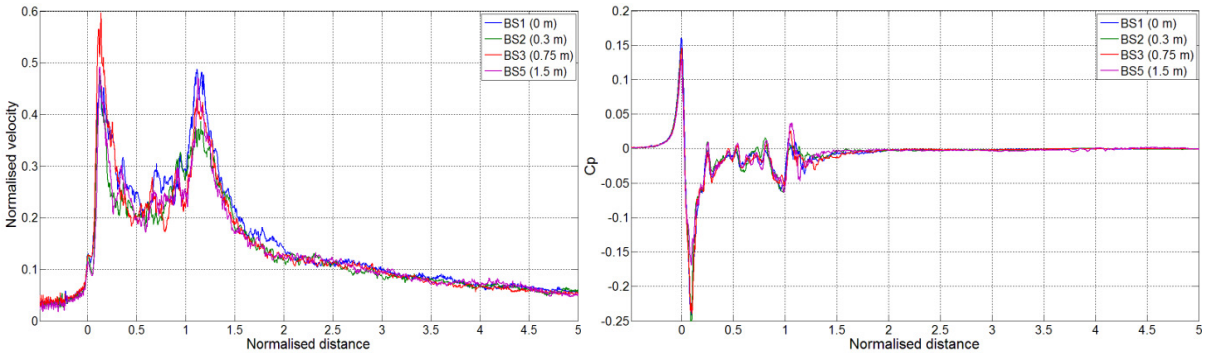

Figure C.2.39 - Slipstream and pressure for HST with BS1, BS2, BS3 and BS5 at y = 2.0 m from COT, z = 0.2 m above TOR.

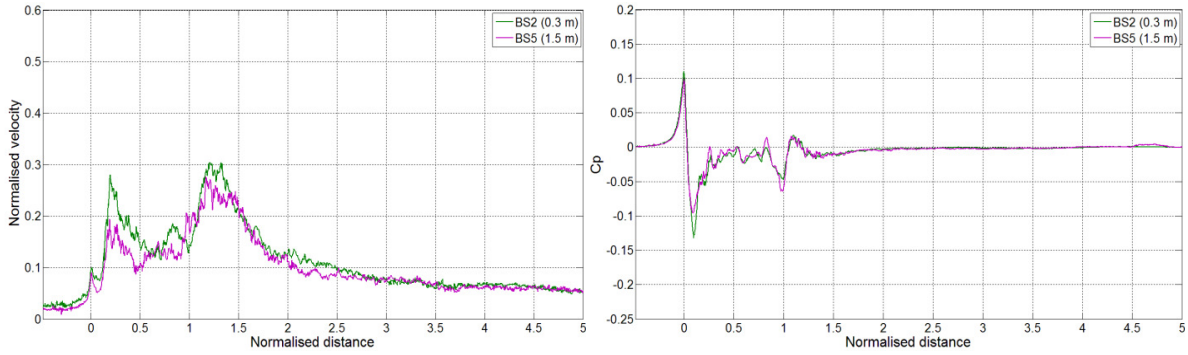

Figure C.2.40 - Slipstream and pressure for HST with BS2 and BS5 at y = 2.5 m from COT, z = 0.2 m above TOR.

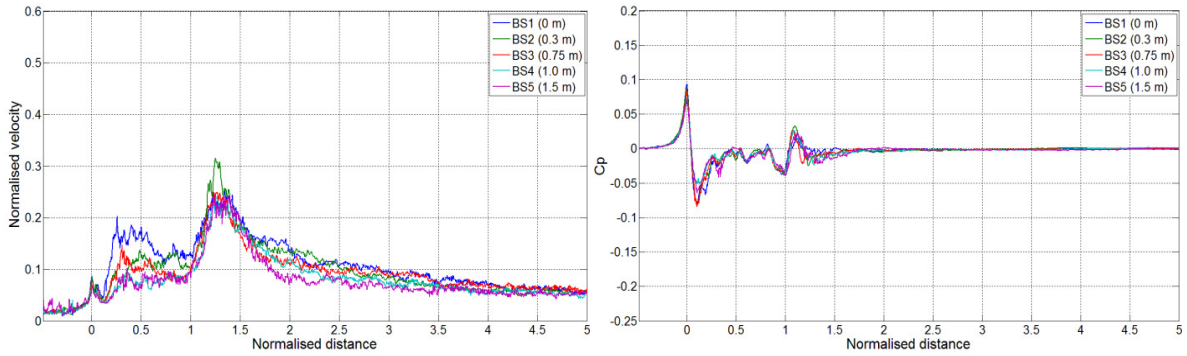

Figure C.2.41 - Slipstream and pressure for HST with BS1, BS2, BS3, BS4 and BS5 at y = 3.0 m from COT, z = 0.2 m above TOR.

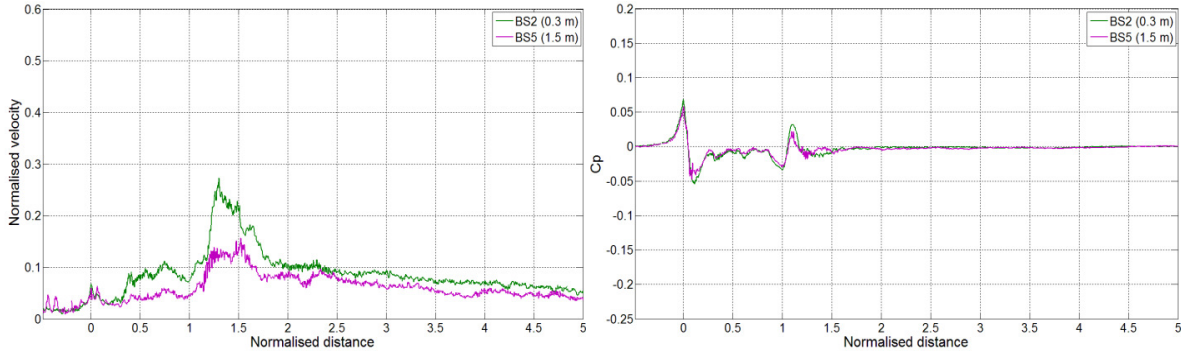

Figure C.2.42 - Slipstream and pressure for HST with BS2 and BS5 at y = 3.5 m from COT, z = 0.2 m above TOR.

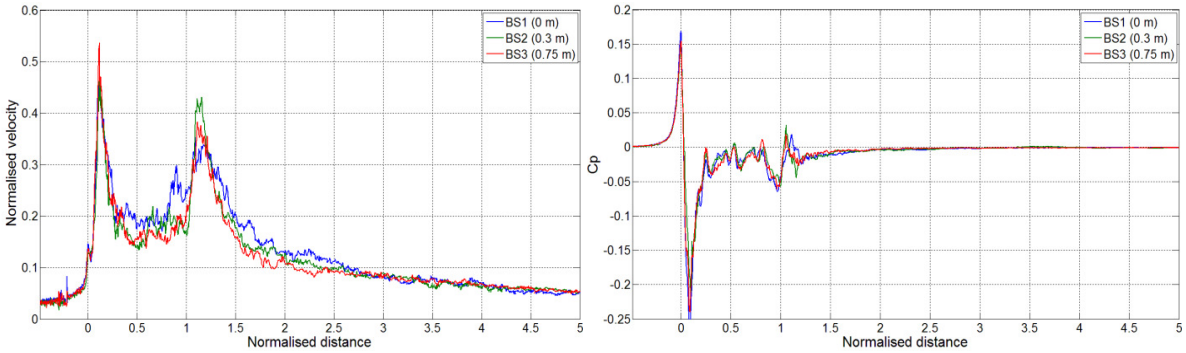

Figure C.2.43 - Slipstream and pressure for HST with BS1, BS2 and BS3 at y = 2.0 m from COT, z = 0.7 m above TOR.

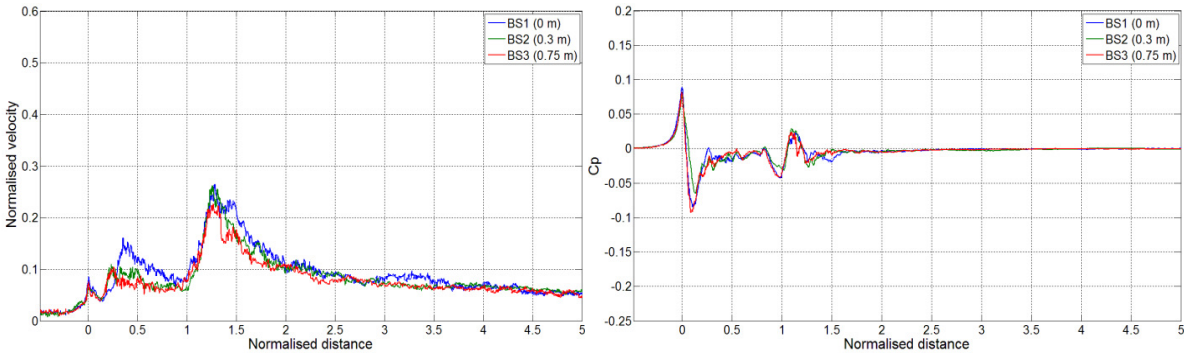

Figure C.2.44 - Slipstream and pressure for HST with BS1, BS2 and BS3 at y = 3.0 m from COT, z = 0.7 m above TOR.

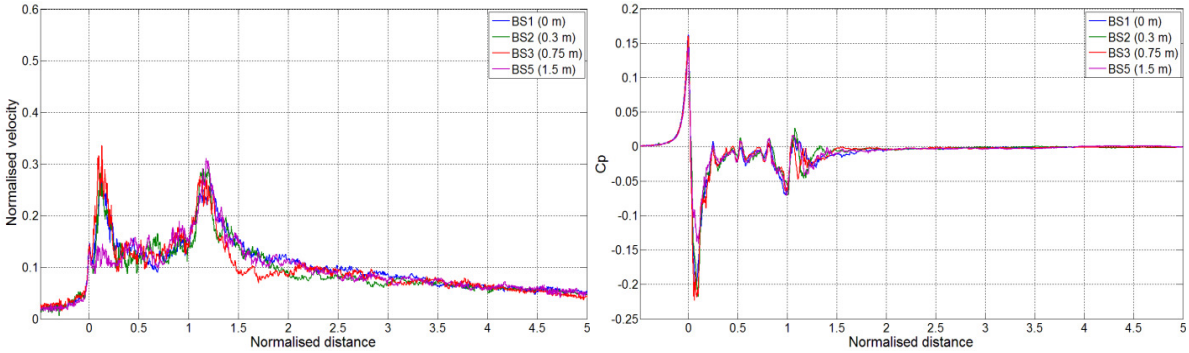

Figure C.2.45 - Slipstream and pressure for HST with BS1, BS2, BS3 and BS5 at y = 2.0 m from COT, z = 1.2 m above TOR.

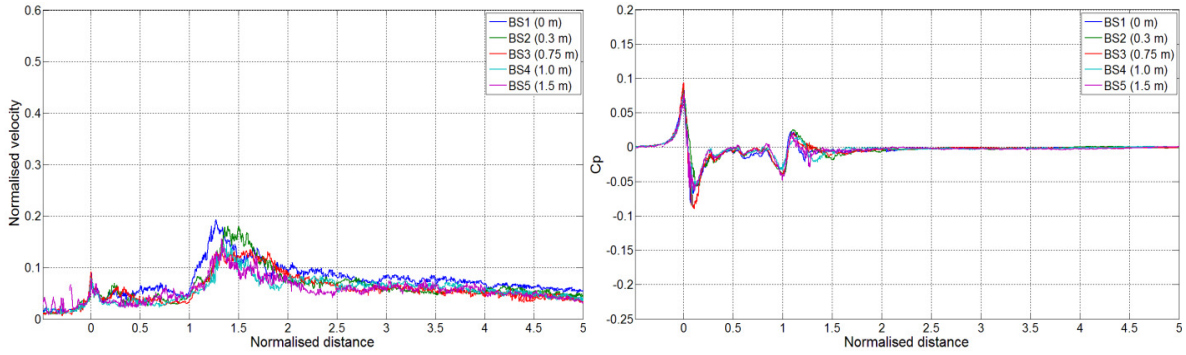

Figure C.2.46 - Slipstream and pressure for HST with BS1, BS2, BS3, BS4 and BS5 at y = 3.0 m from COT, z = 1.2 m above TOR.

C.2.3 Freight results

C.2.3.1 Freight results by height above TOR (z)

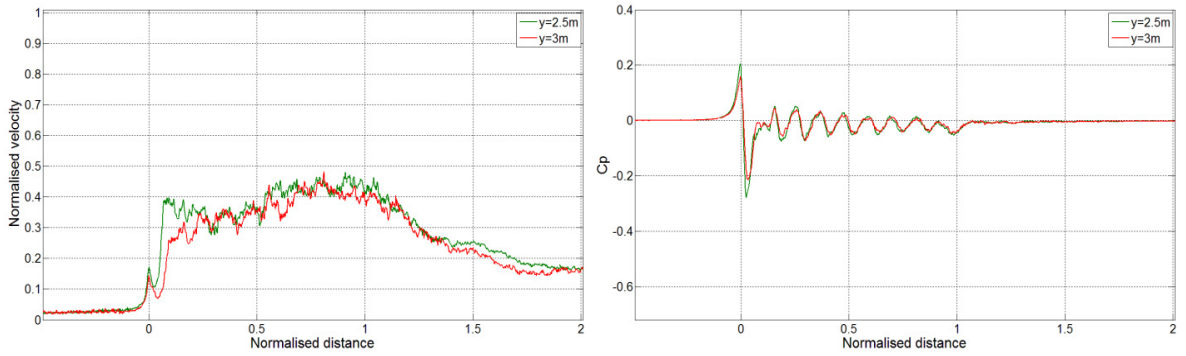

Figure C.3.1 - Slipstream and pressure for freight with BS2 at z = 0.3 m below TOR, y = 2.5 m and 3.0 m from COT.

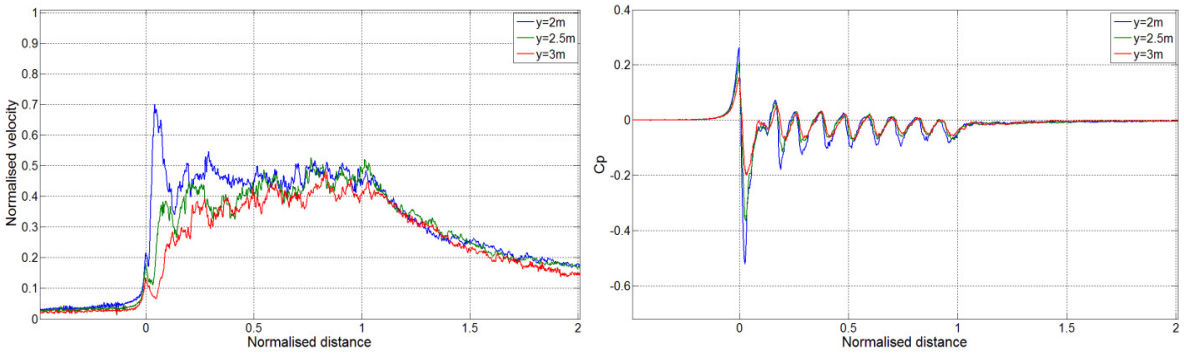

Figure C.3.2 - Slipstream and pressure for freight with BS2 at z = 0.0 m above TOR, y = 2.0 m, 2.5 m and 3.0 m from COT.

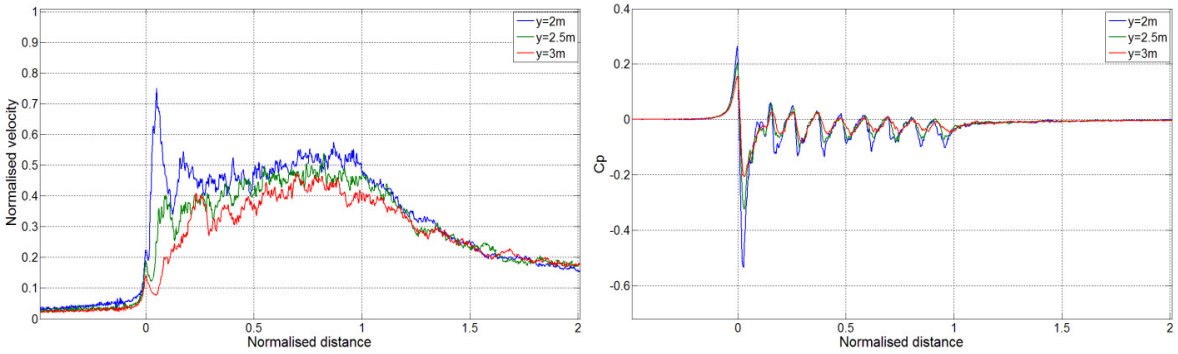

Figure C.3.3 - Slipstream and pressure for freight with BS2 at z = 0.2 m above TOR, y = 2.0, 2.5 m and 3.0 m from COT.

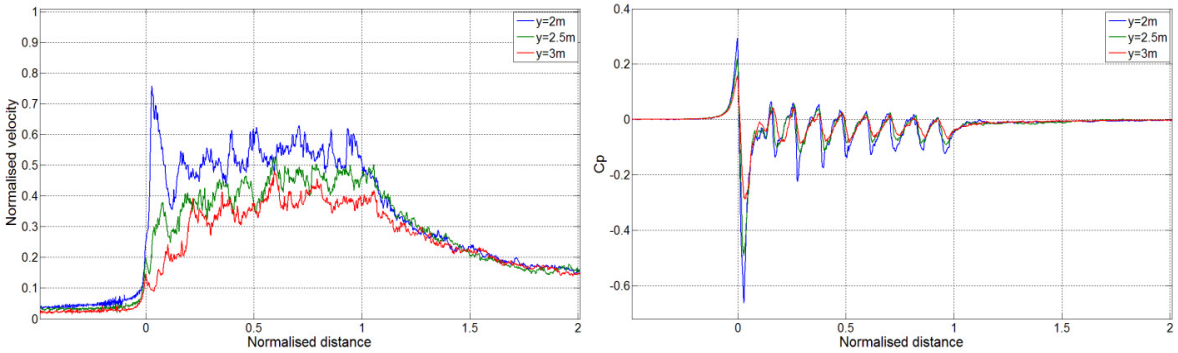

Figure C.3.4 - Slipstream and pressure for freight with BS2 at z = 0.7 m above TOR, y = 2.0, 2.5 m and 3.0 m from COT.

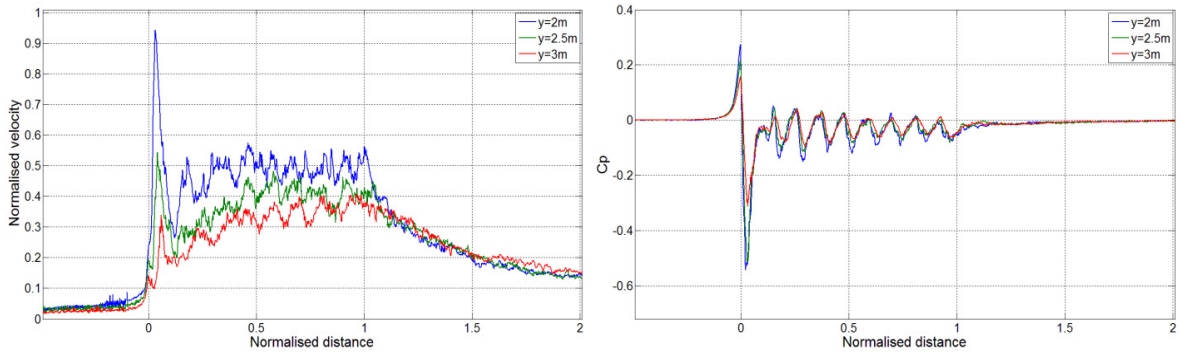

Figure C.3.5 - Slipstream and pressure for freight with BS2 at z = 1.2 m above TOR, y = 2.0, 2.5 m and 3.0 m from COT.

C.2.3.2 Freight results by distance from COT (y)

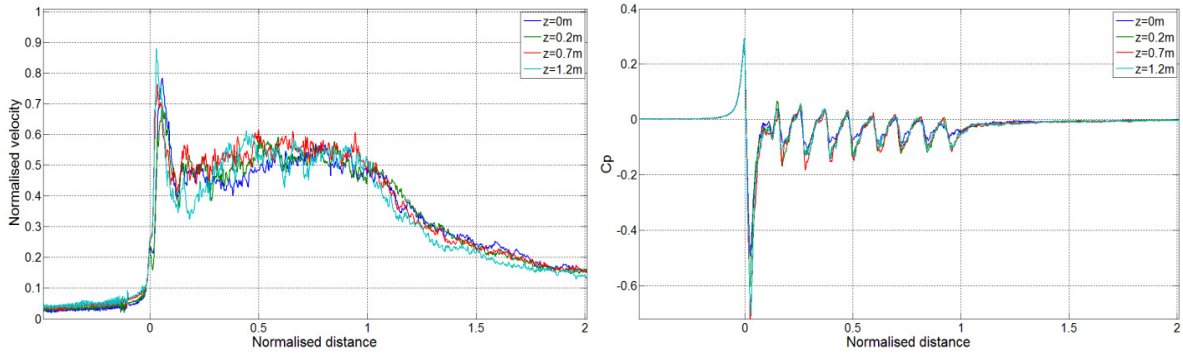

Figure C.3.6 - Slipstream and pressure for freight with BS1 at y = 2.0 m from COT, z = 0.0 m, 0.2 m, 0.7 m and 1.2 m above TOR.

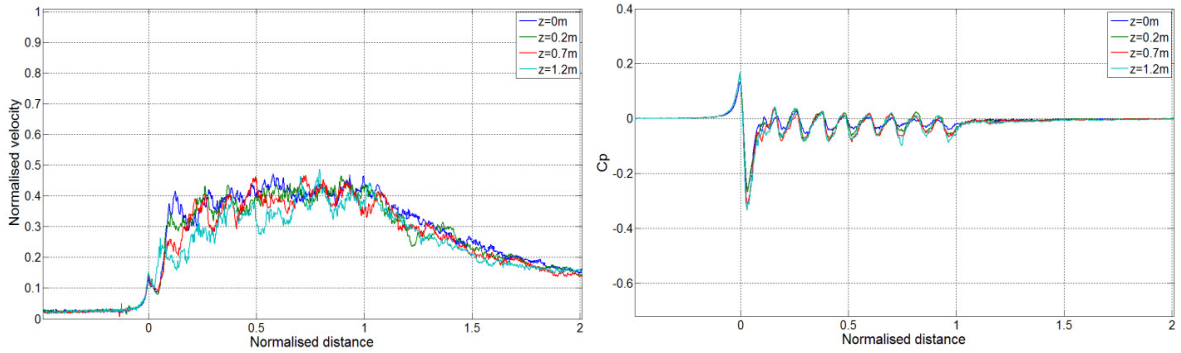

Figure C.3.7 - Slipstream and pressure for freight with BS1 at y = 3.0 m from COT, z = 0.0 m, 0.2 m, 0.7 m and 1.2 m above TOR.

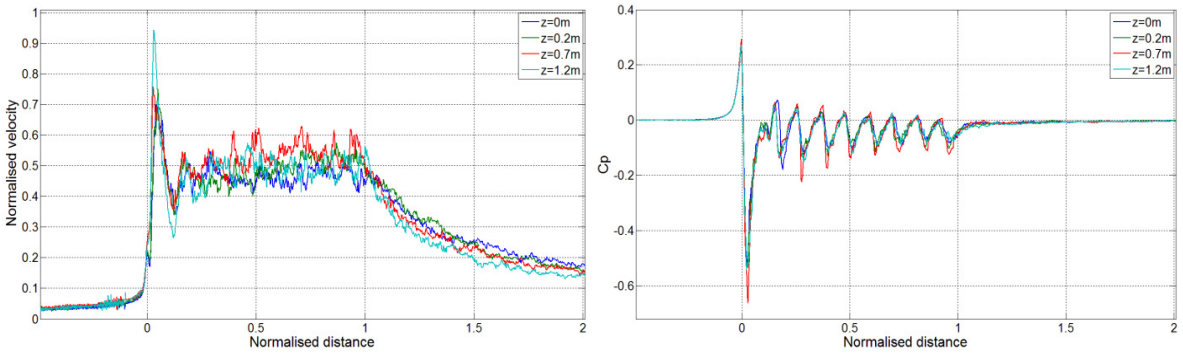

Figure C.3.8 - Slipstream and pressure for freight with BS2 at y = 2.0 m from COT, z = 0.0 m, 0.2 m, 0.7 m and 1.2 m above TOR.

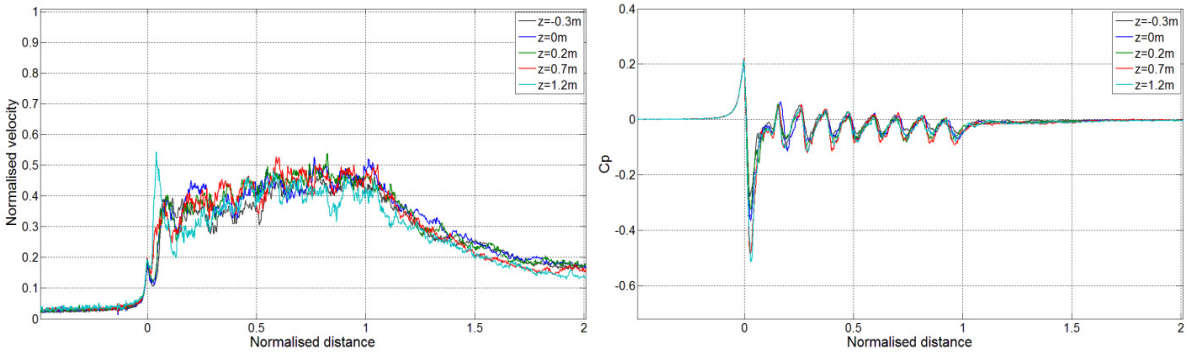

Figure C.3.9 - Slipstream and pressure for freight with BS2 at y = 2.5 m from COT, z = 0.3 m below and 0.0 m, 0.2 m, 0.7 m and 1.2 m above TOR.

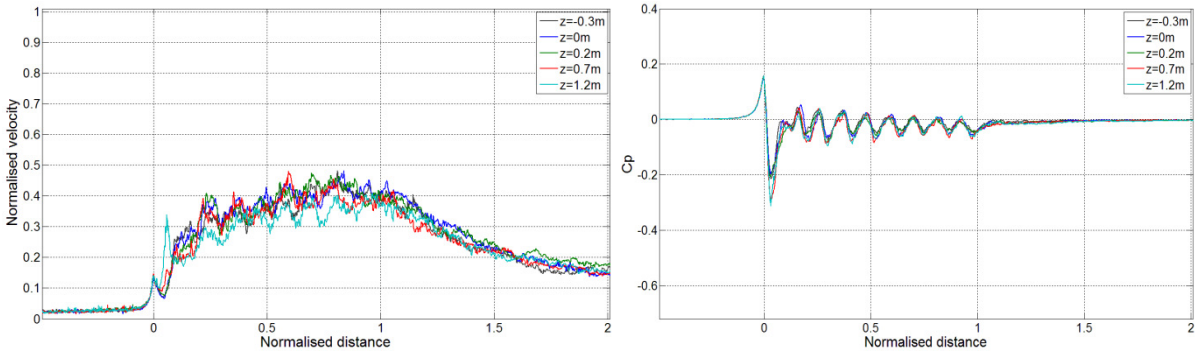

Figure C.3.10 - Slipstream and pressure for freight with BS2 at y = 3.0 m from COT, z = 0.3 m below and 0.0 m, 0.2 m, 0.7 m and 1.2 m above TOR.

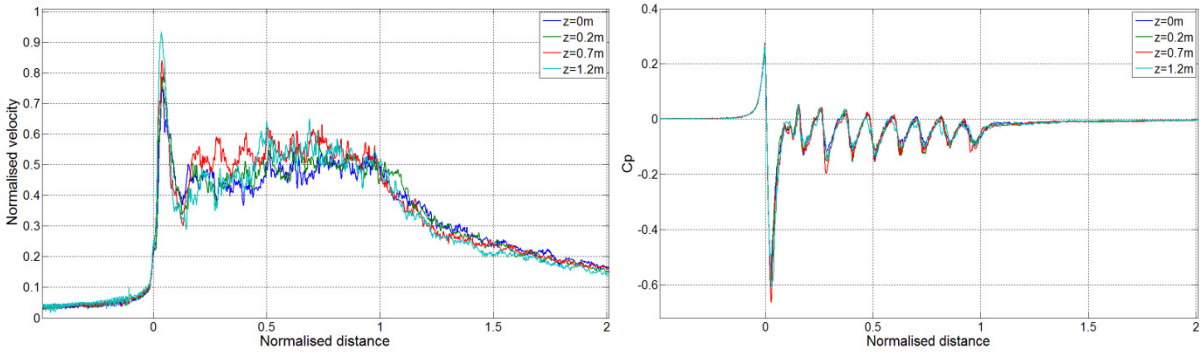

Figure C.3.11 - Slipstream and pressure for freight with BS3 at y = 2.0 m from COT, z = 0.0 m, 0.2 m, 0.7 m and 1.2 m above TOR.

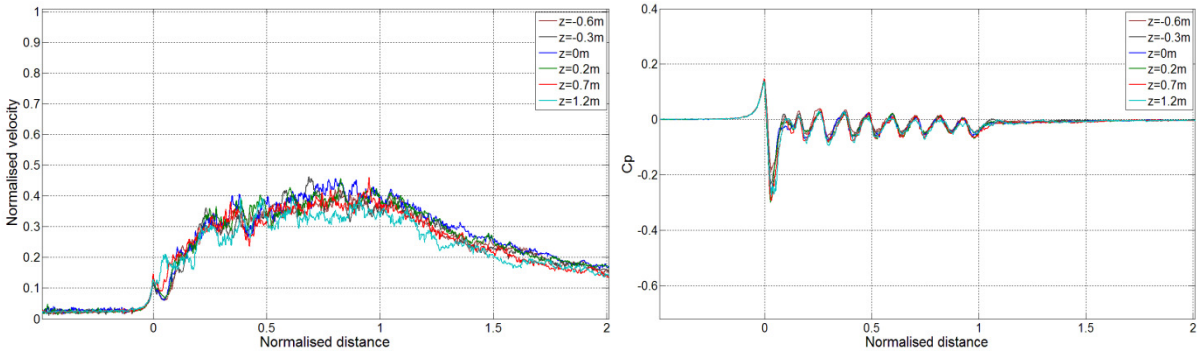

Figure C.3.12 - Slipstream and pressure for freight with BS3 at y = 3.0 m from COT, z = 0.6 m and 0.3 m below and 0.0 m, 0.2 m, 0.7 m and 1.2 m above TOR.

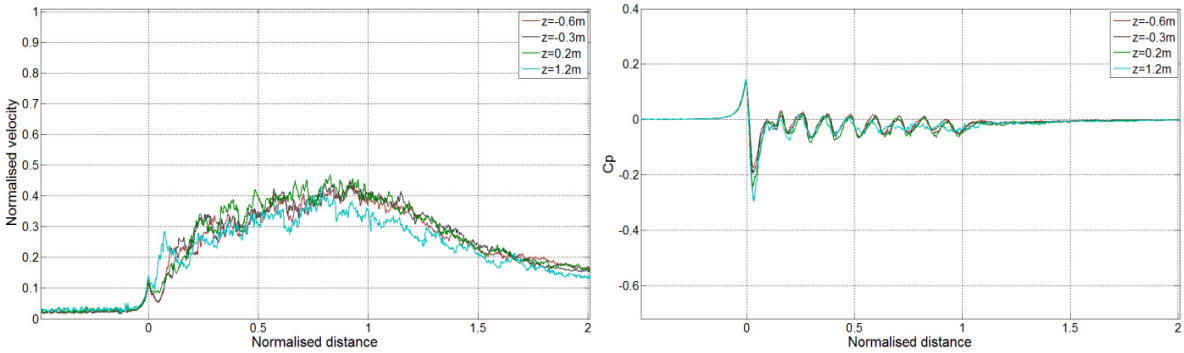

Figure C.3.13 - Slipstream and pressure for freight with BS4 at y = 3.0 m from COT, z = 0.6 m and 0.3 m below and 0.2 m and 1.2 m above TOR.

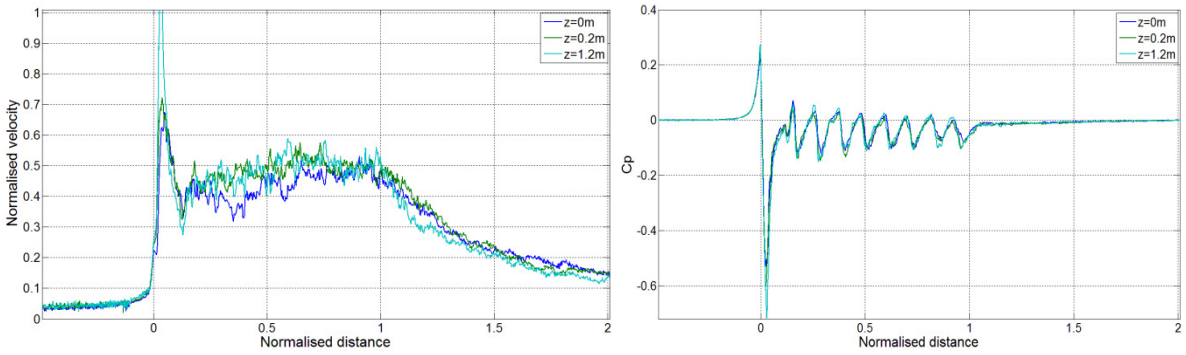

Figure C.3.14 - Slipstream and pressure for freight with BS5 at y = 2.0 m from COT, z = 0.0 m, 0.2 m and 1.2 m above TOR.

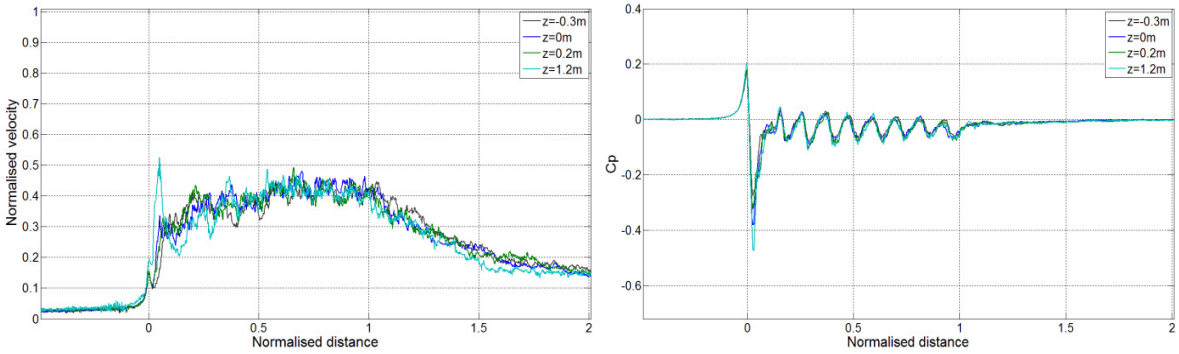

Figure C.3.15 - Slipstream and pressure for freight with BS5 at y = 2.5 m from COT, z = 0.3 m below and 0.0 m, 0.2 m and 1.2 m above TOR.

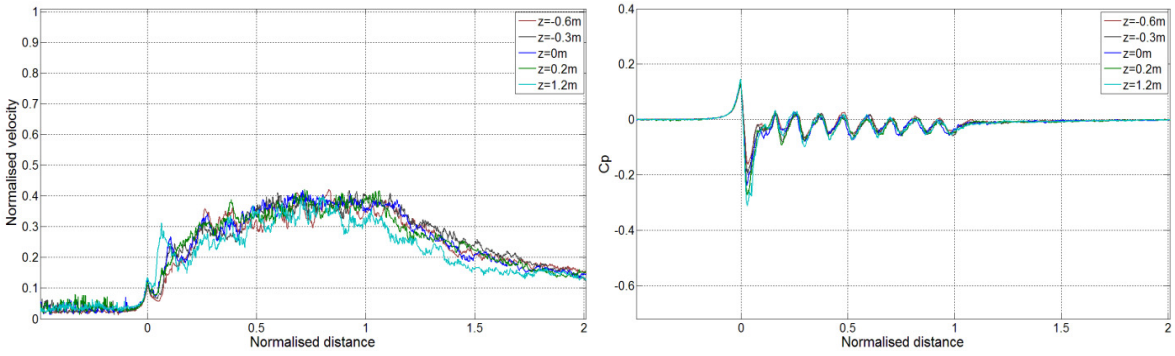

Figure C.3.16 - Slipstream and pressure for freight with BS5 at y = 3.0 m from COT, z = 0.6 m and 0.3 m below and 0.0 m, 0.2 m and 1.2 m above TOR.

C.2.3.3 Freight results by ballast height

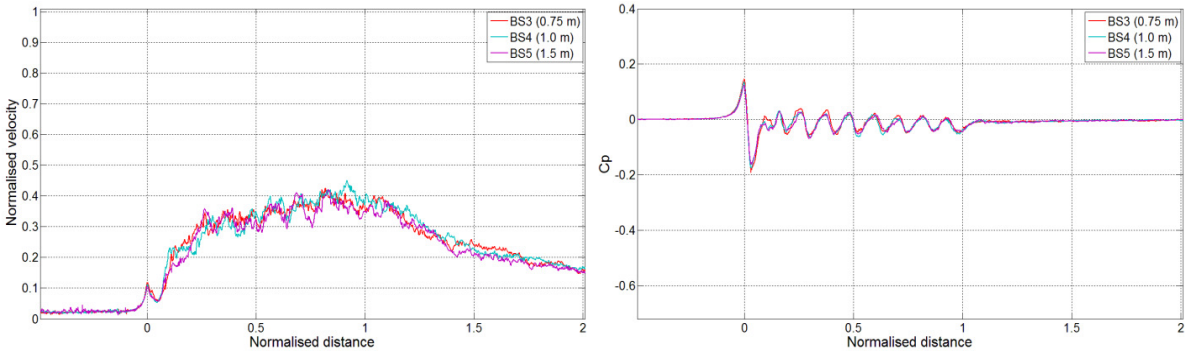

Figure C.3.17 - Slipstream and pressure for freight with BS3, BS4 and BS5 at y = 3.0 m from COT, z = 0.6 m below TOR.

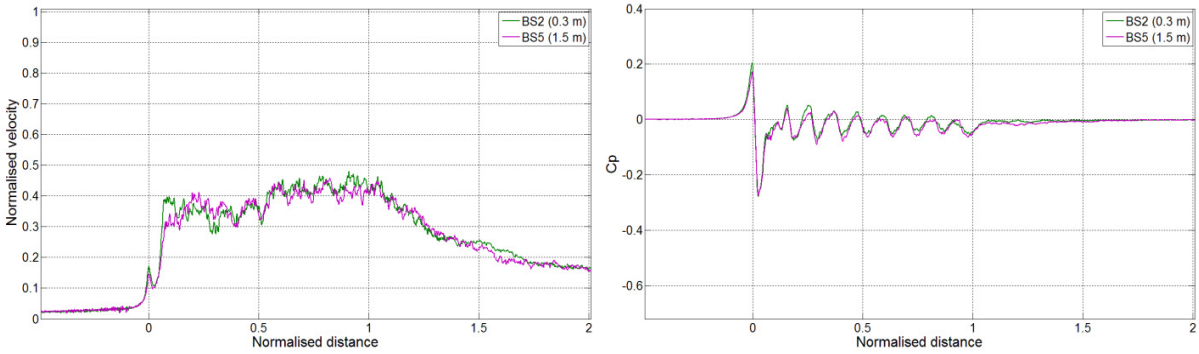

Figure C.3.18 - Slipstream and pressure for freight with BS2 and BS5 at y = 2.5 m from COT, z = 0.3 m below TOR.

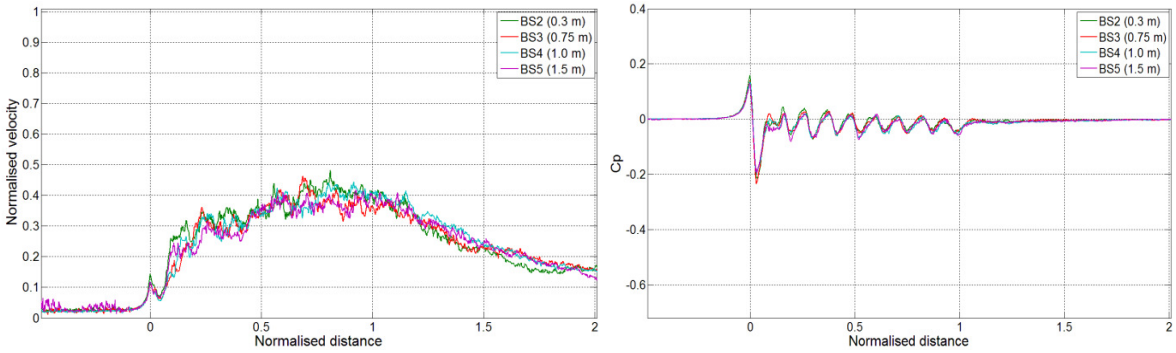

Figure C.3.19 - Slipstream and pressure for freight with BS2, BS3, BS4 and BS5 at y = 3.0 m from COT, z = 0.3 m below TOR.

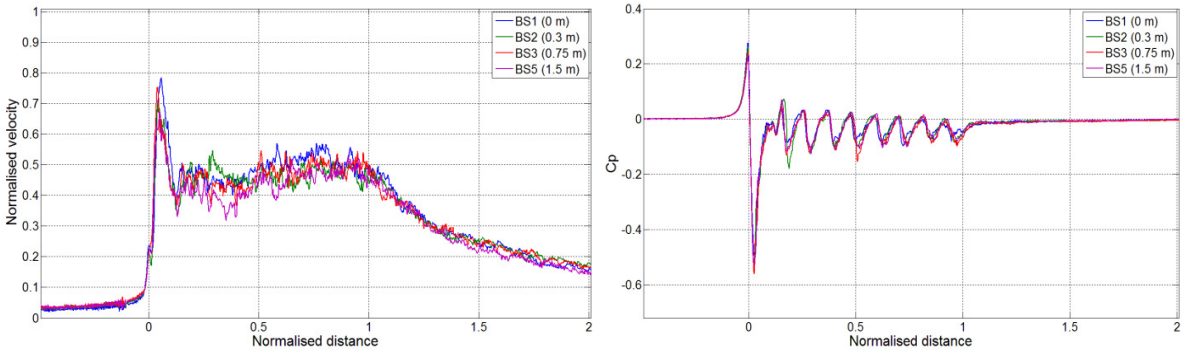

Figure C.3.20 - Slipstream and pressure for freight with BS1, BS2, BS3 and BS5 at y = 2.0 m from COT, z = 0.0 m above TOR.

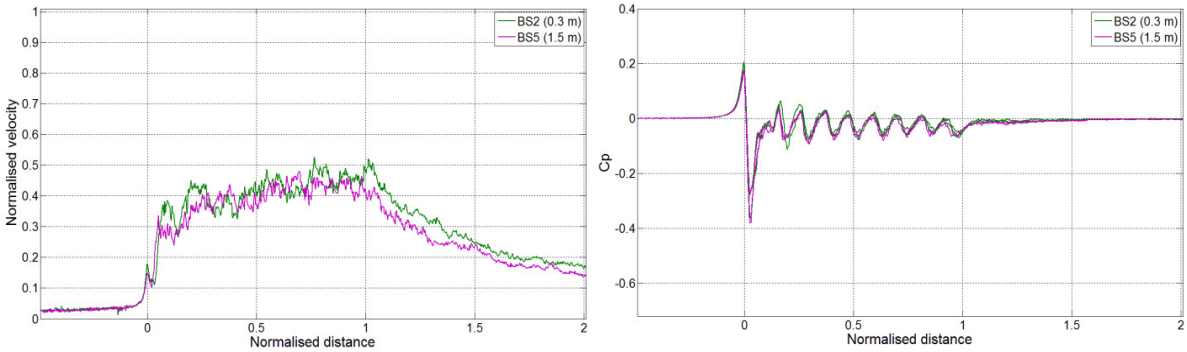

Figure C.3.21 - Slipstream and pressure for freight with BS2 and BS5 at y = 2.5 m from COT, z = 0.0 m above TOR.

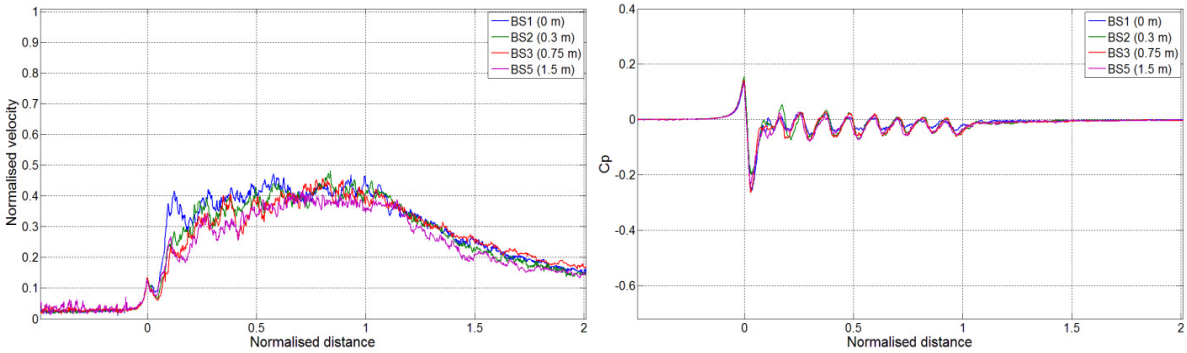

Figure C.3.22 - Slipstream and pressure for freight with BS1, BS2, BS3 and BS5 at y = 3.0 m from COT, z = 0.0 m above TOR.

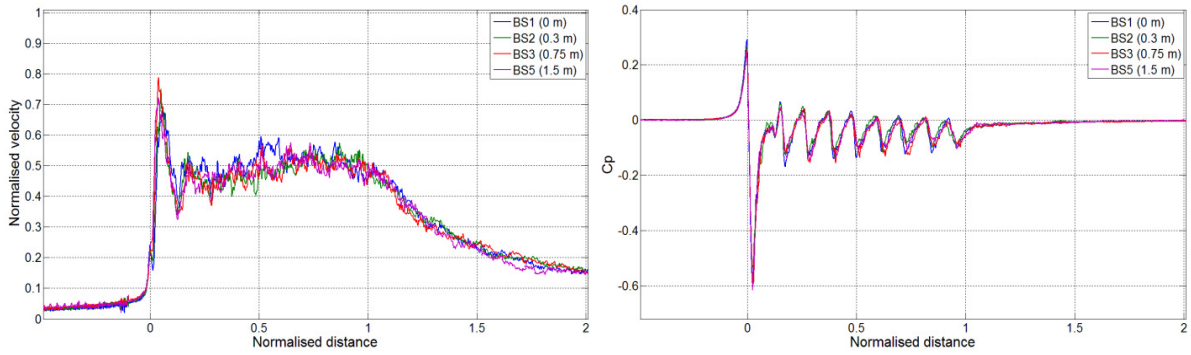

Figure C.3.23 - Slipstream and pressure for freight with BS1, BS2, BS3 and BS5 at y = 2.0 m from COT, z = 0.2 m above TOR.

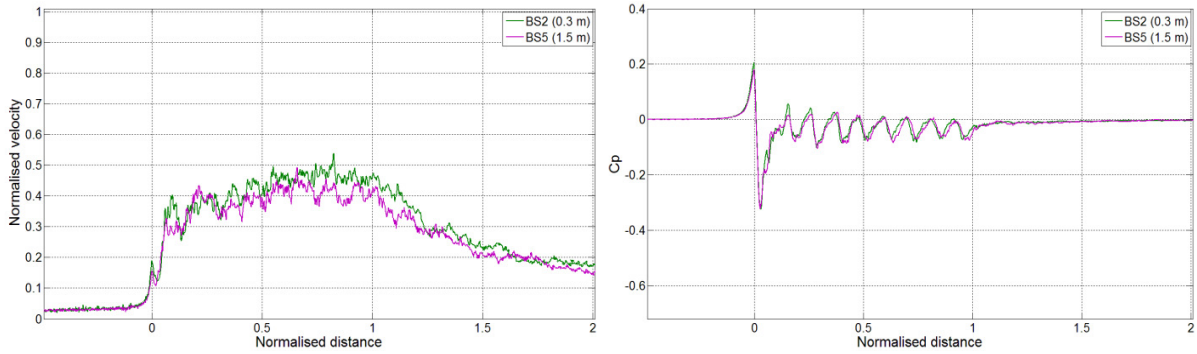

Figure C.3.24 - Slipstream and pressure for freight with BS2 and BS5 at y = 2.5 m from COT, z = 0.2 m above TOR.

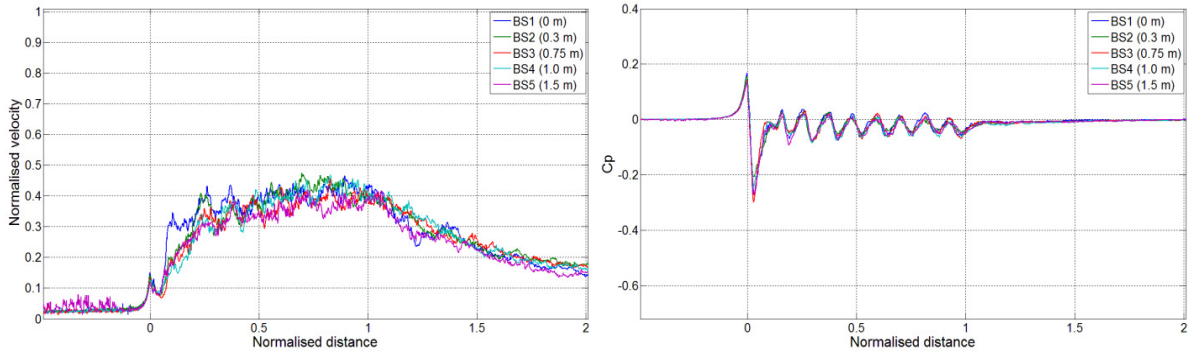

Figure C.3.25 - Slipstream and pressure for freight with BS1, BS2, BS3, BS4 and BS5 at y = 3.0 m from COT, z = 0.2 m above TOR.

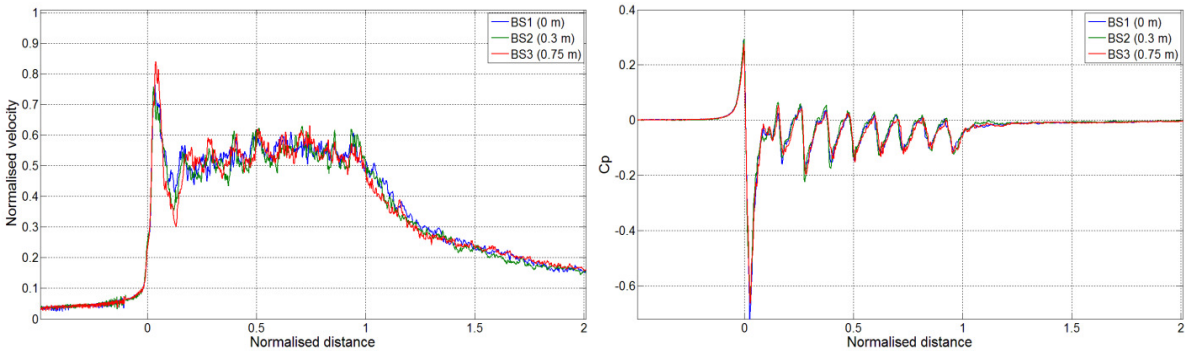

Figure C.3.26 - Slipstream and pressure for freight with BS1, BS2 and BS3 at y = 2.0 m from COT, z = 0.7 m above TOR.

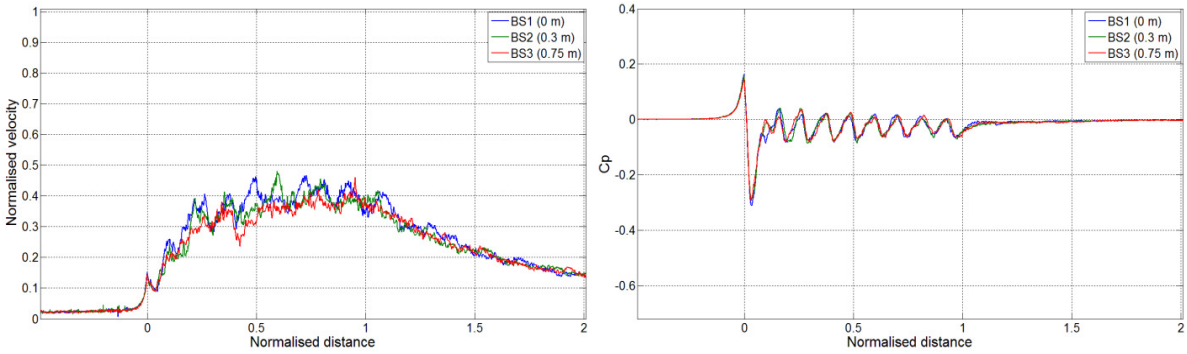

Figure C.3.27 - Slipstream and pressure for freight with BS1, BS2 and BS3 at y = 3.0 m from COT, z = 0.2 m above TOR.

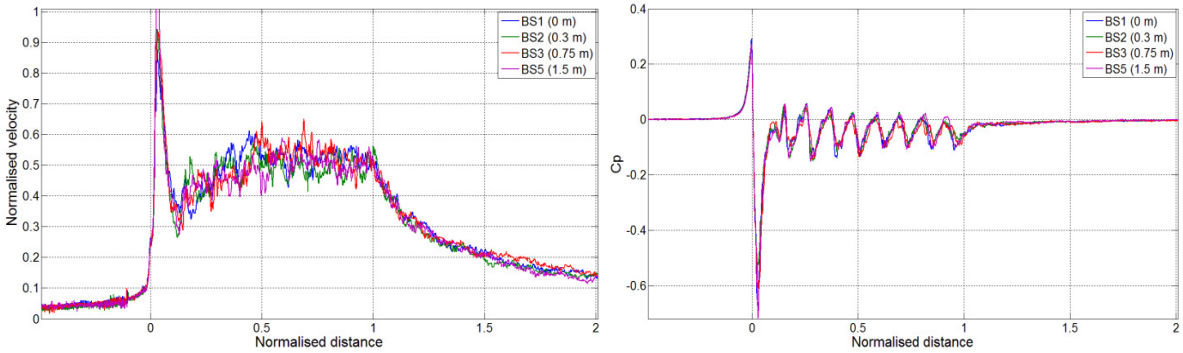

Figure C.3.28 - Slipstream and pressure for freight with BS1, BS2, BS3 and BS5 at y = 2.0 m from COT, z = 1.2 m above TOR.

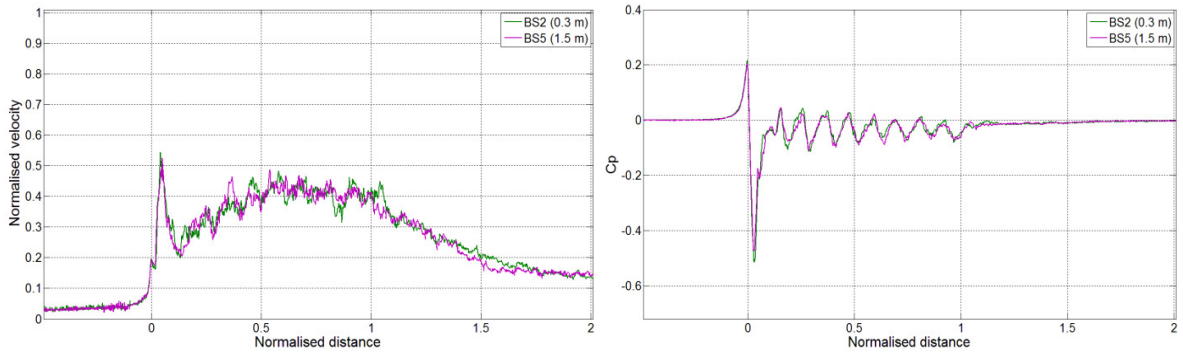

Figure C.3.29 - Slipstream and pressure for freight with BS2 and BS5 at y = 2.5 m from COT, z = 1.2 m above TOR.

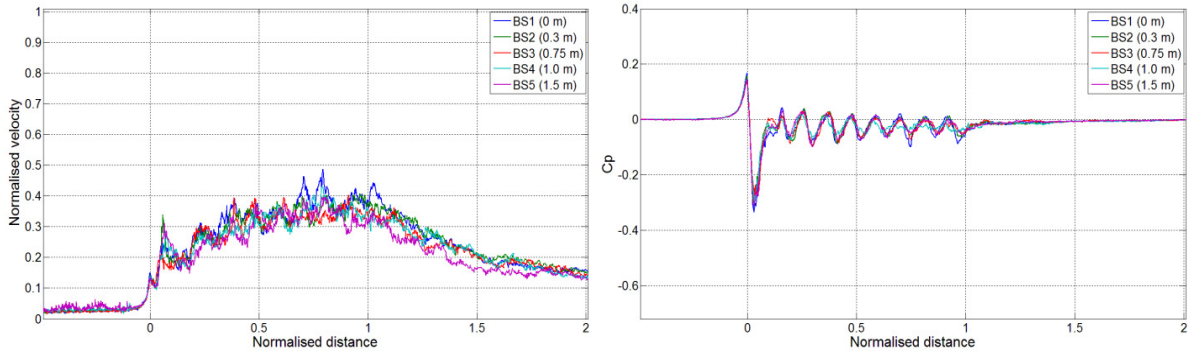

Figure C.3.30 - Slipstream and pressure for freight with BS1, BS2, BS3, BS4 and BS5 at y = 3.0 m from COT, z = 1.2 m above TOR.

C.2.4 ICE2 results

C.2.4.1 ICE2 results by height above TOR (z)

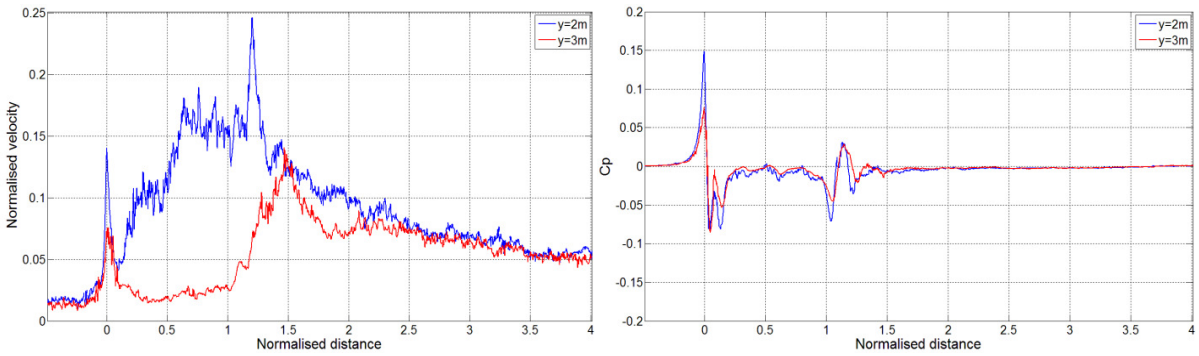

Figure C.4.1 - Slipstream and pressure for ICE2 with BS1 at z = 1.2 m above TOR, y = 2.0 m and 3.0 m from COT.

C.2.4.2 ICE2 results by distance from COT (y)

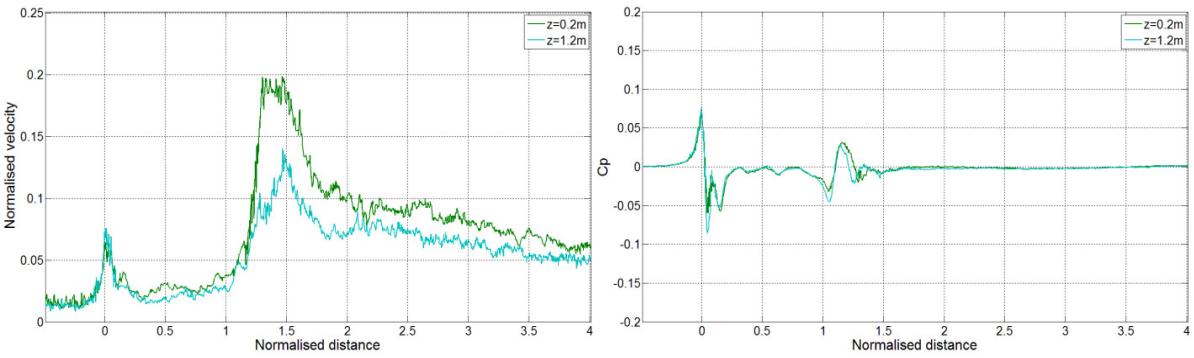

Figure C.4.2 - Slipstream and pressure for ICE2 with BS1 at y = 3.0 m from COT, z = 0.2 m and 1.2 m above TOR.

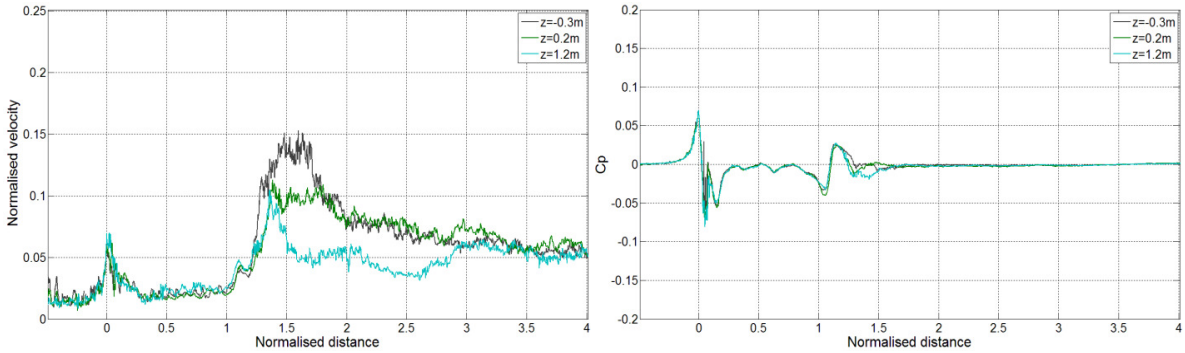

Figure C.4.3 - Slipstream and pressure for ICE2 with BS3 at y = 3.0 m from COT, z = 0.3 m below and 0.2 m and 1.2 m above TOR.

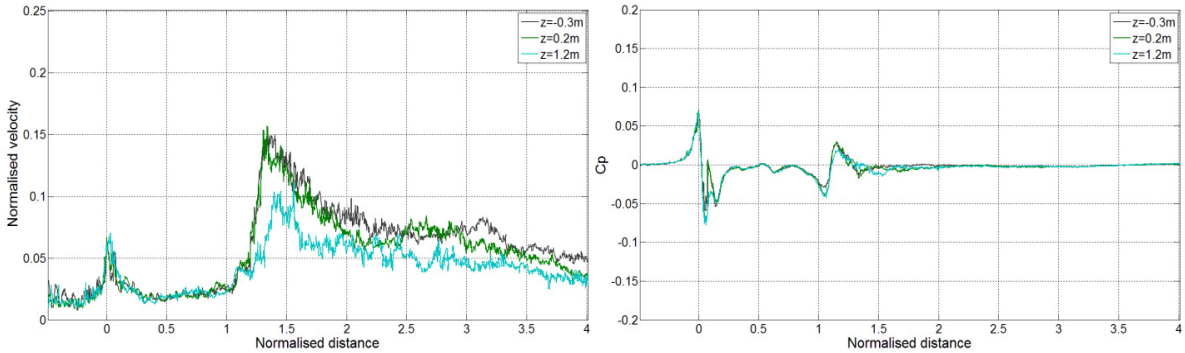

Figure C.4.4 - Slipstream and pressure for ICE2 with BS5 at y = 3.0 m from COT, z = 0.2 m and 1.2 m above TOR.

C.2.4.3 ICE2 results by ballast height

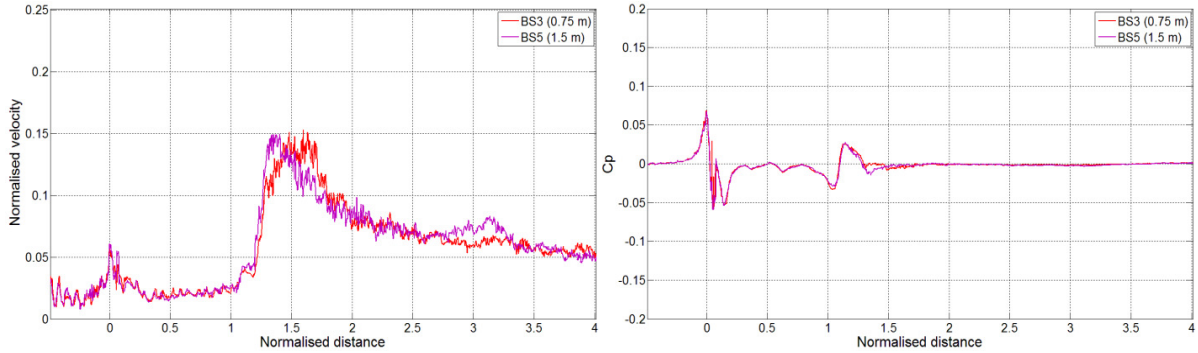

Figure C.4.5 - Slipstream and pressure for ICE2 with BS3 and BS5 at y = 3.0 m from COT, z = 0.3 m below TOR.

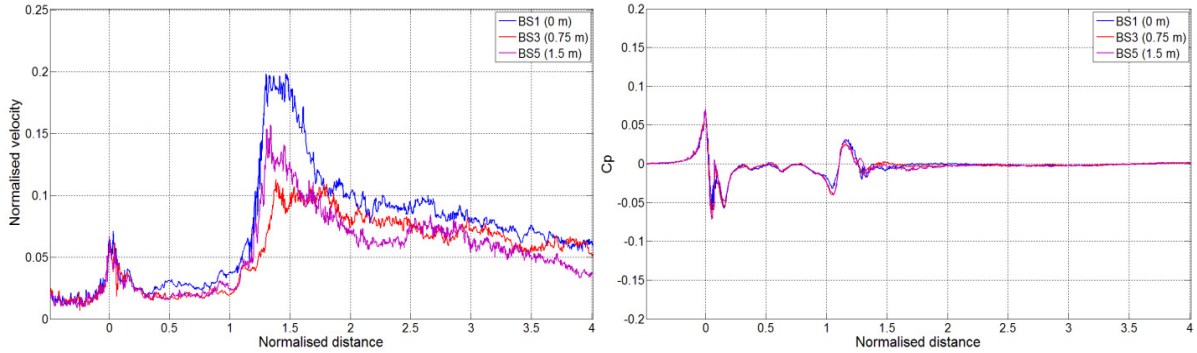

Figure C.4.6 - Slipstream and pressure for ICE2 with BS1, BS3 and BS5 at y = 3.0 m from COT, z = 0.2 m above TOR.

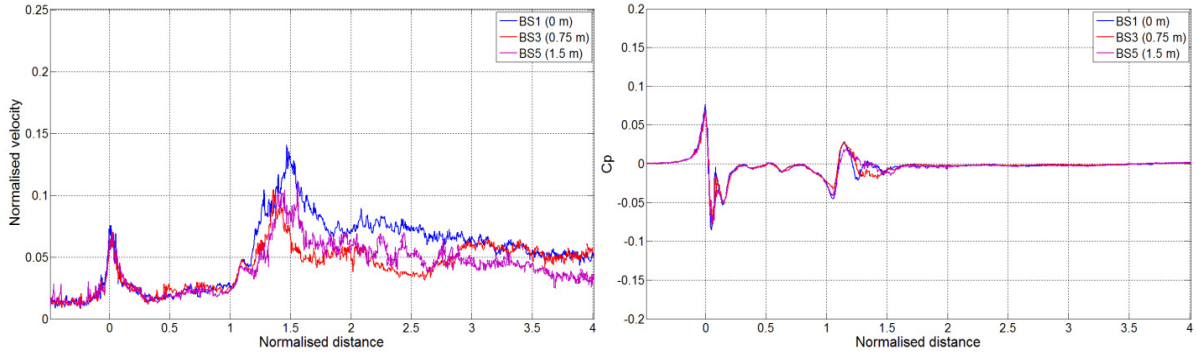

Figure C.4.7 - Slipstream and pressure for ICE2 with BS1, BS3 and BS5 at y = 3.0 m from COT, z = 1.2 m above TOR.

APPENDIX D

FULL-SCALE SLIPSTREAM MEASUREMENTS

D.1 Introduction

Appendix D describes full-scale measurements made by Baker and Quinn, (2012). Full-scale measurements of slipstreams were planned at the Uffington site as part of this project following previous slipstream measurements undertaken by Baker and Quinn, (2012) which identified the site as suitable. However, since the slipstream measurements as part of this PhD study did not take place due to a line speed restriction of 50 mph, the data from Baker and Quinn, (2012) will be presented briefly to allow a limited comparison with the model-scale data obtained from the TRAIN rig (presented in chapter 5). Section D.1.2 describes the background and purpose of the measurements made by Baker and Quinn, (2012). Section D.2 describes the test site, and section D.3 describes the experimental equipment and test procedure. D.4 describes the analytical procedure and presents the slipstream results at a trackside position (0.7 m above TOR, 3 m from COT) that was close to the TSI measurement position for trackside slipstream measurements for the full-scale measurements, and also shows equivalent slipstream measurements made at model-scale at the TRAIN rig. Section

D.5 presents the main conclusions based on consideration of the full-scale data, and the findings from this investigations are discussed in the main body of this thesis in section 5.7.

D.1.1 Background of the tests

Measurements of the slipstream of an HST at full-scale were undertaken between July and August, 2012, by the University of Birmingham in cooperation with Network Rail. The purpose of these tests was to measure the effects of train induced gusts on a road rail vehicle (RRV) shown in figure D.1. The RRVs can have raised baskets for workers to install overhead line equipment, therefore there was concern that the slipstream velocities may be hazardous to workers, and may also cause movement of tools and equipment on the basket floor. Slipstream measurements were also made at a trackside location (close to the TSI position of 3 m from COT and 0.2 m above TOR). The tests were conducted at Uffington on the West Coast Main Line (WCML), and the site is described in section D.2.

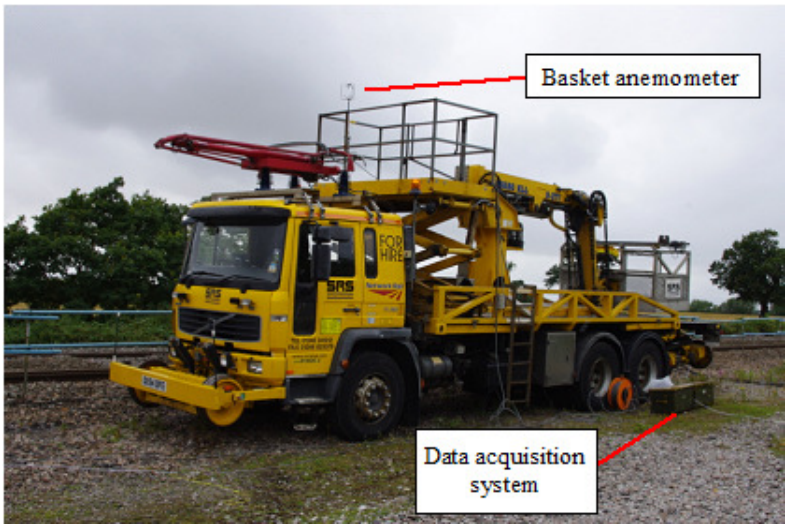

Figure D.1 - Road rail vehicle and basket anemometer (1.5 m above basket floor)

D.2 Uffington test site

The Uffington test site is located on the WCML in Oxfordshire, UK, at the site of the old Uffington station, and is shown on the map in figure D.2. It is a straight section of double track that has a large amount of HST traffic in both directions (about 6 per hour on the near track), usually in a 2+7 or 2+8 configuration (equivalent to train lengths of 200 m and 223 m respectively). Some freight traffic was also observed though the majority of this was during the evenings/nights. The ground configuration is relatively flat - there is a small ballast shoulder that is approximately 0.3 m in height (from top of ballast to cess), though this is somewhat variable/nominal. The site itself is shown in figure D.3.

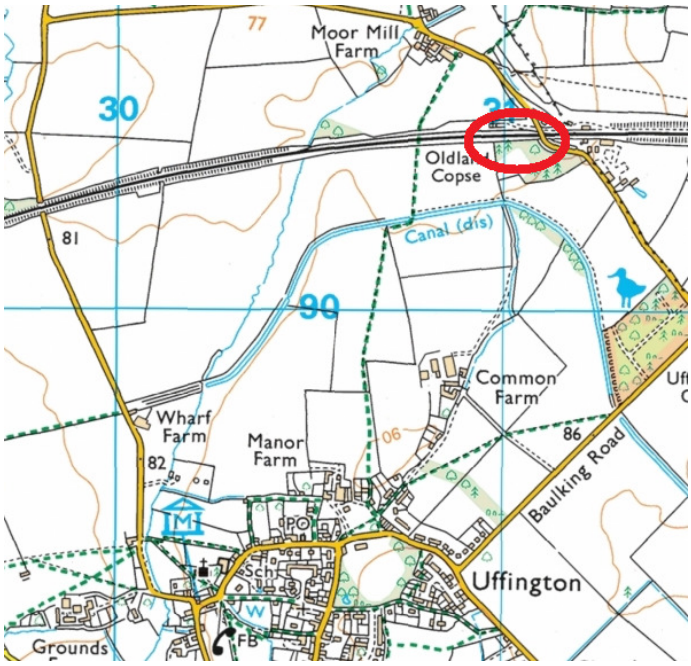

Figure D.2 - Location of Uffington test site (Microsoft Corporation, 2015).

The advantages of this site are that it is relatively secure and that there is space available beside the track to set up equipment. The line has an operating speed of 125 mph (200 kph) which is the maximum operating speed of the HST, and so most of the train passages were

near to the maximum operational speed. The disadvantages are that the site is on relatively open and flat terrain, and therefore ambient winds were often higher than 2 m/s as limited in the TSI.

D.3 Experimental set up and testing procedure

A total of four ultrasonic anemometers were used to sample air speeds at a frequency of 50 Hz. The anemometers were manufactured by Gill Instruments Research (model R3-50) and the dimensions are shown in figure D.4. Two anemometers were placed on the RRV - one at the height of 1.5 m above the base of the basket (and therefore 4.6 m above the cess), the other was laid flat on the basket floor, and both were 3.3 m from the nearest rail. The third anemometer was positioned in open track and 20 m ahead of the RRV so that trains would pass this position before reaching the RRV. The open track anemometer was at a height of 1.1 m above the cess (0.7 m above TOR) and 2.3 m from the nearest rail (3.05 m from COT) - this was as close to the TSI measurement position, 3 m from COT and 0.2 m above TOR, as practicable. The final anemometer was used to record reference wind speeds, and was therefore positioned 2.85 m above the ground level and 24 m from the RRV and track to avoid slipstream effects.

The site was manned during daylight hours. During this time the train types were observed and manually recorded. A video camera was used to record each train passage and the videos were stored on a PC at the end of each day/shift. Train speed was measured using a Decatur RailMaster-VP radar speed gun for each passage, which was found to be accurate to within 1 kph. Two static pressure probes were mounted on a safety fence approximately 1 m above

TOR and 1.3 m from the nearest rail (about 2 m from COT), and on either side of the RRV, 39.5 m apart. The pressure probes were connected to a single box containing Honeywell 164PC01D37 differential pressure transducers. The analogue output voltage from the pressure transducers was converted to a digital signal using an analogue to digital card (Measurement Computing USB-1616FS), and the data was logged onto a Windows PC using bespoke software. The difference in time between the head pressure pulse was used as an independent measure of train speed. Comparisons between the two methodologies of train speed measurement showed agreement to within 2 kph (Baker & Quinn, 2012).

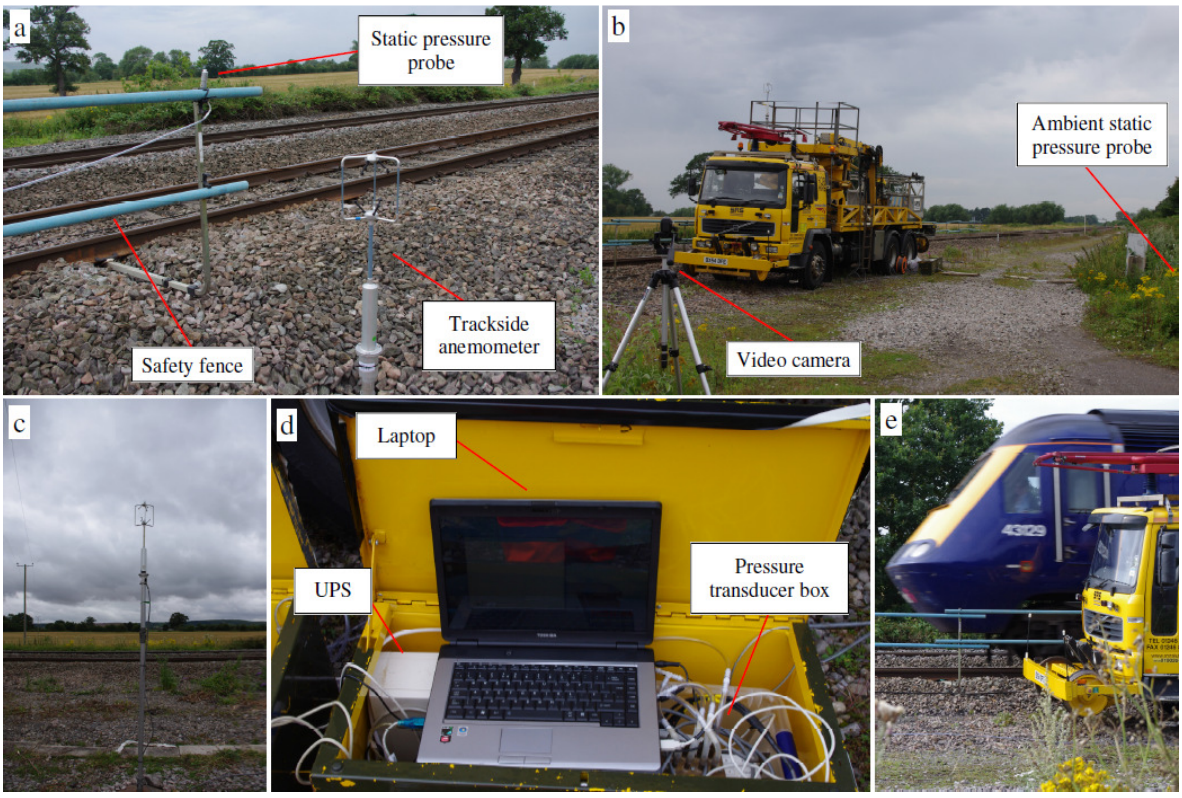

Figure D.3 - Experimental set up at Uffington - (a) trackside anemometer and static pressure probe on safety fence, (b) video camera and reference pressure location, (c) wind speed reference anemometer, (d) data acquisition system (laptop and pressure transducer box), (e) relative height of an HST to RRV and safety fence.

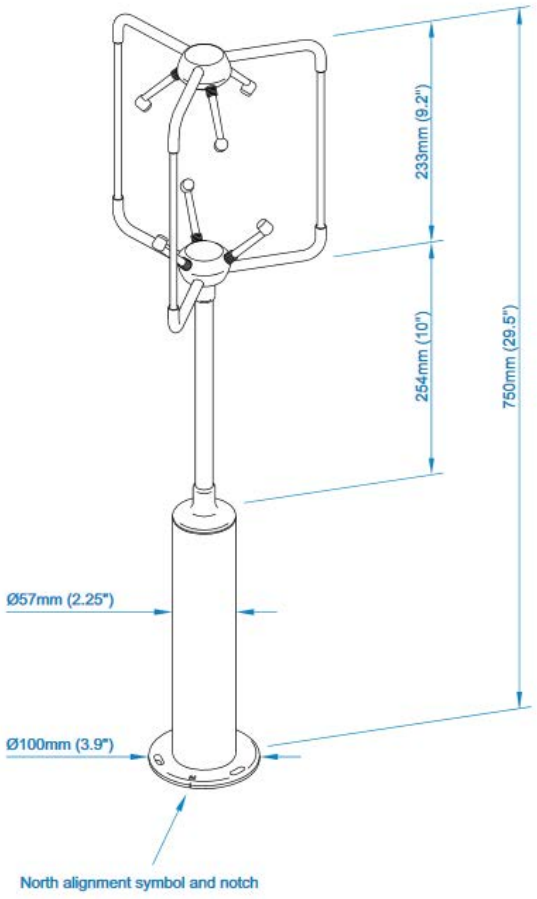

Figure D.4 - Dimensions of Gill R3-50 ultrasonic anemometer (Gill Instruments, 2015)

D.4 Analytical procedure and results

The analytical procedure follows that outlined in section 4.x. Each run was normalised by dividing by train speed. Each run was then resampled to the maximum full-scale train speed of 55.9 m/s, and realigned with x = 0 m as the maximum of the nose velocity peak of U_{res} (only values of U_{res} have been considered in this analysis).

A total of 14 runs were acceptable by the TSI requirements, with 6 runs with a 2+7 configuration and 8 runs for the 2+8 configuration. Section B.2 has shown that the ensemble

mean is sensitive to size with only 14 runs (which is below the minimum of 20 runs in the TSI). Analysis of this limited data set is therefore only briefly considered.

Figures D.5.1 and D.5.2 present the individual runs and ensemble averages of U_{res} for each configuration. The 2+7 slipstream data was then split at the position of the intercarriage gap between the final coach and the trailing power car, and then the split data was aligned to this equivalent position on the 2+8 data, resulting in alignment of the train tail and hence wake between the 2+7 and 2+8 configurations. Figure D.5.3 shows the individual runs from the split 2+7 data and the 2+8 data combined and the resulting 14 run ensemble average.

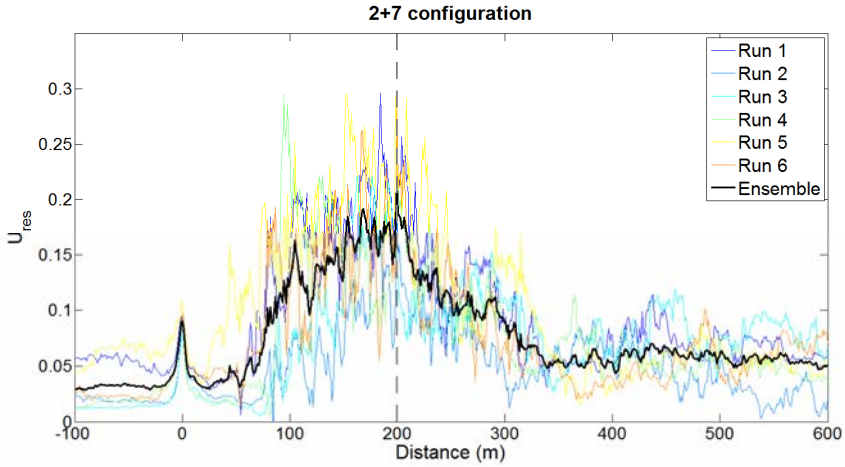

Figure D.5.1 - Full-scale runs and ensemble average of U_{res} for 2+7 configuration at 3 m from COT and 0.7 m above TOR with 0.3 m ballast height. Train tail shown as dashed vertical grey line.

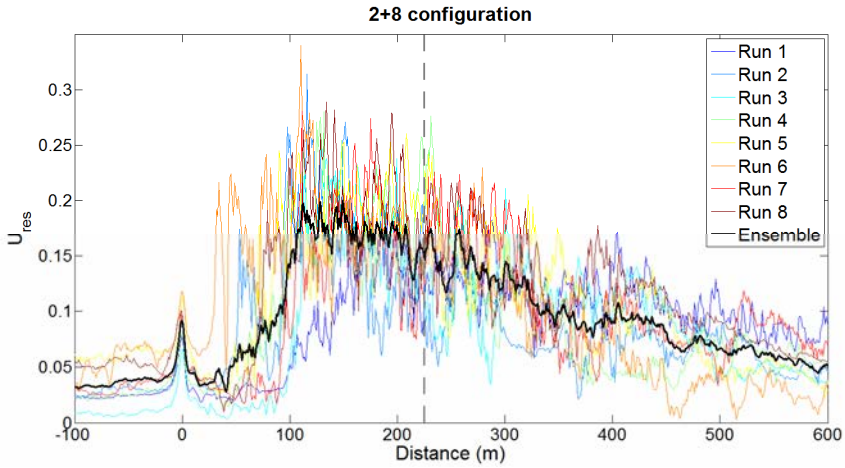

Figure D.5.2 - Full-scale runs and ensemble average of U_{res} for 2+8 configuration at 3 m from COT and 0.7 m above TOR with 0.3 m ballast height. Train tail shown as dashed vertical grey line.

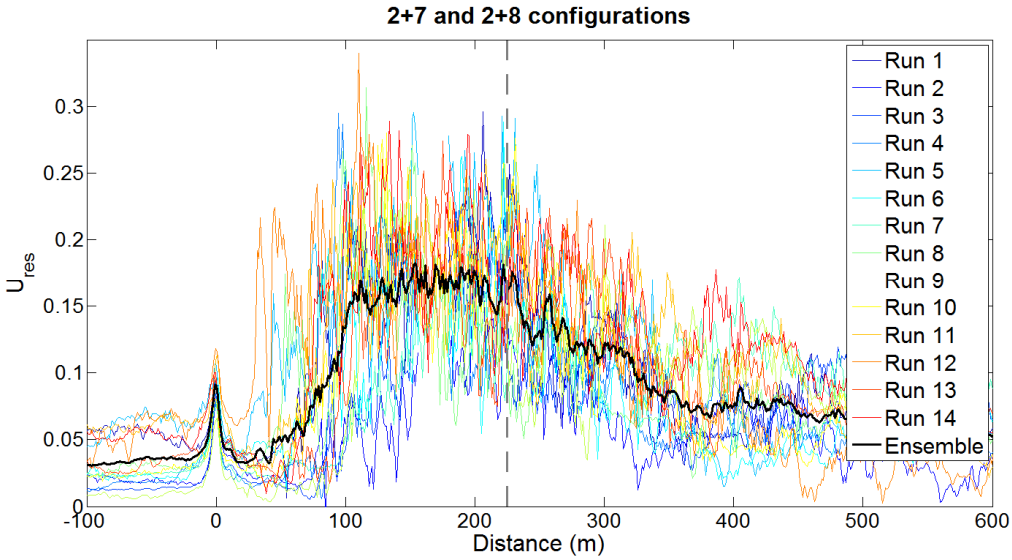

Figure D.5.3 - Full-scale runs and ensemble average of U_{res} for both 2+7 and 2+8 configurations at 3 m from COT and 0.7 m above TOR with 0.3 m ballast height. Train tail shown as dashed vertical grey line.

It must be stressed that the quantity of data obtained at full-scale is insufficient to form a meaningful ensemble. The results from the 2+7 and 2+8 configurations appear to show similar flow characteristics - the nose peak at x = 0 m is clearly defined in both cases and the magnitude appears to depend slightly on ambient wind velocity. Run 5 from the 2.7 configuration (figure D.5.1) and run 6 on the 2+8 configuration (figure D.5.2) shows a velocity peak quite closely after the initial nose peak, similar to that found on the model-scale data, though this peak is not apparent in the ensemble suggesting that it is an intermittent flow. Generally, the largest velocity peaks are within the boundary layer region and the variation between runs is clearly quite large, most likely due to the relative roughness of the HST underbody and the anemometer position close to the ground. Neither the 2+7, 2+8 or combined ensembles show a clear and defined near wake peak - if anything the ensembles show a gradual decrease in ensemble slipstream velocity immediately after the tail passage. However, the conclusion that the HST does not have a near wake peak that is similar to more conventional passenger trains cannot be made due to the low ensemble size.

The equivalent model-scale data is shown in figure D.6. Large velocity peaks can be seen closely after the nose peak, but again these are not apparent in the ensemble average due to the intermittency of these peaks - there is a very poorly defined peak in the ensemble (at x = 20 m to 50 m) though it is of much lower magnitude that the causal velocity peaks in the individual runs. The near wake is well defined at model-scale and there is a sharp peak in the ensemble average velocity immediately after the tail passage. The ensemble averages are compared between full-scale and model-scale in figure D.7 - the TRAIN rig data has been split in the same way as the 2+7 data was split in order to align the train tails. The nose peak at full-scale is larger, possibly due to ambient winds resulting in an increase in the nose peak at full-scale, and also due to the limitations of the Cobra probes used at model-scale which

only record flow within a ± 45° cone of acceptance (and hence the nose peak which is primarily a V component may have been underestimated). The lack of the near wake peak is quite striking when the full-scale data is compared to model-scale data. The velocity decay in the far wake is almost identical between the full-scale and model-scale data.

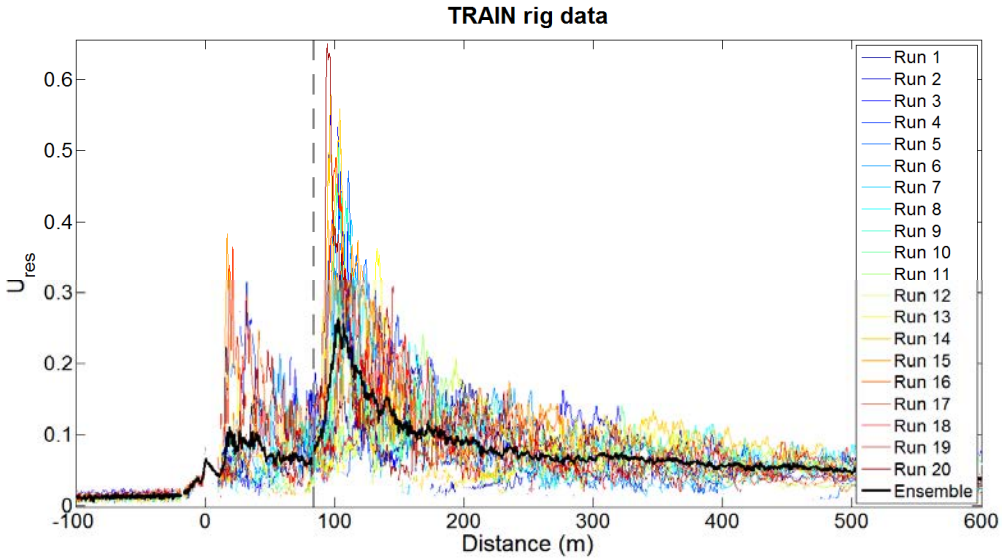

Figure D.6 - Model-scale data from TRAIN rig at 3 m from COT and 0.7 m above TOR with 0.3 m ballast height. Train tail shown as dashed vertical grey line.

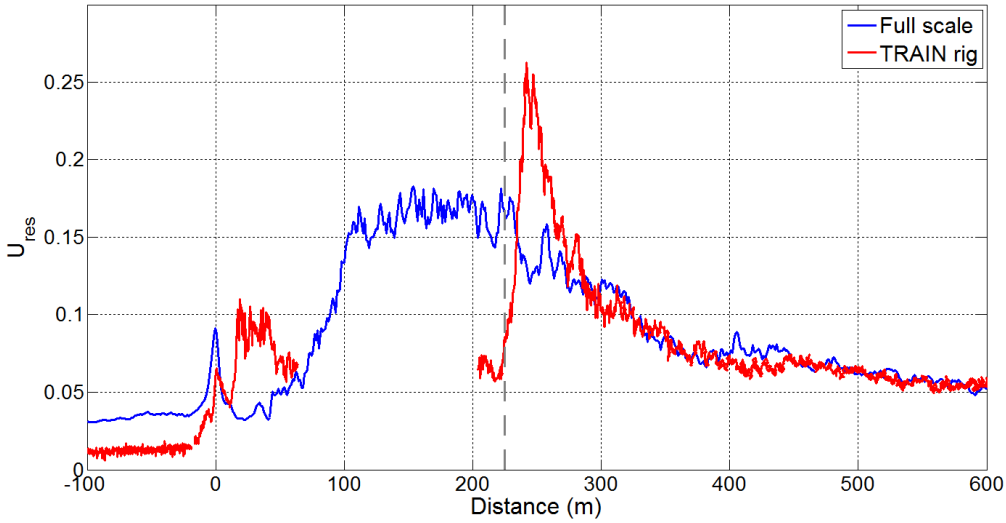

Figure D.7 - Model-scale data from TRAIN rig at 3 m from COT and 0.7 m above TOR with 0.3 m ballast height. Train tail shown as dashed vertical grey line.

D.5 Closing remarks

Full-scale tests were undertaken to measure the slipstream of an HST (and freight trains) on the WCML by Baker and Quinn, (2012), for Network Rail, in order to assess the effects of slipstreams on the stability of workers and tools in HOPS designed to install overhead line equipment. One anemometer was placed at trackside, and a total of 14 acceptable runs (by TSI standards) were obtained, and it should be stressed that the purpose of these tests was not the measurement of trackside slipstream velocities and hence this ensemble size is too low to undertake much detailed analysis.

From the limited data set, and comparison with equivalent model-scale measurements, the following conclusions can be made:

- The nose peak was well defined and of similar magnitude for all full-scale runs.

- The largest velocities of individual runs tended to occur within the boundary layer region (20 m < x < 200 m), and no relationship between x-axis position and velocity was apparent from the low number of full-scale runs, suggesting that these peaks arise due to intermittent flows that are of variable magnitude and x-axis position for each run.
- Large velocity peaks were apparent within the boundary layer at model-scale, though were closer to the train nose and only featured on some of the runs, indicating that these velocity peaks too were intermittent flows.
- The model-scale data showed a clearly defined sharp near wake velocity peak that was not at all apparent on the full-scale data, and while this is unusual and unexpected, a larger quantity of full-scale data is needed before any further explanations and conclusions can be drawn.
- The nose peak at model-scale was lower, which may be due to equipment limitations (Cobra probe cone of acceptance) and also the influence of ambient winds at full-scale.
- The far wake flows were virtually identical between full-scale and model-scale.

APPENDIX E

PRESSURE TRANSDUCER CALIBRATIONS

E.1 Introduction

Appendix E provides the details of the various pressure transducer calibrations that were performed during this PhD project. The methodology presented in this appendix follows that of previous studies using the same type of pressure transducer and calibration equipment (Dorigatti, 2013; Soper 2014).

Section E.2 describes the experimental methodology for the calibration of pressure transducers for the different aerodynamic investigations (such as crosswind tests at the TRAIN rig and full scale on the NMT). Section E.3 describes the analysis of the data from the calibrations, and presents the key results. A brief discussion about the results and how they were using in the experimental studies in this project, and concluding remarks are made in section E.4.

E.2 Calibration methodology

This section describes the experimental procedure and equipment used for the calibrations carried out as part of this project.

E.2.1 Equipment

E.2.1.1 Pressure transducers

Pressure transducers convert a pressure differential to a voltage signal. The pressure transducers used in this project were manufactured by Sensortechnics, and were model number HCLA0050DB (Sensortechnics, n.d.). The transducers have a 5 kPa operating range (±2.5 kPa) which was adequate for the tests undertaken, and the manufacturer's specifications are presented in table E.1. The transducers require a nominal DC supply voltage of 5 V, and the voltage output ranges between 2.25 V ±1.25 V for pressures between 0 Pa ±2500 Pa.

Figure E.1 shows the external dimensions and electrical connections. Each pressure transducer has two pneumatic ports - the high pressure port (HPP) and the low pressure port (LPP). The HPP is typically connected to a pressure tap at the location at which the pressure is to be measured and the LPP is connected to either a reference pressure reservoir or left open to the atmosphere.

Table E.1 - Properties of the differential pressure transducers (Sensortechnics, n.d.)

Pressure transducer model	HCLA0050DB
Operating range (Pa)	±2500
Proof pressure[1] (mbar)	750
Burst pressure[2] (mbar)	1200
Zero pressure offset[3] (mV)	±0.5
Nominal full scale span[3] (mV)	±20.0
Combined non-linearity and hysteresis[4]	±5%
Warm up drift[5] (mV)	±0.05
Long term drift[6] (mV)	±0.1
Temperature effects between 0°c - 70°c (mV)[6]	±0.2

Notes

1. Proof pressure is the maximum pressure that can be applied without causing durable shifts in the electrical parameters of the sensing equipment.
2. Burst pressure is the maximum differential pressure that can be applied without causing leaks to the sensor and housing.
3. These are manufacturer tolerances between the same model of transducer. Zero pressure offset is the expected range in voltages of the different pressure transducers at 0 Pa. Nominal full scale span is the difference between the voltage at the maximum operating pressure and the voltage at 0 Pa pressure, nominally 3.25 V - 2.25 V = 1 V).
4. Difference between linear best fit line and actual measured pressure at the nominal max operating pressure of 2500 Pa.
5. After one hour of excitation of the sensing equipment.
6. After one year.
7. Drifts relative to 25°c.

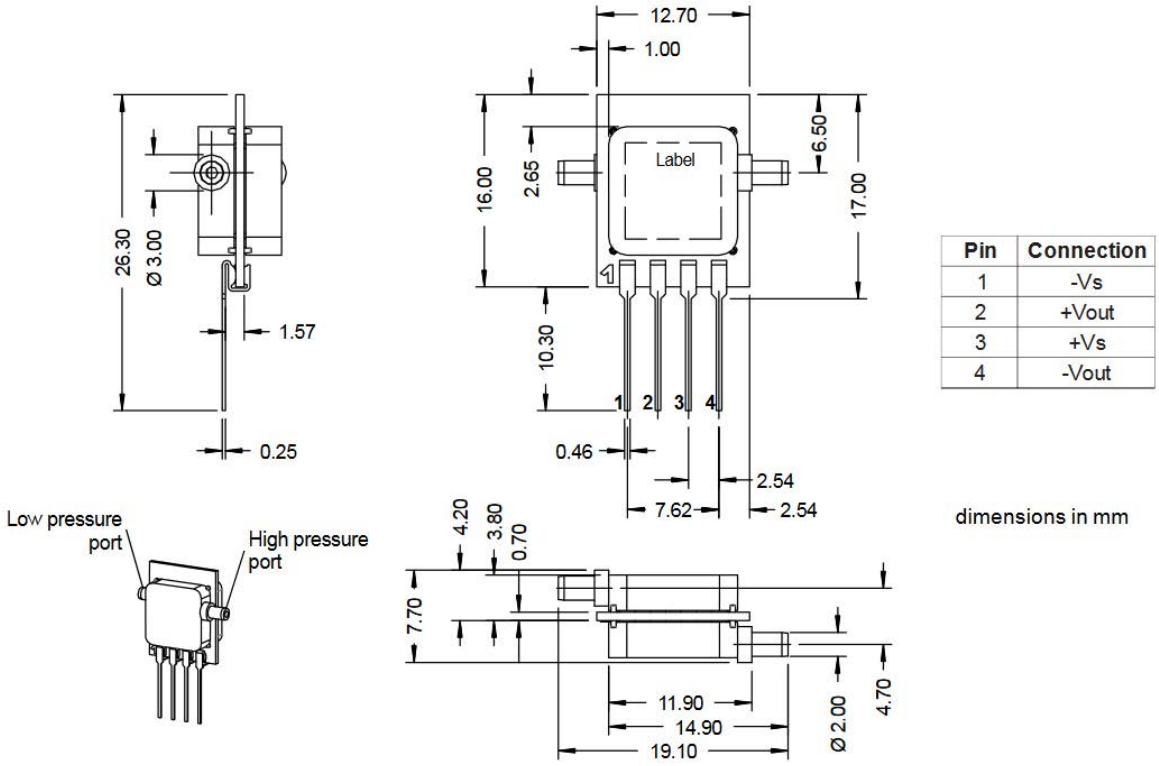

Figure E.1 - Dimensions of HCLA0050DB pressure transducer (Sensortechnics, n.d).

E.2.1.2 Betz manometer

A Betz J-tube manometer was used for applying a known pressure to the transducers during the calibrations. The manometer is capable of measuring a positive pressure up to 2500 Pa and has a scale resolution accurate to 1 Pa. Figure B1 shows the Betz manometer and the connection points for the high and low pressure.

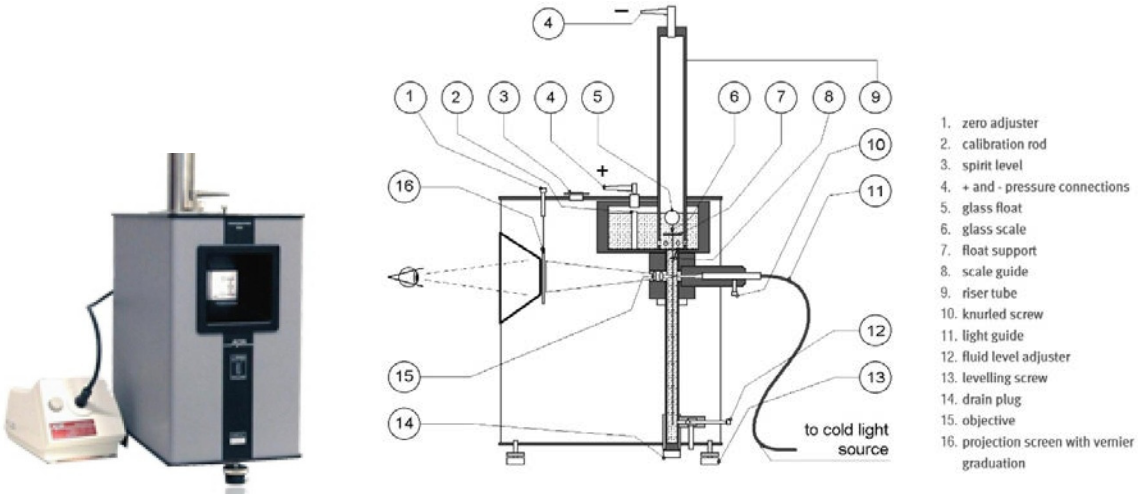

Figure E.2 - Betz Manometer (ACIN, 2014)

E.2.2 Testing procedure

The overall procedure for the pressure transducer calibrations was to apply a known pressure to the pressure transducers and to record the voltage signal from each transducer. The calibrations took place *in situ*, i.e., that the pressure transducers were connected to the experimental system where they would be used during the aerodynamic tests, hence variables such as the power supply, data logger, connecting cables, reference pressure etc were controlled.

The general procedure for a calibration is as follows:

- Setting up the Betz manometer:

  - ensuring that it is level using the spirit level bubble on the top of the body of the Betz and adjusting the three legs for height where necessary;

  - checking that the level of manometer fluid is correct while both of the pressure

connections are open, i.e., the zero on the scale should be visible on the glass scale front when there is no differential pressure acting on the manometer;

- Set up of pneumatic tubing from the pressure transducers to the Betz, and electrical connections from the transducers to the power supply and data logger;
- Testing that the pressure transducers are working (the zero voltage should have been close to 2.25 V), and adjusting/replacing the electrical connections and pressure transducers if necessary;
- Applying a pressure with the hand pump to the manometer and transducers, and then checking that the pressure is stable for the duration of sampling (30 s to 1 minute) by visually inspecting the scale reading on the manometer - if not the pneumatic system was checked for leakage;
- Applying pressures in nominal intervals to test the entire working range of the transducers, and recording the pressure data with the data logger and the environmental conditions for each pressure tested (ambient air pressure, temperature and humidity) using the equipment described in the main body of this thesis, section 3.4.3;
- Repeating the procedure but for the negative pressures.

A total of three calibrations were undertaken for the different elements of aerodynamic work, and these calibration tests are described in the following subsections. Calibrations 1 and 2 followed the methodology and equipment used in previous studies (Dorigatti, 2013 and Soper, 2014). Table E.2 describes the differences between each calibration.

Table E.2 - Details of the different pressure transducer calibrations performed during this project.

	Calibration 1	Calibration 2	Calibration 3
Purpose	General use around TRAIN rig (e.g. tunnel transient measurements)	Crosswind tests at TRAIN rig	In-situ calibration of the NMT system using the portable data logger and pre-calibrated transducers from this calibration.
HCLA0050DB pressure transducers numbers	1 - 16	1 - 15	9, 10, 13
Data logger	Static (Measurement Computing)	Onboard	Onboard
Power supply	5 V DC EPU	Data logger inbuilt battery (5 V nominal)	Data logger inbuilt battery (5 V nominal)
Pressure range tested (Pa)	-2500 to 2500	-1250 to 1500	-2500 to 2500
Sampling duration (s)	60	30	30
Sampling frequency (Hz)	5000	4000	4000
Pneumatic system for positive pressures	Positive pressure applied to HPPs and positive port on Betz. LPPs in closed pneumatic circuit with negative port on Betz.	Same as in calibration 1	Positive pressure applied to HPPs and positive port on Betz. LPPs and negative port on Betz left open to surroundings.
Pneumatic system for negative pressures	Positive pressure applied to LPPs and positive port on Betz. HPPs in closed pneumatic circuit with negative port on Betz.	Same as in calibration 1	Suction pressure applied to HPPs and negative port on Betz. LPPs and positive port on Betz left open to surroundings.

E.3 Analytical procedure and calibration results

E.3.1 Definitions

The pressure applied by Betz manometer was recorded using the visual scale reading on the manometer, and is accurate to 1 Pa. During some of the measurements (during calibrations 1 and 2) it was observed that this pressure would change (by the order of 0 - 10 Pa) during the sampling time. Therefore, the nominal pressure applied to the positive pressure input of the Betz manometer and pressure transducers, P_N, is defined as the mean of the initial and final pressure readings on the Betz manometer. The difference in pressures was 0 Pa in most cases.

The voltages of the output signal were sampled for a given duration, t (in seconds), and at a given frequency, f (in Hz), which are specified in table E.2 for each calibration. The time averaged mean voltages were given by:

$$\overline{V_{P,t}} = \frac{\sum V_{P,t|Samp}}{ft} \tag{E.1}$$

Where $V_{P,t|Samp}$ is the voltage output for each transducer (subscript t) at each individual sample, at a nominal pressure (subscript P).

The output voltage at zero pressure and at the full scale pressure of ±2500 Pa is ratiometric to the voltage of the power supply, therefore because the transducers are sensitive to the power supply voltage they need to be zeroed before any test. The zero voltage (or background voltage) was taken as the mean voltage with no net pressure applied to the transducer.

The difference between the mean voltage at a nominal non-zero applied pressure and the background voltage, $\overline{V_{0,t}}$, for each transducer is:

$$\Delta V_t = \overline{V_{P,t}} - \overline{V_{0,t}} \quad \text{(E.2)}$$

E.3.2 Linear calibration

The raw data from the three calibrations is shown in figure E.3. As specified by the manufacturer, the relationship between differential pressure, P_N, and the output voltage change, ΔV_t, are close to linear for each pressure transducer, and there is very little variation between individual pressure transducers. A nominal linear calibration (NLC) can therefore be adopted to convert the output voltage signal into a differential pressure, ΔP_{NLC}, by:

$$\Delta P_{NLC} = \Delta V_t K_{NLC} \quad \text{(E.3)}$$

Where K_{NLC} is the nominal linear calibration (NLC) factor, which is the same magnitude as half of the operating range of the transducer specified by the manufacturer, i.e., 2500 Pa, but has the units of Pa/V.

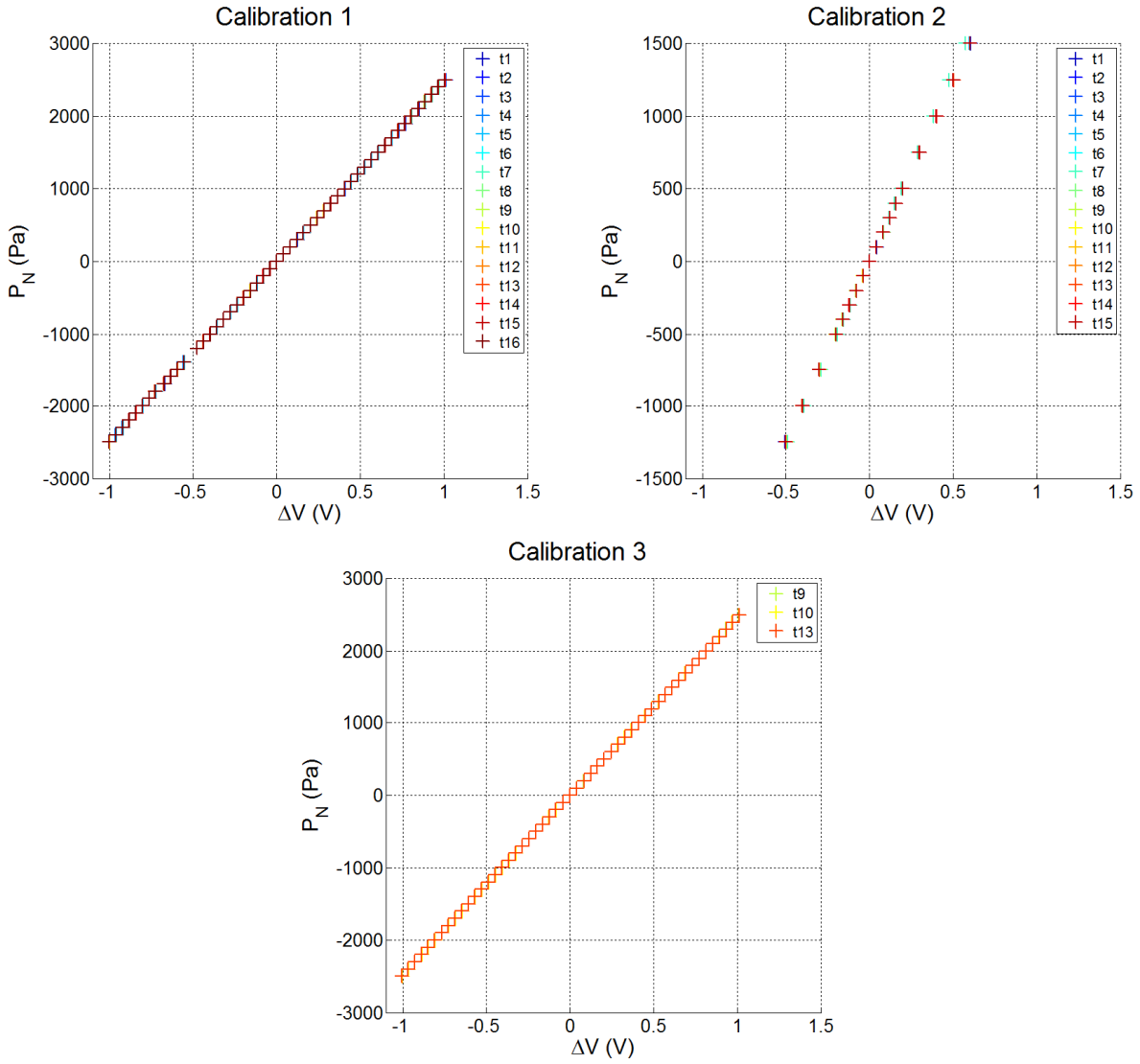

Figure E.3 - Raw data showing relationship between differential pressure, P_N, and change in voltage for all three calibrations.

The idea of a nominal linear calibration error, $E_{NLC}(\Delta P_N)$, can be introduced by considering the difference between the differential pressure from the NLC and the actual pressure applied during the calibration, ΔP_N, measured with the Betz manometer:

$$E_{NLC}(\Delta P_N) = \Delta P_{NLC} - \Delta P_N \tag{E.4}$$

Figure E.4 shows the nominal linear calibration errors obtained from the three different calibrations. Calibration 3 shows that the error appears to show a cubic relationship with the change in voltage which is consistent with previous findings (Dorigatti, 2013 and Soper, 2015). The magnitudes of the NLC error are similar for each of the three calibrations range from ±20 Pa between ±0.5 V, (corresponding to a nominal pressure range of ±1250 Pa), and the error increases up to ±30 Pa at voltage changes close to ±1 V. The NLC errors in calibration 1show a cubic relationship when the positive pressures were tested (i.e., a positive change in voltage) for all pressure transducers. When the negative pressures were tested the errors for each transducer show a similar albeit discontinuous trend, and are of similar magnitudes. This suggests that the pneumatic set up in calibrations 1 and 2 (i.e., a closed circuit at both the HPP and LPP) is an incorrect method of calibrating the negative pressure range of the HCLA0050DB pressure transducers.

An actual linear calibration (ALC) was obtained by fitting a straight line through the data using linear regression on Microsoft Excel, where the x-axis data was ΔV and the y-axis data was ΔP_N and the y-axis intercept was set at 0. ALC factors, K_{ALC}, were obtained for each individual transducer from the gradient of each graph, and are presented in table E.3 for the three calibrations. The actual linear calibration error, $E_{ALC}(\Delta P_N)$, was therefore defined as:

$$E_{ALC}(\Delta P_N) = K_{ALC}\Delta V - \Delta P_N \quad \text{(E.5)}$$

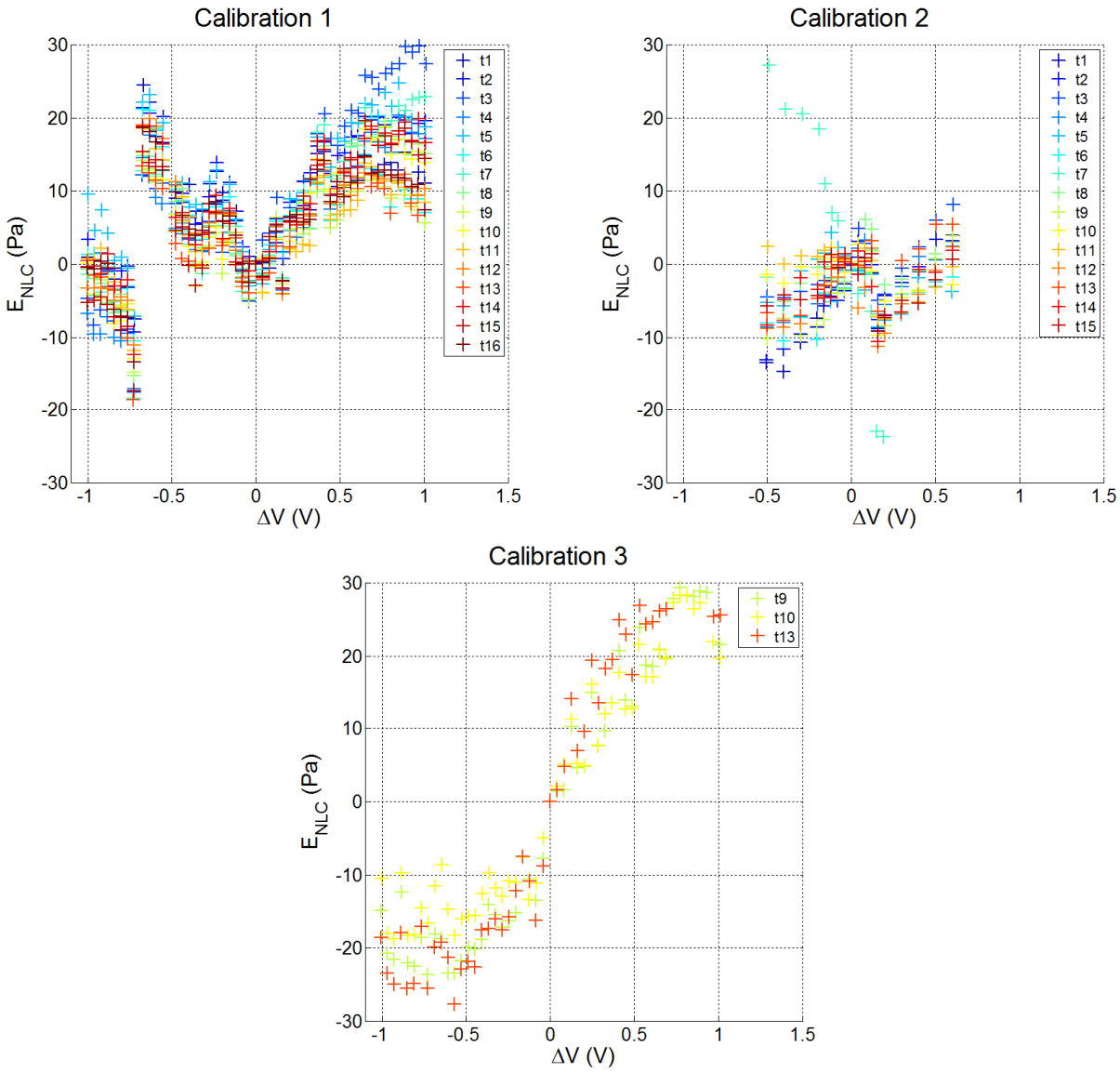

Figure E.4 - NLC errors for each calibration

Table E.3 - Values of K_{ALC} coefficients for the three calibrations.

Transducer	K_{ALC} (Pa/V)		
	Calibration 1	Calibration 2	Calibration 3
1	2495	2487	-
2	2491	2488	-
3	2482	2491	-
4	2488	2493	-
5	2492	2504	-
6	2496	2496	-
7	2487	2600	-
8	2490	2497	-
9	2494	2492	2470
10	2490	2504	2474
11	2496	2507	-
12	2494	2496	-
13	2493	2490	2466
14	2491	2498	-
15	2488	2500	-
16	2494	-	-

The values of K_{ALC} are, in most cases, close to the value of K_{NLC} of 2500 Pa/V (within ± 20 Pa/V), and in most cases lower. Transducer 7 in calibration 2 had a value of = 2600 Pa, and this transducer also showed the largest NLC error. Figure E.5 shows the ALC errors for the three calibrations. When compared with figure E.4, it can be seen that the ALC errors are lower than the NLC errors for calibrations 2 and 3 (i.e., an error range of ± 10 Pa between ± 0.5 V). In calibration 1, the ALC calibration errors are lower than the NLC errors for the positive pressure range, but very similar in magnitude (but offset by about + 5 Pa) for the negative pressure range.

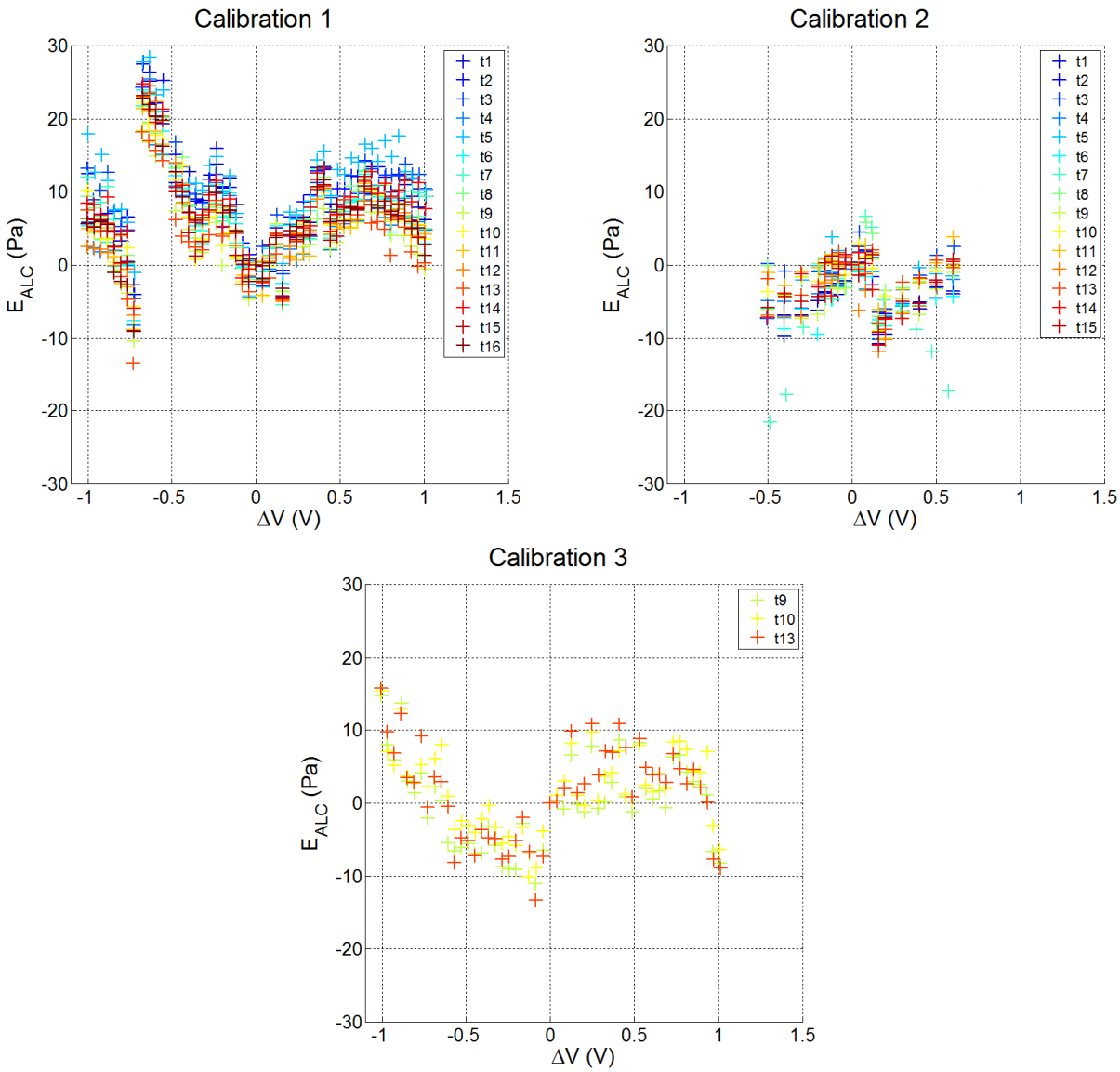

Figure E.5 - Individual ALC errors for all pressure transducers for each calibration

E.3.3 Cubic calibration

From the calibration data, and following observations made in previous studies, the voltage to pressure response was found to fit a cubic best fit (Dorigatti, 2013 and Soper, 2014). The

actual cubic calibration (ACC) equation was obtained using Microsoft Excel by fitting a 3rd order polynomial through the graph of P_N against ΔV and specifying a y-axis intercept of zero. The ACC equation for ΔP_{ACC} is therefore given as:

$$\Delta P_{ACC} = K1_{ACC}\Delta V^3 + K2_{ACC}\Delta V^2 + K3_{ACC}\Delta V \quad \text{(E.6)}$$

Where the coefficients $K1_{ACC}$, $K2_{ACC}$ and $K3_{ACC}$ were obtained for each individual pressure transducer and for each calibration. These coefficients and dimensions are specified for each pressure transducer for calibrations 1, 2 and 3 in tables E.4.1 to E.4.3.

Table E.4.1 - ACC factors for calibration 1

Transducer	$K1_{ACC}$ (Pa/V^3)	$K2_{ACC}$ (Pa/V^2)	$K3_{ACC}$ (Pa/V)
1	-10.57	-13.07	2502
2	-7.968	-17.30	2496
3	-6.907	-17.65	2487
4	-12.33	-9.680	2496
5	-3.256	-21.40	2494
6	-6.626	-10.30	2500
7	-4.360	-14.56	2490
8	-5.678	-12.32	2494
9	-0.305	-6.859	2494
10	-3.136	-10.81	2492
11	-7.667	-9.626	2501
12	-10.08	-9.307	2501
13	3.233	-7.182	2491
14	-7.723	-14.74	2496
15	-3.440	-10.72	2491
16	-5.261	-9.797	2497

Table E.4.2 - ACC factors for calibration 2

Transducer	$K1_{ACC}$ (Pa/V^3)	$K2_{ACC}$ (Pa/V^2)	$K3_{ACC}$ (Pa/V)
1	-59.02	34.48	2495
2	-34.02	30.84	2491
3	-35.27	3.447	2498
4	-36.54	22.24	2497
5	-83.06	-25.35	2518
6	-25.81	-31.37	2497
7	-27.42	77.19	2596
8	-22.92	7.180	2501
9	-48.29	27.78	2498
10	-47.12	15.65	2512
11	-61.44	8.300	2519
12	-85.61	30.80	2510
13	-41.33	13.00	2497
14	-75.97	23.96	2511
15	-70.53	23.39	2512

Table E.4.3 - ACC factors for calibration 3

Transducer	$K1_{ACC}$ (Pa/V^3)	$K2_{ACC}$ (Pa/V^2)	$K3_{ACC}$ (Pa/V)
9	25.71	-3.357	2454
10	19.18	-6.523	2462
13	30.64	-4.862	2446

Similarly, the ACC error, $E_{ACC}(\Delta P_N)$, is therefore defined as:

$$E_{ACC}(\Delta P_N) = \Delta P_{ACC} - \Delta P_N \quad \text{(E.7)}$$

Figure E.6 shows the ACC error for all pressure transducers for the three calibrations.

The magnitudes of the errors in figure E.6are lower than for the NLC and ALC calibrations, i.e., calibration 1 has an error range of ±20 Pa and calibrations 2 and 3 have an error range of ±10 Pa.

Table E.5 presents the values of the absolute maximum errors for each pressure transducer for calibration 2, as these values are used directly in the error analysis presented in appendix F. The calibration data from calibrations 1 and 3 has not been used directly in this study but was presented in this appendix to show the differences between the different calibration set ups using the same differential pressure transducers. Figure E.7 shows the absolute maximum errors as percentages, i.e., the highest value of the modulus of the errors (E_{NLC}, E_{ALC} and E_{ACC}) of all the transducers at a given nominal applied pressure, ΔP_N, as a percentage of ΔP_N.

From figure E.5 it is clear that calibrations 1 and 2 do not show a clear cubic pattern. This may be caused due to residual pressure (possibly temperature effects) in the Betz manometer creating a drift of the zero pressure during the testing of either positive or negative pressures, since all pressures within a range (either positive or negative) were tested without removing the pneumatic seal. Despite this, it is still recommended to use the ACC for these calibrations since the errors are generally lower (see figure E.7).

Table E.5 - Maximum absolute ACC errors for calibration 2 (CWG tests)

Pressure transducer	1	2	3	4	5	6	7	8	9	10	11	12	13	14	15
Max ACC error (Pa)	9	8	5	9	20	20	7	6	8	8	4	9	7	9	7

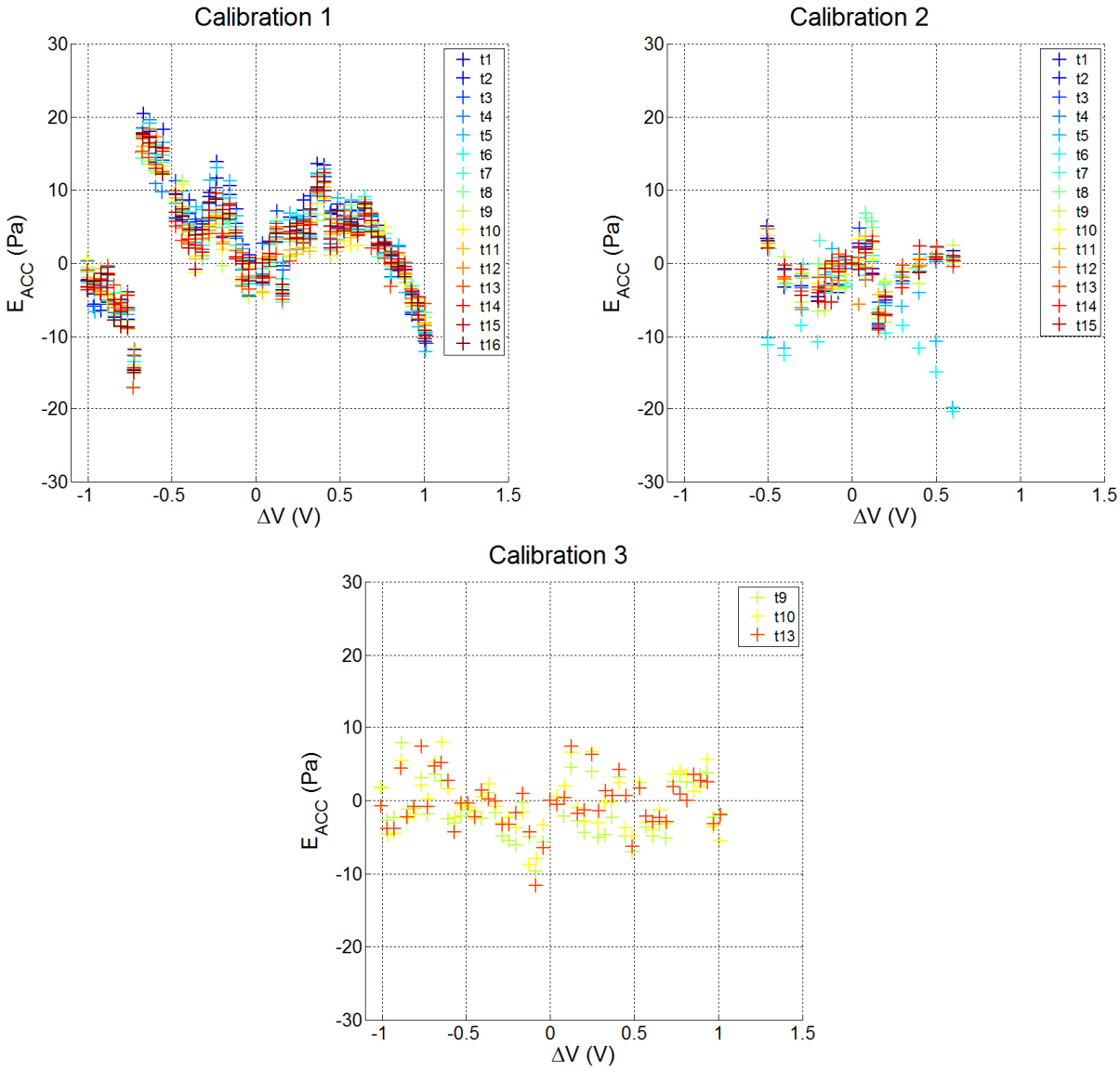

Figure E.6 - Individual ACC errors for all pressure transducers for each calibration

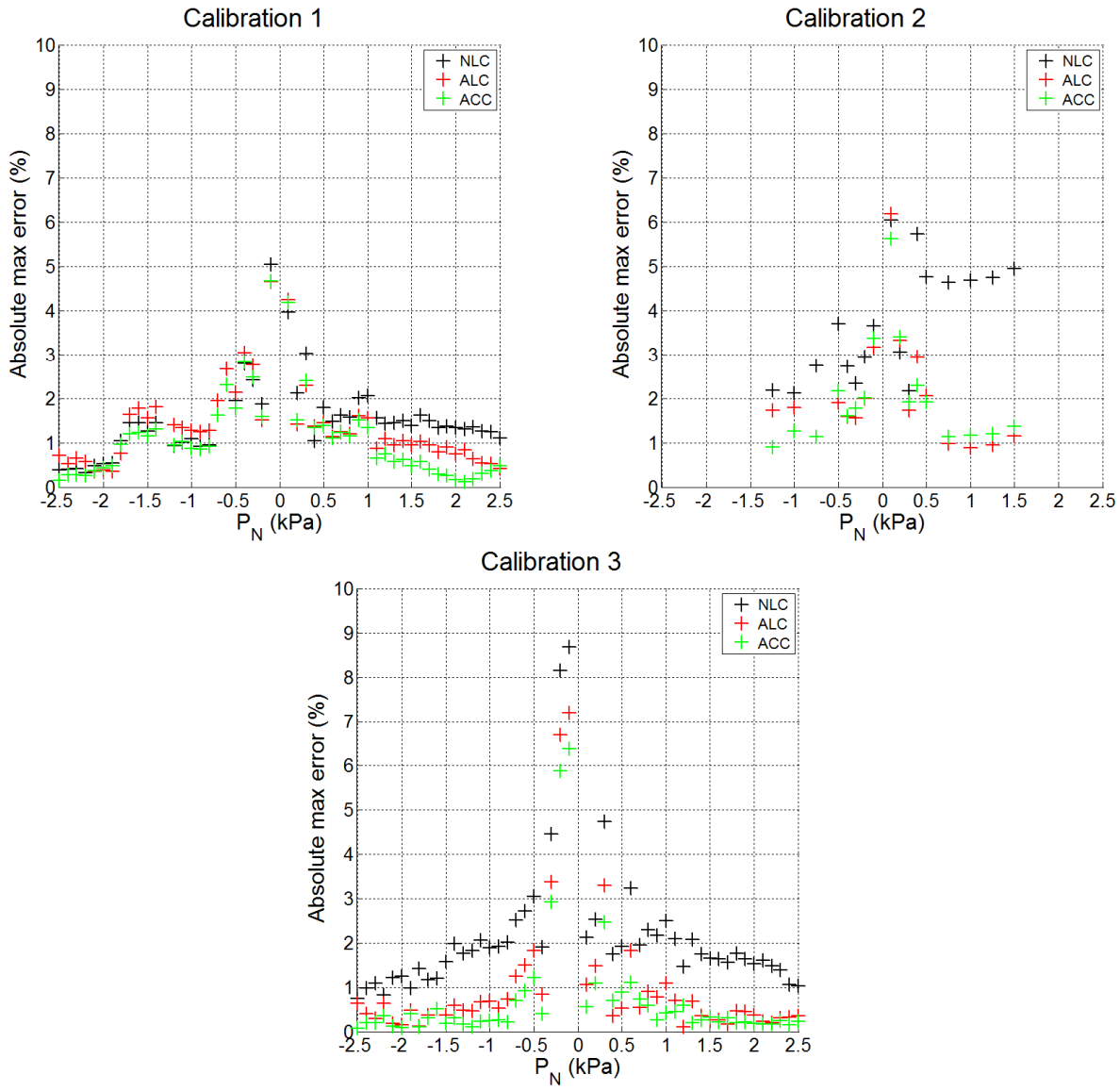

Figure E.7 - Comparison of percentage errors for NLC, ALC and ACC for each calibration

E.4 Conclusions

From the calibrations performed the following conclusions can be made:

- The voltage to pressure response of the HCLA0050DB pressure transducers is almost linear. Three different calibration equations could be used to convert the voltage output of the pressure transducers into a differential pressure.
- Generally speaking, the NLC was the least accurate, and the ACC was the most accurate method of developing a calibration function to obtain differential pressure from the voltage signal of each transducer.
- Using a closed pneumatic circuit when the negative pressures were tested, as in calibrations 1 and 2, gave possibly inaccurate data when the negative pressures were considered. Negative pressures should therefore be tested by applying a suction pressure to the HPP rather than a positive pressure to the HPP.
- When the maximum percentage errors are considered, most of the data shows less than 5% error for the NLC, ALC and ACC for calibrations 1,2 and 3. This is in line with the manufacturer's quoted value of 5% (as in table E.1).
- The largest percentage errors were at the lowest values of nominal applied pressure measured by the Betz manometer. This, combined with the sensitivity to input voltage highlights the importance of zeroing the pressure transducers before any measurements are to be carried out.

APPENDIX F

EXPERIMENTAL ERRORS AND UNCERTAINTY ANALYSIS

F.1 Introduction

Appendix F presents the methodology used in the analysis of uncertainties in the different experiments carried out during this study. The methodology in this error analysis follows the methodology used by Dorigatti, (2013) and subsequently by Soper (2014), in order to allow a comparison between this study and previous studies using the same equipment and testing facility (TRAIN rig). Section F.2 defines the two different components of total uncertainty - bias limit and random uncertainty. Section F.3 shows the calculation of the uncertainties in the slipstream measurements, considering both velocities and static pressures separately. Section F.3.1.2 examines the uncertainty associated with calculations of air density that include or neglect air humidity which is relevant whenever pressure coefficients are calculated. The errors in the moving-model crosswind tests at the TRAIN rig are analysed in section F.4, and the RWDI wind tunnel tests are considered in section F.5. Section F.6 considers the experimental uncertainties associated with the full-scale train based measurements on the NMT.

The errors presented in this appendix are very comprehensive in that they cover all/most of the measurement positions and experimental configurations. Summaries of the errors are presented in the relevant analytical methodology chapters for each experiment based on the values from this appendix.

F.2 Types of uncertainty

An error can be defined as the difference between a measured value and a true value (Taylor, 1997). In this study, errors are considered to have two main components - bias limit - arising from the error of measurement equipment, and random error associated with the fluctuations of a measured value when all other variables are kept constant.

F.2.1 Bias limit

It is conventional for aerodynamic results to be presented in the form of non-dimensional coefficients. Coefficients are calculated from a set of physical variables that are measured with different pieces of equipment, each with an associated error. Table F.2.1 lists all the measurement equipment used in this study and the manufacturer specifications of measurement range, resolution and error. In order to account for the combined effect of these individual errors, the propagation of error theory is used to calculate the uncertainty of a non-dimensional coefficient (Taylor, 1997).

The bias limit calculates the uncertainty of an measured variable, essentially quantifying the difference between the measured value and the true value. By accounting for the instrument

uncertainty (caused by non-linearity and hysteresis) compared with the magnitude of the measured value, the bias limit, E_{BIAS}, is defined by Taylor (1997) as:

$$E_{BIAS} = \sqrt{\sum_{k} \left(\frac{\partial C_{\xi}}{\partial b_k} \delta b_k \right)^2} \tag{F.1}$$

Where C_{ξ} is a non-dimensional aerodynamic coefficient, b_k is an individual physical quantity measured in the calculation of C_{ξ} and δb_k is the associated equipment uncertainty. Essentially, equation F.1 expresses each a specific error (δb_k) as a fraction of the physical value that was measured (∂b_k), multiplied by the magnitude of whatever aerodynamic coefficient was calculated.

F.2.2 Random uncertainty

In this study, aerodynamic coefficients are usually presented as ensemble averaged values. To account for the run to run variability, Dorigatti (2013) defined the random uncertainty, E_{RND}, by assuming a normal statistical distribution of each individual measurement, and considering a 95% confidence level:

$$E_{RND} = \pm 2 \frac{\sigma C_{\xi}}{\sqrt{N}} \tag{F.2}$$

Where σC_{ξ} is the standard deviation of any aerodynamic coefficient with respect to the ensemble, and N is the ensemble size. E_{RND} is therefore twice the standard deviation of the mean value with respect to the ensemble size.

F.2.3 Total uncertainty

The bias and random uncertainties measure different quantities and can be considered independent, therefore the total uncertainty is the algebraic sum of the bias and random uncertainty (Dorigatti, 2013):

$$E_{TOTAL} = E_{BIAS} + E_{RND} \quad \text{(F.3)}$$

The errors presented in this study are always given as absolute values of the various aerodynamic coefficients of interest, and it is assumed that the error is of equal magnitude in both the positive and negative components.

F.3 Slipstream measurements uncertainty

The uncertainties associated with the slipstream measurements (described in chapter 3) are calculated from both the bias and random uncertainties for both maximum velocity and static pressure, where maximum values were obtained in line with the TSI methodology and previous slipstream studies (European Commission, 2008; Gil et al., 2010; Baker et al., 2012; Soper, 2014). The methodology closely follows that of Soper, (2014), which is an adaptation of the error analysis of surface pressure coefficients in crosswind tests by Dorigatti (2013). The only difference between the methodology employed in this error study and the TSI methodology for calculating maximum velocities is that the data has not been filtered with a 1s low-pass moving average filter; maximum velocities, and similarly pressures, are taken directly from the raw data time series.

A range of slipstream measurements were made at the TRAIN rig, both at different measurement positions and with different ballast heights. Analysis in this appendix is undertaken for each measurement position, train type and ballast height investigated.

F.3.1 Slipstream tests bias limit

The bias limit depends on individual equipment inaccuracy and also the magnitude of a measured physical quantity. The equipment inaccuracies are specified in table F.1 below for all equipment used at the TRAIN rig.

Table F.1 - Slipstream tests experimental equipment and errors (TFI, 2012a, b, Greisinger, 2013, Oregon Scientific, 2016).

Measurement type	Symbol	Accuracy	Equipment
Static pressure (Pa)	$\delta\Delta P_{static}$	±5 Pa	Cobra probe
u velocity component (m/s)	δu	0.3 m/s	Cobra probe
v velocity component (m/s)	δv	0.3 m/s	Cobra probe
w velocity component (m/s)	δw	0.3 m/s	Cobra probe
Resultant horizontal velocity (m/s)	δu_{res}	0.3 m/s	Cobra probe
Train speed	δV_{train}	0.1 m/s	Light gate sensors
Air pressure	δP_{AMB}	200 Pa	Digital barometer
Air temperature	δT	1°C	Weather station
Air humidity	$\delta RH_{\%}$	1%	Weather station

F.3.1.1 Slipstream velocity bias limit

Slipstream measurements of air velocity and static pressure were made with Cobra probes, and the train speed was measured using trackside photoelectric position finders (light gates).

In the slipstream tests carried out at the TRAIN rig, the probes were aligned horizontally so that the head was pointing in the opposite direction to the direction of train travel. The positioning of the probes relative to COT and TOR was measured with a ruler (within ±0.5 mm). The angle of the probe head with the primary x-axis was checked visually using a set square, and it is estimated that this is to an accuracy of ±5°, though errors due to positioning errors are not accounted for in this analysis. This error analysis is concerned with measurement of the maximum resultant horizontal velocity, and therefore the bias associated with measurements of u_{res} by propagation of error is:

$$\begin{aligned}\delta u_{res} &= \sqrt{\left(\left(\frac{u}{\sqrt{u^2 + v^2}}\right)du\right)^2 + \left(\left(\frac{v}{\sqrt{u^2 + v^2}}\right)dv\right)^2} \\ &= \sqrt{\left(\left(\frac{u^2}{u^2 + v^2}\right)du^2\right) + \left(\left(\frac{v^2}{u^2 + v^2}\right)du^2\right)} \\ &= \sqrt{\left(\frac{u^2 + v^2}{u^2 + v^2}\right)du^2} \\ &= 0.3\ m/s\end{aligned} \tag{F.4.1}$$

The bias error for each individual TRAIN rig run (subscript r), $E_{BIAS|r}$, was calculated using:

$$E_{BIAS|r} = \sqrt{\left(\frac{C_{\xi|r}}{u_{res(max)|r}}\delta u_{res}\right)^2 + \left(\frac{C_{\xi|r}}{V_{train|LG1|r}}\delta V_{train}\right)^2 + \left(\frac{C_{\xi|r}}{V_{train|LG2|r}}\delta V_{train}\right)^2} \tag{F.4.2}$$

Where $u_{res(max)|r}$ is the maximum resultant horizontal slipstream velocity recorded by the Cobra probe, $V_{train|LGn|r}$ is the train speed of the run recorded by the light sensors

(considered twice for the first and second pair of light gates) and the aerodynamic coefficient, $C_{\xi}|r$, is the maximum of normalised resultant horizontal (U_{res}) velocity of each run:

$$C_{\xi|r} = \frac{u_{res(max)|r}}{V_{train|r}} \tag{F.4.3}$$

It should be noted that a linear deceleration assumed, but error associated with this assumption has not been accounted for in this analysis given the relatively small length of the test section and observed deceleration. Bias limits were calculated for each individual run, giving N bias limits for each individual slipstream measurement position. For the proceeding analysis, the ensemble size (N) was 20 for the all measurement positions and ballast shoulders tested. Figure F.1 shows the bias limits of 20 individual runs at a probe measurement position of 3 m from COT, 0.2 m above TOR with a ballast height of 0.3 m. The bias limits for each show very little variation, which was true for all experimental configurations. The mean bias limit for an ensemble (i.e., N = 20 runs at a given measurement position and ballast shoulder height), $\bar{E}_{BIAS}$, was given as the arithmetic mean of the individual biases, calculated as:

$$\bar{E}_{BIAS} = \frac{\sum_{N} E_{BIAS|r}}{N} \tag{F.4.4}$$

The maximum bias of the ensemble, $E_{BIAS|Max}$, was found by taking the maximum value of all of the individual biases ($E_{BIAS|r}$) in the ensemble. The maximum and mean bias limits are presented in table F.3.1.1 to F.3.3 for the key ballast shoulders and measurement positions tested, along with the random and total uncertainties, and show very little difference between the mean and maximum bias, regardless of train type, measurement position or ballast shoulder height.

F.3.1.2 Error due to neglecting air humidity

Before the errors associated with calculation of pressure coefficients are considered, it is first necessary to consider the error in the calculation of air density when humidity effects are neglected. This section considers the inaccuracy associated with neglecting air humidity from the calculation of air density, and is therefore also relevant to the crosswind tests at the TRAIN rig and full-scale measurements on the NMT.

Air density was calculated according to the ideal gas law for dry air, i.e., humidity effects on air density were neglected. The ideal gas law for dry air is:

$$\rho_d = \frac{P_{AMB}}{R_d T} \tag{F.5.1}$$

Where ρ_d is the density of dry air (zero humidity), P_{AMB} is the ambient pressure, R_d is the gas constant for air (taken as 287 J/kg.K) and T is the temperature (in Kelvin). The ideal gas law can be used to calculate the density of humid air by consider dry air and water vapour separately:

$$\rho_{d+v} = \frac{p_d}{R_d T} + \frac{p_v}{R_v T} \tag{F.5.2}$$

Where p_d is the partial pressure of dry air and p_v is the partial pressure of water vapour, and the gas constants R_v is for water vapour, taken as 461.5 J/kg.K (Wiederhold, 1997). The sum of the partial pressures equals the recorded ambient pressure:

$$P_{AMB} = p_d + p_v \tag{F.5.3}$$

The partial pressure of water vapour is defined as:

$$p_v = RH_{\%} \times p_{sat} \tag{F.5.4}$$

Where $RH_{\%}$ is the relative humidity (recorded by the weather station) and p_{sat} is the saturation pressure of water. The saturation pressure of water is a function of temperature and various empirical equations and tables exist to estimate p_{sat} based on temperature (List, 1971; Tabata, 1973; Wiederhold, 1997). The range of temperatures in this study was within -10°C to 35°C, and therefore the saturation pressures within this temperature range were calculated using a quadratic equation developed by Tabata (1973), who found a good agreement (within 0.2%) between the quadratic equation and existing meteorological reference tables, (List, 1971), within the temperature range of 0°C to 35°C. Saturation pressure was calculated from the following empirical quadratic equation (Tabata, 1973):

$$log_{10} p_{sat} = 8.4293 - 1.8272\left(\frac{10^3}{T}\right) - 0.0712\left(\frac{10^3}{T}\right)^2 \tag{F.5.5}$$

Note that equation F.5.5 gives the pressure in millibars, and T is temperature in Kelvin. The air density was calculated for two extremes - temperatures of -10°C and 35°C, and both at a nominal 100% humidity since this would give the maximum value of p_v (and hence error). The difference between the dry air density and the density of humid air, $\Delta\rho$, is defined as:

$$\Delta\rho = \rho_{d+v} - \rho_d \tag{F.5.6}$$

Note that an upper case delta (Δ) has been used solely to distinguish this term from $\delta\rho$ (defined in equation F.6.1) and does not imply that the difference in air density is large - in fact (from table F.2) the values of $\Delta\rho$ are very low compared to either the dry humid air density.

Table F.2 shows the different parameters calculated. A nominal ambient pressure of 100 kPa was used in the calculations to represent typical conditions. The first two rows of table F.2 are for the extreme of 100% humidity at the maximum and minimum temperatures that could reasonably be expected (i.e., upper bounds of error at a given temperature). The third row is at the normal standard operating conditions of the TRAIN rig - i.e., standard temperature and pressure of 25°C and 100 mbar, and a humidity of 65% (nearest 5%) which was the average humidity of all the readings taken during the experiments (one reading was taken for each run of the TRAIN rig, i.e., 725 runs). The final column in table F.2 is $\Delta\rho_{\%}$ which is $\Delta\rho$ expressed as a percentage of the density of humid air. The percentage error from neglecting humidity of air that was at 100% humidity (i.e., the most extreme case) in the calculation of air density ranged between 0.001 kg/m^3 to 0.024 kg/m^3 (i.e., 0.1% to 2.2%). The most realistic case (i.e., at standard conditions and at 65% humidity) gave the error in air density to be +0.009 kg/m^3, which is an error of less than 1%.

Table F.2 - Calculation steps to compare the density of dry air with the density of humid air

Temperature (°C)	$RH_{\%}$ (%)	P_{AMB} (Pa)	p_{sat} (Pa)	p_d (Pa)	p_v (Pa)	ρ_d (kg/m^3)	ρ_{d+v} (kg/m^3)	$\Delta\rho$ (g/m^3)	$\Delta\rho_{\%}$
0	100	10^5	287	99713	287	1.275	1.274	1.4	0.11
35	100	10^5	5621	94379	5621	1.130	1.107	24	2.17
25	65	10^5	3161	97945	2055	1.168	1.159	9.1	0.78
26	66	9.98 x 10^4	3355	97586	2214	1.162	1.152	9.7	0.84

By including the accuracy of the pressure, temperature and humidity sensors (given in table F.1), the error in air density associated with equipment uncertainty (under nominal standard conditions) was calculated according to upper and lower bounds, and shown in the final row of table F.2. A temperature of 26°C (25°C + 1°C), a humidity of (65% + 1%) and ambient

pressure of 98 mbar (100 mbar - 2 mbar) gave the largest difference in air density error, $\Delta\rho$, to the air density error at nominal standard conditions (penultimate row of table F.2):

9.1 g/m^3 - 9.7 g/m^3 = -0.6 g/m^3

The additional error due to equipment uncertainty in the estimation of error due to neglecting air humidity was very low (0.6 g/m^3), and has therefore been neglected in the calculations of error due to air humidity.

F.3.1.2 Static pressure bias limit

Static pressures were also recorded by the Cobra probes and therefore the error analysis of pressures follows the same methodology as for slipstream velocities. Aerodynamic investigations are usually primarily concerned with the peak to peak pressure of the nose pressure pulse, i.e., the difference between the maximum and minimum static pressure. Error analysis was undertaken twice - once for the maximum and once for the minimum static pressure of each run in an ensemble, then the average of these two errors was found to give a single error per run. For a small number of runs, the maximum or minimum pressure was recorded at the tail passage of the train - in these cases the tail pressure maximum or minimum was used rather than the nose peak.

The equipment errors of the Cobra probes, light sensors and ambient condition sensors are given in table F.1. Pressures were presented in the form of pressure coefficients, which depend on three physical quantities - static pressure, aerodynamic speed and air density.

The error associated with neglecting humidity from the calculation of air density, defined as $\Delta\rho$ in equation F.5.6, (i.e., difference between density of dry air and density of humid air) was

found to have a maximum value of +0.010 kg/m^3 at 65% humidity at 25°C (equivalent to a percentage error of $\Delta\rho_{\%}$= 0.8%). These conditions represent typical conditions (albeit erring towards worst realistic case rather than typical case) for air temperature and pressure, and the average humidity during the tests. The errors associated with equipment inaccuracies were combined the error associated with neglecting air humidity, and the calculation was performed at these typical conditions (T = 25°C, ρ_{air}= 1.2 kg/m^3 and P_{AMB} = 100 kPa) to give:

$$\delta\rho = \sqrt{\left(\frac{1}{RT}\delta P_{AMB}\right)^2 + \left(\frac{-P_{AMB}}{RT^2}\delta T\right)^2 + (\Delta\rho_{\%})^2} \times \rho_{air} \tag{F.6.1}$$

$$\delta\rho = 0.800\% \times 1.2 = 0.01 \text{ kg/m}^3$$

This value of $\delta\rho$ is roughly double the value found by Soper, (2015) who neglected the effects of humidity.

The bias limit of pressure coefficient for each individual run can therefore be expressed, though propagation of error, as:

$$E_{BIAS|r} = \sqrt{\left(\frac{C_{\xi|r(max,min)}}{\Delta P_{Static(max,min)|r}}\delta\Delta P_{Static}\right)^2 + \left(\frac{C_{\xi|r(max,min)}}{V_{train|r}}\delta V_{train}\right)^2 + \left(\frac{C_{\xi|r(max,min)}}{\rho_{air|r}}\delta\rho\right)} \tag{F.6.2}$$

Where $C_{\xi|r(max,\min)}$ is either the maximum or minimum pressure coefficient of each run, $\Delta P_{Static(max,min)|r}$ is the corresponding maximum or minimum pressure recorded during the run and $\rho_{air|r}$ is the dry air density from each run.

The bias limits for static pressure were lower than for velocity, which is due to the ratio of equipment error to magnitude of the physical quantity measured. Across all experimental configurations for the HST, maximum slipstream velocities were 8 m/s to 20 m/s, and static pressures were between -200 Pa and 150 Pa. The run to run variability of bias limit for static pressure was also very low.

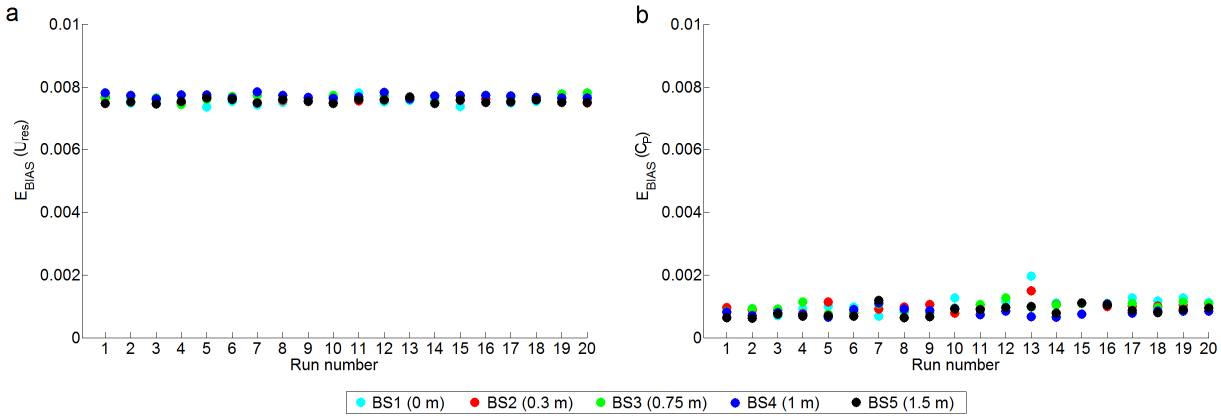

Figure F.1 - Bias limit errors of (a) velocity and (b) static pressure for individual runs at 3 m from COT, 0.2 m above TOR for all ballast shoulder heights

F.3.2 Slipstream tests random uncertainty

F.3.2.1 Slipstream velocity random uncertainty

The random uncertainty for a given ensemble (at a nominal measurement position and ballast shoulder) was calculated according to equation F.2, where σC_{ξ} was the standard deviation of the normalised maximum resultant horizontal velocities ($C_{\xi|r}$) of the ensemble (N = 20 runs). The random uncertainty was therefore a single value for each of the ensembles, which are presented in tables F.3.1.1 to F.3.3.

F.3.2.2 Static pressure random uncertainty

The random uncertainty was found using the same methodology as for slipstream velocities, where an ensemble of 20 measurements of pressure coefficient were considered with a 95% confidence interval. The procedure was carried out twice - once each for the ensembles of maxima and minima of the pressure coefficients, and the mean value taken to give an uncertainty error for each ensemble and these are presented in tables F.3.1.1 to F.3.3.

F.3.3 Slipstream tests total uncertainty

The total uncertainty is the sum of the bias limit and random uncertainty. The maximum and mean total uncertainties were calculated by adding the maximum and mean bias limits to the random uncertainty. Tables F.3.1.1 to F.3.3 presents the bias limits (mean and max from each ensemble), random uncertainties and total mean and maximum errors for each different train, ballast shoulder and probe position configuration. The HST and Class 66 train results have been split into 5 individual tables for each ballast shoulder, whereas the ICE2 results are considered in a single table as only 9 measurement configurations were studied.

Table F.3.1.1 - Errors for HST with 0 m ballast shoulder height

Distance from COT (m)	Distance from TOR (m)	Resultant horizontal velocity					Static pressure				
		E_{BIAS}		E_{RND}	E_{TOTAL}		E_{BIAS}		E_{RND}	E_{TOTAL}	
		Mean	Max		Mean	Max	Mean	Max		Mean	Max
2	0	0.008	0.008	0.033	0.041	0.041	0.002	0.003	0.014	0.016	0.017
2	0.2	0.008	0.008	0.028	0.036	0.036	0.002	0.003	0.020	0.022	0.023
2	0.7	0.008	0.008	0.041	0.049	0.049	0.002	0.003	0.018	0.021	0.021
2	1.2	0.008	0.008	0.037	0.044	0.045	0.002	0.002	0.009	0.011	0.012
3	0	0.008	0.008	0.035	0.043	0.043	0.001	0.002	0.012	0.013	0.014
3	0.2	0.008	0.008	0.036	0.044	0.044	0.001	0.002	0.015	0.016	0.017
3	0.7	0.008	0.008	0.049	0.056	0.057	0.001	0.002	0.011	0.012	0.012
3	1.2	0.008	0.008	0.046	0.053	0.054	0.001	0.001	0.009	0.010	0.010

Table F.3.1.2 - Errors for HST with 0.3 m ballast shoulder height. Note that Pr_n defines the probe numbers used in figure 4.4.

Y from COT (m)	Z from TOR (m)	Pr_n	Resultant horizontal velocity					Static pressure				
			E_{BIAS}		E_{RND}	E_{TOTAL}		E_{BIAS}		E_{RND}	E_{TOTAL}	
			Mean	Max		Mean	Max	Mean	Max		Mean	Max
2	0	1	0.008	0.008	0.031	0.039	0.039	0.002	0.003	0.020	0.022	0.023
2	0.2	2	0.008	0.008	0.021	0.029	0.029	0.002	0.003	0.021	0.023	0.024
2	0.7	3	0.008	0.008	0.042	0.050	0.050	0.002	0.003	0.018	0.020	0.021
2	1	4	0.008	0.008	0.040	0.047	0.048	0.002	0.003	0.018	0.020	0.021
2	1.2	5	0.008	0.008	0.051	0.058	0.059	0.002	0.003	0.018	0.019	0.020
2	1.75	6	0.008	0.008	0.050	0.058	0.058	0.002	0.002	0.018	0.020	0.021
2	2.3	7	0.008	0.008	0.020	0.027	0.028	0.001	0.001	0.007	0.008	0.008
2.5	-0.3	8	0.008	0.008	0.029	0.037	0.037	0.001	0.002	0.012	0.013	0.014
2.5	0	9	0.008	0.008	0.035	0.043	0.043	0.001	0.002	0.011	0.013	0.013
2.5	0.2	10	0.008	0.008	0.039	0.046	0.047	0.001	0.002	0.008	0.010	0.010
2.5	0.7	11	0.008	0.008	0.046	0.054	0.054	0.001	0.002	0.015	0.017	0.017
2.5	1.2	12	0.008	0.008	0.053	0.061	0.061	0.001	0.002	0.009	0.010	0.011
2.5	1.75	13	0.008	0.008	0.053	0.061	0.061	0.001	0.001	0.004	0.006	0.006
2.5	2.3	14	0.007	0.008	0.030	0.038	0.038	0.001	0.001	0.002	0.003	0.003
3	-0.3	15	0.008	0.008	0.025	0.032	0.032	0.001	0.001	0.008	0.009	0.009
3	0	16	0.008	0.008	0.036	0.044	0.044	0.001	0.001	0.009	0.010	0.011
3	0.2	17	0.008	0.008	0.042	0.050	0.050	0.001	0.001	0.008	0.009	0.010
3	0.7	18	0.008	0.008	0.052	0.060	0.060	0.001	0.001	0.008	0.009	0.009
3	1.2	19	0.007	0.008	0.039	0.046	0.046	0.001	0.001	0.006	0.007	0.007
3	1.75	20	0.007	0.008	0.026	0.033	0.034	0.001	0.001	0.005	0.005	0.006
3	2.3	21	0.007	0.008	0.024	0.031	0.031	0.001	0.001	0.003	0.004	0.004
3.5	0.2	22	0.008	0.008	0.041	0.048	0.048	0.001	0.001	0.008	0.009	0.009
3.5	0.7	23	0.008	0.008	0.040	0.047	0.047	0.001	0.002	0.011	0.012	0.012
3.5	1.2	24	0.007	0.008	0.033	0.040	0.040	0.001	0.001	0.003	0.004	0.004
3.5	1.75	25	0.008	0.008	0.042	0.049	0.049	0.001	0.001	0.008	0.009	0.009
3.5	2.3	26	0.007	0.008	0.023	0.030	0.030	0.001	0.001	0.002	0.002	0.002

Table F.3.1.3 - Errors for HST with 0.75 m ballast shoulder height

Distance from COT (m)	Distance from TOR (m)	Resultant horizontal velocity					Static pressure				
		E_{BIAS}		E_{RND}	E_{TOTAL}		E_{BIAS}		E_{RND}	E_{TOTAL}	
		Mean	Max		Mean	Max	Mean	Max		Mean	Max
2	0	0.008	0.008	0.031	0.039	0.039	0.002	0.003	0.023	0.025	0.027
2	0.2	0.008	0.008	0.040	0.048	0.048	0.002	0.003	0.018	0.020	0.021
2	0.7	0.008	0.008	0.042	0.050	0.050	0.002	0.003	0.019	0.021	0.022
2	1.2	0.008	0.008	0.030	0.038	0.038	0.002	0.003	0.025	0.027	0.028
2.5	-0.3	0.008	0.008	0.041	0.049	0.049	0.001	0.002	0.009	0.010	0.011
3	-0.6	0.008	0.008	0.045	0.052	0.052	0.001	0.001	0.007	0.008	0.008
3	-0.3	0.008	0.008	0.039	0.047	0.047	0.001	0.001	0.008	0.008	0.009
3	0	0.008	0.008	0.046	0.054	0.054	0.001	0.001	0.008	0.008	0.009
3	0.2	0.008	0.008	0.039	0.046	0.047	0.001	0.001	0.008	0.009	0.009
3	0.7	0.008	0.008	0.039	0.047	0.047	0.001	0.001	0.008	0.009	0.010
3	1.2	0.008	0.008	0.047	0.055	0.055	0.001	0.001	0.008	0.009	0.009

Table F.3.1.4 - Errors for HST with 1 m ballast shoulder height

Distance from COT (m)	Distance from TOR (m)	Resultant horizontal velocity					Static pressure				
		E_{BIAS}		E_{RND}	E_{TOTAL}		E_{BIAS}		E_{RND}	E_{TOTAL}	
		Mean	Max		Mean	Max	Mean	Max		Mean	Max
3	-0.6	0.008	0.008	0.037	0.045	0.045	0.001	0.001	0.006	0.007	0.008
3	-0.3	0.008	0.008	0.030	0.038	0.038	0.001	0.001	0.008	0.008	0.009
3	0.2	0.008	0.008	0.041	0.049	0.049	0.001	0.001	0.007	0.008	0.008
3	1.2	0.008	0.008	0.032	0.040	0.040	0.001	0.001	0.007	0.007	0.008

Table F.3.1.5 - Errors for HST with 1.5 m ballast shoulder height

Distance from COT (m)	Distance from TOR (m)	Resultant horizontal velocity					Static pressure				
		E_{BIAS}		E_{RND}	E_{TOTAL}		E_{BIAS}		E_{RND}	E_{TOTAL}	
		Mean	Max		Mean	Max	Mean	Max		Mean	Max
2	0	0.008	0.008	0.035	0.043	0.043	0.002	0.002	0.015	0.017	0.017
2	0.2	0.008	0.008	0.028	0.036	0.036	0.002	0.002	0.012	0.013	0.014
2	1.2	0.008	0.008	0.048	0.056	0.056	0.002	0.002	0.011	0.012	0.013
2.5	-0.3	0.008	0.008	0.040	0.048	0.048	0.001	0.001	0.009	0.010	0.010
2.5	0	0.008	0.008	0.044	0.051	0.052	0.001	0.002	0.013	0.014	0.015
2.5	0.2	0.008	0.008	0.035	0.042	0.042	0.001	0.001	0.009	0.010	0.010
3	-0.6	0.008	0.008	0.037	0.044	0.044	0.001	0.001	0.005	0.006	0.006
3	-0.3	0.008	0.008	0.041	0.048	0.048	0.001	0.001	0.009	0.010	0.010
3	0	0.008	0.008	0.036	0.044	0.044	0.001	0.002	0.011	0.012	0.013
3	0.2	0.008	0.008	0.040	0.048	0.048	0.001	0.001	0.010	0.011	0.011
3	1.2	0.007	0.008	0.037	0.045	0.045	0.001	0.001	0.010	0.011	0.011
3.5	0.2	0.008	0.008	0.049	0.056	0.056	0.001	0.001	0.009	0.010	0.011

Table F.3.2.1 - Errors for Class 66 freight train with 0 m ballast shoulder height

Distance from COT (m)	Distance from TOR (m)	Resultant horizontal velocity					Static pressure				
		E_{BIAS}		E_{RND}	E_{TOTAL}		E_{BIAS}		E_{RND}	E_{TOTAL}	
		Mean	Max		Mean	Max	Mean	Max		Mean	Max
2	0	0.010	0.010	0.027	0.037	0.037	0.004	0.005	0.025	0.029	0.030
2	0.2	0.010	0.010	0.026	0.036	0.036	0.005	0.005	0.018	0.023	0.024
2	0.7	0.010	0.010	0.043	0.053	0.053	0.005	0.006	0.030	0.036	0.037
2	1.2	0.010	0.011	0.043	0.053	0.054	0.005	0.007	0.032	0.038	0.040
3	0	0.009	0.010	0.026	0.035	0.036	0.002	0.003	0.019	0.022	0.022
3	0.2	0.009	0.010	0.025	0.034	0.034	0.002	0.003	0.017	0.020	0.020
3	0.7	0.009	0.010	0.019	0.028	0.029	0.003	0.004	0.027	0.030	0.031
3	1.2	0.010	0.010	0.034	0.044	0.044	0.003	0.004	0.024	0.027	0.029

Table F.3.2.2 - Errors for Class 66 freight train with 0.3 m ballast shoulder height

Distance from COT (m)	Distance from TOR (m)	Resultant horizontal velocity					Static pressure				
		E_{BIAS}		E_{RND}	E_{TOTAL}		E_{BIAS}		E_{RND}	E_{TOTAL}	
		Mean	Max		Mean	Max	Mean	Max		Mean	Max
2	0	0.010	0.010	0.028	0.038	0.038	0.004	0.005	0.024	0.028	0.028
2	0.2	0.010	0.010	0.038	0.048	0.049	0.004	0.005	0.020	0.024	0.025
2	0.7	0.010	0.011	0.065	0.076	0.076	0.005	0.006	0.036	0.041	0.043
2	1	0.010	0.011	0.060	0.070	0.070	0.005	0.007	0.037	0.042	0.043
2	1.2	0.010	0.011	0.058	0.069	0.069	0.005	0.006	0.035	0.040	0.042
2.5	-0.3	0.010	0.010	0.033	0.042	0.042	0.003	0.003	0.020	0.023	0.023
2.5	0	0.010	0.010	0.033	0.042	0.043	0.003	0.005	0.029	0.032	0.034
2.5	0.2	0.010	0.010	0.026	0.035	0.036	0.003	0.004	0.021	0.024	0.025
2.5	0.7	0.010	0.010	0.030	0.040	0.040	0.004	0.005	0.031	0.035	0.036
2.5	1.2	0.010	0.010	0.059	0.069	0.069	0.004	0.006	0.035	0.039	0.040
3	-0.3	0.009	0.010	0.016	0.026	0.026	0.002	0.003	0.016	0.019	0.019
3	0	0.009	0.010	0.023	0.032	0.032	0.002	0.003	0.019	0.021	0.022
3	0.2	0.010	0.010	0.022	0.032	0.032	0.002	0.003	0.019	0.022	0.023
3	0.7	0.009	0.010	0.018	0.027	0.027	0.003	0.003	0.018	0.021	0.021
3	1.2	0.009	0.010	0.032	0.041	0.042	0.003	0.004	0.033	0.036	0.038

Table F.3.2.3 - Errors for Class 66 freight train with 0.75 m ballast shoulder height

Distance from COT (m)	Distance from TOR (m)	Resultant horizontal velocity					Static pressure				
		E_{BIAS}		E_{RND}	E_{TOTAL}		E_{BIAS}		E_{RND}	E_{TOTAL}	
		Mean	Max		Mean	Max	Mean	Max		Mean	Max
2	0	0.010	0.010	0.033	0.043	0.043	0.004	0.005	0.032	0.036	0.037
2	0.2	0.010	0.010	0.050	0.060	0.061	0.004	0.005	0.023	0.027	0.028
2	0.7	0.010	0.011	0.053	0.063	0.064	0.005	0.007	0.035	0.040	0.041
2	1.2	0.010	0.011	0.049	0.059	0.060	0.005	0.007	0.057	0.062	0.064
2.5	-0.3	0.009	0.010	0.025	0.035	0.035	0.003	0.003	0.019	0.022	0.022
3	-0.6	0.009	0.009	0.020	0.029	0.029	0.002	0.002	0.018	0.020	0.021
3	-0.3	0.009	0.009	0.019	0.028	0.028	0.002	0.002	0.019	0.021	0.021
3	0	0.009	0.010	0.021	0.031	0.031	0.002	0.002	0.014	0.016	0.016
3	0.2	0.009	0.010	0.024	0.034	0.034	0.002	0.003	0.014	0.017	0.017
3	0.7	0.009	0.010	0.030	0.039	0.039	0.003	0.003	0.018	0.021	0.022
3	1.2	0.009	0.009	0.022	0.031	0.031	0.003	0.004	0.037	0.040	0.042

Table F.3.2.4 - Errors for Class 66 freight train with 1 m ballast shoulder height

Distance from COT (m)	Distance from TOR (m)	Resultant horizontal velocity					Static pressure				
		E_{BIAS}		E_{RND}	E_{TOTAL}		E_{BIAS}		E_{RND}	E_{TOTAL}	
		Mean	Max		Mean	Max	Mean	Max		Mean	Max
3	-0.6	0.009	0.010	0.027	0.037	0.037	0.002	0.003	0.025	0.027	0.028
3	-0.3	0.009	0.010	0.026	0.035	0.035	0.002	0.002	0.017	0.019	0.019
3	0.2	0.009	0.010	0.025	0.034	0.034	0.002	0.003	0.020	0.022	0.023
3	1.2	0.009	0.010	0.036	0.045	0.045	0.003	0.004	0.037	0.040	0.041

Table F.3.2.5 - Errors for Class 66 freight train with 1.5 m ballast shoulder height

Distance from COT (m)	Distance from TOR (m)	Resultant horizontal velocity					Static pressure				
		E_{BIAS}		E_{RND}	E_{TOTAL}		E_{BIAS}		E_{RND}	E_{TOTAL}	
		Mean	Max		Mean	Max	Mean	Max		Mean	Max
2	0	0.010	0.010	0.038	0.047	0.048	0.004	0.005	0.029	0.033	0.035
2	0.2	0.010	0.010	0.034	0.043	0.044	0.005	0.005	0.021	0.025	0.026
2	1.2	0.010	0.011	0.038	0.049	0.049	0.005	0.007	0.046	0.051	0.054
2.5	-0.3	0.009	0.010	0.023	0.033	0.033	0.003	0.003	0.021	0.023	0.024
2.5	0	0.009	0.010	0.025	0.034	0.035	0.003	0.004	0.026	0.029	0.030
2.5	0.2	0.010	0.010	0.028	0.037	0.037	0.003	0.004	0.034	0.037	0.038
2.5	1.2	0.010	0.010	0.046	0.056	0.056	0.004	0.006	0.046	0.050	0.052
3	-0.6	0.009	0.009	0.017	0.026	0.026	0.002	0.002	0.018	0.020	0.020
3	-0.3	0.009	0.010	0.021	0.030	0.030	0.002	0.003	0.016	0.018	0.019
3	0	0.009	0.010	0.023	0.032	0.033	0.002	0.003	0.023	0.025	0.026
3	0.2	0.009	0.010	0.024	0.034	0.034	0.002	0.004	0.024	0.026	0.028
3	1.2	0.009	0.010	0.031	0.040	0.041	0.003	0.004	0.027	0.030	0.031

Table F.3.3 - Errors for ICE2 at all tested ballast shoulder heights

Ballast shoulder height (m)	Distance from COT (m)	Distance from TOR (m)	Resultant horizontal velocity					Static pressure				
			E_{BIAS}		E_{RND}	E_{TOTAL}		E_{BIAS}		E_{RND}	E_{TOTAL}	
			Mean	Max		Mean	Max	Mean	Max		Mean	Max
0	2	1.2	0.008	0.008	0.032	0.039	0.040	0.001	0.001	0.007	0.009	0.009
	3	0.2	0.008	0.008	0.041	0.048	0.048	0.001	0.001	0.011	0.011	0.012
	3	1.2	0.008	0.008	0.039	0.046	0.046	0.001	0.002	0.012	0.013	0.014
0.75	3	-0.3	0.007	0.008	0.034	0.041	0.041	0.001	0.001	0.004	0.004	0.005
	3	0.2	0.007	0.008	0.034	0.042	0.042	0.001	0.001	0.009	0.010	0.011
	3	1.2	0.008	0.008	0.034	0.042	0.042	0.001	0.001	0.008	0.009	0.009
1.5	3	-0.3	0.007	0.008	0.043	0.050	0.050	0.001	0.001	0.005	0.005	0.005
	3	0.2	0.007	0.008	0.045	0.052	0.052	0.001	0.001	0.006	0.007	0.007
	3	1.2	0.007	0.008	0.030	0.037	0.037	0.001	0.001	0.004	0.005	0.005

F.4 Moving model crosswind tests uncertainty

Moving model tests were undertaken at the TRAIN rig through the crosswind generator, and the tests are described in chapters 6 and 7.

F.4.1 Train speed calculation error

Train speed and hence position through the crosswind generator was calculated using a different method to previous studies (Dorigatti, 2013; Soper 2014). Lasers were set up in the crosswind generator at a nominal 2 m spacing down the track which gave the exact train position and allowed the deceleration characteristics of the train through the CWG to be estimated. Pressure and light sensor data were sampled at 4000 Hz by the onboard data logger, and by making the assumption that the position of the voltage peaks from the onboard light sensor (from detecting the laser) are within one sample, at a nominal train speed of

45 m/s (the maximum speed tested) the number of samples between two light sources 2 m apart is 178 samples. If this train speed is recalculated taking the distance as 2 m and the time as (178 ±1)/4000, the possible range in train speed is 44.75 m/s to 45.25 m/s, i.e., an error in train speed of 0.25 m/s. While this error is larger than the error associated with using the light gates, it is believed that using lasers and an onboard light sensor is still more accurate than assuming a linear deceleration through the CWG, with the specific advantage that the train position is marked accurately on the same data time series as the pressure data, and recorded with the same data logger.

F.4.2 Moving model crosswind tests bias limit

The bias limit for the crosswind tests is dependent on the individual accuracies of the measurement equipment, which are specified in table F.1. As before, the bias limit was calculated for each individual run and for each individual pressure transducer. The maximum and mean bias limits for each pressure transducer are specified in table F.4. Bias limit was calculated by:

$$E_{BIAS|r} = \sqrt{\left(\frac{C_{\xi|r}}{\Delta P_{i|r}}\delta\Delta P_i\right)^2 + \left(\frac{C_{\xi|r}}{V_{train|r}}\delta V_{train}\right)^2 + \left(\frac{C_{\xi|r}}{\rho_{air|r}}\delta\rho\right)^2 + \left(\frac{C_{\xi|r}}{\overline{U_{CWG|x}}}\overline{\delta U_{CWG}}\right)^2 + \left(\frac{C_{\xi|r}}{P_{stat|x}}\overline{\delta P_{stat}}\right)^2} \quad \text{(F.7)}$$

Where $\Delta P_{i|r}$ was the mean differential pressure of an individual pressure transducer (subscript i) per run (subscript r), $\delta\Delta P_i$ was the individual maximum error of the transducer (from the calibration in appendix E), and $\overline{\delta U_{CWG}}$ and $\overline{\delta P_{stat}}$ were the crosswind generator velocity perpendicular to train travel and the local static pressure obtained from the flow

characterisation by Dorigatti, (2013). The term $C_{\xi|r}$ is defined as the mean pressure coefficient for a single tap, calculated while the train was through a portion of the CWG where the flow was regarded as stable, in line with previous studies (Dorigatti, 2013 and Soper, 2014). It should be noted that the term $\Delta P_{i|r}$ was calculated from the voltage output of each pressure transducer (from calibrations in appendix E), and therefore the errors were obtained from calibration 2 in appendix E for each pressure transducer, and are given in table E.5.

F.4.3 Moving model crosswind tests random uncertainty

Two methodologies have been used to calculate random uncertainty based on the two different analytical procedures of the CWG data. The ensemble average methodology follows that used by Dorigatti, (2013) and Soper, (2014). The yaw angle bins methodology considers the random uncertainty calculated from the standard deviation of each yaw angle bin and tap. The two methodologies are compared in section F.4.3.3.

F.4.3.1 Ensemble average random uncertainty

The ensemble random uncertainty ($E_{RND,ens}$) was calculated assuming that the mean pressure coefficients for each ensemble were normally distributed, and with a 95% confidence limit as in equation 2. The calculation was performed for each individual mean pressure coefficient (and for each individual pressure transducer/tap) in relation to the ensemble mean for each pressure transducer at each of the yaw angles tested. The number of runs in each ensemble was variable because of the need to conduct a second and briefer set of tests (see section H.2).

In all cases, N was taken as the actual number of runs in the ensemble which ranged from 10 to 15 runs.

F.4.3.2 Yaw angle bin random uncertainty

The yaw bin random uncertainty ($E_{RND,bin}$), i.e., for a single pressure tap at a given yaw angle, described in section 7.3.6), $E_{RND,bin}$, was calculated assuming a normal distribution of pressure coefficients and at a 95% confidence level following equation F.2 where N was taken as the number of samples within each yaw angle bin. The individual bin means, standard deviations and random uncertainties of each bin are given in table 8.2.

F.4.3.3 Comparison of random uncertainties

The values of random uncertainty for each pressure tap are shown on figure F.2.1 where (a) is the ensemble average methodology random error and (b) is the yaw angle bin methodology random error. The random errors were higher when the ensemble average methodology was considered, and this was due to the difference in the value of N; the value of N was typically 3000-6000 for the yaw angle bins methodology whereas for the ensemble methodology N was taken as the number of runs, typically 10 to 15. Generally, the random error increases in magnitude as the yaw angle is increased when $E_{RND,ens}$ is considered. The yaw angle bin errors are fairly consistent for yaw angles from 15° - 25°, though it should be noted that at the nose at 30° yaw angle that the bin errors are approximately twice as large as nose errors at 15° - 25°. The "outliers" in the bin errors are only present at 30° and correspond with pressure taps near to the roof-wall junctions. Larger values of $E_{RND,ens}$ are also seen at these tap

positions, indicating that the roof-wall corners show higher amplitude time domain fluctuation in pressures. Figure F.2.2 compares the individual random errors for both methodologies and shows a positive (albeit fairly spread) correlation, indicating that both methodologies are appropriate in terms of quantifying the random uncertainty. For the purposes of this study, when total errors have been calculated, the larger valued $E_{RND,ens}$ errors have been used to construct error bars in chapter 8.

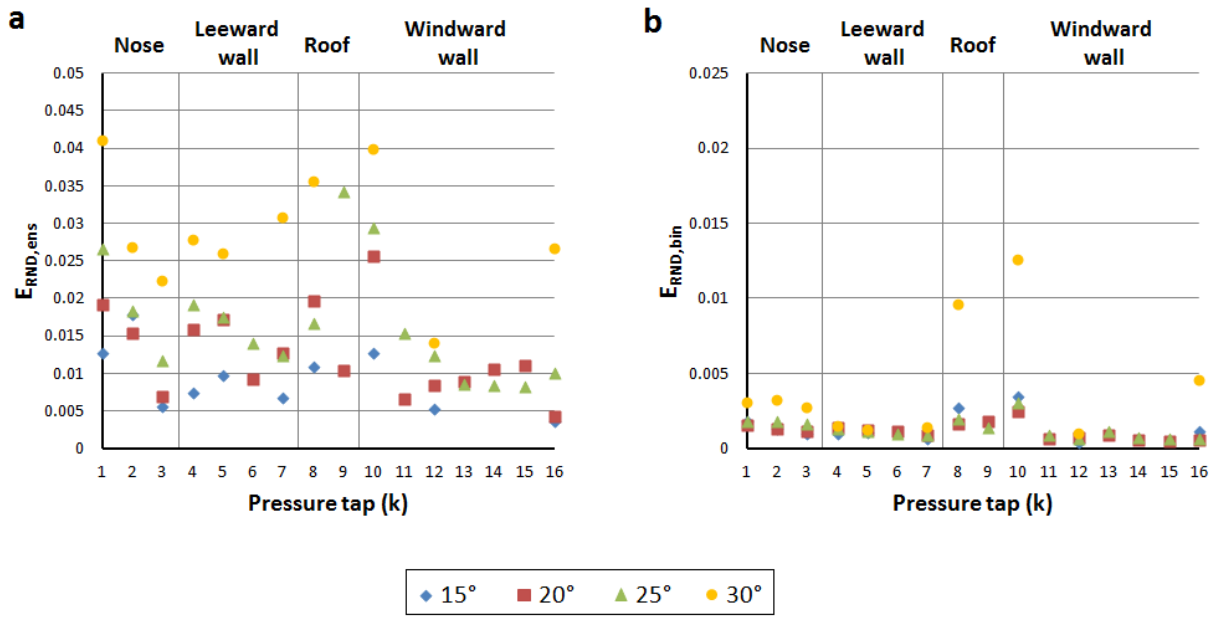

Figure F.2.1 - Random uncertainties for each pressure tap and yaw angle for (a) ensemble of maxima and (b) from each yaw angle bin

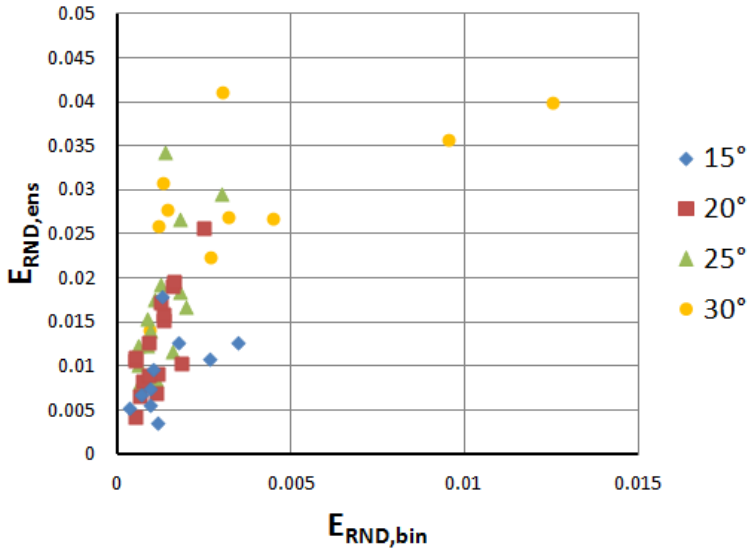

Figure F.2.2 - Scatter plot comparing the random uncertainties SYM and SYM for all pressure taps and yaw angles.

F.4.4 Moving model crosswind tests total uncertainty

The total uncertainty for each pressure tap is the sum of the bias and random uncertainties. Table F.4 lists all of the errors calculated for the CWG tests. The uncertainty for tap L10 was unacceptably high, and as a result of this error analysis this tap has been disregarded from analysis in this study.

Table F.4 - All errors for TRAIN rig CWG tests.

	$E_{BIAS\ (MEAN)}$				$E_{BIAS\ (MAX)}$				E_{RND}				$E_{TOTAL\ (MEAN)}$				$E_{TOTAL\ (MAX)}$			
	15°	20°	25°	30°	15°	20°	25°	30°	15°	20°	25°	30°	15°	20°	25°	30°	15°	20°	25°	30°
N1	0.025	0.023	0.031	0.026	0.026	0.024	0.045	0.029	0.013	0.019	0.027	0.041	0.037	0.042	0.058	0.067	0.039	0.043	0.072	0.070
N2	0.035	0.034	0.033	0.036	0.037	0.036	0.035	0.039	0.018	0.015	0.018	0.027	0.053	0.049	0.052	0.063	0.055	0.051	0.053	0.066
N3	0.038	0.038	0.037	0.037	0.039	0.039	0.038	0.039	0.006	0.007	0.012	0.022	0.044	0.045	0.049	0.060	0.045	0.046	0.050	0.061
L1	0.008	0.011	0.016	0.023	0.009	0.015	0.018	0.026	0.004	0.004	0.010	0.027	0.011	0.015	0.026	0.050	0.012	0.020	0.028	0.053
L2		0.010	0.007			0.024	0.025			0.011	0.008			0.021	0.015			0.035	0.034	
L3		0.006	0.008			0.011	0.028			0.011	0.008			0.017	0.016			0.021	0.037	
L4		0.009	0.010			0.017	0.028			0.009	0.009			0.018	0.019			0.026	0.037	
L5	0.007	0.011	0.017	0.023	0.008	0.015	0.020	0.026	0.005	0.008	0.012	0.014	0.012	0.019	0.029	0.037	0.014	0.024	0.033	0.040
L6		0.010	0.016			0.011	0.020			0.007	0.015			0.016	0.031			0.018	0.036	
L7	0.007	0.015	0.023	0.032	0.012	0.025	0.028	0.039	0.013	0.026	0.029	0.040	0.020	0.040	0.053	0.072	0.024	0.051	0.057	0.079
L8		0.017	0.026			0.018	0.032			0.010	0.034			0.027	0.060			0.029	0.066	
L9	0.008	0.014	0.021	0.027	0.010	0.022	0.024	0.035	0.011	0.020	0.017	0.036	0.018	0.034	0.037	0.063	0.021	0.041	0.041	0.070
L10																				
L11	0.004	0.009	0.013	0.017	0.007	0.015	0.017	0.024	0.007	0.013	0.012	0.031	0.011	0.021	0.026	0.048	0.014	0.028	0.029	0.055
L12		0.026	0.040			0.028	0.050			0.009	0.014			0.035	0.054			0.037	0.064	
L13	0.015	0.024	0.037	0.050	0.059	0.048	0.044	0.060	0.010	0.017	0.018	0.026	0.025	0.041	0.054	0.075	0.069	0.065	0.061	0.086
L14	0.016	0.022	0.034	0.048	0.048	0.043	0.041	0.059	0.007	0.016	0.019	0.028	0.024	0.038	0.054	0.075	0.055	0.059	0.060	0.086

F.4.5 Aerodynamic load uncertainty

The overturning force on the train is calculated by integration of the pressure taps across a discretised train model. For the crosswind tests at the TRAIN rig only a single loop of pressure taps was tested, and because the underbody was neglected, only a side force coefficient was calculated for a 1 m strip centred on the pressure tap loop.

By considering the individual pressure tap measurements (and errors) independent for each pressure tap (subscript i), the total error in the values of an aerodynamic force (side, lift etc) was calculated by propagation of error as (Dorigatti, 2013):

$$E_{TOTAL,C_N} = \sqrt{\sum_j (\sum_i \frac{\partial C_{\xi,j}}{\partial C_{p_{ij}}} E_{TOTAL_{ij}})^2} \quad \text{(F.8)}$$

Where j is the loop number (in the TRAIN rig tests only a single loop was considered, hence j = 1).

Total uncertainties for force and moment coefficients were calculated for yaw angles of 20° and 25° since these were the two cases that had all 14 pressure channels working. Table F.5 presents these errors. The values calculated do not account for the limit in spatial resolution of the pressure taps and the assumption of a uniform pressure distribution in the discretised area of each pressure tap (Dorigatti, 2013). It is therefore acknowledged that the true errors are likely larger than those shown later in figure F.3. The total error in side force coefficient was recalculated at twice the pressure tap resolution (by generating pseudo tap positions halfway between the actual pressure taps, and linearly interpolating the actual recorded pressures and errors to generate corresponding pseudo Cp and error values). No significant differences were

observed between the original total error and the total error at the greater pressure tap resolution, therefore the values presented table F.5 have been used for this study.

Table F.5 - Total error for force and moment coefficients for single loop of pressure taps from CWG tests.

Coefficient	E_{TOTAL} (C_N^*)	
	20°	25°
Side force (C_Y^*)	0.013	0.016
Lift force (C_Z^*)	0.023	0.030
Moment ($C_{M_X}^*$)	0.010	0.012
Lee-rail moment ($C_{M_{X,lee}}^*$)	0.017	0.021

F.5 RWDI wind tunnel tests uncertainty

Two wind tunnel tests were conducted by RWDI, and described in chapters 6 and 7. This section aims to estimate the total uncertainty associated with the wind tunnel measurements, however, the analysis is based on limited information about the experimental set up, and so the values calculated for bias limit should be treated with caution.

F.5.1 Wind tunnel bias limit

No details of the experimental equipment used in the wind tunnel tests was provided, and therefore bias limits cannot be calculated with any certainty. However, for the purpose of this study, nominal equipment uncertainties based on the equipment used for other tests have been used to calculate the bias limit.

The following assumptions were made:

- The mean wind tunnel velocity profiles in the x, y and z directions were uniform. However, a yaw angle offset of about -3° for both was observed at zero yaw, indicating a velocity component in the cross flow (y) direction. It was assumed that there was no boundary layer, though this may be incorrect.
- The static port of the reference pitot-static probe was in a closed pneumatic circuit in parallel with the LPP of each pressure transducer.
- The static pressure at the reference pitot-static probe position (wind tunnel orifice) was the same as the local static pressure at the train model, i.e., no longitudinal pressure gradient in the open air test section.
- The dynamic pressure was measured by the pitot-static probe with a single pressure transducer, where the HPP was connected to the total pressure port of the probe and the LPP of the transducer was connected to the static pressure port of the probe.
- The pressure recorded by each tap was converted to pressure coefficient using equation 7.1, and therefore depended on two measured quantities.
- It was assumed (incorrectly) that the ground set up (turntable and track-ballast) had no affect on the air flow impinging on the train. Appendix I describes a separate wind tunnel test to investigate this assumption which found that the addition of the ballast piece affected the air flow at the train nose at zero yaw angle.
- The ambient conditions (temperature, pressure humidity) and equipment uncertainties pressure transducers were not provided, therefore an estimation of the uncertainty is based on the equipment used in the TRAIN rig tests (as table F.1).

When considering this specific error analysis, the following additional assumptions were made:

- Each pressure tap was measured independently of other pressure taps.
- Wind tunnel velocity was calculated by RWDI from the dynamic pressure measured by the reference pitot static probe using the same type of pressure transducer as for the pressure taps on the train model.
- The velocity calculated at the reference probe location was the same as the air velocity at the location of the train, and the velocity was uniform across the train height and width.
- There were no differences in static pressure at the wind tunnel nozzle and at the train model.
- The errors associated with train positioning and measuring the yaw angle of the train-turntable were neglected.

Given the assumptions in the experimental set up, each pressure coefficient depended on two measured quantities: the pressure at the pressure tap, and the dynamic pressure from the reference probe. The nominal dynamic pressure was calculated from the mean wind tunnel velocity and an air density of 1.2 kg/m^3. Nominal dynamic pressures were therefore 290 Pa and 220 Pa for the 13.2 m/s and 11.5 m/s tests respectively.

The bias limit was calculated for each of the 314 pressure taps at each yaw angle (θ = 0° to 50°) for both of the wind tunnel tests (i.e., 13.2 m/s and 11.5 m/s). By propagation of error, the bias limit was defined as:

$$E_{BIAS|i\varphi} = \sqrt{\left(\frac{C_{\xi|i\varphi}}{\overline{\Delta P}_{i\varphi}}\delta\Delta P_i\right)^2 + \left(\frac{C_{\xi|i\varphi}}{P_{Dynamic}}\delta P_{Dynamic}\right)^2} \quad \text{(F.9)}$$

F.5.2 Wind tunnel random uncertainty

Data was presented as a time series of pressure coefficient for each tapping point, sampled for 120 s at 512 Hz (N = 61440 samples). The random uncertainty was calculated to a 95% confidence interval and assuming that the unsteady pressure fluctuations followed a normal distribution, as in equation F.2. Given that the sampling duration was large and the flow could be considered to have a stable mean for this duration, the random uncertainties were very low - about 0.001 of the mean Cp, and between 1% - 5% of the bias error and therefore have not been presented in this appendix.

F.5.3 Wind tunnel total uncertainty

The total uncertainty for each pressure tap is given as the sum of the bias and random uncertainty.

Tables F.6.1 to F.6.2.7 give the values of total error and have been given only at yaw angles of 0°, 5° 10° 20° and 45° for brevity. Table F.6.1 presents the total errors for all the nose taps, and shows that overall the values of total error at the nose are very similar. The key pressure taps used to calculate yaw angle at full-scale are highlighted in green. Tables F.6.2.1 to F.6.2.7 show the total error for each individual loop of pressure taps around the power car body, and the windward wall taps are highlighted in red, the roof in orange and the leeward side wall in blue. Again, there is very little difference in total error regardless of loop position along the train. Generally, the errors are of highest magnitude over the roof as the yaw angle increases.

Table F.6.1 - Total uncertainties (absolute) for pressure taps on wind tunnel model nose - taps highlighted in green are at same position as on NMT and TRAIN rig CWG tests.

E_{TOTAL} (C_P)												
Tap	0°	5°	10°	20°	45°			0°	5°	10°	20°	45°
A101	0.049	0.050	0.052	0.058	0.049		B112	0.055	0.054	0.052	0.049	0.049
A102	0.055	0.058	0.059	0.058	0.049		B113	0.051	0.057	0.067	0.093	0.089
A103	0.058	0.059	0.058	0.054	0.049		B114	0.054	0.061	0.070	0.086	0.088
A104	0.057	0.055	0.053	0.049	0.057		B115	0.060	0.067	0.072	0.078	0.086
A105	0.049	0.050	0.054	0.071	0.102		B116	0.054	0.062	0.071	0.083	0.090
A106	0.050	0.055	0.062	0.076	0.096		C106	0.054	0.049	0.049	0.053	0.049
A107	0.055	0.051	0.049	0.056	0.099		C107	0.050	0.057	0.068	0.098	0.084
A108	0.063	0.061	0.058	0.052	0.056		C108	0.055	0.064	0.075	0.099	0.081
A109	0.061	0.064	0.065	0.063	0.049		D102	0.053	0.050	0.049	0.050	0.050
A110	0.052	0.057	0.061	0.064	0.049		D103	0.056	0.053	0.050	0.049	0.056
A111	0.052	0.049	0.049	0.056	0.057		D104	0.051	0.050	0.050	0.049	0.053
A112	0.051	0.049	0.050	0.057	0.061		D105	0.049	0.049	0.050	0.050	0.054
A113	0.052	0.056	0.058	0.058	0.049		D106	0.050	0.051	0.052	0.053	0.058
A114	0.055	0.056	0.057	0.054	0.049		D107	0.051	0.054	0.058	0.069	0.069
A115	0.054	0.053	0.052	0.049	0.057		D108	0.051	0.057	0.064	0.087	0.079
A116	0.051	0.057	0.061	0.065	0.081		D109	0.053	0.056	0.060	0.069	0.063
A117	0.050	0.055	0.059	0.071	0.076		E106	0.057	0.052	0.049	0.049	0.049
A118	0.049	0.048	0.048	0.050	0.060		E108	0.057	0.054	0.053	0.051	0.060
A119	0.049	0.049	0.049	0.049	0.050		E109	0.080	0.076	0.072	0.067	0.073
A120	0.048	0.049	0.050	0.051	0.050		E110	0.053	0.053	0.053	0.053	0.057
A121	0.054	0.050	0.049	0.051	0.049		E113	0.054	0.054	0.055	0.055	0.059
B106	0.057	0.051	0.049	0.052	0.058		E115	0.052	0.054	0.055	0.056	0.062
B108	0.057	0.052	0.049	0.052	0.056		E118	0.055	0.059	0.064	0.071	0.079
B109	0.054	0.049	0.049	0.054	0.049		E120	0.055	0.061	0.069	0.081	0.076
B110	0.054	0.055	0.056	0.055	0.055		E121	0.067	0.075	0.080	0.076	0.074
B111	0.056	0.056	0.055	0.052	0.049		E123	0.059	0.066	0.073	0.085	0.076

Table F.6.2.1 - Total uncertainties for pressure taps in loop at X/L = 0.16.

E_{TOTAL} (C_P)											
Tap	0°	5°	10°	20°	45°	Tap	0°	5°	10°	20°	45°
G101	0.049	0.048	0.048	0.049	0.055	G110	0.060	0.061	0.063	0.065	0.076
G102	0.048	0.048	0.048	0.049	0.058	G111	0.052	0.055	0.059	0.065	0.072
G103	0.048	0.048	0.048	0.049	0.057	G112	0.050	0.051	0.053	0.066	0.071
G104	0.049	0.049	0.048	0.049	0.055	G113	0.050	0.051	0.053	0.066	0.070
G105	0.050	0.049	0.048	0.048	0.051	G114	0.049	0.051	0.054	0.062	0.068
G106	0.050	0.049	0.049	0.050	0.064	G115	0.049	0.049	0.051	0.056	0.067
G107	0.050	0.049	0.049	0.050	0.064	G116	0.048	0.049	0.049	0.053	0.065
G108	0.052	0.050	0.050	0.052	0.071	G117	0.048	0.049	0.050	0.054	0.066
G109	0.060	0.060	0.060	0.060	0.072	G118	0.049	0.050	0.052	0.056	0.065

Table F.6.2.2 - Total uncertainties for pressure taps in loop at X/L = 0.27

E_{TOTAL} (C_P)											
Tap	0°	5°	10°	20°	45°	Tap	0°	5°	10°	20°	45°
H101	0.049	0.048	0.048	0.048	0.054	H110	0.048	0.048	0.049	0.053	0.085
H102	0.049	0.048	0.048	0.048	0.056	H111	0.048	0.048	0.049	0.052	0.079
H103	0.048	0.048	0.048	0.048	0.054	H112	0.048	0.048	0.049	0.051	0.063
H104	0.048	0.048	0.048	0.048	0.051	H113	0.048	0.048	0.049	0.051	0.063
H105	0.048	0.048	0.048	0.048	0.048	H114	0.048	0.048	0.049	0.050	0.061
H106	0.048	0.048	0.048	0.051	0.077	H115	0.048	0.048	0.049	0.050	0.060
H107	0.048	0.048	0.049	0.051	0.080	H116	0.048	0.049	0.049	0.051	0.060
H108	0.048	0.048	0.049	0.052	0.089	H117	0.049	0.049	0.050	0.052	0.062
H109	0.048	0.048	0.049	0.053	0.091	H118	0.049	0.049	0.050	0.052	0.062

Table F.6.2.3 - Total uncertainties for pressure taps in loop at X/L = 0.43.

E_{TOTAL} (C_P)												
Tap	0°	5°	10°	20°	45°		Tap	0°	5°	10°	20°	45°
J101	0.048	0.048	0.048	0.049	0.054		J110	0.048	0.048	0.048	0.052	0.087
J102	0.048	0.048	0.048	0.049	0.054		J111	0.048	0.048	0.048	0.051	0.079
J103	0.048	0.048	0.048	0.048	0.052		J112	0.048	0.048	0.048	0.050	0.068
J104	0.048	0.048	0.048	0.048	0.050		J113	0.048	0.048	0.048	0.049	0.060
J105	0.048	0.048	0.048	0.049	0.056		J114	0.048	0.048	0.048	0.049	0.057
J106	0.048	0.048	0.049	0.052	0.096		J115	0.048	0.048	0.048	0.049	0.057
J107	0.048	0.048	0.048	0.051	0.087		J116	0.048	0.048	0.049	0.050	0.058
J108	0.048	0.048	0.048	0.052	0.094		J117	0.048	0.048	0.049	0.051	0.062
J109	0.048	0.048	0.048	0.052	0.093		J118	0.048	0.048	0.049	0.051	0.063

Table F.6.2.4 - Total uncertainties for pressure taps in loop at X/L = 0.60.

E_{TOTAL} (C_P)												
Tap	0°	5°	10°	20°	45°		Tap	0°	5°	10°	20°	45°
K101	0.048	0.048	0.048	0.048	0.053		K110	0.048	0.048	0.049	0.052	0.076
K102	0.048	0.048	0.048	0.048	0.053		K111	0.048	0.048	0.048	0.051	0.064
K103	0.048	0.048	0.048	0.048	0.051		K112	0.048	0.048	0.048	0.050	0.059
K104	0.048	0.048	0.048	0.048	0.049		K113	0.048	0.048	0.048	0.049	0.058
K105	0.048	0.048	0.048	0.049	0.057		K114	0.048	0.048	0.048	0.049	0.057
K106	0.048	0.048	0.049	0.053	0.094		K115	0.048	0.048	0.048	0.049	0.057
K107	0.048	0.048	0.048	0.052	0.084		K116	0.048	0.048	0.049	0.049	0.058
K108	0.048	0.048	0.049	0.053	0.091		K117	0.048	0.048	0.049	0.050	0.059
K109	0.048	0.048	0.049	0.053	0.088		K118	0.048	0.048	0.049	0.050	0.061

Table F.6.2.5 - Total uncertainties for pressure taps in loop at X/L = 0.75

E_{TOTAL} (C_P)											
Tap	0°	5°	10°	20°	45°		Tap	0°	5°	10°	20°	45°
L101	0.048	0.048	0.048	0.048	0.052		L110	0.048	0.048	0.049	0.051	0.063
L102	0.048	0.048	0.048	0.048	0.052		L111	0.048	0.048	0.048	0.050	0.060
L103	0.048	0.048	0.048	0.048	0.051		L112	0.048	0.048	0.048	0.049	0.058
L104	0.048	0.048	0.048	0.048	0.050		L113	0.048	0.048	0.048	0.049	0.057
L105	0.048	0.048	0.048	0.049	0.051		L114	0.048	0.048	0.048	0.049	0.057
L106	0.048	0.048	0.049	0.052	0.076		L115	0.048	0.048	0.048	0.049	0.058
L107	0.048	0.048	0.049	0.053	0.085		L116	0.048	0.048	0.048	0.049	0.061
L108	0.048	0.048	0.049	0.053	0.079		L117	0.048	0.048	0.049	0.050	0.066
L109	0.048	0.048	0.049	0.052	0.073		L118	0.048	0.049	0.049	0.051	0.065

Table F.6.2.6 - Total uncertainties for pressure taps in loop at X/L = 0.88

E_{TOTAL} (C_P)											
Tap	0°	5°	10°	20°	45°		Tap	0°	5°	10°	20°	45°
M101	0.048	0.048	0.048	0.048	0.051		M110	0.048	0.048	0.049	0.050	0.055
M102	0.048	0.048	0.048	0.048	0.052		M111	0.048	0.048	0.048	0.050	0.055
M103	0.048	0.048	0.048	0.048	0.052		M112	0.048	0.048	0.048	0.049	0.055
M104	0.048	0.048	0.048	0.048	0.050		M113	0.048	0.048	0.048	0.049	0.056
M105	0.048	0.048	0.048	0.048	0.049		M114	0.048	0.048	0.048	0.049	0.056
M106	0.048	0.048	0.048	0.051	0.066		M115	0.048	0.048	0.048	0.049	0.056
M107	0.048	0.048	0.049	0.053	0.078		M116	0.048	0.048	0.048	0.049	0.058
M108	0.048	0.048	0.049	0.052	0.067		M117	0.048	0.048	0.049	0.049	0.061
M109	0.048	0.048	0.049	0.052	0.061		M118	0.048	0.048	0.049	0.049	0.066

Table F.6.2.7 - Total uncertainties for pressure taps in loop at X/L = 0.96

E_{TOTAL} (C_P)												
Tap	0°	5°	10°	20°	45°		Tap	0°	5°	10°	20°	45°
N101	0.048	0.048	0.048	0.048	0.050		N110	0.048	0.048	0.048	0.050	0.054
N102	0.048	0.048	0.048	0.048	0.051		N111	0.048	0.048	0.048	0.049	0.054
N103	0.048	0.048	0.048	0.048	0.051		N112	0.048	0.048	0.048	0.049	0.055
N104	0.048	0.048	0.048	0.048	0.050		N113	0.048	0.048	0.048	0.049	0.055
N105	0.048	0.048	0.048	0.048	0.049		N114	0.048	0.048	0.048	0.049	0.056
N106	0.048	0.048	0.048	0.050	0.059		N115	0.048	0.048	0.048	0.049	0.057
N107	0.048	0.048	0.048	0.049	0.057		N116	0.048	0.048	0.048	0.049	0.058
N108	0.048	0.048	0.048	0.050	0.060		N117	0.048	0.048	0.048	0.049	0.058
N109	0.048	0.048	0.048	0.050	0.058		N118	0.048	0.048	0.048	0.049	0.056

F.5.3.1 Aerodynamic load total uncertainty

The calculation of total error was undertaken following the same methodology as for the CWG tests, and following equation F.8. The total uncertainties for each loop of taps at yaw angles from 0° to 45° are given in tables F.7.1 to F.7.4 for both of the wind tunnel tests conducted by RWDI. Figure F.3 compares the errors in force and moment coefficients along the length of the train. Note that the values in tables F.7.1 to F.7.3 and in figure F.3 take a reference side area of 10 m^2 as required in CEN, (2010). The overall values given as the final row in each table take a reference area of 60 m^2 for consistency with the value used by RWDI.

Table F.7.1 - Total errors of side force coefficient for individual loops and overall error

Loop position (X/L)	Tap Ref.	E_{TOTAL} (C_Y)				
		0°	5°	10°	20°	45°
0.16	G	0.001	0.020	0.038	0.069	0.098
0.27	H	0.001	0.026	0.039	0.051	0.054
0.43	J	0.012	0.025	0.039	0.036	0.034
0.60	K	0.022	0.033	0.041	0.024	0.028
0.75	L	0.045	0.022	0.026	0.022	0.043
0.88	M	0.006	0.031	0.024	0.023	0.052
0.96	N	0.024	0.051	0.037	0.043	0.068
OVERALL ERROR		0.005	0.008	0.008	0.010	0.014

Table F.7.2 - Total errors of lift force coefficient for individual loops and overall error

Loop position (X/L)	Tap Ref.	E_{TOTAL} (C_Z)				
		0°	5°	10°	20°	45°
0.16	G	0.076	0.075	0.072	0.067	0.069
0.27	H	0.006	0.001	0.009	0.035	0.082
0.43	J	0.017	0.002	0.028	0.062	0.096
0.60	K	0.047	0.048	0.057	0.076	0.096
0.75	L	0.120	0.148	0.135	0.098	0.093
0.88	M	0.003	0.023	0.048	0.056	0.058
0.96	N	0.009	0.014	0.037	0.040	0.046
OVERALL ERROR		0.013	0.014	0.015	0.015	0.020

Table F.7.3 - Total errors of x-axis moment coefficient for individual loops and overall error

Loop position (X/L)	Tap Ref.	$E_{TOTAL}\ (C_{M_X})$				
		0°	5°	10°	20°	45°
0.16	G	0.000	0.012	0.023	0.041	0.058
0.27	H	0.000	0.015	0.022	0.029	0.031
0.43	J	0.009	0.014	0.024	0.023	0.021
0.60	K	0.014	0.021	0.027	0.015	0.018
0.75	L	0.029	0.023	0.022	0.015	0.025
0.88	M	0.004	0.019	0.014	0.013	0.030
0.96	N	0.015	0.030	0.021	0.025	0.039
OVERALL ERROR		0.005	0.007	0.007	0.008	0.012

Table F.7.4 - Total errors of lee-rail moment coefficient for individual loops and overall error

Loop position (X/L)	Tap Ref.	$E_{TOTAL}\ (C_{M_{X,lee}})$				
		0°	5°	10°	20°	45°
0.16	G	0.014	0.025	0.036	0.054	0.071
0.27	H	0.001	0.015	0.024	0.035	0.046
0.43	J	0.012	0.014	0.029	0.034	0.038
0.60	K	0.006	0.030	0.037	0.029	0.036
0.75	L	0.007	0.050	0.046	0.033	0.042
0.88	M	0.004	0.023	0.023	0.023	0.041
0.96	N	0.014	0.033	0.028	0.032	0.048
OVERALL ERROR		0.003	0.010	0.011	0.012	0.016

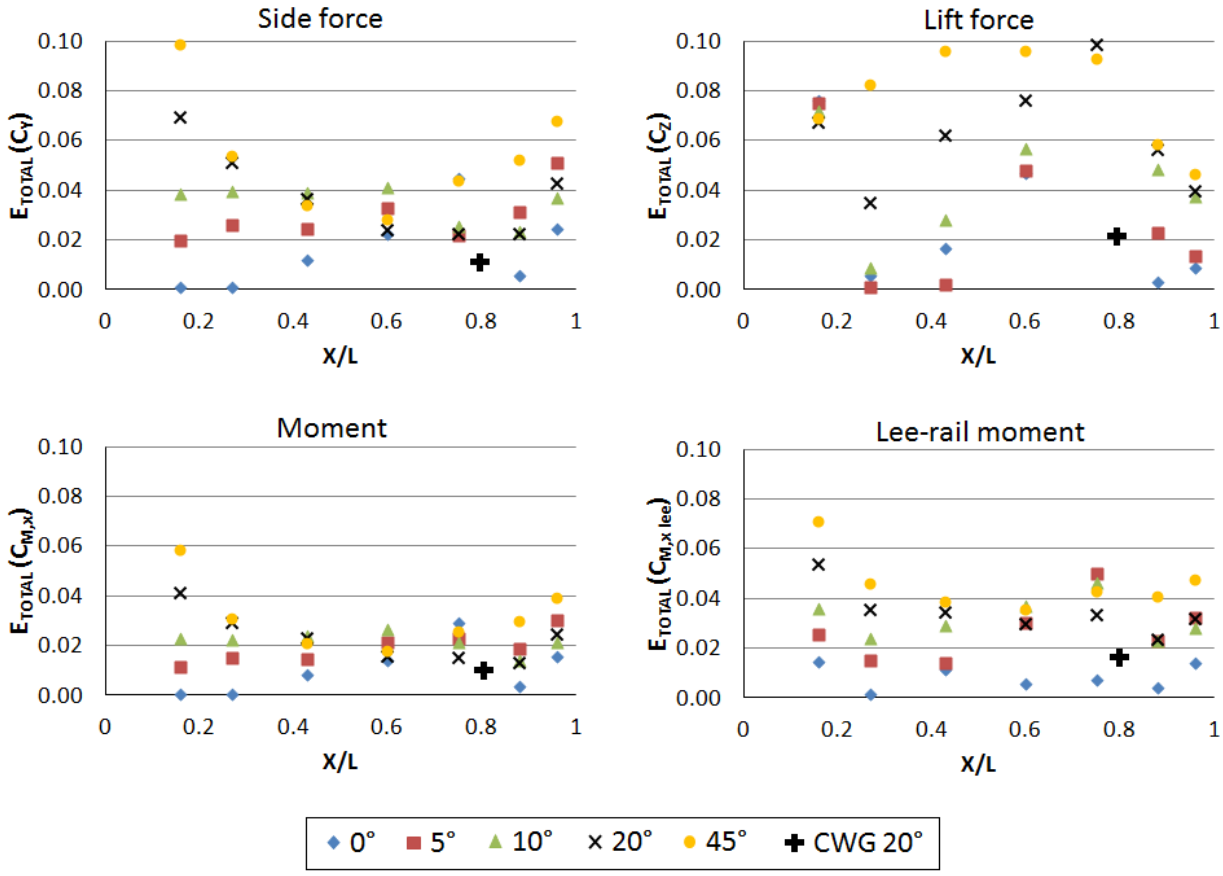

Figure F.3 - Variation of total error along train length at different yaw angles for force and moment coefficients for wind tunnel test (0° to 45°) and also CWG test (at 20° only).

F.5.4 Comparison of wind tunnel test errors

Two wind tunnel tests were conducted by RWDI (described in section 6.2.2). The bias, random error and total errors for all of the pressure taps tested are compared for both tests in figure F.4. It can be seen that the bias error in the lower velocity test is slightly higher, almost certainly as a result of the lower wind speed (therefore a greater fractional contribution of bias error over dynamic pressure). The random uncertainties in the second test are also higher, as a

result of the higher turbulence intensity of the flow which corresponds to higher standard deviations for all of the pressure taps measured and analysed in this study. The total uncertainty for the lower velocity, higher turbulence intensity test was therefore higher than the original test. Another point to note from figure F.4 is that tap numbers up to about 120 show higher magnitudes of bias, random and total error - these are pressure taps located around the nose of the train.

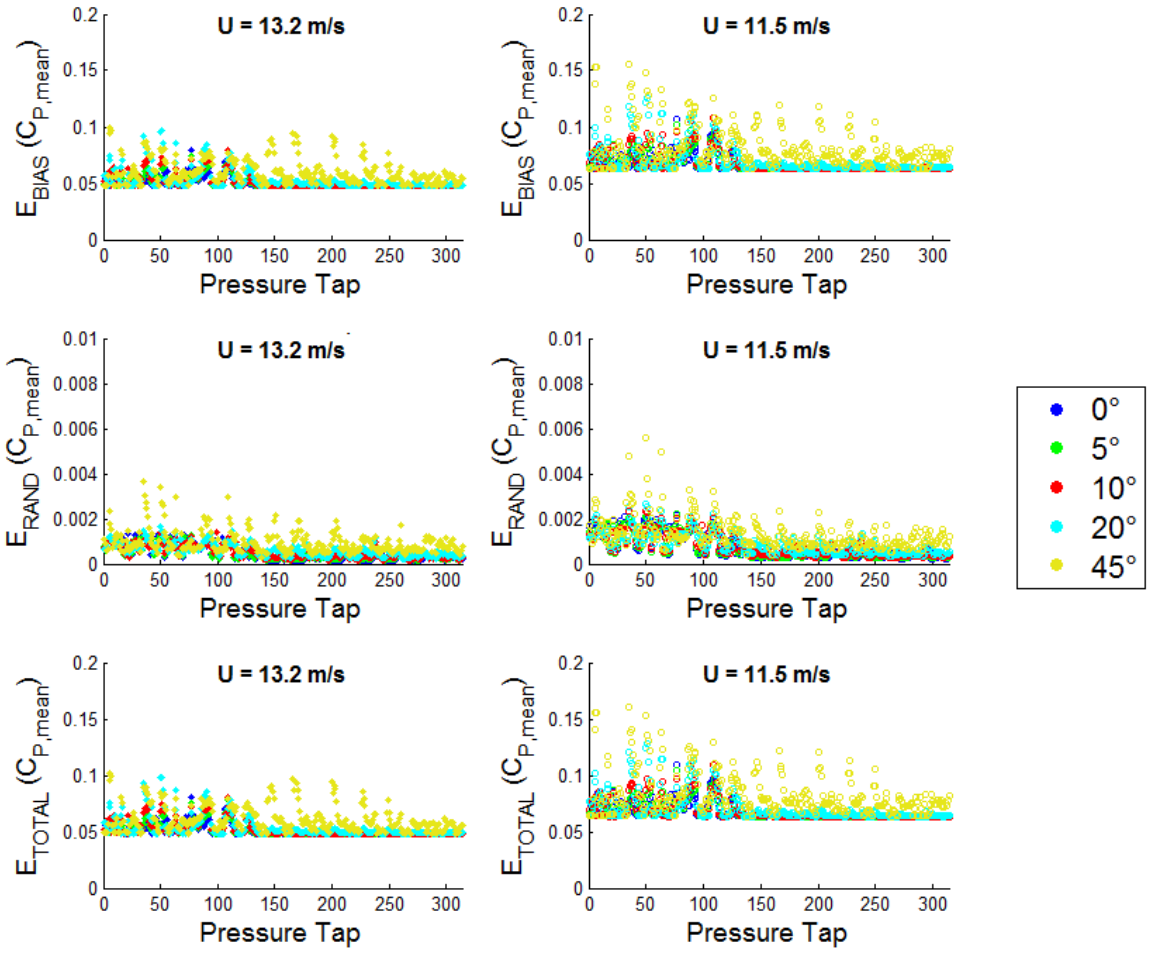

Figure F.4 - Bias, random and total errors for all pressure taps for both RWDI wind tunnel tests

F.6 Full-scale crosswind tests uncertainty

Full-scale errors are calculated following the methodology set out in section F.2, i.e., through calculation of bias limit and random uncertainty. Much of the equipment on the NMT was not calibrated or tested before use, therefore the values of uncertainty obtained in this section are themselves (somewhat ironically) quite uncertain. It should be stressed that the quantity of data obtained from the NMT was very large. While every effort was made to ensure the data quality, through a variety of checks and period manual inspection of the data, it is quite possible that some "bad data" has been used in analysis, given that some faults are difficult to detect without a detailed analysis. The main faults observed are described in section J.5.5. In addition, other effects such as the period negative pressures over the roof (believed to be due to the engine cooling fan and discussed in section J.5.3) will certainly have affected the data quality. Nonetheless, error analysis has been useful in order to quantify the differences in error between pressure taps and also to allow a relative comparison to model-scale.

F.6.1 Bias limit

The bias limit is based on the experimental uncertainties of the equipment used to obtain pressure coefficients (equation F.10). As an introduction to the bias limit calculation, equation F.10 will be considered in terms of the raw measured quantities that were used to obtain C_{P_k}, and the proceeding subsections will consider the errors associated with each measurement type. Bias limits were calculated for each mean pressure coefficient at ±10° yaw angle and are based on the calculation of yaw angle from the wind tunnel coefficients (table 8.1).

Pressure coefficient is given as:

$$C_{P_k} = \frac{\Delta P_k}{\frac{1}{2}\rho U_{res}^2} \tag{F.10}$$

Where ΔP_k was obtained for all channels except dynamic pressure (see section F.6.1.4) by:

$$\Delta P_k = \left(P_{k,HPP} - P_{ref,CS}\right) - \left(P_{ref,CS} - P_{ref,OE}\right) \tag{F.11.1}$$

The terms $\left(P_{k,HPP} - P_{ref,CS}\right)$ and $\left(P_{ref,CS} - P_{ref,OE}\right)$ were calculated physically by each pressure transducer as the differential between the HPP and LPP ($\Delta P_{HPP-LPP}$), which is related to pressure transducer voltage as:

$$\Delta P_{HPP-LPP} = \Delta V_k K_{NLC} \tag{F.11.2}$$

Differential voltage (i.e., the voltage of the output signal of each transducer) is defined for any given instant in time as:

$$\Delta V_k(t) = V_k(t) - V_{0,k}(t) \tag{F.11.3}$$

Errors in the background voltage are considered in section F.6.1.1, and the accuracy of the pressure transducers is considered in section F.6.1.2.

The pressure differential of each tap (ΔP_k) was normalised by $\frac{1}{2}\rho U_{res}^2$. Section 10.2.3.3 describes how U_{res} was calculated, and U_{res} depends on yaw angle (calculated from the nose pressure taps) and the dynamic pressure from the nose mounted pitot-static probe. Section F.6.1.3 considers the error associated with yaw angle calculations (based on the wind tunnel errors from section F.5.3), and section F.6.1.4 considers the errors in the measurement of train speed.

The summary values of the experimental errors associated with equipment are presented in section F.6.1.5 along with a calculation of bias limit for each pressure tap.

F.6.1.1 Background voltages errors

Figure F.5 shows the background voltages of all of the pressure transducers across the entire first year of the experiments - note that segments of bad data have not removed from the figure, but "bad data" has not been included in any of the analysis in this study. The error associated with each background voltage was defined as $\delta V_{0,k}$ and was calculated for each pressure transducer as one standard deviation of each of the background voltages defined for each data file at least 10 minutes long over a one year period. The background voltage was assumed to be constant for each data file (see section 10.2.3.1 for details on how $V_{0,k}$ was obtained). Table F.8 lists the background voltage errors for each transducer as absolute values of the voltages and also as equivalent percentage errors.

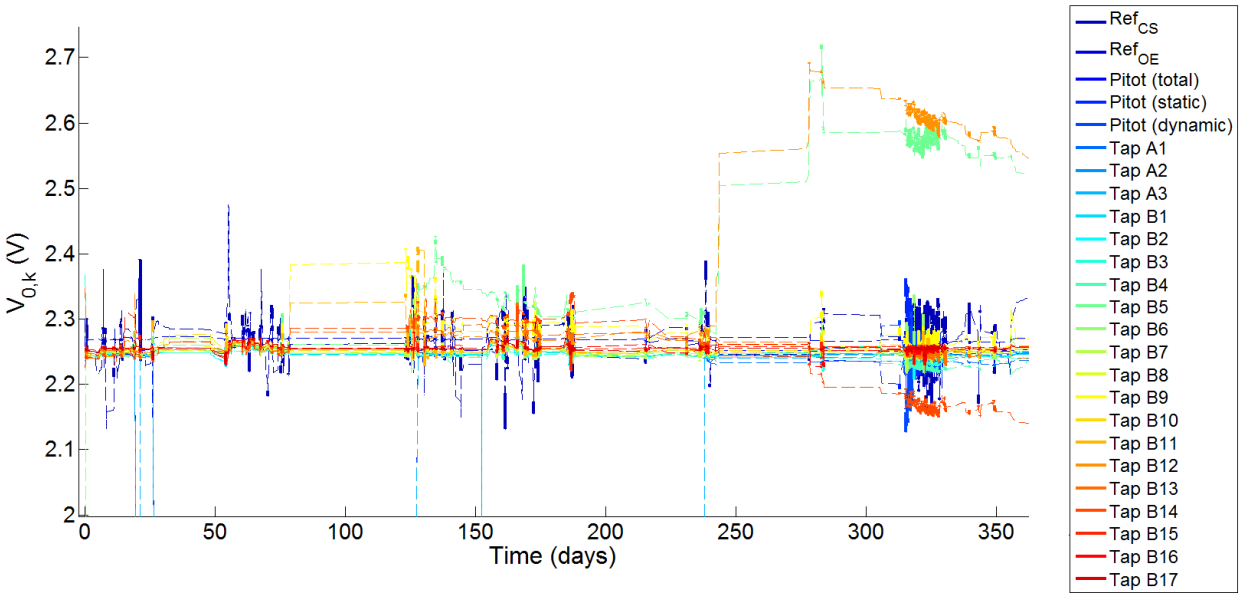

Figure F.5 - Background voltages for first year of NMT experiments - note that bad data has not been removed from the figure. Dashed lines show linearly interpolated data.

Table F.8 - Errors associated with background voltages for each pressure transducer.

Transducer	$\overline{V_{0,k}}$ (V)	$\delta V_{0,k}$	Percentage error
Ref_{CS}	2.278	0.036	1.6
Ref_{OE}	2.267	0.003	0.1
Pitot total	2.252	0.010	0.4
Pitot static	2.245	0.014	0.6
Pitot dynamic	2.246	0.015	0.7
A1	2.235	0.010	0.4
A2	2.245	0.009	0.4
A3	2.243	0.009	0.4
B1	2.246	0.004	0.2
B2	2.251	0.046	2.1
B3	2.280	0.089	3.9
B4	2.263	0.034	1.5
B5	2.390	0.151	6.3
B6	2.255	0.020	0.9
B7	2.246	0.005	0.2
B8	2.252	0.013	0.6
B9	2.267	0.020	0.9
B10	2.253	0.004	0.2
B11	2.255	0.013	0.6
B12	2.486	0.188	7.6
B13	2.263	0.015	0.7
B14	2.202	0.064	2.9
B15	2.257	0.006	0.3
B16	2.255	0.005	0.2
B17	2.256	0.004	0.2

F.6.1.2 Pressure transducer accuracy

The manufacturer specification states that the pressure transducers used on the NMT have an accuracy of 5% within a working range of ±2500 Pa, and because no calibration could be performed on the NMT system, this value of 5% has been assumed as the error of V_k for all pressure transducers.

F.6.1.3 Error associated with yaw angle calculation

Yaw angle was calculated from equation 10.9a based on the coefficients presented in table 8.1 from the higher Re number wind tunnel test. The term "yaw coefficient" is defined as the difference between the windward and leeward pressure taps divided by the central tap. The maximum and minimum yaw coefficient were found by either adding or subtracting the total error for each of the wind tunnel taps to the mean pressure coefficients. Figure F.6 shows the upper and lower bounds of yaw angle - it should be noted that these values are considered "extreme worst case" upper and lower bounds since they depend on all three of the nose pressure taps independently having the maximum total error in the least favourable direction (positive or negative) from the mean.

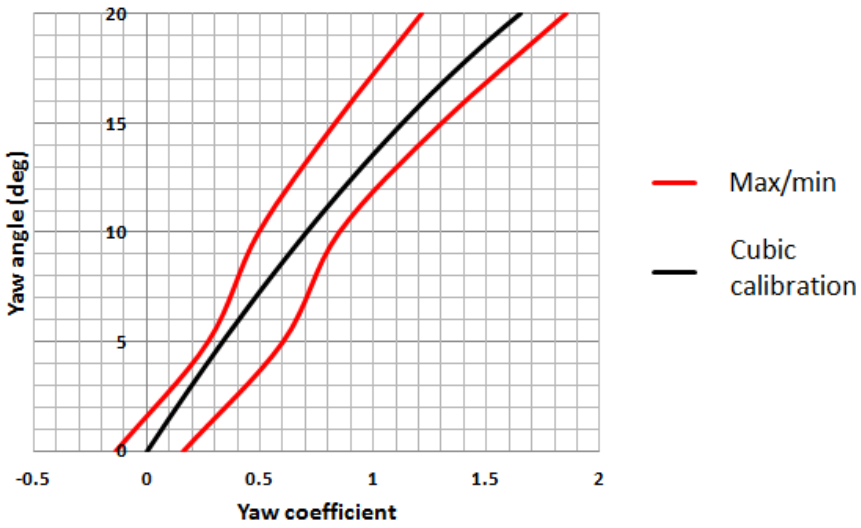

Figure F.6 - "Worst case" upper and lower bounds for yaw angle calculation.

Maximum and minimum yaw angle were calculated based on these "worst case" lower bounds at yaw angles of 0° to 20°, and are given in table F.9.

Table F.9 - "Worst case" upper and lower bounds of yaw angle.

$\theta_{nominal}$ (degrees)	θ_{max} (degrees)	θ_{min} (degrees)
0	2	-1
5	6	2
10	13	7
15	19	13
20	25	18

The error associated with yaw angle can be expressed as:

$$\delta\theta = max[|\theta_{nominal} - \theta_{max}|, |\theta_{nominal} - \theta_{min}|] \quad \text{(F.12)}$$

The values of $\delta\theta$ were assumed to be of equal magnitude for both positive and negative yaw angles.

F.6.1.4 Dynamic pressure and train speed error

Dynamic pressure is defined as:

$$P_{dyn} = P_{total} - P_{stat} \quad \text{(F.13.1)}$$

In this study the value of dynamic pressure measured across a single pressure transducer (HPP = total, LPP = static) has been used, since there is only one measurement of pressure and hence a lower error. By accounting for background voltage, dynamic pressure can be expressed as:

$$P_{dyn} = \left(V_k - V_{0,k}\right) \times K_{NLC} \quad \text{(F.13.2)}$$

Where k refers to the pressure transducer measuring dynamic pressure. Streamwise aerodynamic speed was calculated from dynamic pressure by:

$$U_{uncor} = \sqrt{\frac{2P_{dyn}}{\rho}} \tag{F.13.2}$$

The error related to air density is discussed in section F.3.1.2. In calculations on the NMT, air density was taken as 1.2 kg/m^3 and temperature and humidity effects were not included. If the upper and lower bound analysis presented in section F.3.1.2 is considered for typical extremes of atmospheric pressure, temperature and humidity, then $\delta\rho$ = 0.1 kg/m^3.

By propagation of error, the error associated with streamwise uncorrected aerodynamic speed is:

$$\delta U_{uncor} = \sqrt{\left(\frac{U_{uncor}}{V_k}\delta V_k\right)^2 + \left(\frac{U_{uncor}}{V_{0,k}}\delta V_{0,k}\right)^2 + \left(\frac{U_{uncor}}{\rho}\delta\rho\right)^2} \tag{F.14}$$

At this stage the value of U_{uncor} is multiplied by a correction factor (equal to 2.1) to obtain U_{cor} (see equation 10.7 and figure 10.2). Errors due to the accuracy of this correction factor have not been considered, but it should be noted that the error term is also multiplied by this factor, resulting in:

$$\delta U_{cor} = 2.1 \times \delta U_{uncor} \tag{F.15}$$

F.6.1.5 Calculation of bias limit

The bias limit for any measurement of pressure coefficient, $E_{BIAS|k}$, was found through propagation of error as:

$$E_{BIAS|k} = \sqrt{\left(\frac{C_{P_k}}{V_k}\delta V_k\right)^2 + \left(\frac{C_{P_k}}{V_{0,k}}\delta V_{0,k}\right)^2 + \left(\frac{C_{P_k}}{\rho}\delta\rho\right)^2 + \left(\frac{C_{P_k}}{U_{cor}}\delta U_{cor}\right)^2 + \left(\frac{C_{P_k}}{\theta}\delta\theta\right)^2} \quad \text{(F.16)}$$

One issue noted with equation F.16 is the term $\frac{C_{P_k}}{\theta}\delta\theta$. Most of the data was close to zero yaw, which resulted in this term becoming very large as it tends to infinity as θ tends to zero. At yaw angles of between ±1° this term was omitted from equation F.16 on the basis that at zero yaw $U_{res} = U_{cor}$.

Bias limit was calculated for each individual sample in each of the yaw angle bins and the final values of bias limit were given as the mean plus two standard deviations of the bias limits for each pressure tap yaw angle bin, and are presented in table F.11.

F.6.2 Random uncertainty

The random uncertainty was calculated based on the two methodologies used to analyse the open air data.

F.6.2.1 Scatter plot regression analysis random uncertainty

When the scatter plot regression analysis was considered (see appendix K), random uncertainty was given as the root mean square error (RMSE) of the linear regression model, and taken as the maximum value for each tap from either the positive or negative yaw angle range (i.e., the maximum values from table K.4).

F.6.2.2 Yaw angle bins random uncertainty

When considering the yaw angle bins methodology, random uncertainty was calculated following equation F.2 and considering a 95% confidence limit based on the standard deviation of each yaw angle bin for each individual pressure tap. Tables F.10.1.1 to F.10.1.3 list the standard deviations, bin sizes and random uncertainty for each pressure tap and yaw angle based on the yaw coefficients obtained from the wind tunnel tests, and tables F.10.2.1 to F.10.2.3 show the same properties but based on yaw angle calculated from the CWG tests. Note that the quantity of data (tables F.10.1.2 and F.10.2.2) is in seconds, but the uncertainty calculation was performed based on number of samples (i.e., value in seconds multiplied by 128 Hz).

Table F.10.1.1 - Quantity of data for each yaw angle bin for yaw angles calculated based on WT yaw coefficients.

Tap	Quantity of data (s)								
	-20°	-15°	-10°	-5°	0°	5°	10°	15°	20°
B1	0.2	0.5	71	7510	557031	14198	574	9.1	0.9
B2	0.2	0.5	66	7509	557039	14198	587	9.0	0.9
B3	0.2	0.5	67	7240	527570	13113	577	9.0	0.9
B4	0.2	0.5	70	7239	525180	12760	599	9.4	0.9
B5	NA	NA	9	2632	109836	1570	14	NA	NA
B6	0.2	0.5	66	7507	556867	14154	537	3.8	0.4
B7	0.2	0.5	70	7510	557039	14200	627	9.9	0.9
B8	0.2	0.5	68	7508	557023	14198	581	5.5	0.6
B9	0.2	0.5	62	7505	557039	14198	570	5.0	0.6
B10	0.2	0.5	64	7503	557039	14200	586	4.1	0.5
B11	0.2	0.5	65	7501	557031	14199	597	5.5	0.5
B12	NA	NA	21	3262	157930	3513	171	3.2	0.3
B13	0.2	0.5	69	7508	557039	14198	618	6.2	0.6
B14	0.2	0.5	59	7493	557031	14198	633	8.2	0.9
B15	0.2	0.5	64	7498	557039	14199	627	8.2	0.9
B16	0.2	0.5	59	7496	557031	14198	637	9.1	0.9
B17	0.2	0.5	57	7492	557031	14199	641	9.7	0.9

Table F.10.1.2 - Standard deviation of each yaw angle bin for yaw angles calculated based on WT yaw coefficients.

Tap	$\sigma_k\ (C_P)$								
	-20°	-15°	-10°	-5°	0°	5°	10°	15°	20°
B1	0.213	0.186	0.403	0.047	0.029	0.054	0.266	0.621	0.152
B2	0.206	0.181	0.432	0.072	0.034	0.054	0.272	0.671	0.220
B3	0.210	0.185	0.483	0.082	0.033	0.062	0.271	0.692	0.221
B4	0.239	0.208	0.485	0.073	0.049	0.095	0.315	0.662	0.236
B5	NA	NA	0.514	0.144	0.057	0.054	0.219	NA	NA
B6	0.218	0.191	0.598	0.134	0.087	0.181	0.788	1.294	0.990
B7	0.091	0.072	0.447	0.062	0.027	0.053	0.481	0.660	0.567
B8	0.243	0.210	0.566	0.112	0.084	0.127	0.645	1.004	1.403
B9	0.121	0.105	0.611	0.142	0.073	0.158	0.610	0.919	1.420
B10	0.244	0.215	0.638	0.157	0.041	0.105	0.595	0.961	1.069
B11	0.213	0.187	0.610	0.163	0.059	0.095	0.575	0.906	1.092
B12	NA	NA	0.592	0.152	0.074	0.096	0.474	0.364	0.124
B13	0.288	0.252	0.565	0.098	0.043	0.085	0.562	0.877	1.374
B14	0.256	0.232	0.304	0.104	0.057	0.090	0.482	0.733	0.918
B15	0.248	0.222	0.507	0.086	0.033	0.063	0.493	0.741	0.929
B16	0.232	0.210	0.524	0.085	0.036	0.047	0.445	0.717	0.775
B17	0.209	0.193	0.262	0.084	0.030	0.045	0.410	0.712	0.691

Table F.10.1.3 - E_{RND} for each yaw angle bin for yaw angles calculated based on WT yaw coefficients.

Tap	E_{RND} (C_P)								
	-20°	-15°	-10°	-5°	0°	5°	10°	15°	20°
B1	0.089	0.048	0.008	0.000	0.000	0.000	0.002	0.036	0.028
B2	0.086	0.046	0.009	0.000	0.000	0.000	0.002	0.040	0.041
B3	0.087	0.047	0.010	0.000	0.000	0.000	0.002	0.041	0.041
B4	0.100	0.053	0.010	0.000	0.000	0.000	0.002	0.038	0.044
B5	NA	NA	0.030	0.000	0.000	0.000	0.011	NA	NA
B6	0.091	0.049	0.013	0.000	0.000	0.000	0.006	0.117	0.262
B7	0.038	0.018	0.009	0.000	0.000	0.000	0.003	0.037	0.105
B8	0.101	0.054	0.012	0.000	0.000	0.000	0.005	0.076	0.322
B9	0.050	0.027	0.014	0.000	0.000	0.000	0.005	0.072	0.318
B10	0.102	0.055	0.014	0.000	0.000	0.000	0.004	0.084	0.281
B11	0.089	0.048	0.013	0.000	0.000	0.000	0.004	0.069	0.284
B12	NA	NA	0.023	0.000	0.000	0.000	0.006	0.036	0.037
B13	0.120	0.065	0.012	0.000	0.000	0.000	0.004	0.062	0.311
B14	0.107	0.059	0.007	0.000	0.000	0.000	0.003	0.045	0.170
B15	0.103	0.057	0.011	0.000	0.000	0.000	0.003	0.046	0.173
B16	0.097	0.054	0.012	0.000	0.000	0.000	0.003	0.042	0.144
B17	0.087	0.049	0.006	0.000	0.000	0.000	0.003	0.040	0.128

Table F.10.2.1 - Quantity of data for each yaw angle bin for yaw angles calculated based on CWG yaw coefficients.

Tap	Quantity of data (s)								
	-20°	-15°	-10°	-5°	0°	5°	10°	15°	20°
B1	4.3	240.1	2717	27313	429359	59467	5730	1079	114
B2	2.2	236.0	2717	27313	429367	59467	5730	1084	120
B3	2.9	237.1	2638	26113	406828	55502	5342	1058	118
B4	4.0	238.9	2637	26096	405445	54395	5245	1050	132
B5	NA	56.5	957	6438	86914	10812	487	34	0.9
B6	4.1	233.8	2717	27308	429266	59353	5716	1066	98
B7	4.1	238.9	2718	27316	429367	59470	5731	1094	141
B8	4.1	235.5	2717	27312	429352	59466	5730	1083	117
B9	2.1	230.3	2717	27315	429367	59469	5730	1073	112
B10	4.1	228.8	2717	27314	429359	59469	5730	1085	118
B11	3.9	229.8	2716	27315	429359	59468	5730	1088	124
B12	0.2	87.1	1225	8259	126969	15048	1384	281	38
B13	4.2	235.9	2717	27314	429367	59467	5730	1094	133
B14	3.7	220.3	2712	27313	429359	59467	5730	1093	145
B15	3.8	228.5	2714	27315	429359	59468	5730	1095	138
B16	3.7	221.7	2713	27313	429359	59467	5730	1096	145
B17	3.2	219.4	2711	27315	429359	59467	5730	1097	147

Table F.10.2.2 - Standard deviation of each yaw angle bin for yaw angles calculated based on CWG yaw coefficients.

Tap	$\sigma_k\ (C_P)$								
	-20°	-15°	-10°	-5°	0°	5°	10°	15°	20°
B1	1.141	1.134	1.132	1.143	0.960	1.056	1.141	1.148	1.148
B2	0.561	0.251	0.043	0.028	0.029	0.035	0.055	0.174	0.337
B3	0.689	0.312	0.065	0.034	0.035	0.039	0.054	0.168	0.369
B4	0.624	0.335	0.076	0.039	0.033	0.035	0.065	0.177	0.374
B5	0.573	0.322	0.072	0.056	0.047	0.060	0.104	0.201	0.422
B6	NA	0.453	0.133	0.050	0.059	0.045	0.058	0.156	0.087
B7	0.448	0.445	0.123	0.086	0.083	0.118	0.175	0.548	0.988
B8	0.634	0.297	0.057	0.033	0.026	0.032	0.050	0.249	0.607
B9	0.576	0.425	0.106	0.065	0.089	0.072	0.123	0.420	0.751
B10	1.119	0.494	0.145	0.079	0.071	0.096	0.156	0.420	0.662
B11	0.495	0.521	0.171	0.062	0.040	0.049	0.096	0.381	0.671
B12	0.613	0.516	0.183	0.066	0.060	0.058	0.088	0.352	0.669
B13	0.266	0.482	0.147	0.051	0.079	0.057	0.091	0.260	0.542
B14	0.582	0.417	0.093	0.050	0.042	0.049	0.089	0.310	0.694
B15	0.345	0.246	0.119	0.064	0.057	0.064	0.096	0.241	0.688
B16	0.780	0.288	0.098	0.046	0.033	0.039	0.061	0.232	0.638
B17	0.724	0.271	0.097	0.042	0.037	0.037	0.045	0.200	0.584

Table F.10.2.3 - E_{RND} for each yaw angle bin for yaw angles calculated based on CWG yaw coefficients.

Tap	E_{RND} (C_P)								
	-20°	-15°	-10°	-5°	0°	5°	10°	15°	20°
B1	0.048	0.003	0.000	0.000	0.000	0.000	0.000	0.001	0.006
B2	0.082	0.004	0.000	0.000	0.000	0.000	0.000	0.001	0.006
B3	0.065	0.004	0.000	0.000	0.000	0.000	0.000	0.001	0.006
B4	0.051	0.004	0.000	0.000	0.000	0.000	0.000	0.001	0.007
B5	NA	0.011	0.001	0.000	0.000	0.000	0.000	0.005	0.016
B6	0.039	0.005	0.000	0.000	0.000	0.000	0.000	0.003	0.018
B7	0.055	0.003	0.000	0.000	0.000	0.000	0.000	0.001	0.009
B8	0.051	0.005	0.000	0.000	0.000	0.000	0.000	0.002	0.012
B9	0.137	0.006	0.000	0.000	0.000	0.000	0.000	0.002	0.011
B10	0.043	0.006	0.001	0.000	0.000	0.000	0.000	0.002	0.011
B11	0.055	0.006	0.001	0.000	0.000	0.000	0.000	0.002	0.011
B12	0.116	0.009	0.001	0.000	0.000	0.000	0.000	0.003	0.016
B13	0.050	0.005	0.000	0.000	0.000	0.000	0.000	0.002	0.011
B14	0.032	0.003	0.000	0.000	0.000	0.000	0.000	0.001	0.010
B15	0.071	0.003	0.000	0.000	0.000	0.000	0.000	0.001	0.010
B16	0.067	0.003	0.000	0.000	0.000	0.000	0.000	0.001	0.009
B17	0.031	0.003	0.000	0.000	0.000	0.000	0.000	0.001	0.008

F.6.3 Total uncertainty

The total uncertainty was given as the sum of the bias and random uncertainty, and all errors are presented in table F.11. Figure F.7 shows the bias, random and total errors for each of the loop pressure taps based on the random errors (RMSE) of the scatter plots - i.e., the values from table K.4. The values of these errors have been assumed for both the scatter plot regression and yaw angle bins methodologies since the random errors, when calculated based on equation F.2 and given in tables F.10.1.3 and F.10.2.3, are very low due to the very large quantities of data and intuitively it is felt that they are gross underestimates of the true random

error. The values presented in table F.11 are assumed to be independent of yaw angle, and hence they are most likely conservative at lower yaw angles. When yaw angles of 20° were considered in chapter 11, pressure coefficients were obtained by extrapolation and hence the values of total error were doubled to account for the increased uncertainty.

During analysis of the pressures for each tap (appendix J) it was noted that some taps showed very little variation in pressure coefficient with yaw angle - tap B7 in particular. The total error for this tap is significantly lower than for the adjacent taps, again suggesting that tap B7 may have been blocked or that the pneumatic connections to this tap were unsealed. This may also be true for tap B4.

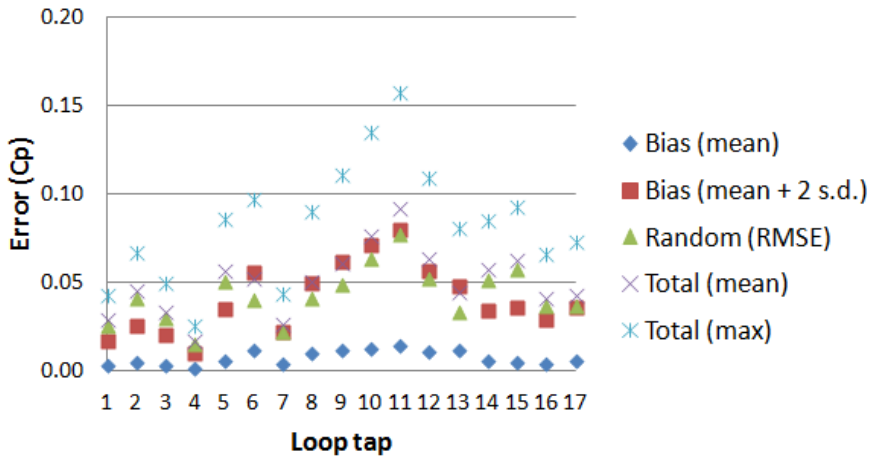

Figure F.7 - Errors for each pressure tap in loop around NMT power car.

Table F.11 - Values of errors for each of the loop pressure taps - random errors given as RMSE of linear regression models (see table K.4).

Tap	E_{BIAS}		E_{RND}	E_{TOTAL}	
	Mean	Max		Mean	Max
B1	0.003	0.017	0.026	0.029	0.043
B2	0.005	0.026	0.041	0.046	0.067
B3	0.003	0.020	0.030	0.033	0.050
B4	0.002	0.010	0.015	0.017	0.025
B5	0.006	0.035	0.051	0.057	0.086
B6	0.012	0.056	0.041	0.053	0.097
B7	0.004	0.022	0.022	0.026	0.044
B8	0.010	0.049	0.041	0.051	0.091
B9	0.012	0.062	0.049	0.061	0.111
B10	0.013	0.071	0.063	0.076	0.135
B11	0.014	0.080	0.078	0.092	0.157
B12	0.011	0.056	0.053	0.064	0.109
B13	0.012	0.048	0.033	0.045	0.081
B14	0.006	0.034	0.051	0.057	0.085
B15	0.005	0.036	0.057	0.063	0.093
B16	0.004	0.029	0.037	0.041	0.066
B17	0.006	0.036	0.037	0.043	0.073

APPENDIX G

WIND TUNNEL TESTS - UNDERBODY PRESSURES

G.1 Introduction

Appendix G provides additional details about the underbody pressures measured during the RWDI wind tunnel test. Section G.2 defines the pressure tap locations and section G.3 considers the underbody pressures in detail.

G.2 Pressure tap set up

The specific locations of all of the pressure taps on the wind tunnel model are shown on figures G.1.1 and G.1.2 for the nose and main power car body respectively.

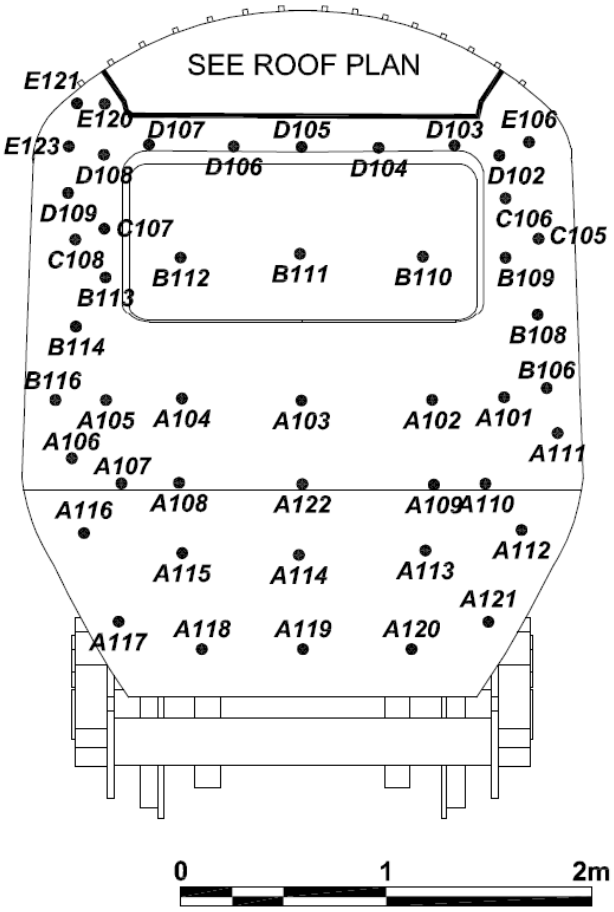

Figure G.1.1 - Positions and letters/numbers of pressure taps on HST wind tunnel model at nose.

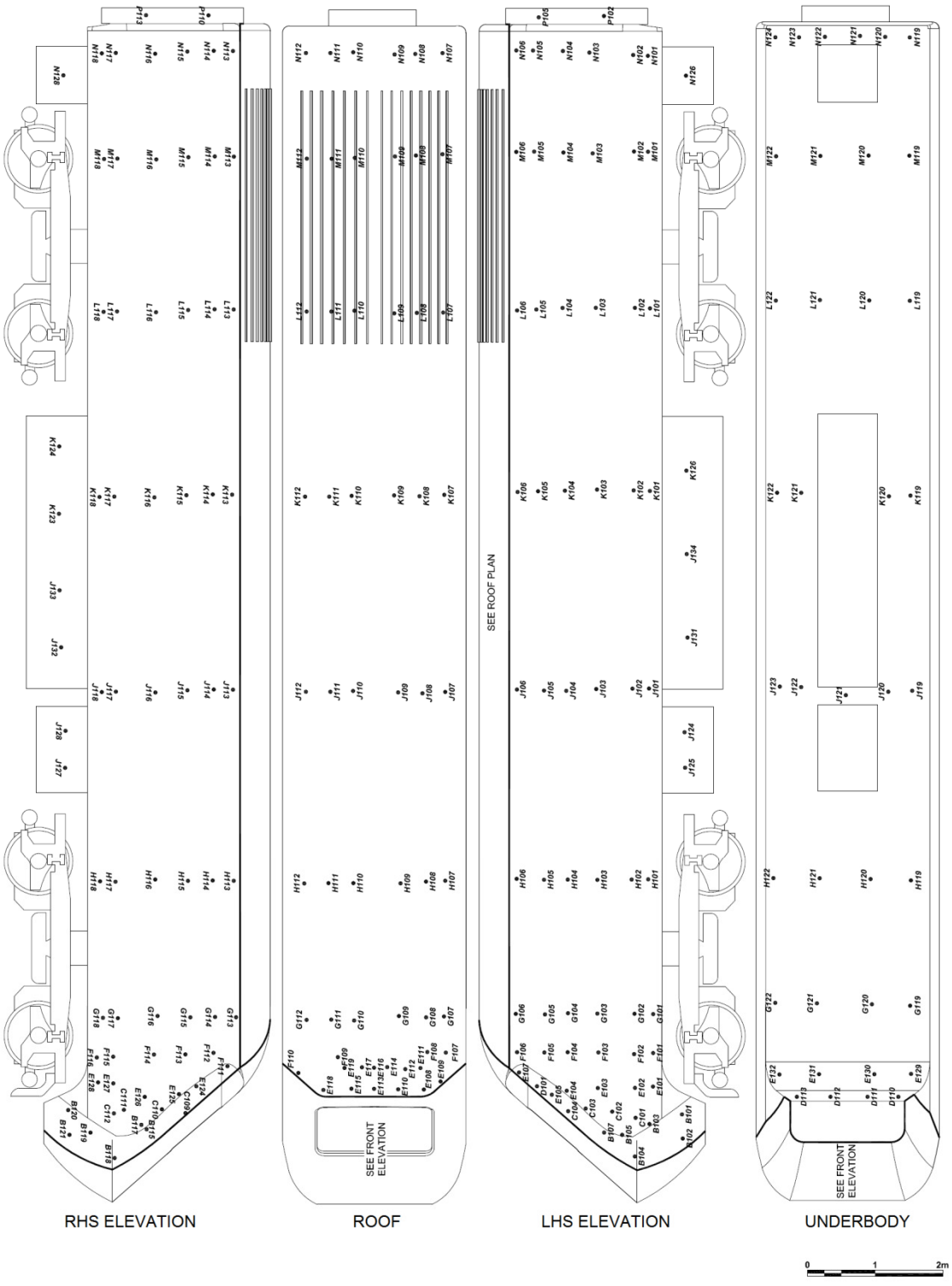

Figure G.1.2 - Positions and letters/numbers of pressure taps on body of HST wind tunnel model.

G.3 Underbody pressures

G.3.1 Experimental set up

The HST power car model was fitted with 31 pressure taps on the flat surface of the underside, which are shown in figure G.2, which also shows the key geometric features of the undercarriage region. All of these taps were part of loops of pressure taps, (loop distances are defined on figure G.2). Underbody pressures are of importance when lift forces and hence lee-rail moment are calculated. It was therefore desirable to consider the underbody pressures of the wind tunnel model in order to calculate moment coefficients for each loop.

The flow beneath a train is complex and has not been considered in this study in much detail - the principal reason for this is that it was not possible to consider the underbody at full scale or with the TRAIN rig crosswind tests. In addition, the underbody geometry was slightly different between the three types of test, and the wind tunnel did not simulate the relative movement between the train and the track.

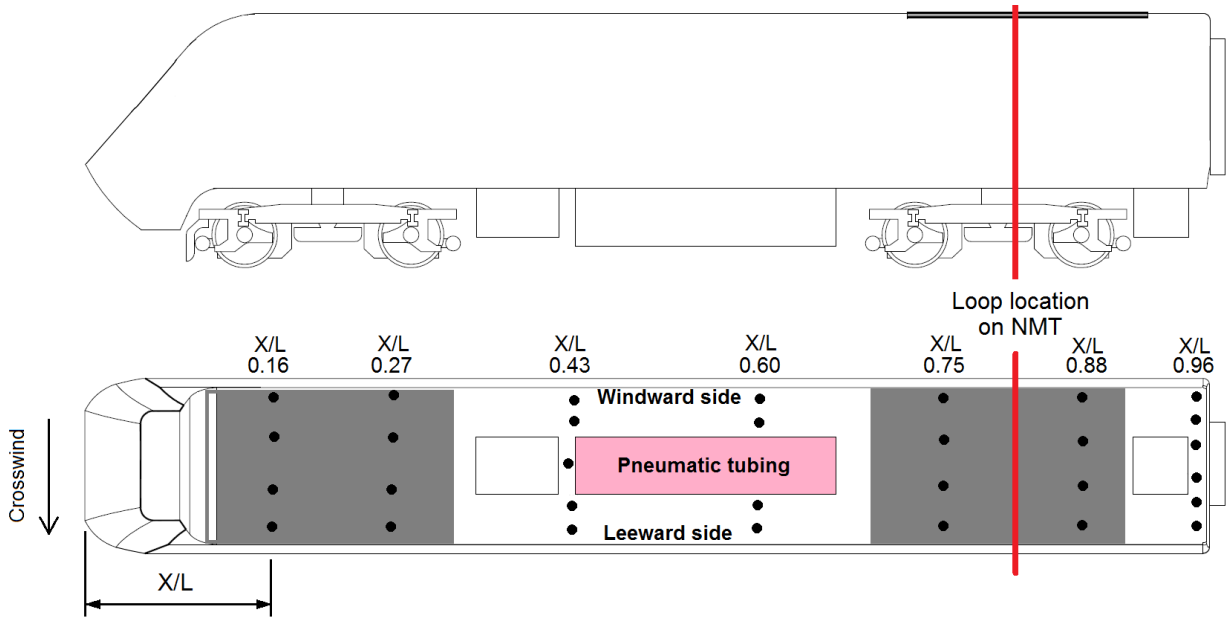

Figure G.2 - Locations of under body pressure taps on wind tunnel model. Bogie areas shaded grey.

G.3.2 Underbody pressure distribution

The mean pressure coefficients for each row of taps, i.e., the underbody taps in a given loop at a given distance (X/L) from the nose were calculated from the pressure coefficient time series for each pressure tap and at different yaw angles (equation 7.1) . Figures G.4.1 to G.4.7 show the pressure coefficients across the underside at ascending the loop locations from the nose shown in figure G.2. Figure G.3 shows a shaded plot of $\overline{C_P}$ at yaw angles of 0° to 30°. It should be noted that when figure G.3 was constructed, the geometrical discontinuities (caused by blocks and bogies) were disregarded, therefore figure G.3 must be interpreted with care. The purpose of figure G.3 is to show the net pressure over the underbody, and shows that there is a low and slightly negative pressure at zero yaw, and that as the yaw angle increases a

positive (uplift) pressure develops on the windward side which will increase the value of $C_{M_{X,lee}}$, though at yaw the magnitudes of the underbody pressures lower than the pressures around the walls and roof (figure 8.5). The effect of the geometric discontinuities is discussed by considering figures G.4.1 to G.4.7.

The pressures either side of the front bogie can be considered by comparing loops at X/L = 0.16 and 0.27, and are shown in figures G.3.1 and G.3.2. Just ahead of the bogie, at X/L = 0.16, the pressure coefficient is about zero at low yaw angles (up to 20°). At higher yaw angles from 30° to 45° there is a negative pressure coefficient, which is most pronounced on the leeward side of the underbody. The loop immediately after the front bogie at X/L = 0.27 shows very similar results, possibly suggesting that this pressure distribution with yaw is similar for any region immediately after some geometrical feature that results in blockage - the pressures immediately downstream of the rearward bogie at X/L = 0.88 (figure G.4.6) are very similar to the pressures downstream of the leading bogie.

The two rectangular "blocks" at about half the power car length represent a geometric simplification of the full scale HST power car. At higher yaw angles and at X/L = 0.43, the windward side taps recorded a positive pressure as the rectangular blocks would have obstructed the flow and caused a region of stagnation. The pneumatic tubing resulted in 100% underbody blockage in the y direction (at X/L ~ 0.5) and may have caused this stagnation pressure to be unrealistically high, and hence also resulted in larger suction pressures around this block (in the vicinity of the tubing) as the air flow was accelerated around this blockage. The central and leeward side pressure taps show a negative pressure coefficient. This pressure distribution shows a similar pattern and magnitude in the loop at X/L = 0.60, though the corresponding figure G.4.4 shows interpolated data, and without the central pressure tap the

pressures between the windward and leeward taps (i.e., at normalised y distances of -0.2 to 0.2) are an arbitrary guess.

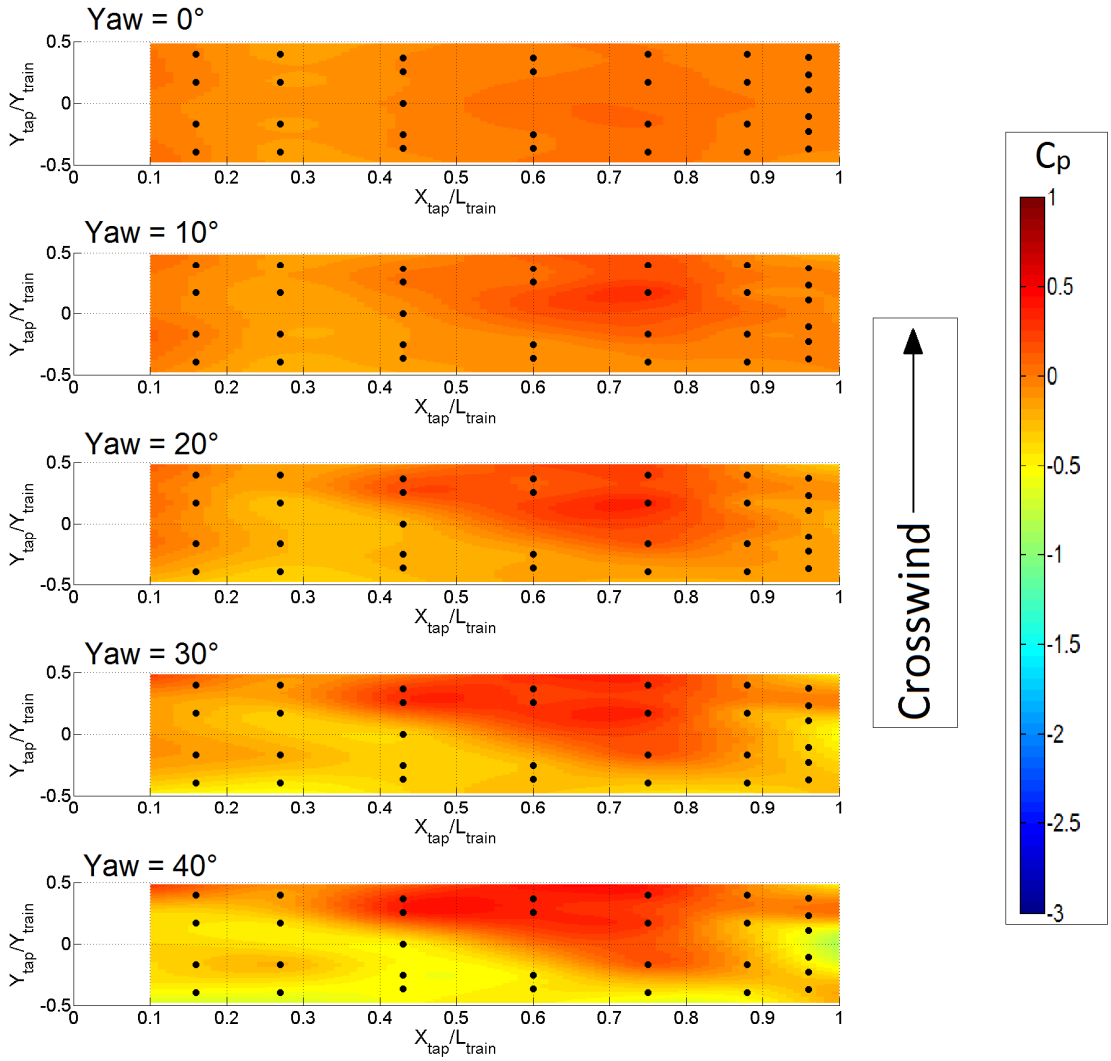

Figure G.3 - Underbody pressure distribution. Note that surfaces and bogies have been omitted during the construction of this plot.

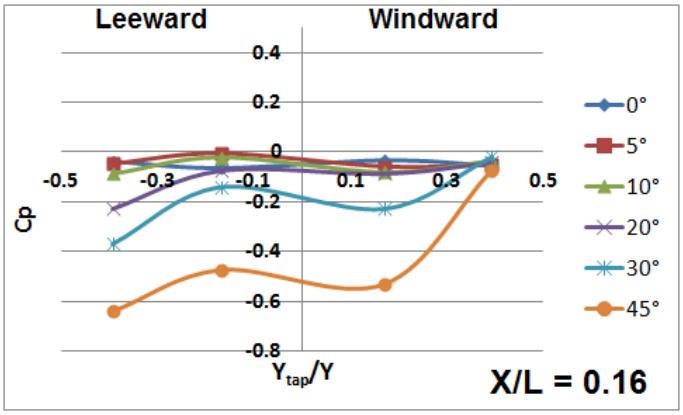

Figure G.4.1 - Pressure coefficients along underbody loop at X/L = 0.16

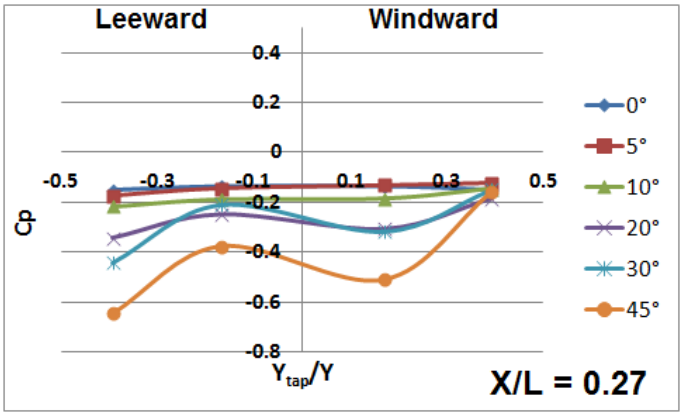

Figure G.4.2 - Pressure coefficients along underbody loop at X/L = 0.27

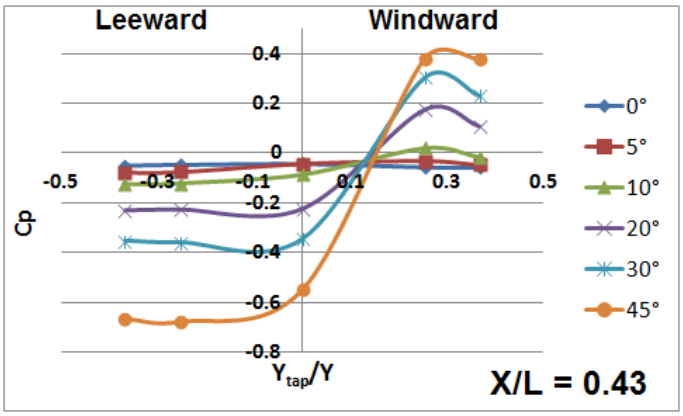

Figure G.4.3 - Pressure coefficients along underbody loop at X/L = 0.43

Figure G.4.4 - Pressure coefficients along underbody loop at X/L = 0.60

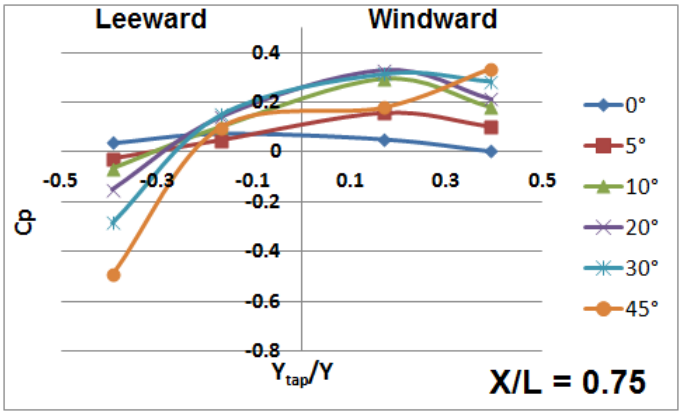

Figure G.4.5 - Pressure coefficients along underbody loop at X/L = 0.75

Figure G.4.6 - Pressure coefficients along underbody loop at X/L = 0.88

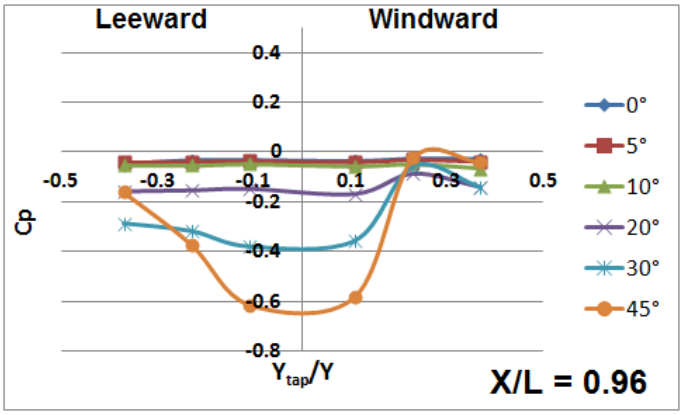

Figure G.4.7 - Pressure coefficients along underbody loop at X/L = 0.96

The main reason for considering underbody pressures is in the calculation of lift force and moment coefficients for the TRAIN rig and NMT work. The location of the NMT (and TRAIN rig) loop of pressure taps is shown in red on figure G.2, and is located at X/L = 0.8. The NMT loop of pressure taps is just offset from the centreline of the rear bogie (slightly towards the end of the carriage - figure G.5). Figures G.4.5 and G.4.6 compare the pressures just in front of and just after the rear bogie. Though there was little notable difference between pressures at the front bogie, the rearward bogie shows significant differences between the loop of taps either side of the bogie centreline (i.e., loops at X/L = 0.75 and 0.88 respectively). Just ahead of the bogie, the pressures are positive at lower yaw angles which is unsurprising as the bogie will create blockage and result in stagnation. As the yaw angle is increased, the positive pressures increase in magnitude and, roughly speaking, the region from the leeward rail to the windward wall experiences a positive pressure. Considering the rearward loop (X/L = 0.88), at low yaw angles the pressure is about zero (but ever so slightly negative) and as the yaw angle is increased a negative pressure coefficient with a spatial average of about 0.2 develops across this strip.

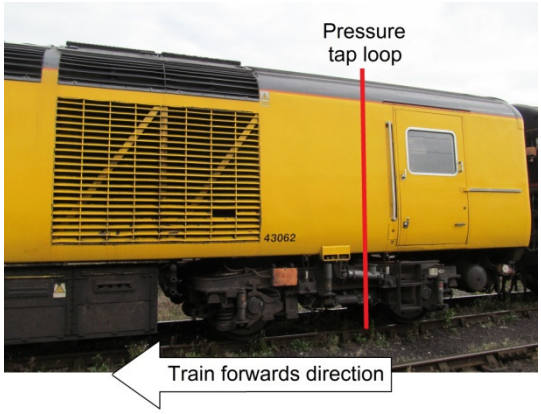

Figure G.5 - Pressure tap loop on NMT at X/L = 0.8.

G.3.3 Calculation of force and moment coefficients

As it was not possible to consider the underbody region for all the tests, partial force and moment coefficients were defined (in equation 7.10) for the lift, moment and lee rail moment coefficients caused by pressures on the roof and walls (the underbody contributions to side force are not considered). The partial force/moment coefficients per unit length $C^*_{\eta,loop}$ and $C^*_{\eta,floor}$ are considered in this section.

The model was discretised following the same methodology adopted in section 7.2.2 - discreet rectangular surfaces were drawn, each "centred" on a single pressure tap, where the edges of the rectangle were at the midpoint of the considered pressure tap and the adjacent pressure tap (or underbody edge when end taps were considered). Figure G.6 shows the discretisation of the train underbody and the areas of each surface are given in table G.1, and the surface numbering convention follows the convention in figure 7.2.1 (hence the surface numbers start at 19 and are numbered ascending from the leeward wall edge, i.e., counter clockwise as in figure 7.2.1). Again, this methodology only considers the coefficient per unit length, i.e., for a

1 m strip centred on each loop of taps. As the underbody surface is flat and horizontal, θ_S was 90° for all the underbody taps, hence side force coefficients would always be zero, and the pressures on the rectangular blocks were not considered - the underbody was treated as a flat plane.

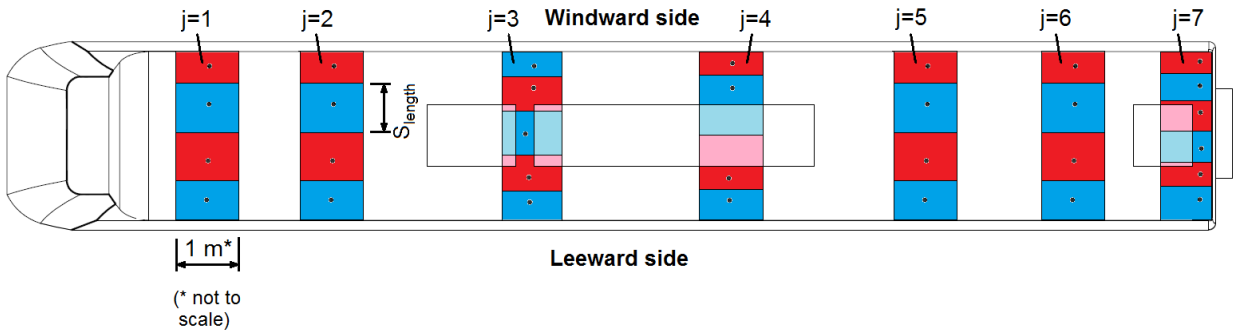

Figure G.6 - Underbody pressure taps and surfaces. Pseudo-surface extensions are shown in light blue and red for loops j = 3, 4 and 7. Width of all surfaces is nominally 1 m (widths are not to scale). Surface 19 for each loop is at bottom of figure always shown in blue and on leeward side.

As shown in figure G.6, due to the rectangular blocks in the underbody region, the model was further simplified. Pseudo-surface extensions were produced where the underbody was considered to be flat (i.e., no rectangular blocks) and the pressures across the "real" surface and the pseudo-surface were assumed equal (shown in faint red and blue for loops j = 3, 4 and 7 on figure G.6). As no pressures were measured on the underside of the blocks, this assumption was made in order to simplify analysis and is expected to lead to a slightly conservative overestimation in the lift force and moment coefficients (as pressures on the

underside of the blocks are expected to be low and negative), and considered to have negligible effect on lee-rail moment given the short distance between the central pseudo surfaces and the lee-rail. The effects of neglecting the side forces on the blocks was expected to have little significance on the lee-rail moment given the short vertical lever arm, and the overall force and moment coefficients calculated solely from the loops of taps compared favourably with the force and moment coefficients calculated by RWDI who included every pressure tap (figure 8.11.3).

Table G.1 - Areas of surfaces (at full scale) for underbody loops considering 1 m strips

Loop number (j)	Distance from nose (X/L)	Equivalent full scale area of surface (m^2)					
		S = 19	S = 20	S = 21	S = 22	S = 23	S = 24
j = 1	0.16	0.46	0.77	0.77	0.46	N/A	N/A
j = 2	0.27	0.46	0.77	0.77	0.46	N/A	N/A
j = 3	0.43	0.38	0.50	0.69	0.50	0.38	N/A
j = 4	0.60	0.38	0.85	0.85	0.38	N/A	N/A
j = 5	0.75	0.46	0.77	0.77	0.46	N/A	N/A
j = 6	0.88	0.46	0.77	0.77	0.46	N/A	N/A
j = 7	0.96	0.41	0.36	0.46	0.46	0.36	0.41

G.3.4 Partial force and moment coefficients per unit length

Values of $C^*_{\eta,floor}$ were calculated for each loop (where η = Z, M_X and $M_{X,lee}$). Values of $C^*_{\eta,floor}$ are compared to values of $C^*_{\eta,loop}$ along the train length in figures G.7.1 to G.7.3 at yaw angles of 0° to 50°. The y axes are different for the loop and underbody coefficients

Broadly speaking, the $C^*_{\eta,floor}$ are one order of magnitude lower than the $C^*_{\eta,loop}$. When $C^*_{Z,floor}$ is considered (figure G.7.1b), the only loop location that has a positive (i.e., upwards) lift coefficient is at X/L = 0.75, i.e., immediately ahead of the rearward bogie. The larger underbody moment coefficients, seen in figure G.7.2 (b) at X/L = 0.43 and 0.60, are caused by the rectangular blocks along the train centreline which cause a relatively large pressure differential either side of the block (seen in figures G.4.3 and G.4.4). It is, however, acknowledged, that these values may be an overestimation due to the geometric simplifications made to the model. The lee rail moment coefficients within the underbody show that the region of the train affected by blockage shows negative (i.e., overturning in the windward direction) lee rail coefficients, though these are an order of magnitude lower than the partial lee rail coefficients from the loop.

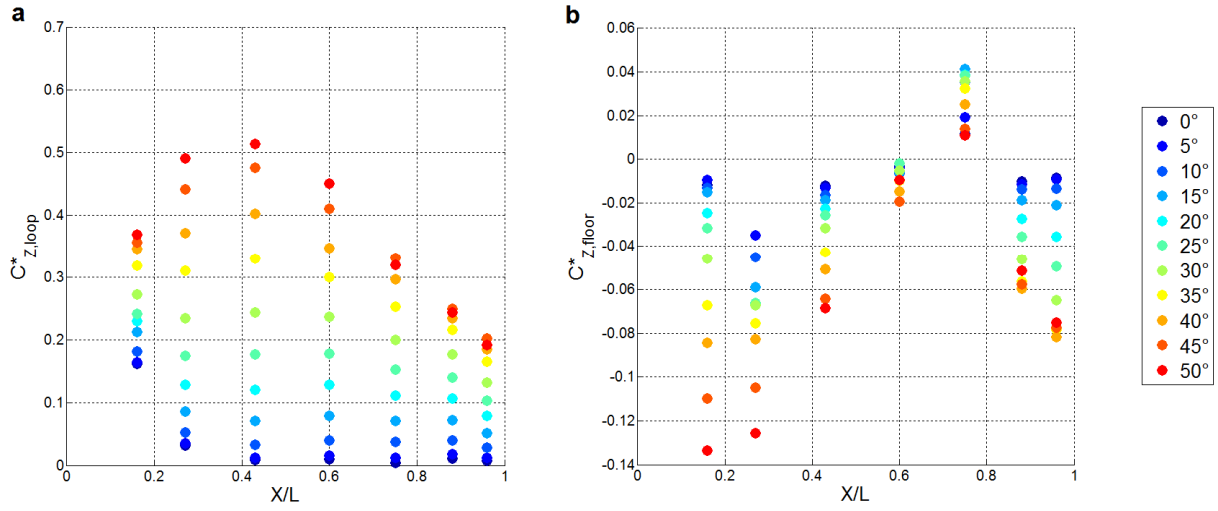

Figure G.7.1 - Comparison of partial lift force (Z) coefficient along train length (a) from loop taps across walls and roof and (b) from underbody only.

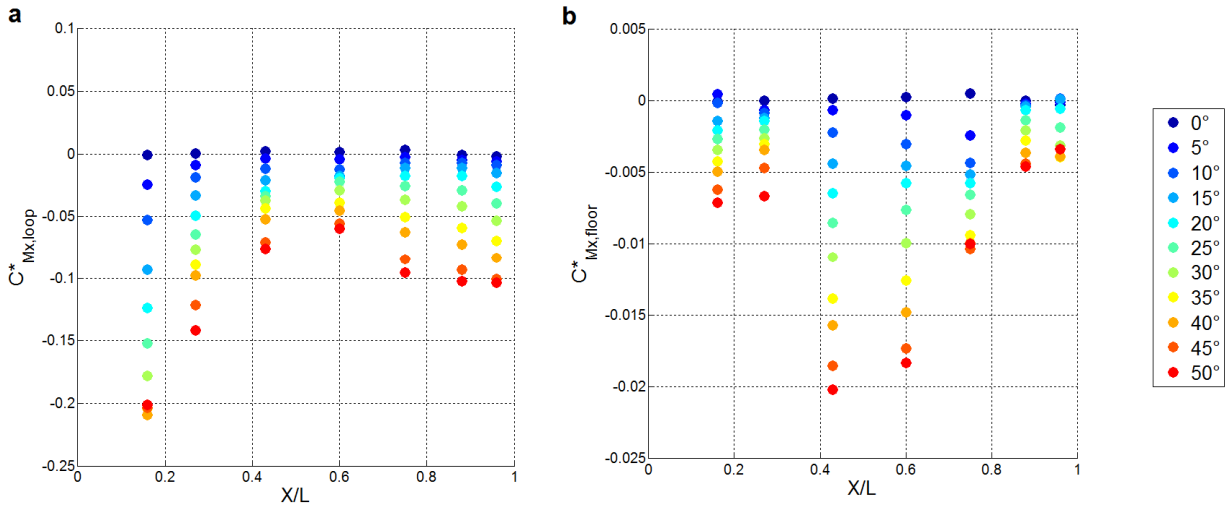

Figure G.7.2 - Comparison of partial moment (M_X) coefficient along train length (a) from loop taps across walls and roof and (b) from underbody only.

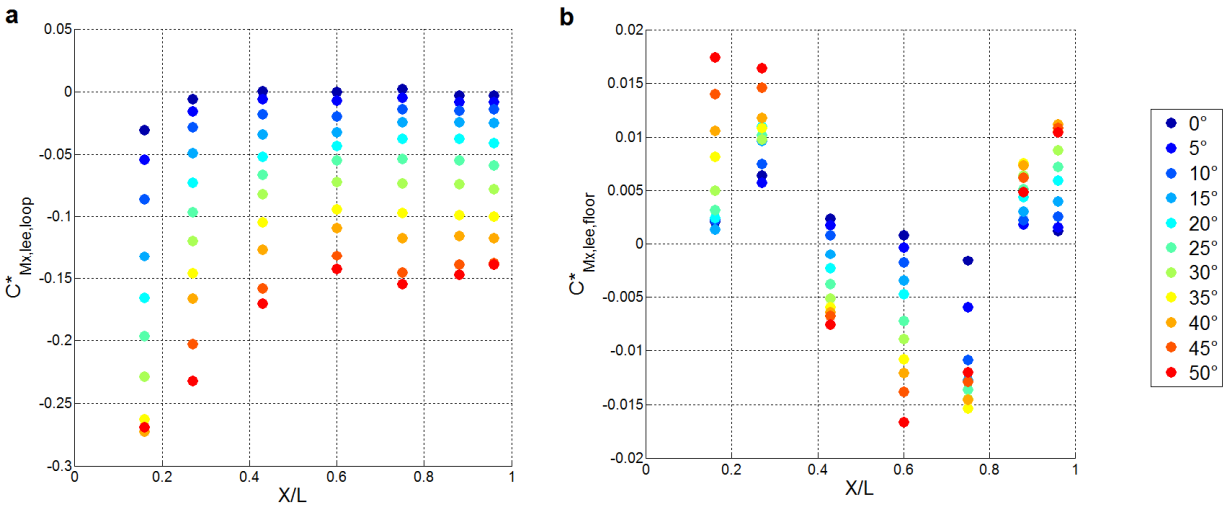

Figure G.7.3 - Comparison of partial lee rail moment ($M_{X,lee}$) coefficient along train length (a) from loop taps across walls and roof and (b) from underbody only.

APPENDIX H

TRAIN RIG CROSSWIND TESTS - ADDITIONAL INFORMATION

H.1 Introduction

Appendix H provides additional information regarding the crosswind tests at the TRAIN rig using the CWG. The details of the experimental procedure are presented in section H.2, with a focus on describing the two sets of tests that took place as a result of broken data channels. Section H.3 described the overall set up of the TRAIN rig during the CWG tests. Section H.4 describes the format of the raw data that was acquired by the data logger and reference probe. Section H.5 describes the process by which an appropriate filter was selected to remove the resonant interference caused by the CWG noted by Dorigatti, (2013). Section H.6 considers a different approach to analysis of the data, by considering span wise ensemble averages rather than the yaw angles procedure described in chapter 7.

H.2 Experimental details

The pressure tap set up was designed assuming that the data logger would work correctly throughout the tests, i.e., that a total of 15 pressure taps could be tested on a given run (the tap positions that were planned are shown in figure H.1). A loop of pressure taps was located around the rear of the power car at the same distance from the nose as on the full scale tests (chapter 9). The data logger, pressure transducers and electrical cables were all housed entirely in the train model, which experienced large acceleration/deceleration forces during the tests. As a result, 5 of the 15 pressure channels developed faults during the tests and were unusable. Given that repairs on the train model were very time consuming when compared to carrying out runs of the TRAIN rig it was necessary to perform the tests without repairing the broken channels. A second test was then carried out to test the pressure tap positions (shown in figure H.1) that were associated with the faulty data logger channels. Throughout this appendix, the two tests will be known as test 1 and test 2, and table H.1 gives the details about the two tests. The second test considered 10 run ensembles at two yaw angles ($\varphi = 20°$ and 25°) yaw angles, i.e., 20 additional acceptable runs - the lower number of runs was due to time constraints on the availability of the TRAIN rig and a second person to assist with the tests. The details of the broken pressure taps and both tests are described in this section. The aim of the test 2 was to test the broken pressure channel tap positions and also some additional tap positions (see figure H.1). The three taps at the nose were kept in order to check for consistency between the two tests and also in order to achieve a larger ensemble size at the nose given that these taps were important in estimating yaw angle at full scale (see section 8.2.2).

Table H.1 - Experimental details for both sets of crosswind tests

	Test 1	Test 2
Yaw angles tested (°)	15, 20, 25, 30	20, 25
Total number of runs	60 (4 sets of 15 runs)	20 (2 sets of 10 runs)

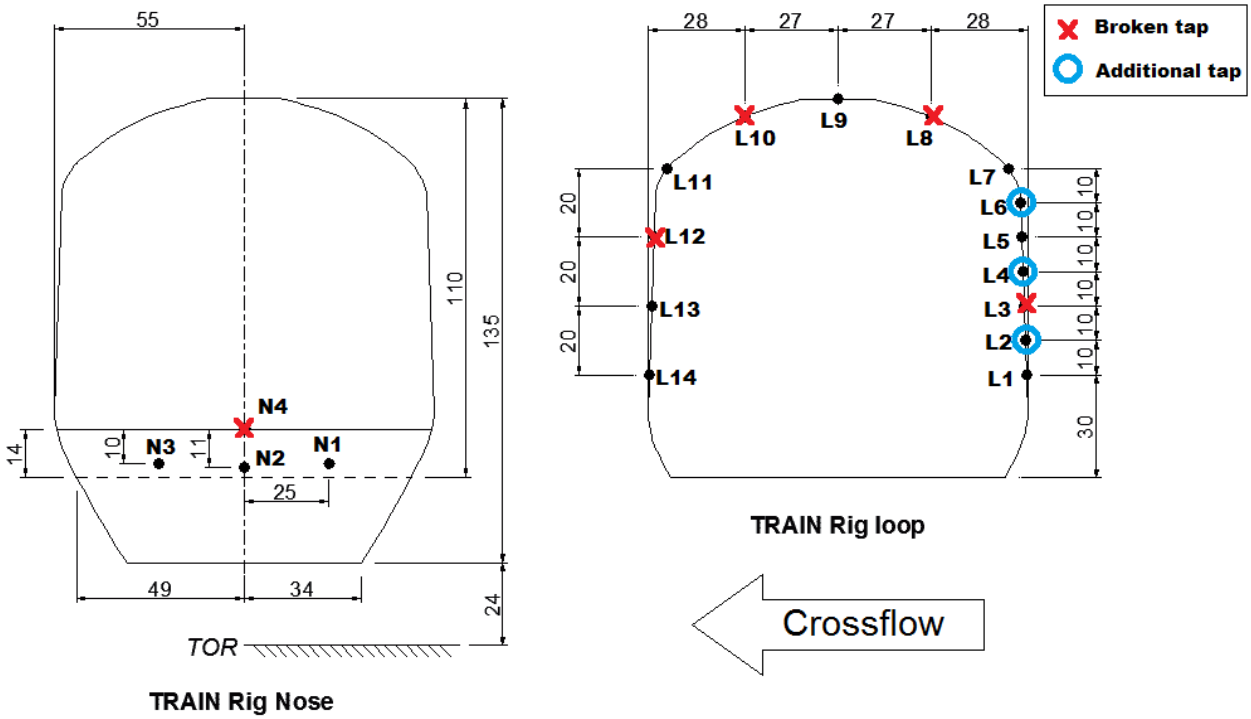

Figure H.1 - All pressure tap positions tested during TRAIN rig crosswind tests.

In figure H.1 the plane of view is looking towards train nose (contrary to direction of travel). Red crosses indicate pressure taps that were not tested during the first set of measurements and were subsequently retested (along with blue circled additional taps). Note that the data from taps N4 and L10 was unacceptable from both test 1 or 2.

Table H.2 - Description of data logger channels and issues.

Channel number	Pressure tap (test 1)	Pressure tap (test 2)	Comments
1	N1	N1	Data OK.
2	N2	N2	Data OK.
3	N3	N3	Data OK.
4	-	-	Broken channel.
5	L14	L12	Data OK.
6	L13	L10	Data OK during test 1. Test 2 data discarded - tap L10 not tested.
7	-	-	Broken channel.
8	L11	L8	Data OK.
9	-	-	Broken channel.
10	L9	L6	Data OK.
11	-	-	Broken channel. Tap 11 retested.
12	L7	L4	Data OK.
13	L5	L3	Data OK.
14	-	-	Broken channel. Tap 14 retested.
15	L1	L2	Data OK.
16	-	-	Used for the onboard light sensor.

H.3 TRAIN rig set up

In addition to the crosswind data, the tests were set up to acquire pressure tap data from passing a stationary freight train and a tunnel transient on the same run. This additional data has not been considered directly in this study, therefore the experimental set up is described only briefly in this section.

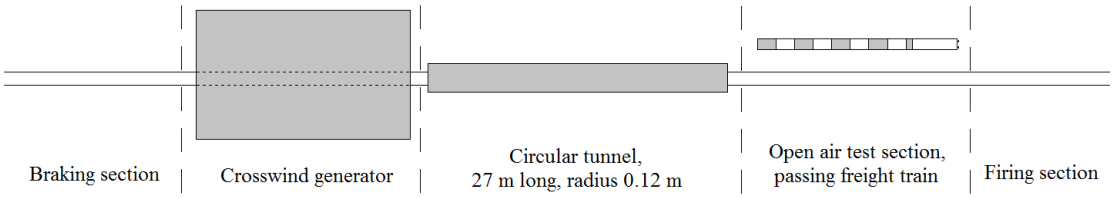

Figure H.2 - Schematic overview of the test set up (train direction is from RHS to LHS).

H.3.1 Open air test section - passing a stationary Class 66 freight train

The open air test section was intended to measure the pressure transient on the HST surface when passing a stationary Class 66 freight train. The pre-tunnel probes were intended to be used solely as a measure of train speed by estimating speed from the probe spacing divided by time between nose pressure transients, though could quite easily have been used to measure slipstreams simultaneously as CWG data, though ideally additional light gates would be positioned either side of the rake of Cobra probes.

Figure H.3 - Cobra probes and freight train containers in open air test section.

H.3.2 Circular tunnel

Pressures were measured in a circular tunnel, 27 m in length with a radius of approximately 0.12 m. The tunnel cross section was centred at the track centreline, and three pairs of pressure transducers were set up at 4 m, 8 m and 20 m from the tunnel entrance, and at the mid-height of the tunnel. The pressure transducers were housed inside "nylon 66" blocks on the exterior surface of the tunnel (with a 3 mm hole about 10 mm from the internal surface), and the reference pressure tubing (lengths of about 1.5 m) was positioned beneath the train rig on the floor.

The train based tunnel data was useful during on-site quality control checks of the data every few runs - given that the tunnel centreline is the COT, and that the tunnel is symmetrical, opposite pressure taps around the loop were checked to ensure that the pressures were of similar magnitude.

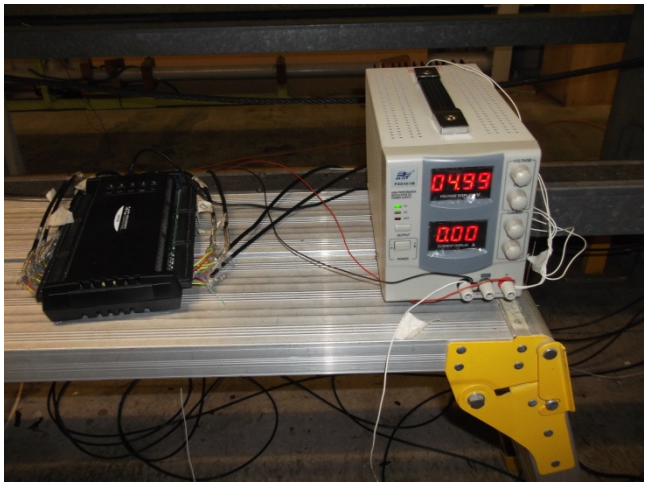

Figure H.4 - Data logger and 5V DC electrical power supply for tunnel pressure transducers.

Figure H.5 - Pressure transducer mounted inside nylon block glued to outer surface of tunnel.

H.4 Data format

The data from the onboard system was returned as a 16 column ".tsv" (tab separated values) file, where each column was the voltage output signal of each transducer (for columns 1 to 15), and the light sensor voltage as the 16th column.

	A	B	C	D	E	F	G	H	I	
1	Experiment Number: 1									
2										
3	Number of Samples: 80591									
4										
5	Started Time : 26/03/2015 14:57:11									
6										
7	Duration: 00:00:20									
8										
9	Battery Voltage: 8.81									
10										
11	Start Block Address: 16384									
12										
13	End Block Address: 21423									
14										
15	Frequency: 4000									
16										
17	Error: 0									
18										
19	Size of Data: 2519KBytes									
20										
21	Channel1	Channel2	Channel3	Channel4	Channel5	Channel6	Channel7	Channel8	Channel9	Char
22	2.269821167	2.257843018	2.262649536	2.264328003	2.267608643	2.26524353	2.214584351	2.261581421	2.275695801	2.25
23	2.26852417	2.253723145	2.265472412	2.265396118	2.262954712	2.26524353	2.214660645	2.265167236	2.274932861	2.25
24	2.266235352	2.256393433	2.264556885	2.261505127	2.261657715	2.265625	2.214508057	2.261123657	2.274703979	2.25
25	2.266540527	2.256011963	2.266693115	2.266845703	2.263031006	2.265319824	2.214355469	2.263793945	2.275238037	2.25
26	2.266311646	2.255783081	2.264328003	2.263412476	2.265777588	2.259368896	2.214508057	2.263336182	2.275314331	2.25

Figure H.6 - Output data file from onboard data logger (viewed in Microsoft Excel).

The Cobra probe data from the reference probe comprised five files per run - the main probe data file which contained individual columns for the three velocity components and the static pressure, and four individual analogue files (a single column of raw voltage time series) for each of the four light gates. The light gate voltage time series (shown in figure H.7) would sharply increase to ~3-4 V when it was broken, and so the first data sample at which the second light gate was greater than 3 V was taken as the alignment row (as this would correspond to the first external light source being aligned with the onboard light detector).

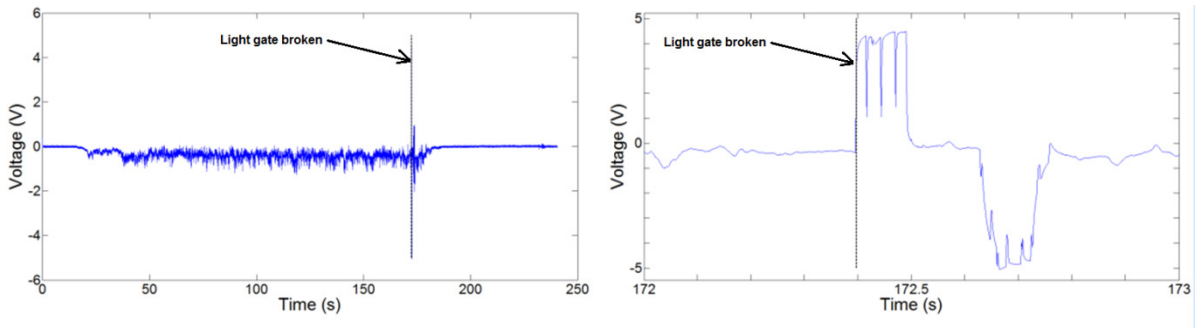

Figure H.7 - Voltage time series for a single light gate (vertical dashed line is defined as the light gate being broken, i.e., the first data point where the voltage is equal to or above 3 V).

When considering data from the reference Cobra probe, Dorigatti, (2013), and Soper, (2014), trimmed a 60 second time series from 50 s before the train entered the CWG to 10 seconds after entry. However, given this author's testing methodology, it was not possible to trim 10 s after the train had entered due to shutting down the CWG earlier in order to reduce the time taken to set up the next run. A 53 s time series was selected (i.e., 3 s after the train had entered the CWG) based on the time between the train passing through the CWG and the shutdown of the CWG for all runs considered. The sampling time of the onboard data logger and the time

of the train passing through the CWG with respect to reference probe velocity is shown in figure H.8.

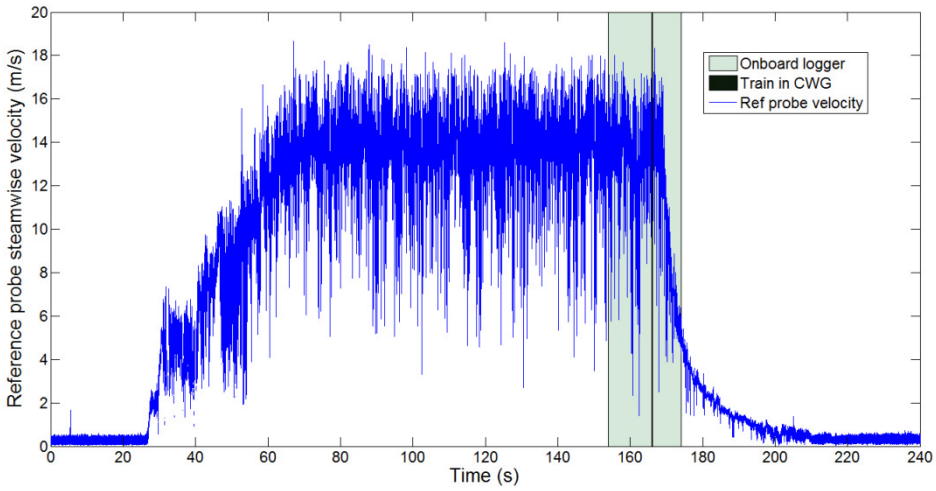

Figure H.8 - Streamwise velocity from reference probe for a single run showing 20 s sampling time for the onboard logger (shaded green) and actual time train is in the CWG as a vertical bar (time of train in CWG was typically 0.1 - 0.3 s).

H.5 Data filtering

The purpose of filtering a time signal is to remove interference that has a known frequency, whilst preserving the original (and real) signal as much as possible. In the CWG tests there are a range of causes of observable frequency phenomena. Unwanted vibration effects could be due to the movement of the model (which would have a frequency proportional to train speed) and vibration of the CWG due movement of the fans which would be independent of train speed. Frequency effects that should not be filtered include the effect of the model moving through the non-uniform velocity profile (section 6.2.1, figure 6.8.1) and also turbulent fluctuations in the air flow which would occur at a range of frequencies.

It was found in a study using the CWG that the movement of the fan blades created interference (Dorigatti, 2013). Figure H.9 shows the power spectrum from this previous study for a single pressure tap and run - a peak can be seen at about 120-150 Hz, and therefore a low-pass filter with a cut off frequency of 70 Hz was applied to the pressure tap data to remove the effects of vibrations due to the fan blades (shown in red on figure H.9) in the previous study (Dorigatti, 2013).

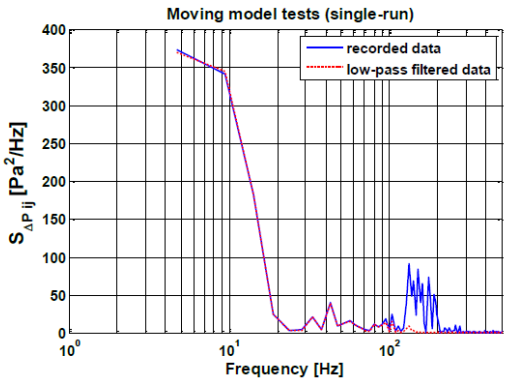

Figure H.9 - Power spectrum for single pressure tap and run showing raw and filtered data (Dorigatti, 2013).

In the analysis for this study, four pressure taps have been considered representative of the nose, windward wall, roof and leeward side wall respectively. The frequency spectra of individual runs were analysed. To consider the effect of train speed on the frequency spectrum, two different train speeds were selected - 44 m/s and 20 m/s (i.e., yaw angles of 15° and 30°).

The voltage time series for each pressure tap was trimmed (as described in section 7.3.4) so only the data through the crosswind generator was considered. This trimmed time series was then decomposed and the fluctuations about the mean considered; the mean of the trimmed voltage time series was subtracted from the time series (and hence the new mean of the

voltage time series for each pressure tap was zero). It should be noted that this methodology makes an incorrect assumption that the mean voltage is uniform across the span which is incorrect, however, it does allow the frequency fluctuations as a result of the non-uniform span wise velocity to also be considered on the power spectrum. A Fourier transform was applied to this unfiltered time series using the fast Fourier transform function "fft" on Matlab to convert it to a frequency domain signal (Mathworks, 2010). The frequency spectra of the raw voltage time series were plotted for each pressure tap (shown in blue on figures H.11.1 to H.11.4). This procedure was repeated for the same data, but with different filters applied in the initial stages of data processing (i.e., immediately after the data had been trimmed). The frequency spectrum of the raw unfiltered data showed a large peak at frequencies just below 200 Hz. For the windward wall tap and the nose tap there is an additional peak at 135 Hz, similar to that found in a previous study (Dorigatti, 2013). It was therefore decided that a low-pass filter was appropriate to remove this noise interference by to preserve the lower frequency portion of the signal which was real. In this study on the HST, a low-pass Butterworth filter was designed using Matlab using the "butter" function, and applied to the data using the "filter" function (Mathworks, 2010). Two filter parameters were investigated - the filter order (filter orders 1, 2 and 3 were considered) and the cut-off frequency (f_{cut}) - given the position of the noise in the unfiltered data cut-off frequencies of 50 Hz, 75 Hz and 100 Hz were considered. Figure H.10 shows the magnitude and phase angle properties of the filters that were investigated.

The position of the noise in the unfiltered data is not dependent on train speed, which implies that it is due to mechanical vibrations caused by the fans. In fact, the train speed appears to have no apparent effect on the frequency spectra when frequency specific peaks are considered. This suggests that the use of the onboard data logger is an effective way of

mitigating vibration caused by the movement of the train on the track compared to the use of a force balance (Sanquer et al., 2004; Dorigatti, 2013). The data at the high train speed is sparser in the x-axis simply because there were fewer data points in the sample due to the higher train speed (and fixed test section length through the CWG, hence lower sample time of the run).

The effect of changing the filter order on the frequency spectrum is shown in different colours in figures H.11.1 and H.11.2 (each figure considers a different run and hence train speed). It was important to preserve the data signal as best as possible at frequencies below frequency of the noise. Different Butterworth filters were applied to the voltage time series, and the power spectra were plotted for a range of train speeds and pressure taps. A first order filter with a cut-off frequency of 100 Hz did not entirely remove the noise peak from the frequency spectra. The second and third order Butterworth filters removed the noise to acceptable levels, but the second order filter appeared to preserve frequencies less than 100 Hz slightly better than the third order filter.

The effect of changing the cut-off frequency is considered with the same data and format, as in figures H.11.3 and H.11.4, for a second order Butterworth filter. All three cut-off frequencies successfully removed the noise peaks at 135 Hz and 200 Hz. Unsurprisingly, cut-off frequencies of 50 Hz and 75 Hz were can be seen to have a greater effect on the signal at frequencies below 100 Hz than a cut-off frequency of 100 Hz.

A second order Butterworth filter with a cut-off frequency of 100 Hz was therefore chosen and applied to all pressure tap data from the CWG tests, as it preserved in data at lower frequencies (< 100 Hz) closest to the original signal, but the noise peak between 135 Hz - 200 Hz was successfully removed.

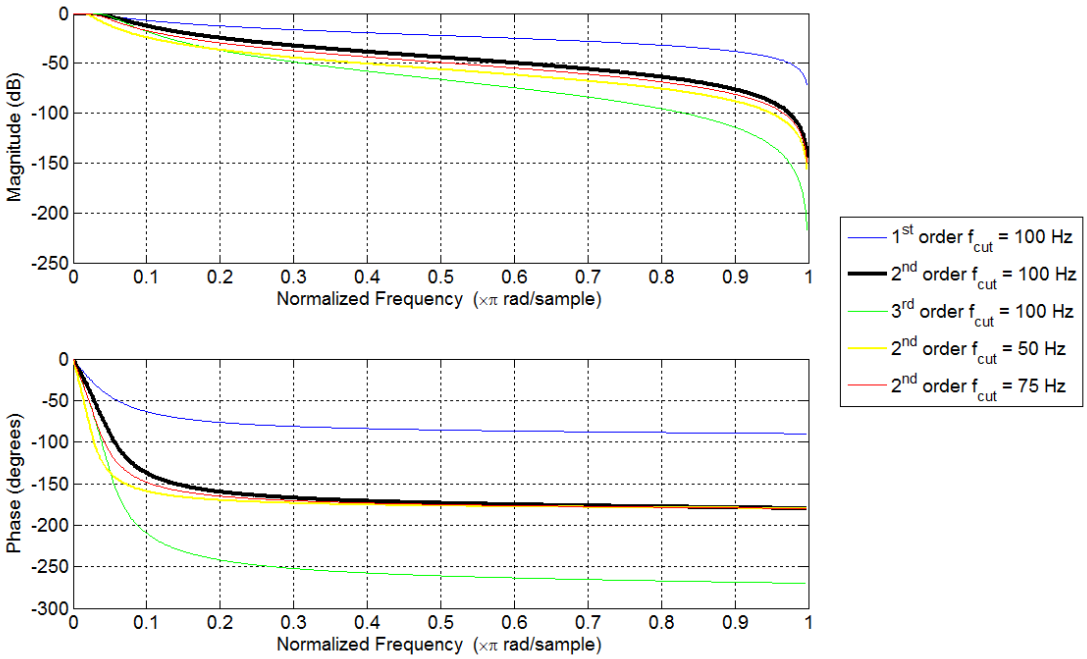

Figure H.10 - Butterworth filters - magnitudes and phases (100 Hz cut off frequency is equivalent to a normalised frequency of 0.05) (Mathworks, 2010).

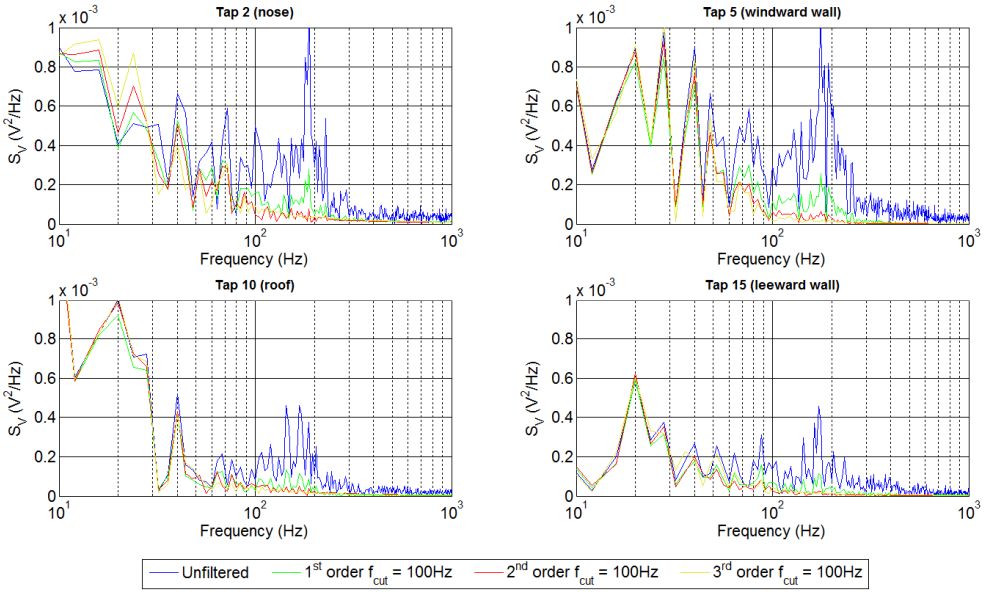

Figure H.11.1 - Frequency spectra of the voltage time series at 44 m/s to compare effect of changing filter order for each pressure tap.

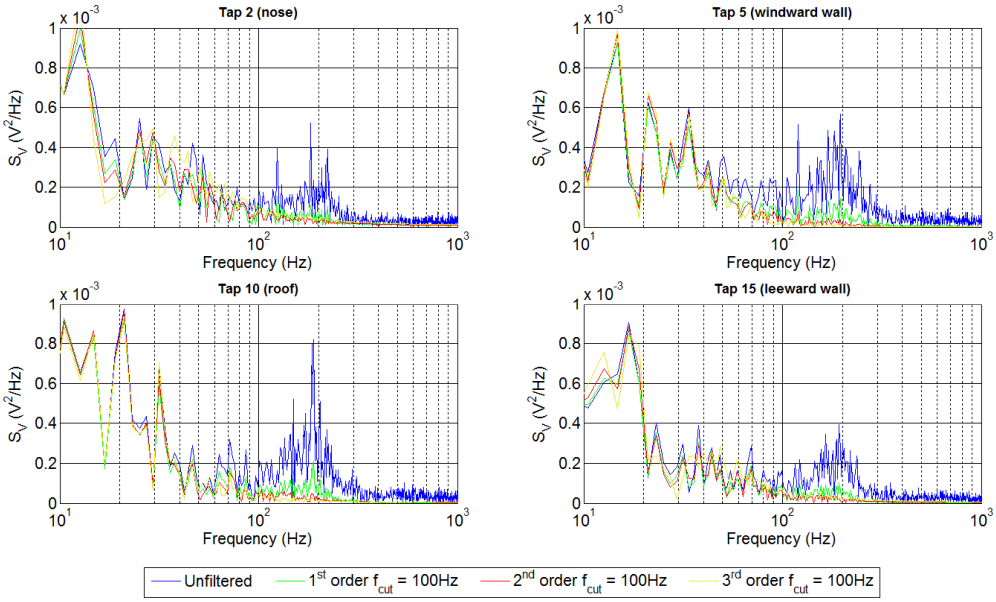

Figure H.11.2 - Frequency spectra of the voltage time series at 20 m/s to compare effect of changing filter order for each pressure tap.

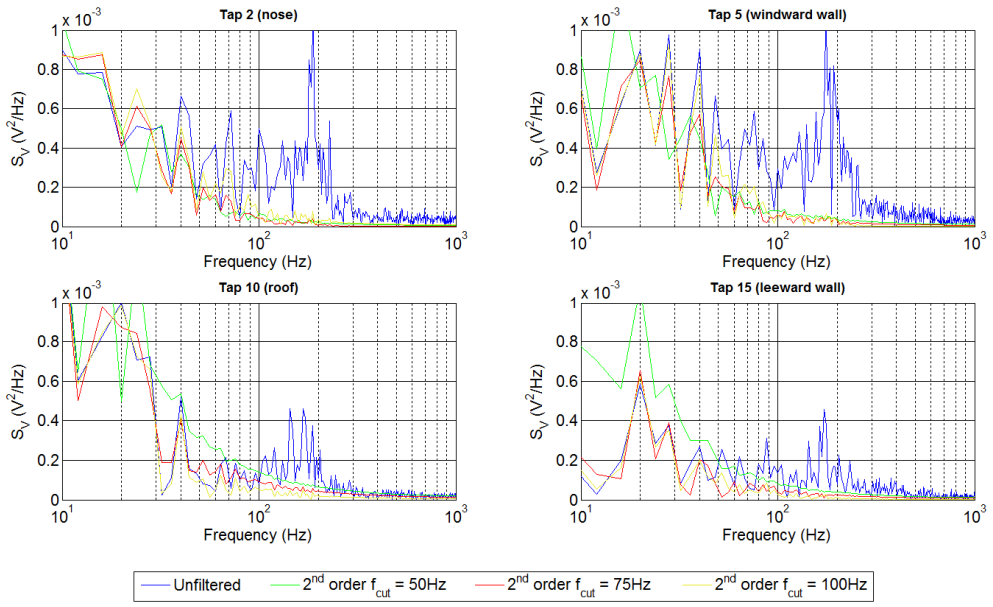

Figure H.11.3 - Frequency spectra of the voltage time series at 44 m/s to compare effect of changing cut-off frequency for each pressure tap.

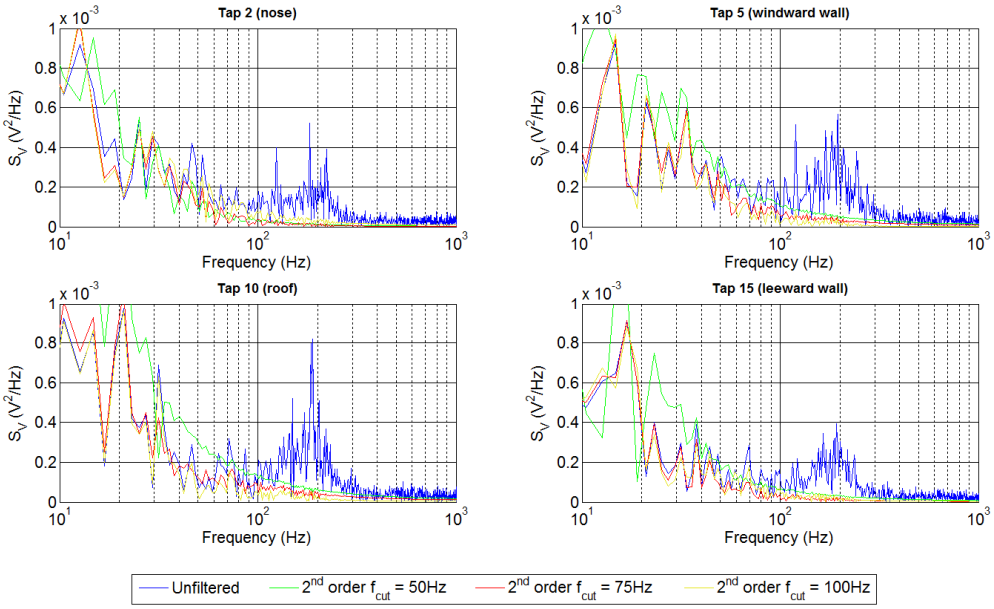

Figure H.11.4 - Frequency spectra of the voltage time series at 20 m/s (φ = 30°) to compare effect of changing cut-off frequency for each pressure tap.

H.6 Span-wise ensemble averages

The CWG has a non-uniform flow along the length of track (defined as the span of the CWG), discussed in section 6.2.1 and also in great detail in Dorigatti, (2013). This section considers an alternative approach to obtaining mean pressure coefficients, based on a span wise ensemble average. This method was used by Dorigatti, (2013) and Soper (2014), and has been used in the uncertainty analysis presented in appendix F. The main results are therefore illustrated in this appendix, but have not been used to obtain any of the mean pressures considered in chapter 8.

H.6.1 Ensemble average methodology

In order to calculate the ensemble averaged pressure for each pressure tap and at a given yaw angle, the data was first split to consider the nose pressure taps and loop of pressure taps separately. Each run was then trimmed to only consider distances between 1.2 m and 5 m through the crosswind generator (measured from the entrance portal inner wall), in order to discard data that was affected by the CWG walls. Instantaneous voltages were then converted to instantaneous pressure coefficients (i.e., equations 7.11 to 7.23 have been performed on the data).

Data was then resampled to the nominal investigative train speed (given in table 6.4 for each yaw angle), resulting in a consistent distance x-axis for each tap and run, therefore the instantaneous pressure coefficient of a given tap, k, was defined at a known distance, x, that was consistent for each of the resampled runs within the ensemble. The result of this procedure was that the sampling frequency changed (see equation 4.9), and each sample was

at a consistent x-axis position. In order to resample the data consistently, train speed was assumed constant through the crosswind generator - no additional resampling of the data due to deceleration took place as this would have added unnecessary complexity to the analysis. The deceleration calculated from the lasers and light sensor was already accounted for during the initial stages of data processing with regard to the distance axis. Consequent errors in the x-axis (i.e., in distance through the crosswind generator) due to resampling were no greater than 10 mm, which indicates an offset equivalent to between 1-2 samples, were therefore neglected. This assumption of constant train speed has only been made in this section in order to calculate ensemble averages.

The ensemble averages and standard deviations were calculated in the conventional way, though are expressed as a function of distance, x, rather than time,

$$\overline{C_{P_k}(x)} = \frac{\sum_N C_{P_{k,run}}(x)}{N} \tag{H.1}$$

Where $C_{P_{k,run}}(x)$ represents a pressure coefficient for a fixed tap and distance for a single run, and N is the number of runs. The standard deviation (used in error analysis) of each tap, $\sigma_{Cp_k}(x)$, was found from the N values of $C_{P_{k,run}}(x)$ at any given x-axis position in the CWG. in relation to the ensemble mean.

H.6.2 Results

The CWG shows span-wise variation in the mean velocities and pressures due to the proximity of the fans and hence low fetch (Dorigatti, 2013; Soper, 2014). The purpose of this section is to illustrate how the fluctuations in the local air flow characteristics affect the surface pressures on the HST.

H.6.2.1 Variation in yaw angle along span

Before considering the ensemble averaged pressures it is useful to first consider the variation in yaw angle along the span of the CWG. The yaw angle of each run (equation 7.22) was calculated from the mean CWG velocities and train speed. Figure H.12 shows the variation in yaw for all of the individual runs for the CWG length considered (1.2 m < x < 5 m). The ensemble average of the yaw angles for each run is shown in bold, and the span-wise average (i.e., the spatial mean of the ensemble average) is shown in green. The yaw angle various significantly across the span of the CWG as a result of the non-uniform span-wise cross flow velocity profile. The span-wise yaw angle is, in all cases, about 1° lower than the investigative yaw angle which suggests that the variation in train speed was low, but that the investigative train speeds were slightly underestimated by using the values for span-wise mean cross flow velocity from Dorigatti, (2013).

As discussed in chapter 8, yaw angle can be calculated from the pressure differential of the two offset nose taps divided by the central tap (equations 8.2 and 8.3). Figure shows the yaw calculated from the nose pressure taps for individual runs, the ensemble average of the yaw for each run and the yaw angles calculated based on the mean velocities and train speed (i.e.,

the ensemble averages from figure H.12). At investigative yaw angles of 15° - 25° there is good agreement between the yaw angle calculated from the nose taps and from the yaw angle calculated from the train speed and mean flow velocities across the span, which indicates that the ensemble sizes were sufficiently large enough to obtain a mean pressure coefficient at any position along the CWG that is representative of the mean CWG flow velocity. The matching positions of the peaks and troughs in the two ensemble averaged yaw angle time histories indicates that measurement of train speeds (and hence distance) and resampling procedure in order to form ensemble averages were accurate. The two different ensemble yaw angles have similar magnitudes at nominal yaw angles of 15° - 25°, suggesting that the nose pressure tap calculation is valid for calculation of mean yaw angles, which is echoed in figure H.14 which shows the nose tap yaw angle plotted against the flow characterisation yaw angle, and has a gradient close to unity (albeit with a lot of scatter).

At 30° there is large disagreement between the yaw angles calculated from the nose taps and the ensemble average yaw from the flow characterisation. This supports the claim that the cubic empirical yaw angle equation (equation 8.3) is only valid up to 25°.

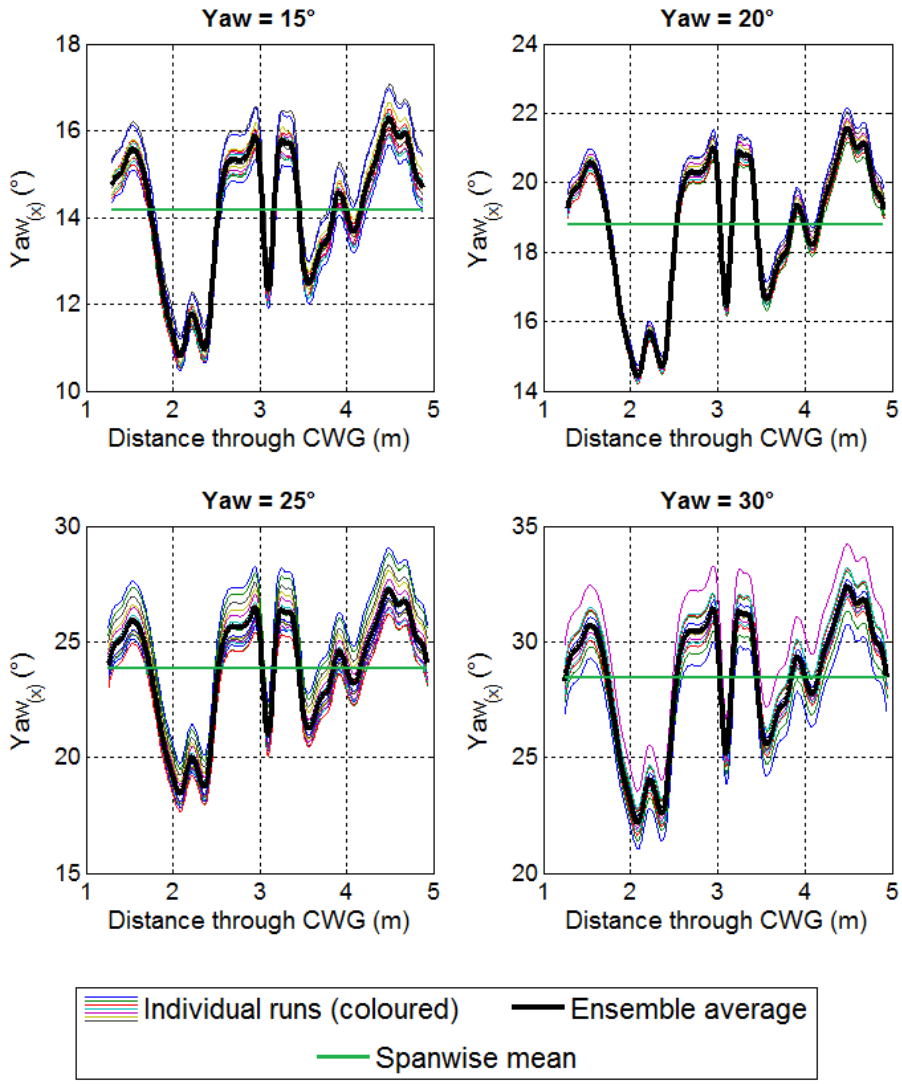

Figure H.12 - Instantaneous yaw angles calculated from the flow characterisation data and train speed, i.e., mean velocity from Dorigatti, (2013) and train speed for individual runs (coloured) and ensemble average along CWG span (from test 1). Span-wise spatial average yaw shown as horizontal green lines.

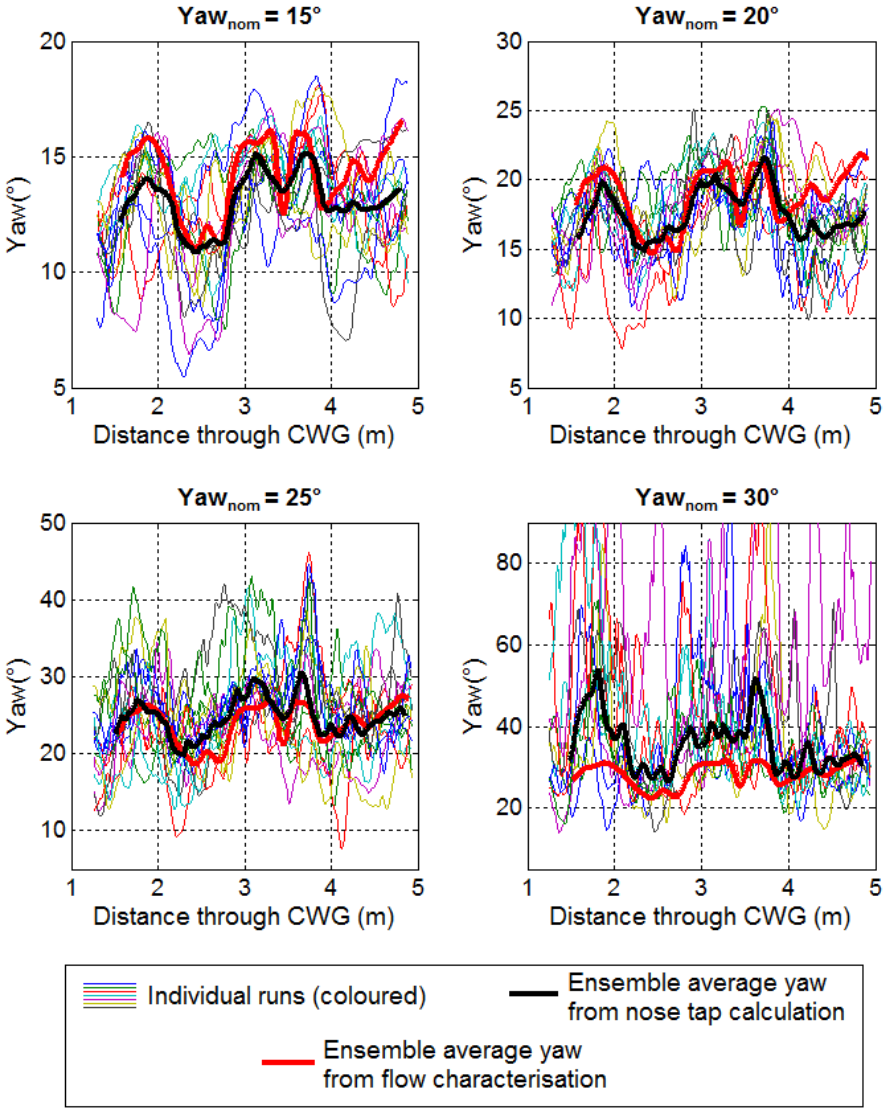

Figure H.13 - Instantaneous yaw angles calculated from the nose pressure tap differentials (equations 8.2 and 8.3) for individual runs and ensemble (black), and also ensemble averaged yaw based on flow characterisation data and train speed.

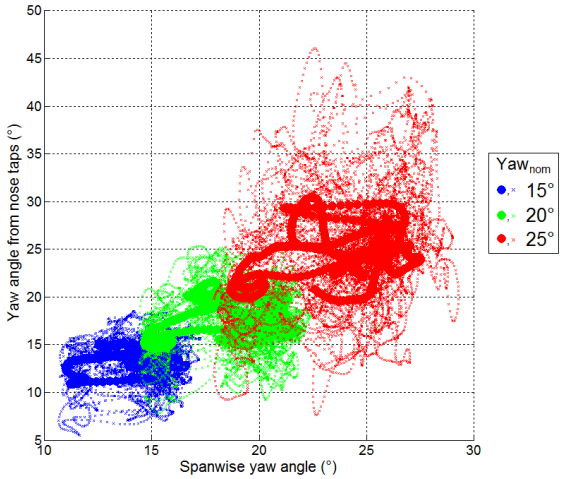

Figure H.14 - Scatter plot of yaw angles calculated from flow characteristics and train speed (x-axis) against yaw angle calculated from nose taps pressures (y-axis) at nominal investigative yaw angles of 15° - 25°. Small crosses are instantaneous values from each run and larger circles are from ensemble averages.

H.6.2.2 Variation in pressures and forces along span

It has been shown that the span wise variation in CWG flow affects the yaw angle, and hence is expected to affect the pressures and overturning forces. The pressures from the individual runs and the ensemble averaged pressures are shown for the key pressure tap positions around the train (same positions as in figures H.11.1 to H.11.4), i.e., tap N2 is at the nose, and for the loop, tap L1 (windward wall), tap L9 (roof centre) and tap L14 (leeward wall). Throughout figures H.15.1 to H.15.4, the individual runs are shown as coloured lines and the ensemble averages as emboldened black lines.

The variations in pressures correspond to the span wise variations in crosswind velocity, which can be seen both in the ensemble averages and the individual runs. The ensemble

averages for pressure taps N2, L1, L9 and L14 are shown at each yaw angle in figure H.16.1, and similarly, the standard deviations are shown in figure H.16.2. At higher yaw angles the standard deviations greatly increase. The increase in the roughness of the ensemble averages and standard deviations is simply due to the larger quantity of data obtained per run.

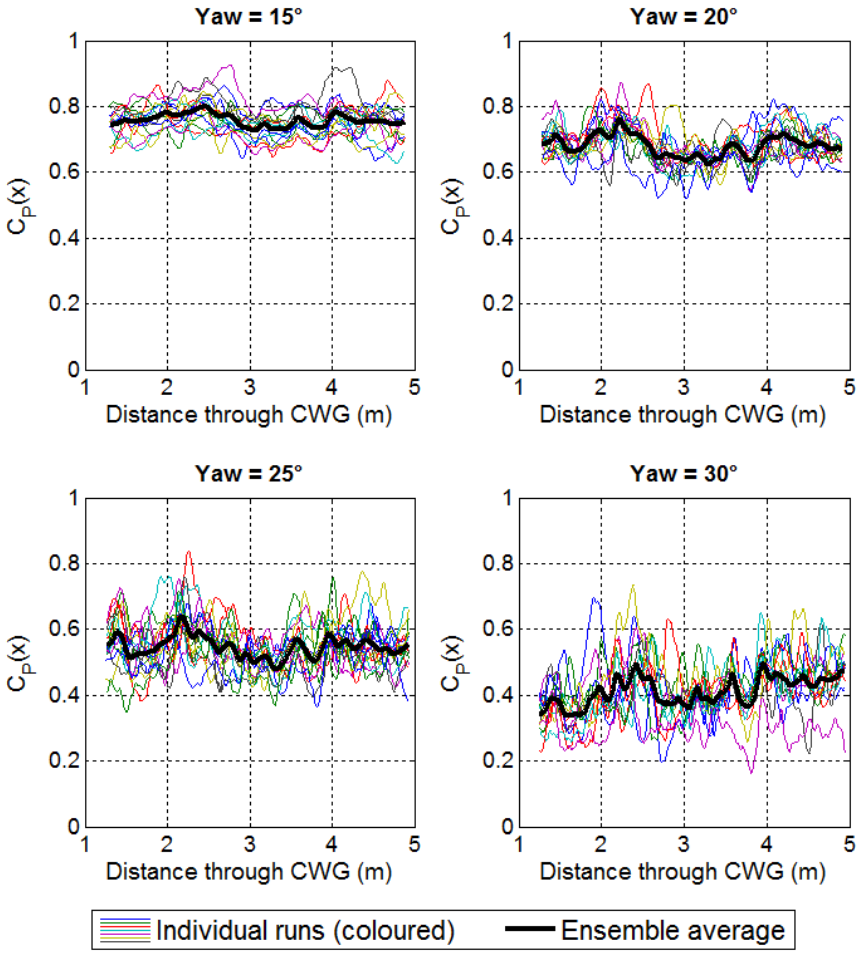

Figure H.15.1 - Individual runs and ensemble average pressure for test 1, tap N2 (central nose).

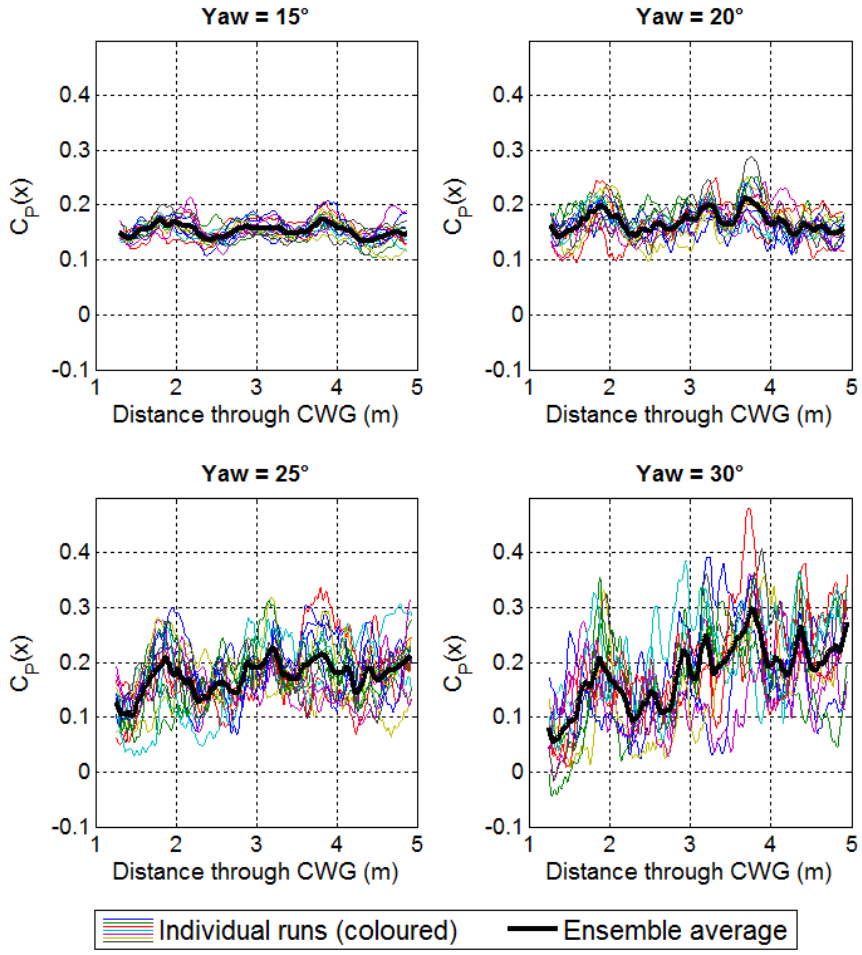

Figure H.15.2 - Individual runs and ensemble average pressure for tap L1 (windward side wall).

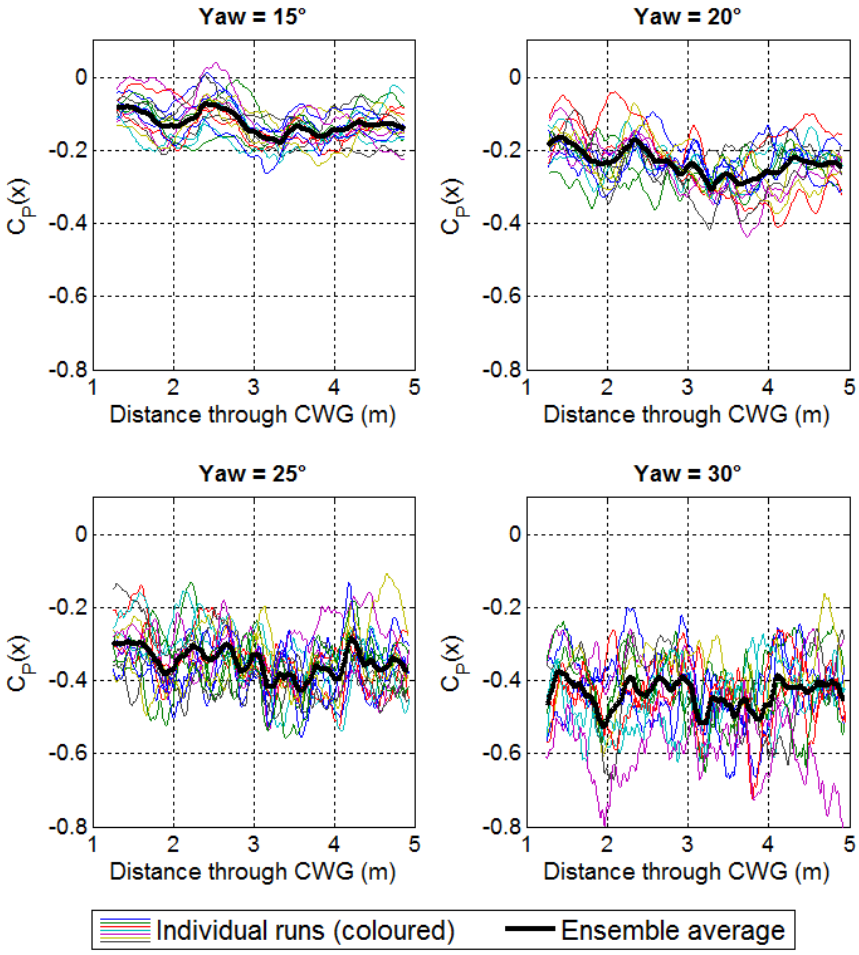

Figure H.15.3 - Individual runs and ensemble average pressure for tap L9 (roof centre).

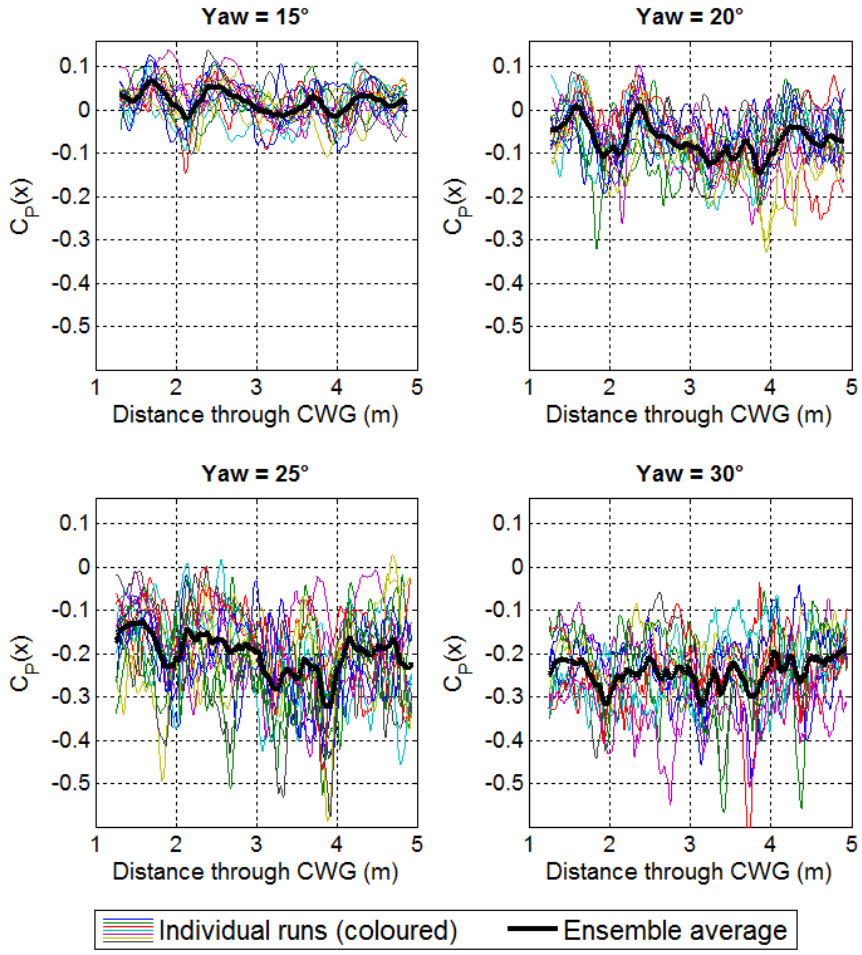

Figure H.15.4 - Individual runs and ensemble average pressure for tap L14 (leeward side wall).

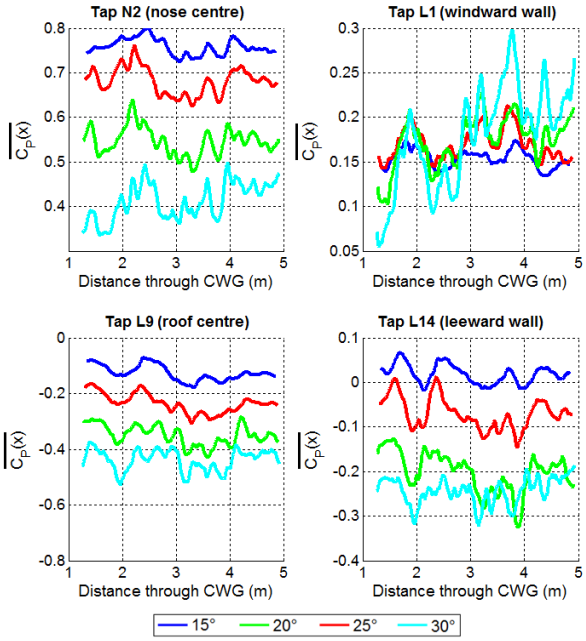

Figure H.16.1 Ensemble averaged pressure coefficient for taps N2, L1, L9 and L14 at yaw angles of 15° to 30°.

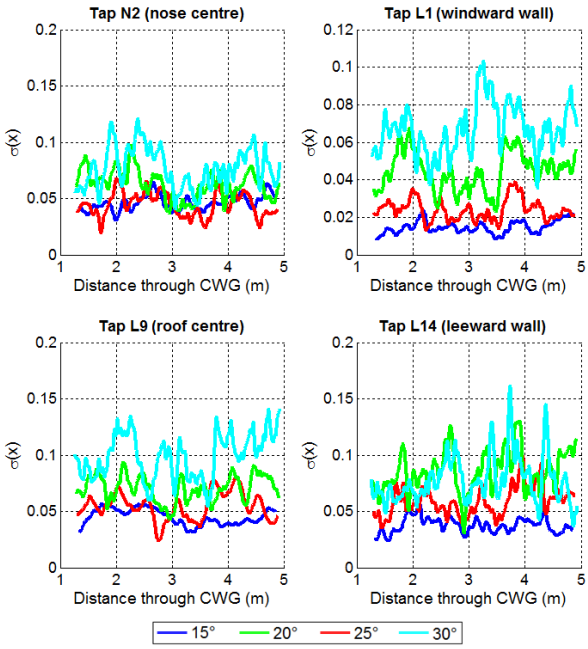

Figure H.16.2 - Standard deviation of pressure coefficient for taps N2, L1, L9 and L14 at yaw angles of 15° to 30°.

H.6.2.3 Variation in force and moment coefficients along span

The ensemble mean pressures at a given position in the CWG (after data had been resampled), $\overline{C_{P,t}(x)}$ were integrated for all pressure taps in the loop, according to the methodology described in section 7.2.2 and the geometrical discretisation described in section 7.3.6. As the data was resampled to give a consistent distance axis, it was possible to consider the two sets of CWG tests within in the same ensemble (though the effect of the lower ensemble size in the second tests has led to an increase in error for the retested pressure taps). Figure H.17 shows the variation of side and lift force coefficient and x-axis lee-rail rolling moment coefficients per unit length across the span of the CWG at yaw angles of 20° and 25°. Force and moment coefficients were not calculated at yaw angles of 15° and 30° due to the much lower number of pressure taps in the loop at these yaw angles. The side and lift force coefficients show similar trends across the span of the CWG to the span wise cross wind velocity and yaw angle. For instance, where the mean crosswind velocity reaches a local maxima, there is a corresponding maxima in side force, and corresponding minima in moments. However, given that these results have not been used directly in this study, this analysis is taken no further.

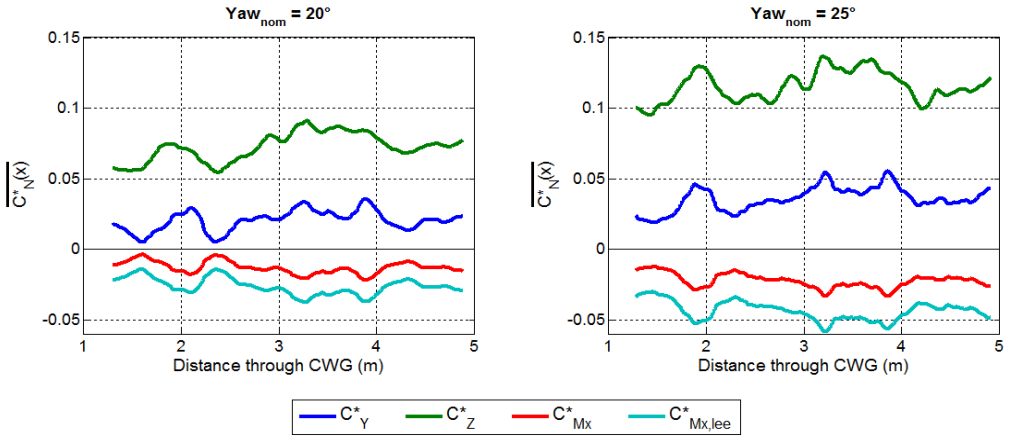

Figure H.17 - Span wise ensemble average force (side and lift) and moment coefficients.

APPENDIX I

WIND TUNNEL TEST IN UOB WIND TUNNEL

I.1 Introduction

Appendix I describes a wind tunnel test that was undertaken during this study using the wind tunnel at the University of Birmingham on the HST model provided by RWDI. The reason for this was that it was observed that the streamwise aerodynamic speed of the NMT, calculated from the dynamic pressure from the pitot static probe, was consistently lower that the vehicle speed recorded by the GPS tracker. Therefore, the aim of the test was to measure the wind velocity at the nose of the train model at the same location as the pitot static probe on the NMT.

It was intended to also record surface pressures at the pre-constructed pressure tap locations. However, due to a technical fault with the data acquisition system, the pressure tap data was not collected.

I.2 Experimental details

I.2.1 Experimental set up

The wind tunnel is shown in figure I.1. Air flow in the wind tunnel was provided by 49 fans (in a 7 x 7 grid) working in a blow through configuration. The fans are followed by a contraction/nozzle and then a hexagonal "honey comb" flow straighter, before the 10 m long, 2m by 2 m square working test section. The velocity along the length of the working section decreases slightly along the wind tunnel length (about an 8% decrease along the total length at the centre of the test section). The turbulence intensity 1 m from the nozzle was 3% and was 8% at the orifice. The location for the test on the HST was 5 m from the nozzle/orifice (i.e., at the centre of the rectangular test section), with a corresponding turbulence intensity of 3-5%, based on previous measurements (using Gill ultrasonic anemometers) by Fintelman (2015). In this study, the streamwise turbulence intensity was found to be about 2% when measured with a Cobra probe, and the streamwise velocity was about 11.5 m/s. Fintelman (2015), obtained parameters based on a wind tunnel speed of about 7-8 m/s and with different equipment, therefore the slight difference in turbulence intensity is of little significance.

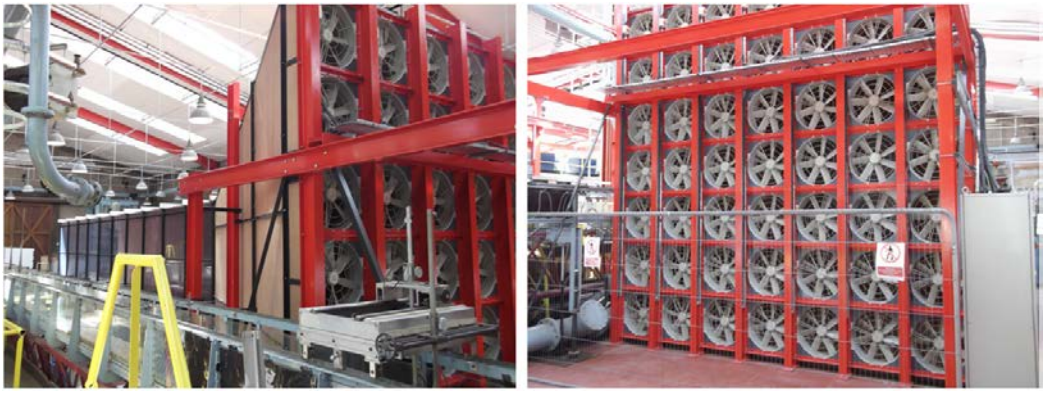

Figure I.1 - Wind tunnel at the University of Birmingham

The HST model, (power car only), was placed on the single track ballast and rail (STBR) ground configuration also supplied by RWDI and fastened together using screws through the ground plane and into the bogies. The train model was located in the centre of the wind tunnel cross section to negate wall boundary layer effects. An initial flow characterisation found that the streamwise velocity was uniform across the train height and width, with a mean streamwise velocity of 11.5 m/s at the centre of the wind tunnel cross section, equivalent to a Re number of about 9×10^4 (lower than the minimum of 2.5×10^5 required in CEN), though very similar to the RWDI test. A small yaw angle offset of 3° was also measured at the centre of the test section. A horizontal ground plane was constructed from 2 m x 1 m sheets of polymer that were 8 mm thick, with a specific focus on causing minimal blockage - the cross sectional area of the ground plane and side supports was 0.04 m^2, i.e., a blockage of 1% due to the ground and supports. When the train model and track and ballast, and the Cobra probe and mounting system are included in the calculation of total blockage, the actual cross sectional area of all the equipment total blockage increases to 2.3% (based on a conservative calculation), and hence no correction was applied to the data. Figure I.2 shows the horizontal ground plane and supports in the wind tunnel - two side supports were fastened to the wind tunnel walls with adhesive and a central support, to reduce the amplitude of any vertical vibration oscillations, was fixed along its bottom edge to the wind tunnel floor and along its upper edge to the horizontal ground plane. The leading edge of the ground plane was chamfered to channel air beneath the horizontal ground plane with minimal effect on the air flow, and to act as a splitter plate. A circular hole was drilled in the centre of the horizontal ground plane, 1 m from the leading edge in the x-axis direction, and a hole was made in the track/ballast piece to allow a Cobra probe to be mounted vertically upwards from beneath the splitter plate and at the train nose at the same position as the pitot-static probe on the NMT.

The Cobra probe was held in a probe holder and mounted on a retort stand that was secured to the wind tunnel floor, and a second stand was fixed to the first stand to reduce the amplitude of any vibrations. The hole for the probe was sealed with clay. Care was taken to ensure that the probe was not directly in contact with the model or ground plane in order to further reduce vibration effects on the probe. The STBR was secured with high-strength adhesive tape to the horizontal ground plane, and the lower edges of the ballast were sealed with tape to prevent air flow beneath the track/ballast piece which could have dislodged the model.

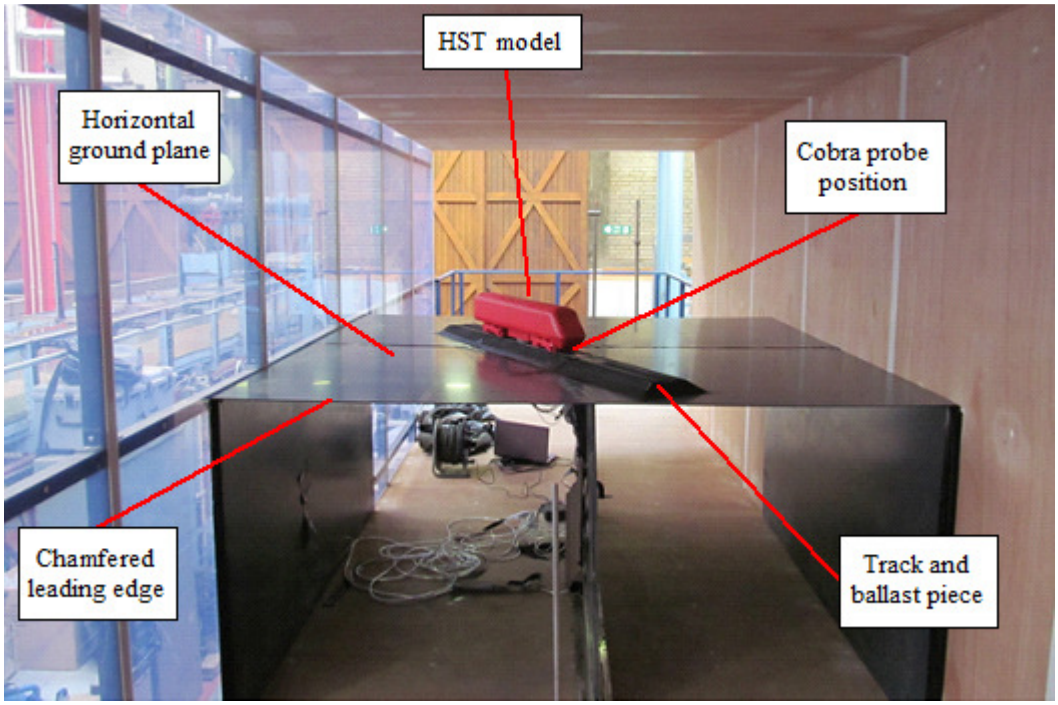

Figure I.2 - Experimental set up in wind tunnel

I.2.2 Test procedure

The wind tunnel velocity was controlled by specifying the power to each fan using bespoke software on a laptop PC. In this test the maximum safe power was supplied to every fan in order to test at the highest possible velocity. The reference tube for the Cobra probe was positioned outside of and beneath the wind tunnel. Before each run of the wind tunnel, the probe was zeroed while there was no air flow. The ambient conditions were recorded using the Oregon Scientific BAR208HGA weather station and GBP3300 Digital Barometer which were used during the TRAIN rig tests (section 3.4.3). The wind tunnel was then started, at a 30 s start up period was allowed for the fans to reach full power. Data was then sampled by the probe (controlled using the bespoke hardware and software provided by TFI) for 120 seconds at 2500 Hz. The wind tunnel was then powered down before any adjustments to the set up were made. The wind tunnel velocities and static pressure during operation are shown in figure I.3 - the wind tunnel was started at 15 seconds and switched off at 95 seconds.

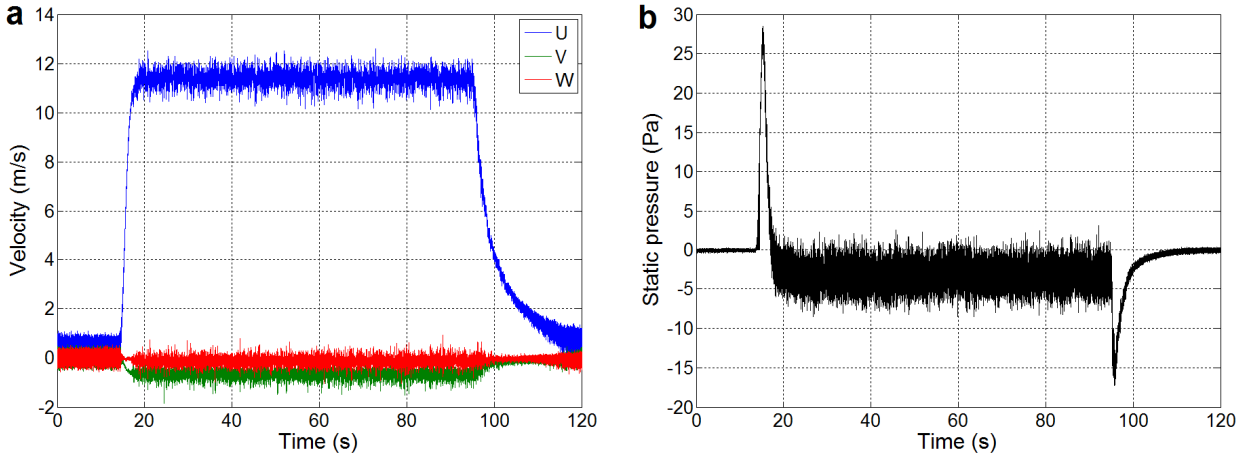

Figure I.3 - Wind tunnel operation (a) velocity components and (b) static pressure time series.

The Cobra probe head was initially positioned at the equivalent position as the pitot-static probe head on the NMT - at a height of 1.1 m above TOR (at full scale), 0.31 m from the train surface in the x direction, and centrally in the y direction (i.e., 1 m from either wind tunnel side wall) - test case 1 (a). A range of longitudinal distances from the train nose were also tested, (table I.1) - test cases 1 (b-d). Additional measurements of velocity were taken at the main test position but with different experimental configurations (test cases 1(a), 2, 3 and 4). Air velocity was measured with the ground plane and track and ballast piece but without the train mode to give an indication of the air velocity without the train (test case 2). Air velocity was also measured with the ground plane only (i.e., no train or track and ballast piece) to give an indication as to the effect of the track and ballast piece on the air flow at the nose of the train (test case 3). Finally, measurements were made without any of the equipment except for the Cobra probe stand (test case 4) to assess the effect of the ground plane splitter plate assembly. The test cases are defined in table I.1 and shown in figure I.4

Table I.1 - Experimental set up for wind tunnel test cases

Test case	Probe distance from pitot-static probe on NMT in x direction (mm)	Experimental details
1(a)	0	With train, track/ballast and ground plane
1(b)	5	
1(c)	10	
1(d)	15	
2	0	Without train. With track/ballast and ground plane.
3	0	Without train or track ballast. With ground plane.
4	0	Without train, track ballast or ground plane.

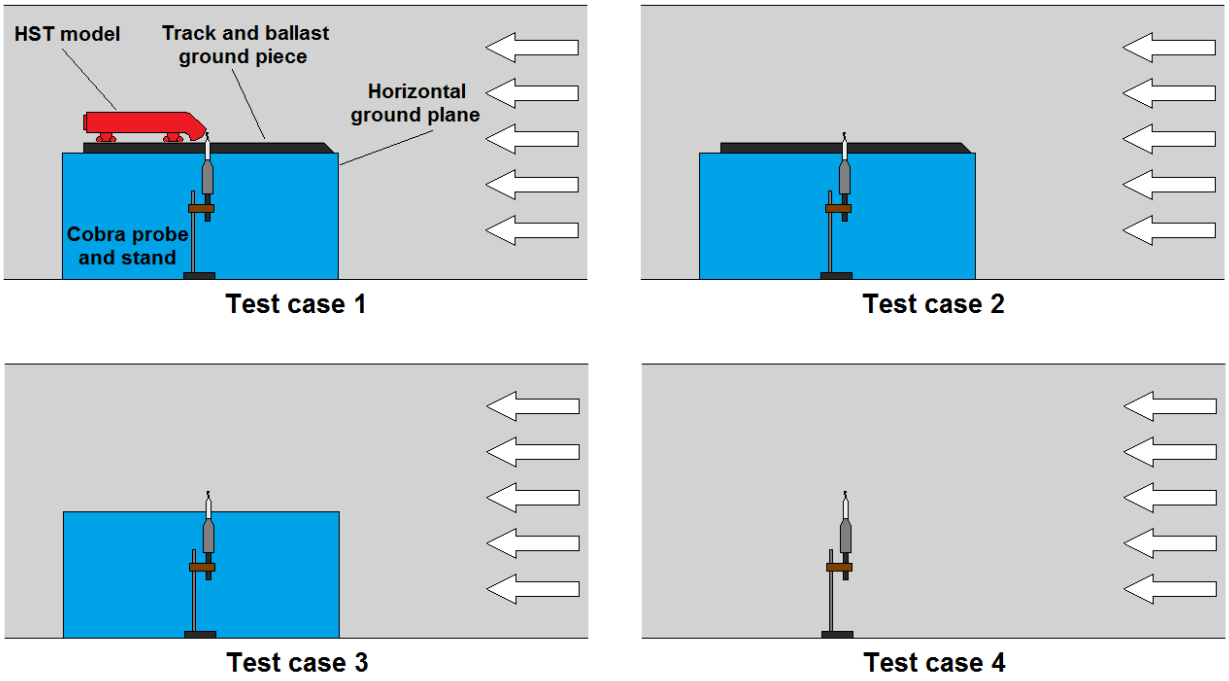

Figure I.4 - Diagrammatic representation of test cases 1 - 4 (not in any way to scale).

I.3 Results and discussion

Velocity time series were obtained for each run. The mean wind tunnel velocity was stable for the duration over which the data was sampled. Data was then filtered using a first order Butterworth filter with a cut-off frequency of 650 Hz, i.e., the maximum frequency response of the Cobra probe. Data was filtered using the "butter" and "filter" functions on Matlab (Mathworks, 2010). It is acknowledged that the vibration effects due to mounting of the Cobra probe may have been at lower frequency that 650 Hz and therefore not mitigated by filtering, however as the vibrations would create oscillations about the mean, and that this investigation was only concerned with obtaining mean velocities and pressures, it has been

assumed that mechanical vibration would have negligible effect on the mean values given the large sampling duration.

Once the data time series was filtered, it was then time averaged. The results are presented in table I.2. Figures I.5 shows a sample five second portion of the time series data for test cases 1(a), 2, 3 and 4 in order to compare the effects of the experimental set up in the wind tunnel. Figure I.6 shows the variation of velocity and static pressure as the distance to the train nose is increased (i.e., test cases 1 (a) to (d)). Note that U is the streamwise component, U is the lateral component (and positive if facing the U-flow and moving towards the LHS) and W is the vertical component (positive in the upwards direction).

Table I.2 - Time averaged velocities, streamwise turbulence intensity, static pressure and yaw angle for each wind tunnel test case.

Test case	U_{mean} (m/s)	V_{mean} (m/s)	W_{mean} (m/s)	I_U (%)	$P_{Static,mean}$ (Pa)	φ_{mean} (°)
1 (a)	4.9	0.6	-3.8	13.3	43.0	7
1 (b)	5.6	0.4	-2.4	15.4	42.2	4
1 (c)	6.1	0.3	-1.9	15.0	40.4	3
1 (d)	6.8	0.4	-1.3	15.2	34.2	3
2	10.2	0.5	0.3	10.9	-4.9	3
3	11.7	0.1	0.2	1.7	-5.2	0.5
4	11.5	0.7	0.5	1.7	-3.7	3

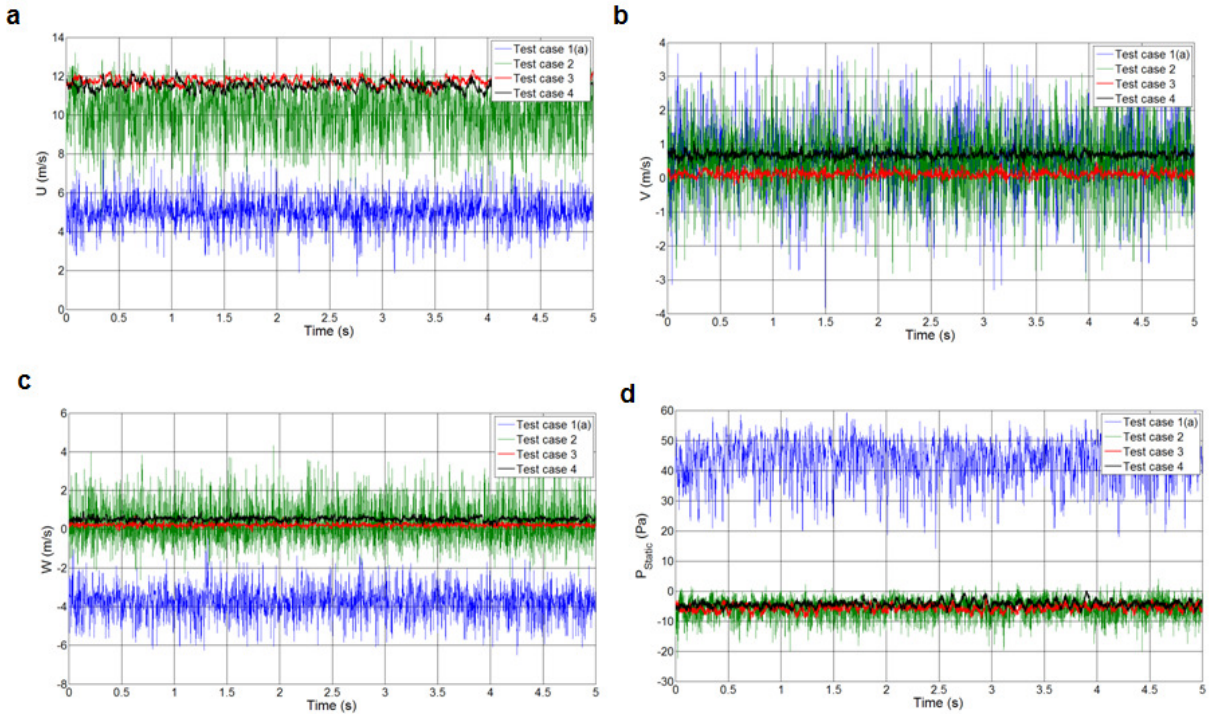

Figure I.5 - Sample 5 s sampling duration for test cases 1(a), 2, 3 and 4 shows (a) U (streamwise), (b) V (lateral), (c) W (vertical) and (d) static pressure.

The effect of the horizontal ground plane and supporting structure on the air flow are compared by considering test cases 3 and 4. The only difference in experimental set up between the two tests was that, test case 4 only the probe and retort stand were in the test and in test case 3 the Cobra probe was mounted vertically upwards (with the same stand) through the ground plane and the hole was sealed with clay. The mean streamwise velocity was the same for test cases 3 and 4, indicating that the splitter plate ground plane had no significant effects on the air flow. Another concern was that vibrations of the ground plane would pass on to the Cobra probe. Test cases 3 and 4 show no difference in the time series or mean values, which suggests that vibrations due to the ground plane were of low significance for this study.

A significant and somewhat concerning finding is that the STBR has a large effect on the flow at the probe position tested. The only difference between the two set ups is that test case 2 had the STBR in place. When test case 2 and 3 are compared, test case 2 shows much larger streamwise velocity fluctuations (hence a streamwise turbulence intensity of 11%) than test case 3 where the turbulence intensity was about 2%. Test case 2 also shows a lower mean velocity. This suggests that the sloped leading edge of the ground piece, which was directly upstream of the Cobra probe, is creating a flow separation and hence turbulence in the region of the HST nose where pressure sensors have been set up on the NMT based on the RWDI wind tunnel findings, which is supported by CFD calculations on the same wind tunnel set up as the RWDI tests reported in Morden et al., (2015). Another possible explanation is that in test case 3 the clay seal would have a much larger (roughly triple) contact area between the Cobra probe/holder and the ground plane and STBR, and would be "better" at transmitting vibration loads to the probe than in test case 4.

Finally, the effect of the train on velocity and pressure can be made by comparing test case 1(a) and test case 2. The mean streamwise velocity, as in table I.2, is about half of what it would be with no train in place. Unexpectedly, the vertical velocity component is about zero when there was no train, but was -3.8 m/s when the train was in place, indicating that the HST nose was channelling air downwards. The implication of this is that the pitot-static probe on the NMT will not record the true streamwise aerodynamic speed of the train. Figure I.6 shows the mean streamwise velocities from test cases 1(a) to (d), i.e., at increased x-distances from the pitot-static probe position on the NMT, normalised by the mean streamwise velocity from test case 2. The mean streamwise velocity appears to follow a linear relationship as the distance from the train nose is increased within the range of distances measured.

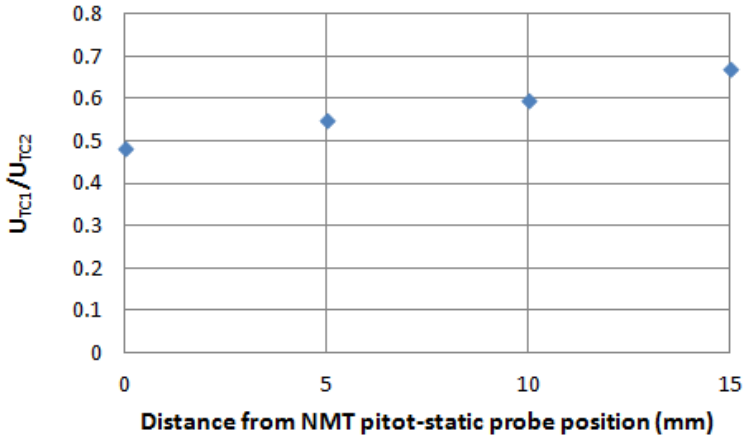

Figure 1.6 - Mean streamwise velocity when HST is in place (test case 1) normalised by mean U with no train (test case 2), at increasing distances from train nose.

I.4 Concluding remarks

The velocity and static pressure were measured at the nose of the HST in the same position as the pitot static probe on the NMT. This investigation was focussed on obtaining mean values, and the effects of mechanical vibration have been accepted, and assumed to have negligible effect on the mean velocities. The horizontal ground plane had no apparent effect on the air flow. The inclusion of the track and ballast piece was shown to affect the flow at the pitot static probe position, and resulted in a slight decrease in mean velocity and an increase in the streamwise turbulence intensity. The inclusion of the train model significantly decreased the velocity measured by the Cobra probe by about half. As a result of the HST nose profile channelling the flow downwards, the magnitude of the vertical velocity component increased as the probe position was moved closer to the train nose, and the magnitude of the streamwise velocity component decreased. A final comment is, from table I.2, that slight changes to the

experimental set up can have a significant effect on the mean yaw angle when low yaw angle ranges are considered.

APPENDIX J

FULL-SCALE CROSSWIND TESTS - DATA PROCESSING PROCEDURE

J.1 Introduction

Appendix J provides additional information about the data processing methodology utilised in the full-scale crosswinds tests on the NMT. Definitions of terms used specifically in this appendix are set out in table J.1. Section J.2 describes the data acquisition procedure and the different sources of data. Section J.3 describes the format of the raw data files used in subsequent analysis. Section J.4 describes initial data processing procedure by which data from different sources were collected together, and the conversion of data to a usable format. Section J.5 describes elements of the analytical procedure that are not directly of relevance to analysis of open air data, but were necessary stages in obtaining and understanding the open air data considered in this study. Section J.5.1 describes the methodology by which pressure transients were identified, categorised and removed. Section J.5.2 describes the reference pressure modification. Section J.5.3 describes the effects of the engine cooling fans on the pressures measured over the roof surface and section J.5.4 considers the resonance effects

related to standing waves in the pneumatic tubing. Section J.6 describes the identification of faults and maintenance and repair work.

Table J.1 - Definitions of terms used in this appendix

File name	Description
Raw data	Raw pressures calculated using nominal background voltages of 2.25 V.
Voltage adjusted data	Pressures recalculated using background voltages obtained from periods where the NMT was stationary.
Reference pressure modified data	Voltage adjusted data with Ref 2 added to account for changes in elevation (i.e., ρgZ) (section 10.2.1.2 defines the reference pressures).
Filtered data[1]	1 s moving average filter applied to reference pressure corrected data.
Unfiltered data[1]	Same data as "reference pressure corrected" but this term is used to distinguish from filtered.
Transient (general)	A fluctuation in pressure about the mean pressure that exceed a nominal threshold pressure.
Identify (transient)	A segment of data was identified as a transient (general) based on a fluctuation of instantaneous pressure about a mean value.
Categorise (transient)	A transient was defined based on the likely cause of the pressure.
Transient (pulse)	Pressure transient caused by a passing train characterised by sinusoidal pulse.
Transient (tunnel)	Pressure transient caused by train passing through tunnel.
Transient (false positive)	Pressure transient was identified by algorithm, but was not caused by a physical object - these generally arise due to high amplitude and high frequency fluctuations of the pressure time series, which themselves could be caused by turbulence/crosswinds or electrical noise.
Transient (misc)	Pressure transient where cause is not certain. May be train, tunnel or bridge, or possibly a false positive.
Crosswind[1]	Data identified by yaw angle peak and corresponding pressure differential on roof and windward side.
Bad data	Data that was not usable for analysis.
Notes: 1. May be considered in terms of dimensional pressures or non-dimensional pressure coefficients.	

J.2 Data acquisition

Data was collected from a range of different sources and sampled by the onboard PC using bespoke software. Data files were saved onto the hard drive of the PC and transferred to the USB flash drive during acquisition and once the file was transferred to the USB flash drive it was cleared from the hard drive to allow space for subsequent data. Data from all of the different data sources were trimmed into blocks of a fixed time duration - usually 15 minutes during normal operation, and were synchronised by the Epoch time stamp (in seconds) which was included in the file name, hence the start time of each data file was within 1 s of the others. Further synchronisation of the start and end times of each file are discussed later in section J.4.1.1. Table J.2 lists all the different files that were collected for each ~ 15 minute time block, the locations of the sensor equipment and the relevant raw data collected. The file names (column 1) in table J.2 have been used to refer to each data file in all subsequent descriptions. Each data filename was recorded by the onboard PC in the format "Filename_Epochtime.txt", where "Filename" is given in table J.2, "TIMESTAMP" was an Epoch timestamp in seconds, and the format of all the files was a "text" file and comma delimited (with the exception of the GPS feeds). The format of each file type is described in section J.3.

All data was sampled at 128 Hz by the onboard PC, with the exception of both GPS feeds - the internal GPS was sampled at 1 Hz and the network GPS was sampled at 50 Hz. The network GPS data gave train speed as a vector and was positive when car 43062 was leading - this would potentially have been useful for analysis but data from the network GPS feed was intermittent as it required the modified measurement Mk. III coach to be powered on which was not always the case during operation. The network GPS data was therefore not used in

any meaningful analysis, but was used in the initial stages to validate the internal GPS data and both showed very good agreement.

Table J.2 - Description of data files

File name	Description	Physical location	Raw data acquired
Interface	Reference data	Internal sensors inside the onboard PC	Reference pressures (Ref. 0, 1 and 2). Temperature. Gyroscopic sensor.
Internal GPS	GPS position tracker	Inside onboard PC	Latitude and longitude, train speed (scalar) and elevation.
Network GPS	GPS position signal from existing onboard feed	Bespoke system in modified Mk. III coach	Latitude and longitude, train speed (vector) and NR track reference.
Module 1	Modular pressure transducer box	Train nose	Pressure taps A1, A2 and A3. Pitot static probe pressures (static, total and dynamic pressures).
Module 2	Modular pressure transducer box	Luggage area - fire extinguisher side wall (driver's LHS)	Pressure taps B1, B2, B3, B4 and B5.
Module 3	Modular pressure transducer box	Luggage area - train roof	Pressure taps B6, B7, B8, B9, B10 and B11.
Module 4	Modular pressure transducer box	Luggage area - cupboard side wall (driver's RHS)	Pressure taps B12, B13, B14, B15, B16 and B17.

J.3 Format of data files

The format of the interface and module data files was similar and shown in figures J.1.1 and J.1.2 below - data has been extracted into Microsoft Excel, and column headings added manually for ease of illustration. It should be noted that the numeric values in these figures are unprocessed 12-bit numbers - the conversion procedure is described later in section J.4.2.

	A	B	C	D	E	F	G	H	I	J	K	L
1	Synch counter	Node	Flags byte	Unused	Temperature	Unused	Gyro	Unused	Reference pressure 2	Reference pressure 1	Reference pressure 0	Node timestamp
2	2478	0	1	4223	14197	16378	4071	16377	3649	3663	4693	1380856053
3	2479	0	1	4222	14197	16378	4053	16377	3648	3662	4693	1380856054
4	2480	0	1	4223	14197	16378	4058	16377	3649	3662	4693	1380856054
5	2481	0	1	4223	14197	16378	4065	16377	3648	3663	4692	1380856054
6	2482	0	1	4223	14197	16378	4074	16377	3649	3663	4693	1380856054
7	2483	0	1	4223	14197	16378	4063	16377	3649	3663	4694	1380856054
8	2484	0	1	4223	14197	16378	4067	16377	3649	3662	4693	1380856054
9	2485	0	1	4223	14197	16378	4065	16377	3648	3663	4693	1380856054
10	2486	0	1	4223	14197	16378	4065	16377	3648	3663	4693	1380856054

Figure J.1.1 - Example of raw interface data file.

	A	B	C	D	E	F	G	H	I	J	K	L
1	Synch counter	Node	Flags byte	Pressure channel 1	Pressure channel 2	Pressure channel 3	Pressure channel 4	Pressure channel 5	Pressure channel 6	Pressure channel 7	Pressure channel 8	Node timestamp
2	2478	3	1	3612	3606	3607	3621	3611	6662	6661	3610	1380856053
3	2479	3	1	3612	3606	3608	3621	3611	6663	6661	3609	1380856054
4	2480	3	1	3612	3606	3608	3622	3612	6663	6661	3610	1380856054
5	2481	3	1	3613	3606	3608	3622	3612	6663	6660	3610	1380856054
6	2482	3	1	3613	3606	3607	3622	3612	6663	6662	3610	1380856054
7	2483	3	1	3612	3606	3607	3621	3611	6663	6661	3609	1380856054
8	2484	3	1	3612	3607	3608	3621	3611	6662	6661	3610	1380856054
9	2485	3	1	3612	3606	3607	3621	3611	6662	6661	3610	1380856054
10	2486	3	1	3611	3606	3607	3621	3612	6662	6661	3609	1380856054

Figure J.1.2 - Example of raw module data file (all four module files are in this format).

The internal GPS data file was slightly more complex and is shown in figure J.2. The relevant data is highlighted - yellow rows are the GPS data that contained latitude and longitude coordinates and train speed (in knots), and green rows are the Epoch time stamp (in

milliseconds). Each "block" (i.e., rows 2 to 12 in figure J.2.) represents a single sample at 1 Hz. Files were always in a consistent format therefore extraction of information could be automated and was relatively straightforward. The text "$GPRMC" allowed each relevant row to be identified and this row always contained 13 comma delimited fields, which were consistently ordered - row 13 in figure J.2 shows red boxes identifying (from left to right) the latitude, longitude and train speed. Train speed (scalar) and latitude and longitude (in decimal degree format) were then extracted from the GPS data and synchronised with the pressure data based on the epoch time series of the GPS and pressure data.

Temperature and gyroscope data was also included in the collated data file - section J.4.2 describe how there were obtained from the raw data feeds.

	A
1	GPS data (unformatted)
2	$GPRMC,040736.00,A,5459.20390,N,00134.01715,W,0.092,,041013,,,A*69
3	$GPVTG,,T,,M,0.092,N,0.170,K,A*2E
4	$GPGGA,040736.00,5459.20390,N,00134.01715,W,1,11,0.97,51.8,M,48.1,M,,*76
5	$GPGSA,A,3,17,18,26,12,01,14,22,15,24,28,25,,1.74,0.97,1.44*0C
6	$GPGSV,4,1,13,01,07,013,28,12,45,213,23,14,14,312,34,15,43,170,28*7B
7	$GPGSV,4,2,13,17,34,067,28,18,23,250,37,22,26,287,42,24,87,269,33*77
8	$GPGSV,4,3,13,25,08,225,28,26,06,144,13,28,05,049,22,33,26,196,*75
9	$GPGSV,4,4,13,39,23,148,*4D
10	$GPGLL,5459.20390,N,00134.01715,W,040736.00,A,A*7C
11	16381
12	1.38086E+12
13	$GPRMC,040737.00,A,5459.20388,N,00134.01709,W,0.099,,041013,,,A*67
14	$GPVTG,,T,,M,0.099,N,0.183,K,A*29
15	$GPGGA,040737.00,5459.20388,N,00134.01709,W,1,11,0.97,51.7,M,48.1,M,,*7C
16	$GPGSA,A,3,17,18,26,12,01,14,22,15,24,28,25,,1.74,0.97,1.44*0C
17	$GPGSV,4,1,13,01,07,013,28,12,45,213,24,14,14,312,34,15,43,170,28*7C
18	$GPGSV,4,2,13,17,34,067,28,18,23,250,36,22,26,287,42,24,87,269,33*76
19	$GPGSV,4,3,13,25,08,225,28,26,06,144,13,28,05,049,22,33,26,196,*75
20	$GPGSV,4,4,13,39,23,148,*4D
21	$GPGLL,5459.20388,N,00134.01709,W,040737.00,A,A*79
22	16381
23	1.38086E+12
24	

Figure J.2 - Example of raw GPS file - yellow rows contain GPS data with red boxes indicating longitude, latitude and train speed (in knots) from left to right.

J.4 Preliminary data processing

This section describes the stages and processes involved in converting the raw data from different sources into a useful format, which was then saved as a single output file. Figure J.3 outlines the overall procedure, and each of the stages are described in the subsections that follow.

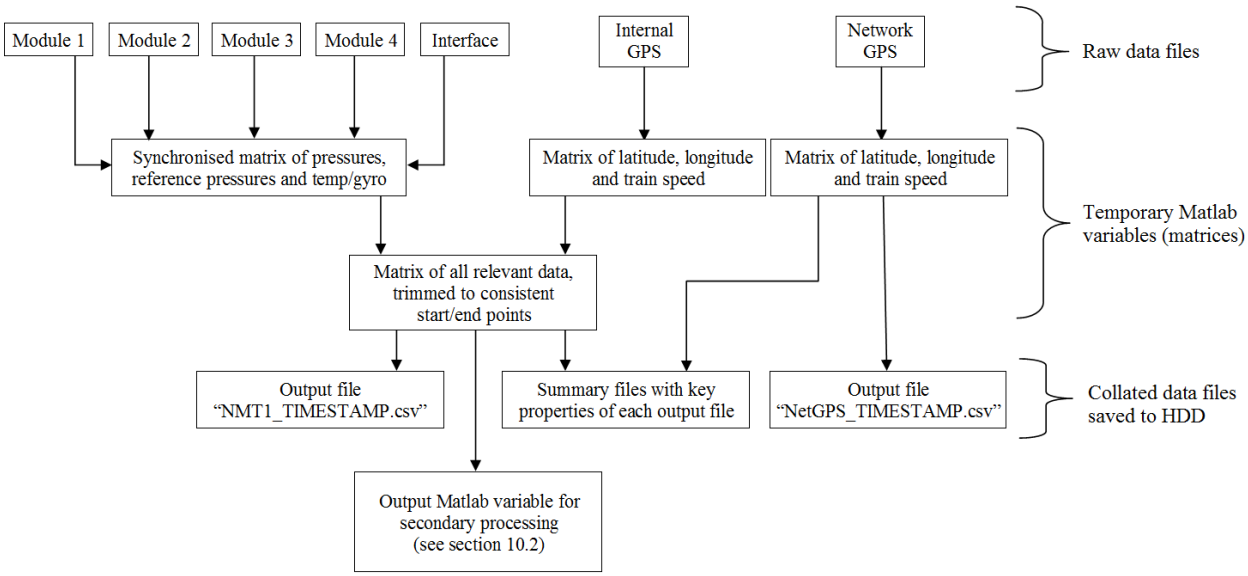

Figure J.3 - Overview of the initial data processing procedure.

J.4.1 Data collation

Data was acquired from a range of different sources by the onboard PC and the first stage in processing was to collect all the data together in a single file with a consistent time history.

J.4.1.1 Synchronisation of the interface and module data files

This section describes the process by which the interface and module data files were synchronised and collated - the GPS data is considered in section 10.3.1.3.

The bespoke software on the PC trimmed the data to consistently sized blocks. The data was then synchronised to a higher accuracy by considering the synch counter (i.e., the first column of each data file as shown in figures J.1.1 and J.1.2). The synch counter would loop from 0 to 16381 with an iteration of +1 per sample and figure J.4 shows the synch counter for a single data file. The maximum of the first value of the synch counter from each data file (i.e., row 1 column 1 as in figures J.1.1 and J.1.2) was found and all data aligned at this synch counter value - any rows that had synch counter values lower than this maximum were discarded. The same process was repeated at the final row of each data file (but considering the minimum synch counter value). In almost all cases the number of rows to remove was zero indicating that the data was already well aligned - the exception was for data files that were less than 15 minutes where the system had been powered down during sampling.

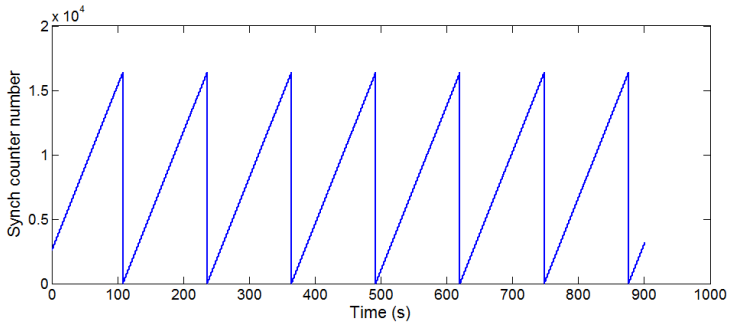

Figure J.4 - Synch counter for duration of 15 minute file

Pressure data (i.e., channels associated with pressure taps) from each of the four module files, and the reference pressures, temperature and gyro data from the interface box were collated together into a single matrix with a single time series for ease of subsequent analysis.

J.4.1.2 Train speed and GPS position information

The numeric values for latitude and longitude shown in figure J.2 were in decimal degree format and are considered as characters - latitudes were in the format HH MM (hours and minutes) and all subsequent characters were fractional minutes, and longitudes were in the format HHH MM and then fractional minutes. Train speed in knots, $V_{train,kn}$ was converted to train speed in metres per second (V_{train}) by taking 1 kn = 1.852 km/h (Posudin, 2014).

GPS data was extracted into a four column matrix containing the GPS coordinates, train speed and epoch time (from the GPS feed). A Matlab script then aligned each row of the GPS matrix with the pressure data matrix by matching each GPS epoch time stamp to the closest epoch time stamp in the pressure data, effectively "stretching" the GPS data to match the pressure data. Because of the different sampling frequencies, it was necessary to then linearly interpolate the GPS data to obtain a continuous data series. It was noted that the first and last GPS epoch time stamps often did not match the first and last pressure data epoch time stamp (by the order of 1-2 seconds) - the additional pieces of "end data" were discarded. The result was a data file containing a time series, the GPS data and the pressure data, which was saved as a comma separated values (".csv") file with the epoch start time included in the file name.

The raw GPS data was used to create a check file (which was created as a temporary Matlab variable). The purpose of this check file was to locate segments of data where the GPS feed

dropped out (i.e., the tracker could not receive a signal). The most common reason for GPS drop out (aside from a power failure) was passing through tunnels, and this temporary check file was used to categorise pressure transients as tunnel transients (see section J.5.1.5).

J.4.2 Data conversion

Pressure data (and also temperature and gyroscopic data) was saved as 12-bit numbers. The numbers were first converted to 16-bit numbers by multiplying by 2^2, resulting in positive 16-bit integer values ranging from 0 to 65536. Any values greater than 32767 were representative of negative pressures, and 65536 was subtracted from any values greater than 32767.

The resulting 16-bit voltage of each pressure transducer was defined as $V_{k,16bit}$, which was converted to the raw voltage output of each pressure transducer, V_k, by:

$$V_k = \frac{V_{k,16bit}}{6553.6} \tag{J.1}$$

For the absolute barometric pressure, the 16 bit voltage was converted to barometric pressure (in mbar) by:

$$P_{AMB} = 80 \times \left(\frac{V_{AMB,16bit} \times 2.125}{6553.6}\right) + 850 \tag{J.2}$$

The resulting voltage of the thermocouple was defined as , and converted to temperature (in °C) by:

$$T = 2037.90503 \times \left(\frac{V_{T,16bit}}{6553.6} - 0.1261\right) \tag{J.3}$$

The 16-bit voltage of the gyroscopic sensor was converted to roll rate (in degrees per second) using:

$$\text{Roll}(^{\circ}\text{s}^{-1}) = \frac{V_{gyro,16bit}}{6553.6 \times 0.02} \quad \text{(J.4)}$$

J.4.3 Final stages of preliminary data processing

A summary file was generated outlining key information from each data file, such as the file duration, max, min, and mean pressures, train speed and train direction (forwards or backwards - inferred quite straightforwardly from the dynamic pressure of the pitot-static probe) for each data file. This summary file aided in the secondary processing described in section 10.2, and allowed for quick fault detection - faults were usually indicated by comparing the max, min or mean pressures from adjacent pressure taps or minimum pressures of approximately -5500 Pa (i.e., zero values in the raw data).

J.5 Data analysis

J.5.1 Pressure transients

Pressure transients were identified based on the pressures from key taps on the side walls, and were categorised as "passing train", "tunnel" and "misc". Of these transients, many were manually identified as "false positives", i.e., the fluctuations in pressure were not caused by a passing train or tunnel (or other trackside structure). Figures J.8.1 to J.8.3 show examples of each type of pressure transient.

The overall process was as follows:

1. Check that data is ok for analysis.
2. Obtain a background mean pressure.
3. Obtain a raw pressure time series for each tap that has very high frequency fluctuations removed.
4. Compare the values of (3) to the values of (1) to identify large pressure fluctuations.
5. Check data to categorise type of transient.
6. Write transient as new data file and remove transient from raw data.

Note that the terms "identify" and "categorise" have very specific meanings and are not interchangeable. This procedure is described in sections J.3.1.1 to J.3.1.7 that follow.

J.5.1.1 Data checking

Two checks were performed on the data:

1. The length of the collated data file was checked, and the data file needed to be greater than 10 s in duration.

If the data file was greater than 10 s:

2. The quality of each pressure channel was checked, which enabled appropriate pressure taps to be used for subsequent identification of transients. The default pressure taps were taps B1 and B16 on the walls. If the data from either of these taps was "bad" then the next adjacent tap was checked and used instead, and so forth.

All data files that met these conditions were analysed regardless of train speed.

The system onboard the NMT is capable of accurately recording magnitudes of pressure transients. Quinn et al., (2016), (included in appendix M) shows an example of two train based pressure transients (one from the NMT data and one from measurements made on an instrumented Class 222 passenger train) and both through the same tunnel (Ampthill). The form and amplitude of the recorded pressures matched very favourably.

J.5.1.2 Obtaining background mean pressure

In order to identify pressure transients, the fluctuation in pressure needed to be quantified with respect to a mean pressure. The reference pressure for each pressure tap was a partially sealed container ($P_{ref,PS}$), and the differential pressure recorded by each transducer is given as equation 10.3. The partially sealed container had a decay time of about 30 s to one minute, which resulted in variation on the mean pressures with respect to altitude (see figure J.5 for example). It was not prudent to apply the reference pressure modification at this stage since this would result in unrealistic magnitudes of pressure transients given that the HST is not at all airtight. To account for pressure variation with respect to elevation changes, a 30 s moving average filter was applied to the data in both the forwards and reverse direction (i.e., starting at the first data sample and shifting the 30 s window 1 sample at a time towards the end of the data file, and then reversing the procedure by starting the filter at the end of the file and shifting the window 1 sample per iteration towards the start of the file). This resulted in a zero phase shifted stable "background mean pressure", defined as $P_{background}$, illustrated on figure J.5 and J.7.

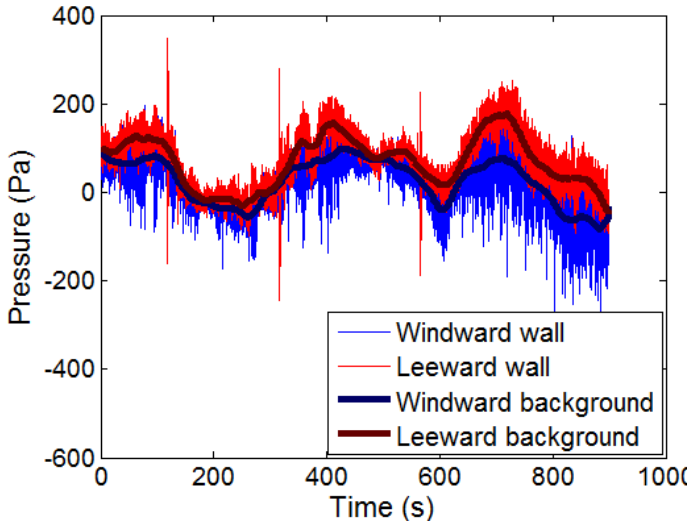

Figure J.5 - Comparison of raw pressure time series for entire run and background mean pressure after 30 s moving average filter applied (and corrected for phase shift).

J.5.1.3 Removal of high frequency fluctuations

It was noted that the pressure time history would often have high frequency and amplitude fluctuations. Given that pressure transients due to passing trains result in a positive and negative peak over a time period of about 0.1 to 0.5 s, the raw pressure data was filtered with a ~0.05 s moving average filter (6 samples at 128 Hz) which damped out very high frequency and high amplitude fluctuations but left the magnitudes of pressure transients relatively unaltered, and is defined as $P_{smoothed}$. The slight phase shift of 6 samples was accounted for by appending a column of six zero values to the beginning of the $P_{smoothed}$ time series. Figure J.6 compares a passing train pressure transient from the raw and 0.05 s filtered data and shows that the magnitudes of the pressure peaks are only slightly decreased (by the order of 10 to 20%).

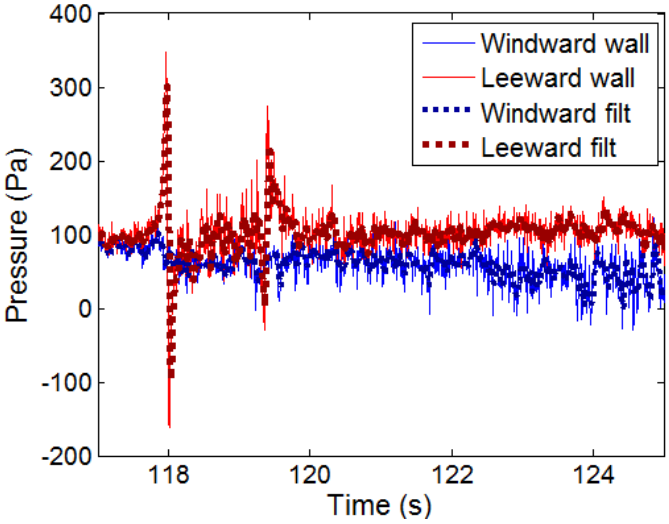

Figure J.6 - Comparison of raw pressure time series for passing train transient and background mean pressure after 0.05 s moving average filter applied (and corrected for phase shift).

J.5.1.4 Identification of transients

The difference between $P_{smoothed}$ (0.05 s filtered data) and $P_{background}$ (the double 30 s filtered background pressures) was found, and compared to a nominal threshold pressure, P_{thres}. Three different threshold pressures were used - 500 Pa, 200 Pa and 80 Pa. Generally speaking, the accuracy of the identification procedure decreased as threshold pressure increased (i.e., many more false positives were detected with an 80 Pa threshold pressure). It is acknowledged that 80 Pa is a very low pressure, however the aim of this analysis was to ensure that only open air data remained, and this process is therefore conservative. False positives identified later as gusts were reintegrated into the open air analysis.

A transient was identified based on the criterion that:

$$P_{smooth} - P_{background} \geq P_{thres} \tag{J.5a}$$

$$P_{background} - P_{smooth} \geq P_{thres} \quad \text{(J.5b)}$$

Note that in most cases equation J.5a defined the transient. Equation J.5b typically defined tunnel transients when the power car was trailing.

Figure J.7 illustrates the background pressures relative to the transient shown in figure J.6, and shows that the background pressure is an accurate representation of the mean pressure.

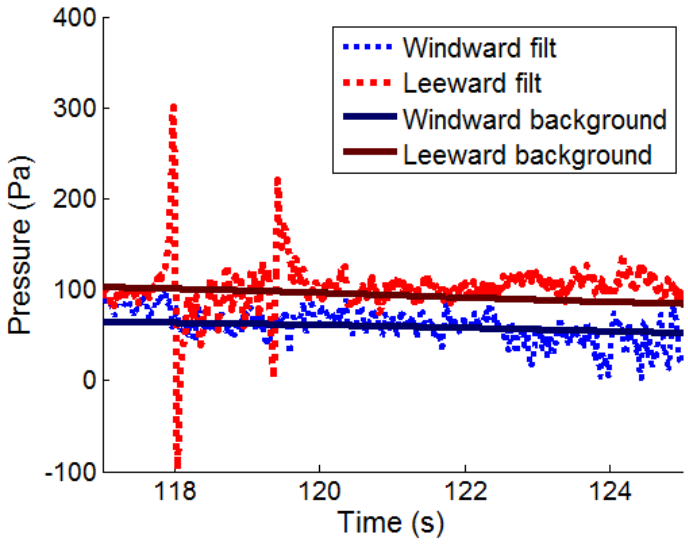

Figure J.7 - Comparison between 0.05 s filtered data and 30 s filtered background pressure.

J.5.1.5 Categorisation of transients

The initial categorisation criterion was the value of P_{thres} for which either equation J.5a or J.5b was satisfied, and transients were thus defined as Cat. 1, Cat. 2 or Cat. 3 for values of P_{thres} of 500 Pa, 200 Pa and 80 Pa respectively.

Pressure pulses from passing trains had to meet two criteria and a check:

1. Equation J.5.a needed to be initially satisfied for either of the wall pressure taps.

2. Equation J.5.b needed to be satisfied for the same pressure tap and within 0.5 s after the first instant in time after equation J.5.a was satisfied (i.e., a positive pressure followed by a negative pressure, and both greater than P_{thres}).

A final check was then performed:

3. The peak to peak pressure within this 0.5 s window was obtained and compared to the peak to peak pressure from the pressure tap on the opposite wall. If the maximum of the peak to peak pressures was at least 3 times greater than the minimum peak to peak pressure, the pulse was sub-classified as a "good pulse".

The reason for this check was that transients due to tunnels could also satisfy criteria (1) and (2), but would typically have similar magnitudes of pressures on the RHS and LHS wall, whereas a passing train creases a large pulse on the nearest wall tap and a very low pressure pulse on the far side wall.

If a transient failed to meet the criteria for a pressure pulse, a check was undertaken to attempt to identify whether it was a tunnel. Tunnels were defined by two different checks. The first check considered data drop out from the raw GPS feed. It was observed that the GPS logging system would record zero values when the train was passing through a tunnel, hence the first tunnel criteria was:

4. If at least one single sample contained GPS "drop out" for 15 s after a transient was identified, it was categorised as a tunnel.

The second check to categorise a transient as a tunnel involved considering the pressures themselves. Tunnel transients (for most tunnels) are categorised by an initial rise in pressure

as the loop taps enter the tunnel, followed by a large negative pressure - see figure J.8.2 for example. The criteria for a tunnel was that:

5. The mean value of ($P_{smooth} - P_{background}$) between 1 s and 5 s after either equation J.5a or J.5b had been satisfied had to be lower than 120 Pa. If this condition was met, the transient was categorised as a tunnel.

If the transient was not identified as a pulse or tunnel it was categorised as "miscellaneous".

J.5.1.6 Transient removal from data

For pressure pulses, data was removed from 3 s before the transient was identified, and 12 s afterwards. For tunnels, pressure data was removed from 10 s before the transient was identified and 60 s afterwards - the reason for such a long trim time for tunnels is that automatically defining an end point for a transient was difficult to automate, and when passing through a tunnel, the partially sealed reference pressure source would develop a more negative pressure than before the tunnel, and given that the decay time of the reservoir was about 30 s, it was necessary to remove any open air data where the reference pressure was decaying.

J.5.1.7 Examples of pressure transients

Figures J.8.1 to J.8.3 show examples of transients categorised as pulses, tunnels and miscellaneous. Considering the transients shown in figure J.8.1, (a) shows a typical passenger train pulse and (b) shows a passenger train pulse with a large pressure peak half-way which

likely indicates two train sets joined together, such as a Class 222 (Quinn et al., 2009). Figure J.8.1 shows a (c) short length 2 car passenger train and (e) likely shows an irregularly loaded freight train (i.e., no consistent geometrical loading such as containers). Figure J.8.1 (d) is quite interesting - the NMT was stationary the GPS position indicated that it was inside a tunnel - a pressure pulse can clearly be seen at 10 s but there are period oscillations in pressure between 5 s and 10 s, almost certainly caused by the reflection of the pressure wake within the tunnel caused by the passing train. Figure J.8.1 (f) shows a pressure pulse that has exceeded the 1.44 kPa safety limit (Johnson, 2011). Considering figure J.8.2, (a) shows a tunnel followed by a passing train, (b) shows two tunnels in very close proximity, (c) and (d) show "typical" tunnel transients, (e) shows two tunnel transients and (f) shows a tunnel transient recorded while the power car was trailing. Considering figure J.8.3, (a) shows a very short tunnel while the power car was trailing, (b) shows an unusually shaped pressure pulse caused by a passing train (the NMT was stationary), (c) and (d) are both examples of crosswinds, (e) shows bad data from the RHS tap (in red) and (e) shows a partial tunnel transient from a tunnel that was not correctly identified.

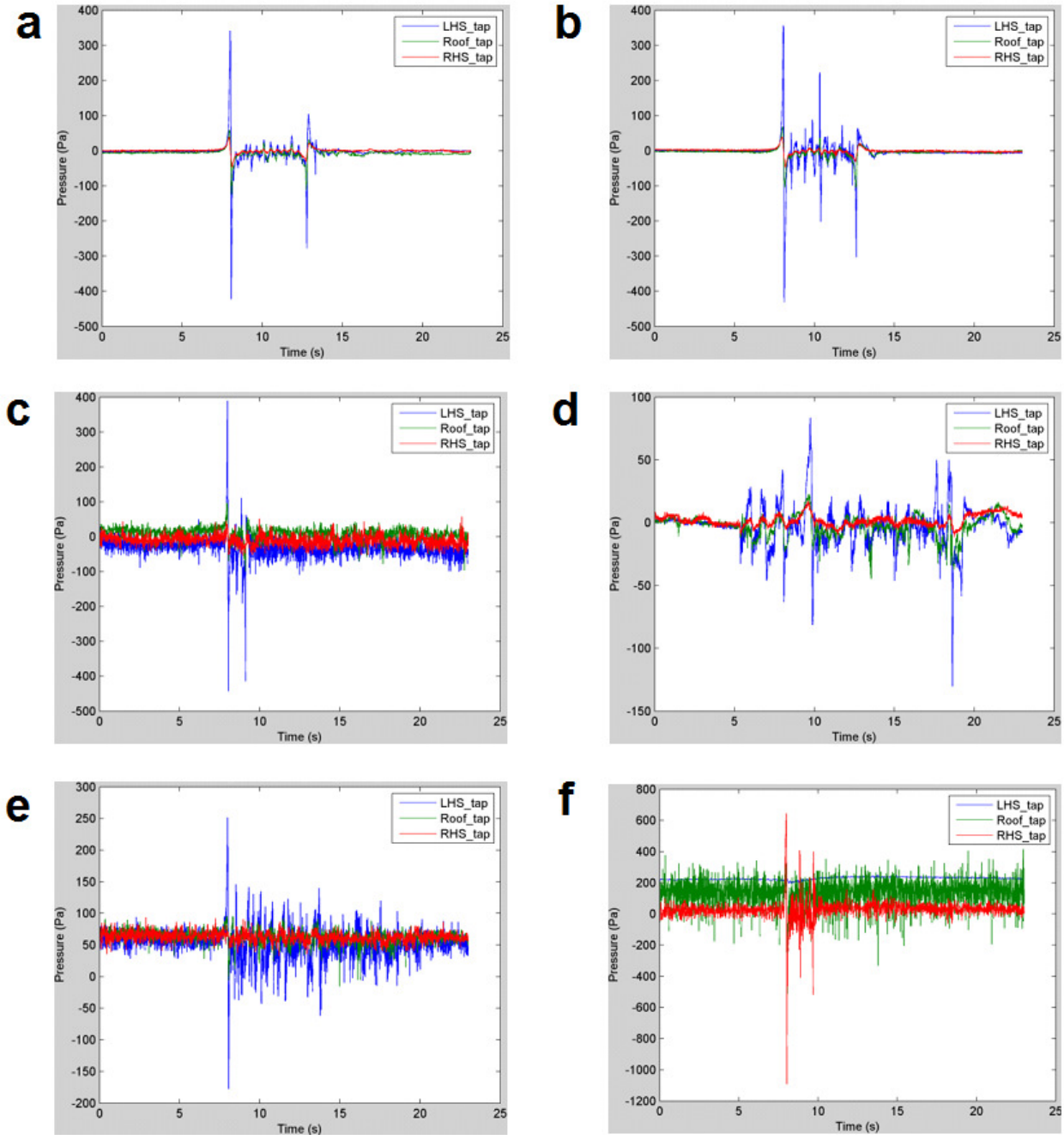

Figure J.8.1 - Examples of pressure pulse (passing train) transients.

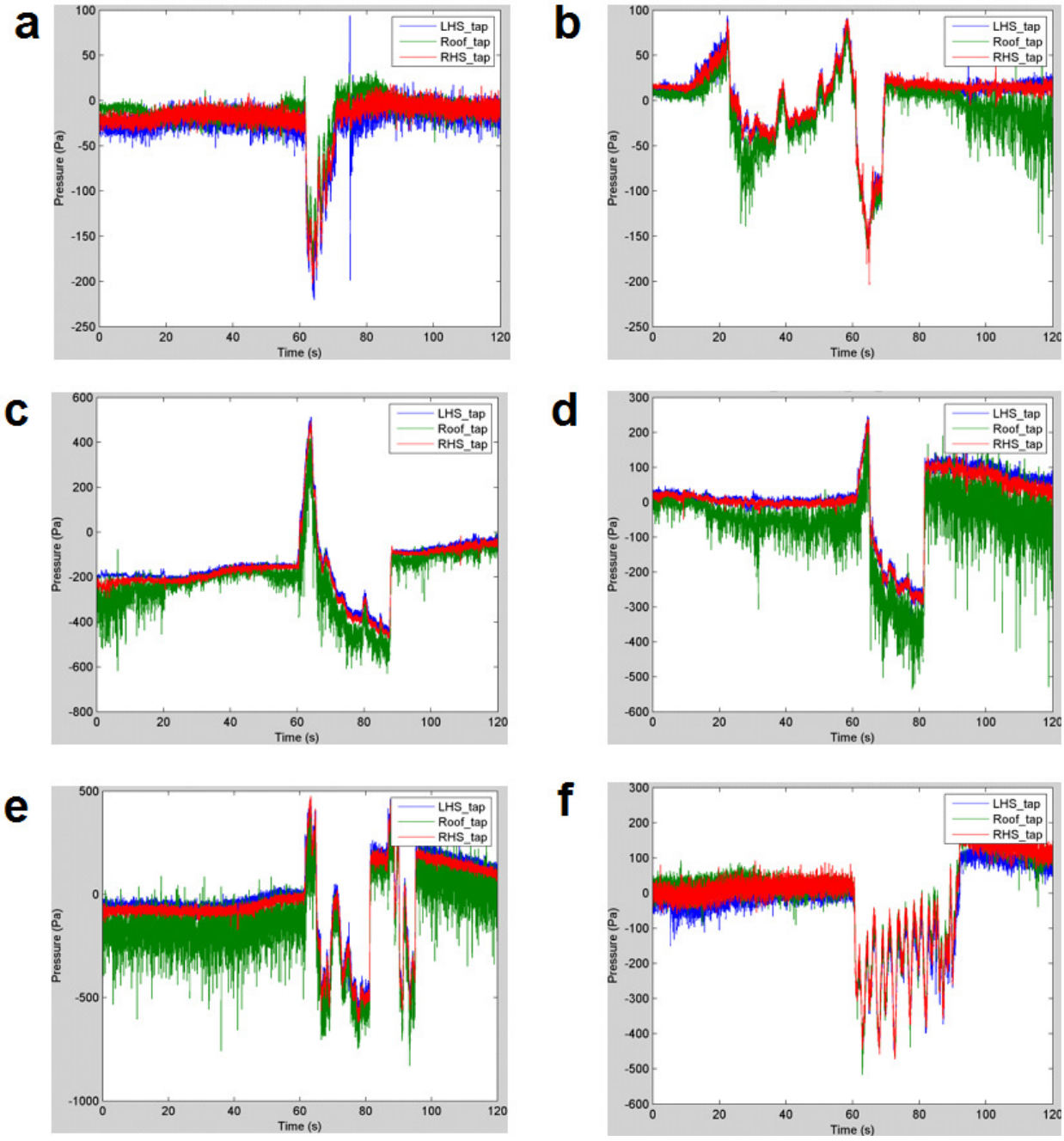

Figure J.8.2 - Examples of tunnel pressure transients.

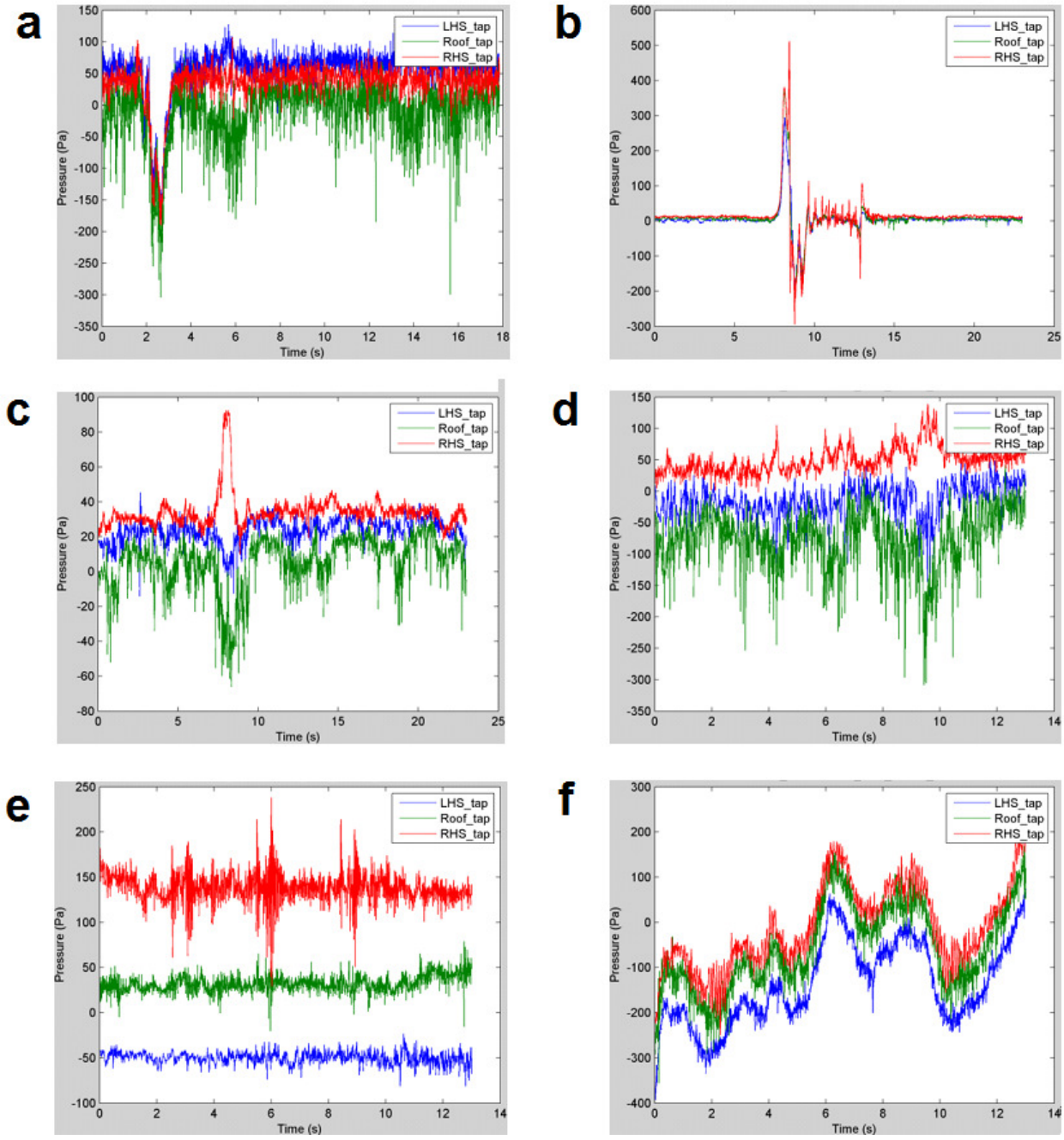

Figure J.8.3 - Examples of miscellaneous transients.

J.5.2 Reference pressure modification

As discussed in section 10.2.3.2, the pressure tap data was modified to take the open ended reference probe as the reference pressure - the reason for this is that the changes in altitude and temperature resulted in variations in pressure that were greater than those caused by crosswind effects. Figure J.9 shows the effect of modifying the normalising reference pressure and shows that the gradual pressure changes (over time periods of 30 s to 200 s) have been greatly reduced. It should be noted that this reference pressure modification took place after the transients had been removed.

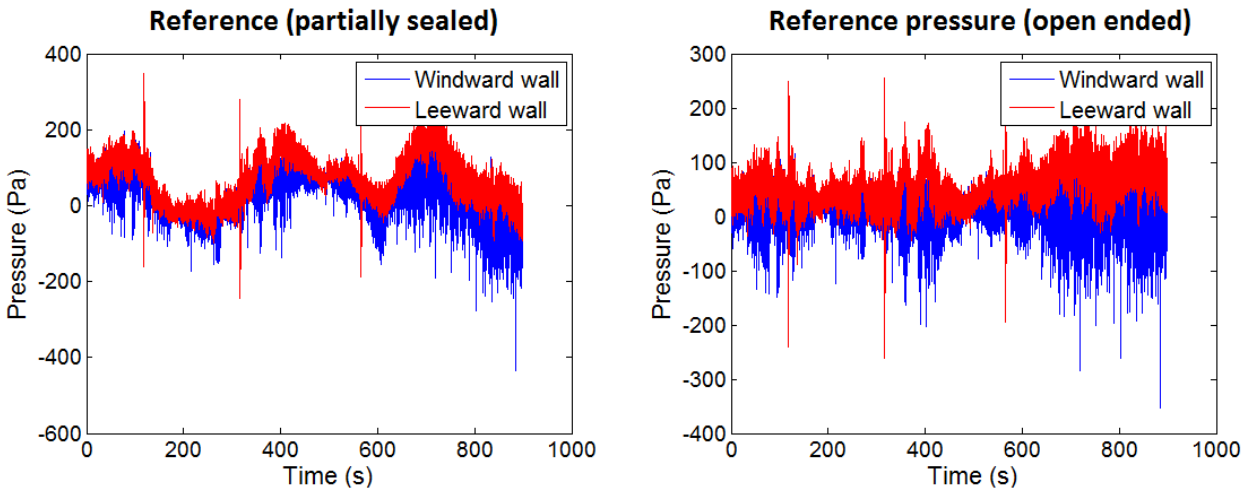

Figure J.9 - The effects of normalising the data with the partially sealed reference pressure compared with the modified open ended reference pressure for a 15 minute data file.

J.5.3 Effect of engine cooling fan on roof pressures.

The main purpose of the low pass 1 s moving average filter was to remove any pressure fluctuations that were as a result of gusts of time scales less than 1 s. However, it was

observed that the pressures over the roof showed quasi-period intervals of large amplitude fluctuations, believed to be caused by the upstream engine cooling fan. Figure J.10 shows two data files and shows the roof pressure time series in green. Note that pressure transients have been removed from the data shown, and as such there are discontinuities in the data. The main point to be made from figure J.10 is that the negative roof pressures are of high magnitude (-200 Pa and - 500 Pa on the LHS and RHS figures) and they show a periodic pattern. It could also be noted that these bursts of negative roof pressure occur either when the train is accelerating (as on the LHS figure) or running close to maximum speed (as on the RHS figure), again suggesting that these negative pressures are a result of the engine cooling fan. It is also worth noting that the side wall tapping points are unaffected.

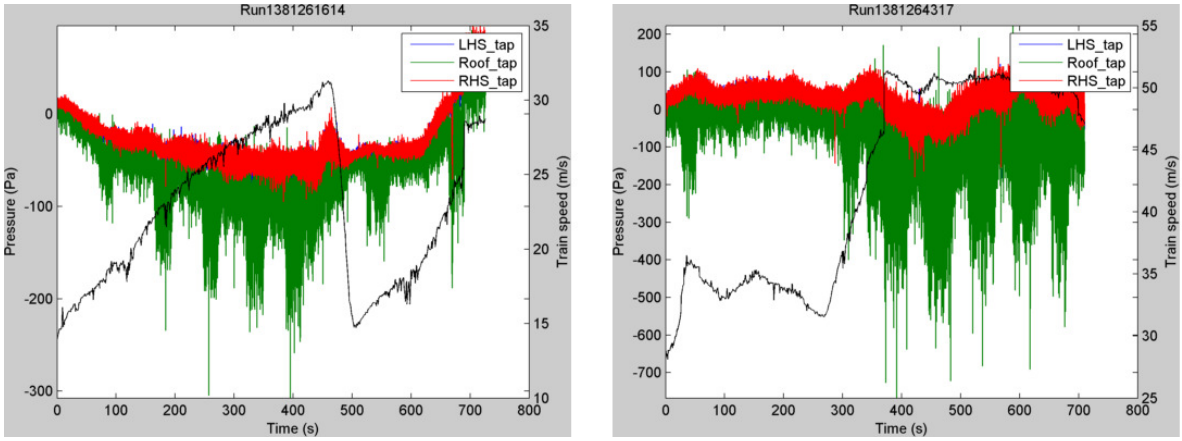

Figure J.10 - Two data files showing bursts of negative pressures recorded by the central roof pressure tap (train speed shown as black line).

In order to further illustrate this negative roof pressure, a 200 s segment of data was considered (shown in figure J.11). This 200 s segment was then divided into "blocks", where 0-40 s and 85-120 s were the unaffected roof pressures (blocks 1 and 2), and between 50-75 s and 130-155s were the affected roof pressures (blocks 3 and 4). Figure J.11 also shows the

filtered data, and there are clearly larger negative pressures within the time intervals specified for blocks 3 and 4. Figure J.12 shows the unfiltered roof pressure time series for each of the blocks. A Fourier transform was performed on the raw data and the 1 s filtered data to obtain the power spectra of the pressure signal for each of the four blocks (figure J.13). Blocks 1 and 2 (no fan) show very similar results, and similarly blocks 3 and 4 are similar. Differences can be seen in the power spectra when comparing blocks 1 and 2 to blocks 3 and 4 (i.e., when the engine fan is turned off compared to when it is turned on). If frequencies greater than 1 Hz are considered, it appears that when the fans are turned on, a much greater portion of the signal power is at frequencies between 1 Hz to 10 Hz than at 10 Hz or greater. When the fans are switched off, the power of this signal is distributed more uniformly across signals of 1 Hz to greater than 10 Hz (note the maximum frequency considered in figure J.13 is 64 Hz, i.e., half of the sampling frequency). This analysis therefore shows that the pressures over the train roof are significantly affected by the roof fans. A 1 s moving average filter is very successful at removing the frequency effects that have been observed, however the effect of the fans on the mean pressure is significant and cannot be mitigated through analytical procedures without the need for some crude data manipulation.

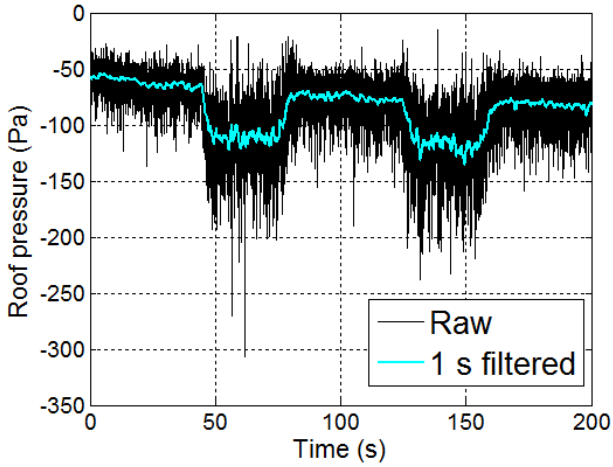

Figure J.11 - 200 s sample of data showing intervals of negative pressures above the roof.

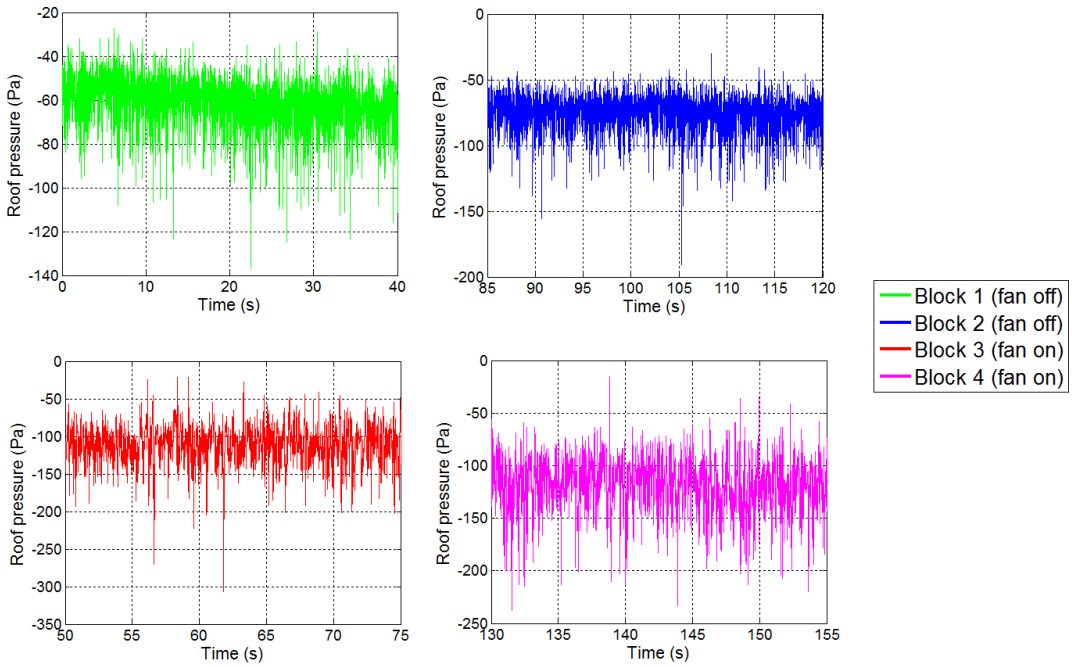

Figure J.12 - Pressure time series for blocks 1 to 4 for roof tapping point.

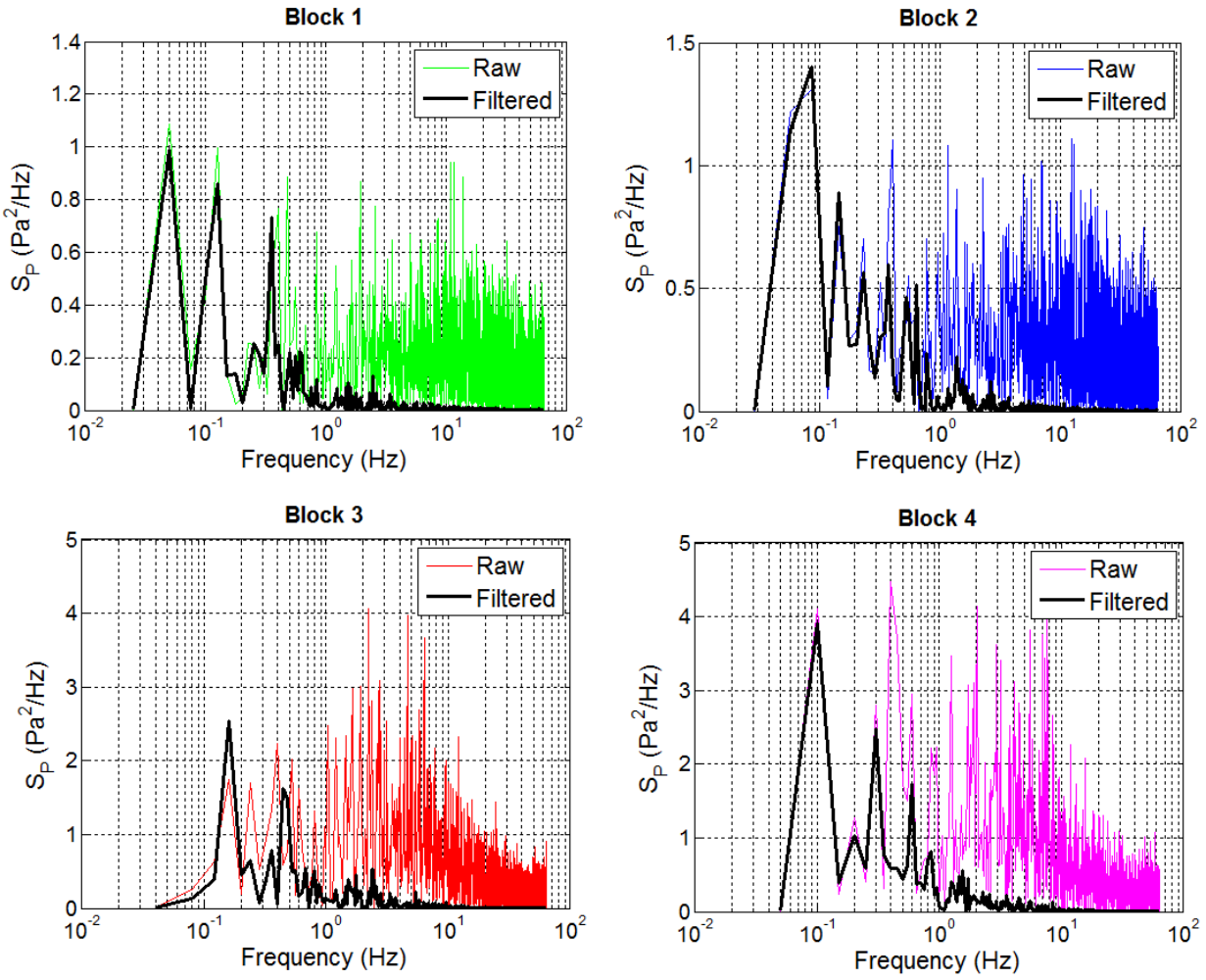

Figure J.13 - Power spectra for blocks 1 to 4 (roof tap pressures) obtained from raw and 1 s filtered data.

J.5.4 Resonance effects in pneumatic tubing

Fluctuations in air pressure can result in standing waves in the pneumatic tubing (Lawson, 2001). The lengths of pneumatic tubing for each tap are given in table J.3. These lengths are to the nearest 5 mm and are the distances from the tap (i.e., the open end) to the front face of the modular transducer box. In all cases, the length of the internal pneumatic tubing inside the

modular transducer box was 120 mm. The tubing was simplified as an open pipe, and hence the resonant frequency of the standing wave was given as:

$$F_{res_k} = \frac{V_{sound}}{2L_{tube_k}} \tag{J.6}$$

Where V_{sound} is the speed of sound in air, taken as 340 m/s and L_{tube_k} was the length of the pneumatic tubing per pressure transducer, k, defined in table J.3.

In reality there is a secondary "pipe" for the loop tapping points as a result of the drainage line junction, though given the small lengths of these secondary pipes (which would result in very high frequency standing waves), these effects were disregarded. The frequency of the primary standing wave for each tube is given in table J.3. The maximum tubing length (and hence lowest resonant frequency) were 1.57 m and 108 Hz respectively. Given that a low pass moving average filter with a 1 s period was applied to all of the data explicitly considered in this study, and that the sampling frequency was relatively low (128 Hz) and close to the minimum value of F_{res_k}, no additional filtering due to the specific resonant frequencies took place. The power spectra in figure J.13 show that frequencies above 1 Hz are effectively damped out to zero power once data has been filtered. If it is desirable to consider the non-1 s filtered data (such as analysis of pressure transients or gusts of period lower than 1 s) it is recommended that a low-pass filter with a cut off frequency of 75 - 100 Hz be applied to the data.

Table J.3 - Tube lengths and corresponding resonant frequencies of standing waves.

Pressure tap	Tubing length to modular box (mm)	L_{tube_k} (m)	F_{res_k} (Hz)
A1	1080	1.2	142
A2	485	0.605	281
A3	1065	1.185	143
PITOT STATIC	480	0.6	283
PITOT TOTAL	445	0.565	301
PITOT DYNAMIC (HPP)	470	0.59	288
B1	365	0.485	351
B2	680	0.8	213
B3	745	0.865	197
B4	845	0.965	176
B5	1165	1.285	132
B6	1280	1.4	121
B7	770	0.89	191
B8	520	0.64	266
B9	335	0.455	374
B10	325	0.445	382
B11	480	0.6	283
B12	1450	1.57	108
B13	1100	1.22	139
B14	645	0.765	222
B15	390	0.51	333
B16	770	0.89	191
B17	865	0.985	173

J.5.5 Fault detection

The NMT is operated by Network Rail and is a critical component of NR's safety system, as its primary role is track inspection. Access to the train was therefore limited and usually only permitted when car 43062 was undergoing routine maintenance work. It was therefore useful to be able to detect faults from the data itself as well as by visual inspection of the equipment. A key element of the data analysis has therefore focussed on fault detection.

Physical problems were often related to the pneumatic tubing to the HPP becoming filled with water, or transducer failure, hence were specific to certain data channels. The modular boxes had 7 PT channels and therefore it was usually possible to switch the pneumatic tubing connection to a different channel to a pressure transducer specific fault. A pressure tap that was blocked with water (or paint) would record pressures of lower magnitude and the standard deviations would be lower than for an adjacent and working pressure tap. Data channels that had broken/faulty pressure transducers may have shown the converse - either larger amplitude mean pressures or significantly larger standard deviations. See figure J.13 for examples of three broken pressure transducers that show either much higher means or much higher standard deviations than working taps. An automated Matlab script was written in order to identify this type of fault by comparing the magnitudes of pressures and standard deviations for segments of good data with adjacent pressure taps - if the standard deviations were different by a factor of 2 then the taps were diagnosed as needing checks. which aided in the physical inspection of equipment. An automated Matlab script was written that considered a segment of open air data within each file and compared the standard deviation and maximum pressures of each pressure tap pair, though manual identification of faults was still required. A second and less apparent issue was that the airtight connections made within the drain plug systems would degrade which would lead to lower recorded pressures (this was hard to pick out from data, and was detected and repaired during physical inspection).

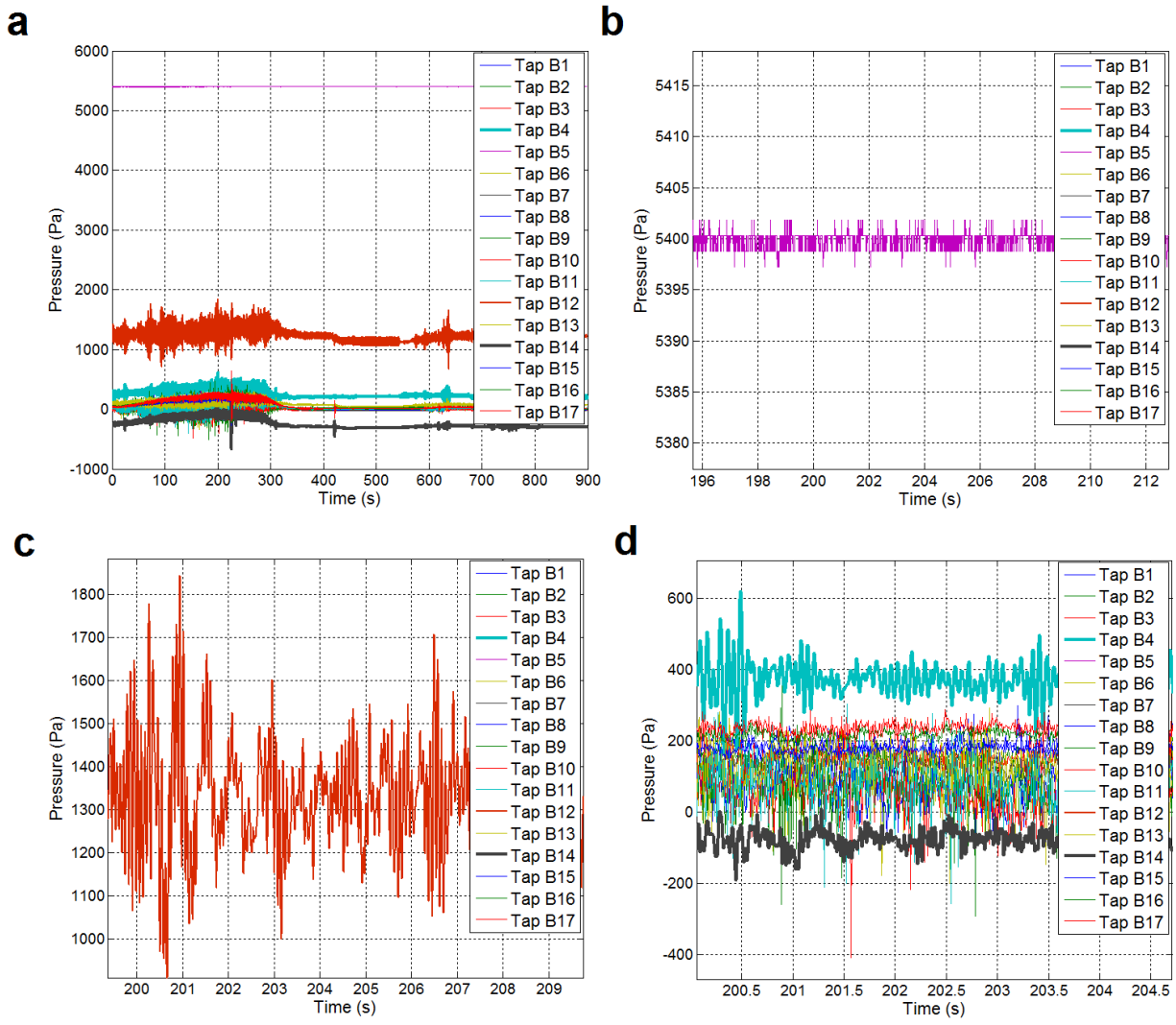

Figure J.13 - Example of data file containing bad data related to individual pressure transducer failures - (a) entire file, (b) tap B5 (c) tap B12 and (d) tap B4.

It was observed that the modular box located at the front of the train on the front panel would often give faulty data (i.e., all the channels showed 0 V) suggesting a power or signal failure. This was most likely due to a loose connection at the rear of the box which was exacerbated by the movement of the "loosely fitting" front nose panel during operation. Once this PT box was replaced, the data feed was far more consistent. Data between 24/10/13 and 06/01/14 and

also between 06/03/14 and 23/05/14 showed large quantities of data drop out from the modular pressure transducer box at the nose. Of the 987 hours of data collected between 24/10/13 and 23/05/14, 757 hours of data were bad - i.e., the front box was recording a zero output. The modular pressure transducer box was replaced with the spare box on 28/05/14 while the train was in the depot undergoing maintenance work and since then this issue has been eliminated. On occasions

An issue was encountered with the pneumatic tubing to the pitot static probe on 20/02/14. The probe was mounted at the maximum vertical height as was practicable but this only left a minimal clearance (1 - 3 mm) between the pneumatic tubing and the edges of the panel hole. The tubing broke and was replaced with the more sturdy PVC tubing on the same day, shown in figure J.14, and since then no issues have been noted with the pneumatic tubing to the pitot probe.

Throughout the entire course of the experiments, the thermocouple gave spurious data. The probe was replaced on 05/03/14 and appeared to give correct data for about 2 weeks, after which the temperature data again became spurious. The former thermocouple was tested in the lab at the UoB and no faults were diagnosed with this sensor. Temperature data has as such not been used in any meaningful was in this study.

Between 11/01/15 and 24/04/15 data at the train nose was affected by blocked taps caused by dry paint, after the NMT had been stopped in a depot for about 3 months undergoing maintenance work and painting. The affected pressure taps at the nose were cleared of paint, however tap B2 had not been cleared and remains blocked.

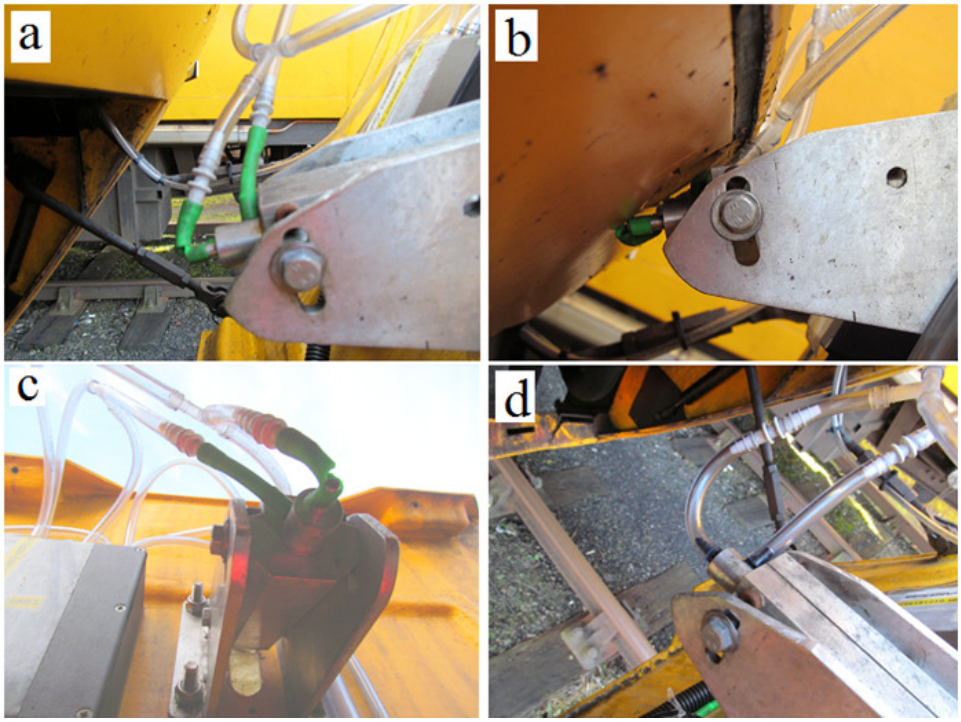

Figure J.14 - Broken pneumatic tubing connected to pitot static probe (a) and (c) show the tear in the tubing, (b) shows the total pressure port of the probe "crushing" against the NMT nose when the drawbar access panel is raised and (d) shows the replacement PVC tubing.

Finally, on 23/05/16 a major fault was detected with the onboard PC. It is believed that the hard drive had developed a serious fault resulting in software corruption and hence the PC was no longer able to start up and sample data. As a closing thought relating to the NMT investigation, when the systems are functioning the NMT acquires data that is potentially very useful, and more "good" data would of course be very useful in further work, particularly with respect to considering the GPS position of pressure transient events and peak gusts. Removal of the onboard PC is required given that it is no longer functional. It is this author's belief that reinstalling the PC would be less time consuming that removal of all equipment, and given the cooperation from Network Rail in these tests, the continued operation of the NMT should be

possible for the foreseeable future (this is true at the time of writing). New modular pressure transducer boxes and a new/repaired PC should be developed and replace the existing system. The pneumatic circuits should be entirely replaced following the same construction as before. The existing conduit runs for cable and reference pressure tubing are intact, and the conduit line beneath the train was difficult and time consuming to install - therefore the fact that it is intact is promising. Finally, Y-shaped connectors should be used in place of T-shaped connectors on some of the T-junctions between the short length of tubing to a pressure tap and the drainage line (figure 9.9), so that the pressure tubing from the junction to the modular transducer box runs upwards and hence preventing any water ingress.

APPENDIX K

FULL-SCALE CROSSWIND TESTS - SCATTER PLOTS AND REGRESSION ANALYSIS

K.1 Introduction

Appendix K considers the experimental procedure and results related to the NMT scatter plot methodology outlined in section 10.3.1. Section K.2 sets out the analytical methodology and three types of regression models. Section K.3 shows the scatter plots of pressure coefficient against yaw angle and illustrates the three regression models. The coefficients of each regression model, as well as key statistical parameters are also given. Section K.4 applies the regression analysis to the wind tunnel and outlines flaws in this methodology related to unrealistic predictions of the quadratic and cubic regression models. Section K.5 shows the pressure distributions obtained from each regression model (and briefly considers the application of this methodology to gusts in section K.5.1). Further discussion is made in section K.6.

K.2 Analytical methodology

Data files that were acceptable for open air analysis were analysed in the usual way (as described chapter 10), resulting in two data files of pressure coefficients and yaw angles (depending on the yaw angle calculation - i.e., one data file using the wind tunnel yaw coefficients and one data file using the TRAIN rig CWG yaw coefficients, as presented in table 8.1). Data was then filtered with a 1 s moving average filter, and then resampled to a frequency of 1 Hz, which was necessary given the large quantity of data and limited computational power of a desktop PC. The result was that the total number of data points was about 80 000, for which it was possible to create scatter plots and undertake a regression analysis. Three best fit regression models - a linear, quadratic and cubic model, were developed by using the "polyfit" function on Matlab (Mathworks, 2010), for both the wind tunnel (WT) and TRAIN rig CWG yaw angle calculation methodologies, which uses a least squares approach to fit a polynomial within scattered data. Higher order polynomials were not considered due to both the limited yaw angle range of the full scale data and the fact that the wind tunnel data was only considered in 5° yaw angle steps (and the main point is a comparison between full scale and model scale), therefore only polynomials of the order of 1 to 3 were appropriate when considering the wind tunnel data (as in section K.4) (Mathworks, 2010). The coefficients of each best fit model are defined as:

Linear:

$$C_{P_k}(t) = C_{NMT|1}\varphi(t) + C_{NMT|0} \quad \text{(K.1)}$$

Quadratic:

$$C_{P_k}(t) = C_{NMT|2}\varphi^2(t) + C_{NMT|1}\varphi(t) + C_{NMT|0} \quad \text{(K.2)}$$

Cubic:

$$C_{P_k}(t) = C_{NMT|3}\varphi^3(t) + C_{NMT|2}\varphi^2(t) + C_{NMT|1}\varphi(t) + C_{NMT|0} \quad \text{(K.3)}$$

Each of equations K.1.1 to K.1.3 are defined independently for positive and negative yaw angles, and were calculated based on yaw angle obtained from the CWG tests or from the wind tunnel tests (abbreviated to WT on figures).

Tables K.1.1.1 and K.1.1.2 in section K.2.2.2 present the values and dimensions of the coefficients $C_{\mathrm{NMT|0,1,2,3}}$ for all pressure taps for both positive and negative yaw angles separately for the WT yaw angle calculation methodology. Similarly, tables K.1.2.1 and K.1.2.2 present these coefficients for the positive and then negative yaw angles for the TRAIN rig CWG yaw angle calculation methodology.

K.3 Scatter plots and regression models (NMT)

Figures K.1.1 to K.1.17 in section K.3.1 show the scatter plots of instantaneous pressure coefficients against instantaneous yaw angle, where (a) shows the data based on yaw angle calculated from the WT yaw coefficients and (b) shows the same data but calculated from the TRAIN rig CWG yaw coefficients. The three regression models are shown and positive and negative yaw angles are considered independently. Section K.3.2 discusses the results and the values of the coefficients of each regression model (as per equations K.1 to K.3) are given later in section K.3.2

K.3.1 Scatter plots

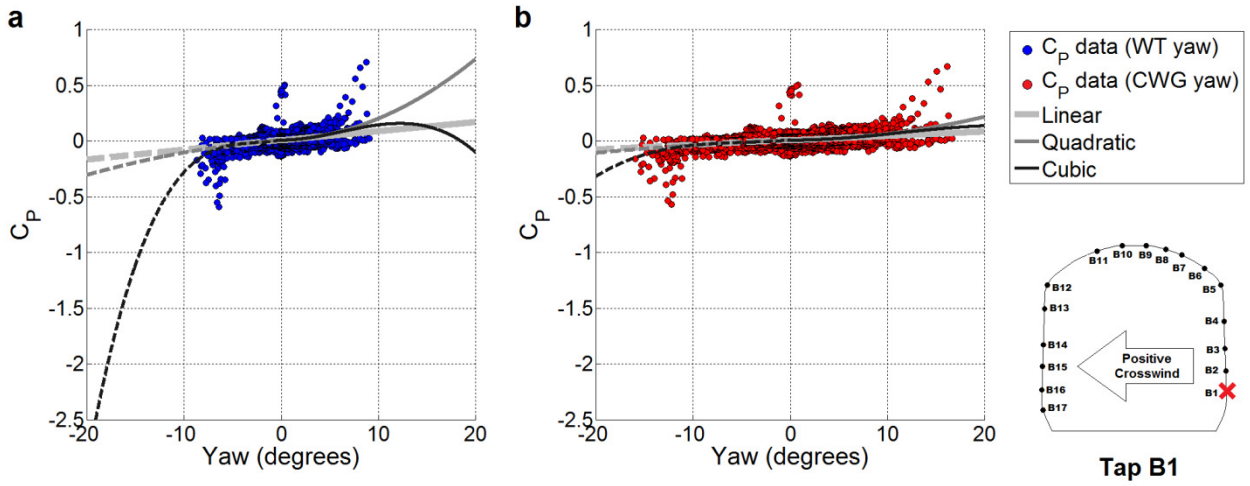

Figure K.1.1 - Scatter plots of $C_{P_k}(t)$ against yaw angle and best fit curves for tap B1 for (a) WT and (b) CWG yaw angle calculation methodologies.

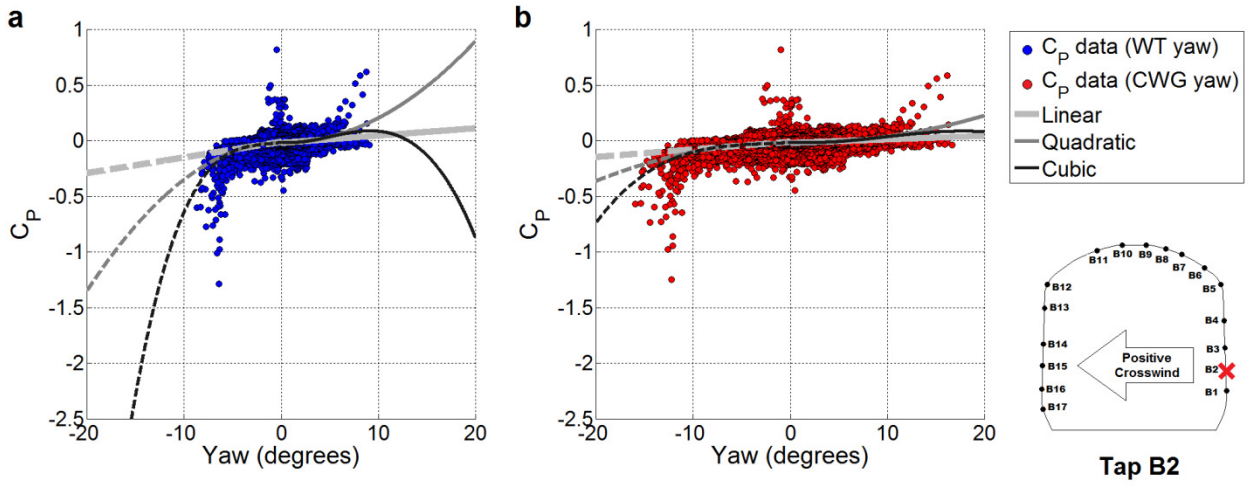

Figure K.1.2 - Scatter plots of $C_{P_k}(t)$ against yaw angle and best fit curves for tap B2 for (a) WT and (b) CWG yaw angle calculation methodologies.

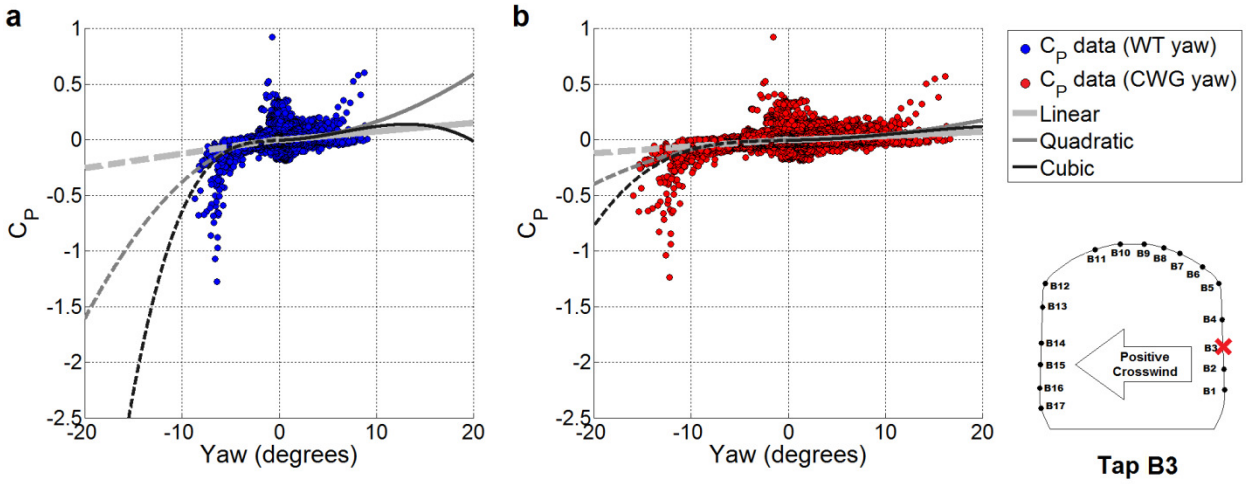

Figure K.1.3 - Scatter plots of $C_{P_k}(t)$ against yaw angle and best fit curves for tap B3 for (a) WT and (b) CWG yaw angle calculation methodologies.

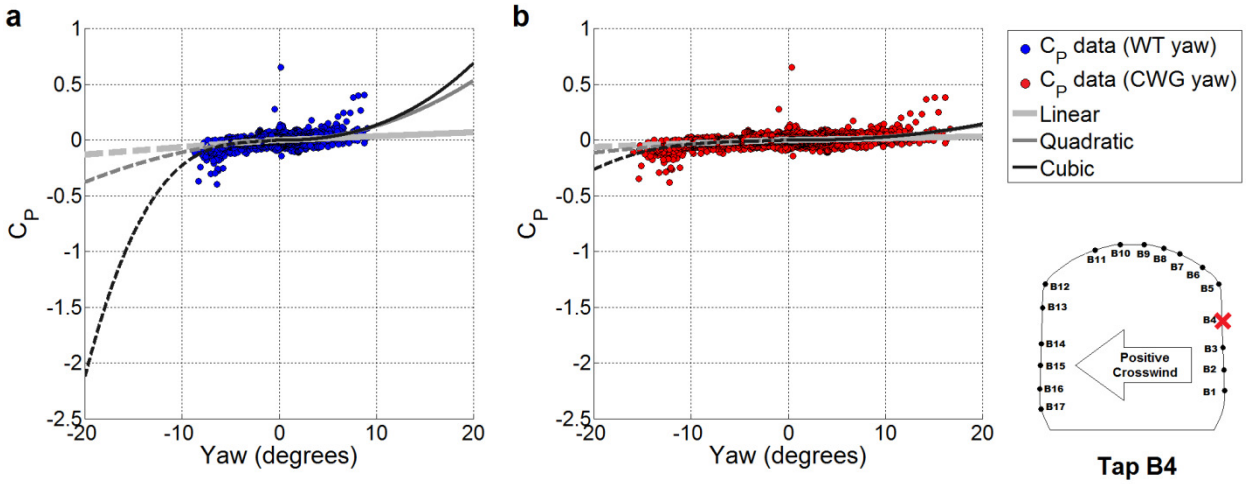

Figure K.1.4 - Scatter plots of $C_{P_k}(t)$ against yaw angle and best fit curves for tap B4 for (a) WT and (b) CWG yaw angle calculation methodologies.

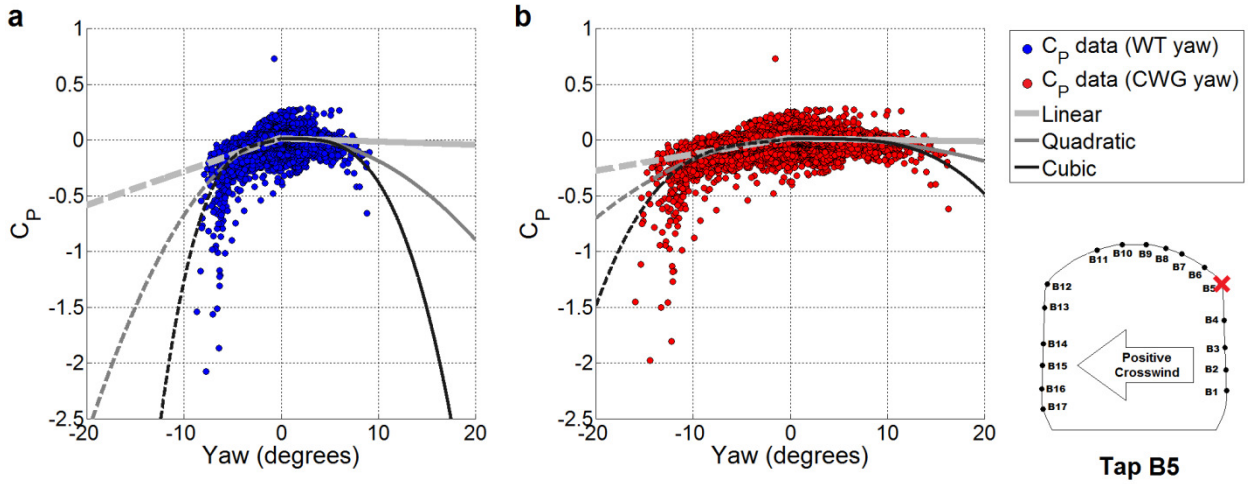

Figure K.1.5 - Scatter plots of $C_{P_k}(t)$ against yaw angle and best fit curves for tap B5 for (a) WT and (b) CWG yaw angle calculation methodologies.

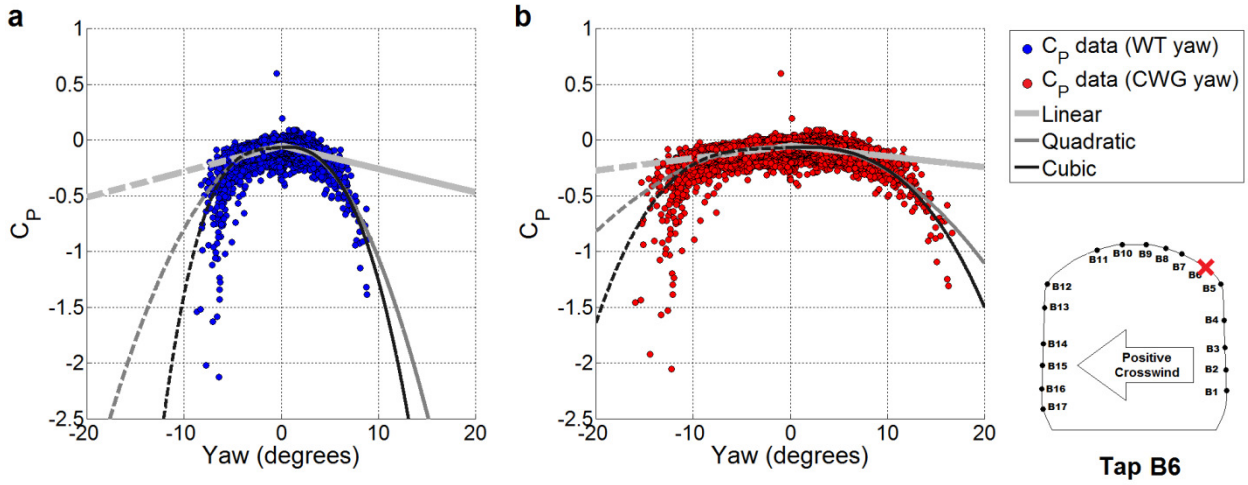

Figure K.1.6 - Scatter plots of $C_{P_k}(t)$ against yaw angle and best fit curves for tap B6 for (a) WT and (b) CWG yaw angle calculation methodologies.

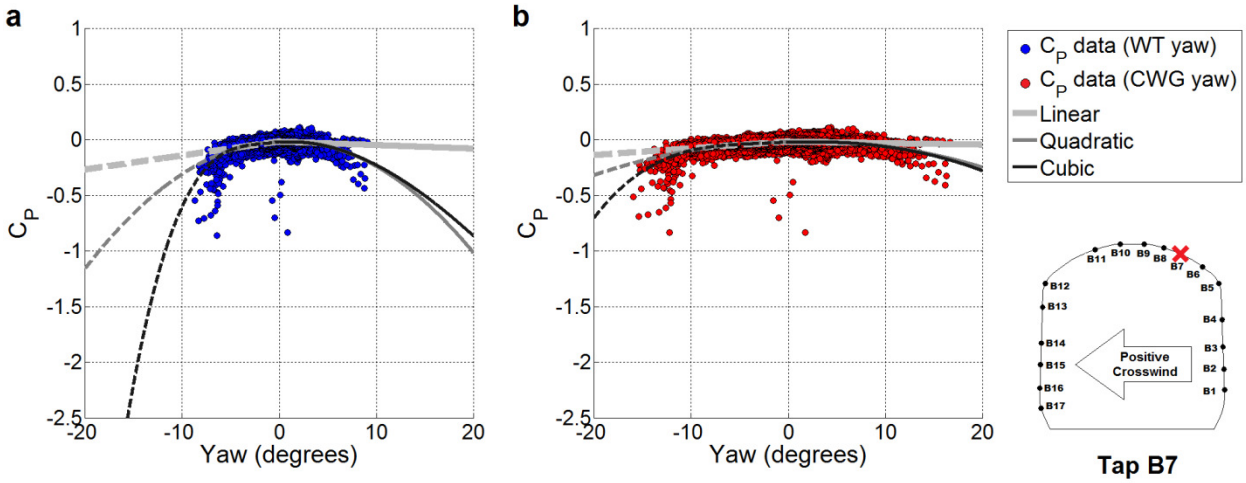

Figure K.1.7 - Scatter plots of $C_{P_k}(t)$ against yaw angle and best fit curves for tap B7 for (a) WT and (b) CWG yaw angle calculation methodologies.

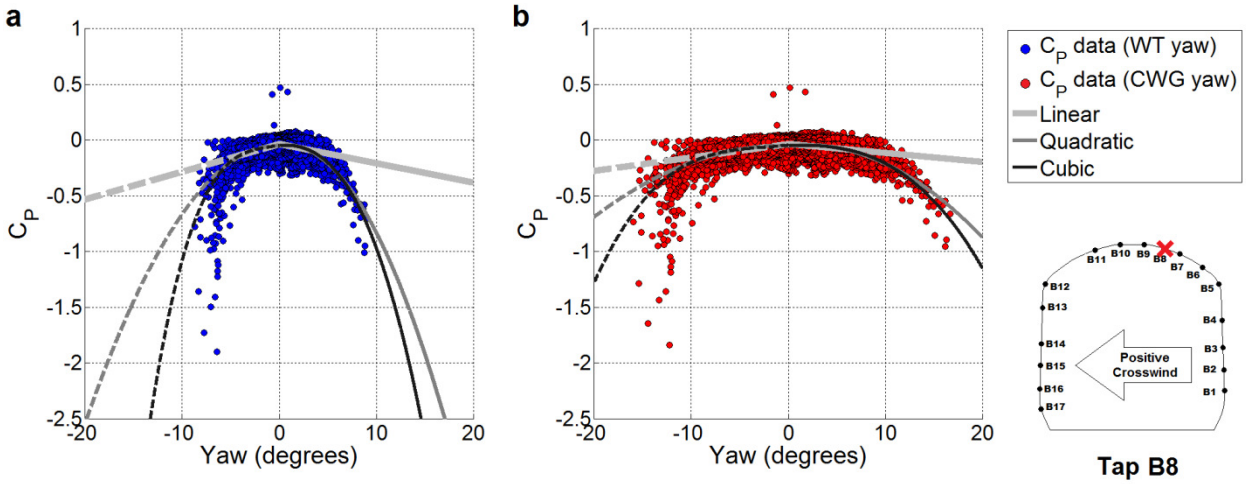

Figure K.1.8 - Scatter plots of $C_{P_k}(t)$ against yaw angle and best fit curves for tap B8 for (a) WT and (b) CWG yaw angle calculation methodologies.

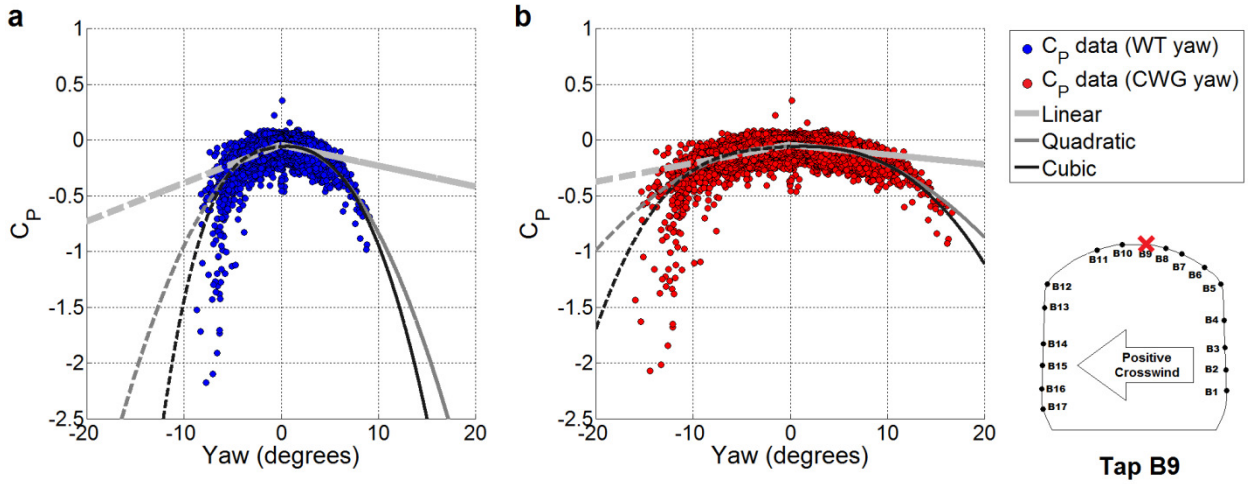

Figure K.1.9 - Scatter plots of $C_{P_k}(t)$ against yaw angle and best fit curves for tap B9 for (a) WT and (b) CWG yaw angle calculation methodologies.

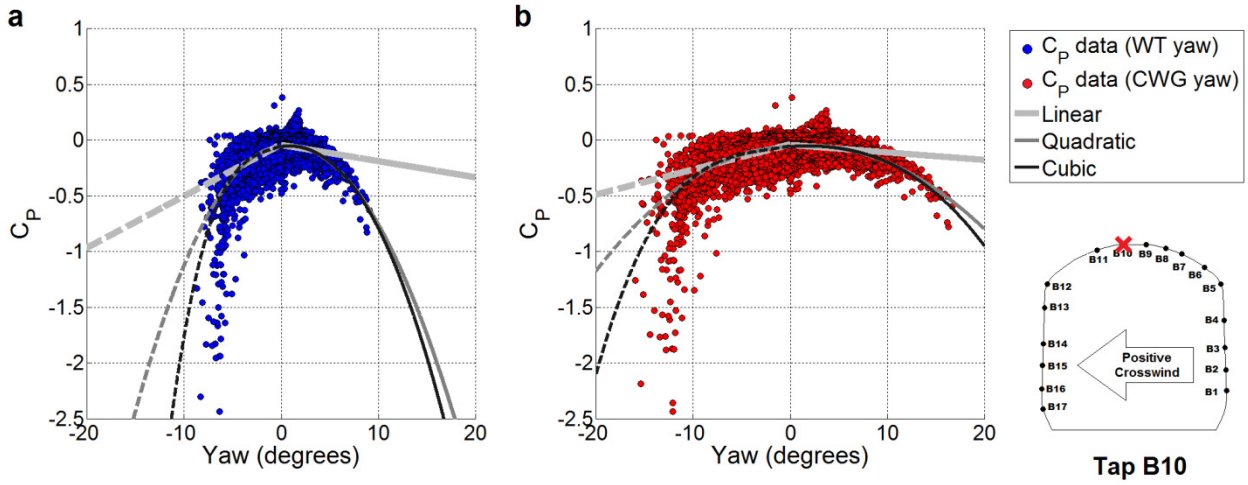

Figure K.1.10 - Scatter plots of $C_{P_k}(t)$ against yaw angle and best fit curves for tap B10 for (a) WT and (b) CWG yaw angle calculation methodologies.

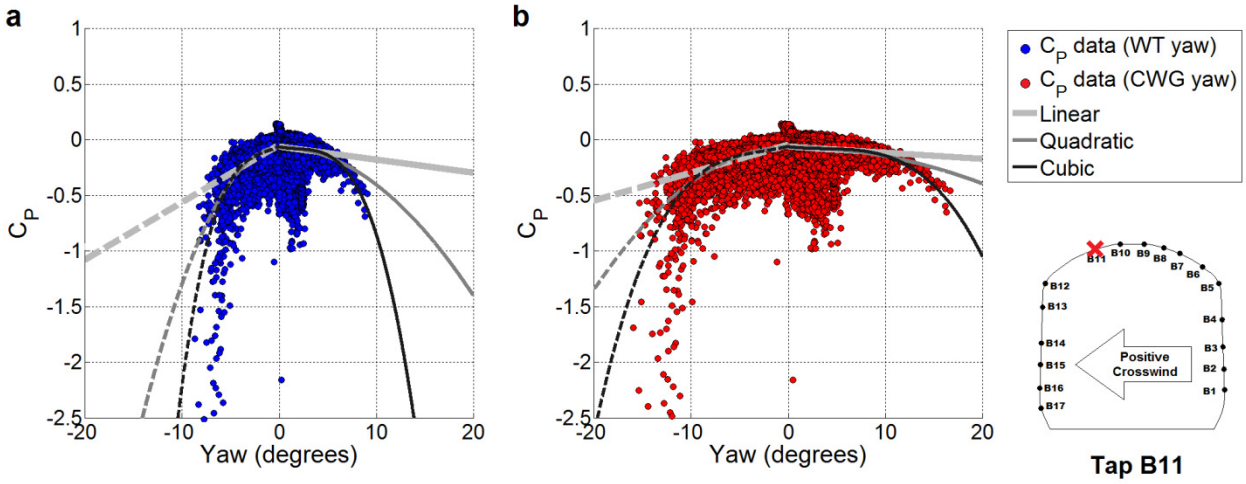

Figure K.1.11 - Scatter plots of $C_{P_k}(t)$ against yaw angle and best fit curves for tap B11 for (a) WT and (b) CWG yaw angle calculation methodologies.

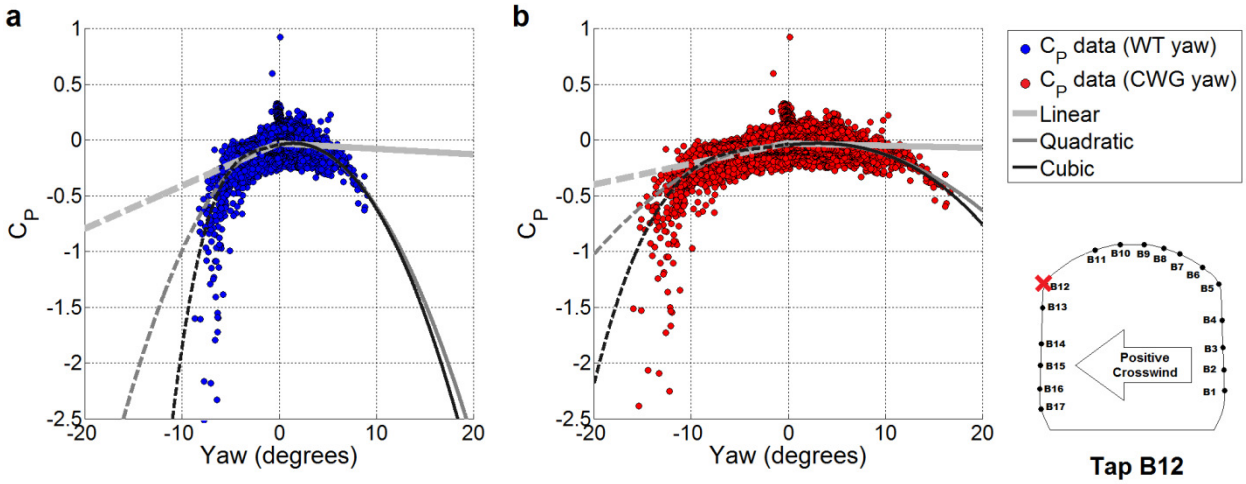

Figure K.1.12 - Scatter plots of $C_{P_k}(t)$ against yaw angle and best fit curves for tap B12 for (a) WT and (b) CWG yaw angle calculation methodologies.

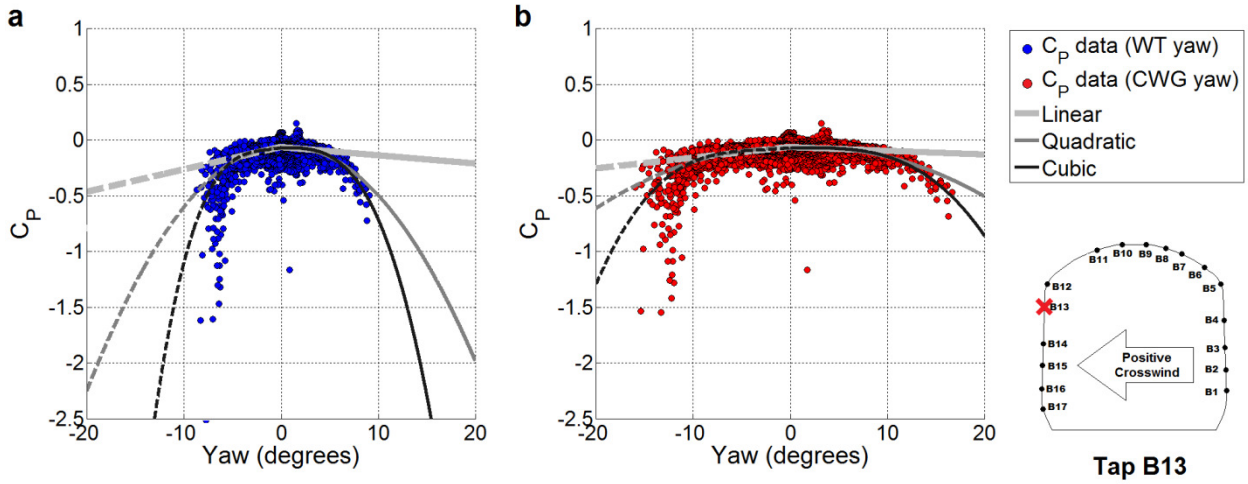

Figure K.1.13 - Scatter plots of $C_{P_k}(t)$ against yaw angle and best fit curves for tap B13 for (a) WT and (b) CWG yaw angle calculation methodologies.

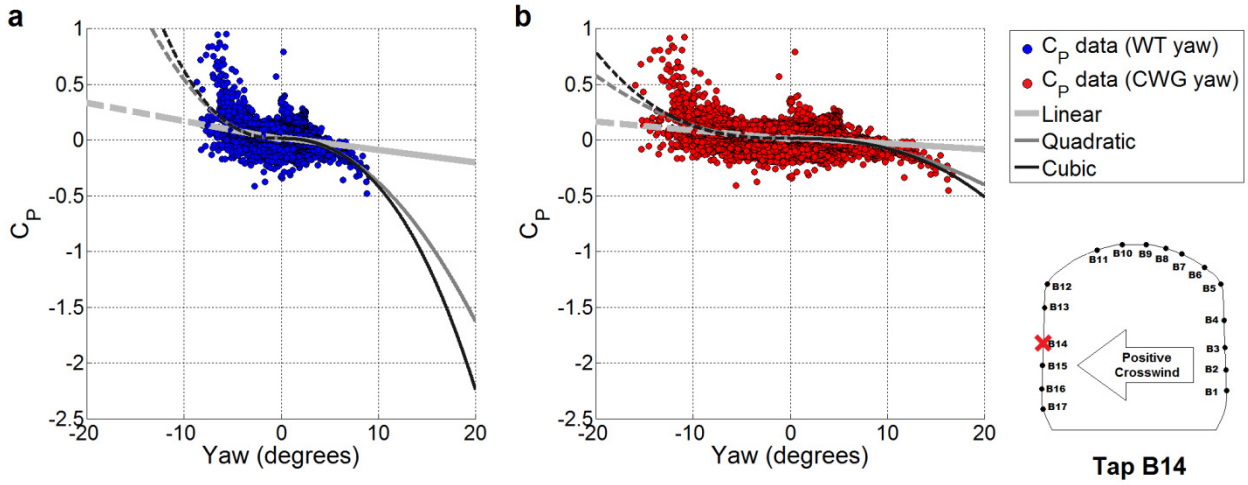

Figure K.1.14 - Scatter plots of $C_{P_k}(t)$ against yaw angle and best fit curves for tap B14 for (a) WT and (b) CWG yaw angle calculation methodologies.

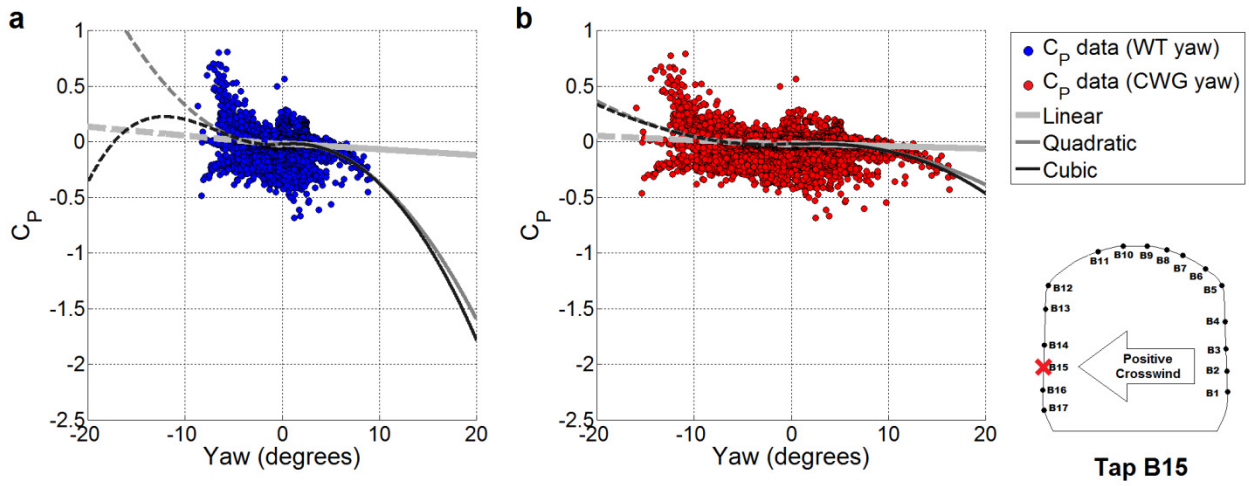

Figure K.1.15 - Scatter plots of $C_{P_k}(t)$ against yaw angle and best fit curves for tap B15 for (a) WT and (b) CWG yaw angle calculation methodologies.

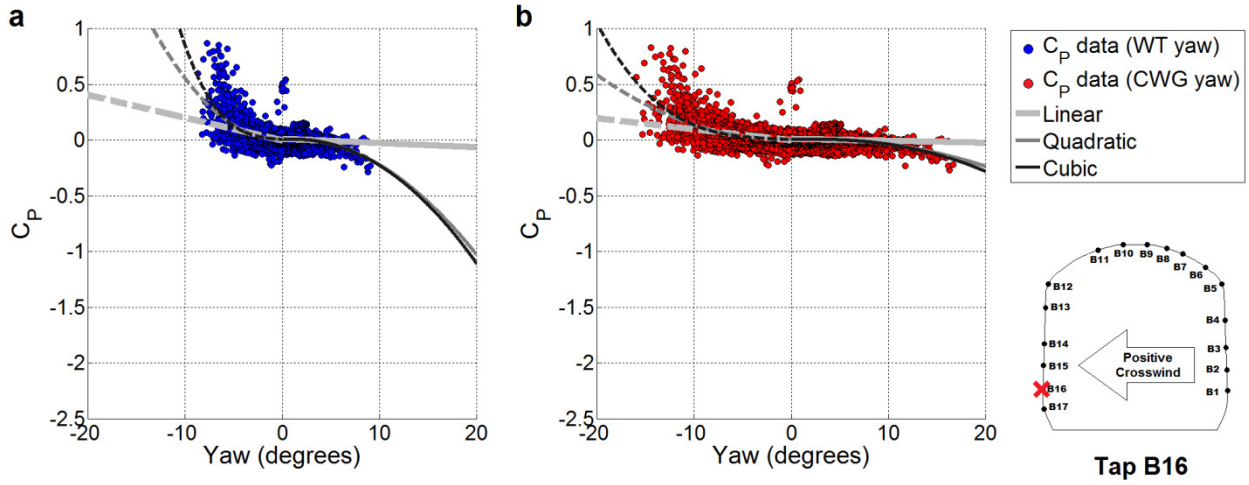

Figure K.1.16 - Scatter plots of $C_{P_k}(t)$ against yaw angle and best fit curves for tap B16 for (a) WT and (b) CWG yaw angle calculation methodologies.

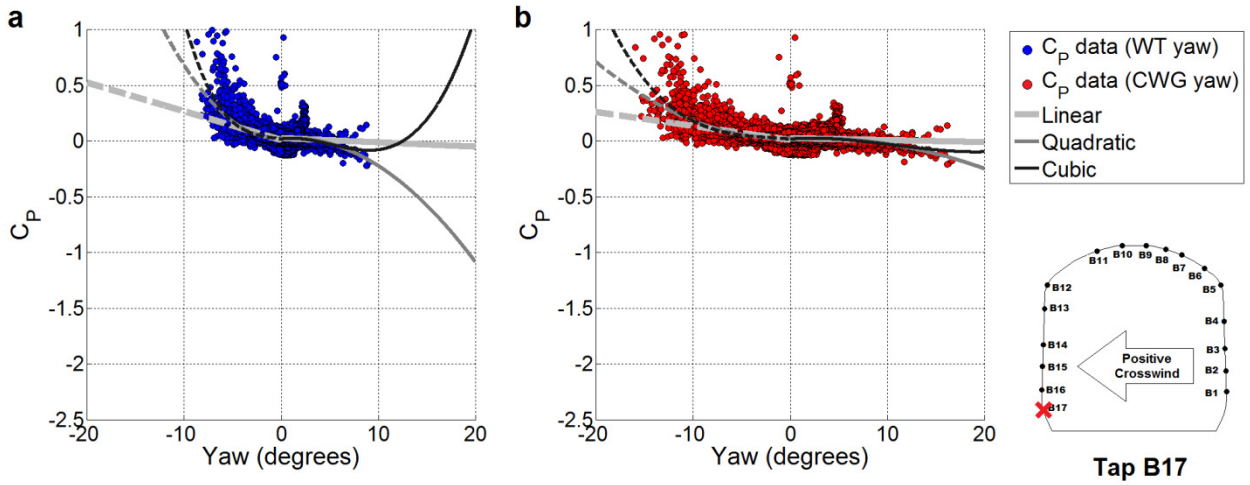

Figure K.1.17 - Scatter plots of $C_{P_k}(t)$ against yaw angle and best fit curves for tap B17 for (a) WT and (b) CWG yaw angle calculation methodologies.

K.3.2 Discussion of scatter plot results

The first point of note from figures K.1.1 to K.1.17 is that the differences between the WT and CWG yaw angle methodologies results in a "stretch" in the x-axis when using the CWG data to calculate yaw angle. This is unsurprising given that the yaw angle calculated from the CWG data was approximately double that of the yaw angle calculated from the WT data. It is also worth noting that the magnitudes of pressure coefficients show little variation, which is also unsurprising given the low yaw angle range considered and hence lower contribution of crosswind velocity to U_{res} which was used to normalised the pressures to coefficients. The second point to note from figures K.1.1 to K.1.17 is that the cubic and quadratic best fit curves are very much unreliable with respect to extrapolation outside of the ranges of yaw angles into which the majority of the data falls. For example, the cubic best fit on figure K.1.2 (a) - tap B2 - shows that during positive yaw angles this pressure tap which is on the

windward side will sharply decrease at yaw angles of 20° or higher, which cannot be true in reality. Figure K.1.14 (a) shows that when tap B14 is considered at negative yaw angles (i.e., tap B14 is on the windward side wall) that both the quadratic and cubic best fit polynomials show a sharp increase in pressure coefficient at yaw angles of greater magnitude than 10°, which would result in the impossible phenomena of a pressure coefficient greater than unity. Care should therefore be taken when interpreting the R^2 values in tables K.2.1 and K.2.2, as a higher value of R^2 does not necessarily correspond to a better best fit model.

Analysis in section 11.2 therefore considers the linear best fits only, though it is acknowledged (see wind tunnel data in section K.2.3) that the linear model does not truly represent the variation of C_P with respect to yaw angle. It should also be noted that pressure taps B4, B7 and B2 show a much lower magnitude of $C_{\mathrm{NMT}|1}$ (i.e., linear gradient) than adjacent pressure taps, possibly indicating faults with these tapping positions.

Ideally, if a larger yaw angle range could be considered, more accurate best fit regression models could be developed. However, at the lower train speeds required for higher yaw angles there is not only an increase in experimental error (due to the fractional contribution of error in train speed measurement to actual aerodynamic vehicle speed), but also the limitations of the nose mounted pitot-static probe and nose pressure taps to accurately measure wind velocity and yaw angle at lower train speeds become significant. The pitot probe points in the streamwise direction, and while it has not been assessed, it is expected that the yaw angle sensitivity at very high yaw angles results in large uncertainties in the measurement on the streamwise velocity (via the dynamic pressure). The physical flow field around the train nose is also affected by yaw angle, and it is believed that at yaw angles of 30° or higher that a separation occurs at the leading edge/side of the train nose, resulting in the

yaw angle calculation from the pressure differential of the nose taps to become invalid. Additionally, given that the pitot static probe does not record a true dynamic pressure due to its position, there may be speed sensitivity of this conversion factor at low train speeds that could potentially result in high errors, though this is purely speculative without further work (such as a set of detailed wind tunnel tests/CFD simulations to consider the effects of train/wind speed on the dynamic pressure recorded by the pitot-static probe). Therefore the linear best fit models have been assumed to be sufficiently accurate within the low yaw angle ranges considered, given that they do not result in entirely unrealistic behaviour, though extrapolation of the data must be treated cautiously.

K.3.3 Tables of regression coefficients and values of R^2 and RMSE

The coefficients of each regression model (defined in equations K.1 to K.3 are presented in tables K.1.1 and K.1.2 for positive and negative yaw angles when data was processed with the WT yaw coefficients and K.2.1 and K.2.2 show the coefficients when the data was processed with the yaw coefficients obtained from the TRAIN rig CWG tests. The R^2 values are compared in tables K.3.1 and K.3.2, and the root mean square error (RMSE) is compared between the positive and negative yaw angles for each tap (based on WT yaw coefficients) - the RMSE of data obtained from the TRAIN rig CWG yaw coefficients is virtually identical. Note that the values of RMSE for the linear regression model have been used in the error analysis presented in section F.6.

Table K.1.1 - Coefficients of best fit curves for NMT scatter plots based on yaw angle calculated from wind tunnel coefficients for each pressure tap at positive yaw.

Tap	Linear		Quadratic			Cubic			
	$C_{NMT\|1}$ (deg^{-1} $\times10^{-2}$)	$C_{NMT\|0}$ (deg^{0} $\times10^{-2}$)	$C_{NMT\|2}$ (deg^{-2} $\times10^{-2}$)	$C_{NMT\|1}$ (deg^{-1} $\times10^{-2}$)	$C_{NMT\|0}$ (deg^{0} $\times10^{-2}$)	$C_{NMT\|3}$ (deg^{-3} $\times10^{-2}$)	$C_{NMT\|2}$ (deg^{-2} $\times10^{-2}$)	$C_{NMT\|1}$ (deg^{-1} $\times10^{-2}$)	$C_{NMT\|0}$ (deg^{0} $\times10^{-2}$)
B1	0.818	0.557	0.171	0.212	0.864	-0.017	0.305	-0.027	0.943
B2	0.659	-2.020	0.237	-0.182	-1.593	-0.035	0.523	-0.691	-1.425
B3	0.783	-0.551	0.132	0.314	-0.313	-0.012	0.229	0.141	-0.256
B4	0.355	-0.235	0.140	-0.142	0.017	0.003	0.114	-0.096	0.002
B5	-0.285	1.368	-0.256	0.625	0.906	-0.059	0.226	-0.234	1.190
B6	-2.097	-4.849	-1.199	2.157	-7.009	-0.064	-0.680	1.233	-6.705
B7	-0.316	-1.695	-0.282	0.684	-2.203	0.003	-0.306	0.727	-2.217
B8	-1.737	-3.460	-0.933	1.575	-5.142	-0.044	-0.577	0.940	-4.933
B9	-1.865	-4.395	-0.901	1.333	-6.019	-0.035	-0.617	0.827	-5.852
B10	-1.451	-4.417	-0.850	1.566	-5.949	-0.012	-0.751	1.388	-5.891
B11	-1.172	-6.194	-0.334	0.014	-6.796	-0.139	0.792	-1.992	-6.134
B12	-0.491	-3.063	-0.777	2.268	-4.464	-0.007	-0.722	2.169	-4.432
B13	-0.736	-6.406	-0.535	1.164	-7.371	-0.068	0.020	0.175	-7.045
B14	-1.116	2.263	-0.430	0.411	1.487	-0.012	-0.330	0.233	1.546
B15	-0.531	-1.500	-0.445	1.048	-2.302	-0.004	-0.414	0.993	-2.284
B16	-0.379	1.072	-0.290	0.650	0.549	-0.002	-0.276	0.626	0.557
B17	-0.385	2.622	-0.313	0.724	2.059	0.044	-0.670	1.360	1.849

Table K.1.2 - Coefficients of best fit curves for NMT scatter plots based on yaw angle calculated from wind tunnel coefficients for each pressure tap at negative yaw.

Tap	Linear		Quadratic			Cubic			
	$C_{\mathrm{NMT}\|1}$ (deg^{-1} $\times 10^{-2}$)	$C_{\mathrm{NMT}\|0}$ (deg^{0} $\times 10^{-2}$)	$C_{\mathrm{NMT}\|2}$ (deg^{-2} $\times 10^{-2}$)	$C_{\mathrm{NMT}\|1}$ (deg^{-1} $\times 10^{-2}$)	$C_{\mathrm{NMT}\|0}$ (deg^{0} $\times 10^{-2}$)	$C_{\mathrm{NMT}\|3}$ (deg^{-3} $\times 10^{-2}$)	$C_{\mathrm{NMT}\|2}$ (deg^{-2} $\times 10^{-2}$)	$C_{\mathrm{NMT}\|1}$ (deg^{-1} $\times 10^{-2}$)	$C_{\mathrm{NMT}\|0}$ (deg^{0} $\times 10^{-2}$)
B1	0.881	0.929	-0.044	0.699	0.844	0.052	0.378	1.501	1.082
B2	1.408	-1.040	-0.333	0.014	-1.691	0.086	0.369	1.348	-1.294
B3	1.290	0.196	-0.426	-0.490	-0.636	0.078	0.209	0.715	-0.278
B4	0.665	0.190	-0.078	0.338	0.038	0.035	0.205	0.875	0.197
B5	3.017	1.855	-0.651	0.294	0.583	0.175	0.774	3.001	1.388
B6	2.309	-5.404	-0.856	-1.272	-7.076	0.175	0.574	1.444	-6.268
B7	1.263	-1.622	-0.281	0.087	-2.171	0.087	0.426	1.430	-1.772
B8	2.485	-3.820	-0.635	-0.170	-5.060	0.123	0.368	1.735	-4.493
B9	3.441	-4.272	-0.937	-0.480	-6.103	0.145	0.247	1.769	-5.434
B10	4.645	-4.046	-1.038	0.302	-6.074	0.188	0.499	3.222	-5.206
B11	5.174	-4.664	-1.226	0.046	-7.058	0.270	0.979	4.234	-5.813
B12	3.849	-2.743	-0.972	-0.216	-4.641	0.257	1.125	3.766	-3.457
B13	2.014	-6.259	-0.562	-0.336	-7.356	0.147	0.640	1.947	-6.678
B14	-1.630	0.804	0.628	0.997	2.031	-0.022	0.445	0.650	1.927
B15	-0.802	-2.509	0.465	1.144	-1.601	0.039	0.785	1.753	-1.420
B16	-2.035	-0.198	0.596	0.459	0.966	-0.087	-0.118	-0.897	0.563
B17	-2.577	1.091	0.693	0.323	2.445	-0.121	-0.295	-1.554	1.887

Table K.2.1 - Coefficients of best fit curves for NMT scatter plots based on yaw angle calculated from TRAIN rig CWG coefficients for each pressure tap at positive yaw.

Tap	Linear		Quadratic			Cubic			
	$C_{\mathrm{NMT}\|1}$ (deg^{-1} $\times 10^{-2}$)	$C_{\mathrm{NMT}\|0}$ (deg^{0} $\times 10^{-2}$)	$C_{\mathrm{NMT}\|2}$ (deg^{-2} $\times 10^{-2}$)	$C_{\mathrm{NMT}\|1}$ (deg^{-1} $\times 10^{-2}$)	$C_{\mathrm{NMT}\|0}$ (deg^{0} $\times 10^{-2}$)	$C_{\mathrm{NMT}\|3}$ (deg^{-3} $\times 10^{-2}$)	$C_{\mathrm{NMT}\|2}$ (deg^{-2} $\times 10^{-2}$)	$C_{\mathrm{NMT}\|1}$ (deg^{-1} $\times 10^{-2}$)	$C_{\mathrm{NMT}\|0}$ (deg^{0} $\times 10^{-2}$)
B1	0.395	0.551	0.049	0.057	0.895	-0.003	0.089	-0.079	0.983
B2	0.318	-2.020	0.068	-0.150	-1.545	-0.005	0.141	-0.400	-1.382
B3	0.380	-0.560	0.039	0.114	-0.290	-0.002	0.066	0.021	-0.229
B4	0.169	-0.233	0.038	-0.095	0.035	0.000	0.033	-0.075	0.022
B5	-0.131	1.356	-0.065	0.319	0.898	-0.010	0.085	-0.195	1.232
B6	-0.974	-4.903	-0.320	1.231	-7.144	-0.013	-0.117	0.534	-6.693
B7	-0.141	-1.714	-0.076	0.380	-2.243	-0.001	-0.061	0.330	-2.211
B8	-0.810	-3.499	-0.250	0.911	-5.249	-0.010	-0.105	0.415	-4.927
B9	-0.873	-4.429	-0.242	0.795	-6.125	-0.008	-0.118	0.369	-5.849
B10	-0.671	-4.457	-0.229	0.904	-6.059	-0.005	-0.148	0.628	-5.881
B11	-0.553	-6.202	-0.082	0.012	-6.776	-0.022	0.257	-1.147	-6.025
B12	-0.204	-3.119	-0.207	1.222	-4.569	-0.004	-0.142	0.998	-4.425
B13	-0.330	-6.442	-0.139	0.626	-7.413	-0.012	0.045	-0.001	-7.006
B14	-0.534	2.258	-0.117	0.275	1.435	-0.004	-0.062	0.086	1.558
B15	-0.240	-1.526	-0.119	0.581	-2.361	-0.003	-0.079	0.445	-2.272
B16	-0.176	1.059	-0.078	0.363	0.511	-0.002	-0.055	0.285	0.561
B17	-0.181	2.610	-0.088	0.423	1.997	0.005	-0.165	0.688	1.824

Table K.2.2 - Coefficients of best fit curves for NMT scatter plots based on yaw angle calculated from TRAIN rig CWG coefficients for each pressure tap at negative yaw.

Tap	Linear		Quadratic			Cubic			
	$C_{\mathrm{NMT}\|1}$ ($\deg^{-1}$ $\times10^{-2}$)	$C_{\mathrm{NMT}\|0}$ ($\deg^{0}$ $\times10^{-2}$)	$C_{\mathrm{NMT}\|2}$ ($\deg^{-2}$ $\times10^{-2}$)	$C_{\mathrm{NMT}\|1}$ ($\deg^{-1}$ $\times10^{-2}$)	$C_{\mathrm{NMT}\|0}$ ($\deg^{0}$ $\times10^{-2}$)	$C_{\mathrm{NMT}\|3}$ ($\deg^{-3}$ $\times10^{-2}$)	$C_{\mathrm{NMT}\|2}$ ($\deg^{-2}$ $\times10^{-2}$)	$C_{\mathrm{NMT}\|1}$ ($\deg^{-1}$ $\times10^{-2}$)	$C_{\mathrm{NMT}\|0}$ ($\deg^{0}$ $\times10^{-2}$)
B1	0.437	0.950	-0.012	0.340	0.859	0.007	0.098	0.741	1.095
B2	0.684	-1.029	-0.088	-0.034	-1.703	0.013	0.108	0.680	-1.282
B3	0.625	0.199	-0.113	-0.294	-0.663	0.013	0.083	0.419	-0.243
B4	0.327	0.202	-0.021	0.155	0.041	0.005	0.057	0.439	0.208
B5	1.476	1.889	-0.174	0.064	0.565	0.027	0.240	1.572	1.453
B6	1.104	-5.415	-0.224	-0.719	-7.125	0.028	0.207	0.852	-6.199
B7	0.613	-1.612	-0.074	0.013	-2.175	0.013	0.127	0.743	-1.745
B8	1.202	-3.807	-0.169	-0.172	-5.096	0.020	0.141	0.956	-4.432
B9	1.664	-4.257	-0.251	-0.376	-6.171	0.024	0.120	0.974	-5.376
B10	2.258	-4.006	-0.280	-0.011	-6.136	0.032	0.209	1.767	-5.088
B11	2.513	-4.626	-0.327	-0.141	-7.115	0.044	0.355	2.343	-5.652
B12	1.868	-2.717	-0.257	-0.215	-4.671	0.040	0.354	2.010	-3.361
B13	0.967	-6.258	-0.147	-0.224	-7.375	0.023	0.211	1.080	-6.607
B14	0.437	0.950	-0.012	0.340	0.859	0.007	0.098	0.741	1.095
B15	0.684	-1.029	-0.088	-0.034	-1.703	0.013	0.108	0.680	-1.282
B16	0.625	0.199	-0.113	-0.294	-0.663	0.013	0.083	0.419	-0.243
B17	0.327	0.202	-0.021	0.155	0.041	0.005	0.057	0.439	0.208

Table K.3.1 - R^2 (as percentage) for positive yaw angle best fit models for yaw angles calculated using both WT and CWG coefficients.

Tap	R^2 based on WT yaw calculation (%)				R^2 based on CWG yaw calculation (%)		
	Linear	Quadratic	Cubic		Linear	Quadratic	Cubic
B1	6.5	7.5	7.6		6.2	7.3	7.4
B2	1.8	2.6	2.7		1.7	2.6	2.6
B3	5.3	5.8	5.8		5.1	5.7	5.7
B4	3.7	5.8	5.8		3.5	5.6	5.6
B5	0.4	1.4	1.7		0.3	1.2	1.6
B6	17.3	37.5	37.8		15.5	35.5	36.2
B7	1.4	5.4	5.4		1.1	5.1	5.1
B8	11.1	22.6	22.8		10.0	21.3	21.6
B9	11.2	20.5	20.6		10.1	19.3	19.5
B10	8.1	18.0	18.0		7.1	16.8	16.9
B11	1.6	2.1	2.5		1.4	1.8	2.4
B12	0.9	8.8	8.8		0.6	8.2	8.3
B13	4.5	12.9	13.7		3.7	11.4	12.5
B14	5.6	8.6	8.6		5.2	8.2	8.3
B15	1.1	4.0	4.0		0.9	3.7	3.7
B16	1.4	4.4	4.4		1.2	4.2	4.2
B17	1.3	4.3	4.7		1.1	4.4	4.6

Table K.3.2 - R^2 (as percentage) for negative yaw angle best fit models for yaw angles calculated using both WT and CWG coefficients.

Tap	R^2 based on WT yaw calculation (%)				R^2 based on CWG yaw calculation (%)		
	Linear	Quadratic	Cubic		Linear	Quadratic	Cubic
B1	13.3	15.6	16.3		15.4	15.5	16.2
B2	19.2	25.7	26.7		12.7	14.9	15.6
B3	25.5	26.6	27.6		18.1	24.5	25.7
B4	31.1	35.6	37.1		24.7	25.8	26.8
B5	29.2	41.6	43.9		30.3	34.8	36.4
B6	30.4	35.0	37.0		27.4	39.6	42.5
B7	33.0	39.6	40.8		29.0	33.5	35.6
B8	38.7	47.5	48.5		31.5	38.1	39.6
B9	40.9	47.1	48.1		37.1	46.1	47.4
B10	36.3	42.5	43.9		39.5	45.9	47.2
B11	40.4	48.4	50.9		34.8	41.1	42.9
B12	32.3	40.0	42.4		38.9	46.8	49.6
B13	11.5	16.7	16.7		30.6	38.1	41.0
B14	2.5	5.0	5.1		10.6	16.0	16.1
B15	28.0	35.4	36.2		2.3	4.9	4.9
B16	38.2	46.7	47.8		26.8	34.4	35.5
B17	13.3	15.6	16.3		36.8	45.4	47.1

Table K.4 - Comparison of RMSE for positive and negative regression models based on yaw calculation from WT coefficients.

Tap	RMSE based on WT yaw calculation for positive yaw (C_P)			RMSE based on WT yaw calculation for negative yaw (C_P)		
	Linear	Quadratic	Cubic	Linear	Quadratic	Cubic
B1	0.026	0.026	0.026	0.023	0.023	0.023
B2	0.041	0.041	0.041	0.041	0.040	0.040
B3	0.028	0.028	0.028	0.030	0.029	0.028
B4	0.015	0.015	0.015	0.013	0.013	0.013
B5	0.040	0.040	0.040	0.051	0.049	0.048
B6	0.038	0.033	0.033	0.041	0.037	0.036
B7	0.022	0.022	0.022	0.022	0.021	0.021
B8	0.041	0.038	0.038	0.040	0.038	0.038
B9	0.044	0.042	0.042	0.049	0.045	0.045
B10	0.041	0.039	0.039	0.063	0.060	0.059
B11	0.077	0.077	0.077	0.078	0.074	0.073
B12	0.044	0.042	0.042	0.053	0.049	0.048
B13	0.029	0.027	0.027	0.033	0.031	0.031
B14	0.038	0.038	0.038	0.051	0.050	0.050
B15	0.042	0.041	0.041	0.057	0.056	0.056
B16	0.026	0.026	0.026	0.037	0.035	0.035
B17	0.028	0.028	0.028	0.037	0.034	0.034

K.4 Wind tunnel data regression analysis

This section briefly considers the wind tunnel data in order to investigate the accuracy of extrapolation from the limited range of yaw angles obtained at full scale. The wind tunnel data was formed by interpolation of the two loops of pressure taps either side of the position of the loop on the NMT. Figure K.2.1 shows the pressure coefficients of each pressure tap across the yaw angle range. Key regions of the train (the windward and leeward side walls, the roof and the windward wall-roof corner) - have been marked by different marker shapes and odd numbered pressure taps have been shown as dashed solely for simplicity of visualisation.

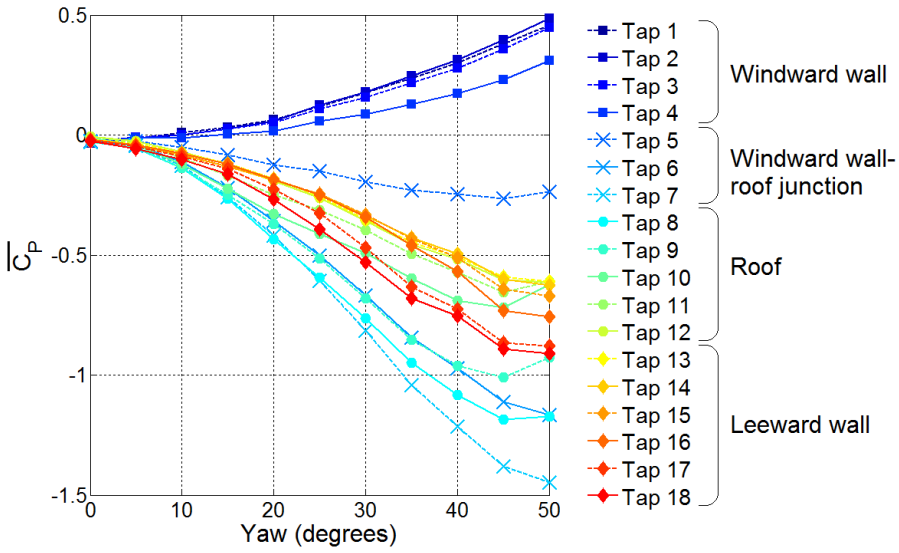

Figure K.2.1 - Wind tunnel data - mean pressure coefficient for each tap at NMT loop position across yaw angle range of 0° - 50°.

Regression analysis was undertaken for each of these wind tunnel taps by fitting polynomials of increasing order to the values of C_P across the entire yaw angle range (0° - 50°). The R^2 values of each tap for increasing polynomial order are shown on figure K.2.2, and this analysis suggests that a 3rd or 4th order polynomial most accurately describes the variation of C_P with yaw angle for the majority of the pressure taps, though the windward wall taps appear to follow a 2nd order polynomial. Figure K.2.2 also shows that a linear regression model is less appropriate for the windward wall taps ($R^2 < 0.95$) than the pressure taps across the roof and leeward side wall ($R^2 > 0.95$).

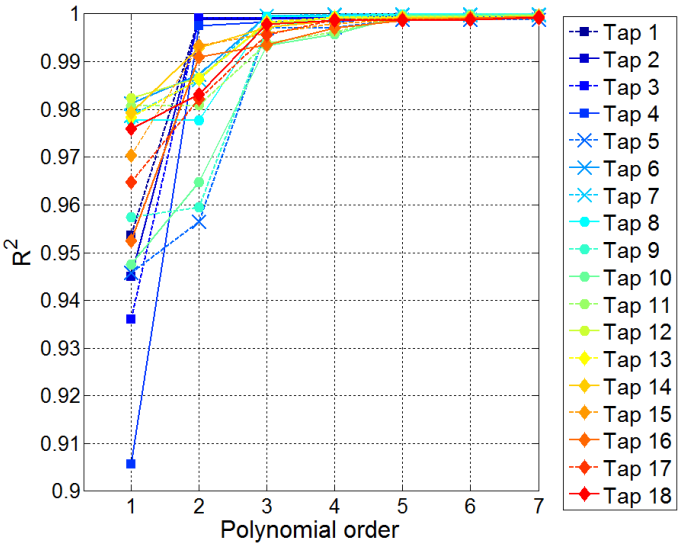

Figure K.2.2 - Values of R^2 for wind tunnel loop taps for best fit polynomials of increasing order (1 to 7).

In order to consider the accuracy of extrapolation from a data set limited to low yaw angles (as is the case for the NMT), best fit curves (linear, quadratic and cubic) were fit to the wind tunnel data at yaw angles of 0° - 15° for pressure taps representative of the different loop regions. Figure K.2.3 shows the actual mean pressure coefficients for these taps at the yaw

angle range of 0° to 30° and the three best fit curves based on the wind tunnel data only within the yaw angle range of 0° to 15°. The main point of figure K.2.3 is to show that there is no consistency between which best fit model works best for each tap - for example a cubic best fit worked well on tap 6, but resulted in large error and unrealistic behaviour on taps 3 and 10. It has therefore been concluded that it is not possible to extrapolate from a low yaw angle range with any confidence since quadratic and cubic regression models may predict very unrealistic phenomena, and linear regression models do not account for the polynomial nature of the variation in Cp with yaw angle for individual pressure taps. The possibility of development of regression models based on the wind tunnel data that could be applied to the NMT has not been explored in this study.

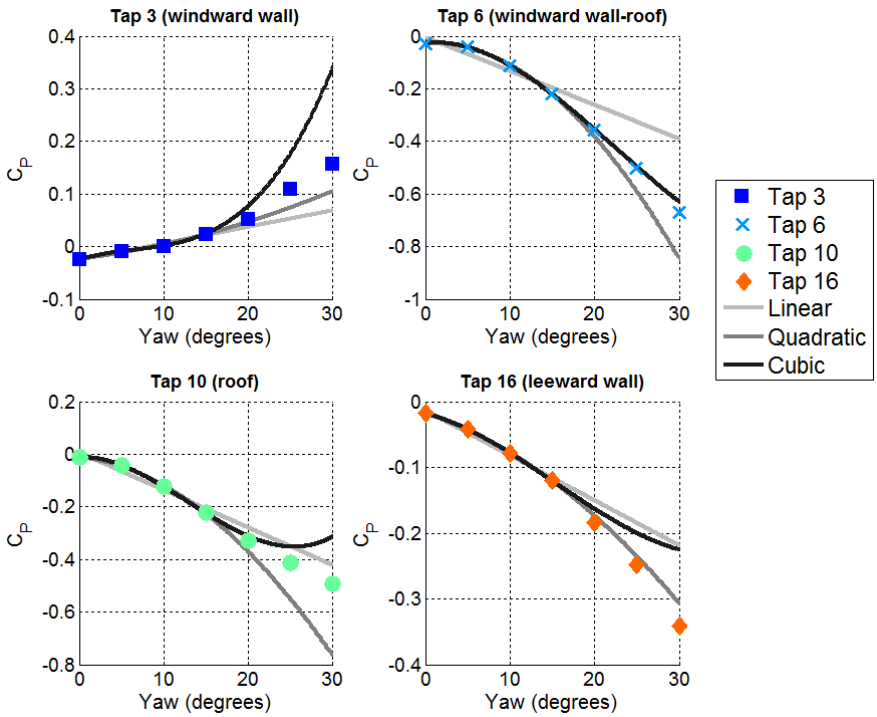

Figure K.2.3 - Mean pressure coefficients at yaw angles between 0° and 30° and regression models fitted to wind tunnel data at for yaw angles of 0° to 15° (i.e., regression curves show extrapolation at yaw angles greater than 15°) for key pressure taps.

K.5 Formed pressure distributions

Distributions of pressures around the loop were formed from the three regression models, and are shown in figures K.3.1 to K.3.4 at yaw angles up to 25°. Each of the figures shows the wind tunnel data and the three regression models. Figure K.3.1 shows the positive yaw range for the data obtained from the WT coefficients and K.3.2 shows the negative yaw angles obtained from the WT coefficients. Figures K.3.3 and K.3.4 are of the same format but obtained from the TRAIN rig CWG yaw coefficients. Note that the tap numbers start with tap B17 on the LHS of the x-axis and tap B1 is on the RHS of the x-axis.

There are two main points to note from figure K.3.1 - firstly that the linear regression model most closely matches the wind tunnel data, and that the overall pressure distribution at full scale shows the expected behaviour - a positive pressure on the windward side, a large suction peak at the windward wall-roof junction and a negative pressure across the roof and leeward side. The quadratic and cubic models show much larger magnitudes of pressure coefficients than the wind tunnel data and linear regression model and as previously discussed show unrealistic phenomena when data is extrapolated (i.e., yaw angles above 10°). The second point to note is that, at full scale, certain pressure taps show very little variation with yaw - this can be seen on figure 3.1 (b) at x = 4.1 m (tap B7). If the scatter graph of this pressure tap is compared to the adjacent pressure taps (as in figures K.1.6 to K.1.8) the scatter of pressure coefficients across the yaw angle range is lower resulting in an almost zero linear gradient of pressure against yaw - it is believed that tap B7 was faulty throughout the course of the NMT tests and this tap has been disregarded from all subsequent analysis. Tap B4 also shows very little variation with yaw angle for both positive and negative yaw angles, and was also discarded from subsequent analysis in chapter 11. Section F.6.3 considers the total errors of

each of the loop taps, and shows that taps B7 and B4 have much lower total errors than adjacent pressure taps, which could imply that the taps were faulty (possibly blocked or unsealed pneumatic connections) resulting in lower mean pressure coefficients (at a given yaw angle) and hence a lower total error. Other taps also show unusual behaviour, for example tap B6 on figure K.3.1b shows a much lower pressure coefficient than adjacent taps, however these issues appear to be specific to the regression model and also whether or not positive or negative yaw angles were considered.

A significant difference is observed between the positive and negative yaw angles, for example a comparison of the linear regression models shown in figures K.3.1 and K.3.2 shows that when negative yaw angles are considered, the pressure distribution matches qualitatively, however at negative yaw angles the magnitudes of pressures are roughly double those at positive yaw angles. This is also true for the data obtained from the TRAIN rig CWG yaw coefficients. The values of R2 (tables K.3.1 and K.3.2) also show significant differences where the negative yaw angles show a much higher value of R^2, though the values of RMSE are very similar between both positive and negative yaw angles. The distribution of quantity of data at different yaw angles was considered and showed a normal distribution though there was possibly a slight skew towards positive yaw angles (see figure 11.1), though given the low yaw angle range and possibility of high uncertainty in estimation of yaw angle this slight positive yaw bias is not a conclusive finding. The scatter plots and regression models (figures K.1.1 to K.1.17) show an asymmetry between positive and negative yaw angles and negative yaw angles have a larger degree of scatter at negative yaw angles of magnitude 5° and greater. One possible explanation is that a lot of the UK rail network is within cuttings and hence quite shielded, and regions of track that are not in cuttings often have trees and fences either side of the tracks, and most of the rail network is at least double track. In the UK trains travel on the

LHS track, therefore the "windward" side (at positive yaw) is closer to the cutting side or fences/trees and thus potentially more shielded than the leeward side. Negative yaw angles may have more data within this "partially shielded" scenario. Therefore, if there are higher magnitude turbulent fluctuations in the ABL at negative yaw angles in the partially shielded scenario, this may explain the higher degree of scatter and higher magnitude of the linear regression gradients at negative yaw angles. Even so, the fact that negative yaw angles effectively show double the pressures at positive yaw angles is concerning as it was expected that the yaw angle measured by the nose taps would represent the magnitude of the crosswind on the train, and therefore if infrastructure effects are the cause of this large discrepancy that there would be a lower quantity of data at higher negative yaw angles. This discrepancy may also be due to inaccuracy in the calculation of yaw angles due to undetected issues (such as offsets or blockage) with one of the nose pressure taps, though nothing in the data used for the scatter graphs suggests any issues with the nose taps.

Finally, when a comparison is made between the pressure distributions obtained from the WT and CWG yaw coefficients (i.e., comparing figures K.3.1 to K.3.3 and figures K.3.2 to K.3.4) similarities can be noted - the faulty pressure taps have the same effects on the pressure distribution and that the qualitative description of the pressure distribution is consistent. The main difference is that the CWG data shows lower magnitudes of pressure coefficient than the data obtained from the WT yaw coefficients.

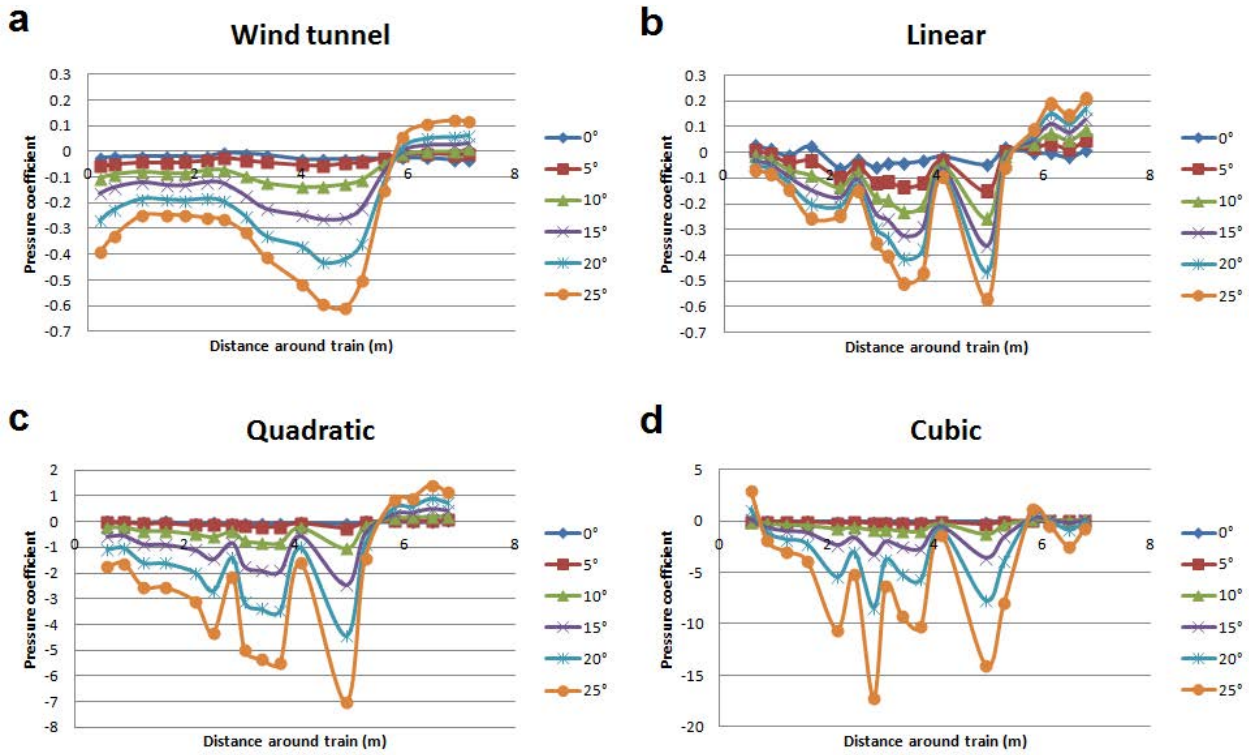

Figure K.3.1 - Comparison of pressure distribution from (a) wind tunnel data, and (b) linear, (c) quadratic and (d) cubic regression models using WT yaw coefficients at positive yaw angles.

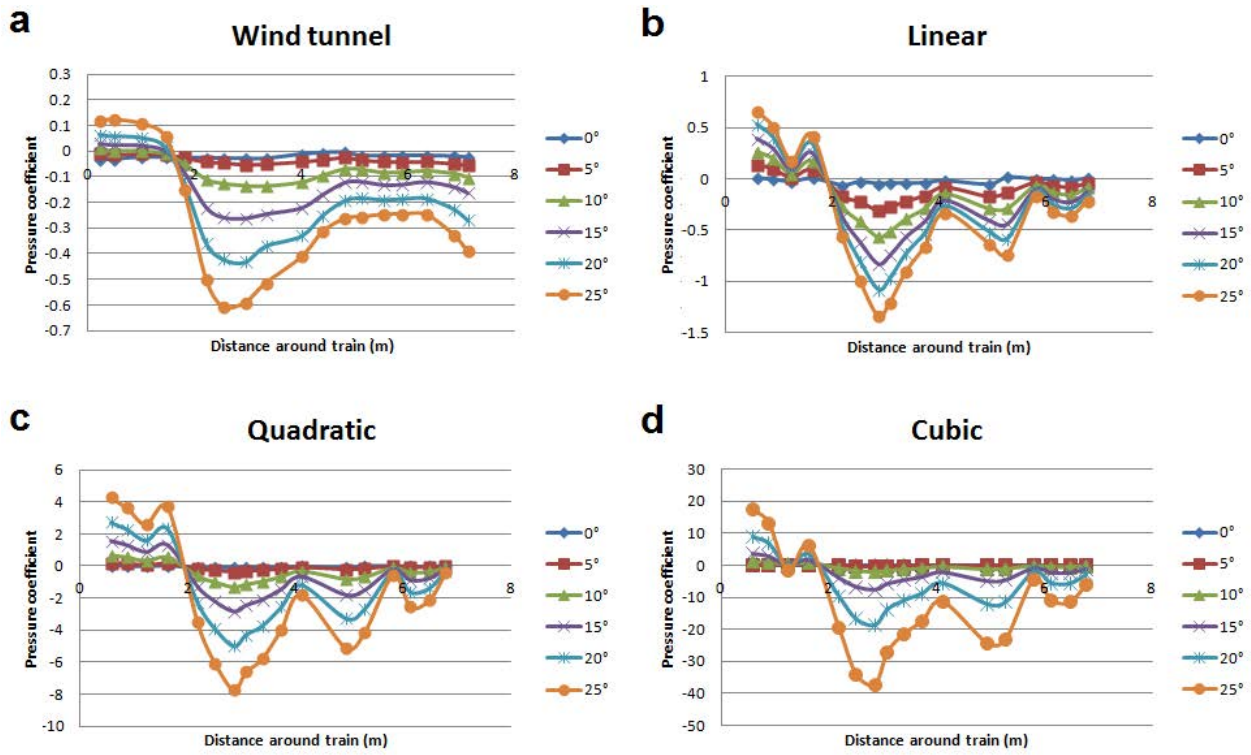

Figure K.3.2 - Comparison of pressure distribution from (a) wind tunnel data, and (b) linear, (c) quadratic and (d) cubic regression models using WT yaw coefficients at negative yaw angles.

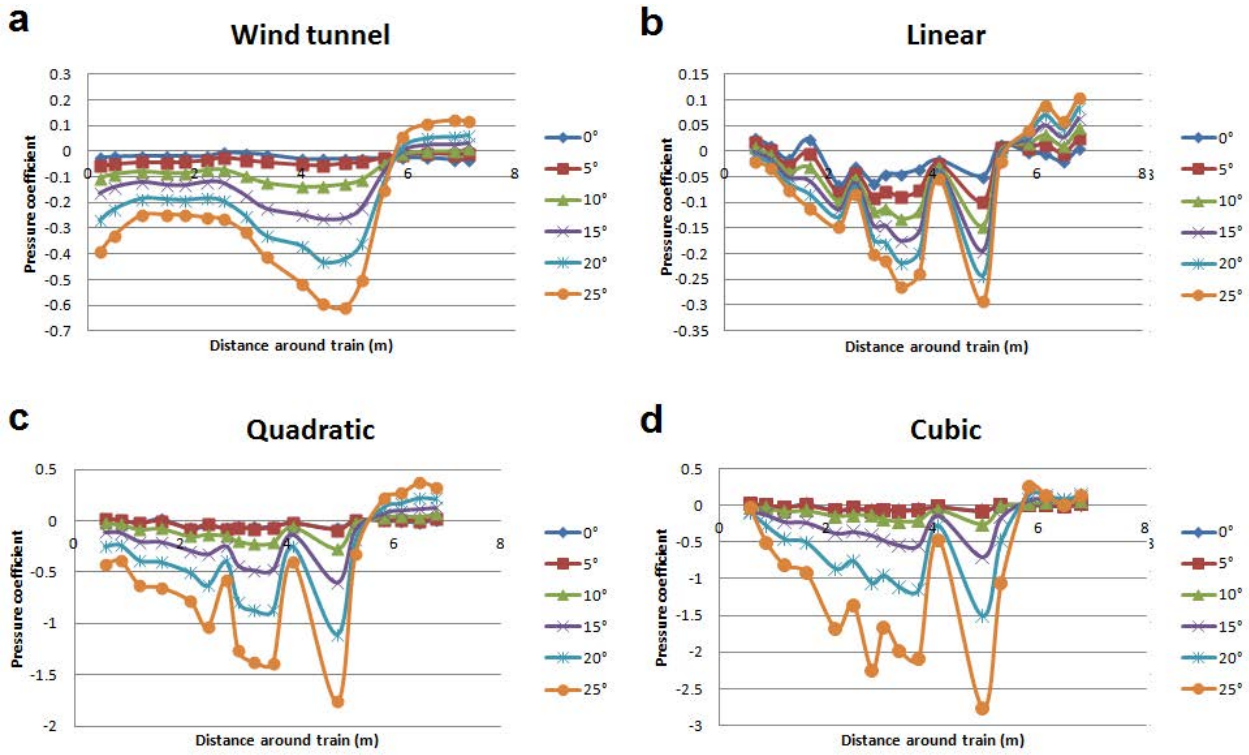

Figure K.3.3 - Comparison of pressure distribution from (a) wind tunnel data, and (b) linear, (c) quadratic and (d) cubic regression models using CWG yaw coefficients at positive yaw angles.

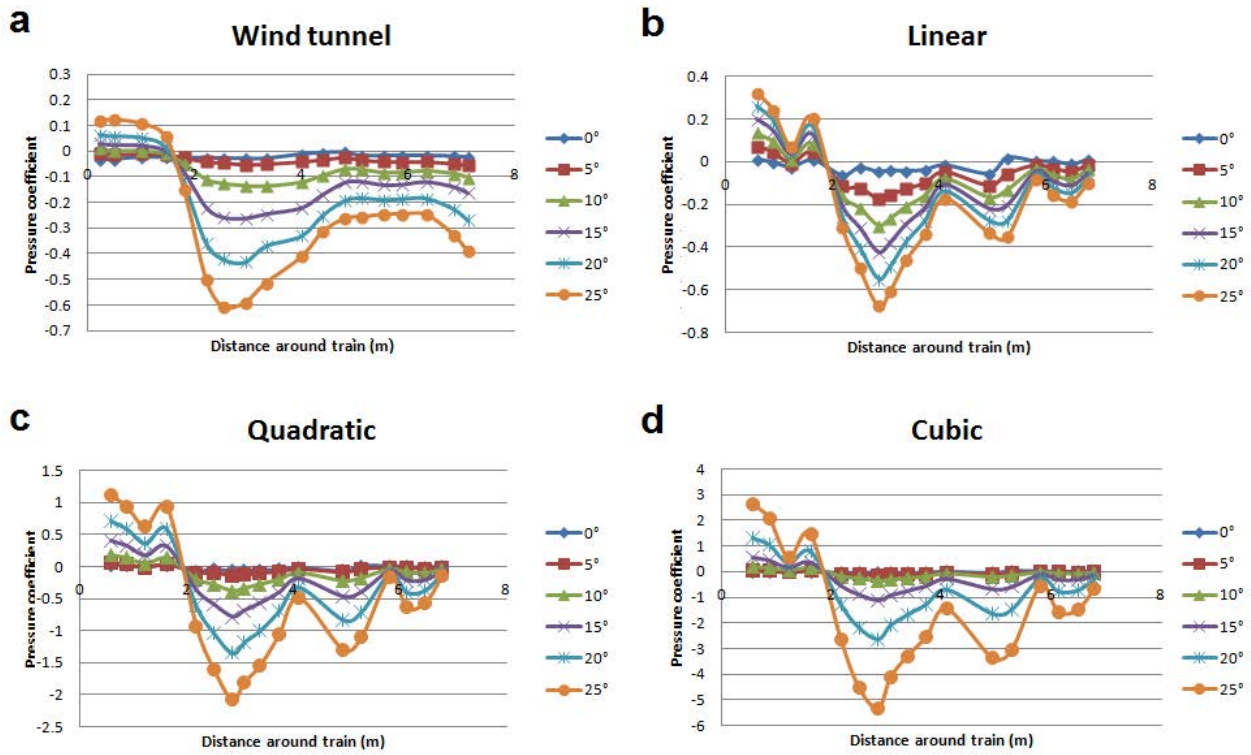

Figure K.3.4 - Comparison of pressure distribution from (a) wind tunnel data, and (b) linear, (c) quadratic and (d) cubic regression models using CWG yaw coefficients at negative yaw angles.

K.5.1 Formed pressure distributions of gusts

Section 10.3.3 introduced the definition of a "gust" which was identified by the yaw angle time history, and section 11.4 showed the pressures and forces for a selection of six gusts. All gusts that were identified were then analysed following the same methodology as described in section 10.3.1 and K.2, and the resulting formed pressure distributions are shown in figure K.4. Note that the gust data was not resampled as the quantity of data was sufficiently low to allow analysis on a desktop PC. Given that the quantity of data used when only considering gusts was lower, only yaw angles of 0° to 15° are considered, and only a linear regression model was considered.

Figure K.4 shows the same qualitative pressure distribution as figures K.3.1 to K.3.4 (considering the linear regression only). It is interesting to note that on figure K.4, in both cases (i.e., both yaw angle calculations) the pressure taps on the leeward wall and roof junction show virtually no dependency on yaw angle - it is believed that this is due to the limitations of the small data quantity of the "gusts" data set. The results in figure K.4 from the WT coefficients show slightly higher pressures than the equivalent data (figure K.3.1) that considered all open air data. This suggests that when all open air data was considered the higher degree of scatter ultimately resulted in lower magnitudes of the linear regression gradients than when gusts were considered. The results obtained from the CWG yaw coefficients compare very favourably between the gust ensemble and all of the open air data (i.e., figure K.3.3) and quite favourably to the wind tunnel data. The quantity of the gusts ensemble cannot be considered exhaustive, but this finding could suggest that analysis of gusts and a smaller data set (that was 100% quality controlled through manual inspection)

yields the most accurate results, and that the TRAIN rig CWG cubic yaw coefficients should be used to calculate yaw angle.

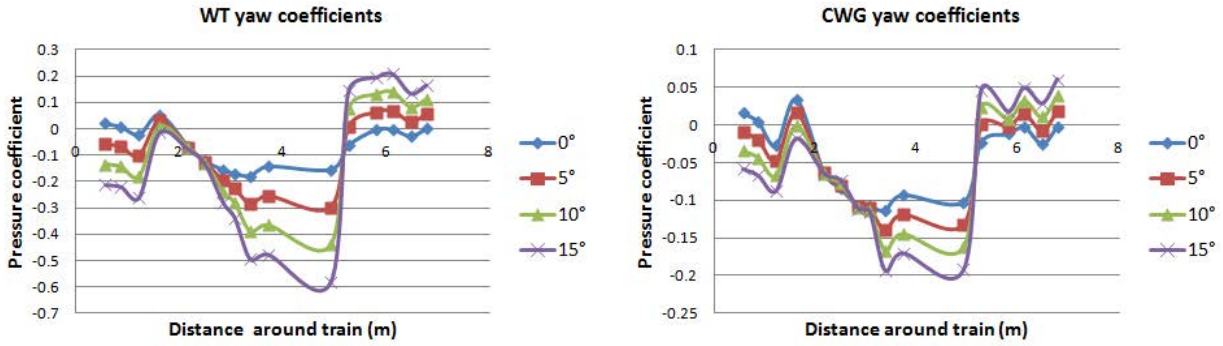

Figure K.4 - Comparison of formed pressure distribution based on linear regression model of gusts. Note that tap B7 has been omitted.

K.6 Closing remarks

From the analysis of the scatter plots from the NMT and analysis of the wind tunnel data the following conclusions can be made:

- The majority of the NMT data is at very low yaw angles, and there is considerable scatter in the data collected.
- Application of a linear regression model to the NMT data is only slightly appropriate and generally results in lower values of R^2 than a quadratic or cubic model, however the advantages of a linear model is that it does not result in unrealistic extrapolation behaviour.

- The wind tunnel data showed that across the yaw angle range of 0° to 50°, the variation of pressure coefficient with respect to yaw angle can be modelled as a cubic best fit for all pressure taps, though windward taps can be modelled with a quadratic best fit. When these models were applied to a limited quantity of wind tunnel data (at yaw angles of 0° to 15°) no single regression model was able to accurately estimate pressure coefficient at yaw angles of 30°, and the same issues were noticed - that quadratic and cubic models can result in unrealistic behaviour.
- When pressure distributions were formed from the scattered data based on the three regression models the linear best fit for the data obtained with the WT yaw coefficients at positive yaw angles showed the closest comparison to the WT pressure distribution. The quadratic and cubic models showed unrealistic phenomena for all cases (positive and negative yaw angles and using the WT or CWG obtained yaw coefficients).
- Negative yaw angles were found to have magnitudes of pressure coefficients that were roughly double the pressure coefficients at positive yaw angles. This may be as a result of infrastructure - at positive yaw the windward side is more likely to be shielded by a cutting or tree line/fence than the leeward wall. Conversely, at negative yaw angles, the windward side of the train is more exposed assuming that the train is on a double track scenario.

APPENDIX L

EPSRC PROJECT INFORMATION

L.1 Introduction

Appendix L contains information from the EPSRC project proposal document for the project "The measurement of train aerodynamic phenomena under operational conditions". All of the text is reproduced *in verbatim* from this document (Baker et al., 2012). The purpose of this appendix is to show how this PhD study fits into the EPSRC funded project. In summary, this PhD study has covered all of the physical experiments undertaken in the EPSRC project. This PhD project has run in parallel with a second PhD study by Justin Morden who undertook the CFD calculations.

L.1.1 Technical information

EPSRC reference number: EP/I03842X/1

Project start date: 01/04/12

Project end date: 31/5/16

L.2 Description of project

L.2.1 Hypothesis

The fundamental hypothesis is that the techniques that have been used to predict aerodynamic effects are likely to predict magnitudes of pressures, velocities, forces etc. that are higher than those observed in practice, where other effects – such as track roughness, variability in meteorological conditions etc. are likely to usually obscure aerodynamic effects to some extent, and because of this some of the current design methodologies are unnecessarily restrictive and conservative.

L.2.2 Aim

To investigate and measure a range of aerodynamic phenomena observed in real train operation, both relative to the train and relative to a fixed point at the trackside, and to compare how such effects match model scale measurements and various types of CFD calculation, and thus to test the validity, or otherwise, of the above hypothesis.

L.2.3 Objectives

a) To carry out a range of conventional physical model tests and computational trials to measure then velocity and pressure field around a Class 43 train, commonly referred to as the HST.

b) To instrument the Network Rail High Speed Measuring Train (NMT - based on Class 43 vehicles) to measure aerodynamic phenomena during its operation on all main line routes in the UK.

c) To carry out a series of measurements at a trackside location on the Midland Main Line, (a route where the Class 43 is widely used), such that the pressure and velocity fields close to such trains can be measured under operational conditions.

d) To compare the results of (a) and (b) to determine the adequacy of the predictions of established test methods to give the cross wind forces, moments, displacements and on-train pressure transients found in operational conditions.

e) To compare the results (a) and (c) to determine the adequacy of predicted slipstream velocities (at the side and underneath the train) and trackside pressure fields with those measured in operational conditions.

f) To thus investigate the fundamental hypothesis outlined above and to develop possible methods in which testing and codification procedures could be changed to make them more adequately reflect operational conditions, and thus to make the design process for new trains less conservative and restrictive.

In addition to addressing the basic hypothesis, the above objectives address a number of issues of direct concern to the UK rail industry (which also have impactions for the travelling public) as follows.

i) Assessment of the adequacy of the CEN codification procedures, based largely on European practice, to the often very different UK railway network (addressed through objectives a-f).

ii) Assessment of the adequacy of current methods for specifying cross wind forces on train, through model scale and measurements and computations with values obtained in train operation (addressed through objectives e and f).

iii) Determination of the range of displacements between pantographs, overhead wires and trackside structures in realistic operational and meteorological conditions, to specify realistic design methods and of the nature of the transient pressure forces experienced by trains in normal operation, both due to passing trains and due to passage through tunnels, and a comparison with the "worst case scenarios" often used in existing design methodology (addressed through objective b).

iv) Determination of the magnitude of train slipstream velocities in operational conditions and an understanding of the nature of the aerodynamic forces on ballast and thus the issue of ballast flight (addressed through objective c).

L.2.3.1 Realisation of objectives in this PhD study

Objective (a) was achieved through undertaking a large number of slipstream measurements at the TRAIN rig, and with a range of ballast heights (see chapters 3 to 5), which can be compared to CFD simulations. Measurements of pressures due to crosswinds were undertaken by RWDI and by this author at the TRAIN rig using the CWG (see chapters 6 to 8).

Objective (b) was achieved (see chapter 9) and the NMT system has been in operation for longer than was originally planned. A large quantity of useful data has been acquired and a framework by which the data can be processed and analysed has been set out in chapter 10 and appendix K.

Objectives (c) (and hence e) were not achieved in the project due to a line speed restriction at the Uffington test site during the time window in which it was possible to undertake the full scale slipstream measurements. A limited quantity of full scale slipstream data was available (Baker and Quinn, 2012) which has been considered in appendix D.

Objective (d) has been realised to some extent. There is not as yet a firm explanation as to why the pressure coefficients at full scale are higher than from the model scale predictions at given yaw angles, though it is believed that the model-scale data used to estimate yaw angle needs reconsideration. Different methods of analysing the full-scale data have yielded different results, and therefore further work is required in order to develop a robust analytical methodology for the full-scale train based data. It is believed that analysis of gusts is potentially the most logical approach, and that an overhaul of the current equipment and calibration of the pressure transducers is essential in obtaining a robust data set. An additional outcome is a large database of pressure transients that is potentially very useful when considering safely limits related to tunnels and passing trains (Johnson, 2011).

Objective (e) was therefore only partially realised given that objective (c) was not realised. The data from Baker and Quinn, (2012), highlighted differences between model-scale and full-scale though the full-scale ensemble sizes were small and only a single trackside measurement position was tested.

Objective (f) has not yet been achieved as this depends on a comprehensive synthesis of results. This study forms part of that procedure. Model scale slipstream tests have shown that changing the ballast height can affect the slipstream within the range of ballast heights permitted in the TSI. Further work is needed to investigate the significance of this finding with respect to different train geometries. The full-scale train based measurements of tunnel

transients could help form part of a database by which computational models could be validated for a range of tunnel geometries. The development of experimental and analytical procedures for moving model crosswind tests may help to allow this type of test to become a permitted methodology for crosswind assessment in CEN part 6 (2010).

J.3 Further information

The project description can be found via the EPRSC website (EPSRC, 2011) and the academic outputs are listed on the Research Councils UK website (Gateway to Research) (RCUK, 2016).

APPENDIX M

AUTHOR'S PUBLICATIONS

Two papers are presented in this appendix:

Quinn et al., (2016);

Soper et al., (2016).

The first paper sets out details about the full-scale crosswind measurements onboard the HST power car of the NMT. The second paper describes experimental work undertaken as part of this study in order to investigate the effect of ballast height on the slipstream of an HST, a Class 66 freight train and an ICE2. Full results for this paper are in appendix C.

[PAPERS ARE NOT PRESENTED IN THIS DIGITAL COPY]